UNIVERSITÄT DUISBURG ESSEN

Offen im Denken

TECHNICAL CHEMISTRY I
BARCIKOWSKI GROUP

Synthesis, surface chemistry, and application of fully inorganic gold nanoclusters by pulsed laser fragmentation in liquids

Dissertation

by

Anna Rosa Ziefuß

born in Mülheim an der Ruhr

for the degree of

Doctor of Natural Science

- Dr. rer. Nat. -

Faculty of Chemistry

University Duisburg-Essen

Germany

Essen, 2021

DOI: 10.17185/duepublico/76118
URN: urn:nbn:de:hbz:465-20220705-104240-5

This thesis has been experimentally conducted from November 2016 till October 2020 in the working group of Prof. Dr. Ing. Stephan Barcikowski at the Technical Chemistry I of the University of Duisburg-Essen.

Referees:

Prof. Dr. Ing. Stephan Barcikowski
University of Duisbug-Essen

Prof. Dr. Wolfgang J. Parak
University of Hamburg

Prof. Dr. Leonid V. Zhigilei
University of Virginia

Chairman:

Prof. Dr. Jochen Niemeyer
University of Duisburg-Essen

Date of Disputation: 07.02.2022

Abstract

In his 1857 lecture, Michael Faraday featured the fascination of the relations of gold with light. His passion is served to the full extent within this thesis as the interaction decisively determines the synthesis and characteristics of colloidal inorganic gold nanocluster. Gold nanoclusters with diameters < 2 nm are known for their fluorescent behavior with quantum yields several orders of magnitude higher than bulk gold, making them interesting candidates for e.g., optical sensing and applications in the field of catalysis. The origin of the fluorescence of noble metal nanoclusters is a controversial topic addressed in many studies but could not been clarified to date. The primary drawback is that current state-of-the-art chemical synthesis methods only give access to ligand-capped systems. Hence, core emission and ligand-to-metal-surface charge-transfer contributions cannot be differentiated. To solve this conundrum and to fundamentally understand the origin of the gold nanoclusters fluorescence, a new class of nanomaterials, fully inorganic ligand-free colloidal nanoclusters, is required.

In this thesis, the size-controlled generation of ligand-free gold nanoclusters with defined surface charge chemistry by a modern laser fragmentation in liquids technique is developed and optimized. This includes experimental series including advanced in-situ methods, linking physical and chemical process parameters to size distribution, yield, and surface chemistry of the fully inorganic gold nanoclusters, with interesting implications on surface oxidation and surface charge. Furthermore, it is discovered that inorganic gold nanoclusters possess pronounced photoluminescence affected by transition states from the core and inorganic surface states controlled by the ionic nano-environment. The study is complemented by experiments demonstrating the impact of core composition on photoluminescence by utilization of AuPt alloy series and scouting experiments on the impact of thiolated and non-thiolated surface ligands on photoluminescence. Finally, the applicability of the generated fully inorganic gold nanoclusters in oxidation catalysis is demonstrated in three independent model reactions.

Overall, fully inorganic ligand-free gold nanoclusters are exploited. The whole process chain from their optimized synthesis and in-depth characterization to applications in catalysis is demonstrated. The emphasis of this work is on their optical properties, which can help to shed light on the highly disputed origin of fluorescence in metal nanoclusters.

Table of content

1. Introduction

Over the last decades, researchers developed a strong interest in the material-dependent properties of nanoparticles (NPs).[1–3] Due to their chemical and physical stability[4,5], as well as their biocompatibility[1,6,7], Au NPs are suitable for a variety of biomedical[8–10] and chemical applications, such as catalysis[11,12]. Furthermore, Au NPs are known to possess a characteristic optical behavior, whereby the most prominent optical feature is the surface plasmon resonance (SPR).[13] However, as particle size decreases, a blue-shifted SPR can be observed.[13,14] Further decrease of the particle size leads to the quantization of electronic states and, thus, a discretization of the energy levels.[15,16] The optical properties of such ultra-small Au NPs or, more precisely, gold nanoclusters (Au NCs) are dominated by a bright fluorescence rather than an SPR and, due to their small size, can bridge the gap between molecules and nanoparticles.[16] This is particularly interesting for catalytic applications, which profit from the high mass-specific surface area and high defect densities, addressed later in more detail, and for biomedical applications as the cellular uptake is described as a function of the nanoparticle size.[17,18] Besides serving as an optical probe inside cells[19,20], Au NCs can penetrate the Blood-Brain Barrier[21] and are, thus, a promising tool for targeted drug transport, which in turn can support the therapeutic success against neurodegenerative diseases[17,22]. Following a recent press release, at least one Au NC-based drug (MTX102 by Midatech Pharma[23]) is in production as an immunotolerant vaccine in the treatment of Type I diabetes. In addition to biomedical applications, Au NCs are promising candidates to increase the efficiency of heterogeneous oxidation-based catalytic reactions. Here it is generally accepted that the adsorption of nanoparticular Au on oxide supports, such as TiO_2, offers active sites that are located at the interface between both.[24] Furthermore, reactions like CO oxidation[25] and selective ethanol oxidation[26] benefit from small particle size and high surface oxidation. However, ligated systems require a calcination step prior to the reaction, which activates the catalyst, but can also change surface chemistry and reduce the specific surface area.

Besides application-oriented research, the fluorescence of Au NCs at a size of ~2 nm has comprehensively and fundamentally been studied in literature[27–29]. However, the results concerning Stokes-shifts, lifetimes, and quantum yields remain surprisingly

diverse. Until now, no clearly discriminating research linking Au NC fluorescence to surface oxidation and charge transfer effects from organic ligands has been established. This is primarily attributed to the fact that during state-of-the-art synthesis of Au NCs, both ligand coverage and surface oxidation are altered simultaneously.[30] Hence, there are no existing reports in the literature that differentiate quantum confinement related to intrinsic size effects of the metallic cores and ligand-induced charge-transfer contributions. This is predominantly caused by the fact that gold clusters are mostly available as metal-organic compounds containing carbon atoms in much greater abundance than gold atoms.[30–33] For example, the Au_{25} 'gold standard' nanoclusters[34] are chemically $Au_{25}(SG)_{18}$ (SG = Glutathione) with only ~4% Au atoms in the cluster.

Additionally, this implies that the influence of the surface charge density in the absence of organic ligands on the optical properties could hardly be researched yet. However, following Scanlon et al.[35], adsorptively bound negative charges on the Au surface can influence the surface potential by pushing electronic density from the surface to the particle's interior. Please note that electronic processes are crucial in considerations of the fluorescence, and thus, changes in the latter are to be expected. Consequently, the primary objective is to fill this gap by employing a laser-based synthesis route to synthesize intrinsically pure and totally inorganic Au NCs. For the first time, this fundamentally elucidates how particle size, surface oxidation, and surface charge transfer by inorganic ions and organic ligands added post-synthesis individually alter photoluminescence in Au NCs. Therefore, this thesis develops a design of a model material suitable to bridge the gap between theoretical predictions and experimental verification.

To this end, the first part of this thesis' (sketched in Figure 1) is the development of an optimized synthesis route for totally inorganic Au NCs. Here, laser synthesis and processing of colloids (LSPC)[36], including pulsed laser ablation in liquids (LAL)[37] combined with subsequent pulsed laser fragmentation in liquids (LFL)[38], are used as key methods to generate inorganic colloidal Au NCs in an aqueous solution with tailored particle characteristics. Downsizing the particle size using a laser post-processing method requires an adequate and generalized process control strategy.[39–41] In addition, it necessitates a comprehensive insight into underlying fragmentation

and ripening mechanisms. Yet, in the case of fragmentation with high-intensity pulsed lasers, the individual mechanistic differentiation between effects from energy deposition kinetics (pulse duration) and driving force for fragmentation (laser intensity) is still challenging, demanding for further insides. Thereto, physical and chemical process parameters of the LFL process are systematically altered, and their effect on size distribution, yield of small particles, surface charge, and surface oxidation is documented. Concerning physical parameters, the initial absorption cross-section of the educt particles, ruled by their diameter and the laser intensity, are used as relevant variables. Chemical process parameters, mostly the composition of the fragmentation medium (e.g., micromolar saline additives), may also have a pronounced impact on the properties of the particles.

Here, the thesis will concentrate on the initial absorption cross-section of the educt nanoparticles produced through LAL and the laser intensity, which can be varied by the pulse energy, repetition rate of pulsed lasers, and pulse duration. Besides this, the colloidal environment presents an important aspect as it hinders particle growth to a certain extent.[37] This work concentrated on purely inorganic substances and, thus, evaluated the influence of the pH value, ionic strength, and addition of oxidizing agents like ozone. We will see that this large amount of experimental data allows mechanistic predictions, validated by experiments on ultra-short time scales. Therefore, in this thesis and in close cooperation with Plech et al. (KIT, Germany) and Glenzer et al. (SLAC, USA), two types of pump-probe experiments were performed. While optical pump-probe spectroscopy allows access to the heat transfer time between electrons and phonons (observable time window approx. 100 fs – 10 ps), in-situ synchrotron X-ray analysis provides structural information on the lattice heating (time window 80 ps – 10 µs) and in-situ size quenching by anions. Here, the extraction of important material parameters, like the electron-phonon coupling time of the educt Au NPs in different colloidal anionic environments or heat transfer dynamics to the environment, are required for density functional calculations on the LFL process in future studies, which will further lead to a deep fundamental understanding of the LFL process.

With respect to the second part of this thesis (see Figure 1), the former will grant access to Au NCs with tailored particle sizes, which are initially free of organic ligands. Size-controlled and purely inorganic Au NCs from LFL-based synthesis were consecutively

used to fundamentally study and mechanistically understand the optical properties of inorganic Au NCs. Thus, these particles offer the possibility to answer one of the most frequently asked questions in this research area: Is the fluorescence of Au NCs an intrinsic effect of the particles, or is it caused by a ligand-metal-charge transfer?[30,42–45] Since previous studies always required a ligand exchange[30], this question could not be answered satisfyingly yet. On the other hand, ligand-free colloidal nanoclusters offer the unique opportunity to study the direct interactions between the ligand and nanocluster surface via different anchor groups (covalently bound thiol vs. coordinatively bound amine). Here, cross-effects[30] caused by other organic molecules already attached to the surface can be avoided entirely, and the onset of ligand-induced photoluminescence can be directly observed.

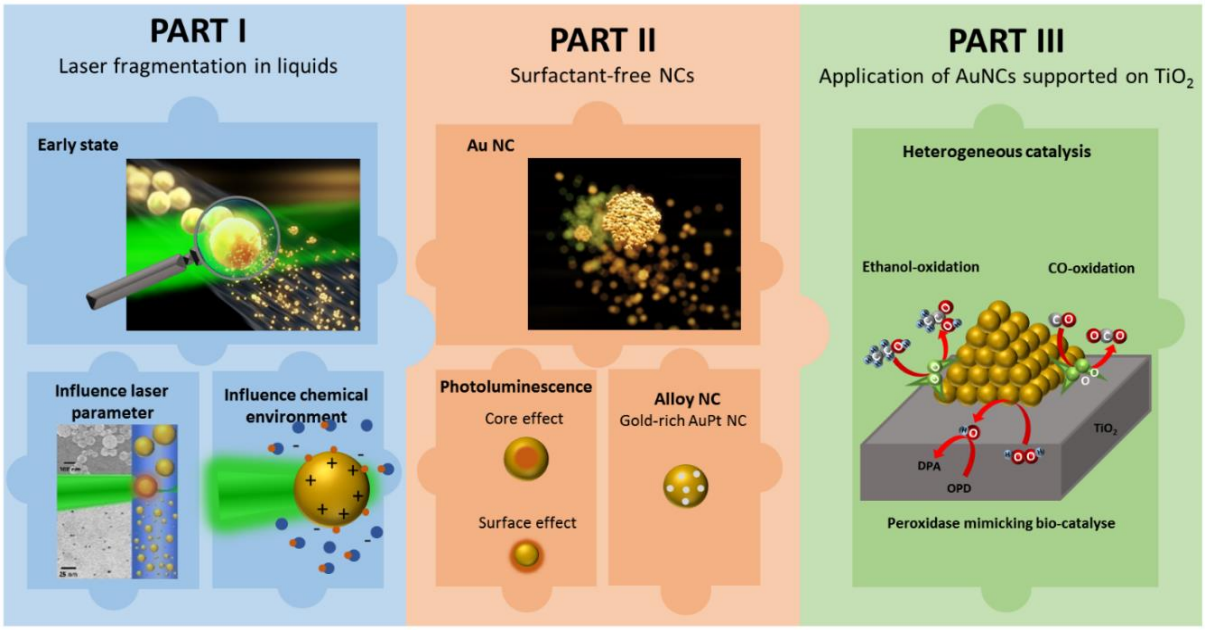

Figure 1: *Shematic illustration of the structure of this thesis. (Part I) Laser-based synthesis route towards fully inorganic gold nanolcusters including an early state analysis via in-situ spectroscopy followed by investigations on the influence of laser parameters and the colloidal nano-enviroment on the final particle properties. (Part II) Characterisation of Au, Pt, and Au rich AuPt alloy nanolcusters including fluorescence, crystal structure, surface charge density, and pump-probe experiments. (Part III) Investigations on the performance of fully inorganic colloidal gold nanoclusters in three heterogeneous oxdation catalysis reactions.*

Furthermore, due to their ligand-free nature, the fully inorganic Au NCs additionally offer the unique opportunity to study more subtle charge transfer effects by the environment on the photoluminescence, especially weak electrostatic interactions caused by ion adsorption or pH changes. These findings could be highly relevant as

the impact of ligands and biomolecules on initially ligand-free nanoclusters is important in case these entities are transferred to biofluids to be used in biomedical imaging applications. In addition to elemental Au NCs, the second part of this thesis provides an insight into the transferability of the laser-based synthesis route to bi-metallic nanoclusters. Here, different gold-rich AuPt alloys are used to study the impact of the chemical composition on the core properties.

To achieve this goal, a large collaboration network has been established, involving the Parak group, the Rübhausen group, the Bester group (all from the University of Hamburg, Germany), the Sures group (UDE, Germany), the Plech group (KIT, Germany) and the Amans group (University of Lyon, France). While the Bester group verified experimental data with density functional theory (DFT), most experimental data such as size, fluorescence (incl. lifetime), and crystal structure were collected in collaboration with the other groups.

An application perspective is provided in the last part of this work (see Figure 1) as these particles were tested in three heterogeneous oxidation catalysis reactions, in collaboration with the Parak (University Hamburg, Germany) and Muhler group (University Bochum, Germany). According to different studies on wet-chemically synthesized NCs, the catalytic activity increases with decreasing particle size and increasing surface oxidation, associated with the increased amount of active sites delivered by the high specific surface area. When wet chemically-synthesized particles are considered, the active sites are initially hidden by ligands, which must be removed by previous calcination steps.[46] The latter, however, results in significant changes in morphology, including particle growth and catalytic properties, and requires ultra-small surfactant-free particles with tunable charge density as model material.

Overall, excess to charge-tunable and size-selected inorganic, colloidal Au NCs will provide a promising tool relevant for fundamentals in photophysics, photochemistry biomedicine, and catalysis. Therefore, their synthesis and properties are systematically investigated in this thesis.

2. State-of-the-art

2.1 Laser excitation of particles in liquids

Excitation of colloidal nanoparticles with coherent light at high intensities allows the fabrication of advanced materials bearing unique properties applicable in a broad range of processes.[36,47,48] The interaction of coherent laser light with metal nanomaterials is dominated by the interactions between photons and electrons, as electrons absorb the energy in an initial step in case photons are neither scattered nor transmitted.[49–51] The resulting hot electron population is balanced by electron-electron scattering within the first ~100 fs, followed by an energy transfer to the lattice via electron-phonon coupling.[52–55] Heating of the material is thus a secondary effect that results from the subsequent interaction of the excited electrons with the lattice. If the lattice temperature reaches the melting point, the irradiated material can be deformed[56,57] (Scheme 1). The irradiation of nanorods, for instance, with low laser intensities results in a change of shape,[58–60] whereas irradiation of aggregates leads to sub-micrometer spheres.[61] Moreover, the irradiation of nearly spherical nanoparticles yields a reshaping of the NPs from an initial faceted shape into an ideal spherical geometry without any observable changes in particle size.[62] If the laser power is further increased, melting is followed by fragmentation of the particles.[63–65] Laser fragmentation in liquids (LFL), i.e., the post-irradiation of nanoparticles with high-intensity lasers, is a complex process that is influenced by the pulse duration.[39,52] LFL can be described as a multi-dimensional problem, influenced by the type of educt (shape, size, etc..)[38,63], laser power[38,63,65–67], pulse duration[49] and surrounding colloidal environment[68]. As it is the key method in this work to synthesize surfactant-free fluorescent gold nanoclusters (Au NCs), the LFL process under variation of the parameters mentioned above will be discussed.

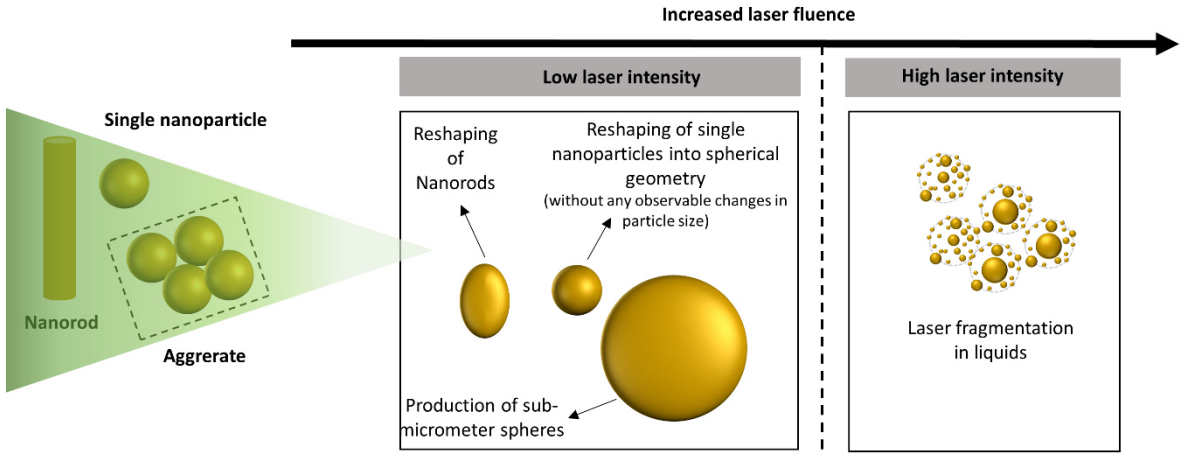

Scheme 2: *Differentiation of processes triggered by laser irradiation of gold nanoparticles, depending on the laser fluence.*

2.2 Fundamentals of laser fragmentation in liquids

To be able to understand and control the laser-induced fragmentation of Au NPs, a review of the previously postulated mechanisms is indispensable. Even though many researchers have explored the mechanism of LFL[38,49,67,68], it is not yet fully understood. Besides an electronically-induced Coulomb explosion (CE)[65,69–71], scientists suggest heating-melting-evaporation (HME)[40,41,57] and other exotic processes[58,72,73] as the underlying mechanism. The following section will introduce several influencing factors that determine the mechanistic path, like laser parameters, the properties of the irradiated colloid, and its chemical environment. To be able to control the LFL and to extract parameters that are important to produce ultra-small particles, those parameters will be discussed step-by-step in the subsequent section.

2.2.1 Differentiation of mechanistic processes during laser fragmentation in liquids depending on laser parameters

The most significant difference becomes visible when considering thermal processes on ultra-short time scales. If the electronic temperature (T_e) is high, an electronically-induced LFL mechanism can be expected[38,65,70], whereas the process at high lattice temperatures (T_l) is more thermally-induced.[49,62,74,75] Therefore, a rough mechanistically differentiation during LFL can be done by using the laser fluence (F) and the pulse duration (τ) (Scheme 2). When the whole energy is transferred before electron-phonon coupling occurs ($\tau_p > \tau_{e\text{-}ph}$), the electrons can heat up strongly and be

partially emitted, generating multiple ionized NPs.[38,70] Zhigilei et al.[76] reported a change in the electronic density when the electronic temperature reached 3000 K. This point is defined as coulomb-instable (CI) as the particles' integrity starts to decline. However, electronically-induced spontaneous fission, the so-called Coulomb explosion (CE), is anticipated for much higher temperatures (> ~ 7000 K[65] – 8150 K[38]) and, following the liquid drop model[38], requires that the coulomb forces exceed the cohesive forces. In this case, the thermal energy stored by the electrons exceeds the difference between the work function of the electrons and the Fermi level, whereby some electrons leave the metal NPs and are solvated in the medium. Then, multiple charged NPs that remain will spontaneously undergo fission if the above-mentioned force balance requirements are met.

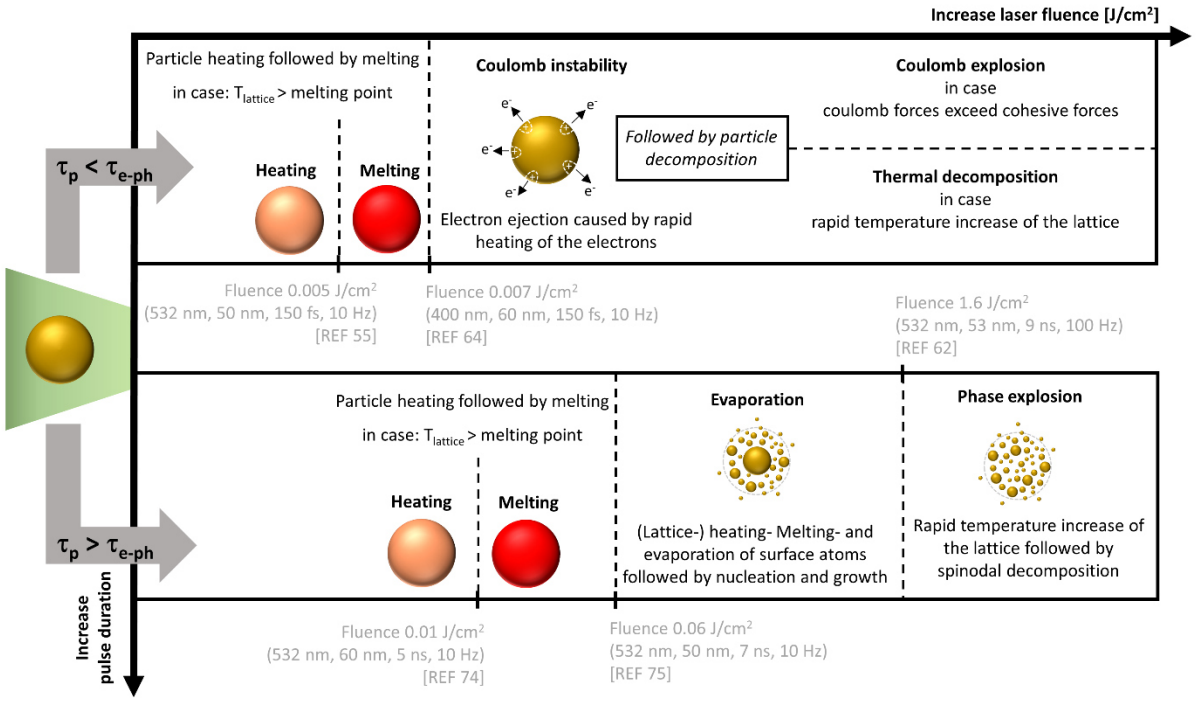

Scheme 3: *Graphical illustration of possible laser fragmentation mechanism depending on the laser fluence and the pulse duration.*

However, experimental proof of this is still needed. In 2006, Marfune et al.[70] monitored the existence of produced solvated electrons by the laser irradiation of Au NPs at 335 nm and found an optical signal that fits in the spectral position and band shape of the 1s→2p transition of solvated electrons. Five years later, Hashimoto et al.[65] were able to identify positively charged gold ions by mass spectrometry after fs-laser excitation at 532 nm and concluded that spontaneous fission of 50 nm Au NPs is

possible for laser fluence above 6 – 7.4 mJ/cm^2 (150 fs, 532 nm, 10 Hz), which is in good agreement with Ref.[77]. However, as stated, further experimental studies are limited, and the occurrence of this mechanism is still under debate.[38,78,79] Specifically, the major uncertainty is if the absorbed laser energy can force enough electrons to leave the particle to initiate CE. For proof, scientists refer to the classical liquid drop model that was initially used to calculate the fission probability into fragments in nuclei[80], which can be compared to nanoparticles[81], although they present a surface-charged system rather than a uniformly charged system.[82] Following the liquid drop model, the degree of instability (fissility factor, X) correlates with the charge state (q) of the particle in relation to the total number of atoms (n):

$$X = 0.9\frac{q^2}{n} \qquad (1)$$

Particle fission is to be expected when $X > 1$. For smaller fissility factors ($0.3 < X < 1$), electronically-induced fission is accompanied by thermal evaporation followed by only evaporation when $X < 0.3$.[83] If not enough electrons are ejected, a thermally-based mechanism is conceivable. Note that spontaneous fission is to be expected for $T_{electrons} > 7000$ K. For lower temperatures, an ejection of electrons will be observed; however, the resulting surface charge will not be large enough for particle fission. In this case, the energy will be transferred to the lattice in a second step, which will lead to a rapid increase in the lattice temperature. The particle will start to melt, followed by evaporation if the particle's temperature exceeds the boiling temperature. Itina et al.[78] described this process theoretically and used the two-temperature model (TTM) to calculate the temperatures of the electrons and of the lattice in two coupled diffusion equations for different particles sizes. Of pertinent mention, the total amount of absorbed energy is a function of size and can be expressed by the absorption cross-section that can be calculated according to the Mie-Theory. Itina et al.[38] found that electrostatic explosion is anticipated for particles < 60 nm. On the other hand, larger particles are expected to undergo thermal fragmentation if a size-dependent threshold fluence exceeds the threshold fluence to reach CE in the same range as the threshold fluence to reach the boiling temperature (Fig. 3).[78] However, a superposition of both mechanisms cannot be excluded.

So far, we have only considered the case for when the laser's energy is transferred to the particle before energy coupling between electrons and the lattice takes place. In case the fragmentation of Au NPs is performed with an ns-laser, the pulse duration is about three orders of magnitude longer than $\tau_{e\text{-}ph}$ of Au NPs. The lattice heats up while further energy is still transferred to the electrons. Hence, the energy absorption processes by the electrons and energy transfer to the lattice are no longer temporarily separated. An electronically-induced LFL mechanism becomes even more unlikely if the increased lattice temperature favors a thermally-based HME mechanism.[40,41,57,79] When the lattice and electrons reach thermal equilibrium, and the absolute lattice temperature exceeds the boiling point, evaporation of the molten particle is likely to occur. Pyatenko et al.[77] found complete evaporation of 68.7 ± 6.3-nm Au NPs after irradiation with a 532 nm Nd:YAG laser with 0.1 J/pulse.

The initial laser intensity must be high enough to allow enough time for boiling before energy is transferred to the medium, increasing the chance for another mechanism already known from laser ablation, i.e., the phase explosion (PE), more likely to occur.[63] According Miotello and Kelly, PE is likely to occur after the lattice temperature reaches the spinodal temperature and results in a homogeneous nucleation of vaporous material throughout the molten ablation zone. This is followed by ejection and spillage and then the formation of bimodal size distribution.[77,84,85] In other words, the material is spontaneously overheated and undergoes explosive boiling once the lattice temperature exceeds the spinodal temperature (80%[85] of the critical temperature).[86]
The occurrence of a phase explosion during LFL is a basic hypothesis in the present thesis and is described in greater detail in Chapter 3.2.1.

Note that the specification of the laser fluence or laser intensity always depends on the initial particle size and laser wavelength since the absorption cross-section and, therefore, the effective energy can be influenced by varying those parameters.[87] Assuming a fixed laser wavelength, a bathtub-like dependence of the threshold fluence for thermal-based LFL on the initial particle diameter can be observed.[66] The lowest threshold fluence was theoretically found for 60 nm Au NPs. Note that heat loss and heat transfer scale with $\sim R^2$ while the absorption-cross section scales with R^3. Therefore, a decrease in particle size is accombined by more heat loss with respect to

absorption, which results in a higher laser fluence threshold for thermally based LFL. For larger particles, the required threshold fluence increases as well, which is based on non-linear effects caused by the size-dependent absorption cross-section.[66]

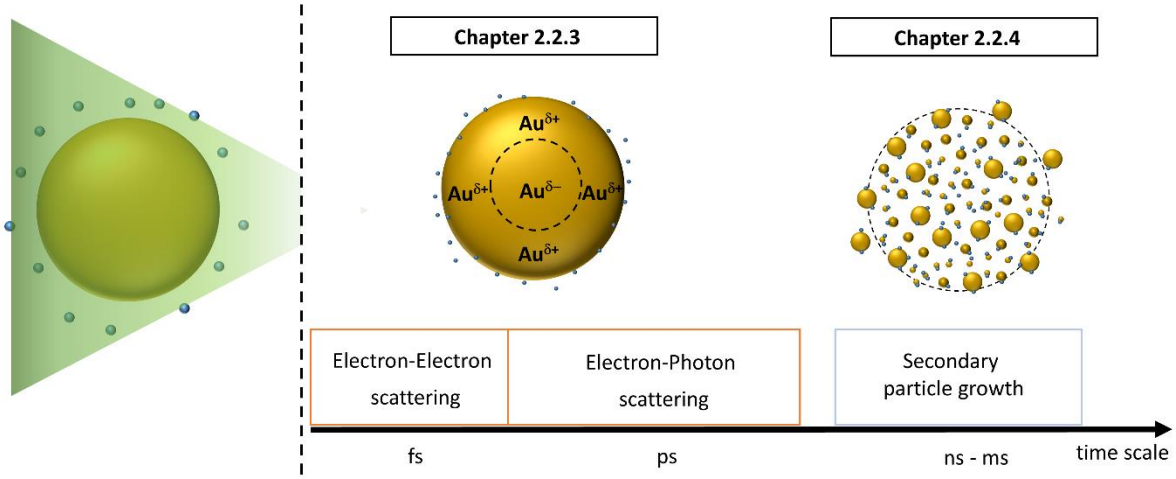

Scheme 3: *Illustration of the influence of the colloidal environment in LFL dependend on the delay time regime.*

Although individual factors that define the quality of the LFL are conceptually known, practical implementation is often hampered by experimental conditions. On the one hand, the laser intensity in a colloid is subject to an axial attenuation due to absorption at the front side, leading to a mixture of different mechanisms in the irradiated colloid volume.[88,89] If fragmentation occurs, e.g., thermally, particles in the front irradiation area can be completely fragmented, while those located further at the backside can only be partially fragmented. On the other hand, besides laser parameters, the colloidal environment represents an important parameter in the LFL process (Scheme 3). While both factors have not been discussed, the following sections will depict why they should not be neglected.

2.2.2 Laser fragmentation in a liquid jet

As mentioned, a mechanistic differentiation during LFL requires homogeneous irradiation of the colloid. Most references describe LFL in a batch system.[39,85,90] The resulting particle size distribution depends critically on laser parameters, the colloidal environment, stirring speed, irradiation time, and absorbance cross-section. Although the colloidal solution is stirred, the resulting particle size distributions are often broad and include fragmented particles together with unfragmented particles. Here, a

mechanical differentiation is hampered by energy gradients and temporal educt particle concentration changes within the batch system. Wagener et al.[91] developed a novel approach based on a liquid jet system that can be considered a continuous flow technique to overcome these limitations. Here, the liquid is pumped through a nozzle generating a thin circular liquid filament (d < 1 mm), adjusted perpendicular to the laser beam. Here, axial dispersions are minimized, allowing control of the product particle properties as well as a more accurate calculation of the mass-specific energy input during LFL.[92] Since then, the liquid jet has been further modified. The basis for this was certainly given by a publication by Waag et al.[93], which presented a detailed raytracing. They calculated the laser energy density distribution within the above-mentioned circular liquid jet. They found that 13.8% of the liquid jet are not sufficiently irradiated by the laser pulses, explainable by refractions at the air-liquid interface. In addition, they found an energy distribution in the remaining areas so that particle melting phenomena next to fragmentation cannot be ruled out. Siebeneicher et al.[94] follow up on this research and present an elliptical jet by which the energy distribution in the liquid becomes more homogeneous. Thereby, there were able to reduce the unirradiated areas to 0.9%, followed by a more homogeneous energy distribution notable by a peak fluence decrease of up to 71% enabling a more precise process control. So far, the development of the liquid jet has not been completed. Zerebecki et al.[95] recently developed a flat jet with a thickness of 130 ± 10 µm in which only a defined area is irradiated. Outer areas show a variation of the thickness and are therefore excluded by using mechanical slits cutting the non-irradiated volume fraction. Please note that the excluded fraction can be recycled, allowing re-use of the nonirradiated colloid. Here, refraction and self-focusing at the air/liquid interface can be avoided, resulting in a significant reduction of laser intensity deviation from 83% (cylindrical jet, ideal top hat) to 20% (flat jet, ideal top hat) and thereby a more homogeneous product particle size distribution, allowing even more precise mechanistic study of the LFL process in future studies.[96]

2.2.3 Influence of surface chemistry on the electron-phonon coupling time

Following recent literature, the colloidal environment can influence physical processes during LFL already on the early time scale, as surface adsorbates possibly affect the coupling time between electrons and phonons during the laser-induced metal heating

process and, with this, the lifetime of excited electrons. As the latter somehow allows a mechanistical differentiation during LFL (as discussed in the previous chapter), knowledge about the influence strength is required to precisely control the LFL process. Electron energy dynamics in metal systems can be resolved using ultrafast optical pump-probe spectroscopy, a method that concerns the measurement of transient changes of the transmission signal that are induced by fs-laser excitation.[97] However, the results found in literature[98–101] are manifold and controversial, which can be explained particularly by the different electronically-induced temperature changes and different particle sizes, but also by the diversity of the surface adsorbates. So far, most studies have concentrated on changes in the maximum electronic temperature after laser excitation and have reported longer $\tau_{e\text{-}ph}$ when the induced temperature change is high.[99] This phenomenon can be explained by the heat capacity, which increases with temperature, leading to a longer electron-phonon coupling time scale at higher laser excitation energy density. Note that the electron heat capacity is certainly not negligible if the evolution of Te is considered, and it exhibits linear temperature dependence in any excitation regime. The temperature change induced in the particles depends on the laser intensity (I_0) and significantly on the effective absorption cross-section ($eff_{abs}^{\lambda}(d_p)$), which in turn is a function of particle size (d_p) and laser wavelength (λ).[77] With increasing particle size, an increase of the absorption cross-section is to be expected, leading to an increased temperature change of the electrons after laser excitation with constant I_0 and λ:

$$\Delta T_{max} = \frac{3}{2} \cdot \frac{I_0}{g} \cdot \frac{eff_{abs}^{\lambda}(d_p)}{d_p} \qquad (2)$$

Although some experimental studies have verified the influence of the colloidal environment and, thus, surface adsorbates on $\tau_{e\text{-}ph}$, this has been neglected in theoretical descriptions on this topic. Moreover, there is no reference for such effects on fully inorganic gold particles.

For instance, Aruda et al.[100] demonstrated that surface adsorbates can accelerate $\tau_{e\text{-}ph}$ by a local screening of coulombic electron interactions explainable by the occurrence of additional decay channels for hot electrons. The lifetime of hot electrons (T_{max} > 2000 K) after laser excitation in thiolated Au NPs was 20% longer than in aminated NPs. Westcott at al.[98] determined the influence of different aminated ligands and found

that the ability to alter $\tau_{e\text{-}ph}$ critically depends on the possibility to induce a dipole moment near the metal NP surface, concluding that the ligand-induced effect is primarily of electronic nature. However, in both studies, the influences of aminated or thiolated organic ligands were investigated as surface adsorbates, which are known to interact with the surface in ligand-metal charge transfer (LMCT) processes resulting in a damping of the plasmon resonance of Au NPs and an altered absorption cross-section. Additionally, because thiolated ligands possess a different electronic heat capacity than aminated ligands, a superimposition of different influence factors on $\tau_{e\text{-}ph}$ makes it difficult to differentiate between them.

In contrast to organic ligands as surface adsorbates, damping of plasmon resonance has yet not been investigated for the adsorption of inorganic ligands. Following Scanlon et al., adsorption of anions at the metal NP surface will produce a shift in the electron density to the interior, causing the particles' surface to become slightly positive (Scheme 4). This should lead to a reduced screening of the core potential and should be observable in an accelerated electron-lattice coupling. Since no proof of these two hypotheses, the role of the amount and type of anions on pulsed laser excitation of colloid can be found in the literature; corresponding experiments were conducted in this work (Chapter 3.2.4).

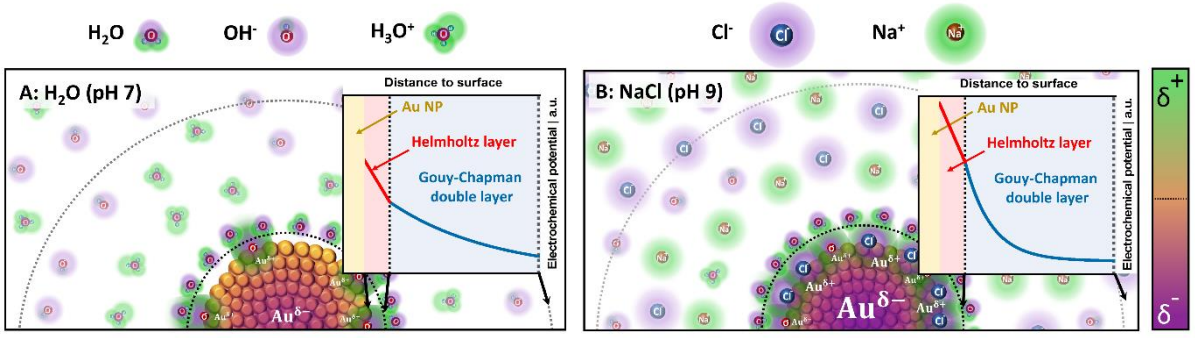

Scheme 4: *Illustration of electronic processes within Au NPs after adsorption of anions on the surface. A) H2O at pH 7, B) NaCl at pH 9*

2.2.4 Influence of surface chemistry on the stability of particles produced by laser fragmentation in liquids

Besides electronic processes on ultra-short time scales, the colloidal environment plays an important role on longer time scales (>>ns). Since ultra-small Au NPs are subject to secondary particle growth due to their high specific surface, the study of such particles must extend beyond physical parameters.[70,102] Mafune et al.[70] observed particle growth after LFL on the ns time scale, then Jendrzej et al.[102] published that such growth processes can last on a time scale of days. Since secondary particle growth processes result in a reduction of the specific surface area (A_{NP}) and, thus, decreased free enthalpy (G) of the system, these processes are thermodynamically favored and must be inhibited for the successful synthesis of ultra-small particles. *In-situ* stabilization of nanoparticles can generally be achieved through one of the following approaches (Scheme 5): i) high dilution of the colloidal solution to increase the interparticle distance (and thereby collision rate), ii) addition of electrochemical stabilizers to force particle repulsion based on charge effects, or iii) addition of steric stabilizers to force the particles to have a certain interparticle distance.[103,104]

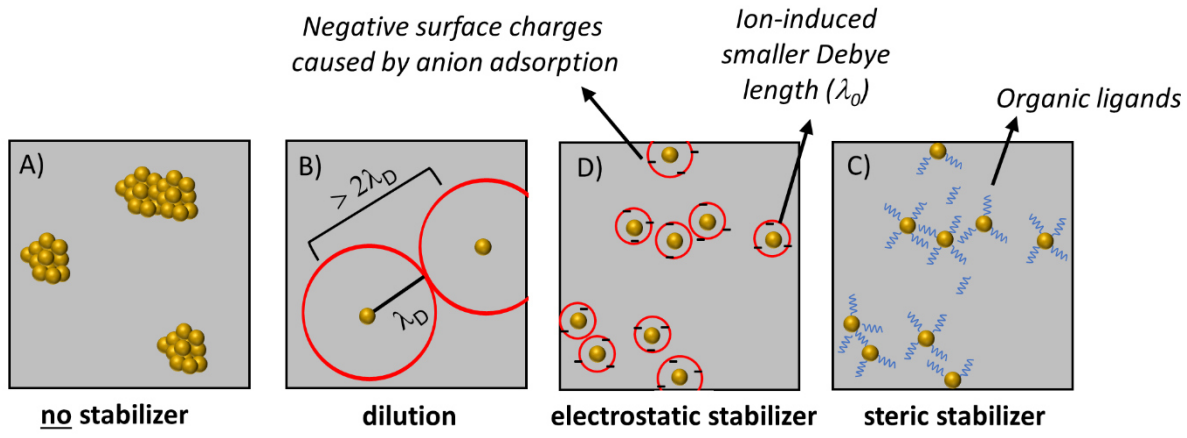

***Scheme 5**: Graphical illustration of (A) undesirable particle aggregates after LFL, (B) dilution strategy, (C) ion-induced electrostatic stabilization, and (D) ligand-induced steric stabilization.*

The first approach, dilution, aims to increase the interparticle distance and hence reduce the collision probability for the particles, slowing down the kinetics of secondary particle growth. The laser-based synthesis of the initial particles used for LFL includes

the formation[105,106] of O_2, H_2, and H_2O_2, which leads to partial oxidation of the particle surface. According to an XPS study, Au^+/Au^{3+} was determined to be 3.3 – 6.6%.[107] In an aqueous environment, a pH-dependent equilibrium of Au-OH/Au-O^- is formed on the surface so that even without further stabilizing agents, electrostatic repulsion can be achieved.[37,108,109] According to the DLVO theory[110,111], the repulsive forces scale with the distance between particles. If the particles come too close to each other, attracting forces predominate, which results in aggregation. The distance needed for electrostatic stabilization is dependent on the debye length (λ_D),[112,113] where instabilities are to be expected for a distance less than 2 λ_D. Dilution of the colloid enables the particles to maintain a certain statistical distance that does not lead to the overlapping of the charge clouds so that stability is guaranteed with sufficient dilution. Based on this approach, the achievable concentration is naturally low, and electrostatic stabilization is often the better choice (Scheme 5C). By adding anions, the ionic strength (IS) of the system is increased. On the one hand, a base can be added to shift the pH-dependent equilibrium of Au-OH/Au-O^- to the deprotonated form. On the other hand, anions can adsorb on the particle surface, which leads to an increased surface charge density and thus increased stabilization by charge repulsion if the ionic strength is sufficiently low to avoid charge screening by counter ions.[37,108] Last but not least, the addition of organic molecules can help to prevent particle growth (Scheme 5D). In steric stabilization, the colloid is mixed with a ligand (polymer, biomolecule, ...) that has a certain affinity to the particle surface. The ligand acts as a protective shell (Born repulsion) and prevents two particles from getting too close. If ligands of neighboring particles cross, there is a decrease in particle mobility, which is thermodynamically unfavorable since this would reduce the entropy of the system.[103,104] Although all three stabilization methods can be used during LFL, the use of organic ligands is usually avoided as they can be degraded in case they are near the metal surface.[114] The formation of toxic by-products also cannot be ruled out[115], so in-situ stabilization using anionic species or dilution is to be favored. Also, ligand-free NPs are an ideal model material. The advantage of premature dilution is that present particles can be irradiated more homogeneously since shielding effects are reduced.[88]

However, the choice of one of these stabilization methods depends strongly on the subsequent application. For basic research, the dilution and electrosteric stabilization approach is often used, as it does not require any further chemicals and allows more

homogeneous irradiation of the whole colloidal volume[88]. For example, Lau et al.[68] used electrostatic stabilization and added H_2O_2 in the basic regime prior to LFL of Au NPs in order to oxidize the particle surface, increase the surface charge density, and increase the amount of ultra-small particles for heterogeneous catalytic applications after absorbing those particles on graphene nano sheets.

2.3 Size effect on optical properties of gold nanoparticles and gold nanoclusters

The optical properties of Au NCs are clearly distinguishable from those of larger Au NPs, allowing evaluation of the LFL process' success. While the properties of metallic bulk material are determined by the metal bands that form due to a periodic linear combination of molecule orbitals, the properties of nanomaterials can be differentiated and show a size-dependent optical behavior.[13,116,117] Coinage metall NPs with sizes smaller than the incident photon wavelength display a so-called surface plasmon resonance (SPR). The incident electric field is able to penetrate those particles, leading to the polarization of conduction band electrons and causing an oscillation displacement of the electron gas around positively charged ions.[13,118] The excitation of SPR is frequency-specific, and the resonant wavelength depends strongly on particle size, shape, and interparticle distance, which gives Au NPs their characteristic reddish color rather than the typical golden color of bulk gold.[13,118–120] A further reduction of particle size leads to a loss of electron mobility and makes the harmonic oscillation of the metal conducting electrons impossible, leading to discrete energy states.[121,122] Following Zhou et al.,[122] this transition between metallic and non-metallic properties can be found for particles smaller than 1.7 nm, while particles between 1.7 nm and 2.3 nm can be either metallic or non-metallic. Whereas metallic nanoparticles are known for their surface plasmon resonance, non-metallic nanoclusters lack this feature and instead exhibit a pronounced photoluminescence behavior.[28,123–125]

The origin of the observable emission behavior that can be found for non-metallic Au NCs is yet not fully understood.[126] Caused by their molecular-like behavior, an intrinsic core effect as a responsible factor must be considered. The optical properties are dependent on the number of free electrons, which can be illustrated by the particle-in-a-box model.[127,128] Following this model, the length of a potential box (in this case, the

size of the nanocluster) behaves anti-proportional to the energy of the quantized states. Consequently, with decreasing particle size, the strength of the quantization increases, influencing the intraband transitions, which are observable by an increasing gap between the highest occupied and lowest unoccupied molecular orbital.[128] The confinement to particles smaller than the Fermi wavelength of an electron (~0.7 nm) can be described by the spherical jellium model, which also considers the electronic dynamic of metallic NCs.[129] This model explains the scaling of transition energies of spherical metal NCs as a function of their atomic number (N): (h = Planck's constant, ω_0 = transition frequency, E_F = Fermi energy):[130]

$$h\omega_0 = E_F \cdot N^{-\frac{1}{3}} \qquad (3)$$

The prerequisites for the applicability of this model include: i) the presence of a delocalized valence electron, ii) the core potential equal to the potential of the delocalized electrons (s-orbital character), and iii) the delocalized electrons surrounding the metal atoms in a shell-like manner, which are subject to the rules of Pauli's exclusion principle. Although this model was initially invented for the gas-phase synthesis of Na NCs[129], their validity in liquid NCs could be proven using PAMAM dendrimer encapsulated Au NCs with N < 40 atoms.[128,131] Following Equation 3, different coinage metal NCs should display comparable emission behavior. However, recent experiments show contradictory results. For instance, Zheng et al.[131] found that dendrimer-encapsulated Au_8 NCs give an emission around 455 nm, while the working group of Pradeep et al.[126] found mercaptosuccinic acid capped Ag_8 NCs emit at 650 nm. Although the jellium model can be used to explain relative particle size effects for ultra-small NCs, it completely ignores the lattice structure[132–135], oxidation state[136–139], and electronic contribution of surface-bound ligands[30,140–144], which will be discussed in the following section.

2.3.1 Influence of lattice structure and NC oxidation state

Besides the size effects on the emission of NCs, a variety of size-independent emission phenomena have been reported. Zhou et al.[137] synthesized 2 nm Au NCs with a 40-50% oxidized surface, which showed a pronounced fluorescence around 550 nm. While the particle size did not change, the addition of the strong reducing agent $NaBH_4$ caused a reduction of Au(I) accompanied by an off-switched fluorescence. This

suggests that the particle surface largely contributes to the fluorescence. Further experiments conducted by Quin et al.[145] and Tian et al.[146] lend contrasting results. Specifically, Quin et al.[145] reported the fluorescence of $Au_{38}(PET)_{24}$ (PET = SCH_2CH_2Ph) NCs, which were also obtained by Tian et al. ten years later.[146] However, Tian found a different emission behavior of these NCs that was contributed to structural isomerism. As the structure of Tian's NCs is thermodynamically less stable, the thermal treatment allowed the transformation, which then displayed the same optical behavior as the particles produced by Quin et al.. While changing the structure of the particle core without changing the surface structure is nearly impossible[147], scientists have succeeded in changing the structure of the particle surface and retaining the core structure.[148,149] Yet, structural surface transformation requires a ligand exchange, making it difficult to differentiate between charging and structural influence factors. Further discussion will consider that organic ligands can change the electronic structure of the surface so that in such cases, it is difficult to distinguish between structure-induced effects and ligand effects, demanding organic ligand-free Au NCs as reference material.

2.3.2 Influence of organic ligands

Almost all observations and results concerning the fluorescence of nanoclusters were gathered for gold nanoclusters in combination with stabilizing organic ligands. The carbon content in such ligand-capped Au NCs often exceeds the Au content (e.g., for $Au_{25}(SG)_{18}$ with SG = Glutathione, the ratio is 1:7)[34], and thus, ligand-to-metal charge transfer (LMCT) processes cannot be excluded as the primary reason for the fluorescence.[30,140–144] Yet, the following two influencing factors for surface ligands on the emission behavior of Au NCs are widely accepted in the literature:

- **Influence of the ligand anchor group** (which points towards the particle surface)[30,131,150]: The anchor group (e.g., Au-S) can interact with the particle surface via direct LMCT processes. The strength of this charge transfer depends critically on the donor ability of the anchor group.
- **Influence of the head group** (which points towards the solution)[30,131,150]: The head group may provide a functional group or electron-rich atoms within the ligand that contribute to the charge density via the donation of delocalized electrons

In both cases, a drastic increase of the fluorescence quantum yield (QY) can be observed[30], which is attributed to a shifted electron density from the surface to the core. This further results in an increased probability of photon emission by reducing the number of non-radiative transitions[30,147,150,151]. Deng et al.[151] found an increase of the QY by 63.2% for 6-aza-2-thiothymine (ATT)-stabilized Au NCs after adding L-arginine to the ligand-shell. The author reported that the strong interaction between L-arginine and ATT strengthened the interactions between the ligand shell and particles' surface. Further, Jin et al.[30] discovered that QY decreases as the distance between the head group and particle surface increases and, thus, the interactions weaken. While the investigation of fully inorganic nanoclusters could help to understand the influence of ligands, structural changes, and charging effects on the fluorescence, the synthesis of NCs is hampered by their expected poor stability due to the very high surface energy. Pérez-Prieto et al.[152] produced fully inorganic nanoclusters (mean diameter > 1.9 nm) by chemical reduction of a gold precursor without needing organic ligands and found no fluorescence. However, adding 11-mercaptoundecanoic acid (MUA) forced a pronounced fluorescence at 540 nm ($\lambda_{excitation}$ = 254 nm), which subsequently resulted in a particle size change (mean diameter 1.35 nm) that the authors ascribe to a pronounced etching. Due to the reduced particle size, a stronger degree of energy level discretization is expected, so that the observed emission in the presence of MUA could be the overlay between LMCT and core emissions stimulated by the reduced size and the more pronounced energy state quantization, which is a function of particle size. But here, two things are changed simultaneously, the size and the presence/absence of ligands. Hence, further studies on this system based on fully inorganic NCs at different sizes would be required.

2.4 Gold nanoclusters as heterogeneous catalyst in selective oxidation reactions

While the bulk gold surface is considered to be catalytically inactive, there is a dramatic increase in catalytic activity when gold is present in NP form.[153] Au NPs exhibit high catalytic activity in various heterogeneous catalytic reactions, where the reactant phase (gas or liquid) differs from the catalyst phase (solid).[154–156] In contrast to homogeneous catalysts, only Au NPs surface atoms participate in the corresponding reaction.

However, the ratio of NPs core to surface atoms may change drastically with further decreasing particle size, and more metal atoms participate in the catalytic reaction.

In addition to their small size and thus increased specific surface area, Au NCs have further unique properties that influence their catalytic behavior dramatically, such as:

- **Lattice structure:** The arrangement of metal atoms in NCs can be completely different from the arrangement in NPs, which possibly alters the reactive sites of the catalysts.[157]
- **Electronic structure**: Quantization leads to a discretization of energy levels, which affords the opportunity of electron transfer between the reactant and quantized electronic orbitals of the metal NCs.[158]
- **Dynamic factors**: Both the above-mentioned criteria can significantly change during catalytic reactions due to exothermicity associated with the adsorption of reactants and chemical reactions.[149,159] Dynamic factors are, thus, primarily attributed to conditions during the reaction (temperature, pressure,…) as they can alter the lattice structure and particle size.

However, the exact influence of these factors on individual reactions cannot be predicted with the current state of research. Here, Zhang et al. compared the CO oxidation, catalyzed by gold nanoparticles supported on TiOs, of laser-generated surfactant-free NPs with wet-chemically produced ligand-protected systems. They found an increased onset temperature for the CO conversion in counter ward of the ligand-protected system and referred this to a preferential depletion of active sites accompanied by a decreased interaction with the oxide support.[160] Please note that the catalysts undergo a calcination step prior to their use, which leads to their activation. However, as shown by Kuhn et al. [161], high-temperature calcination can lead to catalysts poisoning caused by surfactant degradation during this process.

Since the rational design of surface charge-controlled, ligand-free NCs (at constant size) is far from being easily available, most studies are still conducted on a trial-and-error basis.

.

2.5 References

(1) Elahi, N.; Kamali, M.; Baghersad, M. H. Recent biomedical applications of gold nanoparticles: A review. Talanta **2018**, 184, 537–556. DOI: 10.1016/j.talanta.2018.02.088.

(2) Palpant, B.; Prével, B.; Lermé, J.; Cottancin, E.; Pellarin, M.; Treilleux, M.; Perez, A.; Vialle, J. L.; Broyer, M. Optical properties of gold clusters in the size range 2–4 nm. Phys. Rev. B **1998**, 57 (3), 1963–1970. DOI: 10.1103/PhysRevB.57.1963.

(3) Zhang, Y.-x.; Wang, Y.-h. Nonlinear optical properties of metal nanoparticles: a review. RSC Adv. **2017**, 7 (71), 45129–45144. DOI: 10.1039/C7RA07551K.

(4) Zhou, J.; Ralston, J.; Sedev, R.; Beattie, D. A. Functionalized gold nanoparticles: synthesis, structure and colloid stability. Journal of colloid and interface science **2009**, 331 (2), 251–262. DOI: 10.1016/j.jcis.2008.12.002.

(5) Veith, G. M.; Lupini, A. R.; Rashkeev, S.; Pennycook, S. J.; Mullins, D. R.; Schwartz, V.; Bridges, C. A.; Dudney, N. J. Thermal stability and catalytic activity of gold nanoparticles supported on silica. Journal of Catalysis **2009**, 262 (1), 92–101. DOI: 10.1016/j.jcat.2008.12.005.

(6) Tshikhudo, T. R.; Wang, Z.; Brust, M. Biocompatible gold nanoparticles. Materials Science and Technology **2004**, 20 (8), 980–984. DOI: 10.1179/026708304225019849.

(7) Kang, M. S.; Lee, S. Y.; Kim, K. S.; Han, D.-W. State of the Art Biocompatible Gold Nanoparticles for Cancer Theragnosis. Pharmaceutics **2020**, 12 (8). DOI: 10.3390/pharmaceutics12080701.

(8) Bansal, S. A.; Kumar, V.; Karimi, J.; Singh, A. P.; Kumar, S. Role of gold nanoparticles in advanced biomedical applications. Nanoscale Adv. **2020**, 2 (9), 3764–3787. DOI: 10.1039/D0NA00472C.

(9) Kalimuthu, K.; Cha, B. S.; Kim, S.; Park, K. S. Eco-friendly synthesis and biomedical applications of gold nanoparticles: A review. Microchemical Journal **2020**, 152, 104296. DOI: 10.1016/j.microc.2019.104296.

(10) Kundu, S.; Ghosh, B.; Nandi, S.; Ghosh, M.; Pyne, A.; Chatterjee, J.; Sarkar, N. Surface Ligand-Controlled Wavelength-Tunable Luminescence of Gold Nanoclusters: Cellular Imaging and Smart Fluorescent Probes for Amyloid Detection. ACS Appl. Bio Mater. **2020**, 3 (7), 4282–4293. DOI: 10.1021/acsabm.0c00337.

(11) Zhang, Q.-P.; Sun, Y.-l.; Cheng, G.; Wang, Z.; Ma, H.; Ding, S.-Y.; Tan, B.; Bu, J.-h.; Zhang, C. Highly dispersed gold nanoparticles anchoring on post-modified covalent organic framework for catalytic application. Chemical Engineering Journal **2020**, 391, 123471. DOI: 10.1016/j.cej.2019.123471.

(12) Corma, A.; Garcia, H. Supported gold nanoparticles as catalysts for organic reactions. Chemical Society reviews **2008**, 37 (9), 2096–2126. DOI: 10.1039/B707314N.

(13) Amendola, V.; Pilot, R.; Frasconi, M.; Maragò, O. M.; Iatì, M. A. Surface plasmon resonance in gold nanoparticles: a review. Journal of physics. Condensed matter : an Institute of Physics journal **2017**, 29 (20), 203002. DOI: 10.1088/1361-648X/aa60f3.

(14) El-Brolossy, T. A.; Abdallah, T.; Mohamed, M. B.; Abdallah, S.; Easawi, K.; Negm, S.; Talaat, H. Shape and size dependence of the surface plasmon resonance of gold nanoparticles studied by Photoacoustic technique. Eur. Phys. J. Spec. Top. **2008**, 153 (1), 361–364. DOI: 10.1140/epjst/e2008-00462-0.

(15) Jin, R. Quantum sized, thiolate-protected gold nanoclusters. Nanoscale **2010**, 2 (3), 343–362. DOI: 10.1039/B9NR00160C.

(16) Jin, R.; Zhu, Y.; Qian, H. Quantum-sized gold nanoclusters: bridging the gap between organometallics and nanocrystals. Chemistry (Weinheim an der Bergstrasse, Germany) **2011**, 17 (24), 6584–6593. DOI: 10.1002/chem.201002390.

(17) Shilo, M.; Sharon, A.; Baranes, K.; Motiei, M.; Lellouche, J.-P. M.; Popovtzer, R. The effect of nanoparticle size on the probability to cross the blood-brain barrier: an in-vitro endothelial cell model. Journal of nanobiotechnology **2015**, 13, 19. DOI: 10.1186/s12951-015-0075-7.

(18) Chithrani, B. D.; Chan, W. C. W. Elucidating the mechanism of cellular uptake and removal of protein-coated gold nanoparticles of different sizes and shapes. Nano letters **2007**, 7 (6), 1542–1550. DOI: 10.1021/nl070363y.

(19) van de Broek, B.; Devoogdt, N.; D'Hollander, A.; Gijs, H.-L.; Jans, K.; Lagae, L.; Muyldermans, S.; Maes, G.; Borghs, G. Specific cell targeting with nanobody conjugated branched gold nanoparticles for photothermal therapy. ACS nano **2011**, 5 (6), 4319–4328. DOI: 10.1021/nn1023363.

(20) Sun, L.; Liu, D.; Wang, Z. Functional gold nanoparticle-peptide complexes as cell-targeting agents. Langmuir : the ACS journal of surfaces and colloids **2008**, 24 (18), 10293–10297. DOI: 10.1021/la8015063.

(21) Nair, L. V.; Nair, R. V.; Shenoy, S. J.; Thekkuveettil, A.; Jayasree, R. S. Blood brain barrier permeable gold nanocluster for targeted brain imaging and therapy: an in vitro and in vivo study. Journal of materials chemistry. B **2017**, 5 (42), 8314–8321. DOI: 10.1039/C7TB02247F. Published Online: Oct. 23, 2017.

(22) Ruff, J.; Hüwel, S.; Kogan, M. J.; Simon, U.; Galla, H.-J. The effects of gold nanoparticles functionalized with ß-amyloid specific peptides on an in vitro model of blood-brain barrier. Nanomedicine : nanotechnology, biology, and medicine **2017**, 13 (5), 1645–1652. DOI: 10.1016/j.nano.2017.02.013.

(23) MIDATECH PHARMA. MTX102 Safety Results, 2019.

(24) Reichenberger, S.; Marzun, G.; Muhler, M.; Barcikowski, S. Perspective of Surfactant-Free Colloidal Nanoparticles in Heterogeneous Catalysis. ChemCatChem **2019**, 11 (18), 4489–4518. DOI: 10.1002/cctc.201900666.

(25) Falsig, H.; Hvolbæk, B.; Kristensen, I. S.; Jiang, T.; Bligaard, T.; Christensen, C. H.; Nørskov, J. K. Trends in the Catalytic CO Oxidation Activity of Nanoparticles. Angew. Chem. **2008**, 120 (26), 4913–4917. DOI: 10.1002/ange.200801479.

(26) Sun, K.-Q.; Luo, S.-W.; Xu, N.; Xu, B.-Q. Gold Nano-size Effect in Au/SiO2 for Selective Ethanol Oxidation in Aqueous Solution. Catal Lett **2008**, 124 (3-4), 238–242. DOI: 10.1007/s10562-008-9507-4.

(27) Zhang, Y.; Zhang, C.; Xu, C.; Wang, X.; Liu, C.; Waterhouse, G. I. N.; Wang, Y.; Yin, H. Ultrasmall Au nanoclusters for biomedical and biosensing applications: A mini-review. Talanta **2019**, 200, 432–442. DOI: 10.1016/j.talanta.2019.03.068.

(28) Chevrier, D. M. Properties and applications of protein-stabilized fluorescent gold nanoclusters: short review. J. Nanophoton **2012**, 6 (1), 64504. DOI: 10.1117/1.JNP.6.064504.

(29) Liu, M.; Tang, F.; Yang, Z.; Xu, J.; Yang, X. Recent Progress on Gold-Nanocluster-Based Fluorescent Probe for Environmental Analysis and Biological Sensing. Journal of analytical methods in chemistry **2019**, 2019, 1095148. DOI: 10.1155/2019/1095148.

(30) Wu, Z.; Jin, R. On the ligand's role in the fluorescence of gold nanoclusters. Nano letters **2010**, 10 (7), 2568–2573. DOI: 10.1021/nl101225f.

(31) Genji Srinivasulu, Y.; Yao, Q.; Goswami, N.; Xie, J. Interfacial engineering of gold nanoclusters for biomedical applications. Mater. Horiz. **2020**, 7 (10), 2596–2618. DOI: 10.1039/D0MH00827C.

(32) Li, H.; Li, H.; Wan, A. Luminescent gold nanoclusters for in vivo tumor imaging. The Analyst **2020**, 145 (2), 348–363. DOI: 10.1039/C9AN01598A.

(33) Zhu, S.; Wang, X.; Cong, Y.; Li, L. Regulating the Optical Properties of Gold Nanoclusters for Biological Applications. ACS omega **2020**, 5 (36), 22702–22707. DOI: 10.1021/acsomega.0c03218.

(34) Liu, H.; Hong, G.; Luo, Z.; Chen, J.; Chang, J.; Gong, M.; He, H.; Yang, J.; Yuan, X.; Li, L.; Mu, X.; Wang, J.; Mi, W.; Luo, J.; Xie, J.; Zhang, X.-D. Atomic-Precision Gold Clusters for NIR-II Imaging. Advanced materials (Deerfield Beach, Fla.) **2019**, 31 (46), e1901015. DOI: 10.1002/adma.201901015. Published Online: Oct. 1, 2019.

(35) Scanlon, M. D.; Peljo, P.; Méndez, M. A.; Smirnov, E.; Girault, H. H. Charging and discharging at the nanoscale: Fermi level equilibration of metallic nanoparticles. Chemical science **2015**, 6 (5), 2705–2720. DOI: 10.1039/C5SC00461F. Published Online: Mar. 23, 2015.

(36) Zhang, D.; Gökce, B.; Barcikowski, S. Laser Synthesis and Processing of Colloids: Fundamentals and Applications. Chemical reviews **2017**, 117 (5), 3990–4103. DOI: 10.1021/acs.chemrev.6b00468.

(37) Rehbock, C.; Merk, V.; Gamrad, L.; Streubel, R.; Barcikowski, S. Size control of laser-fabricated surfactant-free gold nanoparticles with highly diluted electrolytes and their subsequent bioconjugation. Physical chemistry chemical physics : PCCP **2013**, 15 (9), 3057–3067. DOI: 10.1039/C2CP42641B.

(38) Delfour, L.; Itina, T. E. Mechanisms of Ultrashort Laser-Induced Fragmentation of Metal Nanoparticles in Liquids: Numerical Insights. J. Phys. Chem. C **2015**, 119 (24), 13893–13900. DOI: 10.1021/acs.jpcc.5b02084.

(39) Mafuné, F.; Kohno, J.-y.; Takeda, Y.; Kondow, T. Growth of Gold Clusters into Nanoparticles in a Solution Following Laser-Induced Fragmentation. J. Phys. Chem. B **2002**, 106 (34), 8555–8561. DOI: 10.1021/jp020786i.

(40) Takami, A.; Kurita, H.; Koda, S. Laser-Induced Size Reduction of Noble Metal Particles. The journal of physical chemistry. B **1999**, 103 (8), 1226–1232. DOI: 10.1021/jp983503o.

(41) Hashimoto, S.; Katayama, T.; Setoura, K.; Strasser, M.; Uwada, T.; Miyasaka, H. Laser-driven phase transitions in aqueous colloidal gold nanoparticles under high pressure: picosecond pump-probe study. Physical chemistry chemical physics : PCCP **2016**, 18 (6), 4994–5004. DOI: 10.1039/C5CP07395B.

(42) Qian, H.; Zhu, M.; Wu, Z.; Jin, R. Quantum sized gold nanoclusters with atomic precision. Accounts of chemical research **2012**, 45 (9), 1470–1479. DOI: 10.1021/ar200331z.

(43) Goswami, N.; Yao, Q.; Luo, Z.; Li, J.; Chen, T.; Xie, J. Luminescent Metal Nanoclusters with Aggregation-Induced Emission. The journal of physical chemistry letters **2016**, 7 (6), 962–975. DOI: 10.1021/acs.jpclett.5b02765.

(44) Li, H.; Zhu, W.; Wan, A.; Liu, L. The mechanism and application of the protein-stabilized gold nanocluster sensing system. The Analyst **2017**, 142 (4), 567–581. DOI: 10.1039/C6AN02112C.

(45) Yang, T.; Dai, S.; Tan, H.; Zong, Y.; Liu, Y.; Chen, J.; Zhang, K.; Wu, P.; Zhang, S.; Xu, J.; Tian, Y. Mechanism of Photoluminescence in Ag Nanoclusters: Metal-Centered Emission versus Synergistic Effect in Ligand-Centered Emission. J. Phys. Chem. C **2019**, 123 (30), 18638–18645. DOI: 10.1021/acs.jpcc.9b04034.

(46) Bryant, K.; West, C. W.; Saunders, S. R. Impacts of calcination on surface-clean supported nanoparticle catalysts. Applied Catalysis A: General **2019**, 579, 58–64. DOI: 10.1016/j.apcata.2019.04.016.

(47) Sassaroli, E.; Li, K. C. P.; O'Neill, B. E. Numerical investigation of heating of a gold nanoparticle and the surrounding microenvironment by nanosecond laser pulses

for nanomedicine applications. Physics in medicine and biology **2009**, 54 (18), 5541–5560. DOI: 10.1088/0031-9155/54/18/013.

(48) Cui, M.; Zhao, Y.; Song, Q. Synthesis, optical properties and applications of ultra-small luminescent gold nanoclusters. TrAC Trends in Analytical Chemistry **2014**, 57, 73–82. DOI: 10.1016/j.trac.2014.02.005.

(49) Hashimoto, S.; Werner, D.; Uwada, T. Studies on the interaction of pulsed lasers with plasmonic gold nanoparticles toward light manipulation, heat management, and nanofabrication. Journal of Photochemistry and Photobiology C: Photochemistry Reviews **2012**, 13 (1), 28–54. DOI: 10.1016/j.jphotochemrev.2012.01.001.

(50) Del Fatti, N.; Vallée, F. Ultrafast optical nonlinear properties of metal nanoparticles. Applied Physics B: Lasers and Optics **2001**, 73 (4), 383–390. DOI: 10.1007/s003400100648.

(51) Giustino, F. Electron-phonon interactions from first principles. Rev. Mod. Phys. **2017**, 89 (1), 41. DOI: 10.1103/RevModPhys.89.015003.

(52) Hodak, J. H.; Henglein, A.; Hartland, G. V. Photophysics of Nanometer Sized Metal Particles: Electron−Phonon Coupling and Coherent Excitation of Breathing Vibrational Modes. J. Phys. Chem. B **2000**, 104 (43), 9954–9965. DOI: 10.1021/jp002256x.

(53) Hodak, J.; Martini, I.; Hartland, G. V. Ultrafast study of electron–phonon coupling in colloidal gold particles. Chemical Physics Letters **1998**, 284 (1-2), 135–141. DOI: 10.1016/S0009-2614(97)01369-9.

(54) Lin, Z.; Zhigilei, L. V.; Celli, V. Electron-phonon coupling and electron heat capacity of metals under conditions of strong electron-phonon nonequilibrium. Phys. Rev. B **2008**, 77 (7), 776. DOI: 10.1103/PhysRevB.77.075133.

(55) Dowgiallo, A.-M.; Knappenberger, K. L. Ultrafast electron-phonon coupling in hollow gold nanospheres. Physical chemistry chemical physics : PCCP **2011**, 13 (48), 21585–21592. DOI: 10.1039/c1cp22743b.

(56) Plech, A.; Kotaidis, V.; Grésillon, S.; Dahmen, C.; Plessen, G. von. Laser-induced heating and melting of gold nanoparticles studied by time-resolved x-ray scattering. Physical review. B, Condensed matter **2004**, 70 (19), R13. DOI: 10.1103/PhysRevB.70.195423.

(57) Inasawa, S.; Sugiyama, M.; Yamaguchi, Y. Laser-induced shape transformation of gold nanoparticles below the melting point: the effect of surface melting. J. Phys. Chem. B **2005**, 109 (8), 3104–3111. DOI: 10.1021/jp045167j.

(58) Plech, A.; Ibrahimkutty, S.; Reich, S.; Newby, G. Thermal dynamics of pulsed-laser excited gold nanorods in suspension. Nanoscale **2017**, 9 (44), 17284–17292. DOI: 10.1039/c7nr06125k.

(59) Zijlstra, P.; Chon, J. W. M.; Gu, M. White light scattering spectroscopy and electron microscopy of laser induced melting in single gold nanorods. Phys. Chem. Chem. Phys. **2009**, 11 (28), 5915–5921. DOI: 10.1039/b905203h.

(60) González-Rubio, G.; Mosquera, J.; Kumar, V.; Pedrazo-Tardajos, A.; Llombart, P.; Solís, D. M.; Lobato, I.; Noya, E. G.; Guerrero-Martínez, A.; Taboada, J. M.; Obelleiro, F.; MacDowell, L. G.; Bals, S.; Liz-Marzán, L. M. Micelle-directed chiral seeded growth on anisotropic gold nanocrystals. Science (New York, N.Y.) **2020**, 368 (6498), 1472–1477. DOI: 10.1126/science.aba0980.

(61) Rehbock, C.; Zwartscholten, J.; Barcikowski, S. Biocompatible Gold Submicrometer Spheres with Variable Surface Texture Fabricated by Pulsed Laser Melting in Liquid. Chem. Lett. **2014**, 43 (9), 1502–1504. DOI: 10.1246/cl.140455.

(62) Werner, D.; Hashimoto, S.; Uwada, T. Remarkable photothermal effect of interband excitation on nanosecond laser-induced reshaping and size reduction of pseudospherical gold nanoparticles in aqueous solution. Langmuir : the ACS journal of surfaces and colloids **2010**, 26 (12), 9956–9963. DOI: 10.1021/la100015t.

(63) Ziefuß, A. R.; Reichenberger, S.; Rehbock, C.; Chakraborty, I.; Gharib, M.; Parak, W. J.; Barcikowski, S. Laser Fragmentation of Colloidal Gold Nanoparticles with High-Intensity Nanosecond Pulses is Driven by a Single-Step Fragmentation Mechanism with a Defined Educt Particle-Size Threshold. J. Phys. Chem. C **2018**, 122 (38), 22125–22136. DOI: 10.1021/acs.jpcc.8b04374.

(64) Maximova, K.; Aristov, A.; Sentis, M.; Kabashin, A. V. Size-controllable synthesis of bare gold nanoparticles by femtosecond laser fragmentation in water. Nanotechnology **2015**, 26 (6), 65601. DOI: 10.1088/0957-4484/26/6/065601.

(65) Werner, D.; Furube, A.; Okamoto, T.; Hashimoto, S. Femtosecond Laser-Induced Size Reduction of Aqueous Gold Nanoparticles: In Situ and Pump−Probe Spectroscopy Investigations Revealing Coulomb Explosion. J. Phys. Chem. C **2011**, 115 (17), 8503–8512. DOI: 10.1021/jp112262u.

(66) Metwally, K.; Mensah, S.; Baffou, G. Fluence Threshold for Photothermal Bubble Generation Using Plasmonic Nanoparticles. J. Phys. Chem. C **2015**, 119 (51), 28586–28596. DOI: 10.1021/acs.jpcc.5b09903.

(67) Amendola, V.; Meneghetti, M. Controlled size manipulation of free gold nanoparticles by laser irradiation and their facile bioconjugation. J. Mater. Chem. **2007**, 17 (44), 4705. DOI: 10.1039/B709621F.

(68) Lau, M.; Haxhiaj, I.; Wagener, P.; Intartaglia, R.; Brandi, F.; Nakamura, J.; Barcikowski, S. Ligand-free gold atom clusters adsorbed on graphene nano sheets generated by oxidative laser fragmentation in water. Chemical Physics Letters **2014**, 610-611, 256–260. DOI: 10.1016/j.cplett.2014.07.047.

(69) Besner, S.; Kabashin, A. V.; Meunier, M. Fragmentation of colloidal nanoparticles by femtosecond laser-induced supercontinuum generation. Appl. Phys. Lett. **2006**, 89 (23), 233122. DOI: 10.1063/1.2402944.

(70) Yamada, K.; Tokumoto, Y.; Nagata, T.; Mafuné, F. Mechanism of laser-induced size-reduction of gold nanoparticles as studied by nanosecond transient absorption spectroscopy. The journal of physical chemistry. B **2006**, 110 (24), 11751–11756. DOI: 10.1021/jp061020b.

(71) Kamat, P. V.; Flumiani, M.; Hartland, G. V. Picosecond Dynamics of Silver Nanoclusters. Photoejection of Electrons and Fragmentation. J. Phys. Chem. B **1998**, 102 (17), 3123–3128. DOI: 10.1021/jp980009b.

(72) Kuzmin, P. G.; Shafeev, G. A.; Serkov, A. A.; Kirichenko, N. A.; Shcherbina, M. E. Laser-assisted fragmentation of Al particles suspended in liquid. Applied Surface Science **2014**, 294, 15–19. DOI: 10.1016/j.apsusc.2013.12.174.

(73) Mo, M. Z.; Chen, Z.; Li, R. K.; Dunning, M.; Witte, B. B. L.; Baldwin, J. K.; Fletcher, L. B.; Kim, J. B.; Ng, A.; Redmer, R.; Reid, A. H.; Shekhar, P.; Shen, X. Z.; Shen, M.; Sokolowski-Tinten, K.; Tsui, Y. Y.; Wang, Y. Q.; Zheng, Q.; Wang, X. J.; Glenzer, S. H. Heterogeneous to homogeneous melting transition visualized with ultrafast electron diffraction. Science (New York, N.Y.) **2018**, 360 (6396), 1451–1455. DOI: 10.1126/science.aar2058.

(74) Fales, A. M.; Vogt, W. C.; Pfefer, T. J.; Ilev, I. K. Quantitative Evaluation of Nanosecond Pulsed Laser-Induced Photomodification of Plasmonic Gold Nanoparticles. Scientific reports **2017**, 7 (1), 15704. DOI: 10.1038/s41598-017-16052-7. Published Online: Nov. 16, 2017.

(75) Stuart, B. C.; Feit, M. D.; Herman, S.; Rubenchik, A. M.; Shore, B. W.; Perry, M. D. Optical ablation by high-power short-pulse lasers. J. Opt. Soc. Am. B **1996**, 13 (2), 459. DOI: 10.1364/JOSAB.13.000459.

(76) Lin, Z.; Zhigilei, L. V. Thermal excitation of d band electrons in Au: implications for laser-induced phase transformations. In High-Power Laser Ablation VI; Phipps, C. R., Ed.; SPIE, 2006; 62610U. DOI: 10.1117/12.674636.

(77) Pyatenko, A.; Yamaguchi, M.; Suzuki, M. Mechanisms of Size Reduction of Colloidal Silver and Gold Nanoparticles Irradiated by Nd:YAG Laser. J. Phys. Chem. C **2009**, 113 (21), 9078–9085. DOI: 10.1021/jp808300q.

(78) Itina, T. E.; Gouriet, K.; Zhigilei, L. V.; Noël, S.; Hermann, J.; Sentis, M. Mechanisms of small clusters production by short and ultra-short laser ablation. Applied Surface Science **2007**, 253 (19), 7656–7661. DOI: 10.1016/j.apsusc.2007.02.034.

(79) Strasser, M.; Setoura, K.; Langbein, U.; Hashimoto, S. Computational Modeling of Pulsed Laser-Induced Heating and Evaporation of Gold Nanoparticles. The Journal of Physical Chemistry C, 118(44), 25748-25755 **2014.** DOI: 10.1021/jp508316v.

(80) Cohen, S.; Plasil, F.; Swiatecki, W. J. Equilibrium configurations of rotating charged or gravitating liquid masses with surface tension. II. Annals of Physics **1974**, 82 (2), 557–596. DOI: 10.1016/0003-4916(74)90126-2.

(81) Grigoryev, S. Y.; Lakatosh, B. V.; Krivokorytov, M. S.; Zhakhovsky, V. V.; Dyachkov, S. A.; Ilnitsky, D. K.; Migdal, K. P.; Inogamov, N. A.; Vinokhodov, A. Y.; Kompanets, V. O.; Sidelnikov, Y. V.; Krivtsun, V. M.; Koshelev, K. N.; Medvedev, V. V. Expansion and Fragmentation of a Liquid-Metal Droplet by a Short Laser Pulse. Phys. Rev. Applied **2018**, 10 (6), 1589. DOI: 10.1103/PhysRevApplied.10.064009.

(82) Rayleigh. XX. On the equilibrium of liquid conducting masses charged with electricity. The London, Edinburgh, and Dublin Philosophical Magazine and Journal of Science **1882**, 14 (87), 184–186. DOI: 10.1080/14786448208628425.

(83) Muto, H.; Miyajima, K.; Mafuné, F. Mechanism of Laser-Induced Size Reduction of Gold Nanoparticles As Studied by Single and Double Laser Pulse Excitation. J. Phys. Chem. C **2008**, 112 (15), 5810–5815. DOI: 10.1021/jp711353m.

(84) Miotello, A.; Kelly, R. Laser-induced phase explosion: new physical problems when a condensed phase approaches the thermodynamic critical temperature. Appl Phys A **1999**, 69 (S1), S67-S73. DOI: 10.1007/S003399900296.

(85) Pyatenko, A.; Wang, H.; Koshizaki, N.; Tsuji, T. Mechanism of pulse laser interaction with colloidal nanoparticles. Laser & Photonics Reviews **2013**, 7 (4), 596–604. DOI: 10.1002/lpor.201300013.

(86) Miotello, A.; Kelly, R. Laser-induced phase explosion:New physical problems when a condensed phase approaches the thermodynamic critical temperature. Appl Phys A **1999**, 69 (S1), S67-S73. DOI: 10.1007/s003399900296.

(87) Chen, H.; Kou, X.; Yang, Z.; Ni, W.; Wang, J. Shape- and size-dependent refractive index sensitivity of gold nanoparticles. Langmuir : the ACS journal of surfaces and colloids **2008**, 24 (10), 5233–5237. DOI: 10.1021/la800305j.

(88) Waag, F.; Gökce, B.; Kalapu, C.; Bendt, G.; Salamon, S.; Landers, J.; Hagemann, U.; Heidelmann, M.; Schulz, S.; Wende, H.; Hartmann, N.; Behrens, M.; Barcikowski, S. Adjusting the catalytic properties of cobalt ferrite nanoparticles by pulsed laser fragmentation in water with defined energy dose. Scientific reports **2017**, 7 (1), 13161. DOI: 10.1038/s41598-017-13333-z.

(89) Siebeneicher, S.; Waag, F.; Escobar Castillo, M.; Shvartsman, V. V.; Lupascu, D. C.; Gökce, B. Laser Fragmentation Synthesis of Colloidal Bismuth Ferrite Particles. Nanomaterials (Basel, Switzerland) **2020**, 10 (2). DOI: 10.3390/nano10020359. Published Online: Feb. 19, 2020.

(90) Gelesky, M. A.; Umpierre, A. P.; Machado, G.; Correia, R. R. B.; Magno, W. C.; Morais, J.; Ebeling, G.; Dupont, J. Laser-induced fragmentation of transition metal nanoparticles in ionic liquids. Journal of the American Chemical Society **2005**, 127 (13), 4588–4589. DOI: 10.1021/ja042711t.

(91) Wagener, P.; Barcikowski, S. Laser fragmentation of organic microparticles into colloidal nanoparticles in a free liquid jet. Appl. Phys. A **2010**, 101 (2), 435–439. DOI: 10.1007/s00339-010-5814-x.

(92) Lau, M.; Barcikowski, S. Quantification of mass-specific laser energy input converted into particle properties during picosecond pulsed laser fragmentation of zinc oxide and boron carbide in liquids. Applied Surface Science **2015**, 348, 22–29. DOI: 10.1016/j.apsusc.2014.07.053.

(93) Waag, F.; Gökce, B.; Kalapu, C.; Bendt, G.; Salamon, S.; Landers, J.; Hagemann, U.; Heidelmann, M.; Schulz, S.; Wende, H.; Hartmann, N.; Behrens, M.; Barcikowski, S. Adjusting the catalytic properties of cobalt ferrite nanoparticles by pulsed laser fragmentation in water with defined energy dose. Scientific reports **2017**, 7 (1), 13161. DOI: 10.1038/s41598-017-13333-z. Published Online: Oct. 13, 2017.

(94) Siebeneicher, S.; Waag, F.; Escobar Castillo, M.; Shvartsman, V. V.; Lupascu, D. C.; Gökce, B. Laser Fragmentation Synthesis of Colloidal Bismuth Ferrite Particles. Nanomaterials (Basel, Switzerland) **2020**, 10 (2). DOI: 10.3390/nano10020359. Published Online: Feb. 19, 2020.

(95) Zerebecki, S.; Reichenberger, S.; Barcikowski, S. Continuous-Flow Flat Jet Setup for Uniform Pulsed Laser Postprocessing of Colloids. The journal of physical chemistry. A **2020**, 124 (52), 11125–11132. DOI: 10.1021/acs.jpca.0c08787. Published Online: Dec. 16, 2020.

(96) Zerebecki, S.; Reichenberger, S.; Barcikowski, S. Continuous-Flow Flat Jet Setup for Uniform Pulsed Laser Postprocessing of Colloids. The journal of physical chemistry. A **2020**, 124 (52), 11125–11132. DOI: 10.1021/acs.jpca.0c08787. Published Online: Dec. 16, 2020.

(97) Hodak, J. H.; Martini, I.; Hartland, G. V. Spectroscopy and Dynamics of Nanometer-Sized Noble Metal Particles. J. Phys. Chem. B **1998**, 102 (36), 6958–6967. DOI: 10.1021/jp9809787.

(98) Westcott, S. L.; Averitt, R. D.; Wolfgang, J. A.; Nordlander, P.; Halas, N. J. Adsorbate-Induced Quenching of Hot Electrons in Gold Core−Shell Nanoparticles. The journal of physical chemistry. B **2001**, 105 (41), 9913–9917. DOI: 10.1021/jp011213t.

(99) Mongin, D.; Maioli, P.; Burgin, J.; Langot, P.; Cottancin, E.; D'Addato, S.; Canut, B.; Treguer, M.; Crut, A.; Vallée, F.; Del Fatti, N. Ultrafast electron-lattice thermalization in copper and other noble metal nanoparticles. Journal of physics. Condensed matter : an Institute of Physics journal **2019**, 31 (8), 84001. DOI: 10.1088/1361-648X/aaf7eb. Published Online: Jan. 8, 2019.

(100) Aruda, K. O.; Tagliazucchi, M.; Sweeney, C. M.; Hannah, D. C.; Schatz, G. C.; Weiss, E. A. Identification of parameters through which surface chemistry determines the lifetimes of hot electrons in small Au nanoparticles. Proceedings of the National

Academy of Sciences of the United States of America **2013**, 110 (11), 4212–4217. DOI: 10.1073/pnas.1222327110.

(101) Dowgiallo, A.-M.; Knappenberger, K. L. Ultrafast electron-phonon coupling in hollow gold nanospheres. Physical chemistry chemical physics : PCCP **2011**, 13 (48), 21585–21592. DOI: 10.1039/C1CP22743B. Published Online: Nov. 4, 2011.

(102) Jendrzej, S.; Gökce, B.; Amendola, V.; Barcikowski, S. Barrierless growth of precursor-free, ultrafast laser-fragmented noble metal nanoparticles by colloidal atom clusters - A kinetic in situ study. Journal of colloid and interface science **2016**, 463, 299–307. DOI: 10.1016/j.jcis.2015.10.032.

(103) Lourenco, C. Steric stabilization of nanoparticles: Size and surface properties. International Journal of Pharmaceutics **1996**, 138 (1), 1–12. DOI: 10.1016/0378-5173(96)04486-9.

(104) Mo, S.; Shao, X.; Chen, Y.; Cheng, Z. Increasing entropy for colloidal stabilization. Scientific reports **2016**, 6, 36836. DOI: 10.1038/srep36836.

(105) Barmina, E. V.; Gudkov, S. V.; Simakin, A. V.; Shafeev, G. A. Stable products of laser-induced breakdown of aqueous colloidal solutions of nanoparticles. http://arxiv.org/pdf/1707.02357v2.

(106) Kalus, M.-R.; Reimer, V.; Barcikowski, S.; Gökce, B. Discrimination of effects leading to gas formation during pulsed laser ablation in liquids. Applied Surface Science **2019**, 465, 1096–1102. DOI: 10.1016/j.apsusc.2018.09.224.

(107) Muto, H.; Yamada, K.; Miyajima, K.; Mafuné, F. Estimation of Surface Oxide on Surfactant-Free Gold Nanoparticles Laser-Ablated in Water. J. Phys. Chem. C **2007**, 111 (46), 17221–17226. DOI: 10.1021/jp075582m.

(108) Merk, V.; Rehbock, C.; Becker, F.; Hagemann, U.; Nienhaus, H.; Barcikowski, S. In situ non-DLVO stabilization of surfactant-free, plasmonic gold nanoparticles: effect of Hofmeister's anions. Langmuir : the ACS journal of surfaces and colloids **2014**, 30 (15), 4213–4222. DOI: 10.1021/la404556a.

(109) Pfeiffer, C.; Rehbock, C.; Hühn, D.; Carrillo-Carrion, C.; Aberasturi, D. J. de; Merk, V.; Barcikowski, S.; Parak, W. J. Interaction of colloidal nanoparticles with their local environment: the (ionic) nanoenvironment around nanoparticles is different from bulk and determines the physico-chemical properties of the nanoparticles. Journal of the Royal Society, Interface **2014**, 11 (96), 20130931. DOI: 10.1098/rsif.2013.0931.

(110) VERWEY, E. J. W. Theory of the stability of lyophobic colloids. The Journal of physical and colloid chemistry **1947**, 51 (3), 631–636. DOI: 10.1021/j150453a001.

(111) Derjaguin, B. On the repulsive forces between charged colloid particles and on the theory of slow coagulation and stability of lyophobe sols. Trans. Faraday Soc. **1940**, 35, 203. DOI: 10.1039/tf9403500203.

(112) Makino, K.; Ohshima, H. Electrophoretic mobility of a colloidal particle with constant surface charge density. Langmuir : the ACS journal of surfaces and colloids **2010**, 26 (23), 18016–18019. DOI: 10.1021/la1035745.

(113) Doane, T. L.; Chuang, C.-H.; Hill, R. J.; Burda, C. Nanoparticle ζ -potentials. Accounts of chemical research **2012**, 45 (3), 317–326. DOI: 10.1021/ar200113c.

(114) Mafuné, F.; Kondow, T. Selective laser fabrication of small nanoparticles and nano-networks in solution by irradiation of UV pulsed laser onto platinum nanoparticles. Chemical Physics Letters **2004**, 383 (3-4), 343–347. DOI: 10.1016/j.cplett.2003.10.149.

(115) Sylvestre, J.-P.; Tang, M.-C.; Furtos, A.; Leclair, G.; Meunier, M.; Leroux, J.-C. Nanonization of megestrol acetate by laser fragmentation in aqueous milieu. Journal of controlled release : official journal of the Controlled Release Society **2011**, 149 (3), 273–280. DOI: 10.1016/j.jconrel.2010.10.034.

(116) Maier, S. A. Plasmonics:Fundamentals and applications; Springer, 2007. DOI: 10.1007/0-387-37825-1.

(117) Geddes, C. D., Ed. Reviews in plasmonics 2010; Reviews in plasmonics; Springer, 2012.

(118) Mie, G. Beiträge zur Optik trüber Medien, speziell kolloidaler Metallösungen. Ann. Phys. **1908**, 330 (3), 377–445. DOI: 10.1002/andp.19083300302.

(119) Willets, K. A.; van Duyne, R. P. Localized surface plasmon resonance spectroscopy and sensing. Annual review of physical chemistry **2007**, 58, 267–297. DOI: 10.1146/annurev.physchem.58.032806.104607.

(120) Petryayeva, E.; Krull, U. J. Localized surface plasmon resonance: nanostructures, bioassays and biosensing--a review. Analytica chimica acta **2011**, 706 (1), 8–24. DOI: 10.1016/j.aca.2011.08.020.

(121) Alvarez, M. M.; Khoury, J. T.; Schaaff, T. G.; Shafigullin, M. N.; Vezmar, I.; Whetten, R. L. Optical Absorption Spectra of Nanocrystal Gold Molecules. J. Phys. Chem. B **1997**, 101 (19), 3706–3712. DOI: 10.1021/jp962922n.

(122) Zhou, M.; Zeng, C.; Chen, Y.; Zhao, S.; Sfeir, M. Y.; Zhu, M.; Jin, R. Evolution from the plasmon to exciton state in ligand-protected atomically precise gold nanoparticles. Nature communications **2016**, 7, 13240. DOI: 10.1038/ncomms13240.

(123) Sun, J.; Jin, Y. Fluorescent Au nanoclusters: recent progress and sensing applications. J. Mater. Chem. C **2014**, 2 (38), 8000–8011. DOI: 10.1039/C4TC01489H.

(124) Chakraborty, I.; Pradeep, T. Atomically Precise Clusters of Noble Metals: Emerging Link between Atoms and Nanoparticles. Chemical reviews **2017**, 117 (12), 8208–8271. DOI: 10.1021/acs.chemrev.6b00769.

(125) Jin, R.; Zeng, C.; Zhou, M.; Chen, Y. Atomically Precise Colloidal Metal Nanoclusters and Nanoparticles: Fundamentals and Opportunities. Chemical reviews **2016**, 116 (18), 10346–10413. DOI: 10.1021/acs.chemrev.5b00703.

(126) Yang, T.-Q.; Peng, B.; Shan, B.-Q.; Zong, Y.-X.; Jiang, J.-G.; Wu, P.; Zhang, K. Origin of the Photoluminescence of Metal Nanoclusters: From Metal-Centered Emission to Ligand-Centered Emission. Nanomaterials (Basel, Switzerland) **2020**, 10 (2). DOI: 10.3390/nano10020261.

(127) Schmid, G. Nanoparticles:From Theory to Application; Wiley-VCH, 2010.

(128) Zheng, J.; Nicovich, P. R.; Dickson, R. M. Highly fluorescent noble-metal quantum dots. Annual review of physical chemistry **2007**, 58, 409–431. DOI: 10.1146/annurev.physchem.58.032806.104546.

(129) Knight, W. D.; Clemenger, K.; Heer, W. A. de; Saunders, W. A.; Chou, M. Y.; Cohen, M. L. Electronic Shell Structure and Abundances of Sodium Clusters. Phys. Rev. Lett. **1984**, 52 (24), 2141–2143. DOI: 10.1103/PhysRevLett.52.2141.

(130) Cantelli, A.; Guidetti, G.; Manzi, J.; Caponetti, V.; Montalti, M. Towards Ultra-Bright Gold Nanoclusters. Eur. J. Inorg. Chem. **2017**, 2017 (44), 5068–5084. DOI: 10.1002/ejic.201700735.

(131) Zheng, J.; Zhang, C.; Dickson, R. M. Highly fluorescent, water-soluble, size-tunable gold quantum dots. Physical review letters **2004**, 93 (7), 77402. DOI: 10.1103/PhysRevLett.93.077402.

(132) Jadzinsky, P. D.; Calero, G.; Ackerson, C. J.; Bushnell, D. A.; Kornberg, R. D. Structure of a thiol monolayer-protected gold nanoparticle at 1.1 A resolution. Science (New York, N.Y.) **2007**, 318 (5849), 430–433. DOI: 10.1126/science.1148624.

(133) Zhu, M.; Aikens, C. M.; Hollander, F. J.; Schatz, G. C.; Jin, R. Correlating the crystal structure of a thiol-protected Au25 cluster and optical properties. Journal of the American Chemical Society **2008**, 130 (18), 5883–5885. DOI: 10.1021/ja801173r.

(134) Aikens, C. M. Electronic and Geometric Structure, Optical Properties, and Excited State Behavior in Atomically Precise Thiolate-Stabilized Noble Metal Nanoclusters. Accounts of chemical research **2018**, 51 (12), 3065–3073. DOI: 10.1021/acs.accounts.8b00364.

(135) Yu, P.; Wen, X.; Toh, Y.-R.; Ma, X.; Tang, J. Fluorescent Metallic Nanoclusters: Electron Dynamics, Structure, and Applications. Part. Part. Syst. Charact. **2015**, 32 (2), 142–163. DOI: 10.1002/ppsc.201400040.

(136) Pyo, K.; Thanthirige, V. D.; Kwak, K.; Pandurangan, P.; Ramakrishna, G.; Lee, D. Ultrabright Luminescence from Gold Nanoclusters: Rigidifying the Au(I)-Thiolate Shell. Journal of the American Chemical Society **2015**, 137 (25), 8244–8250. DOI: 10.1021/jacs.5b04210.

(137) Zhou, C.; Sun, C.; Yu, M.; Qin, Y.; Wang, J.; Kim, M.; Zheng, J. Luminescent Gold Nanoparticles with Mixed Valence States Generated from Dissociation of Polymeric Au (I) Thiolates. J. Phys. Chem. C **2010**, 114 (17), 7727–7732. DOI: 10.1021/jp9122584.

(138) Zhu, M.; Eckenhoff, W. T.; Pintauer, T.; Jin, R. Conversion of Anionic [Au 25 (SCH 2 CH 2 Ph) 18] − Cluster to Charge Neutral Cluster via Air Oxidation. J. Phys. Chem. C **2008**, 112 (37), 14221–14224. DOI: 10.1021/jp805786p.

(139) Negishi, Y.; Chaki, N. K.; Shichibu, Y.; Whetten, R. L.; Tsukuda, T. Origin of magic stability of thiolated gold clusters: a case study on Au25(SC6H13)18. Journal of the American Chemical Society **2007**, 129 (37), 11322–11323. DOI: 10.1021/ja073580.

(140) Eichelbaum, M.; Rademann, K.; Hoell, A.; Tatchev, D. M.; Weigel, W.; Stößer, R.; Pacchioni, G. Photoluminescence of atomic gold and silver particles in soda-lime silicate glasses. Nanotechnology **2008**, 19 (13), 135701. DOI: 10.1088/0957-4484/19/13/135701.

(141) Helmbrecht, C.; Lützenkirchen-Hecht, D.; Frank, W. Microwave-assisted synthesis of water-soluble, fluorescent gold nanoclusters capped with small organic molecules and a revealing fluorescence and X-ray absorption study. Nanoscale **2015**, 7 (11), 4978–4983. DOI: 10.1039/c4nr07051h.

(142) Le Guével, X.; Hötzer, B.; Jung, G.; Hollemeyer, K.; Trouillet, V.; Schneider, M. Formation of Fluorescent Metal (Au, Ag) Nanoclusters Capped in Bovine Serum Albumin Followed by Fluorescence and Spectroscopy. J. Phys. Chem. C **2011**, 115 (22), 10955–10963. DOI: 10.1021/jp111820b.

(143) Lemke, K.; Prietzel, C.; Koetz, J. Fluorescent gold clusters synthesized in a poly(ethyleneimine) modified reverse microemulsion. Journal of colloid and interface science **2013**, 394, 141–146. DOI: 10.1016/j.jcis.2012.11.057.

(144) Goldys, E. M.; Sobhan, M. A. Fluorescence of Colloidal Gold Nanoparticles is Controlled by the Surface Adsorbate. Adv. Funct. Mater. **2012**, 22 (9), 1906–1913. DOI: 10.1002/adfm.201102057.

(145) Qian, H.; Eckenhoff, W. T.; Zhu, Y.; Pintauer, T.; Jin, R. Total structure determination of thiolate-protected Au38 nanoparticles. Journal of the American Chemical Society **2010**, 132 (24), 8280–8281. DOI: 10.1021/ja103592z.

(146) Tian, S.; Li, Y.-Z.; Li, M.-B.; Yuan, J.; Yang, J.; Wu, Z.; Jin, R. Structural isomerism in gold nanoparticles revealed by X-ray crystallography. Corrected. Nature communications **2015**, 6, 8667. DOI: 10.1038/ncomms9667.

(147) Higaki, T.; Li, Q.; Zhou, M.; Zhao, S.; Li, Y.; Li, S.; Jin, R. Toward the Tailoring Chemistry of Metal Nanoclusters for Enhancing Functionalities. Accounts of chemical research **2018**, 51 (11), 2764–2773. DOI: 10.1021/acs.accounts.8b00383.

(148) Zeng, C.; Li, T.; Das, A.; Rosi, N. L.; Jin, R. Chiral structure of thiolate-protected 28-gold-atom nanocluster determined by X-ray crystallography. Journal of the American Chemical Society **2013**, 135 (27), 10011–10013. DOI: 10.1021/ja404058q.

(149) Chen, Y.; Liu, C.; Tang, Q.; Zeng, C.; Higaki, T.; Das, A.; Jiang, D.-e.; Rosi, N. L.; Jin, R. Isomerism in Au28(SR)20 Nanocluster and Stable Structures. Journal of the American Chemical Society **2016**, 138 (5), 1482–1485. DOI: 10.1021/jacs.5b12094.

(150) Kang, X.; Zhu, M. Tailoring the photoluminescence of atomically precise nanoclusters. Chemical Society reviews **2019**, 48 (8), 2422–2457. DOI: 10.1039/C8CS00800K.

(151) Deng, H.-H.; Shi, X.-Q.; Wang, F.-F.; Peng, H.-P.; Liu, A.-L.; Xia, X.-H.; Chen, W. Fabrication of Water-Soluble, Green-Emitting Gold Nanoclusters with a 65% Photoluminescence Quantum Yield via Host–Guest Recognition. Chem. Mater. **2017**, 29 (3), 1362–1369. DOI: 10.1021/acs.chemmater.6b05141.

(152) Londoño-Larrea, P.; Vanegas, J. P.; Cuaran-Acosta, D.; Zaballos-García, E.; Pérez-Prieto, J. Water-Soluble Naked Gold Nanoclusters Are Not Luminescent. Chemistry (Weinheim an der Bergstrasse, Germany) **2017**, 23 (34), 8137–8141. DOI: 10.1002/chem.201700913.

(153) Tian, S.; Cao, Y.; Chen, T.; Zang, S.; Xie, J. Ligand-protected atomically precise gold nanoclusters as model catalysts for oxidation reactions. Chemical communications (Cambridge, England) **2020**, 56 (8), 1163–1174. DOI: 10.1039/C9CC08215H.

(154) Sankar, M.; He, Q.; Engel, R. V.; Sainna, M. A.; Logsdail, A. J.; Roldan, A.; Willock, D. J.; Agarwal, N.; Kiely, C. J.; Hutchings, G. J. Role of the Support in Gold-Containing Nanoparticles as Heterogeneous Catalysts. Chemical reviews **2020**, 120 (8), 3890–3938. DOI: 10.1021/acs.chemrev.9b00662.

(155) Kawawaki, T.; Negishi, Y. Gold Nanoclusters as Electrocatalysts for Energy Conversion. Nanomaterials (Basel, Switzerland) **2020**, 10 (2). DOI: 10.3390/nano10020238.

(156) Higaki, T.; Li, Y.; Zhao, S.; Li, Q.; Li, S.; Du, X.-S.; Yang, S.; Chai, J.; Jin, R. Atomically Tailored Gold Nanoclusters for Catalytic Application. Angewandte Chemie (International ed. in English) **2019**, 58 (25), 8291–8302. DOI: 10.1002/anie.201814156.

(157) Xu, H.; Cheng, D.; Gao, Y.; Zeng, X. C. Assessment of Catalytic Activities of Gold Nanoclusters with Simple Structure Descriptors. ACS Catal. **2018**, 8 (10), 9702–9710. DOI: 10.1021/acscatal.8b02423.

(158) Liu, J.; Krishna, K. S.; Losovyj, Y. B.; Chattopadhyay, S.; Lozova, N.; Miller, J. T.; Spivey, J. J.; Kumar, C. S. S. R. Ligand-stabilized and atomically precise gold nanocluster catalysis: a case study for correlating fundamental electronic properties

with catalysis. Chemistry (Weinheim an der Bergstrasse, Germany) **2013**, 19 (31), 10201–10208. DOI: 10.1002/chem.201300600.

(159) Wan, X.-K.; Wang, J.-Q.; Nan, Z.-A.; Wang, Q.-M. Ligand effects in catalysis by atomically precise gold nanoclusters. Science advances **2017**, 3 (10), e1701823. DOI: 10.1126/sciadv.1701823.

(160) Zhang, J.; Chen, G.; Chaker, M.; Rosei, F.; Ma, D. Gold nanoparticle decorated ceria nanotubes with significantly high catalytic activity for the reduction of nitrophenol and mechanism study. Applied Catalysis B: Environmental **2013**, 132-133, 107–115. DOI: 10.1016/j.apcatb.2012.11.030.

(161) Kuhn, J. N.; Tsung, C.-K.; Huang, W.; Somorjai, G. A. Effect of organic capping layers over monodisperse platinum nanoparticles upon activity for ethylene hydrogenation and carbon monoxide oxidation. Journal of Catalysis **2009**, 265 (2), 209–215. DOI: 10.1016/j.jcat.2009.05.001.

3. Results

3.1 – PART 0

Analytical ultracentrifugation of fully inorganic colloids

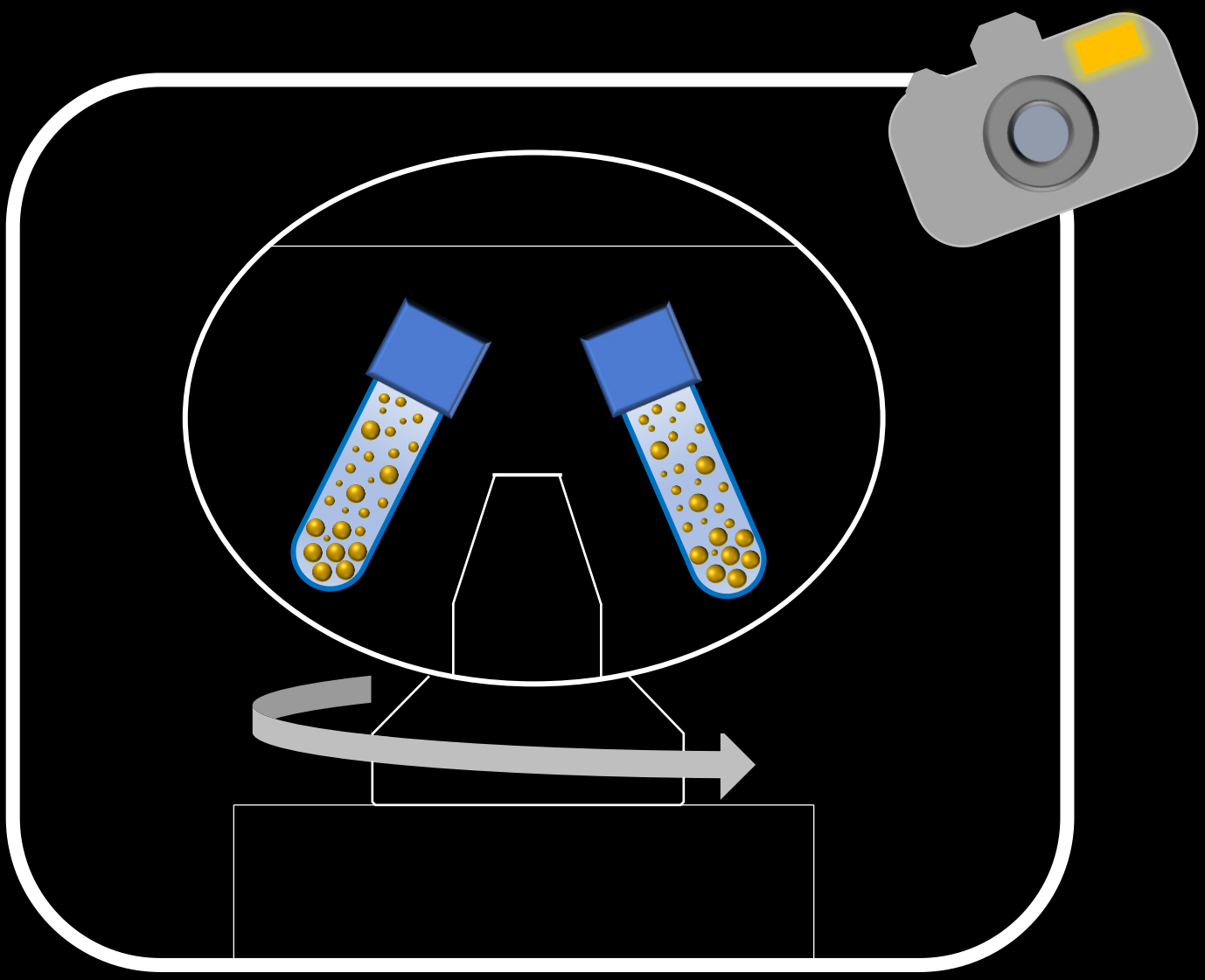

3.1.1 Determination of suitable parameters for AUC of inorganic gold colloids

Synopsis:

As the size of NPs decreases, the number of suitable methods to determine the particle diameter also decreases drastically. While larger particles (> 3 nm) can be analyzed using commercially available lab analysis methods, like analytical disc centrifugation (ADC), transmission electron microscopy (TEM), and dynamic light scattering (DLS), the determination of particle sizes smaller than 3 nm is far more complicated. Particularly, ADC and DLS are no longer suitable as they require sufficient absorbances at 405 nm (ADC) and 633 nm (DLS), which do not necessarily exist in diluted, ligand-free Au NCs. Moreover, the resolution limits TEM to particle sizes of 1-2 nm, and it was already reported that this method cannot compete with the AUC's angstrom resolution.[1] This limit can be overcome using high-resolution TEM, which is a prominent way to determine the size of such ultra-small particles. However, Au NCs lose their phase contrast with decreasing particle size, making it difficult to determine their size microscopically. Electrospray ionization mass spectroscopy (ESI-MS), which is a mass analysis method associated with less particle fragmentation, is an alternative method employed by scientists to determine the size of NCs.[2] The result is a mass-to-charge ratio, which requires some knowledge about possible ionization products to calculate the intensity of each mass fraction (more information about this method can be found in chapter 3.3.1). While the analytical ultracentrifuge (AUC) technique is less prominent, it can also be used to measure the particle size of NCs.[3] Thus far, scientists have applied AUC only for investigations on organic ligand-capped Au NCs.[1,4] However, within and beyond this thesis, the application field was extended to fully inorganic colloidal NPs and NCs, leading to four publications that include AUC measurement of inorganic NPs:

- A. Ziefuß et al, J. Phys. Chem. C, **2020**, 124, 38 (Chapter 6.1.1)
- A. Ziefuß et al., Langmuir, **2019**, 35, 6630-6639 (Chapter 5.1.2)
- F. Waag et al., JPCC, **2019**, 9, 18547-18558 (not part of this work)
- A. Letzel et al., Appl. Surf. Sci., **2018**, 473 (not part of this work)

It is pertinent to mention that the description of the device and choice of experimental parameters were not discussed in detail in the above publications but will be elaborated on in this chapter.

References

(1) Carney, R. P.; Kim, J. Y.; Qian, H.; Jin, R.; Mehenni, H.; Stellacci, F.; Bakr, O. M. Determination of nanoparticle size distribution together with density or molecular weight by 2D analytical ultracentrifugation. *Nature communications* **2011**, *2*, 335. DOI: 10.1038/ncomms1338. Published Online: Jun. 7, 2011.

(2) Mercogliano, C. P.; DeRosier, D. J. Gold nanocluster formation using metallothionein: mass spectrometry and electron microscopy. *Journal of molecular biology* **2006**, *355* (2), 211–223. DOI: 10.1016/j.jmb.2005.10.026. Published Online: Nov. 8, 2005.

(3) Cölfen, H.; Völkel, A. Analytical ultracentrifugation in colloid chemistry. In *Analytical Ultracentrifugation VII*; Lechner, M. D., Börger, L., Eds.; Springer Berlin Heidelberg, **2004**; pp 31–47. DOI: 10.1007/b98011.

(4) Cölfen, H., Ed. *Analytical Ultracentrifugation V*; Progress in Colloid and Polymer Science; Springer Berlin Heidelberg, **1999**. DOI: 10.1007/3-540-48703-4.

Analytical ultra-centrifugation of fully inorganic gold nanocluster

(unpublished results)

Anna. R. Ziefuss, Florian de Kock, Christoph Rehbock, Stephan Barcikowski

University of Duisburg-Essen, Technical chemistry I and Center for Nanointegration Duisburg-Essen (CENIDE), 45141 Essen, Germany

Analytical ultracentrifugation (AUC) was developed in 1923 by Svedberg and Nicholas as a method to measure colloidal particle size distribution.[1] Their idea was to measure the movement of particles while applying a known centrifugal force and using a modified Stokes law to determine the sedimentation behavior.[1] Only 3 years later, Svedberg was honored with the Nobel Prize in chemistry for his work on dispersal systems, including developing the first AUC. Although the device was intended to study the behavior of dispersed metal particles, it was mainly used to analyze biological systems in the following decades.[2,3] It is only in the last few decades that the utilization of AUC was finally established in its original field, and to date, there are still only a few groups that use the instrument intensively for the characterization of colloidal systems.[4–6] Most studies are done on wet-chemical synthesized particles. The determination of the sedimentation and diffusion coefficients offers the opportunity to calculate the particle shape, the hydrodynamic diameter (and distribution shape), and molecular weight. Nevertheless, a transfer of this knowledge to colloidal metal particles without organic ligands is almost completely missing. In the last 2 years, the AUC has been employed in the characterization of laser-generated silver[7], gold[8,9], and high entropy[6] alloy systems, mainly addressing the particle size distribution without specifying the choice of measurement parameters. However, the considerations behind this are a prerequisite for proper interpretation of AUC data of ligand-free Au NPs and Au NCs and will therefore be presented in the following.

Principles of AUC

During AUC, a small sample volume of 350 µL is exposed to a centrifugal field which is supposed to force particle sedimentation. This will lead to a temporal concentration profile within the sample, which can be tracked over the whole radial position by optical systems (Fig. 1A).

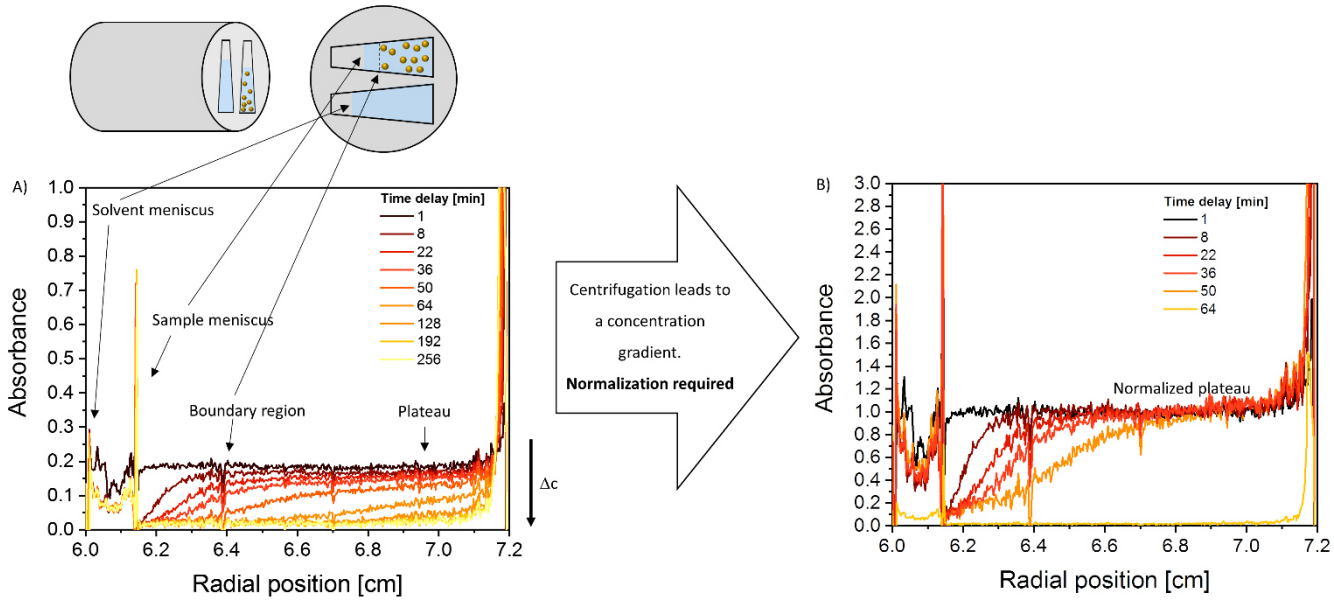

Figure 1: *Raw data of a sedimentation velocity run at 30000 rpm, 20°C. A) Graphical explanation of the raw data based on the changes in absorbance of Au NPs after laser fragmentation in liquids (LFL) (measured at 380 nm), at different times during centrifugation and over the entire radial range. B) During measurement, there is a change in particle concentration over the radial range, so that in the first step of the data evaluation a normalization of the raw data to c_{max} must be carried out. However, the spectrum after 64 min shows already a full depletion of particles. The corresponding spectrum was not normalized in order to clearly demonstrate the depletion of particles.*

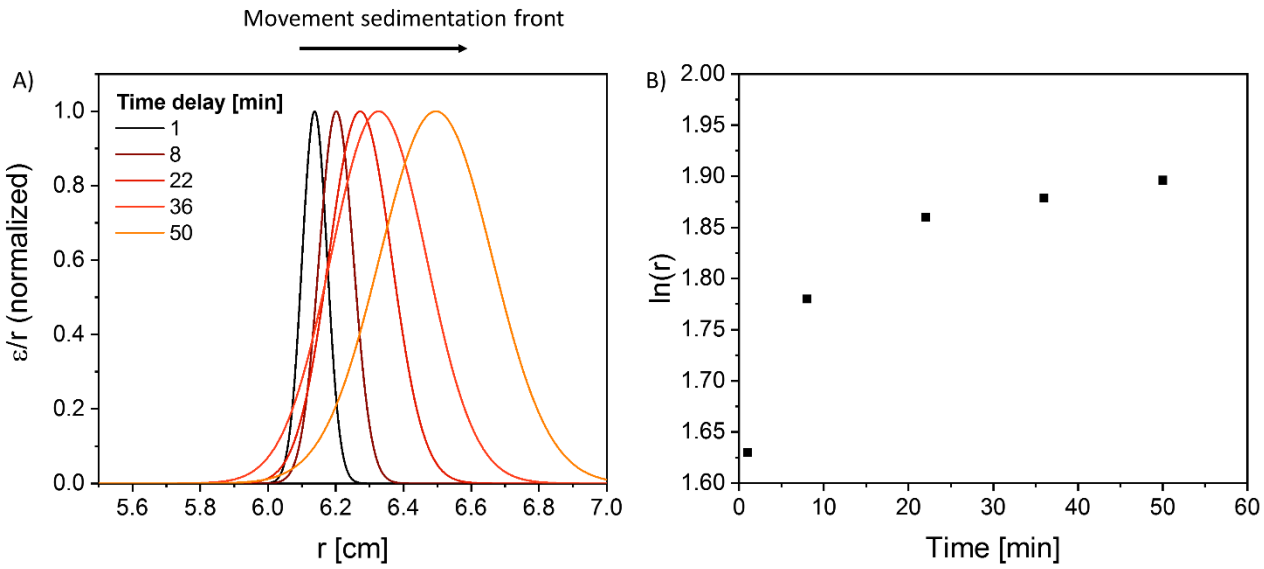

Figure 2: *A) Sedimentation front after deviation of the raw data (normalized to 1). From a subsequent plot of the logarithmic radial position against time the S-value can be calculated (B).*

The radial displacement of the sedimentation front (S-front) is of particular interest, as its temporal change allows the determination of the sedimentation coefficient (S-value).[10] However, the centrifugation will lead to a concentration gradient within the sample cell, which requires normalization to the maximal local concentration in the first step (Fig. 1B). Thereby, the sedimentation front (boundary region) in Fig. 1B is derived, and a representation of the sedimentation front by Gaussian curves is obtained (Fig. 2A). By plotting the logarithmic radial position against time, an S-value distribution can be obtained (Fig. 2B). Due to the high computing power required for this last step, we use the license-free software sedfit. Note that the S-front can be influenced by strong diffusion of the particles or charge effects.[11] While charging effects (as a directed counterforce to sedimentation) can lead to a reduction of the S-value, diffusion should lead to a broadening of the S-front (Fig. 2). Fig. 1 and 2 show the data obtained for gold nanoparticles (Au NPs) after laser fragmentation in liquids. Following Ref.[3] we expect a multimodal particle size distribution with particles sizing from 0.5 – 4 nm. Due to their smaller mass, small particles show a stronger tendency for diffusion in a centrifugal field than large particles. This can be well illustrated using the Au NPs that we study within this research. Following Fig. 2, the S-front broadens with increasing centrifuge time. With increasing centrifugation time, the sedimentation front is only determined by the smaller particle fraction since larger particles could already sediment to the bottom. The distribution width of the smaller S-values is thus determined by the particles diffusion constant. However, the AUC can be operated with different rotation speeds. If large g-forces are generated, diffusion can be suppressed to a large extent, but this in turn makes simultaneous detection of large and small particles difficult.

We almost exclusively used absorption optics to perform optical detection of the s-front. Beside the strength of the centrifugal field, a suitable detection wavelength must be found, that is able to detect large (and therefore plasmonic) and small (protoplasmic) Au

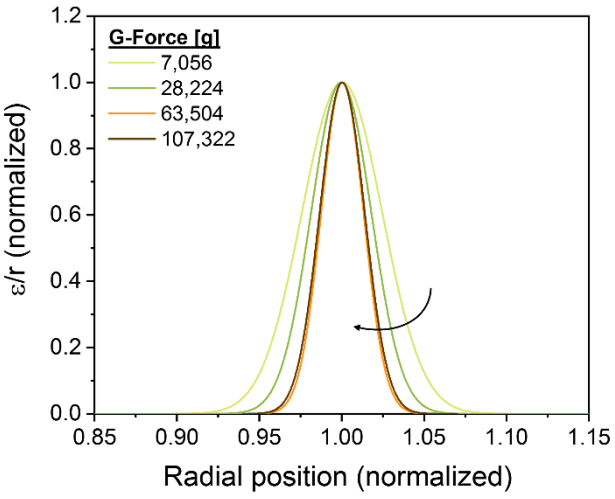

Figure 3: *Sedimentation front after deviation of raw data using different g-forces. For a fair comparison we plotted those data which should already show a depletion of particles > 3nm. The data are measured after 265 min (at 7,065 g), 66 min (at 28,224 g), 29 min (at 63,504 g), and 17 min (107,322 min).*

NPs sufficiently. Further, we need to investigate the influence of charging effects since fully inorganic colloidal Au NPs are subject to electrostatic stabilization by anions. The influence of all three factors on the S-value distribution of the Au NPs is examined below. Note that we have only performed sedimentation-velocity runs, which do not allow the quantitative description of diffusion coefficients as the latter requires sedimentation-equilibrium runs.[11]

Influence of centrifugal speed on the shape of the sedimentation-front

To achieve rapid sedimentation and minimize diffusion, we altered the centrifugal field stepwise. We plotted the deviated sedimentation front after the solution was already considerably depleted of particles < 3 nm (Fig. 3). To calculate the nominal time required for particles > 3 nm to sediment, we calculated the change in particle size over time, assuming a mean sedimentation velocity (parameters see Table 2).

$$\frac{dr}{dt} = \frac{d^2 \cdot (\rho_P \cdot \rho_f)}{18 \cdot \eta} \cdot (2 \cdot \pi \cdot d)^2 \cdot r \qquad (1)$$

The sedimentation time is observed after integration (from $t_0 = 0$ to t_A and r_0 to r_i):

$$t_A = \frac{18 \cdot \eta}{d^2 \cdot (\rho_P \cdot \rho_f)(2 \cdot \pi \cdot \eta)^2} \cdot \ln\left(\frac{r_0}{r_i}\right) \qquad (2)$$

Following Fig. 3 the sedimentation can be sufficiently suppressed using a centrifugal force of 63,504 g while higher centrifugal fields showed no further changes. Therefore, we decided to measure Au NPs with a mean diameter < 3 nm at 63,504 g (equals 30,000 rpm in the Beckman optima XL-I, 8-channel rotor) as it constitutes the ideal compromise eliminating diffusion, while further

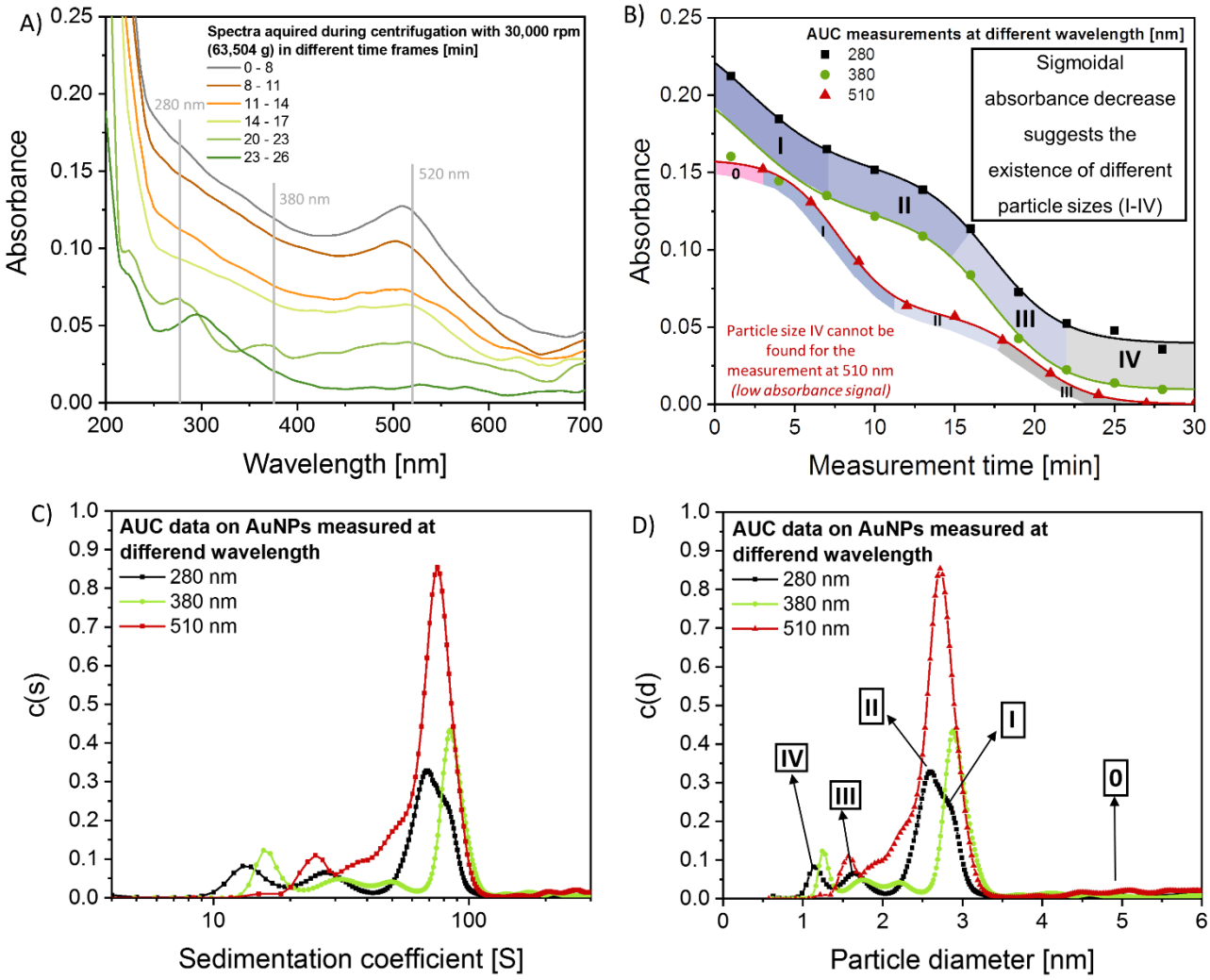

***Figure 4**: A) Absorption spectra (measured at r = 6.5 cm) at different times during AUC after acceleration to 30000 rpm B) Absorption (measured at 280 nm, 380 nm, 510 nm) of the measured sample over time. C) Concentration distribution of the sedimentation coefficient determined after measurement at 3 different wavelengths. D) Size distribution calculated from this (density of bulk Au used*

limitations of the measurable size-range due to even higher rotations speeds can be avoided.

Influence of the absorbance wavelength on the measurable s-value range

While plasmonic Au NPs absorb almost over the entire UV-Vis range with special regions near the interband and ~520 nm (surface plasmon resonance), protoplasmic and fully inorganic Au NPs absorb particularly well in the UV range[5], which requires a careful choice of the wavelength that we use for the detection of the sedimentation velocity. To select the optimal wavelength for laser-generated Au NPs, we used AUC to perform absorbance scans between 200 and 700 nm at different times at a fixed radial position while performing centrifugation with 63,504 g. The results are shown in Fig. 4A. During the first 8 minutes, an absorption spectrum typical for Au NPs is obtained. The next measurements already show a slight blue-shift of the SPR (from 510 nm to 502 nm) until the SPR disappears completely after about 20-23 min. Instead, we observe absorption behavior that is typical for inorganic Au NCs [see Ref.[5] and Fig. S1A)].

In order to find a wavelength at which both plasmonic and protoplasmic AuNPs can be measured, we have carried out measurements at 3 different wavelengths (280 nm, 380 nm, 510 nm).

In all three cases, a clear sedimentation front can be detected. However, the maximum measured absorption at the plateau is different and changes i) with the excitation wavelength and ii) over time (Raw data can be found in Fig. S1). Figure 4B shows the relationship between maximum absorption at the plateau, the excitation wavelength and the measurement time and we observe a sigmoidal decrease of the absorbance over time for all excitation wavelengths. It can be assumed that as soon as the solution is depleted of one particle size (complete centrifugation), the absorption is dominated by another particle size (whose absorption is lower). A rapid decrease in absorption thus indicates sedimentation of, e.g., species I. At a certain time point, the slope decreases, indicating a signal superposition of two similarly absorbing but differently fast sedimentation species occurs until the solution is finally depleted of species I and the sedimentation behavior is dominated by species II. While the curves measured at 380 nm and 280 nm are comparable, the curve measured at 510 nm shows a clear deviation (Fig. 4C) and would measure a distinguishable different sedimentation behavior in contrast to the other wavelength. The sedimentation was then evaluated with the license-free software sedfit (Fig. 4C), and we plotted the sedimentation concentration ($c(S) = dc/dt$) assuming a frictional ratio of 1 and the specific volume of bulk gold. The c(S) distribution describes the changes in the sedimentation concentration over time and can be described using the Lamm equation, which is the basic equation for all AUC experiments.[12]

$$\frac{dc}{dt} = \frac{1}{r} \cdot \frac{d}{dr} \cdot (r \cdot D \cdot \frac{dc}{dr} - s \cdot \omega^2 \cdot r^2 \cdot c) \qquad (3)$$

While we are able to detect a broad S-value range using 280 nm and 380 nm excitation (~8 - 300 S), the measurement at 510 nm cannot resolve s-values < 20 S. If the distributions in Fig. 4C are examined in more detail, further differences become obvious. For example, the resolution of S-values between 40 and 100 S is higher at 280 nm, which we attribute to the

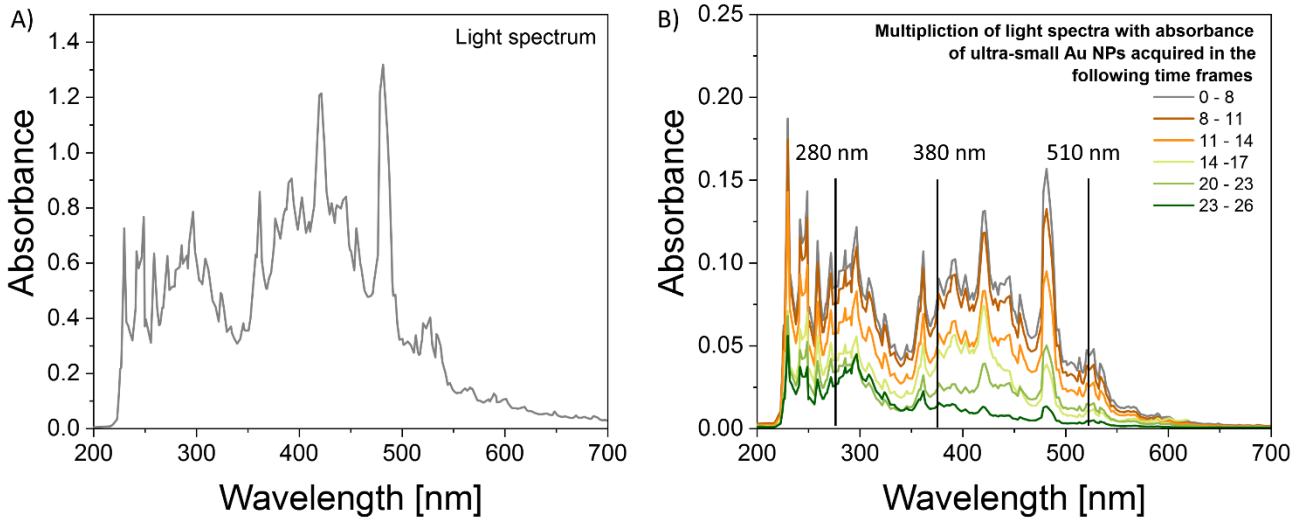

Figure 5: *Light spectra of the AUC device. Lamp spectra multiplicated with the absorbance spectra in Fig. 4A.*

higher absorption measured at this wavelength (Figure 5A). In the next step, we converted the S-value distribution into a particle size distribution assuming the validity of Stokes' law and the density of bulk gold using the following equation, which was already described by Svedberg in 1924.[13]

$$d_i = \sqrt{\frac{18 \cdot \eta \cdot s_i}{\rho_P - p_f}} \quad (4)$$

The calculated particle size distributions can be found in Fig 4D, and we clearly observe the number of size fractions that we already expected in Fig. 4B.

In summary, laser fragmented gold colloids that include plasmonic and protoplasmonic particles, are analyzed best by AUC with an excitation wavelength at 280 nm or 380 nm. Note that besides the absorbance behavior, the lamp spectra (Figure 5A) must be considered. Following ref.[14], the latter shows certain peaks which intensity changes over time. While a fresh lamp shows dominant peaks in the UV, an aged lamp can show dominant features in the visible range. If the absorption behavior of all (sub-) species is known, they can be additionally aligned with the lamp spectrum to determine a measuring wavelength for other materials. We demonstrated this in Figure 5B for the Au colloid discussed above. With increasing run time, the absorbance is dominated by the NC observable by a clear absorbance in the UV range. While initially, the strongest signal could be observed around 490 nm, after some minutes, the signal around 300 nm starts dominating. Note that we will not consider measurements at the peak maximum around 240 nm as this will be overshadowed by anions that are possible in solution for stabilization. With this, we can conclude that the altered absorbance behavior of ultra-small Au NPs accompanied by aging of the lamp makes it difficult to find a suitable measurement wavelength. However, the measurement at 280 nm works well, and we are may able to improve the signal strength by switching to a wavelength of 300 nm.

So far, we have focused on measurement parameters that can be set by the device itself; however, we will see in the next chapter that surface charges adjustable by the pH value can also influence the sedimentation behavior.

Influence of surface charges on the sedimentation behavior

As already mentioned above, the sedimentation coefficient can be influenced by surface charges as those give a repulsive inter-particle force, which counteracts the sedimentation. This point is of particular importance in the characteristics of laser-generated NP in the aqueous milieu, as LFL leads to an oxidized surface which enables the adsorption of anionic species.[15] In the case of Au NPs in H_2O, the surface carries OH/O^- groups which show a pH-depended equilibrium. In this work, we used colloids at a pH of 11, where we expect that the majority of OH groups at the surface are deprotonated[16], which leads to good colloidal stability caused by electrostatic repulsion. However, surface charge density possibly influenced the sedimentation behavior. To check this, we altered the pH value by adding HCl, which should lead to protonation of O^- at the surface. We have only slightly changed the pH range to prevent aggregation of the particles. We tracked the number of surface charges by zeta potential measurements, which allow a statement on electrostatic field strength at the slipping plane (while we measure the electrophoric mobility). Following Ref.[17], we were able to calculate the surface charge density (Table 1). Subsequently, multiplication by the total surface of one particle (assuming a mean particle diameter of 2.9 nm) divided by the elementary charge gives the total number of negative charges on the particle surface. Although we only slightly varied the pH value, we reduced the number of surface charges per particle by nearly 40 % (from -3.8 to -2.3). We measured both colloids using the above-discussed parameters (30,000 rpm, 280 nm) and plotted the detected c(s) distributions in Fig. 6.

Table 1: *Summary of the investigated charge properties at the different pH values. The zeta potential was measured using a Malvern nano z, followed by a calculation of the surface charge density according to Ref.[17].*

	pH 11	pH 9.9
Zeta potential [mV]	-80	-50
Surface charge density [C/m²]	$-31 \cdot 10^{-3}$	$-19 \cdot 10^{-3}$
Negative surface charges per particle	-3.8	-2.3

Following Fig. 6, a decrease of the surface charges by 40% leads only to small changes in the hydrodynamic particle size distribution.

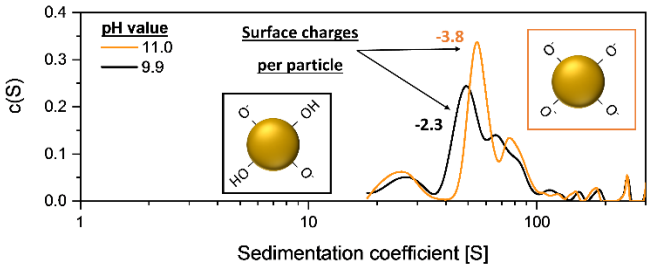

Figure 6: *Sedimentation coefficient of AuNPs after LFL measured at different pH values.*

With increasing surface charges per particle, the AUC detects slightly larger sedimentation coefficients which is referable to the higher number of negative charges which posse a repulsive interplay force. However, the changes are small, and will not be further considered.

This work is a basic building block for the following chapters as the AUC will turn out to be an important method for the size characterization of ultra-small Au NCs in the following. We evaluated the influence of the centrifugal speed on the shape of the sedimentation-front, the influence of the absorbance wavelength on the measurable s-value range, and the influence of surface charges on the overall sedimentation behavior. We extracted the following parameters to be general useful for colloids which contain Au NCs and small Au NPs:

Table 2*: Enumeration of parameters important in this work. Variable parameters have been discussed in the chapter title and are summarized here (red: sample-dependent parameters, black: constants).*

Parameter	**Value or range for which this work is suitable** *(not all parameters are known)*
r = rotor radius	6.4 cm
r_0 = rotor radius (cell bottom)	
r_i = rotor radius (meniscus)	
t = centrifugal time	0 - 64 min
d = particle diameter	0.5 – 4 nm
ρ_P = particle denisty	19.32 g/cm^3
ρ_f = fluid density	0.997 g/cm^3
η = fluid viscosity	1 cP
t_A = sedimentation time	
c = local concentration	< 7.5 mg/L
t = time	< 12 h
D = Diffusion coefficient	
s = sedimentation coefficient	
ω = rotor angular velocity	

References

(1) Svedberg, T.; Nichols, J. B. Determination of size and distribution of size of particle by centrifugal methods, *J. Am. Chem. Soc.* **1923**, *45* (12), 2910–2917. DOI: 10.1021/ja01665a016.

(2) Lebowitz, J.; Lewis, M. S.; SCHUCK, P. Modern analytical ultracentrifugation in protein science: a tutorial review. *Protein science : a publication of the Protein Society* **2002**, *11* (9), 2067–2079. DOI: 10.1110/ps.0207702.

(3) Liu, J.; Andya, J. D.; Shire, S. J. A critical review of analytical ultracentrifugation and field flow fractionation methods for measuring protein aggregation. *The AAPS journal* **2006**, *8* (3), E580-9. DOI: 10.1208/aapsj080367. Published Online: Sep. 22, 2006.

(4) Cölfen, H., Ed. *Analytical Ultracentrifugation V*; Progress in Colloid and Polymer Science; Springer Berlin Heidelberg, 1999. DOI: 10.1007/3-540-48703-4.

(5) Anna. R. Ziefuss, Torben Steenbock, Dominik Benner, Melissa Teubner, Christoph Rehbock, Clothilde Zerbino, David Amans, Indranath Chakraborty, Gabriel Bester, Michael Rübhausen, Wolfgang J. Parak, Stephan Barcikowski. *Photoluminescence of fully inorganic colloidal gold nanocluster and their manipulation using surface charge effects*, 2020 (unpublished).

(6) Waag, F.; Li, Y.; Ziefuß, A. R.; Bertin, E.; Kamp, M.; Duppel, V.; Marzun, G.; Kienle, L.; Barcikowski, S.; Gökce, B. Kinetically-controlled laser-synthesis of colloidal high-entropy alloy nanoparticles. *RSC Adv.* **2019**, *9* (32), 18547–18558. DOI: 10.1039/C9RA03254A.

(7) Letzel, A.; Santoro, M.; Frohleiks, J.; Ziefuß, A. R.; Reich, S.; Plech, A.; Fazio, E.; Neri, F.; Barcikowski, S.; Gökce, B. How the re-irradiation of a single ablation spot affects cavitation bubble dynamics and nanoparticles properties in laser ablation in liquids. *Applied Surface Science* **2019**, *473*, 828–837. DOI: 10.1016/j.apsusc.2018.12.025.

(8) Ziefuß, A. R.; Barcikowski, S.; Rehbock, C. Synergism between Specific Halide Anions and pH Effects during Nanosecond Laser Fragmentation of

Ligand-Free Gold Nanoparticles. *Langmuir,* **2019**, *35* (20), 6630–6639. DOI: 10.1021/acs.langmuir.9b00418.

(9) Ziefuß, A. R.; Haxhiaj, I.; Müller, S.; Gharib, M.; Gridina, O.; Rehbock, C.; Chakraborty, I.; Peng, B.; Muhler, M.; Parak, W. J.; Barcikowski, S.; Reichenberger, S. Origin of Laser-Induced Colloidal Gold Surface Oxidation and Charge Density, and Its Role in Oxidation Catalysis. *J. Phys. Chem. C* **2020**, *124* (38), 20981–20990. DOI: 10.1021/acs.jpcc.0c06257.

(10) Cölfen, H.; Völkel, A. Analytical ultracentrifugation in colloid chemistry. In *Analytical Ultracentrifugation VII*; Lechner, M. D., Börger, L., Eds.; Springer Berlin Heidelberg, 2004; pp 31–47. DOI: 10.1007/b98011.

(11) Planken, K. L.; Cölfen, H. Analytical ultracentrifugation of colloids. *Nanoscale* **2010**, *2* (10), 1849–1869. DOI: 10.1039/c0nr00215a.

(12) Stafford, W. F. [22] Boundary analysis in sedimentation velocity experiments. In *Part B: Numerical Computer Methods*; Methods in Enzymology; Elsevier, 1994; pp 478–501. DOI: 10.1016/S0076-6879(94)40061-X.

(13) Svedberg, T.; Rinde, H., The ultracentrifuge, a new instrument for the determination of size and distribution of size of particles in amicroscopic colloids, *J. Am. Chem. Soc.* **1924**, *46* (12), 2677–2693. DOI: 10.1021/ja01677a011.

(14) Greg Ralston. *Introduction to analytical ultracentrifugation*.

(15) Merk, V.; Rehbock, C.; Becker, F.; Hagemann, U.; Nienhaus, H.; Barcikowski, S. In situ non-DLVO stabilization of surfactant-free, plasmonic gold nanoparticles: effect of Hofmeister's anions. *Langmuir : the ACS journal of surfaces and colloids* **2014**, *30* (15), 4213–4222. DOI: 10.1021/la404556a.

(16) Pfeiffer, C.; Rehbock, C.; Hühn, D.; Carrillo-Carrion, C.; Aberasturi, D. J. de; Merk, V.; Barcikowski, S.; Parak, W. J. Interaction of colloidal nanoparticles with their local environment: the (ionic) nanoenvironment around nanoparticles is different from bulk and determines the physico-chemical properties of the nanoparticles. *Journal of the Royal Society, Interface* **2014**, *11* (96), 20130931. DOI: 10.1098/rsif.2013.0931. Published Online: Apr. 23, 2014.

(17) Makino, K.; Ohshima, H. Electrophoretic mobility of a colloidal particle with constant surface charge density. *Langmuir,* **2010**, *26* (23), 18016–18019. DOI: 10.1021/la1035745.

3.2 – PART I

Synthesis of ultra-small gold nanoparticles

by

pulsed laser fragmentation

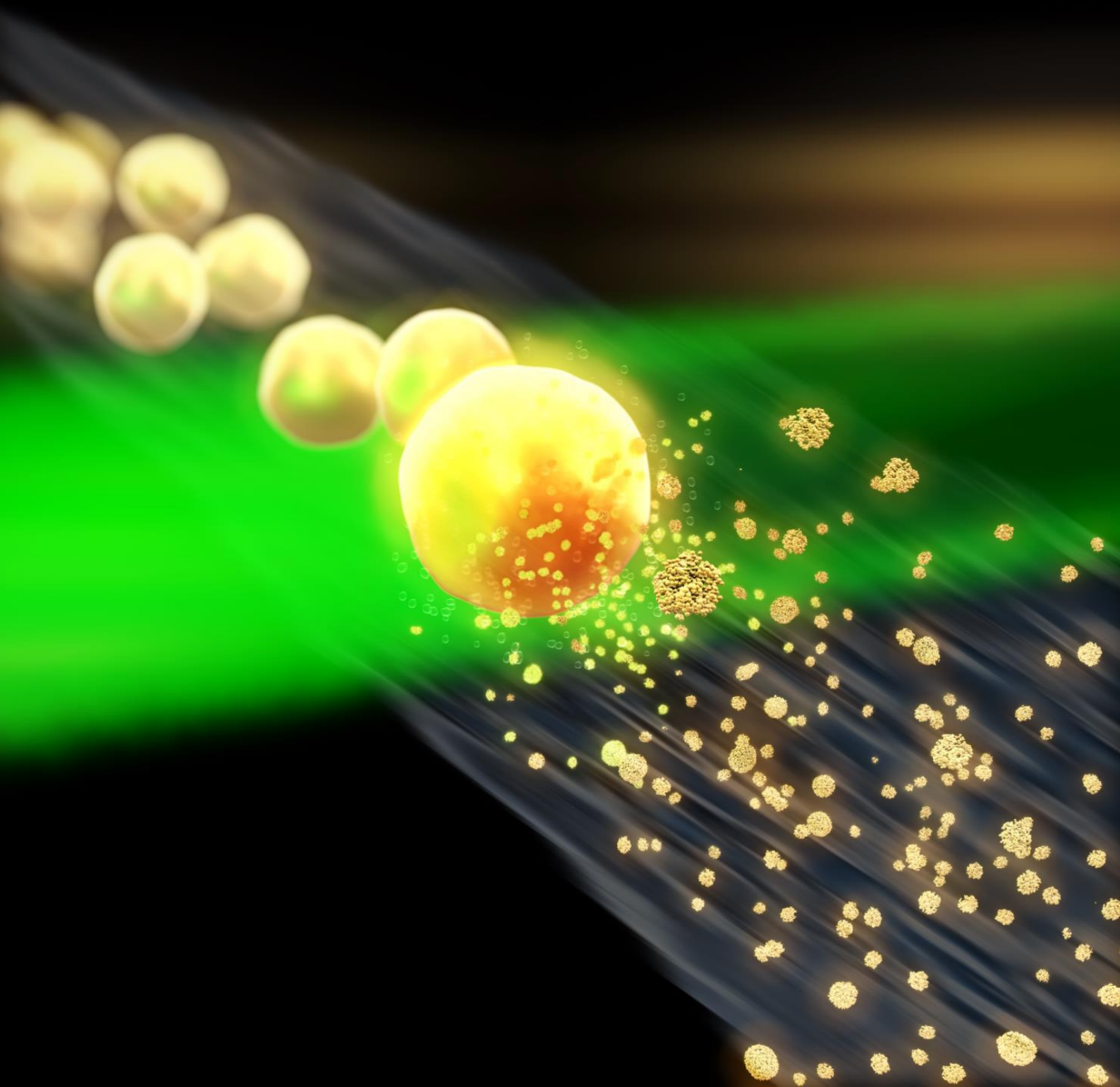

3.2.1 Laser fragmentation of colloidal gold nanoparticles with high-intensity nanosecond pulses is driven by a single-step fragmentation mechanism with defined educt particle size threshold

Synopsis:

Pulsed laser fragmentation in liquid is a useful tool to control the particle size of laser-fabricated nanoparticles, but adequate process control requires a proper understanding of the underlying mechanisms. Typically, the pulse duration is discussed as a decisive criterion ruling the fragmentation process. Commonly, distinctions are made between electronically-induced Coulomb explosion for high laser peak powers (ultrashort pulses) and thermally-induced evaporation for low laser peak powers (ns-pulses at moderate intensities). For the fragmentation with high-intensity ns pulses, however, the mechanism is poorly understood. While photothermal mechanisms are often assumed with the electrons and the lattice being in thermal equilibrium, ejection of electrons was also reported.

In this work, we systematically examine the pulsed laser fragmentation of gold nanoparticles in liquids with high-intensity picosecond and nanosecond pulses, varying the educt particle size, the number of pulses, and the laser intensity. All experiments were carried out in a liquid flow passage reactor, which allows precise control of the energy input per gold colloid volume. We could conclusively prove for the first time that the fragmentation process of gold nanoparticles is a one-pulse and one-step event, yielding monomodal ultra-small nanoparticles in case a pulse peak power of 1.62×10^{12} W/m^2 is exceeded, and all educt particles are larger than 13.4 ± 2.1 nm. For lower peak powers, we found a bimodal size distribution, which can be explained by theoretical calculations. Furthermore, we found strong evidence that the number of irradiation cycles can be used to tune the surface charge density of the resulting ultra-small nanoparticles in an aqueous medium, which was verified by titration curves and zeta potential measurements.

This paper was published in the Journal of Physical Chemistry C on August 30, 2018.

THE JOURNAL OF PHYSICAL CHEMISTRY C

Article

Cite This: J. Phys. Chem. C 2018, 122, 22125–22136

pubs.acs.org/JPCC

Laser Fragmentation of Colloidal Gold Nanoparticles with High-Intensity Nanosecond Pulses is Driven by a Single-Step Fragmentation Mechanism with a Defined Educt Particle-Size Threshold

Anna R. Ziefuß,[†] Sven Reichenberger,[†] Christoph Rehbock,[†] Indranath Chakraborty,[‡] Mustafa Gharib,[‡] Wolfgang J. Parak,[‡] and Stephan Barcikowski*[,†]

[†]Technical Chemistry I and Center for Nanointegration Duisburg-Essen (CENIDE), University of Duisburg-Essen, Universitaetsstrasse 7, 45141 Essen, Germany

[‡]Fachbereich Physik und Chemie, and Center for Hybrid Nanostructure (CHyN), Universität Hamburg, 22761 Hamburg, Germany

Supporting Information

ABSTRACT: Laser-inducd fragmentation is a promising tool for controlling the particle size of ligand-free colloidal nanoparticles and to synthesize ligand-free gold nanoclusters. However, because the underlying mechanisms are not fully understood, increasing the yield of this process remains challenging. In this work, we examine the pulsed laser fragmentation of gold nanoparticles in liquid under statistical single-pulse conditions with high-fluence nanosecond pulses and correlate them with the educt particle size, number of pulses, and laser fluence. We conclusively prove that the fragmentation process of gold nanoparticles is a one-pulse and one-step event, which yields monomodal particles of ≪10 nm down to 2.8 +/- 0.1 nm when exceeding a pulse peak power of 1.6×10^{12} W/m^2 and when all educt particles are larger than 13.4 nm. This size threshold for quantitative fragmentation fits well with the size limit of 13.1 nm calculated with respect to the evaporation–heat–energy balance. Furthermore, we found strong evidence that the number of irradiation cycles, varied within the regime of one to four laser pulses/colloid volume, can be used to tune the surface chemistry and surface charge of the resulting nanoparticles in an aqueous medium.

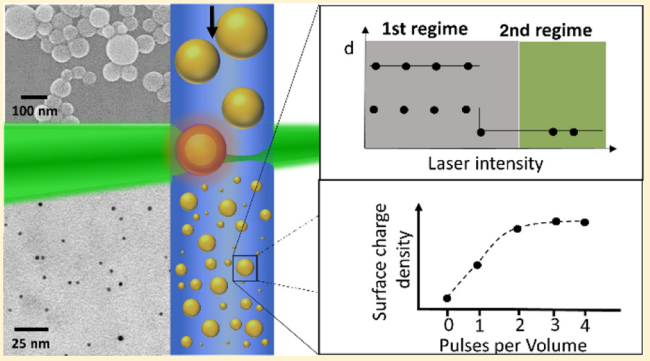

INTRODUCTION

Plasmonic gold nanoparticles (AuNPs) are of great interest in the fields of biology and medicine[1−3] as well as in catalysis research,[4−8] particularly due to their respective optical and selective oxidation properties. On the other hand, protoplasmonic gold nanoparticles (NPs) smaller than 3 nm, which are often called nanoclusters, can function as fluorophores because of their unique photoluminescence properties[9−11] or even affect the local crystal structure of support materials like TiO_2.[6]

The laser-based production of AuNPs is an emerging technique within these fields of research and is yielding crystalline particles of high purity.[12−14] The surfaces of these particles carry no surfactants or only those that are desired, which makes them useful in both biological and catalytic applications. This is because the toxic cross effects from surfactants or their respective residuals after calcination, which can limit cell proliferation or catalytic reactions, can be efficiently avoided.[1,5,15,16] However, as pulsed laser ablation in liquids (LALs) generally yields AuNPs with broad size distributions, their targeted size adjustment and the generation of monomodal particle fractions is of great interest. A commonly applied approach for reducing the polydispersity of colloids synthesized by the LAL method is *in situ* salt quenching.[17,18] In this process, a low concentration of chaotropic anions is added to the liquid used during LAL, which electrostatically stabilizes the AuNPs during the growth process and leads to smaller particles (about 5 nm) with narrow size distributions.[17,18] However, this method cannot be used to synthesize AuNPs with average sizes <5 nm.[18] An alternative approach is the post irradiation of AuNPs produced by LAL with pulsed lasers, which induces a size reduction by a process termed pulsed laser fragmentation in liquids (LFLs).[13,19−21] The use of LFL to generate AuNPs <3 nm (gold nanoclusters) has been studied by several groups.[19,20,22] In 2014, Lau et al. reported the advantages of oxidative LFL and showed that the choice of suitable inorganic additives

Received: May 14, 2018
Revised: August 29, 2018
Published: August 30, 2018

leads to a product that contains these ultrasmall nanoparticles.[20]

The laser-induced excitation of AuNP for "nanobubble" formation was well established both theoretically and experimentally by Hashimoto[23] and Baffou,[24] including its size–fluence threshold effects. The mechanism of LFL, which naturally includes high fluences, has also been investigated[13,20,23,25] but as yet is much less well understood. In particular, the influence of educt particle size and pulse number effect on the efficiency of LFL have not yet been addressed in detail. We know that when a plasmonic gold nanoparticle absorbs a laser pulse of resonant wavelength (e.g., 532 nm wavelength in the case of AuNPs), various processes occur. In the following discussion, we list a series of sequences without going into detail regarding their superimposition occurrence. In the first step, the electrons absorb the laser pulse through an inverse bremsstrahlung mechanism,[26] in which thermally excited electrons interact with the cold conduction-band electrons of the material via scattering. A thermal equilibrium of the electrons occurs, which yields hot electrons and a cold lattice before electron–phonon coupling occurs. Finally, the energy and temperature of the lattice increases and is partially released into the medium due to heat transfer processes.[23,27] The reduction in particle size can be predicted by considering different experimental parameters. Typically, the pulse peak power, comprising the laser fluence (driving force) and the pulse duration (energy transfer kinetics), is considered to be the decisive criterion. In the case of picosecond (ps) or even femtosecond (fs) laser pulses, a huge fraction of the absorbed pulse energy is taken up by the electrons before electron–phonon relaxation occurs (ultrashort pulses), thus strongly increasing the kinetic energy of the electrons (electron temperature). If the peak intensity (laser fluence divided by pulse duration) exceeds a certain threshold, electrons can overcome the work function of the gold and be ejected from the nanoparticle, which can induce a so-called Coulomb explosion (CE).[28] Due to the electron deficiency, a positively charged particle remains, which undergoes spontaneous fission once the Coulomb forces exceed the cohesive forces of the particle.[23,27] Researchers have reported that the size of the resulting particles after a CE is only dependent on the properties of the colloid (concentration and matrix) and does not scale with the laser fluence once the onset threshold for the CE is exceeded.[20,29] On the other hand, if the temperature within the particle becomes slightly higher than the boiling temperature of gold[30] and the laser pulse duration is long enough to allow the electrons and the lattice to reach thermal equilibrium, a photothermal mechanism for size reduction has also been observed and reported in the literature, known as the heating–melting–evaporation (HME) mechanism.[23,25,27,28] Accordingly, during nanosecond (ns) pulse irradiation, the electron–phonon and the electron–electron relaxation for gold occur on time scales more than 2–3 orders of magnitude shorter than the pulse duration so this mechanism is suspected to be dominant during fragmentation with ns pulses.[23,31] Since the boiling process is very slow in terms of ns time scales, with removal rates of less than 0.1 monolayers per ns, superheating of the nanomaterial must be considered.[30,32] Once the temperature of the educt particle exceeds the spinodal temperature[24] in a range of ~80[33] to ~90% of the critical temperature,[30,32,34] explosive boiling of the superheated liquid droplet is likely to occur. To date, this mechanism has only been discussed in terms of laser ablation[32−34] or fundamental theory[30] and has rarely been addressed as a potential laser fragmentation mechanism. According to Miotello and Kelly, the essence of phase explosion is the homogeneous nucleation of vaporous material throughout the molten ablation zone once the spinodal temperature is reached,[30] which leads to ejection and spillage[30,32−34] and the formation of bimodal size distributions.[34] To the best of our knowledge, this scenario has not been modeled in terms of a fragmentation process of spherical nanomaterials. Hence, we can only speculate whether bimodal or monomodal size distributions occur in this case. Additionally, the laser intensity threshold at which the fragmentation mechanism changes from an HME mechanism to phase explosion is yet to be addressed. Pyatenko et al. calculated that the minimum laser intensity for the CE of AuNPs is 1.50×10^{12} W/m^2 (λ = 532 nm, $d_{particle}$: 50–100 nm) when the laser beam is focused on the liquid jet.[32] It is difficult to calculate the electron temperature of the particles along the focused laser beam and to do so requires many assumptions, so a complete CE can only be initiated at a laser intensity of 10^{13} W/m^2 (λ = 532 nm, $d_{particle}$: 50–100 nm),[33] which is in the range of common ps-laser pulses rather than ns-laser pulses. However, Yamada et al. observed the ejection of photoelectrons during irradiation with ns pulses and thus concluded that a CE had occurred.[28] On the basis of the above reports, we conclude that the mechanism of LFL by ns pulses is yet to be fully understood.

To resolve this knowledge gap and elucidate the fragmentation mechanism, using a liquid-flow setup, we performed a series of systematic experiments in which we varied both the laser peak intensity and the educt particle size during ns-laser LFL in steady-state conditions. By analyzing the size distributions of the AuNP products, we first verified that quantitative laser fragmentation of AuNPs requires a fluence-dependent, minimal educt particle size. Next, we determined that this is a one-step mechanism that produces monomodal product particles with complete conversion, ideally with high portions of protoplasmonic particles with diameters of <3 nm.

EXPERIMENTAL METHODS

Pulsed Laser Irradiation of Gold Nanoparticles in Liquid. In our experiments, for use as educt colloids, ligand-free AuNPs with different size distributions are required, which we produced by pulsed laser ablation in water (LAL) using a Nd:YAG laser (Ekspla, Atlantic series, 10 ps, 1064 nm, 9.6 mJ, 100 kHz, 10 min) and subsequent centrifugation. We calculated the centrifugal parameters for particle size separation on the basis of the Svedberg equation and obtained different particle sizes by the fractional centrifugation of the same colloid in multiple consecutive steps. From the pellet, we isolated particle fractions with the desired size and then exposed the supernatants to further centrifugation steps at a higher *g*-force and longer centrifugation times, as specified in Table 1.

We determined the particle concentrations after centrifugation by inductively coupled plasma mass spectrometry (ICP-MS; PerkinElmer Sciex-ELAN 6000). Prior to the fragmentation experiments, we diluted all the resulting colloids to a universal mass concentration of 7.5 mg/L. Each sample also contained 0.3 mM NaOH and 0.3 mM NaCl. We performed the LFL in a free liquid jet using two ns lasers (high and low repetitions rates) and a ps laser. The two ns lasers have similar intensities but differ in their maximal repetition rates (RRs) by

DOI: 10.1021/acs.jpcc.8b04374
J. Phys. Chem. C 2018, 122, 22125–22136

Table 1. Summary of Post Synthesis Centrifugation Parameters Used To Synthesize Gold Nanoparticles with Different Particle Diameters after LAL,[a] as Educt Particles for LFL

Centrifugation force (g)	centrifuge time (min)	particle diameter after centrifugation (nm)
16.8	15	67
67.1	70	53
268.3	20	40
268.3	60	25
603.7	60	19
3286.92	30	13

[a] x_c value of the mass weighted determined diameter by analytical disc centrifuge (ADC).

a factor of 20, and the ps laser provides a 1000 times higher intensity as well as a high repetition rate (Table 2).

The setup of the liquid jet reactor, which is described elsewhere in more detail,[34,35] is shown in Figure 1.

We used a cylindrical lens to focus the laser beam at a perpendicular angle. The liquid beam was located 1.5 cm in front of the focus to guarantee the complete illumination of the 1.1 cm liquid jet. The irradiated areas (detected by a picture of the spot on photo paper) are 5.7×10^{-6} m^2 for the "ns-low RR," 7.8×10^{-7} m^2 for the "ns-high RR," and 3.9×10^{-7} m^2 for the "ps-high RR," which produce fluences of (a) 1.5 J/cm^2 (unless otherwise stated), (b) 2 J/cm^2, and (c) 0.03 J/cm^2. We can calculate how often a laser pulse hits a colloid volume element by considering the flow rate, the area of the liquid jet (as determined from this analysis of the liquid jet), and the repetition rate of the laser. The volume flow rate was kept constant at 6.0×10^{-7} m^3/s throughout all experiments, which was made possible by the use of a Mariotte's bottle. For this purpose, the reactor was closed by a perforated plug into which we fitted a capillary. In each passage of ns-low RR, one volume element is hit exactly once, but at ns-high-RR (which has a smaller beam diameter), the number of pulses per volume element is 1.7. We can calculate how often a laser pulse hits a colloid volume element by the residence time of the colloid in the irradiated volume multiplied by the laser repetition rate. Specifically, this calculation considers the liquid-flow velocity, the height of the irradiated section, and the repetition rate of the laser. As the energy per pulse is known, we can calculate the energy per particle as well, together with the number of laser pulses per volume. Due to attenuation of the energy density by the absorption and scattering processes of the colloid, we can assume that particles along the beam propagation direction will no longer be illuminated at full power so that all given fluence values can be seen as an upper limit. Hence, a value of 1 nominal pulse per volume (PPV) guarantees an equal number of pulses per particle but cannot guarantee that every particle is illuminated with the same energy density. To eliminate these attenuation effects, we used comparably small concentrations of the colloids (7.5 mg/L). As has been recently quantified, laser beam refraction at the curved liquid jet leaves a small volume fraction unirradiated.[36] Hence, increasing yield can be achieved by multiple passages so that every preceding fragmentation included four cycles (passages), unless otherwise stated. The interval between these passages is around 10−20 s. We also note that the liquid jet runs continuously for 6.4 cm after leaving the capillary and then begins to disintegrate into separate droplets. Fragmentation takes place ∼1 cm after the liquid jet has left the capillary. Within the capillary, we calculated the Reynolds number to Re = 779, yielding laminar flow conditions. As soon as the liquid jet leaves the capillary, gravitational forces play an important role and the liquid jet gradually goes into free fall-like profile. Once gravitational forces become large compared with inertial forces (proportional to the flow rate), the laminar velocity profile of the liquid jet converges toward a plug flow-like velocity profile of a falling liquid. The influence of gravitation can be estimated by the dimensionless Froud number. In our case, Fr^2 = 4 (1 cm behind the nozzle) is calculated. Accordingly, near-free-fall conditions are present and the velocity profile is already plug flow-like. Hence, the nanoparticles pass the irradiated area with nearly the same residence time and single-pulse conditions are valid.

Characterization Methods. We measured the absorbance of the educt and product particles on a Thermo Scientific (Evolution 201) UV/vis spectrometer in a wavelength range from 190 to 900 nm. We measured the hydrodynamic particle size with an analytical disk centrifuge (ADC, CPS Instrument DC 24000) at 24 000 rpm, 10 min after LFL. The measured volume for each sample was 0.1 mL, and the measurement time was 25 min. To demonstrate the quality of the ADC, we also used an analytical ultracentrifuge (AUZ, Beckman Coulter, Proteomelab XL-I) to determine the hydrodynamic particle diameter, in which the rotor rotation force was 16 350g and we recorded 250 absorption data points at a wavelength of 520 nm. We determined the Feret diameter by the manual measurement of particles in the transmission electron microscopy (TEM) images acquired on a Zeiss EM 910 transmission electron microscope, using a 5 μL sample volume prepared on a carbon-coated copper 400-mesh grid. We manually measured the particle diameters from the images (1000 in each case) with the assistance of ImageJ software. For the titration curves, we used 0.1 M HCl and 0.1 M NaOH solutions. After fragmentation, we treated 1 mL of the colloids with 30 μL of NaOH to achieve a more alkaline pH. We added the HCl in 2 μL steps while simultaneously recording the pH value. To quantify the stability of the particles against the addition of salt, we measured the hydrodynamic particle diameter using a Malvern Zetasizer Nano Z, after the addition of eight different concentrations of NaCl (purchased from Roth).[37]

In the experiments, we performed fragmentation at a laser wavelength of 532 nm. Under these conditions, plasmonic AuNPs have their highest extinction cross section, compared to

Table 2. Specification of Laser Parameters for the Lasers Used[a]

manufacturer	type	τ	RR (Hz)	λ (nm)	I (W/m^2)	fluence (J/cm^2)
ns-low RR	innolas	9 ns	100	532	1.6×10^{12}	1.6
ns-high RR	edgewave	7 ns	2000	532	2.8×10^{12}	2
ps-high RR	edgewave	10 ps	80 000	532	1.6×10^{15}	0.03

[a] Specified are the pulse duration (τ), repetition rate (RR), wavelength (λ), laser intensity (I) and the laser fluence.

DOI: 10.1021/acs.jpcc.8b04374
J. Phys. Chem. C 2018, 122, 22125−22136

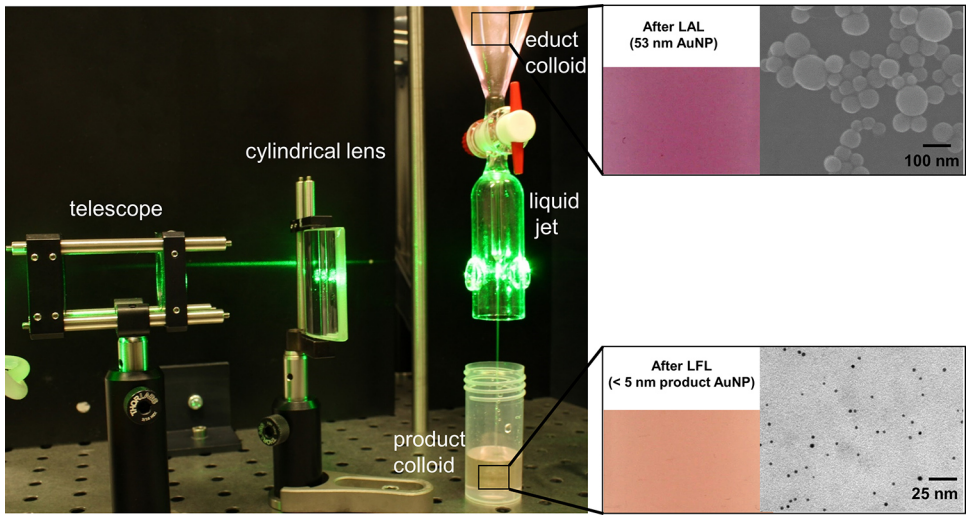

Figure 1. Setup of the ns-laser fragmentation process in liquid on 53 nm educt particles, as an example. The insets show an scanning electron microscopy image of the educt particles (top) and an exemplary transmission electron microscopy (TEM) image of the ultrasmall particles after laser fragmentation (bottom).

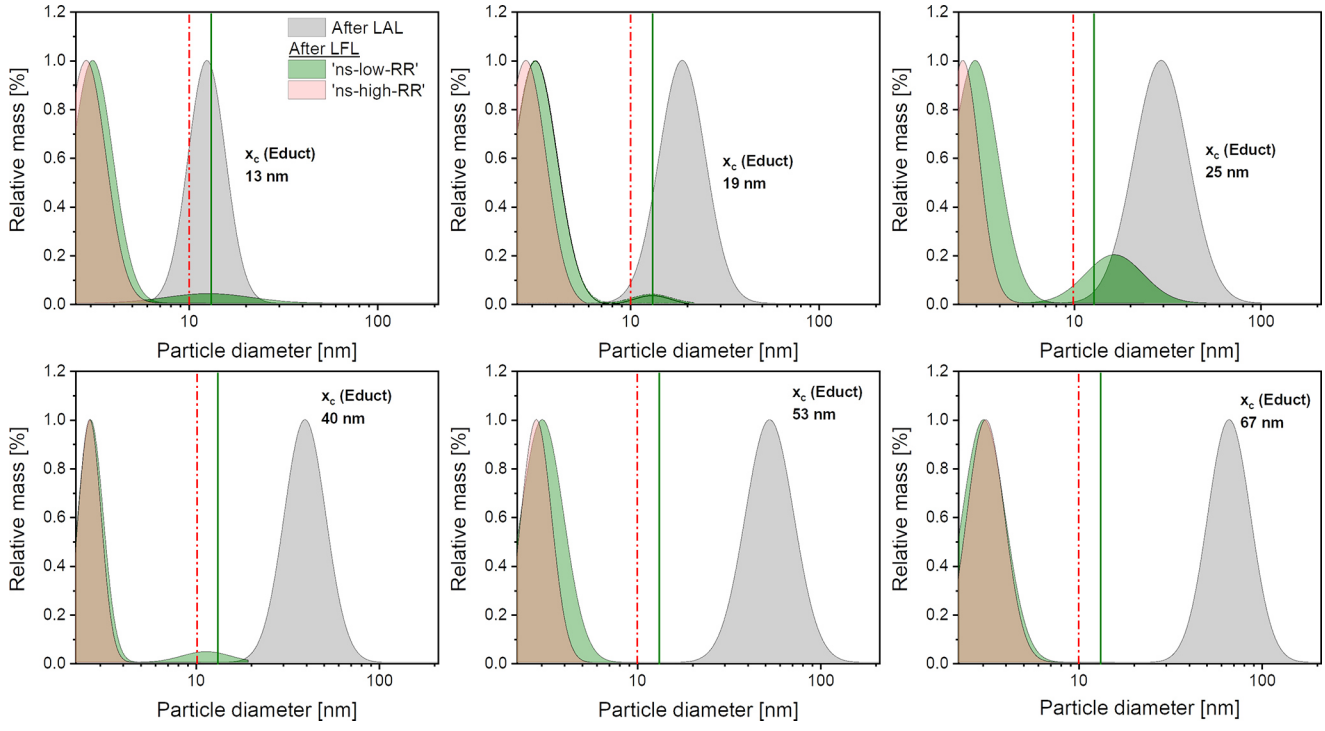

Figure 2. Effect of educt hydrodynamic diameters of gold nanoparticles after LAL and centrifugation (gray) on fragmentation by LFL with two different lasers (green and brown). The particles after LAL were used as starting material for LFL. The size (x_c value of the mass-weighted distributions) of these educt nanoparticles increases in (A)−(F) from 13 to 67 nm. The continuous green line indicates the smallest calculated nanoparticle (NP) diameter that can be evaporated, on the basis of temperature calculations using ns-low RR (green). The dashed line indicates the corresponding value for the ns-high RR laser (brown).

1064 or 355 nm as reported in the literature,[38,39] and consequently, high fragmentation efficiencies are to be expected.[40−42] Additionally, the products of the fragmentation process, predominantly protoplasmonic AuNPs, show a strongly quenched absorption cross section at this wavelength.[43−45] Due to the low concentration of 7.5 mg/L used, the quantitative absorption and hence the reirradiation of the AuNP products can be neglected. In an initial experiment, all laser parameters, including the fluence, repetition rate, pulse duration, and number of pulses per volume were kept constant, while varying the particle sizes of the educt material. Although one passage through the flow reactor should be sufficient to illuminate each volume element, we performed four passages to compensate for the refraction and absorption effects,[36,36] as specified above, and to ensure that every particle was hit by at least one pulse. After only four passages, we could find no more educt particles in the samples (experimental evidence follows below, Figure 4A).

Influence of the Educt Gold Nanoparticle Size. According to the literature, the particle size of educt

DOI: 10.1021/acs.jpcc.8b04374
J. Phys. Chem. C 2018, 122, 22125−22136

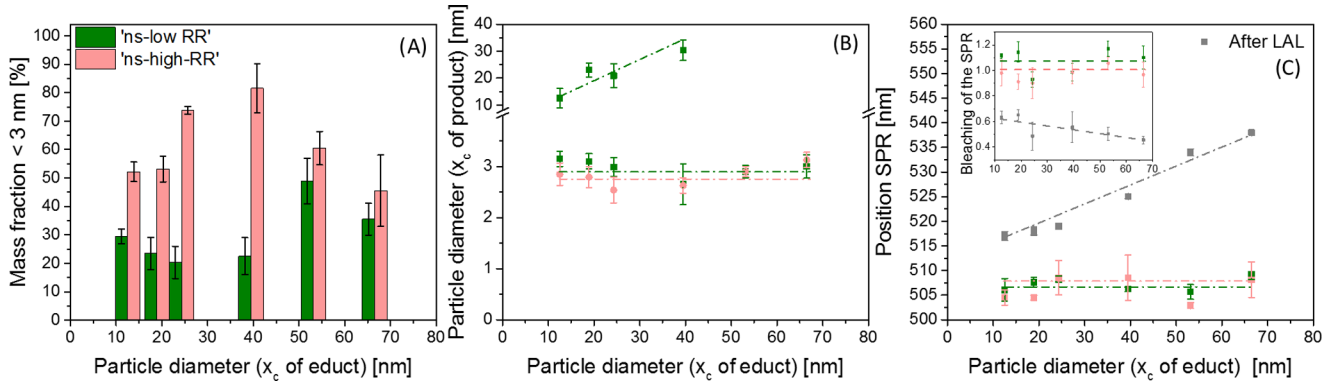

Figure 3. (A) Educt particle diameter effect on mass yield of particles smaller than 3 nm, as determined by ADC measurements. (B) Peak position of the relative mass distribution (ADC) after LFL of different educt particles. (C) Position of the surface plasmon resonance (SPR) peak (before and after LFL) in relation to particle size, with the SPR bleaching of the absorbance spectra as inset. The *x* axis in (A)−(C) represents the x_c values of the educt particles used. Corresponding size distributions and cutoffs are shown in Figure 2 (gray).

nanoparticles determines the energy absorption (gain) and heat transfer (loss) into a liquid.[24,25,46,47] The latter causes significant bubble formation once the temperature of the liquid surrounding the nanoparticle reaches it's spinodal temperature.[24,48] In the case of 532 nm laser pulses, Metwally et al. found that the absorption cross section of AuNPs smaller than 60 nm decreases with particle size by $\sim R^3$.[24] In turn, heat transfer and heat loss, respectively, scale with R^2. Accordingly, the smaller the educt particle size, the more heat loss occurs with respect to absorption, which results in a higher laser fluence threshold for the thermally based fragmentation of AuNPs <60 nm.[24] Due to the Kapitza resistance, heat transfer is delayed when ultrashort (fs, ps) laser pulses are applied, which leads to higher temperatures within the nanoparticles, compared with the surrounding liquid. For ns-laser pulses, heat transfer appears to be quasistatic without significant delay.[24,24] Additionally, temperature-dependent plasmon bleaching further reduces the absorption and fragmentation efficiencies during ns-laser treatment.[47] Considering the impact of AuNP educt particle size on the fragmentation process, we synthesized educt particles of different sizes and fragmented them with different ns-laser intensities to gain further insight into the fragmentation mechanisms. The gray areas in Figure 2 show the size distributions of the different educt particles used in this study.

The particle size distribution after fragmentation with ns-low RR is shown in green, in which, irrespective of the educt particle size, a particle fraction with a size smaller than 5 nm is formed. The figure also shows that only if there are educt particles present that are smaller than 13.4 ± 2.1 nm in diameter, a second particle fraction emerges. Please note that the threshold value of 13.4 ± 2.1 nm does not represent the x_c value of the educt particle size distribution but rather a cutoff value, which is indicated as a green line in Figure 2. This means that for quantitative conversion into smaller NPs, all educt particle sizes in the distribution must be larger than 13.4 ± 2.1 nm. According to the literature, fragmentation with ns pulses is caused by photothermal evaporation.[23] On this basis, the emergence of a second particle fraction can be explained in two ways. In the first, the energy is not high enough to completely evaporate large educt particles. Hence, the evaporated particle volume comprises the small particle fraction, whereas the residual bodies of particles not completely evaporated comprise a second fraction. A second hypothesis assumes that educt particles in the range of 13.4 ± 2.1 nm were already present in the educt solution. For the two larger educt fractions, this seems unlikely, because the size distributions of these particles show no particles in this range. The histograms of the educt particles with an x_c range of 13−25 nm, however, overlap with the second product mode. Although the intermediate educt size with an x_c of 40 nm does not overlap with the product fraction, its smallest detected diameters are quite close to that value, so the presence of a minor fraction of educt particles in the product range cannot be totally excluded. Altogether, an educt particle size with a median diameter well above a defined threshold diameter seems to be a prerequisite for a monomodal product. If the fragmentation threshold for this particle fraction exceeds the applied laser fluence, these particles are not fragmented at all and appear as a second particle fraction, whereas the larger educt particles shown in Figure 2 (gray) are completely fragmented and form the smaller fraction. Although the term "evaporated" indicates the HME mechanism that will take place, evaporation is not necessarily the only mechanism responsible for the fragmentation of these particles, as we discuss later. If the critical temperature is reached and if the thermal process takes place outside the thermal equilibrium, phase explosion could also be responsible for the formation of two particle fractions.[49,50] We note that a distinction between HME mechanism and phase explosion cannot be made without temperature measurements or corresponding simulations, so we make no distinction below as to whether thermal processes take place in thermal equilibrium or far from it. In addition, according to Pyatenko et al.,[32] laser excitation can also lead to the emission of electrons, by which educt particles are cleaved (Coulomb explosion). Of course, the threshold for particle fission also critically depends on the energy uptake of the particle by the incident laser pulse and hence the extinction cross section. If the particles are small, more energy is needed to stimulate the emission of electrons. If not enough electrons are ejected, there can be no particle cleavage and no fragmentation. With reference to a simulation by Baffou et al.,[24] we know that the value of the particle size that cannot be fragmented can be calculated from the maximum temperature after a pulse. If the maximum temperature generated by the absorption of the pulse energy in the interior of the particle is known, it is possible to estimate how much energy is available for the evaporation of the particle. Hence, we note that metastable

DOI: 10.1021/acs.jpcc.8b04374
J. Phys. Chem. C 2018, 122, 22125−22136

states, which may result in a phase explosion, cannot be considered. However, on the basis of these calculations, only particles with diameters >13.1 nm can be fragmented using ns-low RR. As this value describes the Feret diameter of the particles, which is generally smaller than the hydrodynamic diameter determined in this study by analytical disc centrifugation,[51] there is excellent agreement between experimentally determined and theoretically calculated threshold diameters. If a higher energy density (2 J/cm^2, 2.8 × 10^{12} W/m^2 instead of 1.5 J/cm^2, 1.6 × 10^{12} W/m^2) is experimentally applied to the colloid, educt particles of every size are successfully fragmented and only one particle fraction is produced (Figure 1, orange). Due to the shorter pulse duration and the higher fluence, the peak power of ns-high RR is significantly higher and hence all particles >10.0 nm should be completely evaporated. As all educt particles are >10.0 nm, quantitative conversion occurs in all samples. Figure 3A shows the mass fraction of particles smaller than 3 nm for ns-low RR and ns-high RR. Please note that, in this case, the x_c values of the corresponding educt particle size distributions, as depicted in Figure 2, are plotted as particle diameters. Naturally, we found a much higher fraction of particles smaller than 3 nm for fragmentation with ns-high RR.

Interestingly, we found differences in particle productivity (<3 nm) between the ns-low RR and ns-high RR to be less pronounced for larger particle fractions corresponding to Figure 2E,F (x_c = 53 and 67 nm, respectively). On the other hand, we detected bigger differences for particles with x_c values <40 nm (Figure 2A–D). This is probably attributable to the fact that under these conditions, fragmentation with ns-low RR is consistent with second-mode formation, which naturally limits the mass yield of particles <3 nm. Notably, the average diameter of the small fraction is independent of laser type and educt particle size (see Figure 3B). Interestingly, the position of the surface plasmon resonance peak (shown in Figure 3C), after fragmentation with both lasers, is nearly the same and independent of the educt particle diameter. Even if a second particle fraction forms after fragmentation occurs, there is no change in the size of the first particle fraction. However, due to the presence of the larger particle fraction, a slightly higher SPR wavelength would be expected in the ns-low RR case. Obviously, contributions of small mass fraction in the particle size distribution have only minute effects on the position of the plasmon resonance and hence are not useful for determining the exact particle size of particles of this size via the Mie theory.[52] In accordance with the position of the plasmon resonance, SPR bleaching is evident (see inset of Figure 3C). Here, we define bleaching as the ratio between the absorbance in the interband (@λ = 380 nm) and the absorbance at the SPR peak maximum.[53] The differences in the bleaching of the plasmon band of particles before and after fragmentation is most dominant after the fragmentation of 53 and 67 nm educt particles, which correlates with a high amount of proto-plasmonic particles after LFL treatment of these samples.

To determine the changes occurring during each passage, we conducted fragmentation experiments with educt particles 54 nm in size (which contained no particles smaller than 13.43 ± 2.1 nm), since no second fraction of particles had formed after four passages for either laser parameters analyzed. This optimal particle size for the most efficient photofragmentation process correlates nicely with reports in the literature, where the lowest threshold fluence for bubble formation has also been found to be in this size regime.[25,24,46]

Influence of the Number of Pulses per Volume. Having clarified the effect of particle size, in our next experiments, we investigated how the fragmentation process is affected by the laser parameters. We systematically varied the pulse energy and the number of pulses per particle (with otherwise constant parameters) and examined the effect on the particle size distributions of the product particles for each passage. We chose educt particles with average diameters of x_c = 53 nm, as they contain no particles <13.4 ± 2.1 nm and hence can be completely converted into ultrasmall particles after four passages. To minimize multipulse postirradiation processes and adjust the single-pulse conditions, we used ns-low RR for these experiments due to its lower repetition rate. For the 20-time higher repetition rate of ns-high RR, much higher flow rates (very small residence time) would have been required, which means ns-low RR was the ideal system for verifying whether or not one laser pulse is sufficient to achieve complete fragmentation. Figure 4A shows the results regarding

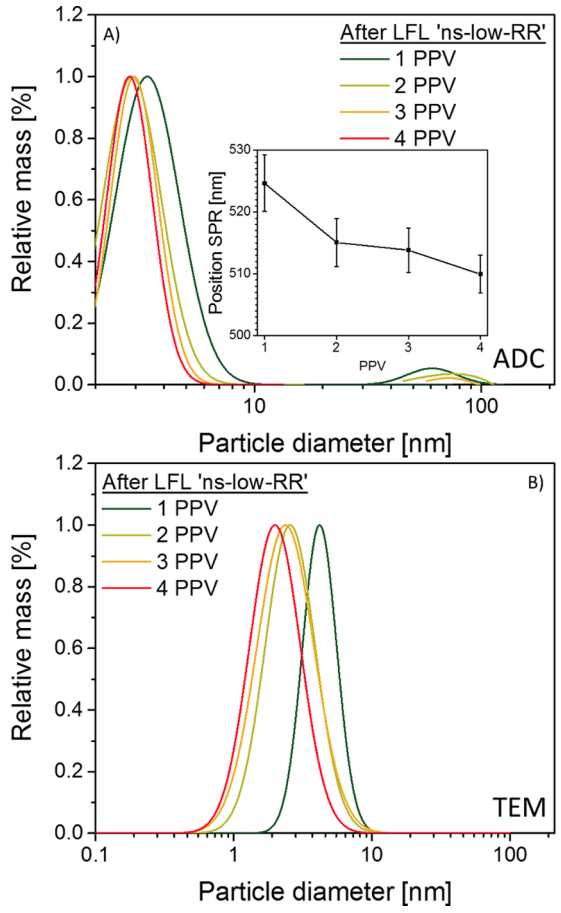

Figure 4. Product particle characterization correlated with the number of pulses per volume (PPV). (A) Relative mass distribution (log normal fit) in relation to the nominal number of pulses per particle, with the position of the SPR after LFL as inset and (B) corresponding TEM data (after measuring 1000 particles).

the variation of the number of passages. After only one passage, most of the mass fraction (about 70%) of gold was completely converted into particles <3 nm. As mentioned above, during each passage, we applied only one laser pulse at each volume in the steady-state conditions of liquid-flow LFL. We adjusted the area of the laser spot to ensure that the jet was almost fully illuminated. However, in accordance with the ray-tracing

DOI: 10.1021/acs.jpcc.8b04374
J. Phys. Chem. C 2018, 122, 22125–22136

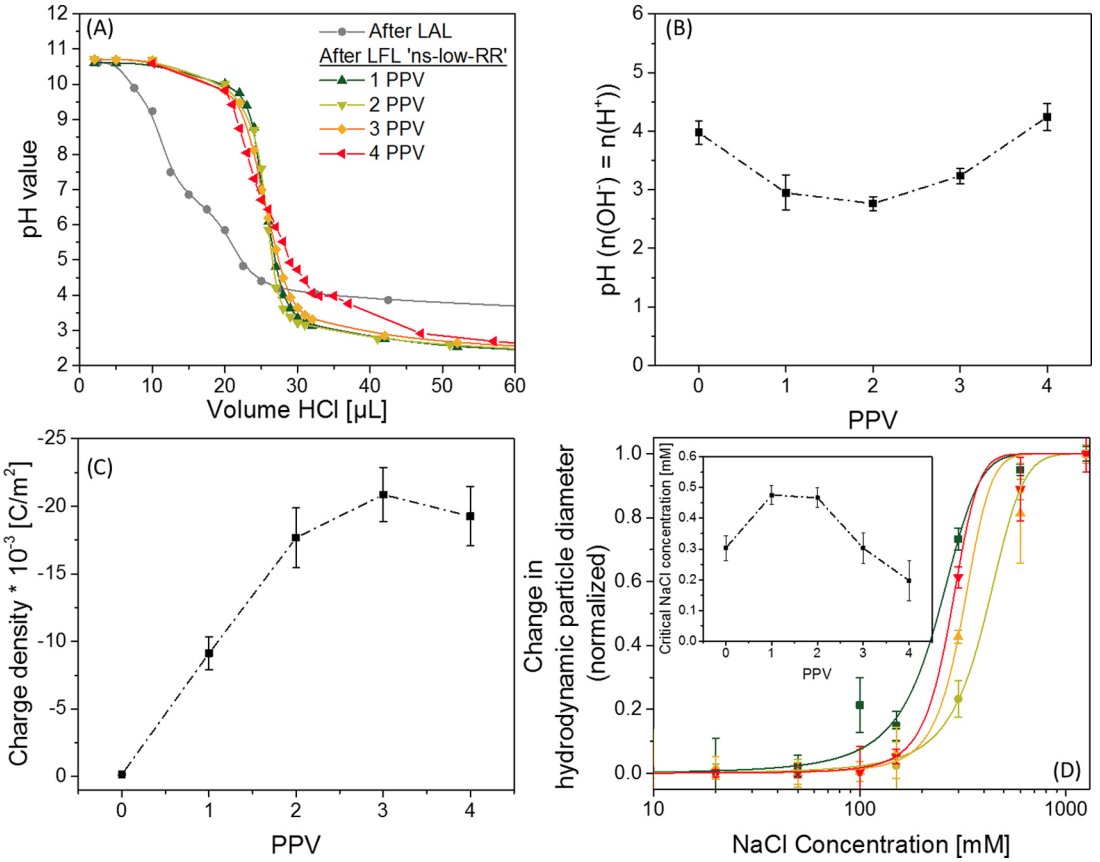

Figure 5. (A) Titration curves of the colloids before and after LFL. (B) Plot of the pH value with which it compensates for the protons and hydroxide ions after 0−4 PPVs (pK_a value). (C) Representation of the surface charge density calculated from the ζ potential for different PPVs. (D) Change in the hydrodynamic particle diameter after the addition of different amounts of salt to the colloids after 1−4 PPVs. The inset shows the critical NaCl concentration to identify the stress resistance of the colloidal particles.

calculations performed recently by Waag et al. for the same liquid jet system, beam refraction at the curved liquid jet surface and attenuation of the intensity of the laser in the colloid may cause a small fraction of particles to fail to undergo full fragmentation.[36] In fact, we could still observe a fraction of educt particles in the product after the first passage most likely due to these refraction and attenuation processes.[36] However, as shown in Figure 4A, this fraction had been eliminated after four passages. Additionally, we can also see a peak shift in the particle size distribution to smaller particle diameters, along with a narrowing of the particle fraction. The SPR peak (Figure 4A, inset) also shifts to smaller wavelengths over all four passages, even though the strongest tendency seems to occur between 1 PPV and 2 PPVs, due to the large error bars. These high error bars are due to the small number of reruns; hence, we used high student factors in our error bar calculations. The error was found to be $\Delta SPR \approx 5$ nm, whereas the signal difference between 1 PPV and 4 PPVs is more than 3 times this value (≈16 nm). Hence, we observed a significant SPR blue shift in our experiments. This fact is striking because the calculation of the critical particle size for fragmentation using ns-low RR, when assuming HME mechanisms, yielded a critical particle size of 13.1 nm.

Generally, the heat transfer (heat loss) increases with increasing surface area, whereas the ernergy gain by absorption decreases proportinal to the particle volume (for NP < 60 nm)[24], as mentioned earlier. In case of an evaporation based fragmentation as discussed here, the temperature of particles smaller than this threshold cannot exceed the boiling temperature under the given conditions.[24,25] In addition to the data from the ADC, Figure 4B shows the relative mass distribution obtained by measuring the particles in the TEM images. The educt particle fraction does not appear in the histograms since our TEM image analysis lacks statistical robustness, although we measured the size of more than 1000 particles to determine the size distribution. To understand the impact of subsequent laser treatment on the surface chemistry (acidity and surface charge density) of the nanoparticles, we conducted pH titration experiments after each passage. Beginning with laser-treated nanoparticles containing 0.3 mM NaOH, we measured the amount of acid added while stirring, as well as the resulting pH value (Figure 5A). Within these considerations, we focused on the point at which the amount of H^+ solution used for the titration corresponded to the amount of OH^- contained in the colloid. Following the Henderson−Hasselbalch equation, we can define the pH value of a gold colloid containing equal amounts of acid and base ($n_{acid} = n_{base}$) as the pK_a value of the gold nanoparticles. Figure 5B shows a plot of the pK_a value of the laser-generated (educt) and fragmented (product) AuNPs, in which the AuNPs obtained a pK_a value of about 4 after laser ablation synthesis, which decreased during consecutive laser fragmentations. However, after 3 PPVs, the pK_a value seems to be restored, reaching the initial value of the educt nanoparticles after 4 PPVs. From the literature, we know that the AuNP surface is partially oxidized and covered with hydroxyl groups and other

DOI: 10.1021/acs.jpcc.8b04374
J. Phys. Chem. C 2018, 122, 22125−22136

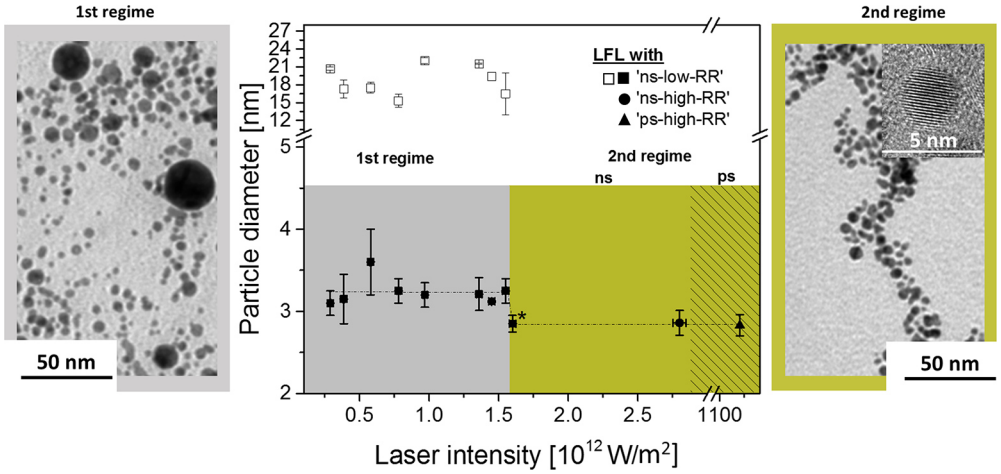

Figure 6. Plot of the resulting particle sizes after fragmentation at different laser pulse intensities. Squares show the results after fragmentation at ns-low RR, circles at ns-high RR, and triangles after LFL at ps-high RR. Marked data points (*) show statistically significant differences from the predecessor data.

anionic species.[17] Hence, the AuNPs are electron acceptors and represent a Lewis acid. From these results and Figure 5B, we can infer that the strength of the Lewis-acidic AuNPs increases within the first two pulses. An increase in acidity indicates the appearance of an increasing number of defects, such as gold atoms with low coordination (kinks, edges, etc.), on the nanoparticle surfaces after laser fragmentation. This is consistent with the observation of hydroxides preferably forming at the corners and on the edges of the surface.[54] In addition, the atoms of the AuNP surfaces are considered to have a reduced melting temperature so that transformations are favored.[46,55] On the other hand, after the third passage, the acid strength of the AuNP colloid decreases (see Figure 5B), reaching the initial value of the unfragmented particles after 4 PPV.

The third and fourth pulses would thus result in a decrease in hydroxide-acceptor ability and could be categorized as a type of surface healing, which shapes the final structure of the particles after the fourth passage. This process would only have a limited influence on the primary particle size, but it should impact the surface charge density and colloidal stability.[56] Unfortunately, it was not feasible to directly measure the surface charge by X-ray photoelectron spectroscopy due to the low colloid concentrations even after cumulating multiple drops of colloid. Another indicator of the surface chemistry is the surface charge density. On the basis of the spherical Poisson−Boltzman equation, Ohshima and co-workers derived two analytical equations to approximate the surface charge density based on the electrophoretic mobility/ζ potential.[57,58] The equations were shown to be valid for AuNPs of various sizes and electrolyte concentrations (KCl),[58] with AuNPs typically having a negative ζ potential over a wide range, due to Au−O^- as well as adsorbed anions.[17] The addition of acid causes a protonation of the Au−O^- surface groups that act as Brønsted acids in this context (Au^+ = Lewis acid). From the ζ potential, we estimated the surface charge density for an increasing number of PPVs using the model developed by Ohshima and co-workers (Figure 5C).[58] For the given AuNP size (a = 3 nm) and ionic strength ($I = 10^{-4}$ mol/L yielding the Debye parameter $\kappa = 0.033$ nm^{-1}), the error of the applied approximation in our case ($\kappa \cdot a \approx 0.1$) is less than 4%.[58] As shown in Figure 5C, during the first two passages, the surface charge density significantly increases and becomes more negative whereas there is no change if additional laser pulses are applied. Hence, the surface charge density stagnates at about −20 mC/m^2. Consequently, this increased surface charge density would improve the colloidal stability of the AuNPs and we could attribute the reduced particle sizes detected between passages 1 and 2 (Figure 4) to postsynthesis electrostatic particle repulsion. To examine the stability of various particles in more detail, we stressed them by the addition of NaCl. In these experiments, the hydrodynamic diameter detected by dynamic light scattering served as the measured parameter. After addition of 10−1250 mM salt concentrations, we observed a sigmoid change in the hydrodynamic diameter, which is expected for colloidal AuNP (Figure 5D). In the following, the turning point of the sigmoidal function is defined as the critical destabilizing salt concentration. We note that this is a purely mathematical formulation. Aggregations of particles are already present at significantly lower salt concentrations. Nevertheless, the critical destabilizing salt concentration correlates directly with the colloidal stability of the particles, as more pronounced changes at lower salt concentrations are expected for less stable particles. Figure 5D shows a plot of these data for the particles for 0−4 PPVs. After 1 PPV element, the particles show the highest stability against salts, which greatly decrease after 2 PPVs and returns to the stability of the educt particles (0 PPV) after four pulses. We observed a similar trend in their optical spectra, where the plasmonic peak gradually shifted with increasing salt concentrations. These results fit well with the previous experimental data, which clearly showed the change in surface chemistry with an increasing number of PPV element. The particles with the most defect rich surface exhibit the best stability against salt. With an increasing number of PPVs, a healing of the surface was evident in the above titration experiments, in which the particles had a nearly unchanged surface charge density and their salt stability approached that of unfragmented educt particles.

On the basis of these findings, we conclude that the size reduction of the 53 nm particles into fractions ≪10 nm is caused by a single-pulse, single-step mechanism. However, due to the attenuation and reflection inside the liquid jet, as noted above, two laser pulses are practically required to achieve

DOI: 10.1021/acs.jpcc.8b04374
J. Phys. Chem. C 2018, 122, 22125−22136

complete fragmentation. The produced particles have poorly coordinated Au surface defects that act as Lewis acids. The origin of these defects is likely to be thermally driven evaporation and fast nucleation after the application of the first laser pulse. Due to much higher heat loss and far lower absorption cross section of the formed nanoparticles, consecutive laser pulses can cause no further evaporation. However, elevated temperatures, even those that eventually reach the melting temperature, induce a curing of the defects from the first fragmentation step. In this context, it is significant that the adjustment of the surface charge density by varying the number of PPVs without significantly changing the particle size distribution could be a valuable approach to better understanding the effect of defect density on, e.g., catalytic properties.

Influence of Laser Intensity. To further explore the fragmentation mechanism, we systematically varied the laser intensity (Figure 6).

If a particle is evaporated by a single laser pulse, there is a threshold energy below which the absorbed energy is no longer high enough to reach the boiling point of 3129 K[33] and overcome the evaporation enthalpy to evaporate the whole nanoparticle. Hence, if the laser pulse energy is just below this threshold, only a fraction of the nanoparticle surface evaporates, leaving a second particle fraction behind. These conclusions are backed by the results shown in Figure 6. First, we discuss the data points shown as squares in this figure, which show the results of fragmentation with ns-low RR. An increase in the laser intensity is achieved by successively increasing the pulse energy. Up to a laser intensity of 1.6×10^{12} W/m^2, the fragmentation leads to a bimodal particle size distribution with particle sizes of 3.2 ± 0.2 and 18.8 ± 2.5 nm in diameter. Beyond a laser intensity of 1.6×10^{12} W/m^2, a significant change is observed. The first particle fraction becomes smaller (2.9 ± 0.02 nm), and the second particle fraction disappears. In one approach, the occurrence of a bimodal size distribution in the low-intensity regime ($<1.6 \times 10^{12}$ W/m^2) can be explained by the photothermic evaporation mechanism, which is favored by researchers in the literature as the explanation for fragmentation with ns-pulsed lasers. Furthermore, the emergence of a second particle fraction at 18.8 nm $\pm$ 2.5 nm, which is independent of the laser intensity is clear evidence that a certain fraction of particles is only partially evaporated, which is probably attributable to fluctuations in intensity because of the Gaussian energy distribution of the laser beam. Consequently, it may be assumed that in the low-intensity regime (1st regime), partial ($evap_{part}$) and complete ($evap_{quant}$) evaporation of the particles may occur simultaneously. The ratio $evap_{part}/evap_{quant}$ would naturally shift to lower values with increasing laser intensity. If the laser intensity exceeds a certain threshold value (1.6×10^{12} W/m^2) and the educt particle size is sufficiently large, evaporation of the AuNPs occurs and the formation of the vapor phase is thermodynamically favored. Particle formation from the vapor phase is consecutively affected by two basic phenomena, nucleation and particle growth. The rate of nucleation is dependent on the interfacial tension γ between the vapor and the resulting liquid gold germs by the $e^{\gamma^{-6}}$ approach. According to the Eötvös rule, the interfacial tension γ decreases with increasing temperature[59] so that the nucleation rate increases at high temperatures. In addition, nucleation is favored by a high saturation of the gas phase.[60] Consequently, on the basis of the high temperatures and high local gold vapor concentrations due to particle evaporation, we can conclude that nucleation is favored over particle growth, which results in the rather small particle fractions of 3.3 ± 0.2 and 2.9 ± 0.02 nm in regimes 1 and 2, respectively. This process is complemented by an electrostatic stabilization of the resulting particles due to their interactions with matrix components, which is identical for all samples due to the constant medium composition. However, the occurrence of a second, larger fraction in the 1st regime seems to indicate that the evaporation in this case was not complete. During a partial evaporation, the available energy is sufficient only to evaporate the surface of the particles. However, when the laser intensity is increased in the 1st regime, a correspondingly higher volume of the particle can be evaporated, so that the remaining particle core (second fraction) decreases with increasing laser intensity. This trend is observed up to a value of 0.76×10^{12} W/m^2. However, with further increasing fluences, the $evap_{part}/evap_{quant}$ decreases so that the final concentration of the second fraction falls below the detection limit of the ADC, as previously determined by Letzel et al.[61] Consequently, the particle size of the residual larger fraction can no longer be quantitatively determined. However, since evaporation is a very slow process that is especially slowed down in an aqueous environment, a phase explosion can occur instead of evaporation. In summary, the mechanism behind the formation of particles after fragmentation in the 1st regime (low intensities) can be assigned to a photothermal fragmentation mechanism. However, a significant change is noticeable in the particle size of the first smaller fraction and the disappearance of the second (larger) particle fraction for a laser intensity of $>1.6 \times 10^{12}$ W/m^2. Assuming that in the 1st regime there is a superposition between the vaporization of the surface of the particle and the complete vaporization of the particle, the 2nd regime (high intensities) could initially be the result of a complete evaporation, with the resulting particle size of 2.9 ± 0.02 nm. According to Pyatenko et al.,[32] however, an electronically induced mechanism cannot be ruled out. To check this, we added two more experimental data points to the diagram in Figure 6. These data points correspond to the results after fragmentation at an ns-high RR (circle) and ps-high RR (triangle), and we can see that the fragmentation by these lasers results in a particle size of 2.8 ± 0.1 nm, which is quite similar to the size after fragmentation with ns-low RR in the 2nd regime. This result is extremely interesting. ps-high RR is an ultrashort pulsed laser with a pulse duration of 10 ps. Even though the duration of this pulse is in the same regime as the electron−phonon coupling of gold (about 3 ps) and a clear temporal separation between photon−electron and electron−phonon coupling as in fs-LFL is not possible, the peak intensity 1.6×10^{15} W/m^2 is 3 orders of magnitude higher than that of ns-low RR and ns-high RR. In addition, to the best of our knowledge, the plasma shielding commonly observed during ns-LAL has not been reported during ns-LFL. On this basis, we can assume that the energy is sufficient to reach an electron deficiency in the particle, whereby a positively charged particle core remains, which undergoes spontaneous fission once the Coulomb forces exceed the cohesive forces of the particle.[23,25] The mechanism of fragmentation with ps-high RR can thus be determined to be CE. Of course, this does not automatically mean that the fragmentation with ns-low RR and ns-high RR at laser intensities higher than 1.6×10^{12} W/m^2 also occur by this mechanism so the question of the fragmentation mechanism

DOI: 10.1021/acs.jpcc.8b04374
J. Phys. Chem. C 2018, 122, 22125−22136

with ns in the 2nd regime cannot be answered by the experimental data. Either fragmentation there also proceeds according to an electronically induced or photothermally induced mechanism. Regardless of this question, the results indicate that the resulting particle size cannot be changed by laser intensities ranging between 1.6×10^{12} and 1.6×10^{15} W/m^2. Similar to LAL, however, we can expect some influence for LFL by the ions used in the liquid matrix on the resulting particle size.[17,18] However, we did not address these effects in this work.

CONCLUSIONS

On the basis of our particle size analysis, we can conclude that nanosecond laser fragmentation can be divided into two regimes depending on the laser intensity. In the 1st regime, the particles are formed either according to a heating−melting−evaporation mechanism whereby the particles are partially vaporized up to a defined laser intensity threshold or by a phase explosion, which could be also responsible for the formation of two particle populations. For laser intensities exceeding 1.6×10^{12} W/m^2, no more changes in the size distribution occur even if the intensity is increased 3 orders of magnitude higher than that for ns-low RR and ns-high RR. The mechanism for nanosecond fragmentation in this regime is still unclear, but the resulting particle size is comparable to that achieved by ps fragmentation at high peak intensity, where Coulomb explosions cannot be ruled out. A closer look at this regime indicates that fragmentation is a one-step one-pulse event, in which educt particles exceeding a certain critical particle size (>13.4 nm) are completely converted into much smaller particles. These product particles are ligand-free nanoclusters with a monomodal mass-weighted diameter of <3 nm. Furthermore, we determined that the surface chemistry of the particles is significantly affected by the number of pulses and that the surface charge density increases with an increasing number of irradiation cycles. The proposed method yields ligand-free gold nanoclusters in a size regime that is highly interesting for applications, e.g., in heterogeneous catalysis or biomedicine. The upscaling of this process also benefits from the fact that it has been realized in a steady-state flow setup. Due to beam refraction of the liquid jet, in practice, four passages are still required to realize perfect colloid quality but physically, only one laser pulse per volume is required, which means the throughput can be simply scaled via the laser repetition rate. Another important point is that all LFL processes studied in this work were performed in the presence of electrolytes (micromolar sodium chloride). Similar to LAL,[17,18] the influence of the ions used in the matrix on the resulting particle could also be true for LFL and should be studied in more detail in the future.

ASSOCIATED CONTENT

Supporting Information

The Supporting Information is available free of charge on the ACS Publications website at DOI: 10.1021/acs.jpcc.8b04374.

Size distributions of all educt AuNPs (Figure S1); calculations of the flow behavior of the free liquid jet (Figure S2); calculated absorption cross section of AuNPs (Figure S3); comparison of the quality of three different methods for obtaining particle size distributions of particles after fragmentation (Figure S4); theoretical consideration of the temperatures in nanoparticles according to LFL (Figure S5); absorption spectra of nanoparticles before and after LFL (Figure S6); TEM images (Figure S7) and absorbance spectra (Figure S8) after fragmentation with different PPVs; hydrodynamic diameters of AuNPs after 4 PPVs and after subsequent ex situ addition of different amounts of NaCl (Figure S9); experimental observation of laser intensity (Figure S10); influence of pulse intensity on product particle size (Figure S11) (PDF)

AUTHOR INFORMATION

Corresponding Author

*E-mail: stephan.barcikowski@uni-due.de.

ORCID

Indranath Chakraborty: 0000-0003-4195-9384
Wolfgang J. Parak: 0000-0003-1672-6650
Stephan Barcikowski: 0000-0002-9739-7272

Notes

The authors declare no competing financial interest.

ACKNOWLEDGMENTS

We gratefully acknowledge the DFG Deutsche Forschungsgemeinschaft for its financial support under Project No. BA 3580/22-1 and PA 794/28-1. I.C. was supported by an Alexander von Humboldt fellowship. The authors also thank Jurij Jacobi for his experimental support in producing the TEM images and Dario Becker for the evaluation of these data (both from the University Duisburg-Essen). Dr. Marcus Heidelmann (ICAN) is acknowledged for assistance with HRTEM measurments. Prof. Zhigilei from the University of Virginia deserves special thanks; we particularly appreciate his valuable insights concerning nonequilibrium processes during laser-based particle heating.

REFERENCES

(1) Gamrad, L.; Mancini, R.; Werner, D.; Tiedemann, D.; Taylor, U.; Ziefuß, A.; Rehbock, C.; Klein, S.; Kues, W.; Barcikowski, S.; et al. Triplex-Hybridizing Bioconjugated Gold Nanoparticles for Specific Y-Chromosome Sequence Targeting of Bull Spermatozoa. *Analyst* **2017**, *142*, 2020−2028.

(2) Baretto, J. A.; O'Malley, W.; Kubeil, M.; Graham, B.; Stephan, H.; Spiccia, L. Nanomaterials: Applications in Cancer Imaging and Therapy. *Adv. Funct. Mater.* **2011**, *23*, H18−H40.

(3) Veigas, B.; Fernandes, A. R.; Baptista, P. V. AuNPs for Identification of Molecular Signatures of Resistance. *Front. Microbiol.* **2014**, *5*, 455.

(4) Gu, S.; Kaiser, J.; Marzun, G.; Ott, A.; Lu, Y.; Ballauff, M.; Zaccone, A.; Barcikowski, S.; Wagener, P. Ligand-Free Gold Nanoparticles as a Reference Material for Kinetic Modelling of Catalytic Reduction of 4-Nitrophenol. *Catal. Lett.* **2015**, *145*, 1105−1112.

(5) Dong, W.; Reichenberger, S.; Chu, S.; Weide, P.; Ruland, H.; Barcikowski, S.; Wagener, P.; Muhler, M. the Effect of the Au Loading on the Liquid-Phase Aerobic Oxidation of Ethanol Over Au/TiO_2 Catalysts Prepared by Pulsed Laser Ablation. *J. Catal.* **2015**, *330*, 497−506.

(6) Pougin, A.; Lüken, A.; Klinkhammer, C.; Hiltrop, D.; Kauer, M.; Tölle, K.; Havenith-Newen, M.; Morgenstern, K.; Grünert, W.; Muhler, M.; et al. Probing Oxide Reduction and Phase Transformations at the Au-TiO_2 Interface by Vibrational Spectroscopy. *Top. Catal.* **2017**, *60*, 1744−1753.

(7) Stratakis, M.; Garcia, H. Catalysis by Supported Gold Nanoparticles: Beyond Aerobic Oxidative Processes. *Chem. Rev.* **2012**, *112*, 4469−4506.

(8) Zhang, Y.; Cui, X.; Shi, F.; Deng, Y. Nano-Gold Catalysis in Fine Chemical Synthesis. *Chem. Rev.* **2012**, *112*, 2467−2505.
(9) Goldys, E. M.; Sobhan, M. A. Fluorescence of Colloidal Gold Nanoparticles is Controlled by the Surface Adsorbate. *Adv. Funct. Mater.* **2012**, *22*, 1906−1913.
(10) Shang, L.; Azadfar, N.; Stockmar, F.; Send, W.; Trouillet, V.; Brund, M.; Gerthsen, D.; Nienhaus, G. U. One-Pot Synthesis of Near-Infrared Fluorescent Gold Clusters for Cellular Fluorescence Lifetime Imaging. *Small* **2011**, *7*, 2614−2620.
(11) Chakraborty, I.; Pradeep, T. Atomically Precise Clusters of Noble Metals: Emerging Link between Atoms and Nanoparticles. *Chem. Rev.* **2017**, *117*, 8208−8271.
(12) Murphy, C. J. Sustainability as an Emerging Design Criterion in Nanoparticle Synthesis and Applications. *J. Mater. Chem.* **2008**, *18*, 2173.
(13) Amendola, V.; Meneghetti, M. Controlled Size Manipulation of Free Gold Nanoparticles by Laser Irradiation and their Facile Bioconjugation. *J. Mater. Chem.* **2007**, *17*, 4705.
(14) Zhang, D.; Gökce, B.; Barcikowski, S. Laser Synthesis and Processing of Colloids: Fundamentals and Applications. *Chem. Rev.* **2017**, *117*, 3990−4103.
(15) Rehbock, C.; Jakobi, J.; Gamrad, L.; van der Meer, S.; Tiedemann, D.; Taylor, U.; Kues, W.; Rath, D.; Barcikowski, S. Current State of Laser Synthesis of Metal and Alloy Nanoparticles as Ligand-Free Reference Materials for Nano-Toxicological Assays. *Beilstein J. Nanotechnol.* **2014**, *5*, 1523−1541.
(16) Xu, Z.; Quintanilla, M.; Vetrone, F.; Govorov, A. O.; Chaker, M.; Ma, D. Harvesting Lost Photons. Plasmon and Upconversion Enhanced Broadband Photocatalytic Activity in Core@Shell Microspheres Based on Lanthanide-Doped $NaYF_4$, TiO_2 and Au. *Adv. Funct. Mater.* **2015**, *25*, 2950−2960.
(17) Merk, V.; Rehbock, C.; Becker, F.; Hagemann, U.; Nienhaus, H.; Barcikowski, S. In Situ Non-DLVO Stabilization of Surfactant-Free, Plasmonic Gold Nanoparticles: Effect of Hofmeister's Anions. *Langmuir* **2014**, *30*, 4213−4222.
(18) Rehbock, C.; Merk, V.; Gamrad, L.; Streuble, R.; Barcikowski, S. Size Control of Laser-Fabricated Surfactant-Free Gold Nanoparticles with Highly Diluted Electrolytes and their Subsequent Bioconjugation. *Phys. Chem. Chem. Phys.* **2013**, *15*, 3057−3067.
(19) Mafuné, F.; Kohno, J.-y.; Takeda, Y.; Kondow, T. Growth of Gold Clusters into Nanoparticles in a Solution Following Laser-Induced Fragmentation. *J. Phys. Chem. B* **2002**, *106*, 8555−8561.
(20) Lau, M.; Haxhiaj, I.; Wagener, P.; Intartaglia, R.; Brandi, F.; Nakamura, J.; Barcikowski, S. Ligand-Free Gold Atom Clusters Adsorbed on Graphene Nano Sheets Generated by Oxidative Laser Fragmentation in Water. *Chem. Phys. Lett.* **2014**, *610−611*, 256−260.
(21) Kim, K. K.; Know, H. J.; Shin, S. K.; Song, J. K.; Park, S. M. Stability of Uncapped Gold Nanoparticles Produced by Laser Ablation in Deionized Water. The Effect of Post-Irradiation. *Chem. Phys. Lett.* **2013**, *588*, 167−173.
(22) Giammanco, F.; Giorgetti, E.; Marsili, P.; Guisti, A. Experimental and Theoretical Analysis of Photofragmentation of Au Nanoparticles by Picosecond Laser Radiation. *J. Phys. Chem. C* **2010**, *114*, 3354−3363.
(23) Hashimoto, S.; Werner, D.; Uwada, T. Studies on the Interaction of Pulsed Lasers with Plasmonic Gold Nanoparticles Toward Light Manipulation, Heat Management, and Nanofabrication. *J. Photochem. Photobiol., C* **2012**, *13*, 28−54.
(24) Metwally, K.; Mensah, S.; Baffou, G. Fluence Threshold for Photothermal Bubble Generation Using Plasmonic Nanoparticles. *J. Phys. Chem. C* **2015**, *119*, 28586−28596.
(25) Delfour, L.; Itina, T. E. Mechanisms of Ultrashort Laser-Induced Fragmentation of Metal Nanoparticles in Liquids. Numerical Insights. *J. Phys. Chem. C* **2015**, *119*, 13893−13900.
(26) Farrashbandi, N. F.; Gholamzadeh, L.; Eslami-Kalantari, M.; Sharifian, M.; Sid, A. Investigation of the Effect of Laser Pulse Length on the Inverse Bremsstrahlung Absorption in Laser−Fusion Plasma. *High Energy Density Phys.* **2015**, *16*, 32−35.
(27) Itina, T. E.; Gouriet, K.; Zhigilei, L. V.; Nöel, S.; Hermann, J.; Sentis, M. Mechanisms of Small Clusters Production by Short and Ultra-Short Laser Ablation. *Appl. Surf. Sci.* **2007**, *253*, 7656−7661.
(28) Yamada, K.; Tokumoto, Y.; Nagata, T.; Mafuné, F. Mechanism of Laser-Induced Size-Reduction of Gold Nanoparticles as Studied by Nanosecond Transient Absorption Spectroscopy. *J. Phys. Chem. B* **2006**, *110*, 11751−11756.
(29) Jendrzej, S.; Gökce, B.; Amendola, V.; Barcikowski, S. Barrierless Growth of Precursor-Free, Ultrafast Laser-Fragmented Noble Metal Nanoparticles by Colloidal Atom Clusters - A Kinetic In Situ Study. *J. Colloid Interface Sci.* **2016**, *463*, 299−307.
(30) Miotello, A.; Kelly, R. Laser-Induced Phase Explosion. New Physical Problems When a Condensed Phase Approaches the Thermodynamic Critical Temperature. *Appl. Phys. A* **1999**, *69*, S67−S73.
(31) Inasawa, S.; Sugiyama, M.; Yamaguchi, Y. Laser-Induced Shape Transformation of Gold Nanoparticles Below the Melting Point: the Effect of Surface Melting. *J. Phys. Chem. B* **2005**, *109*, 3104−3111.
(32) Pyatenko, A.; Yamaguchi, M.; Suzuki, M. Mechanisms of Size Reduction of Colloidal Silver and Gold Nanoparticles Irradiated by Nd. YAG Laser. *J. Phys. Chem. C* **2009**, *113*, 9078−9085.
(33) Pyatenko, A.; Wang, H.; Koshizaki, N.; Tsuji, T. Mechanism of Pulse Laser Interaction with Colloidal Nanoparticles. *Laser Photonics Rev.* **2013**, *7*, 596−604.
(34) Lau, M.; Straube, T.; Aggarwal, A. V.; Hagemann, U.; de Oliveira Viestel, B.; Hartmann, N.; Textor, T.; Lutz, H.; Gutmann, J. S.; Barcikowski, S. Gradual Modification of ITO Particle's Crystal Structure and Optical Properties by Pulsed UV Laser Irradiation in a Free Liquid Jet. *Dalton Trans.* **2017**, *46*, 6039−6048.
(35) Lau, M.; Ziefuss, A.; Komossa, T.; Barcikowski, S. Inclusion of Supported Gold Nanoparticles Into their Semiconductor Support. *Phys. Chem. Chem. Phys.* **2015**, *17*, 29311−29318.
(36) Waag, F.; Gökce, B.; Kalapu, C.; Bendt, G.; Salamon, S.; Landers, J.; Hagemann, U.; Heidelmann, M.; Schulz, S.; Wende.; et al. Adjusting the Catalytic Properties of Cobalt Ferrite Nanoparticles by Pulsed Laser Fragmentation in Water with Defined Energy Dose. *Sci. Rep.* **2017**, *7*, No. 13161.
(37) Hühn, J.; Carrillo-Carrion, C.; Soliman, M. G.; Pfeiffer, C.; Valdeperez, D.; Masood, A.; Chakraborty, I.; Zhu, L.; Gallego, M.; Yue, Z.; et al. Selected Standard Protocols for the Synthesis, Phase Transfer, and Characterization of Inorganic Colloidal Nanoparticles. *Chem. Mater.* **2017**, *29*, 399−461.
(38) Bohren, C. F.; Huffman, D. R. *Absorption and Scattering of Light by Small Particles*; Wiley-VCH: Weinheim, 2008.
(39) Johnson, P. B.; Christy, R. W. Optical Constants of the Noble Metals. *Phys. Rev. B* **1972**, *6*, 4370−4379.
(40) Baffou, G.; Rigneault, H. Femtosecond-Pulsed Optical Heating of Gold Nanoparticles. *Phys. Rev. B* **2011**, *84*, No. 035415.
(41) Jain, P. K.; Lee, K. S.; El-Sayed, I. H.; El-Sayed, M. A. Calculated Absorption and Scattering Properties of Gold Nanoparticles of Different Size, Shape, and Composition: Applications in Biological Imaging and Biomedicine. *J. Phys. Chem. B* **2006**, *110*, 7238−7248.
(42) Maximova, K.; Aristov, A.; Sentis, M.; Kabashin, A. V. Size-Controllable Synthesis of Bare Gold Nanoparticles by Femtosecond Laser Fragmentation in Water. *Nat. Nanotechnol.* **2015**, *26*, No. 065601.
(43) Zheng, J.; Zhang, C.; Dickson, R. M. Highly Fluorescent, Water-Soluble, Size-Tunable Gold Quantum Dots. *Phys. Rev. Lett.* **2004**, *93*, No. 077402.
(44) Zhou, C.; Sun, C.; Yu, M.; Qin, Y.; Wang, J.; Kim, M.; Zheng, J. Luminescent Gold Nanoparticles with Mixed Valence States Generated from Dissociation of Polymeric Au (I) Thiolates. *J. Phys. Chem. C* **2010**, *114*, 7727−7732.
(45) Kreibig, U.; Vollmer, M. *Optical Properties of Metal Clusters*; Springer: Heidelberg, 1995.
(46) Werner, D.; Furube, A.; Okamoto, T.; Hashimoto, S. Femtosecond Laser-Induced Size Reduction of Aqueous Gold Nanoparticles. In Situ and Pump−Probe Spectroscopy Investigations

DOI: 10.1021/acs.jpcc.8b04374
J. Phys. Chem. C 2018, 122, 22125−22136

Revealing Coulomb Explosion. *J. Phys. Chem. C* **2011**, *115*, 8503−8512.
(47) Strasser, M.; Setoura, K.; Langbein, U.; Hashimoto, S. Computational Modeling of Pulsed Laser-Induced Heating and Evaporation of Gold Nanoparticles. *J. Phys. Chem. C* **2014**, *118*, 25748−25755.
(48) Katayama, T.; Setoura, K.; Werner, D.; Miyasaka, H.; Hashimoto, S. Picosecond-to-Nanosecond Dynamics of Plasmonic Nanobubbles from Pump-Probe Spectral Measurements of Aqueous Colloidal Gold Nanoparticles. *Langmuir* **2014**, *30*, 9504−9513.
(49) Zhigilei, L. V.; Lin, Z.; Ivanov, D. S. Atomistic Modeling of Short Pulse Laser Ablation of Metals. Connections between Melting, Spallation, and Phase Explosion. *J. Phys. Chem. C* **2009**, *113*, 11892−11906.
(50) Shih, C.-Y.; Streubel, R.; Heberle, J.; Letzel, A.; Shugaev, M. V.; Wu, C.; Schmidt, M.; Gökce, B.; Barcikowski, S.; Zhigilei, L. V. Two Mechanisms of Nanoparticle Generation in Picosecond Laser Ablation in Liquids: the Origin of the Bimodal Size Distribution. *Nanoscale* **2018**, *10*, 6900−6910.
(51) Petersen, S.; Barcikowski, S. In Situ Bioconjugation. Single Step Approach to Tailored Nanoparticle-Bioconjugates by Ultrashort Pulsed Laser Ablation. *Adv. Funct. Mater.* **2009**, *19*, 1167−1172.
(52) Haiss, W.; Thanh, N. T. K.; Aveyard, J.; Fernig, D. G. Determination of Size and Concentration of Gold Nanoparticles from UV−vis Spectra. *Anal. Chem.* **2007**, *79*, 4215−4221.
(53) Ahmadi, T. S.; Logunov, S. L.; El-Sayed, M. A. Picosecond Dynamics of Colloidal Gold Nanoparticles. *J. Phys. Chem.* **1996**, *100*, 8053−8056.
(54) Narayanan, R.; El-Sayed, M. A. Catalysis with Transition Metal Nanoparticles in Colloidal Solution: Nanoparticle Shape Dependence and Stability. *J. Phys. Chem. B* **2005**, *109*, 12663−12676.
(55) González-Rubio, G.; Guerrero-Martínez, A.; Liz-Marzán, L. M. Reshaping, Fragmentation, and Assembly of Gold Nanoparticles Assisted by Pulse Lasers. *Acc. Chem. Res.* **2016**, *49*, 678−686.
(56) Pfeiffer, C.; Rehbock, C.; Hühn, D.; Carrillo-Carrion, C.; de Aberasturi, D. J.; Merk, V.; Barcikowski, S.; Parak, W. J. Interaction of Colloidal Nanoparticles with their Local Environment: the (Ionic) Nanoenvironment Around Nanoparticles is Different from Bulk and Determines the Physico-Chemical Properties of the Nanoparticles. *J. R. Soc., Interface* **2014**, *11*, No. 20130931.
(57) Ohshima, H.; Healy, T. W.; White, L. R. Accurate Analytic Expressions for the Surface Charge Density/Surface Potential Relationship and Double-Layer Potential Distribution for a Spherical Colloidal Particle. *J. Colloid Interface Sci.* **1982**, *90*, 17−26.
(58) Makino, K.; Ohshima, H. Electrophoretic Mobility of a Colloidal Particle with Constant Surface Charge Density. *Langmuir* **2010**, *26*, 18016−18019.
(59) Hofmann, G. *Kristallisation in der Industriellen Praxis*; Wiley-VCH: Weinheim, 2005.
(60) Werner, D.; Hashimoto, S. Improved Working Model for Interpreting the Excitation Wavelength- and Fluence-Dependent Response in Pulsed Laser-Induced Size Reduction of Aqueous Gold Nanoparticles. *J. Phys. Chem. C* **2011**, *115*, 5063−5072.
(61) Letzel, A.; Gökce, B.; Menzel, A.; Plech, A.; Barcikowski, S. Primary Particle Diameter Differentiation and Bimodality Identification by Five Analytical Methods Using Gold Nanoparticle Size Distributions Synthesized by Pulsed Laser Ablation in Liquids. *Appl. Surf. Sci.* **2018**, *435*, 743−751.

DOI: 10.1021/acs.jpcc.8b04374
J. Phys. Chem. C 2018, 122, 22125−22136

3.2.2 In-situ structural kinetics of picosecond laser-induced heating and fragmentation of colloidal gold spheres

Synopsis:

Since LFL is ideally conducted with high-intensity pulsed lasers, the individual mechanistic differentiation between the effects from energy deposition kinetics (pulse duration) and driving force for fragmentation (laser intensity) is still challenging. The nanoscale environment has demonstrated significant influence on particle growth on ultra-short time scales and, hence, requires attention.

As this was not investigated on a ps- to ns-scale in-depth yet, we systematically examined the LFL of Au NPs in situ, using wide (WAXS) and small-angle (SAXS) time-resolved X-ray scattering to differentiate the effects of both the laser irradiation and chemical nature of the surrounding medium. Laser-material interaction leads to a temperature increase within the particles and subsequently the medium, causing phase transitions, such as particle melting, bubble growth in aqueous solution seen in WAXS, particle decomposition, and the formation of new product particles seen in SAXS. For instance, an increase in the SAXS signal after the vapor bubble vanishes (> 10-20 ns) correlates with the formation of new particles, for which the signal was monitored up to a delay of 10 µs.

We found indications of a quenched growth and higher diffusion-limitation after 1 µs for samples in micromolar saline compared to water, leading to a final particle size of 3–4 nm. Interestingly, we also discovered clusters of a finite initial size already after a few ps, which excludes a pure evaporation and condensation process and can be explained by the occurrence of a phase explosion as already suspected in the previous chapter.

This paper was published in Physical Chemistry Chemical Physics on February 14, 2020. It was awarded as the “PCCP 2020 Hot Article”.

.

PCCP

ROYAL SOCIETY OF CHEMISTRY

PAPER

View Article Online
View Journal | View Issue

Cite this: *Phys. Chem. Chem. Phys.*, 2020, **22**, 4993

In situ structural kinetics of picosecond laser-induced heating and fragmentation of colloidal gold spheres†

Anna Rosa Ziefuss,[a] Stefan Reich,[b] Sven Reichenberger,[a] Matteo Levantino [c] and Anton Plech *[b]

Received 20th September 2019,
Accepted 14th February 2020

DOI: 10.1039/c9cp05202j

rsc.li/pccp

Fragmentation of colloidal 54 nm gold nanoparticles by picosecond laser pulses is recorded by time-resolved X-ray scattering, giving access to structural dynamics down to a 80 ps resolution. Lattice temperature and energy dissipation have been quantified to verify that the maximum applied fluence of 1800 J m^{-2} heats up the particles close to boiling. Already within 30 ns, particles with significantly lower particle sizes of 2 to 3 nm are detected, which hints towards an ultrafast process either by a thermal phase explosion or Coulomb instability. An arrested growth is observed on a microsecond time scale resulting in a final particle size of 3–4 nm with high yield. In this context, the fragmentation in a NaCl/NaOH solution seems to limit growth by electrostatic stabilization of fragments, whereas it does not modify the initial product sizes. The laser-induced fragmentation process is identified as a single-step, instantaneous reaction.

A synthesis method that is mainly driven by physical mechanisms rather than chemical potential has a number of benefits, such as obtaining particles from a wide class of educt materials, a possible scale up of the process or particle suspensions that are less contaminated by reactants or byproducts than for instance in chemical synthesis. Such a process is the synthesis by laser ablation in liquids (LAL) that has gained wide popularity because of its straightforward applicability with limited technological efforts. Nevertheless, size definition has shown to be a delicate issue, as final sizes in LAL-produced nanoparticle batches will depend on a number of interrelated, hierarchical processes. While primary particle sizes are defined by the laser-induced educt decomposition, including phase explosion, evaporation or plasma-aided decomposition, further steps add to ripening and thus particle size growth. Particularly, very small particles (<3 nm) are difficult to obtain and stabilize. In noble metal systems, such as gold, these are labelled protoplasmonic. Their properties change from a quantum regime to a size-scaling regime and may offer a number of unique properties, such as permeability in biological systems[1,2] or higher catalytic activity.[3,4]

While LAL has been intensively investigated[5] and up-scaling routines have been defined,[6] the tendency is to add a second process to reduce sizes and achieve a well-defined size definition by laser-induced fragmentation in liquids (LFL).[7–9] In LFL, a laser pulse intersects the particle suspension such that the particles preferentially absorb energy and transiently pass through a high energy density state that ends in small fragments. The principal advantage of a separation of processes compared to LAL (where LFL would also happen parasitically in most cases) is that the optical properties, the distribution of particles in the suspension and the energy deposition can be well controlled. To that end, the process cascade would be uniform across the ensemble and decomposition would deliver a homogeneous final distribution.

The investigation of structural relaxation processes, particularly in metal nanoparticle excitation and LFL is a topic of current research, also in the view of nanophotonic applications. Energy absorption in the particles and the surrounding medium lead to a cascade of relaxations, partly reversible or irreversible. This can be harnessed in biological applications, including the hybridization with proteins, specifically with antibodies for *in vitro* and *in vivo* targeting or in nanoscale material processing.[10–12] Transfection through cell membranes by transiently enhanced permeation[1,13,14] has been described. A large number of studies have focused on the effect of laser-heated particles, in particular of gold for cell destruction.[15–18]

[a] *Department of Technical Chemistry I and Center for Nanointegration Duisburg-Essen CENIDE, University of Duisburg-Essen, Universitätsstrasse 7, D-45141 Essen, Germany*
[b] *Institute for Photon Science and Synchrotron Radiation, Karlsruhe Institute of Technology, Postfach 3640, D-76021 Karlsruhe, Germany. E-mail: anton.plech@kit.edu*
[c] *European Synchrotron Radiation Facility, 71, avenue des Martyrs, F-38043 Grenoble, France*

† Electronic supplementary information (ESI) available. See DOI: 10.1039/c9cp05202j

Fragmentation includes several levels of particle excitation both in energy and ultrafast time scales. Due to these complications the understanding of the mechanisms is far from being agreed to, despite many available theoretical models. Basically, the photo-excited particles would transform the energy into lattice-thermal degrees of freedom and electron emission within few picoseconds. A slower increasing lattice temperature, for instance in nanosecond excitation, could lead to a pure heating-melting-evaporation pathway, where the particle temperature essentially follows the binodal to reach melting and evaporation. Evaporated atoms and clusters would undergo a subsequent nucleated growth to form new, small particles.[19] Growth can be limited by stabilization and/or kinetic arrest, which can be complicated by pre-existing surfactants in chemically synthesized particles.

Further, the importance of initial particle shape on the fragmentation efficiency of plasmonic nanoparticles has been discussed in literature. For instance, the effect of near-field enhancement even led to more exotic and specialized fragmentation, like near-field ablation,[20] which has been discussed in case of rod-like Au nanoparticles.[21] On the other hand, ultrashort-pulse excitation may lead to a non-equilibrium pathway in the phase diagram that eventually would allow to cross the spinodal line of the material.[22] The consequence would be a violent explosion, or spinodal decomposition. This may directly lead to small particles with a distribution in sizes. A more exotic pathway has been discussed earlier, involving a massive electron emission[23] (particularly in metal nanoparticles) that would destabilize a molten sphere to emit particles and clusters to reduce the Coulomb forces. This Coulomb instability (sometimes called 'explosion', referring to a related effect in molecules and clusters[24]) has been proposed based on observed laser-induced electron ejection[9,25] and is still under debate.[26–30] However, it should not be forgotten that finite-size effects not only encompass thermal properties, but also the spatial mode of fragmentation can be affected by geometry. It has been predicted in simulations that a strain-induced decomposition may be induced,[29] if the photothermal excitation is faster than the particle acoustic eigenmodes. Recently, femtosecond-resolved diffraction experiments on single particles have witnessed such a behaviour.[31]

An approach that is able to shed light on the manifold of proposed reactions needs to resolve the caloric balance of the system (*i.e.* the observation of educts and products as function of energy input), and as well allow for a kinetic determination of structure formation on an ultrafast time scale. The first has been done repeatedly by observing the final particle population and transient optical spectroscopy.[19,32–35] Meanwhile, it is difficult to get access to nanoscale structures on a time scale from picoseconds to microseconds.[36–38] Here, we present results on time-resolved X-ray scattering (small and wide angle) on a surfactant-free gold nanoparticle suspension, excited by picosecond laser pulses of up to 1800 J m^{-2} in a time interval from 100 picoseconds to 100 microseconds to address temporal pathways of energy relaxation as well as the detection of product particles, including particles sizes, mass abundance and crystallinity.

1 Experimental setup

1.1 Gold particle colloidal synthesis

Gold nanoparticles have been produced by pulsed laser ablation in liquids (LAL) by ablating a gold target in ultra-pure water (MilliQ, Millipore) in a batch chamber with a Nd:YAG laser (Ekspla, Atlantic Series, 10 ps, 1064 nm, 9.6 mJ, 100 kHz, 10 min), containing typically a multimodal size distribution.[39–41] To get a well size-separated sample for the study, a centrifugal step (Hettich, 67.1 g, 70 min) had been added. The obtained pellet is left for one week to force coalescence processes[42] and is subsequently diluted to 100 mg L^{-1} either in ultra-pure water or in an aqueous solution containing 0.3 mM NaOH and 0.3 mM NaCl each. These nanoparticles are surfactant-free. Exemplary TEM images of the educt particles can be found in Fig. 1 (top) together with extinction spectra (Thermo Scientific: Evolution 201 spectrometer) of the educt and product particles below.

1.2 *Ex situ* analysis of fragmentation

Fragmentation for an analysis of the irradiated final particles has been done by a picosecond laser (Edgewave) with 10 ps pulses at 532 nm and 80 kHz. A fluence of 300 J m^{-2} was used. Fragmentation was performed in a free liquid jet as described earlier.[41,43] Fragmentation has been performed either in ultra-pure water or in a solution of 0.3 mM NaCl and 0.3 mM NaOH.[44] Transmission electron micrographs (TEM) have been

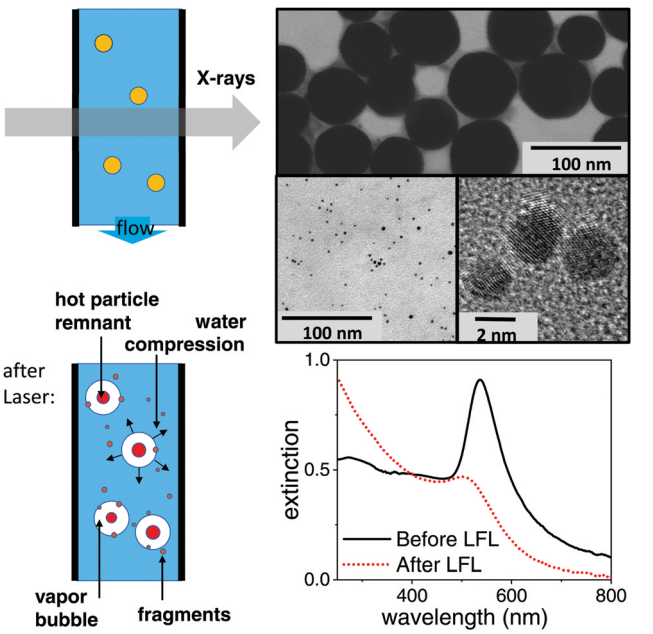

Fig. 1 Left: Sketch of the dominant structure modifications of a metal nanoparticle photo-excitation in aqueous suspension. Possible relaxations include particle heating, fragmentation and vapour bubble formation. In an isochoric situation within the first tens of nanoseconds the expanding bubbles demand for a corresponding compression of the water bulk. Possible scenarios of particle destruction include a partial ablation for fragments around a remaining (size-reduced) parent particle or a complete explosion. Right: Transmission electron micrographs of the educt particles (top), product suspension (centre) together with the corresponding extinction spectra after LFL with 10 ps pulses at 300 J m^{-2}.

acquired on a Zeiss EM 910 (80 kV). Size analysis of the Feret diameter has been done by the software ImageJ. The size distribution in suspension has been derived by an analytical disc centrifuge (ADC, CPS Instrument DC 24 000) at 24 000 rpm. TEM images and extinction spectra after LFL are shown in Fig. 1 and the TEM histogram of product particles in the ESI.† No aggregates were detected by ADC. This is supported by the measured zeta potential. During LFL the zeta potential value of the nanoparticle colloids increased from −36.7 mV before to −75.5 mV after LFL, indicating high colloidal stability of the fragmented particles. Zeta potential measurements (Malvern Zetasizer Nano Z) were performed at a constant pH of 9.

1.3 *In situ* pulsed X-ray scattering of fragmentation

Time-resolved X-ray scattering has been performed at the beamline ID09 at the European Synchrotron Radiation Facility by a pump–probe setup at 1 kHz repetition rate. The suspension was pumped through a quartz capillary (Hilgenberg) of 0.35 mm diameter at a throughput of 2 ml min^{-1}, such that the sample aliquot is replaced after each pulse pair, as indicated in Fig. 1. This assures single-pulse excitation of every part of the sample. The pump laser for fragmentation was a regenerative amplifier on Ti:Sa basis (Coherent Legend), whose fundamental at 800 nm and 2 ps pulse length has been converted into 532 nm light by an optical parametric amplifier (Light Conversion, TOPAS). The pulse length was thus reduced to $\leq$1 ps. The laser light at 532 nm was attenuated by a combination of polarizer (Glan Laser) and motorized waveplate retarder to control the fluence on the sample. Focusing to a 0.26 mm spot size (fwhm) was done by a 500 mm lens. The capillary was irradiated at an angle of 80 degrees, while the illuminated portion of the liquid was at the same time intersected by the X-ray beam.

Pulsed X-rays at 15.2 keV for probing were produced by a single-line undulator[45] and further monochromatized by a multilayer pair of ruthenium/B_4C to a 0.17 keV bandwidth. The pulse train from the storage ring was reduced to 1 kHz by an ultrasonic chopper wheel.[46] Scattered X-rays were detected by a CCD camera (charge coupled device) after conversion to visible light in a scintillator with fiber coupling (Rayonix 170). The transmitted X-ray beam was shielded from the detector by a millimetre-sized metal cylinder as beam stop. A short distance (0.12 m) between capillary and detector screen allowed to cover a solid angle of 60 degrees (wide-angle scattering, WAXS) to record different portions of the scattering yield, such as the liquid scattering from water, the powder rings from the suspended crystalline gold particles and also scattering at low angles related to mesoscopic structures (*e.g.* particle shapes). The small-angle scattering (SAXS) part could be further resolved to smaller angles by increasing the capillary-detector distance to 0.65 m. The images accumulated the scattering from typically 3000 pulses in SAXS and 30 000 pulses in WAXS geometry.

The data acquisition was repeated both for a given delay between X-ray pulses and laser pulses and for a negative delay (−2 ns) in order to isolate signal changes that were linked to photo-excitation. At a (negative) delay of −2 ns the laser pulse followed X-ray scattering, such that only a non-excited sample was probed. The time resolution was given by the X-ray pulse length (about 80 ps) rather than the timing jitter between laser and X-rays (<10 ps). The average fluence is calculated from the intensity distribution of the laser pulses across the X-ray probed central area (0.04 × 0.06 mm^2).

1.4 Data analysis

The 2D X-ray scattering images were subjected to standard image corrections (dark current, flat field, solid angle coverage of different pixels and masking invalid pixels) and integrated azimuthally to get a scattering function $S(q)$ with q being the scattering vector $q = 4\cdot\pi/\lambda\cdot\sin(2\Theta/2)$, with X-ray wavelength λ and the solid angle of scattering 2Θ.

The scattering is dominated by the liquid scattering of water and the capillary scattering. The latter is removed by the process of taking differences $\Delta S(q) = S(q)_\tau - S(q)_{-2ns}$ between the scattering at delay τ and the negative delay. The liquid scattering is only modified slightly, if the liquid undergoes changes in volume and/or temperature.[47] In the difference curve the very weak change in bond angle in such a situation is prominently visible as smooth difference features, as indicated in Fig. 2. As this change in scattering is stationary (only scales with amplitude of change in T and V, but does not shift) in the linear approximation, it can serve to quantify the amount of change. In particular the derivatives $dS/dT|_p$ and $dS/pV|_T$ are known.[47,48] By using the thermal expansion coefficient of water we can translate the signal height into change in volume of the liquid phase. The basic assumption here is that once vapour bubbles form around the excited nanoparticles (and vapour contributing only as background to the scattering curve), the bulk of water needs to be compressed to accommodate the bubbles. After some 100 nanoseconds the liquid column may react by a macroscopic expansion. In this scenario, the total bubble volume can be derived directly (open circles in Fig. 2b).

Gold particles crystallized in an fcc structure give rise to lattice planes that diffract X-rays. The corresponding powder peaks (particles are randomly oriented in the suspension) are seen in the difference scattering in Fig. 2a as sharp negative peaks, as order is lost during photo excitation. The shift in peak position reflects thermal expansion, while the peak intensity is related to the amount of remaining crystalline material and to a lesser extent to thermal-vibration induced intensity reduction (Debye–Waller factor). Here, we mainly analyse the peak intensity, as due to the X-ray bandwidth the resolution of crystalline grain size is limited to below 14 nm. The integral over the (111) peak in Fig. 2a is displayed as crosses in Fig. 2b.

Small angle scattering changes due to several effects: once by the formed vapour bubbles[37,49] and secondly by size changes of the laser-fragmented gold particles. A loss of intensity at scattering vector $q \ll 0.01$ $Å^{-1}$ is found, if the parent particles are destroyed, while an increase at $q > 0.015$ $Å^{-1}$ is observed, if new fragments appear (see Fig. 2a). The integration of $S(q)\cdot q^2$ (Porod invariant) from 0.015 $Å^{-1}$ to 0.5 $Å^{-1}$ serves as a measure for the total mass of small fragments (filled bullets in Fig. 2b). Overall, the observables in Fig. 2b allow for disentangling the temporal evolution of particle crystallinity, size and bubble formation, as discussed in Section 2.2.

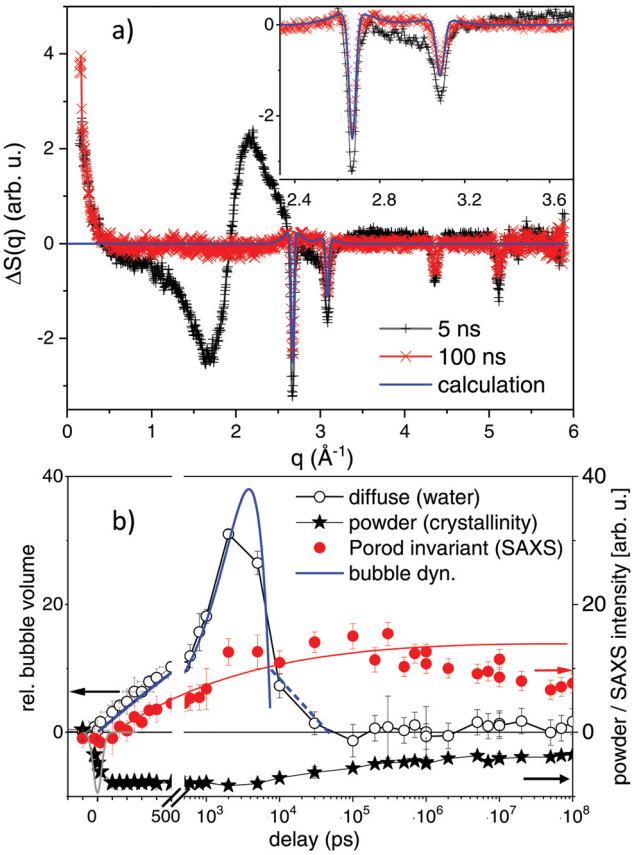

Fig. 2 (a) Selected difference scattering curves after excitation at maximum fluence (1800 J m^{-2}). Black crosses mark the signal at a delay of 5 ns with large excursions around the liquid water peak of 2.2 Å^{-1}. The 100 ns delay is shown by red crosses. The inset magnifies the small-signal region together with a line plot of a simulation of powder scattering, see text. (b) Observables for time-dependent transients: diffuse scattering signal for water changes, SAXS Porod invariant (<0.3 Å^{-1}) reflecting formation of new, small particles and the loss in powder intensity of the (111) reflection, showing particle melting and recrystallization. The thick blue line indicates parabolic kinetic trace indicative of bubble dynamics together with possible rebound stages (dashed line). The thin red line is a guide to the eye for the SAXS signal evolution. The grey (Gaussian) line around zero delay indicates the temporal resolution of the X-ray pulses.

2 Results and discussion

The understanding of photo-reactions in gold nanoparticles requires the definition of the thermal and structural pathway. In particular, phase transitions and dissipative channels are of importance. The concept that the laser light is preferentially absorbed in the nanoparticles embedded in the medium is central. The energy is quickly transformed into heat (except for non-thermal relaxations, such as near-field effects[20] or electron,[25] light, and shock wave emission). The temperature increase of the particles and subsequently the medium leads to structural changes, such as particle melting, bubble formation in water or particle decomposition. Quantifying the contribution of each process is not trivial. In the following we discuss a caloric and a kinetic verification of the state of matter.

2.1 Caloric prediction of phase behaviour

In a caloric approach the absorbed energy is compared to the latent heat of the particles, including heat capacities and heat of melting and fusion.[19,28,34,50] This can be done by (i) an estimation of the absorbed energy from incident fluence and particle-related optical properties. The extinction cross section for spherical particles can be derived by Mie theory.[51,52] Alternatively, (ii) the absorbed energy can be estimated from the extinction of the suspension and a known particle mass density in the suspension. In this case, however, absorption needs to be detailed out, as scattering may contribute to extinction but not to energy uptake.

Both approaches have been used in literature. A direct access to temperature may also be available through (iii) recording temperature-dependent properties, such as elastic moduli[53,54] or thermal expansion.[50] This breaks down for plastic or irreversible relaxations, such as melting or decomposition. Nevertheless, it is possible to nominally estimate the energy uptake by extrapolating the slope of *e.g.* thermal expansion *versus* applied fluence, given that the absorption process (within the pulse length) is shorter than the onset of irreversible relaxations (*e.g.* melting). Further care has to be taken to not neglect transient loss mechanisms, such as intrapulse extinction change through transient bleaching or other energy dissipation.

Dissipation can happen *via* heat conduction or liquid-vapour formation. Heat transfer calculations based on continuum models are successful below bubble formation.[37,50,55] Bubble formation isolates the particles thermally from the liquid, which requires numerical modelling and assumptions about lifetimes or effective transfer coefficients.[56–60] In the present experiment, the pulse length of 1 ps assures that laser energy is absorbed before major structural relaxations and dissipation occur (the latter is slower than the 80 ps observation delay), such that the absorbed energy is localized in the particle.

We have used a laser fluence of 1800 J m^{-2} in the X-ray probed portion of the liquid jet, which afforded a pulse energy after the OPA of 160 μJ. The direct access to mean particle temperature of the crystalline fraction consists in the *in situ* analysis of the powder scattering from the gold fcc lattice. The intensity will drop and finally vanish at the melting transition, while the position of the peaks (for instance the (111) reflection) will shift towards lower angles, reflecting lattice expansion. The lattice expansion at 80 ps delay together with peak intensity is shown in Fig. 3 as function of fluence. With a 80 ps time resolution and cooling times of about 0.3–1 ns[50,61] the observed expansion within the time resolution is expected to record the maximal value and represent the most strongly heated state. At the same time, local thermal equilibrium is supposed to be reached. We observe that the expansion initially scales linearly with fluence, showing a slope of (8.5 ± 0.8) K (J m^{-2})$^{-1}$. Around 80–120 J m^{-2} the slope strongly decreases, while the scattering intensity drops. The extrapolated linear expansion would reach the value of 1.78%,[62] which is the maximum lattice expansion of gold at the melting point. Melting point depression is only expected to amount for about 10 K,[63] while the (initial) lattice

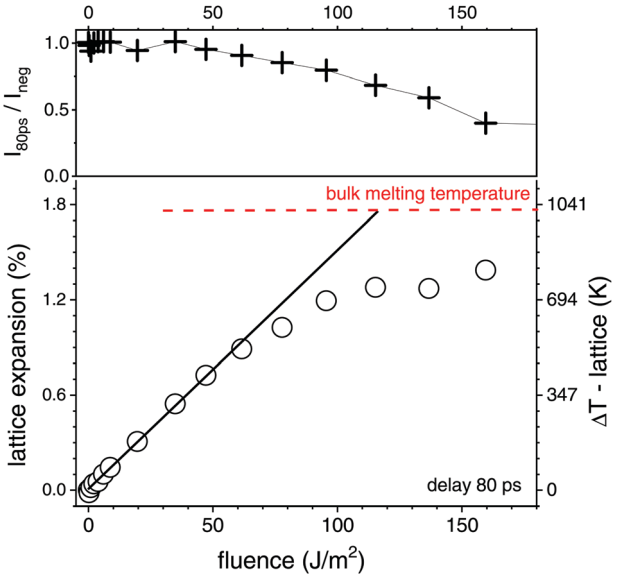

Fig. 3 Top: Change of the intensity of the (111) powder peak at delay τ = 80 ps as function of laser fluence relative to the non excited suspension (τ = −2 ns). Bottom: Lattice expansion (correlated to temperature increase ΔT) as function of fluence at τ = 80 ps, the size of the open circles represents the error margin. The horizontal dashed line marks the maximum expansion at the melting point of gold. The full line indicates the initial slope of the expansion *versus* fluence.

expansion of gold nanoparticles is found not to deviate strongly from the bulk value.[64] It should be noted that an onset of melting removes the hottest particles from observation such that the apparent temperature is lower than the full ensemble average. This can explain the reduction of the slope above 80 J m^{-2}. Consequently, the transition to complete melting is manifested at a fluence F above 120 J m^{-2}. One has to take into account that the real transition even in an individual particle may be smeared out in fluence due to the finite size and distribution of the absorbed energy between lattice heating and (surface) melting.

A calculation of expected heating ΔT as function of fluence according to approach (i) requires to calculate the change in temperature *via*:

$$\Delta T = \frac{\Delta Q}{c_p \cdot m} = \frac{K_{abs} \cdot \pi r^2}{c_p \cdot m_p}, \quad (1)$$

with ΔQ being the absorbed energy per particle as derived by the physical cross section with radius r and the absorption efficiency K_{abs} together c_p and m_p being the mass-specific heat capacity and particle mass, respectively. By taking the absorption efficiency of a particle of 54 nm diameter from a standard Mie calculation[52] and the heat capacity for bulk gold a slope of 31 K (J m^{-2})$^{-1}$ is calculated. Alternatively, using (ii) the macroscopic extinction of the suspension, OD (0.35 mm) at a capillary thickness of 0.35 mm, the absorbed energy in the liquid column with surface area A gets $\Delta Q_V = (1 - 10^{-OD}) \times A \times F$. The gold concentration was measured using inductively coupled plasma mass-spectroscopy (ICP-MS, PerkinElmer Sciex, ELAN 6000) after aqua regia decomposition to a precision of 2%. The extinction of a sample is easy to measure, however, the scattering contribution has to be singled out, which is also done *via* the Mie calculation. A slope of (33 ± 5) K (J m^{-2})$^{-1}$ is derived (main errors are the OD and capillary thickness), following this approach. This value is quite close to approach (i), which reassures that sample properties (under cw illumination as in UV-Vis spectroscopy) match the expectation from Mie theory. A finite size dispersion may lead to a smaller real slope of the heating, in particular in approach (i). By using the size dispersion (27% Gaussian width) we estimate from the variation in plasmon resonance that the slope could be reduced by 12% relative to the ideal value above. The experimentally determined slope of 8.5 K (J m^{-2})$^{-1}$ by (iii) is found to be much lower than the predicted ones. This points to yet not fully understood loss mechanisms, possibly due to electron or plasmon dynamics. Earlier, a discrepancy was found between the predicted and measured slope with excitation at 400 nm with a difference less than a factor of 2.[37,61] Additionally, it has been reported that excitation at (or close to) the plasmon resonance (here 532 nm) is less efficient due to delocalized field distribution[65,66] or ultrafast plasmon band bleaching.[67] Indicative of the latter is also the observation the bubble formation threshold in the current experiment is found at about 56 J m^{-2}, which is not much lower than the previously recorded threshold of 80 J m^{-2} at 400 nm (femtosecond pulses)[61] or 50 J m^{-2} at 355 nm (picosecond pulses)[68] for similarly sized gold particles, despite the absorption cross section being enhanced by a factor of 2 at 532 nm.

Altogether, we can secure the general caloric scale for the excitation of the gold nanoparticle suspension, noting that melting is observed above 120 J m^{-2}. Using the experimentally determined slope of 8.5 K (J m^{-2})$^{-1}$, fully melted particles are expected above 165 J m^{-2}, while full evaporation may be achieved above 2000 J m^{-2}.[34] This, however, does not include nonlinearity in absorption (such as bleaching or plasma formation[69]) or possible loss mechanisms, such as heat dissipation during particle overheating, additional scattering or bubble formation. We note that the applied maximum laser fluence of 1800 J m^{-2} is barely able to fully evaporate the particles, in particular with unquantified loss mechanisms. Thus, a pure evaporation mechanism is unlikely.

2.2 Kinetic identification of structural pathways

In a kinetic approach, structure relaxations may be identified in a time-resolved manner by observing abrupt (discontinuous) changes of properties, such as probe light absorption.[28,70] A well-documented case is the appearance of vapour bubbles on heated nanoparticles, which changes the particle extinction as well as adding light scattering pathways.[37,68]

In optical measurements different relaxation pathways can be correlated to the changes in the extinction, mainly around the plasmon resonance. However, specific transients (shift of the plasmon resonance due to changes in the particle electron density or refractive index of the liquid)[33,68,71,72] mix with unspecific transients, such as scattering from particles and bubbles[70] or aggregated nanoparticles. In X-ray scattering, due to separation of length scales in reciprocal space, different structural reorganization

can be discerned. The first discussed feature is the lattice expansion and loss of crystallinity seen at the gold powder scattering. In Fig. 2a scattering difference curves of the excited suspension at given delay are displayed in a wide range of scattering vector q. The loss of crystallinity is seen as sharp dips at several q positions, related to the different gold fcc reflections. The angular resolution is slightly lower than required to resolve the Scherrer width of the educt due to the finite bandwidth of the X-rays, but sufficient for quantifying the peak shift. The scattering difference at the (111) peak at 2.67 $Å^{-1}$ is negative at 1800 J m^{-2} due to the complete melting at 5 ns. This is still the case at 100 ns, while at this delay a positive contribution at the sides of the peak appears. This can be modelled by assuming additional powder scattering from crystalline particles with the same lattice parameter, but much broader Scherrer width (indicated a bold line in the inset of Fig. 2a). An estimate of the crystalline size from the Scherrer width returns about 2 nm in diameter. The kinetics of the powder scattering intensity loss in Fig. 2b shows that the powder peaks are lost within the time resolution of the experiment to only partly reappear after some 100 to 500 ns. Most of the intensity is lost throughout the probed delay range, indicating liquefied or fragmented particles.

A prominent part of scattering change is the broad modulation around 1.7, 2.2 and 3 $Å^{-1}$, which is related to the position of the (twin) liquid water peak. It has been shown earlier that this can be interpreted as thermodynamic change of the water phase,[47] in the present case a water compression following vapour bubble expansion.[48,49,65] The kinetics show a rise and decay within a 10 ns interval after excitation, which is compatible with a parabolic (ballistic) growth and recess known from bubble dynamics theory.[73] Such bubble dynamics can show multiple oscillations, which in the present case can not be temporally resolved due to the differences in lifetimes between individual bubbles in the ensemble.[49,60,68] Yet, it appears that most of the bubble signal has decayed within 30 ns. It can be inferred that when bubbles have vanished the transiently hot nanomaterial (product and educt particles) would cool down within 1–2 ns.[50,55]

Most interestingly in view of the envisaged fragmentation, a prominent SAXS signal starts to appear at low q (<0.3 $Å^{-1}$). This holds 3 contributions, SAXS from the appearing bubbles,[49] a loss in scattering, if the large educt particles are destroyed and a positive scattering contribution for newly formed small product particles. The achieved lower resolution limit in q, however, gives limited access to the educt particles and bubbles. Due to their large size, the corresponding scattering is strongest below 0.015 $Å^{-1}$,[74] which is close to our lower limit (0.01 $Å^{-1}$). Therefore, the main part of SAXS is positive in Fig. 2b, being related to formation of new product particles.

Within the first 10 ns the Porod invariant, as a measure for the total particle mass of particles below about 15 nm, increases monotonously, similar to bubble growth at early delay (see Fig. 2b). It is difficult to quantify the exact magnitude of the invariant while vapour bubbles are still present. Nevertheless, after bubbles have vanished after 10–30 ns, the SAXS signal persists and tends to grow slightly until a delay of 1 μs. Afterwards, it decays slightly, but one should be aware that the flow in the capillary transports the excited plug out of the probed region.

Overall, particle melting, disintegration (persistent loss of crystallinity) and bubble formation are seen in the kinetic traces. Energy dissipation is almost complete after 10–20 ns of bubble lifetime, which may prevent more rapid thermal dissipation. Therefore, the time window of violent particle modifications is limited to that interval, which is corroborated by the stationary Porod invariant after this delay and the characterization as single-step process.[41]

2.3 Fragmentation

The scenario for fragmentation through evaporation as opposed to decomposition *via* spinodal decay and Coulomb instability would be a complete particle atomization, followed by nucleated growth of atom clusters. A direct appearance of product particles of different sizes, respectively in spinodal or Coulomb decomposition[75] would take place. The Coulomb instability suggests that the creation of daughter particles of some nanometre size would be an efficient pathway to lower the surface charge density of the excited (molten) particles.[9,25,29,76] A current study reports on the observation of Coulomb fission in silica-shell gold particles, that show a signature of small product droplets ejected after femtosecond excitation.[30] A recent structural resolution of gold particle excitation and fragmentation in air on a substrate has shown a stress-mediated explosion at relatively low fluence just above melting.[31] Such a scenario may not be distinguishable from spinodal decomposition with the fragment size depending on the level of overheating.[29] Stronger overheating will produce smaller fragments together with evaporation.

At the earliest delay of 30 ns, which is not mixed any more with bubble signal in SAXS, we already observe a distinct scattering distribution below 0.5 $Å^{-1}$. This scattering persists and changes shape only slightly for increasing delay. Fig. 4a shows the scattering distribution as Kratky representation at 1 μs. Qualitatively, maxima in this plot mark distinct size fractions (1–3 nm and 10–25 nm), whose diameters scale inversely with the corresponding scattering vector. A simulation of the scattering has been done by a reverse Monte Carlo approach,[77] optimizing a freely adjustable distribution of spheres in a large size interval. The resulting mass-weighted histogram shows a predominant population of 2–3 nm particles, accompanied by larger particles (Fig. 4b) at a delay of 1 μs for the gold colloid with NaCl/NaOH. The distribution is fairly narrow, also for earlier times. This would be even more peaked at 2–3 nm in a size-weighted distribution as often presented for *ex situ* characterization. A comparison to the size analysis by ADC and TEM of the final irradiated particles shows a comparable distribution, which is shifted slightly towards larger particles in TEM (see ESI†). This could be induced by drying of the colloid when preparing the TEM grid, sensitivity of the (Feret) diameter in TEM on anisotropy during deposition[78] or selective detection of larger (higher-contrast) particles. Fig. 4c shows the temporal evolution of the small particle fraction with the delay. The hydrodynamic diameter of post-synthesis analysis by ADC (ESI†) fits the *in situ* size distribution quite well.

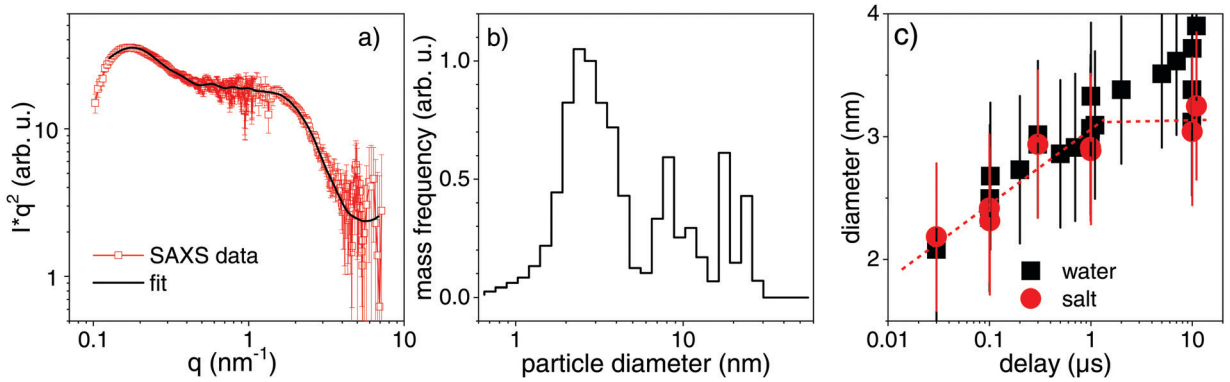

Fig. 4 (a) Scattering distribution at low angles (SAXS) at a delay of 1 µs together with a simulation according to a reverse Monte Carlo optimization. (b) Size distributions as derived from the SAXS simulation at 1 µs. (c) Evolution of the particle size as function of delay for the dominant size fraction. Black squares represent fragmentation in pure water and red bullets fragmentation in a micromolar (300 µM) NaCl/NaOH solution. The symbol size indicates the error in mean size determination, while the error bars reflect the root mean square distribution width.

We find fragments of 2 nm diameter both in pure water and aqueous NaCl/NaOH directly after bubble disappearance. The diameter undergoes a growth phase with the largest particles being observed at the longest analyzed delay of 10 µs. It seems that fragments in NaCl/NaOH solution do not grow as strongly as in pure water on the microsecond time scale, limited by the statistical significance. For delays <1 µs the particle size evolution seems not to be affected by the electrolyte content, whereas later the electrolytes appear to quench growth. Further studies need to clarify this transition and the time scale of size quenching. Nevertheless, it should be emphasized that the dominant fragment nanocluster population of 2–3 nm is quantitatively resolved already after 30 ns and is qualitatively indicated on a sub-nanosecond scale. This should be put in perspective to the early expansion phase of the fragmented particles and bubble. Therefore, we expect that fragmentation at a fluence close to complete evaporation of the gold particles would produce clusters of finite initial size together with atoms and ions as opposed to a pure evaporation and condensation process. Our present level of structure resolution does not yet allow to conclude on the quantitative partition between phase explosion, charge instability or evaporation.

Besides, these early fragments tend to grow in a limited fashion, in particular, if micromolar concentrations of anions are present. Recently, Ziefuß *et al.* studied the role of anions during LFL and found synergism between specific halide anions and basic pH on yielding narrow nanocluster size distributions.[44] The profile of powder scattering in Fig. 2 as well suggests that apart from the scattering loss due to molten educt particles the additional scattering on the wings of the powder peaks indicates that smaller fragments (<2 nm) have formed and have rapidly crystallized as soon as getting in contact with water.

Both Coulomb instability and spinodal decomposition above the boiling point would deliver small product particles as a single-step, instantaneous (on the scale of the local dynamics) reaction. These mechanisms are yet not discriminated. A pure (surface) evaporation process is unlikely here due to the fast onset of product signal. Earlier reports have inspected the emerging fragments by electron microscopy and have found small spherical clusters similar to our observations as well as fingering structures.[9,79] This fingering could be a result of a beginning phase explosion with a fast crystallization as soon as the fragments get in contact to the liquid due to the faster cooling of smaller structures.

The notion of a single-step, instantaneous process has important implications. First, a single-step process is capable of producing the desired fragment particles in one laser irradiation shot. Therefore, processing in a flow reactor or jet[41] is achievable by one passage for an optimized throughput. Secondly, the results show that nanoparticles are produced instantaneously, *i.e.* not requiring a certain delay or incubation time, notwithstanding limited ripening. In an evaporation and growth process, the diffusion and coalescence of fragmented species would dictate the quality of the fragment output. This would be disturbed when adding surface charge delivering additives for preventing ripening.[44] In the instantaneous process of educt particle explosion, the product particles are directly formed and could be size-quenched, if desired. The process would also be biased by external parameters, such as educt concentration, if further secondary processes would define the products. This would limit the generalization of the description and definition of the process.

3 Conclusions

The calorics and kinetics of structure formation during laser-induced fragmentation of spherical gold particles in aqueous suspension, respectively containing a minute amount of ions, has been investigated by direct time-resolved and structural access *in situ*. The results are based on a laser-pump and X-ray-probe setup that allows to irradiate each volume element by a single laser pulse by employing a jet flow. At a fluence of 1800 J m^{-2}, which is close to full evaporation of the educt particles, an almost complete transformation into 2–3 nm particles could be observed. On a time scale of up to 10 µs, a slight growth was observed, quenched by ion adsorption. Above

10 μs, trends indicate further limited particle growth but was not resolved by the experiment. In turn, the adsorption process of anions on the nanoparticle surface improving the colloidal stability has to occur already on time scales below 1 μs.

Note that energy losses also occur *via* dissipation by heat transfer into water and subsequent water boiling and probably non-linear plasmon bleaching during the laser pulse duration. Although the fluence is compatible to an evaporation process followed by a secondary particle nucleation and growth, we could quantify product particles of 2 nm as early as 30 ns after excitation. The given time scale is very short for effective diffusional growth from atoms. Therefore, it is concluded that the fragmentation should include direct fragmentation into nm sized products. Yet, we can not distinguish between different phenomena, such as stress mediation, phase explosion or Coulomb instability.

Nevertheless, the picosecond laser fragmentation process is classified as a single-step, instantaneous reaction. This represents an important aspect for the application as a high-throughput method for production of small, protoplasmonic gold particles in an upscaled thoughput.

Conflicts of interest

The authors declare that no conflicts of interest exist.

Acknowledgements

The research is funded by the Helmholtz Association under the topic "from matter to materials and life" and German Science foundation under contract BA 3580/22-1. The ESRF is acknowledged for provision of beamtime and funding. Support by M. Sander is gratefully acknowledged. AP acknowledges the support from the DFG within the Heisenberg fellowship. We would like to thank L. Zhigilei for fruitful discussions. Jurij Jakobi (U. Duisburg-Essen) is acknowledged for the provision of the TEM micrographs.

Notes and references

1 C. Yao, X. Qu, Z. Zhang, G. Hüttmann and R. Rahmanzadeh, *J. Biomed. Opt.*, 2009, **14**, 054034.
2 Y. Zhang, C. Zhang, C. Xu, X. Wang, C. Liu, G. I. N. Waterhouse, Y. Wang and H. Yin, *Talanta*, 2019, **200**, 432–442.
3 T. Higaki, Y. Li, S. Zhao, Q. Li, S. Li, X.-S. Du, S. Yang, J. Chai and R. Jin, *Angew. Chem., Int. Ed.*, 2019, **58**, 8291–8302.
4 S. Reichenberger, G. Marzun, M. Muhler and S. Barcikowski, *ChemCatChem*, 2019, **11**, 4489–4518.
5 D. Zhang, B. Gökce and S. Barcikowski, *Chem. Rev.*, 2017, **117**, 3990–4103.
6 R. Streubel, S. Barcikowski and B. Goekce, *Opt. Lett.*, 2016, **41**, 1486–1489.
7 F. Mafuné, J. y. Kohno, Y. Takeda and T. Kondow, *J. Phys. Chem. B*, 2002, **106**, 8555–8561.
8 S. Inasawa, M. Sugiyama, S. Noda and Y. Yamaguchi, *J. Phys. Chem. B*, 2006, **110**, 3114–3119.
9 S. Hashimoto, T. Katayama, K. Setoura, M. Strasser, T. Uwada and H. Miyasaka, *Phys. Chem. Chem. Phys.*, 2016, **18**, 4994–5004.
10 A. Podlipensky, A. Abdolvand, G. Seifert and H. Graener, *Appl. Phys. A: Mater. Sci. Process.*, 2005, **80**, 1647–1652.
11 Z. Peng, T. Walther and K. Kleinermanns, *J. Phys. Chem. B*, 2005, **109**, 15735–15740.
12 V. Resta, J. Siegel, J. Bonse, J. Gonzalo, C. N. Afonso, E. Piscopiello and G. V. Tenedeloo, *J. Appl. Phys.*, 2006, **100**, 084311.
13 C. Yao, R. Rahmanzadeh, E. Endl, Z. Zhang, J. Gerdes and G. Hüttmann, *J. Biomed. Opt.*, 2005, **10**, 064012.
14 J. Krawinkel, U. Richter, M. L. Torres-Mapa, M. Westermann, L. Gamrad, C. Rehbock, S. Barcikowski and A. Heisterkamp, *J. Nanobiotechnol.*, 2016, **14**, 2.
15 X. Huang, I. H. El-Sayed, W. Qian and M. A. El-Sayed, *J. Am. Chem. Soc.*, 2006, **128**, 2115–2120.
16 L. R. Hirsch, R. J. Stafford, J. A. Bankson, S. R. Sershen, B. Rivera, R. E. Price, J. D. Hazle, N. J. Halas and J. L. West, *Proc. Natl. Acad. Sci. U. S. A.*, 2003, **100**, 13549–13554.
17 C. M. Pitsillides, E. K. Joe, X. Wei, R. R. Anderson and C. P. Lin, *Biophys. J.*, 2003, **84**, 4023–4032.
18 N. S. Abadeer and C. J. Murphy, *J. Phys. Chem. C*, 2016, **120**, 4691–4716.
19 A. Takami, H. Kurita and S. Koda, *J. Phys. Chem. B*, 1999, **103**, 1226–1232.
20 A. Plech, V. Kotaidis, M. Lorenc and J. Boneberg, *Nat. Phys.*, 2006, **2**, 44–47.
21 G. González-Rubio, P. Díaz-Núñez, A. Rivera, A. Prada, G. Tardajos, J. González-Izquierdo, L. Bañares, P. Llombart, L. G. Macdowell, M. A. Palafox, L. M. Liz-Marzán, O. Peña-Rodriguez and A. Guerrero-Martínez, *Science*, 2017, **358**, 640–644.
22 M. E. Povarnitsyn, T. E. Itina, P. R. Levashov and K. V. Khishchenko, *Phys. Chem. Chem. Phys.*, 2013, **15**, 3108–4114.
23 P. V. Kamat, M. Flumiani and G. V. Hartland, *J. Phys. Chem. B*, 1998, **102**, 3123–3128.
24 T. Döppner, T. Fennel, T. Diederich, J. Tiggesbäumker and K. H. Meiwes-Broer, *Phys. Rev. Lett.*, 2005, **94**, 013401.
25 K. Yamada, Y. Tokumoto, T. Nagata and F. Mafuné, *J. Phys. Chem. B*, 2006, **110**, 11751–11756.
26 S. Hashimoto, D. Werner and T. Uwada, *J. Photochem. Photobiol., C*, 2012, **13**, 28–54.
27 T. E. Itina, K. Gouriet, L. V. Zhigilei, S. Noël, J. Hermann and M. Sentis, *Appl. Surf. Sci.*, 2007, **253**, 7656–7661.
28 M. Strasser, K. Setoura, U. Langbein and S. Hashimoto, *J. Phys. Chem. C*, 2014, **118**, 25748–25755.
29 L. Delfour and T. E. Itina, *J. Phys. Chem. C*, 2015, **119**, 13893–13900.
30 J. M. Voss, P. K. Olshin, R. Charbonnier, M. Drabbels and U. J. Lorenz, *ACS Nano*, 2019, **13**, 12445–12451.
31 Y. Ihm, D. H. Cho, D. Sung, D. Nam, C. Jung, T. Sato, S. Kim, J. Park, S. Kim, M. Gallagher-Jones, Y. Kim, R. Xu, S. Owada, J. H. Shim, K. Tono, M. Yabashi, T. Ishikawa, J. Miao, D. Y. Noh and C. Song, *Nat. Commun.*, 2019, **10**, 2411.

32 S. Link, Z. L. Wang and M. A. El-Sayed, *J. Phys. Chem. B*, 2000, **104**, 7867–7870.
33 D. Werner, A. Furube, T. Okamoto and S. Hashimoto, *J. Phys. Chem. C*, 2011, **115**, 8503–8512.
34 A. Pyatenko, H. Wang, N. Koshizaki and T. Tsuji, *Laser Photonics Rev.*, 2013, **7**, 596–604.
35 D. Werner and S. Hashimoto, *Langmuir*, 2013, **29**, 1295–1302.
36 C.-Y. Ruan, Y. Murooka, R. K. Raman and R. A. Murdick, *Nano Lett.*, 2007, **7**, 1290–1296.
37 A. Siems, S. A. L. Weber, J. Boneberg and A. Plech, *New J. Phys.*, 2011, **13**, 043018.
38 J. N. Clark, L. Beitra, G. Xiong, D. M. Fritz, H. T. Lemke, D. Zhu, M. Chollet, G. J. Williams, M. M. Messerschmidt, B. Abbey, R. J. Harder, A. M. Korsunsky, J. S. Wark, D. A. Reis and I. K. Robinson, *Proc. Natl. Acad. Sci. U. S. A.*, 2015, **112**, 7444–7448.
39 S. Reich, P. Schönfeld, P. Wagener, A. Letzel, S. Ibrahimkutty, B. Gökce, S. Barcikowski, A. Menzel, T. dos Santos Rolo and A. Plech, *J. Colloid Interface Sci.*, 2017, **489**, 106–113.
40 S. Reich, A. Letzel, A. Menzel, N. Kretzschmar, B. Gökce, S. Barcikowski and A. Plech, *Nanoscale*, 2019, **11**, 6962–6969.
41 A. R. Ziefuß, S. Reichenberger, C. Rehbock, I. Chakraborty, M. Gharib, W. J. Parak and S. Barcikowski, *J. Phys. Chem. C*, 2018, **122**, 22125–22136.
42 S. Jendrzej, B. Gökce, V. Amendola and S. Barcikowski, *J. Colloid Interface Sci.*, 2016, **463**, 299–307.
43 M. Lau and S. Barcikowski, *Appl. Surf. Sci.*, 2015, **348**, 22–29.
44 A. R. Ziefuß, S. Barcikowski and C. Rehbock, *Langmuir*, 2019, **35**, 6630–6639.
45 A. Plech, R. Randler, A. Geis and M. Wulff, *J. Synchrotron Radiat.*, 2002, **9**, 287–292.
46 M. Cammarata, L. Eybert, F. Ewald, W. Reichenbach, M. Wulff, P. Anfinrud, F. Schotte, A. Plech, Q. Kong, M. Lorenc, B. Lindenau, J. Räbiger and S. Polachowski, *Rev. Sci. Instrum.*, 2009, **80**, 15101.
47 M. Cammarata, M. Lorenc, T. K. Kim, J. H. Lee, Q. Y. Kong, E. Pontecorvo, M. L. Russo, G. Schiró, A. Cupane, M. Wulff and H. Ihee, *J. Chem. Phys.*, 2006, **124**, 124504.
48 A. Plech, V. Kotaidis, M. Lorenc and M. Wulff, *Chem. Phys. Lett.*, 2005, **401**, 565–569.
49 V. Kotaidis and A. Plech, *Appl. Phys. Lett.*, 2005, **87**, 213102.
50 A. Plech, V. Kotaidis, S. Grésillon, C. Dahmen and G. von Plessen, *Phys. Rev. B: Condens. Matter Mater. Phys.*, 2004, **70**, 195423.
51 G. Mie, *Ann. Phys.*, 1908, **4**, 377–445.
52 P. Laven, 2005, http://www.philiplaven.com/mieplot.htm.
53 G. V. Hartland, M. Hu and J. E. Sader, *J. Phys. Chem. B*, 2003, **107**, 7472–7478.
54 H. Petrova, J. P. Juste, I. Pastoriza-Santos, G. V. Hartland, L. M. Liz-Marzán and P. Mulvaney, *Phys. Chem. Chem. Phys.*, 2006, **8**, 814–821.
55 O. M. Wilson, X. Hu, D. G. Cahill and P. V. Braun, *Phys. Rev. B: Condens. Matter Mater. Phys.*, 2002, **66**, 224301.
56 S. Merabia, S. Shenogin, L. Joly, P. Keblinski and J.-L. Barrat, *Proc. Natl. Acad. Sci. U. S. A.*, 2009, **106**, 15113–15118.
57 J. Lombard, T. Biben and S. Merabia, *Phys. Rev. Lett.*, 2014, **112**, 105701.
58 K. Metwally, S. Mensah and G. Baffou, *J. Phys. Chem. C*, 2015, **119**, 28586–28596.
59 J. Lombard, T. Biben and S. Merabia, *Nanoscale*, 2016, **8**, 14870–14876.
60 A. Dagallier, E. Boulais, C. Boutopoulos, R. Lachaine and M. Meunier, *Nanoscale*, 2017, **9**, 3023–3032.
61 V. Kotaidis, C. Dahmen, G. von Plessen, F. Springer and A. Plech, *J. Chem. Phys.*, 2006, **124**, 184702.
62 Y. S. Touloukian, R. K. Kirby, R. E. Taylor and P. D. Desai, *Thermal expansion – Metallic elements and alloys*, IFI Plenum, New York, Thermodynamical properties of matter edition, 1975, vol. 12.
63 P. Buffat and J.-P. Borel, *Phys. Rev. A: At., Mol., Opt. Phys.*, 1976, **13**, 2287–2298.
64 A. Plech, B. Krause, T. Baumbach, M. Zakharova, S. Eon and H. Bracht, *Nanomaterials*, 2019, **9**, 501.
65 A. Plech, S. Ibrahimkutty, S. Reich and G. Newby, *Nanoscale*, 2017, **9**, 17284–17292.
66 M. Magnozzi, R. Proietti Zaccaria, D. Catone, P. O'Keeffe, A. Paladini, F. Toschi, A. Alabastri, M. Canepa and F. Bisio, *J. Phys. Chem. C*, 2019, **123**, 16943–16950.
67 X. Zhang, C. Huang, M. Wang, P. Huang, X. He and Z. Wei, *Sci. Rep.*, 2018, **8**, 10499.
68 T. Katayama, K. Setoura, D. Werner, H. Miyasaka and S. Hashimoto, *Langmuir*, 2014, **30**, 9504–9513.
69 E. Boulais, R. Lachaine and M. Meunier, *J. Phys. Chem. C*, 2013, **117**, 9386–9396.
70 E. Lukianova-Hleb, Y. Hu, L. Latterini, L. Tarpani, S. Lee, R. A. Drezek, J. H. Hafner and D. O. Lapotko, *ACS Nano*, 2010, **4**, 2109–2123.
71 S. Link and M. A. El-Sayed, *Int. Rev. Phys. Chem.*, 2000, **19**, 409–453.
72 G. V. Hartland, *Phys. Chem. Chem. Phys.*, 2004, **6**, 5263–5274.
73 M. S. Plesset and A. Prosperetti, *Annu. Rev. Fluid Mech.*, 1977, **9**, 145–185.
74 A. Plech, V. Kotaidis, K. Istomin and M. Wulff, *J. Synchrotron Radiat.*, 2007, **90**, 022905.
75 F. Giammanco, E. Giorgetti, P. Marsili and A. Giusti, *J. Phys. Chem. C*, 2010, **114**, 3354–3363.
76 U. Näher, S. Bjørnholm, S. Frauendorf, F. Garcias and C. Guet, *Phys. Rep.*, 1997, **285**, 245–320.
77 B. R. Pauw, J. S. Pedersen, S. Tardif, M. Takata and B. B. Iversen, *J. Appl. Crystallogr.*, 2013, **46**, 365–371.
78 A. Letzel, B. Gökce, A. Menzel, A. Plech and S. Barcikowski, *Appl. Surf. Sci.*, 2018, **435**, 743–751.
79 S. Inasawa, M. Sugiyama and Y. Yamaguchi, *J. Phys. Chem. B*, 2005, **109**, 9404–9410.

3.2.3 Synergism between specific halide anions and pH effect during nanosecond laser fragmentation of ligand-free gold nanoparticles

Synopsis:

Previous studies have shown that next to physical (laser-) parameters, the particle's liquid environment plays a key role in synthesizing ultra-small gold nanoparticles as it supports colloidal stability (see chapter 2.2.4). Although the influence of the colloidal environment was systematically studied in the case of LAL, its effect on LFL is not well understood. Especially regarding the synthesis of completely inorganic Au NCs by LFL, such consideration is important since the ultra-small particles show a large specific surface area and are prone to undergo secondary particle growth without stabilization.

Therefore, in this experimental study, we investigated the extent to which the ionic strength, the anion type, and pH value during laser fragmentation in liquid influences the surface chemistry, electrostatic stabilization, and particle size distributions of the produced Au NCs. Our findings highlight a reduction of the mean particle size and increased mass yield of particles < 3 nm up to ~70% in the presence of halide anions and at alkaline pH. Interestingly, the synergism between the ionic strength and pH value leads to a maximum amount of Au NCs. Furthermore, we propose that this effect is anion-specific for a series of homologous halides as it mechanistically follows a direct Hofmeister's series at neutral pH and a reversal series in the alkaline regime. The herein proposed high-yield synthesis of ligand-free Au NCs, as well as tuning of their surface charge density, are a key prerequisites for the mechanistical study on the photoluminescence of fully inorganic Au NCs (Chapter 3.3) and their performance in heterogenous catalysts (chapter 3.4)

This paper was published in Langmuir on April 26, 2019.

LANGMUIR Article
Cite This: Langmuir 2019, 35, 6630–6639
pubs.acs.org/Langmuir

Synergism between Specific Halide Anions and pH Effects during Nanosecond Laser Fragmentation of Ligand-Free Gold Nanoparticles

Anna Rosa Ziefuß, Stephan Barcikowski,* and Christoph Rehbock*

University of Duisburg-Essen and Center for Nanointegration Duisburg-Essen (CENIDE), Essen 45145, Germany

Supporting Information

ABSTRACT: Gold nanoclusters (AuNCs) with diameters smaller than 3 nm are an emerging field of research because they possess interesting optical properties, such as photoluminescence. However, to date, it is still difficult to distinguish whether these properties originate from the cores of the nanoparticles or from the adsorbates on their surfaces. Hence, there is a high demand for ligand-free, ultra-small particles because they make it possible to study ligand and core effects separately. Pulsed laser fragmentation in liquids (LFL) is a convenient route for the synthesis of ligand-free AuNCs. The influence of physical parameters, such as melting and evaporation, on the LFL process is well understood both theoretically and experimentally. However, the impact of the chemical composition of the medium during LFL, which critically affects the particle formation process, has been less well examined. Therefore, in this work, we elucidate the extent to which the ionic strength, the pH value, and the nature of the halide anion that is present, that is, F^-, Cl^-, Br^-, or I^-, influence the particle size distribution of the LFL product and the mean yield of small particles (<3 nm) of the product. We showed that the yield of small particles can be enhanced by the synergism between pH and specific ion effects, which probably is attributable to the adsorption of specific anions. In addition, our findings indicated that anion-based stabilization depends critically on the type of anion. A direct Hofmeister effect was observed for anions in the neutral pH regime, whereas an indirect Hofmeister series was reported in alkaline solution, which probably was due to the more hydrophilic surfaces of the AuNCs that were formed.

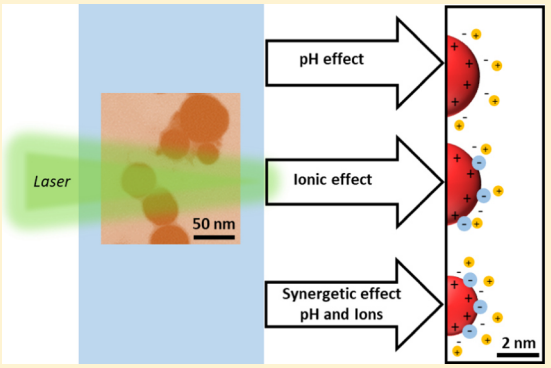

INTRODUCTION

For many decades, the properties of gold nanoparticles (AuNPs) have been studied intensively, and these nanoparticles are used now in many different applications. In addition to other areas, the use of AuNPs in nanobiotechnology has proven to be particularly beneficial.[1,2] Ultra-small AuNPs, called gold nanoclusters (AuNCs), are of particular interest because they exhibit interesting optical properties due to their reduced size (<3 nm).[3] The synthesis of AuNCs is primarily done by chemical methods, however, only in the presence of ligands.[3−5] Each of these wet chemical syntheses results in particles with surfaces that are occupied by organic ligands. Although many groups have worked on ligand-exchange procedures, these endeavors are almost never quantitative.[6−8] The study of the ligand-occupied surfaces of particles is difficult because the first two atomic layers appear amorphous due to organic ligands,[5] and the chemical nature of the surface is dominated by the properties of the ligands rather than the properties of gold.[9] The effects of the ligands and the core cannot be differentiated, so there is a demand for ligand-free AuNCs that are not accessible by chemical synthesis.

Pulsed laser ablation in liquid (LAL) is an alternative synthesis route that allows particles to be generated in pure water and without surface ligands.[10−12] The size distributions obtained usually are very broad, but they can be caused to vary significantly by the in situ addition of salts in the micromolar concentration range,[13] which leads to the quenching of the particle size already within the cavitation bubble.[14] Recent studies have shown that the formation of molecular O_2 and H_2, as well as H_2O_2, occurs during laser ablation.[15,16] the surfaces of the AuNPs after LAL are partially oxidized to Au^+/Au^{3+}, so that there is a pH-dependent equilibrium between Au−OH/AuO^-.[17] According to Merk et al.,[18] the oxidized proportion of surface gold atoms after LAL in pure water is 5.3%, which corresponds well with the estimation of 3.3−6.6% provided by Mafuné et al.[17] Even higher levels of oxidation (7.3%) were reported when ablation was conducted in sodium iodide.[18] However, to date, the correlation between LAL parameters and surface oxidation is not fully understood. The fact that salts can influence the chemistry of both flat and curved surfaces has been known for a long time. This effect is called the Hofmeister effect (first mentioned in 1888 in the field of protein preparation[19]), and it is caused by both anions and cations.[20−23] AuNPs are hydrophobic[24] because of their

Received: February 11, 2019
Revised: April 17, 2019
Published: April 26, 2019

relatively low surface oxidation and they have a negative surface charge.[25] Schwierz et al. used modeling approaches and predicted that the stabilities of such surfaces would be improved based on a direct Hofmeister series (HS) of halides, and their stabilizing effects were sorted as $F^- < Cl^- < Br^- < I^-$.[26] If the surfaces of such particles become more hydrophilic or if the surface charge becomes more positive, the anions may have the reverse influence.[26] Merk et al. showed the transferability of this concept to the stability of laser-fabricated Au colloids in situ stabilized by the adsorption of anions at low ionic strengths (ISs). Cosmotropic anions (e.g., F^-) exhibit no impact on colloidal stability because they are highly hydrated and cannot interact with the surfaces of the particles (Helmholtz layer) because of the compacted charge. However, chaotropic anions (Cl^-, Br^-, and I^-) have a low number of hydration, which allows them to interact with the highly polarizable surface of gold and increase the stability of the colloid, which probably is due to the increased charge density on the surface, which enhances electrostatic stabilization.[18]

According to the literature, LAL of AuNPs does not provide particle sizes smaller than 5 nm.[13,18] However, the synthesis of ligand-free particles with a size distribution in the range of less than 5 nm can be highly beneficial in nanobiotechnology. New possibilities emerge, especially in the field of imaging, because AuNPs smaller than ∼3 nm have fluorescent properties.[4] If these so-called AuNCs are present along with plasmonic AuNPs (>3 nm), optical detections can target both the plasmon band and the emission band. Lau et al. presented a method for synthesizing AuNCs by pulsed laser fragmentation in liquid (LFL).[27,28] For this purpose, a laser with a wavelength close to the plasmon band was used to reirradiate AuNPs produced by LAL. Amendola and Meneghetti showed an exponential progression of the resulting particle size after fragmentation in correlation with the incident fluence, and they observed a saturation of the particle diameter at 4 nm.[11] The resulting particle size after LFL of AuNPs depends on several different parameters. According to the literature, nanosecond LFL can be explained by a photothermal mechanism called heating–melting–evaporation mechanism.[29−32] In short, as soon as a particle absorbs a laser pulse, heat gain and heat loss processes occur that depend mainly on the driving force (laser fluence) and the kinetics of energy transfer. If the temperature of the electrons and the temperature of the lattice of a particle are in equilibrium and the temperature within the particles is high enough to exceed the boiling point of gold, the particle begins to evaporate, and this is followed by nucleation processes.[33] We know from the literature[34] that heating is a comparably slow process, and it is slowed down further in aqueous solution. As soon as the spinodal temperature is reached (>80% of the critical temperature[34]), the particles may overheat, resulting in explosive boiling and the additional formation of liquid droplets. Coalescence processes are to be expected because the surface energy of the ultra-small particles is very high, which can be considered as the driving force for the growth of particles.[35]

In addition to the laser parameters[29,30] and the particle size of the educt,[36] the properties of the matrix are particularly important for the recrystallization of the particles.[27] Lau et al. showed that the combined influence of oxidants and sodium hydroxide allows a further decrease in the particle size of the product down to less than 3.5 nm.[27,28] Ziefuß et al. recently demonstrated that an exchange of the oxidizing agent (H_2O_2) with sodium chloride in accordance with a significant reduction of the educt particle concentration results in an even smaller particle size distribution with a mode size of 2.9 nm. A high laser intensity of 1.6×10^{12} W/m^2 results in a monomodal fraction of AuNPs, which is yielded statistically by single laser pulse LFL conditions in liquid flow.[37] In addition, it was shown that the surface chemistry of these particles was impacted significantly by the number of laser pulses applied per particle.[37] With respect to the LAL synthesis of AuNPs,[18,38] it may be expected that the stability of the colloids generated during LFL could also be affected by higher homologues of the HS (e.g., Br^-, I^-). Note that the ex situ addition of salt to the AuNPs after LAL had no effect because the surface already was in an equilibrium state at this time.[18] Hence, the potential impacts of the IS, the pH value, and the type of anion, present during fragmentation, on the particle size distributions yielded by LFL may be anticipated, and they are elucidated systematically in this work.

MATERIALS AND METHODS

Pulsed LAL. As a starting material, ligand-free AuNPs with the size of 53 nm were synthesized by LAL of a gold target in ultrapure water by an Nd/YAG laser (Ekspla, Atlantic Series, 10 ps, 1064 nm, 9.6 mJ, 100 kHz, 10 min). The ablated AuNPs had a broad size distribution, including particles that ranged in size from 8 to 200 nm (Figure S1). The particles were double-centrifuged to separate the sizes (Hettich, 67.1g, 70 min). The unstabilized colloidal solution was left at a high concentration (1 g/L) for 1 week in order to get rid of residual small particles, which were depleted by the ripening process.[35]

Pulsed LFL. As stated above, the gold nanoparticles produced by LAL serve as the educt material for the process of pulsed laser fragmentation in a free liquid jet. A dropping funnel was filled with the gold colloid and the liquid jet (d = 1.1 mm), and it was illuminated with a nanosecond laser (Innolas, 9 ns, 100 Hz, 84 mJ, 532 nm, 1.6×10^{12} W/m^2, $A = 5.7 \times 10^6$ m^2) (Figure 1). The laser beam was

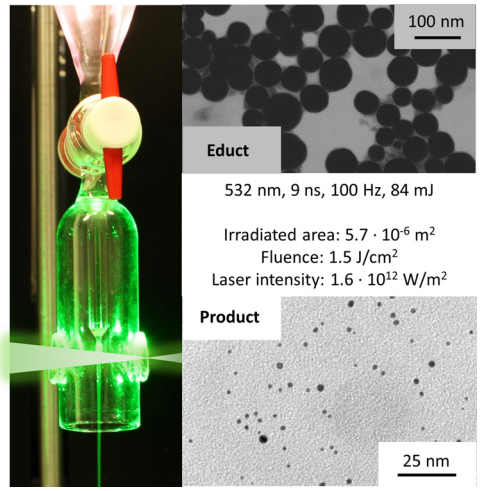

Figure 1. Image of the dropping funnel used during LFL in liquid flow with the axis of the laser beam arranged perpendicular to the direction the liquid was flowing.

focused with a cylindrical lens, and the flow velocity (0.64 m/s) was adapted to the spot size and repetition rate of the laser to ensure that each volume element was hit only once per run (passage).[37] However, because of the absorbance of the particles dispersed in the liquid jet, the laser beam was attenuated in the axial direction so that the particles, which were located away from the entry point, received less energy. In addition, note that the impact of the laser beam on the liquid jet resulted in the diffraction of the light and that the energy of the laser beam was distributed in a Gaussian shape in both space and

DOI: 10.1021/acs.langmuir.9b00418
Langmuir 2019, 35, 6630–6639

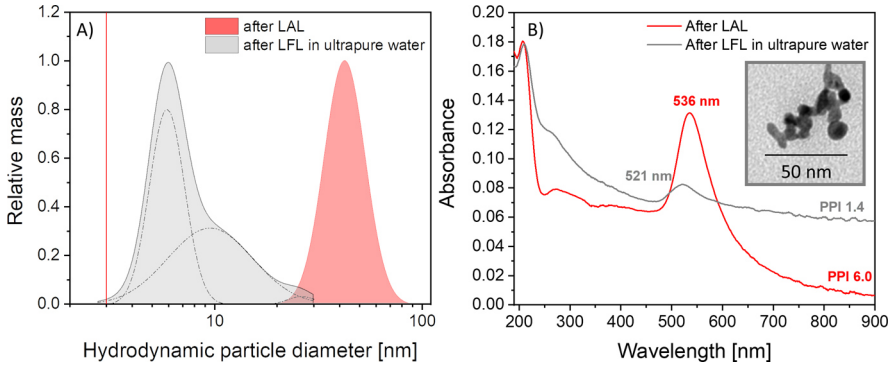

Figure 2. LFL in pure water: (A) log-normal fitted mass-weighted particle size distribution; (B) absorbance spectra of the AuNPs before and after LFL in deionized water (inset: exemplary TEM image of AuNPs after LFL in pure water). The red line marks the size transition between AuNPs and AuNCs at 3 nm.

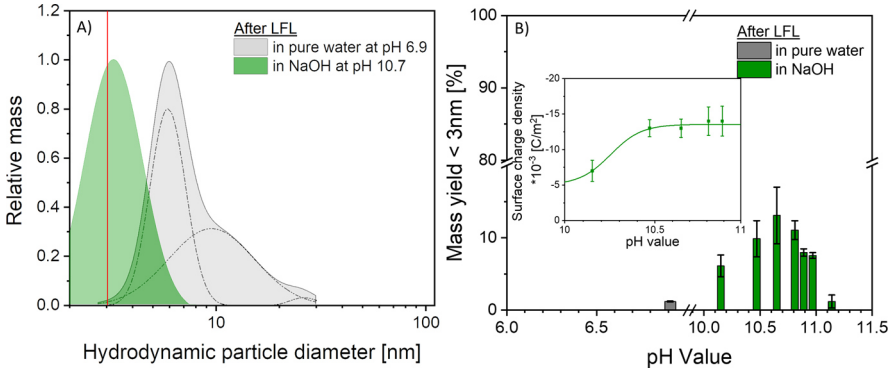

Figure 3. (A) Comparison of the particle size distribution (log-normal fitted mass-weighted distribution) after LFL at pH 6.9 (ultrapure water) and pH 10.7 (adjusted with 0.3 mM NaOH); (B) mass yield of AuNPs smaller than 3 nm in correlation with the pH value during fragmentation (adjusted by adding different amounts of NaOH before LFL). The red line marks the size transition between AuNPs and AuNCs at 3 nm. Error bars obtained by performing the experiments three times. The inset in B indicates surface charge densities at pH = 10−11.

time. A closer examination of these statistical effects has been presented elsewhere.[39] According to the literature, full fragmentation of all particles occurs after four passages.[37] In this work, we investigated the influence of pH and ions on the particle size and stability of the sample. The corresponding additives were added before LFL to study the in situ effects. The pH value was adjusted by sodium hydroxide, which was purchased from Bernd Kraft. We used monovalent sodium salts for the analysis of the influence of ions, that is, sodium fluoride (NaF), sodium chloride (NaCl), sodium bromide (NaBr), and sodium iodide (NaI). NaCl and NaBr were purchased from AnalaR NORMAPUR, and NaF and NaI were purchased from Sigma-Aldrich.

Analysis Methods. We used an analytical disk centrifuge (ADC, CPS Instrument DC 24000) at 24 000 rpm to determine the hydrodynamic diameter. The measuring principle was based on the sedimentation of the particles through a sugar gradient and time-dependent detection of the particles at a wavelength of 405 nm. A 0.1 mL sample was required for each measurement, and the runtime was 25 min. We used an analytical ultracentrifuge (AUC) to obtain high-resolution spectra (Beckman Optima XL-I, An-60 Ti-rotor, 12 mm path length, double-sector epon centerpieces). Sedimentation was detected over 200 scans by an absorbance detector at 380 nm, and 20 °C. The centrifugal speed was 16 350*g*. The Ferret diameters of the particles were determined by transmission electron microscopy (TEM) (Zeiss EM 910) and scanning TEM (JOEL JSM-7500F). We used a sample volume of 5 μL prepared on a carbon-coated copper 400-mesh grid. For the determination of the optical properties, absorbance spectra were recorded with a Thermo Scientific Evolution 201 UV−vis spectrometer in the wavelength range of 190−900 nm. The electronic properties of the resulting AuNCs were determined via zeta potential measurements (Malvern Zetasizer—Nano ZS). X-ray photoelectron spectroscopy (XPS) spectra were measured using a monochromatic aluminum anode with a Kα line at 1486.6 eV and a spot size of 100 μm. We used a hemispherical analyzer (with an angle of 45° between the surface of the sample and the analyzer) and dual-beam charge neutralization. All of the spectra were referenced to the $2p_{3/2}$ Cu peak. The reference was introduced into the vacuum together with the sample and was sputtered with Ar ions, to avoid contaminations and ensure that the reference surface was clean. Casa XPS was used to analyze the spectra.

■ RESULTS AND DISCUSSION

First, control LFL was conducted in ultrapure water in the absence of any salts so that we could evaluate the effects of ions and the pH value on the particle size distributions and particle yields during laser fragmentation. The fragmentation resulted in a broad particle size distribution that was deconvoluted by Gaussian fits into three peaks with maxima at 5.7 ± 0.5, 10.0 ± 1.5, and 25 ± 2.5 nm. The mass fraction of particles smaller than 3 nm was less than 1% (Figure 2A). This finding was significantly different from the results obtained by Amendola and Meneghetti when they conducted cuvette experiments with a similar laser. Although the positions of the first peaks were similar, they observed more narrow particle size distributions (number weighted), even at lower fluences.[11] A closer examination of the extinction spectra after fragmentation shown in Figure 2B indicated that the primary particle index (PPI) decreased drastically during LFL, from 6.0 to 1.4.

DOI: 10.1021/acs.langmuir.9b00418
Langmuir 2019, 35, 6630−6639

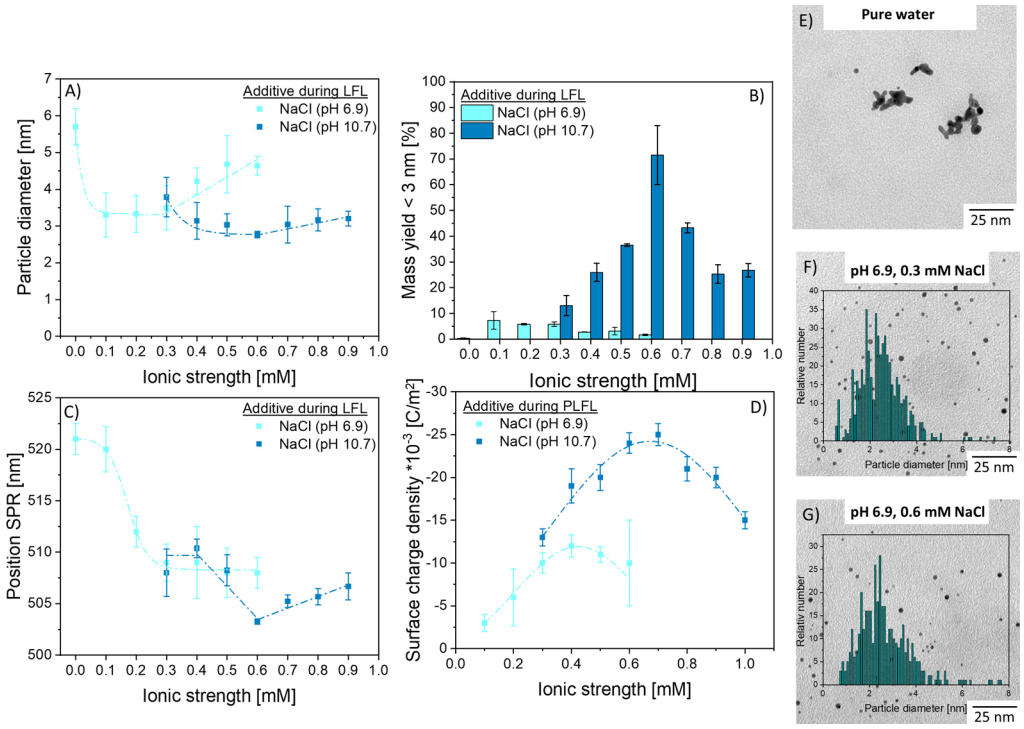

Figure 4. Influence of the IS of NaCl at neutral (light blue) and basic pH (blue) on (A) product particle diameter (x_c-value of the mass-weighted hydrodynamic size distribution, determined by ADC); (B) mass yield of particles smaller than 3 nm (determined by ADC), the position of the SPR peak, and the surface charge density (determined by zeta potential measurements). The pH value was adjusted by adding 0.3 mM NaOH; (E–G) TEM images and corresponding histograms (N = 1000) of the sample after LFL at pH 6.9 in pure water in 0.3 mM NaCl and in 0.6 mM NaCl. Error bars obtained by performing the experiments three times.

The PPI is defined as the ratio of extinction at 380 nm (interband) to extinction at 800 nm (scattering).[13] If there is an increase in extinction at 800 nm, it indicates the formation of aggregates and, hence, an unstable sample in water. In addition to the absorbance measurement, the TEM images showed a distinct sintering of the sample, which confirmed the assumption of colloidal instability (Figure 2B, inset).

Influence of pH. It is known that alkaline conditions improve the stability of AuNPs, so the pH was adjusted to increase the colloidal stability of the particles yielded by LFL.[13,40] The LAL of gold is an oxidative process[13,24] and thus leads to a partially oxidized particle surface.[15] Because of the partial surface charge, a pH-dependent equilibrium between Au–OH and AuO^- has been reported frequently. Consequently, alkaline conditions lead to the deprotonation of hydroxide groups on the surfaces of the NPs, which results in an increase of the negative charge on the surface and thus enhanced electrostatic stabilization.[13] Because the small particles generated during LFL will benefit from this electrostatic potential barrier as soon as they are produced, the consecutive growth of these particles is slowed down,[35] and smaller particles are formed. In accordance with the findings from size quenching during LAL, smaller particles indicate in situ particle stabilization.[13] Figure 3A shows a direct comparison of the relative distributions of mass-weighted particle sizes after fragmentation at pH 6.9 (neutral) and pH 10.7 (basic).

Fragmentation in the basic regime results in a more narrow size distribution with smaller mean particle diameters. In addition, deprotonation of the hydroxides on the surface should go along with a reduction of the solution pH after fragmentation, as protons are released into the medium. This was confirmed by our experiments in which the pH decreased significantly (by about 0.5) after fragmentation in the basic regime. However, fragmentation in a neutral solution produced no significant changes in the pH. In addition to the size distribution, the mean yield of particles with sizes <3 nm is another relevant criterion that indicates the efficiency of the LFL process. Figure 3B shows that increasing the pH, up to an optimum at pH 10.7, resulted in a significantly higher abundance of particles smaller than 3 nm, which most likely was due to the stabilization of the particles by deprotonation. However, for pH values >10.7, the yield of particles <3 nm in diameter decreased, so we assumed that an impaired stabilization occurred in this regime. This probably could be attributed to the fact that increasing the concentration of NaOH while altering the pH also increases the IS. Because higher ISs lead to a reduction of the Debye length (the so-called salt screening), the in situ stabilization of the particles formed during LFL is impaired and larger particles are formed. Therefore, it can be stated that an increase of the pH value has a positive effect on the fragmentation because, up to a pH value of 10.7, a sufficient number of OH groups can be deprotonated on the surfaces of the AuNPs. However, if the pH value is increased further by the addition of NaOH, the increasing IS and the corresponding reduction of the Debye length become more dominant, which has a negative influence on the production of small particles during the fragmentation process. The fact that further addition of NaOH beyond pH = 10.7 has no further beneficial impact on the stability of the resulting colloids was confirmed by the surface charge density (Figure 3B, inset), which stagnated at pH levels exceeding 10.5. The surface charge density was calculated from the zeta potential (Figure S3) based on an assumption from Makino

DOI: 10.1021/acs.langmuir.9b00418
Langmuir 2019, 35, 6630–6639

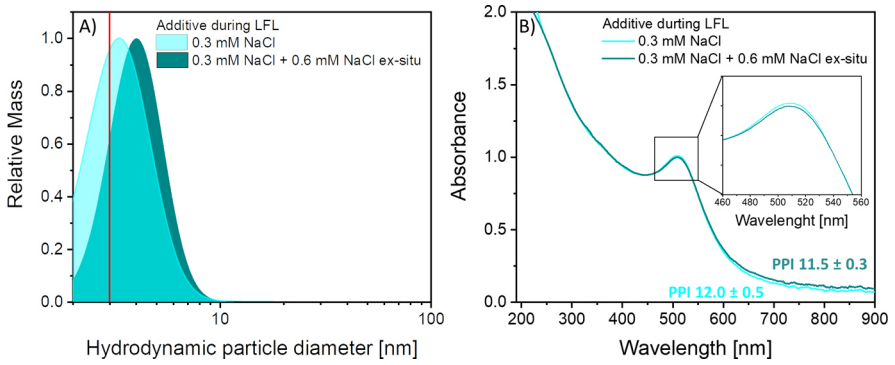

Figure 5. Influence of ex situ addition of 0.6 mM NaCl to particles after LFL in the presence of 0.3 mM NaCl: (A) log-normal fitted mass distribution obtained during ADC measurement and (B) absorbance spectra.

and Ohshima.[41] In summary, we can say that both the IS and the pH value influence the resulting particle size. The influence of the IS alone is examined in the following paragraph using NaCl as a pH-neutral salt.

Influence of IS. According to the results obtained during LAL, salts can interact with the surfaces of AuNPs. Their anions may lead to an oxygen substitution at the surfaces of the particles or to the specific adsorption of the anions by the hydrophobic patches on the surface of gold.[18] In order to evaluate the influence of salts during LFL, first, we varied the IS by adding different amounts of NaCl to the educt colloids in pure water before LFL (Figure 4, light blue).

A significant reduction in the sizes of the hydrodynamic particles during LFL was already evident at small amounts of NaCl (0.1 mM). This was in good agreement with the data from LAL, where an electrostatic stabilization effect of chloride was reported in the micromolar concentration regime.[13] This was also consistent with an increase of the yield of particles in the size range <3 nm. However, for IS greater than 0.3 mM, the resulting hydrodynamic particle size was shifted linearly to larger values, and the mass fraction of particles smaller than 3 nm decreased. This trend was expected because an increasing IS reduces the Debye length (l_D) according to $\left(\lambda_D \approx \sqrt{\frac{1}{IS}}\right)$.[41,42] At an IS of >0.3 mM, a minimum hydrodynamic diameter was reached, and further addition of salt resulted in a linear increase of the hydrodynamic diameter because the destabilizing effects from charge screening were equal to or overshadowed the electrostatic stabilization caused by the adsorption of specific ions. These trends in size basically are also represented in the position of the surface plasmon resonance (SPR) (Figure 4C) and in the data of the surface charge density (Figure 4D) (light blue graphs). The position of the SPR decreases exponentially when the size is reduced, and the surface charge density increases, indicating the presence of stabilizing charges. For ISs >0.3 mM, the linear increase of the particle diameter goes along with a reduced surface charge density, while the SPR position is not affected. This increase of the hydrodynamic diameter can be either due to instability because the maximum electrostatic stabilization is reduced, as the reduced surface charge density may indicate or due to the growth of the hydrodynamic shell (the Gouy−Chapman layer) from the further addition of ions. In the following, we show that the second assumption is more likely.

We added a larger amount of NaCl (0.6 mM) to the product particles after LFL with 0.3 mM NaCl, and we plotted the hydrodynamic, mass-weighted particle size distribution and the absorbance spectra in Figure 5. The ex situ addition of NaCl leads to a shift of the hydrodynamic size distribution to larger sizes, but no differences in the absorbance spectra were observed, so it was assumed that a higher IS leads to an enlarged ion envelope around the particles, which did not affect the Ferret diameter or the stability of the particles.

In summary, the increase of the IS during LFL at the constant, neutral pH leads to two different regimes of mean hydrodynamic particle diameters and AuNC yields. Up to an IS of 0.3 mM, the particle size decreases and reaches a minimum size of 3.5 ± 0.6 nm, whereby the yield of particles smaller than 3 nm increases in comparison to LFL in pure water. In case of even higher IS, a linear increase in the hydrodynamic particle diameter was observed and a decrease in the mass yield of particles <3 nm occurred. However, the TEM size histograms and the SPR peaks indicate that the Ferret diameter was not affected significantly.[43] Of course, it can be assumed that an additional increase of the IS would lead to aggregation, but this well-known salt-screening range was not the focus of our experiments.

Synergetic Effects of IS and pH Value. To this point, we have addressed the effects of the IS for fragmentation at neutral pH. However, as already shown, fragmentation is most effective in the basic regime, so, in the following experimental series, a variation of the IS of NaCl was conducted at a pH of 10.7 (adjusted by adding 0.3 mM NaOH) when LFL was most effective based on Figure 3B. The results are shown in Figure 4 (dark blue). It should be noted that an IS of 0.3 mM already had been achieved by the addition of NaOH for pH adjustment. At an IS of 0.4 mM, the solution consisted of three parts of NaOH and one part of NaCl. Consequently, all of the curves in Figure 4 that show the results of the fragmentations in the alkaline regime (dark blue curves) shifted by 0.3 mM compared to the data with NaCl only. The trend of the hydrodynamic particle diameter with increasing salinity was comparable to the fragmentation at neutral pH. However, the minimum particle size of 2.8 ± 0.9 nm was achieved at an IS of 0.6 mM. Interestingly, the addition of sodium chloride resulted in a significant increase in the mass of particles smaller than 3 nm up to an IS of 0.6 mM (0.3 mM NaOH + 0.3 mM NaCl), and there was a simultaneous increase of the position of the SPR peak. For IS values >0.6 mM, the hydrodynamic diameter increased again, the yield of particles <3 nm decreased, and the position of the SPR peak shifted to longer wavelengths, so that growth or agglomeration of the particles was suspected. This onset of agglomeration, which was not observed in pure water, probably was

DOI: 10.1021/acs.langmuir.9b00418
Langmuir 2019, 35, 6630−6639

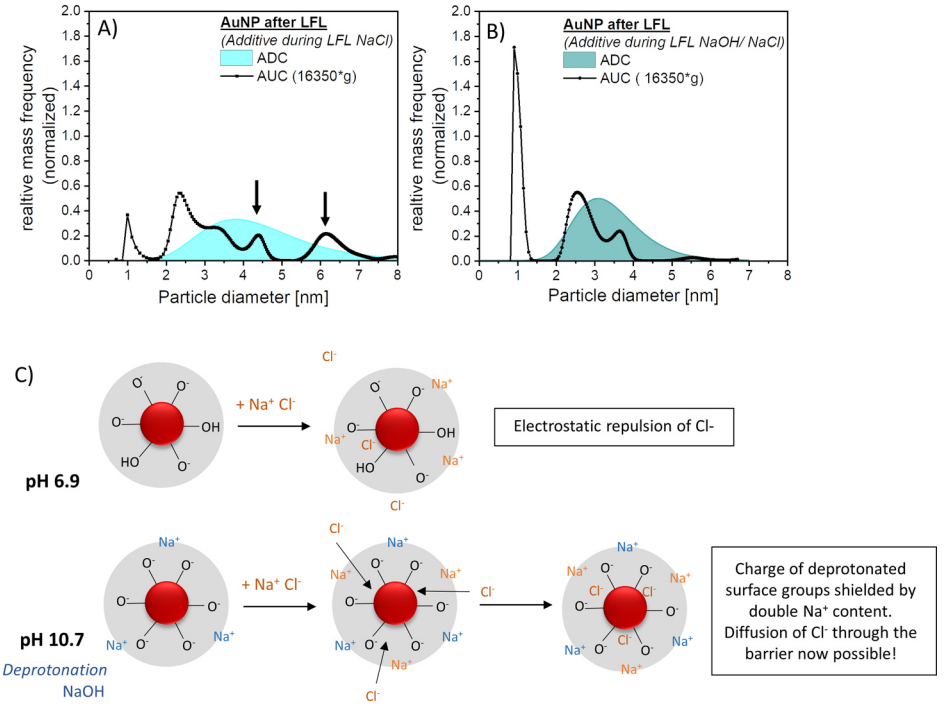

Figure 6. Comparison of ADC and AUC data of samples after LFL with (A) 0.3 mM NaCl and (B) 0.3 mM NaOH + 0.3 mM NaCl. (C) Schematic illustration of the stabilization through anions during LFL at a neutral pH (6.9) and a basic pH (10.7).

attributable to the overall higher IS, which was not reached in pure water, which may push the system beyond the threshold where agglomeration occurs.

The most striking feature of the fragmentation with NaCl at the alkaline pH was the very high yield (up to 71.5 ± 0.3 weight percent) of particles <3 nm, which was a factor of 100 higher than that achieved by NaCl alone and a factor of 4.5 higher than that achieved by pH adjustment alone. On the basis of this, we concluded that the combined pH change and ion addition have a synergetic effect that was much more pronounced than the sum of its individual constituents. This phenomenon is explained below. To understand how the synergism works, size distributions acquired by AUC are shown in Figure 6, comparing particles fragmented in NaCl (IS = 0.3 mM) and NaCl/NaOH (IS = 0.6 mM). The size distributions obtained by AUC show a resolution in the angstrom range,[44] that is, the resolution is many times higher than that derived from data of the ADC, so that small changes in particle size can be detected easily. It was clearly apparent that the addition of both Cl^- and OH^- resulted in the quenching of the particle fraction >4 nm and that the synergism led to a substantial increase in the mass fraction of particles smaller than 2 nm. This cannot be resolved by ADC measurements, but it can be resolved by AUC. Therefore, the process known as salt quenching was more effective during fragmentation in the presence of OH^-.

The laser-based production of gold nanoparticles is known to be an oxidative process that results in the surfaces of the particles being partially oxidized. Barmina et al. showed that LAL of a metallic target leads to the production of O_2, H_2, and H_2O_2 as the result of plasma generation.[15,16] As suggested by Lau et al.,[27] it can be assumed that the surfaces of the particles also are oxidized after LFL, causing a pH-dependent equilibrium between Au−OH/AuO^-. By the addition of NaOH, this equilibrium shifts to the deprotonated form, resulting in an electrostatic stabilization of the particles. This deprotonation results in an increased number of negative charges around the particles. Naturally, this goes along with a more pronounced accumulation of cations in the outer Helmholtz layer. These cations could shield the negative charges of the O^- ions on the surfaces, making it easier for the chloride ions to reach or stay at the surfaces of the nanoparticles. Hence, this local charge screening at the nanoenvironment of the particle could shift the adsorption equilibrium of the chloride to the adsorbed form and increase the number of adsorbed chloride anions. As a consequence, more pronounced chloride adsorption would lead to a more negative charge on the surfaces of the AuNCs, which would result in a more efficient in situ repulsion between particles and an improved electrostatic stabilization against coalescence or ripening (Figure 6C). This is also reflected by the surface charge density (Figure 4D), which is significantly more negative than it is when only chloride or hydroxide is present (compare Figure 3B, inset). Our data seem to indicate that the processes of deprotonation of the surface hydroxides and adsorption of chloride ions are not independent; rather, they synergetically augment each other, leading to improved electrostatic stabilization in situ.

Specific Anion Effects during LFL. Considering the impact of pH and IS discussed above, the literature clearly indicates that the quality of stabilization can also depend on the type of the halide anion that is used. During LAL, the quality of stabilization correlates with the stabilizing effect described by a direct HS.[18,45] The stabilization is based on different affinities to the surfaces of the AuNPs, which increases with increasing ion diameter and polarizability and decreases with higher degrees of hydration, along with the stabilization series of $F^- < Cl^- < Br^- < I^-$.[18,19] Hence, in the last part of this manuscript, we aim to systematically elucidate whether the ion effects observed during LFL are anion-specific.

DOI: 10.1021/acs.langmuir.9b00418
Langmuir 2019, 35, 6630−6639

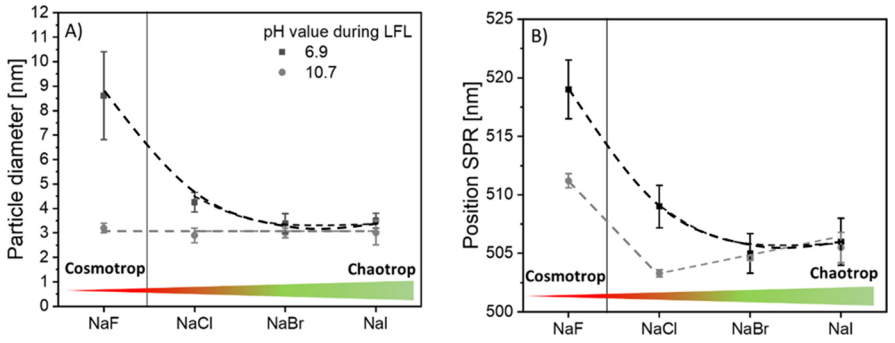

Figure 7. Influence of halide salts after LFL at different pH values on the (A) particle diameter and (B) position of the SPR. Error bars obtained by performing the experiments three times. The black line has no physical meaning; it solely separates the chaotropic anions from the cosmotropic anions.

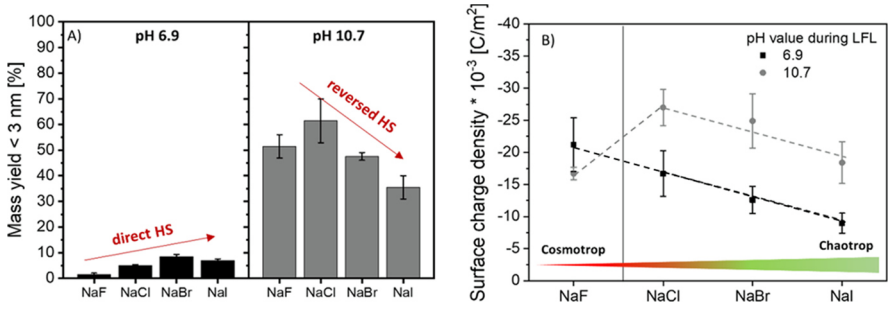

Figure 8. Influence of halide salt LFL results of the different pH values on the (A) mass yield of particles smaller than 3 nm (hydrodynamic x_c value at two different pH values) and on the (B) surface charge density. Error bars obtained by performing the experiments three times.

Therefore, we studied the influence of a Hofmeister anion series on particle size (Figure 7A) and yield of particles <3 nm (Figure 8A) during LFL comparing the homologous halides F^-, Cl^-, Br^-, and I^-. The IS of each salt is 0.3 mM, and the pH value varies and is either neutral (pH = 6.9) or basic (pH = 10.7). First of all, we consider the influence of salts in the neutral pH range (Figure 8). The results clearly show that the mean particle diameter derived from ADC decreases with increasing chaotropicity (polarizability) of the present anion, which resulted in a significantly more pronounced size quenching effect for Br^- and I^- than for Cl^-. The largest particles and the lowest size quenching effectivity during LFL were observed for the cosmotropic F^-. This was complemented by a significant blue shift of the SPR maximum for bromide and iodide (Figure 7B). We already knew about this behavior from the LAL of gold,[18] in which the influence of the same salts on the particle size after LAL was investigated, and it was also in accordance with the expected trends that are characteristic of a direct HS. In accordance with the trends found for laser ablation,[18] the mass yield <3 nm in the presence of iodide is slightly lower than expected based on a pure HS. These deviations may be attributed to the fact that iodide forms strong covalent bonds with gold and may hence alter the gold surface, which may impede stabilization.

However, if the LFL takes place in the alkaline regime, a different behavior emerges. The hydrodynamic diameters of the particles remain approximately the same, but the SPR peak shows a clear red shift tendency with increasing chaotropicity. An exception here is the influence of fluoride, which also leads to the most red-shifted SPR in the basic regime, but it does not show any influence on the particle size. This behavior of fluoride is surprising because it belongs to the cosmotropic anions and can be described as a hard Lewis-base according to the hard and soft acids and base concept. In solution, fluoride is present as a highly hydrated anion, which means that interactions with the partially oxidized surfaces, but mostly hydrophobic metal surfaces of the AuNPs (soft Lewis acid), are possible only to a limited extent.[46] The fact that the use of fluoride produces ultrasmall particles can be explained by the synergism with surface deprotonation, which seems to make halide-based stabilization independent of the type of ion. The data on the position of the SPR peak in the alkaline regime are best discussed in conjunction with the mass yield of particles smaller than 3 nm (Figure 8). We already know that the mass fraction of ultra-small particles is significantly larger after fragmentation in the alkaline range (Figure 3), which is also reflected by these data.

Although the mass of particles smaller than 3 nm increases in the neutral regime when the chaotropicity of the anions increases from fluoride to iodide, this trend in the alkaline regime, with the exception of fluoride as mentioned above, is reversed with the highest yields produced in the presence of Cl^- and the lowest yields obtained with iodide.

This behavior is also correlated nicely with the UV−vis data shown in Figure 7B, where the most blue-shifted SPR peak position was found for chloride, whereas the peak positions for bromide and iodide were red-shifted. As mentioned above, the mass of particles smaller than 3 nm can be seen as an LFL product stability criterion. If the stabilization of the product particles is sufficiently high, the coalescence processes are suppressed, and the particles do not grow because of strong, electrostatic, interparticle repulsions. According to Schwierz et al.,[26] halide anions, in the presence of hydrophobic surfaces with a negative surface charge density, follow a direct HS. As a result, the stability of the gold particles should be increased in the presence of chaotropic anions,[47,48] which was confirmed

DOI: 10.1021/acs.langmuir.9b00418
Langmuir 2019, 35, 6630−6639

directly by our data for LFL at neutral pH. However, if LFL takes place in the alkaline regime, this behavior can no longer be observed. Although the mean value of the hydrodynamic particle diameter is comparable for each salt, the mass fraction of particles smaller than 3 nm increases with increasing cosmotropicity in this case, which is an indication of a partially indirect HS. At this point, we would like to mention that the results are not only valid for the fragmentation in the liquid jet. A validation of the trend by LFL in a cuvette can be found in Figure S8 of the Supporting Information.

To date, indirect HSs have been found either for hydrophobic colloids with a positive surface charge or for hydrophilic colloids with a negative surface charge.[26,48] In the laser-fabricated colloidal nanoparticles, however, two surface features exist in parallel at all times. We always see the presence of a hydrophobic gold surface and negatively charged deprotonated surface groups, which exist independent of the pH (indicated by all negative surface charge densities in Figure 8B). At neutral pH, the hydrophobic features are dominant and a direct HS is observed. However, a shift of the pH into the alkaline regime will increase the number of charged surface groups by deprotonation. As a result, the charged character of the surface becomes dominant and a reversal of the HS is initiated.[26] In this context, it should be mentioned that only a partial reversal of the HS series was found, which according to findings by[49] indicates that the surface is neither fully dominated by hydrophobicity nor by surface charge effects alone.

There are different explanations as to why the number of charged surface groups increases during laser fragmentation at alkaline pH. One explanation could be the presence of a significantly elevated number of oxidized gold atoms on the surface, which could lead to a higher portion of deprotonated surface hydroxides. To test this hypothesis, we characterized AuNCs after LFL with NaCl in basic and neutral solution with XPS. The corresponding spectra (Figure S7) clearly showed an overall oxidation between 10 and 15% for both samples, with no significant differences. Based on this, we concluded that surface oxidation of the inner Helmholtz layer alone does not account for increased surface charge. The next, most obvious explanation would be that the deprotonation of the surface hydroxides (in the outer layer) in the alkaline regime would increase the surface charge density measured in the colloidal state. Figure 3B shows that there is an obvious shift from $(-16.7 \pm 3.5) \times 10^{-3}$ to $(-27.0 \pm 2.8) \times 10^{-3}$ C·m^{-2} for samples with NaCl at pH values of 6.9 and 10.7, respectively. The surface charge density of samples after LFL with 0.3 mM NaOH was $(-13.0 \pm 1.3) \times 10^{-3}$ C·m^{-2}. Thus, the addition of NaCl to samples with NaOH leads to a significant increase in the density of the surface charge, which cannot be achieved either by LFL with NaOH or by LFL with NaCl alone.

CONCLUSIONS

In this work, we showed that, during LFL, specific anion effects and pH effects have significant influence on the size and yield of particles with diameters <3 nm. In particular, we showed that both effects work synergistically and augment each other, so the combined effect is significantly (factor of 20−100 higher AuNC yield) more pronounced than that of the individual constituents. Also, we verified that size quenching and electrostatic stabilization during LFL are anion specific, like in LAL, and follow the rules of HS. However, direct (neutral pH) and indirect (basic pH) series were found, depending on the pH of the medium. Without using organic (electrostatic or steric) stabilizers, the yield of AuNCs with diameters <3 nm was 71.5 ± 0.3 wt %. This work constitutes a significant advancement because, in contrast to most other works in the field, it did not focus on physical parameters, such as, for example, laser fluence; rather, it stressed the importance of chemical effects during the formation of particles by LFL. Hence, we developed a precise protocol for the effective synthesis of these particles, which could stimulate future applications in biomedicine and catalysis. For catalytic applications, such as the oxidation of CO, it is well-known that surface adsorbates may block the active sites of a catalyst and hinder the adsorption of reactants in oxidation reactions.[50]

ASSOCIATED CONTENT

Supporting Information

The Supporting Information is available free of charge on the ACS Publications website at DOI: 10.1021/acs.langmuir.9b00418.

Educt particles for LFL (Figure S1), influence of pulses per volume element (Figure S2), influence of pH and ions on the zeta potential (Figure S3), effect of different pH values on the particle diameter after LFL (Figure S4), influence of different halide salts on the properties of the particles after LFL (Figure S5), TEM histograms before and after ex-situ addition of NaCl (Figure S6), surface oxidation of AuNPs after LFL (Figure S7), and transfer of the experimental findings to LFL in the batch process (Figure S8) (PDF)

AUTHOR INFORMATION

Corresponding Authors

*E-mail: Stephan.barcikowski@uni-due.de (S.B.).
*E-mail: Christoph.rehbock@uni-due.de (C.R.).

ORCID

Stephan Barcikowski: 0000-0002-9739-7272
Christoph Rehbock: 0000-0002-4708-5246

Notes

The authors declare no competing financial interest.

ACKNOWLEDGMENTS

The authors gratefully acknowledge the DFG Deutsche Forschungsgemeinschaft for its financial support under Project No. BA 3580/22-1. The authors thank Jurij Jacobi for his experimental support in producing the TEM images and Dario Becker for the evaluation of these data (both from the University of Duisburg-Essen).

REFERENCES

(1) Petersen, S.; Barcikowski, S. Conjugation Efficiency of Laser-Based Bioconjugation of Gold Nanoparticles with Nucleic Acids. *J. Phys. Chem. C* **2009**, *113*, 19830−19835.
(2) Gamrad, L.; Mancini, R.; Werner, D.; Tiedemann, D.; Taylor, U.; Ziefuß, A.; Rehbock, C.; Klein, S.; Kues, W.; Barcikowski, S.; et al. Triplex-hybridizing Bioconjugated Gold Nanoparticles for Specific Y-chromosome Sequence Targeting of Bull Spermatozoa. *Analyst* **2017**, *142*, 2020−2028.
(3) Zheng, J.; Zhang, C.; Dickson, R. M. Highly Fluorescent, Water-Soluble, Size-Tunable Gold Quantum Dots. *Phys. Rev. Lett.* **2004**, *93*, 77402.
(4) Chakraborty, I.; Pradeep, T. Atomically Precise Clusters of Noble Metals: Emerging Link between Atoms and Nanoparticles. *Chem. Rev.* **2017**, *117*, 8208−8271.

(5) Jin, R.; Zeng, C.; Zhou, M.; Chen, Y. Atomically Precise Colloidal Metal Nanoclusters and Nanoparticles: Fundamentals and Opportunities. *Chem. Rev.* **2016**, *116*, 10346−10413.
(6) Rostek, A.; Mahl, D.; Epple, M. Chemical Composition of Surface-functionalized Gold Nanoparticles. *J. Nanopart. Res.* **2011**, *13*, 4809−4814.
(7) Watanabe, N.; Fujihara, S. Chemical Purification of ZnO Nanoparticles by Dialyzing Treatments and Their Use in Fabricating Luminescent Antireflective Nanocomposite Thin Films. *Ind. Eng. Chem. Res.* **2011**, *50*, 5611−5617.
(8) La Spina, R.; Spampinato, V.; Gilliland, D.; Ojea-Jimenez, I.; Ceccone, G. Influence of Different Cleaning Processes on the Surface Chemistry of Gold Nanoparticles. *Biointerphases* **2017**, *12*, 031003.
(9) Dinkel, R.; Jakobi, J.; Ziefuß, A. R.; Barcikowski, S.; Braunschweig, B.; Peukert, W. Role of Citrate and NaBr at the Surface of Colloidal Gold Nanoparticles during Functionalization. *J. Phys. Chem. C* **2018**, *122*, 27383−27391.
(10) Murphy, C. J. Sustainability as an Emerging Design Criterion in Nanoparticle Synthesis and Applications. *J. Mater. Chem.* **2008**, *18*, 2173.
(11) Amendola, V.; Meneghetti, M. Controlled Size Manipulation of Free Gold Nanoparticles by Laser Irradiation and their Facile Bioconjugation. *J. Mater. Chem.* **2007**, *17*, 4705.
(12) Zhang, D.; Gökce, B.; Barcikowski, S. Laser Synthesis and Processing of Colloids: Fundamentals and Applications. *Chem. Rev.* **2017**, *117*, 3990−4103.
(13) Rehbock, C.; Merk, V.; Gamrad, L.; Streubel, R.; Barcikowski, S. Size Control of Laser-Fabricated Surfactant-free Gold Nanoparticles with Highly Diluted Electrolytes and their Subsequent Bioconjugation. *Phys. Chem. Chem. Phys.* **2013**, *15*, 3057−3067.
(14) Letzel, A.; Gökce, B.; Wagener, P.; Ibrahimkutty, S.; Menzel, A.; Plech, A.; Barcikowski, S. Size Quenching during Laser Synthesis of Colloids Happens Already in the Vapor Phase of the Cavitation Bubble. *J. Phys. Chem. C* **2017**, *121*, 5356−5365.
(15) Barmina, E. V.; Gudkov, S. V.; Simakin, A. V.; Shaffev, G. A. Stable Products of Laser-Induced Breakdown of Aqueous Colloidal Solutions of Nanoparticles. *J. Laser Micro/Nanoeng.* **2017**, *12*, 254−257.
(16) Kalus, M.-R.; Reimer, V.; Barcikowski, S.; Gökce, B. Discrimination of Effects Leading to Gas Formation during Pulsed LaserAblation in Liquids. *Appl. Surf. Sci.* **2019**, *465*, 1096−1102.
(17) Muto, H.; Yamada, K.; Miyajima, K.; Mafuné, F. Estimation of Surface Oxide on Surfactant-Free Gold Nanoparticles Laser-Ablated in Water. *J. Phys. Chem. C* **2007**, *111*, 17221−17226.
(18) Merk, V.; Rehbock, C.; Becker, F.; Hagemann, U.; Nienhaus, H.; Barcikowski, S. In Situ Non-DLVO Stabilization of Surfactant-free, Plasmonic Gold Nanoparticles: Effect of Hofmeister's Anions. *Langmuir* **2014**, *30*, 4213−4222.
(19) Hofmeister, F. Zur Lehre von der Wirkung der Salze. *Arch. Exp. Pathol. Pharmakol.* **1888**, *24*, 247−260.
(20) Medda, L.; Barse, B.; Cugia, F.; Boström, M.; Parsons, D. F.; Ninham, B. W.; Monduzzi, M.; Salis, A. Hofmeister Challenges: Ion Binding and Charge of the BSA Protein as Explicit Examples. *Langmuir* **2012**, *28*, 16355−16363.
(21) Kunz, W. Specific Ion Effects in Liquids, in Biological Systems, and at Interfaces. *Pure Appl. Chem.* **2006**, *78*, 1611−1617.
(22) Lo Nostro, P.; Ninham, B. W. Hofmeister Phenomena: an Update on Ion Specificity in Biology. *Chem. Rev.* **2012**, *112*, 2286−2322.
(23) Hladílková, J.; Heyda, J.; Rembert, K. B.; Okur, H. I.; Kurra, Y.; Liu, W. R.; Hilty, C.; Cremer, P. S.; Jungwirth, P. Effects of End Group Termination on Salting-Out Constants for Triglycine. *J. Phys. Chem. Lett.* **2013**, *4*, 4069−4073.
(24) Sylvestre, J.-P.; Kabashin, A. V.; Sacher, E.; Meunier, M.; Luong, J. H. T. Stabilization and Size Control of Gold Nanoparticles during Laser Ablation in Aqueous Cyclodextrins. *J. Am. Chem. Soc.* **2004**, *126*, 7176−7177.
(25) Petersen, S.; Barcikowski, S. In Situ Bioconjugation. Single Step Approach to Tailored Nanoparticle-Bioconjugates by Ultrashort Pulsed Laser Ablation. *Adv. Funct. Mater.* **2009**, *19*, 1167−1172.
(26) Schwierz, N.; Horinek, D.; Netz, R. R. Reversed Anionic Hofmeister Series: the Interplay of Surface Charge and Surface Polarity. *Langmuir* **2010**, *26*, 7370−7379.
(27) Lau, M.; Haxhiaj, I.; Wagener, P.; Intartaglia, R.; Brandi, F.; Nakamura, J.; Barcikowski, S. Ligand-Free Gold Atom Clusters Adsorbed on Graphene Nano Sheets Generated by Oxidative Laser Fragmentation in Water. *Chem. Phys. Lett.* **2014**, *610*−*611*, 256−260.
(28) Lau, M.; Barickowski, S. Process for the Preparation of Pure, in Particular Carbon-Free Nanoparticles, European Patent no. 2735390, 2012.
(29) Delfour, L.; Itina, T. E. Mechanisms of Ultrashort Laser-Induced Fragmentation of Metal Nanoparticles in Liquids. Numerical Insights. *J. Phys. Chem. C* **2015**, *119*, 13893−13900.
(30) Hashimoto, S.; Werner, D.; Uwada, T. Studies on the Interaction of Pulsed Lasers with Plasmonic Gold Nanoparticles Toward Light Manipulation, Heat Management, and Nanofabrication. *J. Photochem. Photobiol., C* **2012**, *13*, 28−54.
(31) Itina, T. E.; Gouriet, K.; Zhigilei, L. V.; Noël, S.; Hermann, J.; Sentis, M. Mechanisms of Small Clusters Production by Short and Ultra-Short Laser Ablation. *Appl. Surf. Sci.* **2007**, *253*, 7656−7661.
(32) Yamada, K.; Tokumoto, Y.; Nagata, T.; Mafuné, F. Mechanism of Laser-Induced Size-Reduction of Gold Nanoparticles as Studied by Nanosecond Transient Absorption Spectroscopy. *J. Phys. Chem. B* **2006**, *110*, 11751−11756.
(33) Miotello, A.; Kelly, R. Laser-Induced Phase Explosion. New Physical Problems when a Condensed Phase Approaches the Thermodynamic Critical Temperature. *Appl. Phys. A: Mater. Sci. Process.* **1999**, *69*, 67−73.
(34) Pyatenko, A.; Wang, H.; Koshizaki, N.; Tsuji, T. Mechanism of Pulse Laser Interaction with Colloidal Nanoparticles. *Laser Photon. Rev.* **2013**, *7*, 596−604.
(35) Jendrzej, S.; Gökce, B.; Amendola, V.; Barcikowski, S. Barrierless Growth of Precursor-Free, Ultrafast Laser-Fragmented Noble Metal Nanoparticles by Colloidal Atom Clusters - A Kinetic in Situ Study. *J. Colloid Interface Sci.* **2016**, *463*, 299−307.
(36) Metwally, K.; Mensah, S.; Baffou, G. Fluence Threshold for Photothermal Bubble Generation Using Plasmonic Nanoparticles. *J. Phys. Chem. C* **2015**, *119*, 28586−28596.
(37) Ziefuß, A. R.; Reichenberger, S.; Rehbock, C.; Chakraborty, I.; Gharib, M.; Parak, W. J.; Barcikowski, S. Laser Fragmentation of Colloidal Gold Nanoparticles with High-Intensity Nanosecond Pulses is Driven by a Single-Step Fragmentation Mechanism with a Defined Educt Particle-Size Threshold. *J. Phys. Chem. C* **2018**, *122*, 22125−22136.
(38) Pfeiffer, C.; Rehbock, C.; Huhn, D.; Carrillo-Carrion, C.; de Aberasturi, D. J.; Merk, V.; Barcikowski, S.; Parak, W. J. Interaction of Colloidal Nanoparticles with their Local Environment: the (Ionic) Nanoenvironment around Nanoparticles is Different from bulk and Determines the Physico-Chemical Properties of the Nanoparticles. *J. R. Soc. Interface* **2014**, *11*, 20130931.
(39) Waag, F.; Gökce, B.; Kalapu, C.; Bendt, G.; Salamon, S.; Landers, J.; Hagemann, U.; Heidelmann, M.; Schulz, S.; Wende, H.; et al. Adjusting the Catalytic Properties of Cobalt Ferrite Nanoparticles by Pulsed Laser Fragmentation in Water with Defined Energy Dose. *Sci. Rep.* **2017**, *7*, 13161.
(40) Raveendran, P.; Fu, J.; Wallen, S. L. Completely "Green" Synthesis and Stabilization of Metal Nanoparticles. *J. Am. Chem. Soc.* **2003**, *125*, 13940−13941.
(41) Makino, K.; Ohshima, H. Electrophoretic Mobility of a Colloidal Particle with Constant Surface Charge Density. *Langmuir* **2010**, *26*, 18016−18019.
(42) Doane, T. L.; Chuang, C.-H.; Hill, R. J.; Burda, C. Nanoparticle ζ -Potentials. *Acc. Chem. Res.* **2012**, *45*, 317−326.
(43) Haiss, W.; Thanh, N. T. K.; Aveyard, J.; Fernig, D. G. Determination of Size and Concentration of Gold Nanoparticles from UV-Vis Spectra. *Anal. Chem.* **2007**, *79*, 4215−4221.

DOI: 10.1021/acs.langmuir.9b00418
Langmuir 2019, 35, 6630−6639

(44) Cölfen, H.; Pauck, T. Determination of Particle Size Distributions with Angström Resolution. *Colloid Polym. Sci.* **1997**, *275*, 175−180.
(45) Nelson, E. M.; Rothberg, L. J. Kinetics and Mechanism of Single-Stranded DNA Adsorption onto Citrate-stabilized Gold Nanoparticles in Colloidal solution. *Langmuir* **2011**, *27*, 1770−1777.
(46) Pearson, R. G. Hard and soft acids and bases—the evolution of a chemical concept. *Coord. Chem. Rev.* **1990**, *100*, 403−425.
(47) Oncsik, T.; Trefalt, G.; Borkovec, M.; Szilagyi, I. Specific Ion Effects on Particle Aggregation Induced by Monovalent Salts within the Hofmeister Series. *Langmuir* **2015**, *31*, 3799−3807.
(48) López-León, T.; Santander-Ortega, M. J.; Ortega-Vinuesa, J. L.; Bastos-González, D. Hofmeister Effects in Colloidal Systems. Influence of the Surface Nature. *J. Phys. Chem. C* **2008**, *112*, 16060−16069.
(49) Schwierz, N.; Horinek, D.; Sivan, U.; Netz, R. R. Reversed Hofmeister series—The rule rather than the exception. *Curr. Opin. Colloid Interface Sci.* **2016**, *23*, 10−18.
(50) Klyushin, A. Y.; Greiner, M. T.; Huang, X.; Lunkenbein, T.; Li, X.; Timpe, O.; Friedrich, M.; Hävecker, M.; Knop-Gericke, A.; Schlögl, R. Is Nanostructuring Sufficient to Get Catalytically Active Au? *ACS Catal.* **2016**, *6*, 3372−3380.

DOI: 10.1021/acs.langmuir.9b00418
Langmuir 2019, 35, 6630−6639

3.2.4 Inorganic anions linearly tune the electron-coupling time of colloidal gold nanoparticles

Synopsis:

Physical interactions between metal nanoparticles and light have remained an important and controversial topic. The quantitative understanding of energy relaxation in laser-excited colloidal gold nanoparticles is highly relevant for a variety of applications, ranging from hot-electron electrochemical catalysis to biomedical optoporation. In this context, the influence of the chemical environment on energy relaxation is currently underexplored in literature, particularly the impact of anions on these fundamental processes. However, controlling the anion effect is a prerequisite for realistic hot-electron applications in aqueous media under non-deionized conditions that are widely used in catalysis and biomedicine. Therefore, this work was aimed to demonstrate that the simple application of highly dilute salt solutions provides a novel technique to control the hot electron lifetime through precision measurements.
While numerous theoretical and experimental works exist, they mainly focus on varying the physical parameters but mostly ignore surface chemistry. To fundamentally understand the influence of anion surface adsorbates on the hot electron lifetime, we show that surfactant-free colloids are required.
By means of optical pump-probe spectroscopy, we investigated the influence of anions on the energy transfer time between electrons and phonons in colloidal gold nanoparticles via the effect of electron density spill-out on the particle surface. Driven by the valence and ionic strength of the anion, we linearly tuned this electron screening effect and achieved accelerated energy coupling on the picosecond time scale. In other words, anions offer a cheap, mild, and easily controllable tool to manipulate the lifetime of hot electrons with constant laser excitation parameters.

The validate hypothesis on electronic spill-out effects created by anion surface adsorbates on Au NPs could also explain the occurrence of certain optical phenomena in ligand-free inorganic colloidal gold nanoclusters, as indicated in chapter 3.3.

Inorganic anions linearly tune the electron-coupling time of colloidal gold nanoparticles *(unpublished results)*

Anna R. Ziefuß[1], Christoph Rehbock[1], Sven Reichenberger[1], Alexander Letzel[1], Zhijiang Chen[2], Benjamin K. Ofori-Okai[2], Matthias Hoffmann[2], Chandra B. Curry[2,3], Siegfried H. Glenzer[2], Stephan Barcikowski[1]*

[1] University of Duisburg-Essen and Center for Nanointegration Duisburg-Essen (CENIDE), 45141 Essen, Germany.
[2] High Energy Density Science Division, SLAC National Accelerator Laboratory, Menlo Park, California 94025, USA
[3] Department of Electrical and Computer Engineering, University of Alberta, Edmonton, Alberta T6G 1H9, Canada

Abstract

Tuning photophysical interactions at the liquid-nanoparticle interface provides significant insights into electron-phonon coupling processes, particularly in determining the lifetime of the optically induced hot electron population. Such understanding is essential for a variety of applications, ranging from hot electron electrochemical catalysis to biomedical optoporation.

To understand the effects of the physical and chemical environment on the dynamics of electronic processes, we performed ultrafast laser pump-probe measurements on surfactant-free Au nanoparticles in solutions under ambient conditions. These ultra-pure nanoparticles permit a systematic study of the influence of surface chemistry on the interactions of metal nanoparticles with light in a regime that approaches millimolar saline conditions. Varying the concentration, valence of inorganic and polarizability of anions in the micromolar regime provides a powerful and inexpensive tool to measure anionic effects on the energy transfer time between electrons and phonons. Our results resolve the kinetics of energy transfer in colloidal states, enabling to tune excited state lifetimes at low excitation regime, just by adding ions such as table salt, with stronger effect for more polarizable anions such as bromine.

Introduction

In the past decade, interactions between Au nanoparticles (NPs) and light have gained attention in a manifold of applications, including hot electrons[1–4], catalysis[5–7], and biological tissue treatments like cancer destruction by photoacoustic therapy[8], and optoporation[9]. However, the fundamental understanding of the energy uptake after laser excitation of NPs is a complex problem due to the hierarchical time and energy scales of these absorption and equilibrium processes.[9–11] Molecular dynamic simulations provide valuable insights into size- and laser-intensity dependent heat accumulation and transfer.[12] This involves assumptions of the material response to electronic excitations and electron-phonon equilibration. Despite numerous efforts, the existing data are controversial[13–15] because theoretical and experimental works often focus on isolated physical parameters while ignoring surface chemistry.

Colloid synthesis is usually performed with residual reactants like citrate[16–18] (for gold nanospheres) and surfactants like cetyltrimethylammoniumbromide[19–21] for gold nanorods covering the particles' surface, developing generalized conclusions on electron-phonon coupling require the detailed study of the NPs' surface chemistry.

The two-temperature model (TTM) is commonly used to describe the thermalization within metals and includes the heat conduction of both the electrons and the lattice.[22] Irradiation of metals with light first leads to energy absorption by the electronic subsystem. This induces a hot electron population, which thermalizes in the conduction band by electron-electron scattering processes that occur on time scales of ~100 fs.[21] Energy is transferred to the lattice via electron-phonon coupling, followed by phonon-phonon interactions.[23,24] Therefore, the optically induced hot electron population determines the heat transfer dynamics[5,25] and is, thus, responsible for the transfer of excess electronic energy to the lattice and the heat generation within metallic NPs.[23,26–29] The dynamics of the electron distribution have been modeled using novel ab initio methods. Besides the theory on their generation and transport in nanostructures, detailed information on their stabilization and accumulation is of particular interest as it would pave the way towards better understanding and harvesting plasmon-induced catalysis and photochemistry effects.[30 31,32]

Many studies focus on changes in the maximum electron temperature, T_e, after excitation at various laser intensities.[23,33] The electron heat capacity is certainly not negligible if we are considering the evolution of T_e, and it exhibits linear temperature dependence in any excitation regime.[23] The electron heat capacity is certainly not negligible if we are considering the evolution of T_e, and it exhibits linear temperature dependence in any excitation regime.

While the influence of particle size on the phonon-phonon interaction is described in the literature[34], the effects of a colloidal environment on the early relaxations of NPs remain controversial. For instance, Mongin et al. found no influence of the colloidal environment on electronic cooling.[23] In contrast, Westcott et al. reported that organic surface adsorbates can introduce an additional channel for hot electrons to decay after laser excitation, resulting in a local screening of Coulomb interactions and, therefore, an accelerated energy transfer time.[35] Although Aruda et al.[36] verified this result, both studies utilized aminated or even thiolated organic ligands as surface adsorbates. These additives are known to etch the Au surface [37] and to interact with the surface in ligand-to-metal charge transfer (LMCT) processes,[38] resulting in a damping of the plasmon resonance of Au NPs. Interestingly, the reduced lifetime of hot electrons can be explained by an increased induced dipole moment of the surface adsorbate combined with an ultra-fast chemical interface scattering.[35,36] Henglein et al. found that chemisorbed anions on metallic surfaces alter the local charge density at the surface, subsequently changing the surface potential.[39,40] This effect indeed influences the electron density and, therefore, should result in an accelerated energy transfer time between electrons and phonons ($\tau_{e\text{-}ph}$), a fact that has been ignored in hot-electron literature so far.

To address the inconsistencies and understand the influence of surface chemistry on the interaction of light and colloidal NPs surfaces, we performed ultrafast optical laser pump-probe measurements in a transmission geometry on surfactant-free (that is, free of any reactants, dielectric coatings, and organic molecules) gold nanoparticles (Au NPs) produced through Laser Ablation in Liquids (LAL) (see Methods). These naked nanoparticles prepared by laser ablation in liquids[9] represent an appropriate model system as they solely possess electrostatically stabilized metal surface atoms, which make them very sensitive to their chemical environment.[9,41] In this work, the local nanoparticle environment was controlled by varying the charge and concentration of different anionic species.In order to study the effect of the local environments on $\tau_{e\text{-}ph}$. we used a probe beam to detect changes of the dielectric constant after laser photoexcitation of the electronic nanoparticle system.

We selected a probe laser wavelength of 527 nm near the surface plasmon resonance (SPR), providing a sensitive tool for surface adsorbates.[41–43] In theory, alterations in transmission are indicative of electron-phonon coupling, and the corresponding time behavior is directly related to the electron distribution around the Fermi level and, thus, to the internal thermalization dynamics.[44] Note that the electron-phonon coupling strength is a function of the pump energy in the high excitation regime but can be assumed to be almost constant in the weak excitation regime (Further information, see section VII in the SI).[45]

Results and Discussion

To gain clear insight into the interaction between anions and the particle surface, we first determined the coupling time of Au NPs of two different sizes in pure water after excitation with different laser energies. This initial step allowed us to study surface effects in the absence of organic ligands on the energy coupling times of laser-generated surfactant-free Au NPs. Thereby we varied the ionic strength of monovalent salts and the salts valency in a second step.

Influence of deposited energy and particle size

Absorbance spectra of the 23 nm and 53 nm sized monomodal colloids (Fig. 1A) before excitation are shown in Fig. 1B. The feature at 400 nm is mainly due to the interband transition from 5d to 6sp bands in gold.[29] Since the absorbance wavelengths of both colloids at the pump wavelength are on the same order of magnitude (Fig. 1B), a similar electronic temperature at comparable laser intensities can be expected. We excited the particles with three different laser intensities, ranging from $3.6*10^{14}$ to $1.0*10^{15}$ W/m^2, leading to an electronic temperature of 3900–5600 K (according to TTM). The bleaching of the absorbance signal observed in Fig. 1C resulted in a higher transmission, which is caused by an ultrafast alteration of the dielectric constant.[44] Consistent with literature, the subsequent exponential decay time is dependent on the laser intensity and induces a longer energy transfer time between electrons and phonons with increased pump energy. Following Figure 1D, we detect small changes in the coupling time between electrons and phonons at constant pump energy. Note that the particle size as well as the specific surface area in both cases is different. In the following control experiment we aimed to elucidate whether nanoparticle size or the surface area are driving factors. Therto we changed the total surface area of our colloids I) by changing the particle size and II) by changing the nanoparticle mass

c

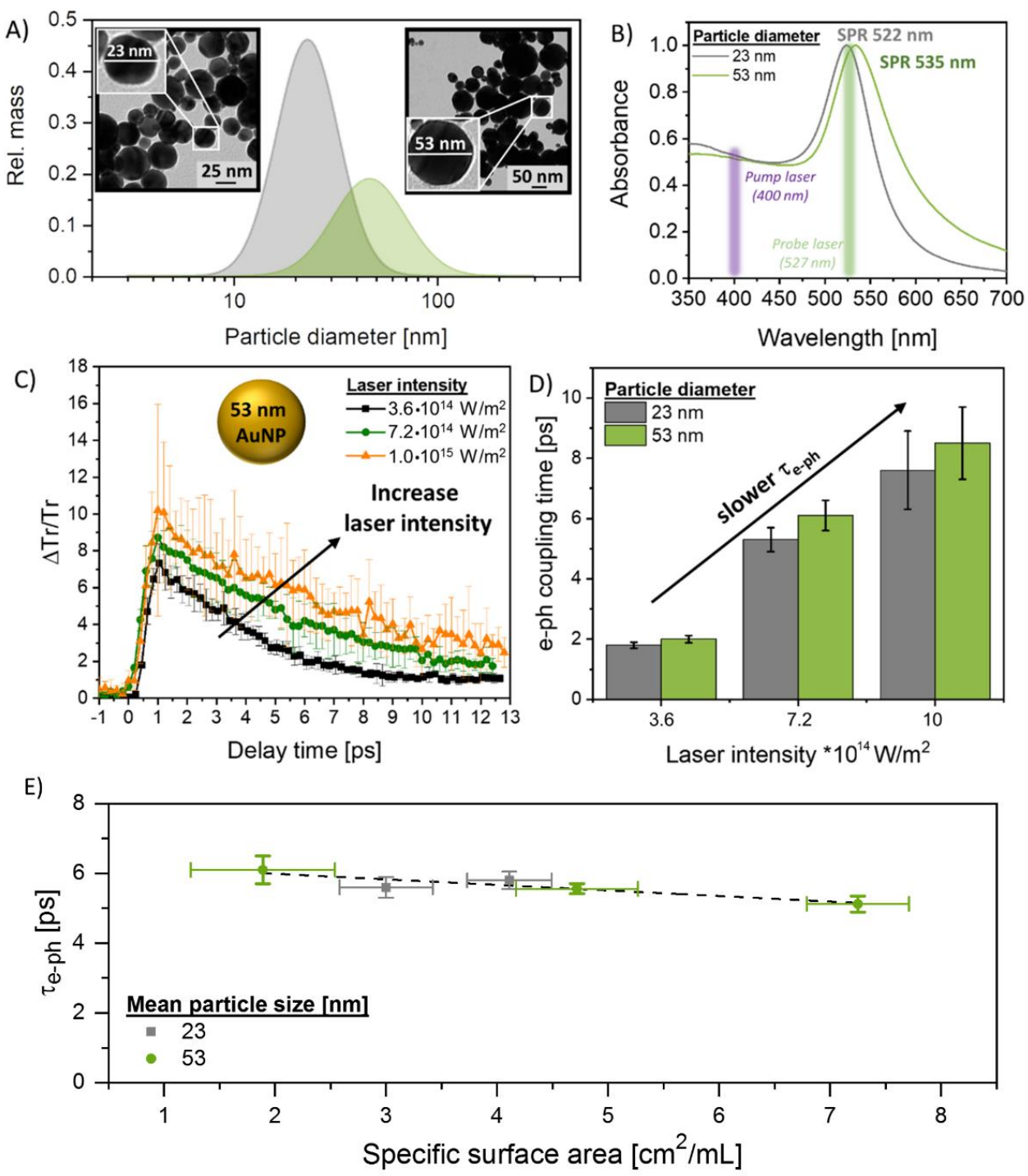

Figure 1: *(A) The particle size analysis for laser ablation in liquids nanoparticles and subsequent centrifugation is shown. The figure shows the mass-weighted size distribution (gained from analytical disc centrifugation) and representative transmission electron microscopy images of 23 nm and 53 nm particles. B) The absorbance spectra of both colloids in ultra-pure water are shown for two types of nanoparticles. C) The transient transmission change is shown after the laser excitation of 53 nm Au nanoparticles in H_2O as a function of delay time with different laser intensities. D) Energy transfer time between electrons and phonons of 23 nm and 53 nm Au nanoparticles measured after excitation with three different laser intensities indicates small deviations between absolute values. E) Dependence of $\tau_{e\text{-}ph}$ on the specific surface area in laser-generated Au NPs adjusted by different particle sizes and altered mass concentrations. The linear behavior (R^2 = 0.978) between $\tau_{e\text{-}ph}$ and the specific surface area points at surface-specific rather than size effects.*

$_{ph}$ and the specific surface area (Figure 1E) but no distinctive size effect. This finding is in good agreement with literature.[23] Although size effects on the energy coupling time have been reported, they have been mainly described for particles much smaller than 20 nm.[23,27] For larger particles, the differences were negligible within the laser intensity ranged used in this work. Now the question arises why there is a correlation between $\tau_{e\text{-}ph}$ in fully inorganic AuNPs and particle surface area. This phenomenon can only be correlated with interactions between the particle and its chemical environment. As the total surface area increases the interactions between nanoparticles and their environment intensified, which resulted in a decrease of the electron-phonon coupling time. This effect is more closely examined in the consecutive paraphs.

Influence of colloidal environment on different particle diameters and at different laser intensities

We investigated the influence of micromolar NaCl in a basic pH-regime on the energy transfer time, as the mixture of salt and base has previously been found to sufficiently stabilize NPs by preventing agglomeration.[46] In short, nanoparticles produced through LAL are partially oxidized, and the interaction with ultra-pure water leads to a pH-dependent equilibrium of OH/O^- on the particle surface.[47,48] Supplemented alkaline additives shift this equilibrium to the deprotonated form, while the addition of anions leads to anion adsorption even on non-oxidized surface atoms.[49] Both additions can increase the density of negative charges at the surface of the particles and, thus, enhance electrostatic stabilization (Fig. 2). This effect was first discovered when Au NPs were synthesized in the presence of corresponding electrolytes, though stabilizing effects by ex-situ addition are also expected to occur in the low salinity regime.[47,50] According to the Stern model[51], the anions in the vicinity of a solid surface will orientate in an electrochemical double layer. The electrochemical potential caused by the anions adsorbed on the particle decreases linearly in the rigid layer (Helmholtz layer) and exponentially in the diffuse layer (Gouy-Chapman layer) with the distance from the surface. Note that the smaller particles have a larger specific surface area, resulting in fewer anions in the near vicinity of each particle. In turn, the gold surface-specific anion dose is higher for larger gold nanoparticles in colloids at the same AuNP mass concentration, causing stronger anion effects on the electron-phonon coupling times for larger nanoparticles (which experience stronger polarization effects by higher surface-specific anion dose). For further information, see also section II in the supporting information.Figure 3 shows the energy transfer times as a function of the pump-laser energy. We included a 92% confidence interval that fits the laser system's signal-to-noise ratio (see also section III of the SI). While we are not able to detect an influence of anions on the smaller-sized particles (within the given sensitivity of the system), Figure 3A shows differences after anion addition for larger particles. To validate the anion-polarisation-based explanation of the results of the dynamic measurement, we performed static experiments probing how the AuNP´s SPR depends on the addition of anions, in a Hofmeister series of increased anion polarizability. This series shows that more polarizable, chaotropic anions (Br-) have a stronger effect on the SPR of fully inorganic gold nanoparticles, and that the larger particles (that are prone to higher surface-specific anion dose) show a stronger SPR shift (section VI on static UV-Vis measurements in the SI). This data proves our herein presented model of anion effects on the AuNP´s electron density. In a simplified picture, one may assume that a Au NP surface atom, which carries an

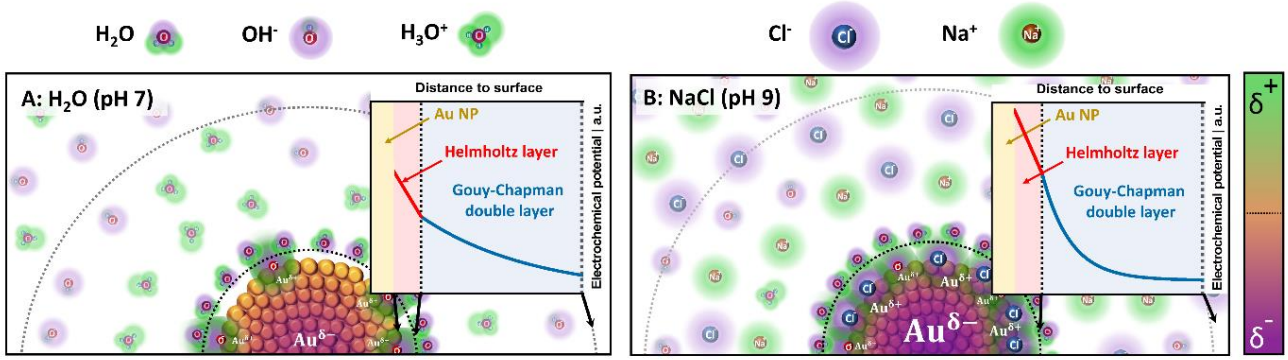

Figure 2: Graphical illustration of anion-specific effects during the interaction between Au NPs with the colloidal, aqueous micromolar saline environment. A) Au NPs in pure water at pH 7 and B) Au NPs in saline solution at pH 9.

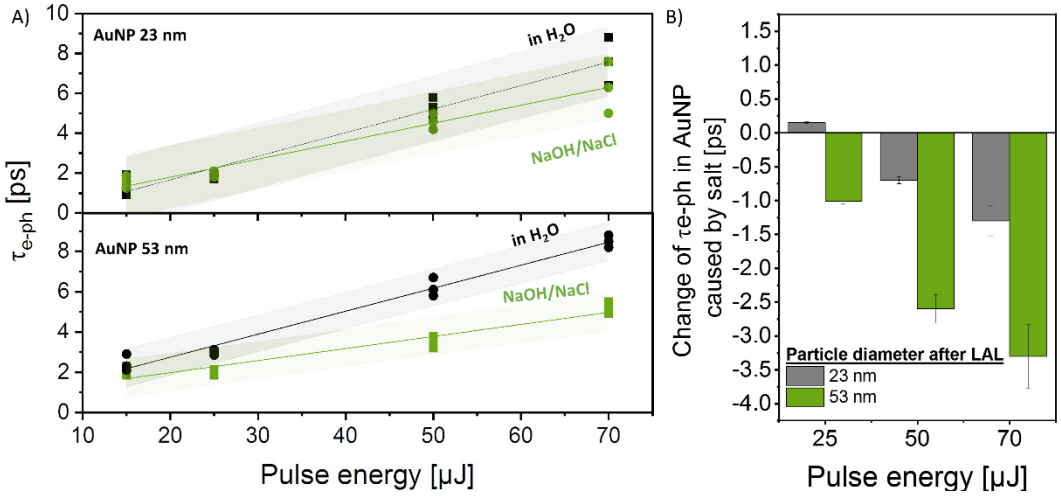

Figure 3: *A) The electron-phonon coupling times of 23-nm (top) and 53-nm (bottom) Au NPs are shown after excitation with different pulse energies, measured for colloids in water (black) and colloids in 0.3 mM NaOH/NaCl (green). The data are fitted with a linear regression with a confident interval of 92% (see SI). B) Changes of the electron-phonon coupling times of 23-nm Au NPs (black) and 53-nm Au NPs (green) are shown.*

anion, will acquire a slightly positive charge, and the excess electron density will move to the NP interior.[40] The presence of the anion will reduce the electron density at the particle surface, such that less electronic screening and, therefore, a faster electron cooling after photon absorption are to be expected. In other words, the particle surface becomes less noble.[40] Many studies have greatly contributed to understanding electron-phonon scattering processes in metal nanoparticles considering non equilibrium electronic processes based on hot electron dynamics[51], which have been used to improve interpretation of pump probe measurements[52]. However, little is known about how an external electric field caused by charge density transfer by anion adsorption would contribute to these processes.

This effect should happen independently of the particle size. However, we used colloids in the same mass concentration, which leads to a higher anion-to-particle ratio in the case of the larger sphere (higher surface-specific anion dose), which results in a stronger observed effect. While differences due to the particle size can be explained by the altered specific surface area (Figure 1E), the anion effects need consideration of anion per particle surface (see also section II in the SI).

The surface of a single spherical 53-nm particle is larger than that of a 23-nm particle, so that the number of anions per particle is higher at constant anion concentration (see also section I in the SI), which leads to a higher surface charge on a single particle. Furthermore, the data in Figure 3A hint towards an increased anion influence with increasing pulse energy. This is very interesting and could explain differences in recent literature. For example, Mongin et al.[23] induced electronic temperature changes of 200 K in Cu NPs and found no influence of the environment, while Westcott et al.[35] induced a temperature change of >2700 K and found a strong influence of the colloidal environment. The influence of surface chemistry on the energy transfer time can, therefore, only be detected after sufficiently strong excitation, whereby the determination of a threshold value is beyond the scope of this publication. However, based on the experimental data, we cannot fully explain the effect of the pulse energy, but we believe this gives an impetus for further studies. To prove the existence of an anion-induced electronic density push from the surface towards the Au NP core, we performed additional static UV-Vis measurements, which show a red-shifted absorbance (see SI). Note that we excluded aggregation-induced plasmon coupling effects by hydrodynamic size measurements (Fig S9). As we cannot explain the observation of increasing anionic influence with increasing pulse energies based on the experimental data, we performed further experiments at a fixed pulse energy of 50 µJ to ensure constant conditions.

We also observed that the influence of anions in the colloidal environment on $\tau_{e\text{-}ph}$ increases for larger NPs (Fig. 2C). The specific surface of spherical 53-nm

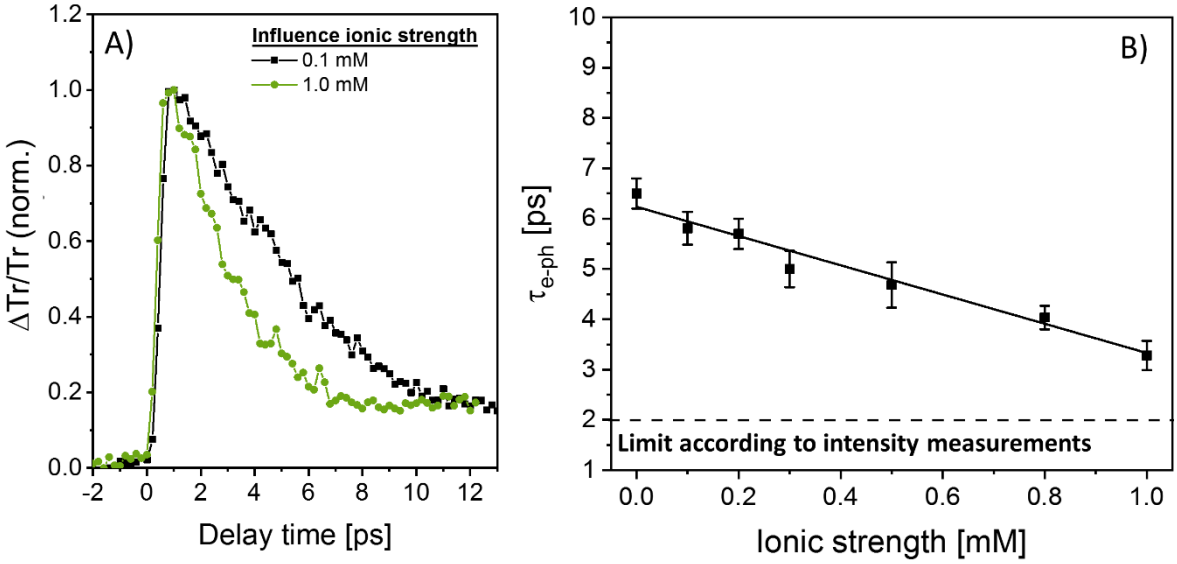

Figure 4: The influence of different ionic strengths of NaCl on the electron-phonon coupling time, $\tau_{e\text{-}ph}$, of 60-nm Au NPs and at a laser pulse energy of 55 µJ is shown; A) comparison of the decay curve measured at 0.1 mM and 1 mM NaCl; B) summary of all measured $\tau_{e\text{-}ph}$.

particles is larger than that of 23-nm particles, so that the number of anions per particle in the colloid with larger particles at constant anion concentration (see also section I in the SI), which leads to a higher surface charge density per particle.

In our experiments, charge transfer effects are more pronounced in larger spheres, indicating that both surface-bound ligands and anions that electrostatically interact with the surface alter the electronic system of the Au NPs.

Influence of the ionic concentration of monovalent salt

To further validate accelerated $\tau_{e\text{-}ph}$ by increasing the anion adsorbate surface density, we varied the ionic strength (IS) of anions in the colloidal solution. According to $IS = \frac{1}{2}\sum_A c_A \cdot z_A^2$, this can be confirmed by either changing the ionic concentration (c_A) or the anion valence (z_A). First, we will consider the impact of the salt concentration on $\tau_{e\text{-}ph}$ using the larger (more sensitive) spheres and aqueous NaCl as a model-system for a monovalent salt (now at neutral pH), probed after excitation with 55 µJ, as the biggest changes occur at high pulse energies. Fig. 4 shows that $\tau_{e\text{-}ph}$ decreases linearly with IS, which is probably due to a linear increase in anion adsorption and, hence, charge transfer to the particles, as previously explained. The linear trend seems to indicate that adsorption follows a Henry-based adsorption isotherm. However, this behavior can also be explained considering the Gouy-Chapman model, which describes the interaction between anions and metal NPs creating a diffuse layer of anions in the nano-environment of a colloidal particle. Accordingly, the electrostatic potential decreases exponentially with distance to the metal surface, while the anion concentrations at the particle surface are far higher than those in the bulk liquid[48] and further increase with IS. Evidently, the highest NaCl concentration that we used (1 mM) accelerates the energy transfer between electrons and phonons by a factor of 2. Following this linear trend, we can assume an even stronger influence for higher salt concentrations. However, higher IS will reduce the Debye-length so that the purely electrostatic stabilization of the colloidal particles is impaired. Subsequently, agglomeration or even aggregation of the NPs[46] occurs, which would dynamically shift the particle's SPR and impair our measurements.

Thus, we conclude that monovalent anion surface adsorbates can accelerate $\tau_{e\text{-}ph}$ by a factor of 2, simply by adding table salt to the aqueous colloid. Their influence is much stronger than the influence of the particle size found in Ref.[23] as well as to the influence caused by an increase in surface area (Figure 1E) and is quantitatively comparable with the well-known influence of the pulse energy. In other words, anions offer to be an inexpensive, mild, and easily-controllable means to manipulate the lifetime of hot electrons at constant laser excitation parameters

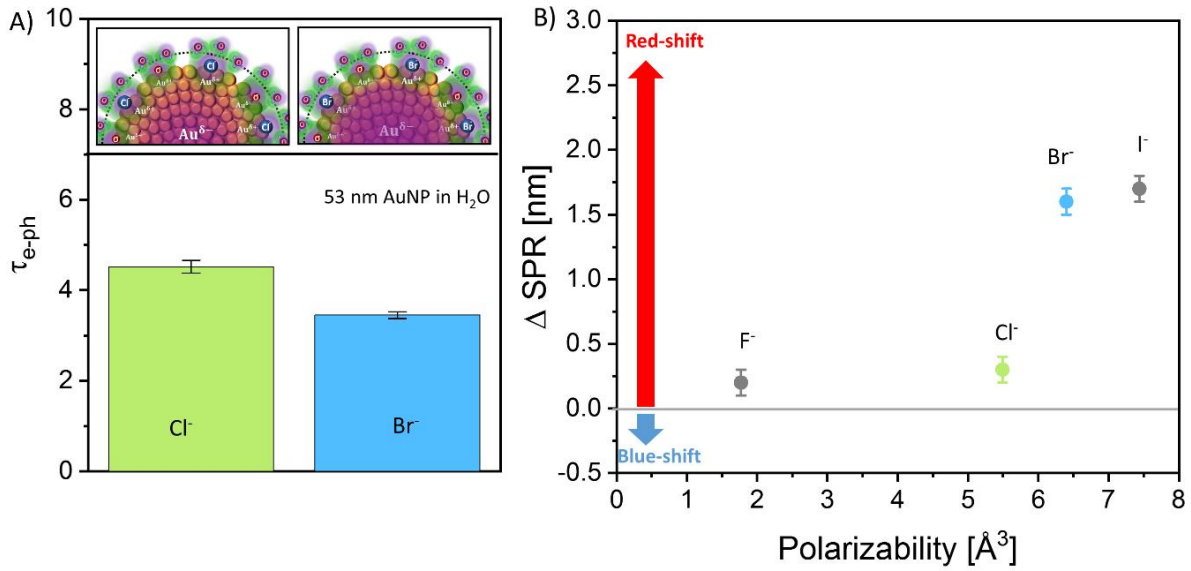

Figure 5: *Comparison of $\tau_{e\text{-}ph}$ of Au NPs in H_2O, NaCl, and NaBr at the constant specific surface area of 4.5 cm^2/mL and ionic strength of 0.5 mM. B) Position of the SPR after adding different halide anions, measured by static UV-Vis extinction spectroscopy*

Influence of different monovalent halide anions

In the next step, we tested the influence of different monovalent, halide anions on their impact on the electronic structure of the large NPs spheres. Note that the polarisability of these anions increases with increasing order in the periodic table (F^- < Cl^-< Br^- <I^-). Following the logic laid out above, the anions' impact should increase, with increasing ability to interact with the Au surface. Following Pearson's concept of hard and soft acids and bases, a better polarizable charge, like that of soft Lewis-base bromide, should interact more intensively with the soft Lewis-acidic gold surface. Therefore, we expected a higher impact on $\tau_{e\text{-}ph}$ and were able to verify this by dynamic pump-probe measurements (see Figure 5). Br^- has a ~20% higher polarizability than Cl^- and accelerates $\tau_{e\text{-}ph}$ by ~15% (further data are shown in section VI of the SI). Besides, we performed static UV-Vis extinction spectroscopy measurements and recorded the position of the SPR after the addition of four different halide anions. The addition of strongly polarizable anions leads to a strong red-shift of the SPR. Note that the hydrodynamic particle size was not affected by the salts at the given concentration (see also Figure S11) so that aggregation-induced plasmon coupling effects can be excluded.

Influence of anion valency

So far, we have considered the influence of NaCl in the neutral and basic regimes. In the next step, we expand the spectrum of anions to sodium dihydrogenphosphate (NaH_2PO_4) as another monovalent salt, followed by the bivalent equivalent disodium hydrogenphosphate (Na_2HPO_4) and the trivalent sodium citrate ($Na_3C_6H_5O_7$). The concentration of the salts in the colloid was adjusted to 0.5 mM, while IS varied due to the different valencies (Fig. 6). In comparison with our previous result, changing the IS by altering the ionic valence at a constant ion concentration has only a small effect on $\tau_{e\text{-}ph}$ (Fig. 6B), which we confirmed by UV vis extinction spectroscopy measurements. While the addition of chlorine anions leads to a red-shift of the SPR, and an even stronger effect is observed for bromine, this effect is negligible for the anions having a higher number of hydrations, as probed for NaH_2PO_4, Na_2HPO_4, and $Na_3C_6H_5O_7$..

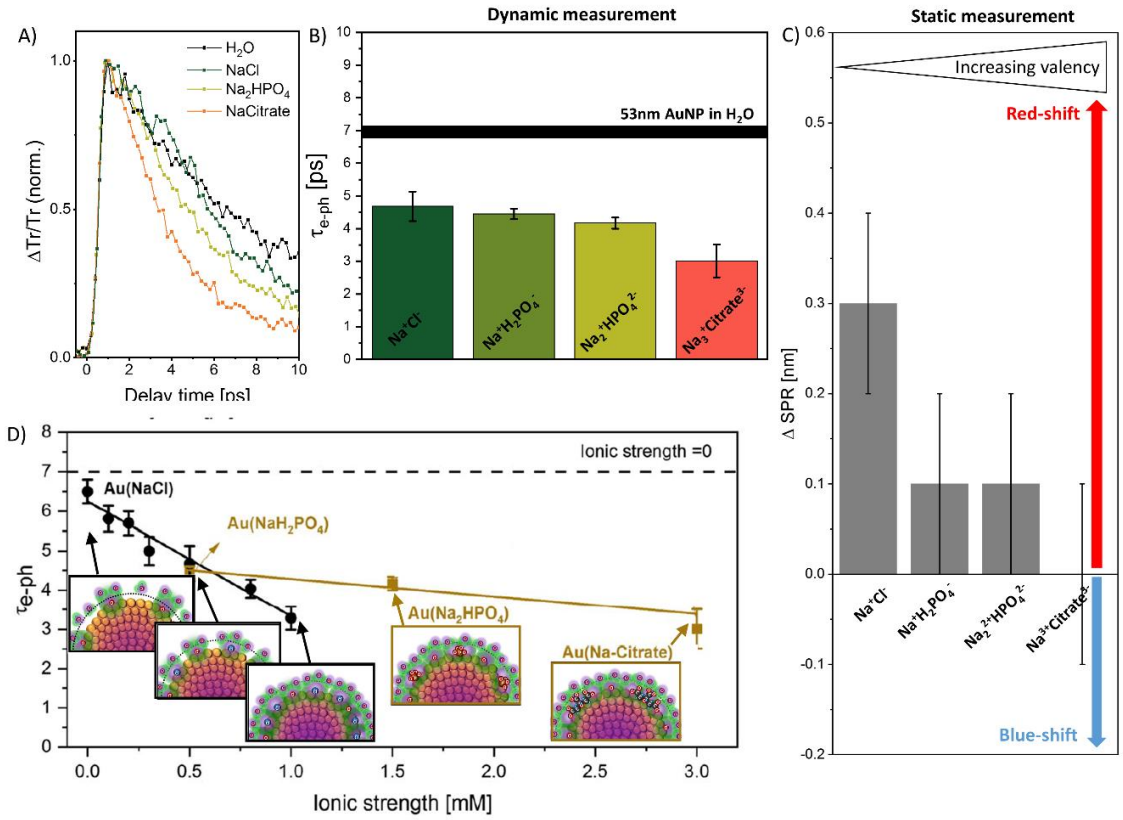

***Figure 6**: A) Influence of varied IS, depending on different anion valences, on the decay curve of 60 nm Au NPs at a pulse energy of 55 µJ. B) Comparison of $\tau_{e\text{-}ph}$ of Au NPs in H_2O, NaCl, NaH_2PO_4, Na_2HPO_4, and $Na_3C_6H_5O_7$. C) Position of the Au NP´s SPR after addition of different valent sodium salts. D) Influence of IS on $\tau_{e\text{-}ph}$; IS is varied by either the concentration or anionic valence*

The electron screening ability on the particle surface is, therefore, higher for monovalent anions than for their higher valent equivalences, which is counter-intuitive as the adsorption enthalpy should be a function of valence.[53] As mentioned above hard and soft acids and bases should interact less with the soft Lewis-acid gold surface and should be adsorbed in lower quantities. In addition, anion surface adsorption of highly charged anionic species, which influences the electron density leaking into the nanoparticle, is hampered due to the kosmotropic character correlated with the charge density of the ions.[54] This stronger hydration of the more kosmotropic multivalent anions weakens the anions' bulk concentration effects on the NPs' surface charge density (see section IV of the SI). Besides, the adsorption capacity for strongly hydrated ions usually decreases.[53] Consequently, the influence of anion valence on the screening of Au NPs surface electrons is observed as expected but is weakened by the kosmotropic effect. In turn, more chaotropic anions, such as chloride and bromide, are more effective surface adsorbates for Au NPs and allow linearly tuning of the hot electron lifetime.

Conclusion

We provide insight into how the nano-environment affects the energy transfer time between electrons and the lattice of laser-excited colloidal nanoparticles without cross-effects produced by organic ligands, such as thiols or amines. Hot electron lifetime is a key factor for light-triggered processes studies in aqueous media, such as catalysis and biophysics. Yet, electron-phonon relaxation processes are rarely performed in anion-free environments such that the effect of adsorbed anions has been neglected in the literature thus far. Our work investigated surfactant-free colloidal gold nanoparticles as the ideal building blocks to probe relaxation tuning using anions to avoid the cross-effects posed by surfactants or thiols. Using optical pump-probe spectroscopy, we analyzed the electron-phonon relaxation on the picosecond time scale, demonstrating that increasing ionic strength (concentration) of

monovalent anions strongly reduces $\tau_{e\text{-}ph}$ by up to a factor of 2. This effect was found to be more pronounced for larger particles with smaller volume-specific surface area, offering a potential explanation for the discrepancies in literature. Among the previous works, the use of particles of smaller diameters led to open questions on the effect of the dielectric environment on the electron-phonon-relaxation times of nanoparticles. Interestingly, tuning the ionic strength of mono-valent NaCl linearly accelerated relaxation and was far more pronounced than the influence of varying anionic valence. We contribute the latter result to the kosmotropic character of anions, which weakens the electronic contribution to the Au NPs surface and accordingly reduces the influence on $\tau_{e\text{-}ph}$. Overall, the valence and concentration of anions allow tuning of this electron screening effect at the nanoparticle surface accelerating the energy transfer time by serval picoseconds.

Understanding the influence of an-ions is not only a prerequisite for hot electron applications in aqueous media under non-deionized conditions, such as catalysis or biomedicine, but may also be a useful tool to tune excited state lifetimes for higher pump energies reaching laser fragmentation regime, recent findings[55] indicate that anions arrest the particle growth on a µs time scale. Hence, anions play an important role in both weakly pumped and strong excitation regimes. In turn, as the lifetime serves as a fingerprint of the surface charge density, this correlation could be employed in future scans of the ionic concentration in administered particles on the nanoscale.

Optical pump-probe spectroscopy was performed using a Ti-Sapphire laser with a pulse duration of 45 fs. After splitting the laser beam into two independent beam paths, we used a BBO ($Ba(BO_2)_2$) crystal to frequency double Ti:Sapphire output to the second harmonic and an optical parametric amplifier (OPA) to produce a probe pulse with a wavelength of 527 nm. The laser signal stability for both laser arms is given in Fig S1 and S2. The pump and probe beams enter the sample from the front surface of the cuvette with a relative angle of 45 degrees and overlap in the middle of a cuvette filled with the colloidal sample. Photodiodes were used to measure the incident energy of the probe laser before crossing the sample and the transmission signal after the sample (Fig. 1C) at different delay times (Δt = 100 fs), which were adjusted by varying the pump laser beam path using a physical delay stage. To increase the signal to noise ratio, we measured each data point 240 times and performed at least 5 runs. Data collection was performed using custom LabVIEW software and a National Instruments data acquisition card.[56] Data evaluation was conducted in OriginPro 2018. Optical pump-probe spectroscopy was performed on Au NPs in ultra-pure water or aqueous solutions containing NaCl, NaOH/NaCl, NaH_2PO_4, Na_2HPO_4, and Na-Citrate.

Laser ablation in liquids

Mixture of Au NPs with diameters of 23 and 53 nm were produced according to the method proposed in Ref.[50,55] using laser ablation in liquids (LAL) with a Nd:YAG laser (Ekspla, Atlantic series, 10 ps, 1064 nm, 88 µJ, 100 Hz). The ablation was performed in a continuously stirred batch chamber for 10 min, resulting in a colloid with a broad size distribution. To separate 23-nm and 53-nm particles with a narrow size distribution, we

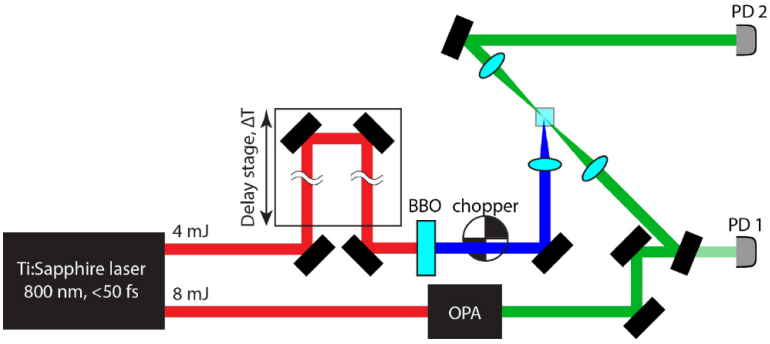

Figure 7: Experimental optical pump-probe set up using a Ti-Sapphire laser at 400 nm (violet: pump laser beam pathway) and 527 nm (green: probe laser pathway, wavelength adjusted using an OPA) with a pulse duration of 45 fs.

Methods

Optical pump-probe spectroscopy

performed centrifugal fractionation. Further information on particle characterization can be found in the SI. The respective salts were all purchased from Sigma Aldrich

as solids and mixed with corresponding volumes of deionized water.

Data availability

The data that support the findings of this study are available from the corresponding author upon reasonable request.

Authors contribution

The research has been designed by SB, SG, AZ, and SR. The experimental technique has been developed by ZC, BO, and CC. The experiments have been performed by AZ, AL, CC, ZC and BO. Data analysis has been done by AZ with support by ZC and BO. The manuscript has been written by AZ. All authors discussed the results and commented on the manuscript.

Conflicts of interest

There are no conflicts to declare.

Acknowledgments

We gratefully acknowledge the Deutsche Forschungsgemeinschaft for its financial support under Project No. BA3580/22-1. This work was further supported by the U.S. Department of Energy SLAC Contract No. DE- AC02-76SF00515 and by the U.S. DOE Office of Science, Fusion Energy Sciences under FWP 100182. AZ was financially supported by the DAAD – German academic exchange service and CENIDE – Center for Nanointegration Duisburg – Essen. CC acknowledges support from the Natural Sciences and Engineering Research Council of Canada (NSERC). The pump-probe experiments were performed in the HEDS Sector 10 Laser Laboratory at SLAC National Accelerator Laboratory. The authors thank Jurij Jacobi for his experimental support in producing the TEM and Prof. Sokolowski-Tinten for discussion. In addition, all authors thank Prof. Zhigilei and Huang Hao for their support and various discussions related to the theoretical background disussed here.

References

1. Hoang, C. V., Hayashi, K., Ito, Y., Gorai, N., Allison, G., Shi, X. Interplay of hot electrons from localized and propagating plasmons. Nat. commun. **8,** 771, (2017).

2. Dubi, Y., Sivan, Y. “Hot” electrons in metallic nanostructures—non-thermal carriers or heating? Light: Sci. Appl. **8,** 1–8; (2019)

3. Besteiro, L. V., Yu, P., Wang, Z., Holleitner, A. W., Hartland, G., Wiederrecht, G.P., Govorov, A. O. The fast and the furious: Ultrafast hot electrons in plasmonic metastructures. Size and structure matter. Nano Today **27,** (2019).

4. Sun, Y., Tang, Z. Photocatalytic hot-carrier chemistry. MRS Bull. **45,** 20–25, (2020).

5. Cortés, E., Xie, W., Cambiasso, J., Jermyn, A. S., Sundararaman, R., Narang, P. Plasmonic hot electron transport drives nano-localized chemistry. Nat. commun. **8,** 1292-1301, (2017).

6. Chu, W., Saidi, W. A., Prezhdo, O. V. Long-Lived Hot Electron in a Metallic Particle for Plasmonics and Catalysis: Ab Initio Nonadiabatic Molecular Dynamics with Machine Learning. ACS nano **14,** 10608–10615, (2020).

7. Wu, K., Chen, J., McBride, J. R. & Lian, T. CHARGE TRANSFER. Efficient hot-electron transfer by a plasmon-induced interfacial charge-transfer transition. Science **349,** 632–635, (2015).

8. Kang, B., Yu, D., Dai, Y., Chang, S., Chen, D., Ding, Y. Cancer-cell targeting and photoacoustic therapy using carbon nanotubes as "bomb" agents. Small, **5,** 1292–1301, (2009).

9. Zhang, D., Gökce, B., Barcikowski, S. Laser Synthesis and Processing of Colloids: Fundamentals and Applications. Chem. Rev. **117,** 3990–4103, (2017).

10. Kochuveedu, S. T., Jang, Y. H., Kim, D. H. A study on the mechanism for the interaction of light with noble metal-metal oxide semiconductor nanostructures for various photophysical applications. Chem. Soc. Rev. **42,** 8467–8493, (2013).

11. Kamat, P. V. Photophysical, Photochemical and Photocatalytic Aspects of Metal Nanoparticles. J. Phys. Chem. B **106,** 7729–7744, (2002).

12. Zeng, Q., Dai, J. Structural transition dynamics of the formation of warm dense gold: From an atomic scale view. Sci. China: Phys. Mech. Astron. **63,** 1017, (2020).

13. Lin, Z., Zhigilei, L. V., Celli, V. Electron-phonon coupling and electron heat capacity of metals under conditions of strong electron-phonon nonequilibrium. Phys. Rev. B **77,** 776, (2008).

14. Giustino, F. Electron-phonon interactions from first principles. Rev. Mod. Phys. **89,** 41, (2017).

15. Sadasivam, S., Ye, N., Feser, J. P., Charles, J., Miao, K. Kubis, T., Fisher, T. Thermal transport across metal silicide-silicon interfaces: First-principles calculations and Green's function transport simulations. Phys. Rev. B **95**, (2017).

16. Polte, J., Ahner, T.T., Delissen, F., Sokolov, S., Emmerlig, F., Thünemann, A. F., Kraehnert, R. Mechanism of gold nanoparticle formation in the classical citrate synthesis method derived from coupled in situ XANES and SAXS evaluation. J. Am. Chem. Soc. **132,** 1296–1301, (2010).

17. Daruich De Souza, C., Ribeiro Nogueira, B., Rostelato, M. E. C.M. Review of the methodologies used in the synthesis gold nanoparticles by chemical reduction. J. Alloys Compd. **798,** 714–740, (2019).

18. Bajaj, M., Wangoo, N., Jain, D. V. S., Sharma, R. K. Quantification of adsorbed and dangling citrate ions on gold nanoparticle surface using thermogravimetric analysis. Sci. rep. **10,** 8213, (2020).

19. Grzelczak, M., Pérez-Juste, J., Mulvaney, P., Liz-Marzán, L. M. Shape control in gold nanoparticle synthesis. Chem. Soc. Rev. **37,** 1783–1791, (2008).

20. Salley, D. Keenan, G., Grizou, J., Sharma, A., Martin, S., Cronin, L. A nanomaterials discovery robot for the Darwinian evolution of shape programmable gold nanoparticles. Nat. commun. **11,** 2771, (2020).

21. Orendorff, C. J., Sau, T. K., Murphy, C. J. Shape-dependent plasmon-resonant gold nanoparticles. Small **2,** (2006).

22. Chen, J. K., Tzou, D. Y., Beraun, J. E. A semiclassical two-temperature model for ultrafast laser heating. Int. J. Heat Mass Transfer **49,** 307–316, (2006).

23. Mongin, D., Maioli, P., Burgin, J., Langot, P., Cottancin, E., D'Addato, S. et al. Ultrafast electron-lattice thermalization in copper and other noble metal nanoparticles. J. Phys.: Condens. Matter **31,** 84001, (2019).

24. González-Rubio, G., Díaz-Núñez, P., Rivera, A., Prada, A.; Tardajos, G., González-Izquierdo, J., Bañares, L.. ; Llombart, P.; Macdowell, L. G.; Alcolea Palafox, M., Liz-Marzán, L. M. et al. Femtosecond laser reshaping yields gold nanorods with ultranarrow surface plasmon resonances. Science **358,** 640–644; (2017).

25. Saavedra, J. R. M., Asenjo-Garcia, A., García de Abajo, F. J. Hot-Electron Dynamics and Thermalization in Small Metallic Nanoparticles. ACS Photonics **3,** 1637–1646, (2016).

26. Hartland, G. V. Measurements of the material properties of metal nanoparticles by time-resolved spectroscopy. Phys. Chem. Chem. Phys. **6,** 5263, (2004).

27. Hodak, J., Martini, I., Hartland, G. V. Ultrafast study of electron–phonon coupling in colloidal gold particles. Chem. Phys. Lett. **284,** 135–141, (1998).

28. Manjavacas, A., Liu, J. G., Kulkarni, V., Nordlander, P. Plasmon-induced hot carriers in metallic nanoparticles. ACS nano **8,** 7630–7638, (2014).

29. González-Rubio, G., Guerrero-Martínez, A. & Liz-Marzán, L. M. Reshaping, Fragmentation, and Assembly of Gold Nanoparticles Assisted by Pulse Lasers. *Acc. of chem. res.* **49,** 678–686, (2016).

30. Sundararaman, R., Narang, P., Jermyn, A. S., Goddard, W. A. & Atwater, H. A. Theoretical predictions for hot-carrier generation from surface plasmon decay. *Nat. commun.* **5,** 5788, (2014).

31. Narang, P., Sundararaman, R. & Atwater, H. A. Plasmonic hot carrier dynamics in solid-state and chemical systems for energy conversion. *Nanophotonics* **5,** 96–111, (2016).

32. Brown, A. M., Sundararaman, R., Narang, P., Goddard, W. A. & Atwater, H. A. Nonradiative Plasmon Decay and Hot Carrier Dynamics: Effects of Phonons, Surfaces, and Geometry. *ACS nano* **10,** 957–966; (2016).

33. Groeneveld, R. H. M., Sprik, R., Lagendijk, A. Effect of a nonthermal electron distribution on the electron-phonon energy relaxation process in noble metals. Phys. Rev. B: Condens. Mater. **45,** 5079–5082, (1992).

34. Dowgiallo, A.-M., Knappenberger, K. L. Ultrafast electron-phonon coupling in hollow gold nanospheres. Phys. Chem. Chem. Phys. **13,** (2011).

35. Westcott, S. L., Averitt, R. D., Wolfgang, J. A., Nordlander, P., Halas, N. J. Adsorbate-Induced Quenching of Hot Electrons in Gold Core−Shell Nanoparticles. J. Phys. Chem. B **105,** 9913–9917, (2001).

36. Aruda, K. O., Tagliazucchi, M., Sweeney, C., Hannah, D. C., Scatz, G. C., Weiss, E. A. Identification of parameters through which surface chemistry determines the lifetimes of hot electrons in small Au nanoparticles. Proc. Natl. Acad. Sci. U. S. A. **110,** 4212–4217, (2013).

37. Chen, X., Wei, M., Jiang, S. & Förster, S. Two Growth Mechanisms of Thiol-Capped Gold Nanoparticles Controlled by Ligand Chemistry. Langmuir **35,** 12130–12138, (2019).

38. Jin, R., Zeng, C., Zhou, M., Chen, Y. Atomically Precise Colloidal Metal Nanoclusters and Nanoparticles: Fundamentals and Opportunities. Chem. Rev. **116,** 10346–10413, (2016).

39. Jin, R., Zeng, C., Zhou, M., Chen, Y. Atomically Precise Colloidal Metal Nanoclusters and Nanoparticles: Fundamentals and Opportunities. Chem. Rev. **116,** 10346–10413, (2016).

40. Scanlon, M. D., Peljo, P., Méndez, M. A., Smirnov, E. & Girault, H. H. Charging and discharging at the nanoscale: Fermi level equilibration of metallic nanoparticles. Chem. Sci. **6,** 2705–2720, (2015)

41. Amendola, V., Pilot, R., Frasconi, M., Maragò, O. M., Iatì, M. A. Surface plasmon resonance in gold nanoparticles: a review. Journal of physics. Condens. Matter Phys. J. **29,** 203002, (2017).

42. Geddes, C. D. Reviews in plasmonics, Springer, (2012)

43. Pastoriza-Santos, I., Sánchez-Iglesias, A., García de Abajo, F. J., Liz-Marzán, L. M. Environmental Optical Sensitivity of Gold Nanodecahedra. Adv. Funct. Mater. **17,** 1443–1450, (2007).

44. Del Fatti, N., Vallée, F. Ultrafast optical nonlinear properties of metal nanoparticles. Appl. Phys. B: Lasers Opt. **73,** 383–390, (2001).

45. Mo, M. Z. *et al.* Heterogeneous to homogeneous melting transition visualized with ultrafast electron diffraction. *Science* **360,** 1451–1455, (2018).

46. Ziefuß, A. R., Barcikowski, S., Rehbock, C. Synergism between Specific Halide Anions and pH Effects during Nanosecond Laser Fragmentation of Ligand-Free Gold Nanoparticles. Langmuir **35,** 6630–6639, (2019).

47. Rehbock, C., Merk, V., Gamrad, L., Streubel, R., Barcikowski, S. Size control of laser-fabricated surfactant-free gold nanoparticles with highly diluted electrolytes and their subsequent bioconjugation. Phys. Chem. Chem. Phys. **15,** 3057–3067, (2013).

48. Pfeiffer, C. Rehbock, C., Hühn, D., Carrillo-Carrion, C., Aberasturi, D. J., Merk, V., Barcikowski, S. Parak, W. J. Interaction of colloidal nanoparticles with their local environment: the (ionic) nanoenvironment around nanoparticles is different from bulk and determines the physico-chemical properties of the nanoparticles. J. R. Soc., Interface **11,** (2014).

49. Lipkowski, J., Shi, Z., Chen, A., Pettinger, B., Bilger, C. Ionic adsorption at the Au(111) electrode. Electrochim. Acta **43,** 2875–2888, (1998).46. Ziefuß, A. R., Reichenberer, S. Rehbock, C., Chakraborty, I., Gharib, M., Parak, W. J., Barcikowski, S.Laser Fragmentation of Colloidal Gold Nanoparticles with High-Intensity Nanosecond Pulses is Driven by a Single-Step Fragmentation Mechanism with a Defined Educt Particle-Size Threshold. J. Phys. Chem. C **122,** 22125–22136, (2018).

50. Ziefuß, A. R., S. Reichenberger, C.Rehbock, I. Chacraborty, M. Gharib, W. J. Parak, S. Barcikowski, Laser Fragmentation of Colloidal Gold Nanoparticles with High-Intensity Nanosecond Pulses is Driven by a Single-Step Fragmentation Mechanism with a Defined Educt Particle-Size Threshold. *J. Phys. Chem. C* **122,** 22125–22136; (2018).

51. Brown, A. M., Sundararaman, R., Narang, P., Goddard, W. A. & Atwater, H. A. Ab initio phonon coupling and optical response of hot electrons in plasmonic metals. *Phys. Rev. B* **94,** 776; (2016).

52. Brown, A. M. *et al.* Experimental and Ab Initio Ultrafast Carrier Dynamics in Plasmonic Nanoparticles. *Phys. Rev. Lett.* **118,** 87401; (2017).

53. Adapa, S., Malani, A. Role of hydration energy and co-ions association on monovalent and divalent cations adsorption at mica-aqueous interface. Sci. rep. **8,** 12198, (2018).

54. Collins, K. D. Charge density-dependent strength of hydration and biological structure. Niophys. J. **72,** 65–76, (1997).49. Werley, C. A., Teo, S. M., Nelson, K. A. Pulsed laser noise analysis and pump-probe signal detection with a data acquisition card. Rev. Sci. Instrum. **82,** 123108, (2011).

55. Ziefuss, A. R., Reich, S., Reichenberger, S., Levantino, M., Plech, A. In situ structural kinetics of picosecond laser-induced heating and fragmentation of colloidal gold spheres. Phys. Chem. Chem. Phys. **22,** 4993–5001, (2020).

56. Werley, C. A., Teo, S. M. & Nelson, K. A. Pulsed laser noise analysis and pump-probe signal detection with a data acquisition card. *The Review of scientific instruments* **82,** (2011).

3.3 – PART II

Characterization of ultra-small gold nanoparticles

3.3.1 Photoluminescence of fully inorganic colloidal nanocluster and their manipulation using surface charge effects

Synopsis:

While the previous chapter elucidates the laser-based synthesis route to inorganic gold nanoclusters, this chapter focuses on their size separation and optical properties.
The origin of the fluorescence of noble metal nanoclusters is a controversial topic that has been addressed in many studies but could not been clarified to date. The primary drawback is that the current state-of-the-art chemical synthesis methods only give access to ligand-capped nanoclusters. Hence, core emissions and ligand to metal-surface charge-transfer contributions cannot be differentiated. A new class of nanomaterials, i.e. fully inorganic colloidal nanoclusters, is required to solve this conundrum.
This work demonstrates the size-controlled generation of these ligand-free gold nanoclusters by a modern laser-based synthesis method. These species exhibit a bright blue fluorescence, for which the intensity is a direct function of the surface charge density easily adjusted by the pH of the surrounding medium. DFT calculations further confirm the correlation between surface charge and photoluminescence. Finally, this work elucidates how fluorescence emission, even in the absence of ligands, can be dedicated to core and surface state transitions, which are predominantly influenced by particle diameter and surface charge density.

This paper was published in Advanced Materials on June 24, 2021

ADVANCED MATERIALS
www.advmat.de

Photoluminescence of Fully Inorganic Colloidal Gold Nanocluster and Their Manipulation Using Surface Charge Effects

*Anna R. Ziefuss, Torben Steenbock, Dominik Benner, Anton Plech, Jörg Göttlicher, Melissa Teubner, Benjamin Grimm-Lebsanft, Christoph Rehbock, Clothilde Comby-Zerbino, Rodolphe Antoine, David Amans, Indranath Chakraborty, Gabriel Bester, Milen Nachev, Bernd Sures, Michael Rübhausen, Wolfgang J. Parak, and Stephan Barcikowski**

Fully inorganic, colloidal gold nanoclusters (NCs) constitute a new class of nanomaterials that are clearly distinguishable from their commonly studied metal–organic ligand-capped counterparts. As their synthesis by chemical methods is challenging, details about their optical properties remain widely unknown. In this work, laser fragmentation in liquids is performed to produce fully inorganic and size-controlled colloidal gold NCs with monomodal particle size distributions and an fcc-like structure. Results reveal that these NCs exhibit highly pronounced photoluminescence with quantum yields of 2%. The emission behavior of small (2–2.5 nm) and ultrasmall (<1 nm) NCs is significantly different and dominated by either core- or surface-based emission states. It is further verified that emission intensities are a function of the surface charge density, which is easily controllable by the pH of the surrounding medium. This experimentally observed correlation between surface charge and photoluminescence emission intensity is confirmed by density functional theoretical simulations, demonstrating that fully inorganic NCs provide an appropriate material to bridge the gap between experimental and computational studies of NCs. The presented study deepens the understanding of electronic structures in fully inorganic colloidal gold NCs and how to systematically tune their optical properties via surface charge density and particle size.

1. Introduction

Noble metal nanoclusters (NCs), particularly those composed of Au, have attracted significant attention over the last two decades[1,2] due to their photoluminescent properties. For instance, Au NCs exhibit small sizes and quantum yields (QY) several orders of magnitude higher than bulk gold,[3,4] making them interesting candidates in bioimaging,[4,5] sensing,[6] catalysis,[7,8] among other potential applications. In addition, Au NCs are highly interesting from a fundamental viewpoint as they bridge the gap between surface plasmon resonant nanoparticles (NPs) and quantized single atoms.[1,9] In this context, it is important to differentiate between colloidal Au NCs synthesized in the presence of organic and inorganic ligands. Specifically, metal–organic compounds possess a very low Au-to-heteroatom ratio (e.g., for $Au_{25}(SG)_{18}$ with SG = glutathione, the

A. R. Ziefuss, Dr. C. Rehbock, Prof. S. Barcikowski
Technical Chemistry I and Center for Nanointegration Duisburg-Essen (CENIDE)
University of Duisburg-Essen
Universitätsstraße 1-7, 45141 Essen, Germany
E-mail: Stephan.Barcikowski@uni-due.de
Dr. T. Steenbock, D. Benner, Prof. G. Bester
Department of Chemistry
Universität Hamburg
Institute for Physical Chemistry
Luruper Chaussee 149, HARBOR, Building 610
D-22761 Hamburg, Germany
The ORCID identification number(s) for the author(s) of this article can be found under https://doi.org/10.1002/adma.202101549.

DOI: 10.1002/adma.202101549

Dr. A. Plech, Dr. J. Göttlicher
Institute for Photon Science and Synchrotron Radiation
Karlsruhe Institute of Technology
Hermann-von-Helmholtz-Platz 1
76344 Eggenstein-Leopoldshafen, Germany
M. Teubner, Dr. B. Grimm-Lebsanft, Prof. M. Rübhausen
Institut für Nanostruktur und Festkörperphysik
Center for Free Electron Laser Science (CFEL)
Universität Hamburg
Luruper Chaussee 149, 22761 Hamburg, Germany
M. Teubner
Department of Inorganic Chemistry
RWTH Aachen University
Landoltweg 1, 52074 Aachen, Germany
C. Comby-Zerbino, R. Antoine, Prof. D. Amans
Univ Lyon
Université Claude Bernard Lyon 1
CNRS
UMR5306
Institut Lumière Matière
Villeurbanne F-69100, France

ratio is 1:7),[4] while fully inorganic Au NCs are electrostatically stabilized in liquid by adsorbed ions.

The vast majority of published studies address the photoluminescence of ligand-capped Au NCs.[7,10,11] The findings remain diverse, and a multitude of different electronic processes seem to be involved. Thus, a clear distinction must be made between a few-atom NCs with particle sizes up to ≈1 nm and NCs in a size regime from ≈1 to 3 nm.[10] The photoluminescence of few-atom clusters with known structures, especially $Au_{25}(SR)_{18}$, is relatively well understood, most likely attributed to the fact that these species can be synthesized with single atomic precision.[4,12] In this case, photoluminescence could be clearly correlated to quantized electronic states of the core material involving interband (d–sp) and intraband (HOMO–LUMO) transitions with lifetimes in the nanosecond regime and constant Stokes shifts of ≈50 nm.[13] The emission energy decreases with increasing NCs size,[14] which is induced by decreased density of states, resulting in a smaller gap between the highest occupied and lowest unoccupied molecule orbital (HOMO and LUMO). However, the colloidal environment can also influence the photoluminescence properties.[1,15,16] In the case of thiolate-capped Au NCs, visible as well as near infrared (NIR) emission with large Stokes shifts >100 nm occurs.[17] Red to NIR emissions are attributed to a charge transfer from the thiolate ligand to the non-oxidized metal core. The quantum yield could be significantly increased by the application of electron donor moieties in the applied thiol ligands.[15,16] Wu and Jin demonstrated that the photoluminescence of $Au_{25}(SR)_{18}$ NCs can be enhanced by increasing the donor ability of the surface ligands or the electropositivity of the metal core.[15] Besides that, the nuclear charge, size of the NCs, and structure of the ligand are decisive for the QY. Moreover, Wang and co-workers found that the QY caused by lipoic acid ligands on the Au NCs depends on their oxidation state. The oxidation of sulfur bound to the gold surface leads to an increase in the quantum yield of the photoluminescence by up to 10%.[18] In another case, photoluminescence emission was significantly blueshifted (0.1 eV) to the orange and yellow range when Au NCs were fabricated in the presence of glutathione.[19] This phenomenon was attributed to the presence of abundant oxidized Au(I) species,[20] which was considered to be a necessary prerequisite for photoluminescence in the observed system. Furthermore, photoluminescence was occasionally observed in larger plasmon-resonant Au NPs, where a reduction of grain size on a single particle induced the parallel occurrence of red single-particle luminescence and plasmon resonance.[21] Other studies observed blue photoluminescence in Au NPs, while particle size, surface oxidation, and predominantly surface ligands influenced the excitation and emission wavelengths and the luminescence intensity.[22]

Contrarily, totally inorganic colloidal Au NCs have been sparsely studied, considering that they are difficult to fabricate by chemical synthesis routes, as organic ligands are required as reducing/etching agents and/or to produce sufficient colloidal stability. Note that it is impossible to quantitatively remove ligands, once they are on the colloidal particle surface.[23] Pérez-Prieto and co-workers reported on a chemical reduction procedure of gold precursors in NaOH, yielding organic ligand-free, nonluminescent Au NCs.[24] Contrarily, the group of Scaffardi and co-workers[25,26] recently succeeded in producing organic ligand-free highly fluorescent few-atom Ag NCs using femtosecond-laser pulses ablating a solid target. The collected colloid includes a broad range of particle sizes that required a further mechanical centrifugation step to fractionate the few-atom NCs. The results revealed a broad photoluminescence after UV excitation, which could be explained by the large range of different sizes that were present in the plasmon-bleached colloids. Many questions about the origin of the photoluminescence of fully inorganic fluorescent colloidal NCs remain unanswered, especially the impact of surface charge density, due to the highly limited number of studies.

In this work, we fabricated inorganic NCs using laser fragmentation in liquids (LFL), which allows for the production of ultrasmall particles (<<5 nm) using ns-laser pulses applied to larger noble metal particles.[27–29] In short, this process is based on the following principle. After a plasmonic Au NP absorbs photons from a laser pulse, hot electrons form and interact with the cold electrons of the conduction band via electron–electron scattering. Thermal equilibrium of the electron gas is reached in less than 100 fs, before electron–phonon coupling occurs within a few picoseconds.[30] The heated lattice may lead to fragmentation, including phase explosion or Coulomb instability. If the laser pulse duration is longer than the characteristic times of the excitation and phase transitions, the reduction of particle size in the LFL process can be explained by a photothermal evaporation mechanism.[27,29,31]

In advancement to previous works on LFL, we applied a purification strategy based on ultrafiltration to yield monomodal and monodisperse Au NCs, which, in the initial state, were only exposed to NaOH and NaCl. Based on these colloids that lack organic ligands, we studied the photoluminescence properties of different size regimes and experimentally evaluated the impact of surface charge density on the photoluminescence. Additionally, the density functional theory (DFT) and screened configuration interaction singles (SCIS) calculations were carried out to acquire a deeper understanding of the quantum mechanical processes that are induced by surface charges.

2. Results and Discussion

LFL provides a method to produce ultrasmall colloidal Au NCs without additional contribution of organic surface

Dr. I. Chakraborty, Prof. W. J. Parak
Department of Physics and Center for Hybrid Nanostructure (CHyN)
Universität Hamburg
Luruper Chaussee 149, 22761 Hamburg, Germany
Prof. G. Bester
Department of Physics
Universität Hamburg
Institut für Nanostruktur und Festkörperphysik
Luruper Chausee 149, HARBOR, 22761 Hamburg, Germany
Dr. M. Nachev, Prof. B. Sures
Department of Aquatic Ecology and Centre for Water and Environmental Research
University of Duisburg-Essen
Universitätsstraße 5, 45141 Essen, Germany
Prof. W. J. Parak
Department of Chemistry
Universität Hamburg
Grindelallee 117, 20146 Hamburg, Germany

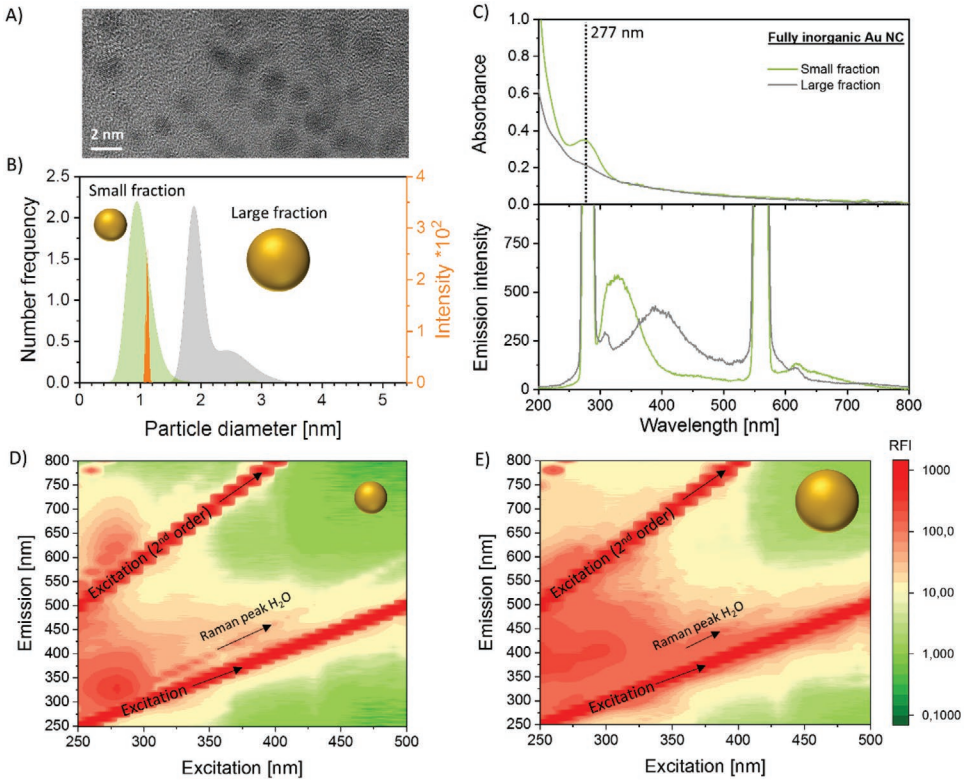

Figure 1. Photoluminescence of small and large, fully inorganic colloidal Au NCs. A) High-resolution transmission electron microscopy (HR-TEM) image of Au NCs after LFL and ultracentrifugation with a 50 kDa centrifugal filter. B) Number-weighted size distribution (measured with analytical ultracentrifugation (AUC)) after further ultracentrifugal steps with 3 kDa centrifugal filters (green, small fraction/gray, large fraction). Note that we additionally measured the smaller size fraction with ESI-MS (orange) (further information can be found in the Supporting Information). C) Absorbance spectra (top) and emission spectra (bottom, excitation 277 nm) after excitation of large and small Au NCs. D,E) 2D emission spectra of small (D) and large (E) Au NCs.

adsorbates. Although the produced colloid already contains Au NCs, a further size separation step is required in order to quantitatively remove plasmonic fractions. Scaffardi and coworkers[25,26] employed mechanical centrifugation to produce inorganic Ag NCs; however, the resulting size distribution was rather broad, making it difficult to study the intrinsic particle properties in detail. In the present study, we used ultracentrifugation together with centrifugal filters containing a regenerated cellulose membrane for a more precise size separation (**Figure 1**). The use of filters with a molecular weight cut-off (MWCO) of 50 kDa was sufficient to quantitatively remove plasmonic NPs, leading to a colloid with particle sizes between 0.5 and 3 nm (Figure 1A; Figure S1, Supporting Information). Since the utilization of filters with a smaller MWCO allows for further size separation, we applied filters with a MWCO of 3 kDa and were able to produce a smaller size fraction (located in the filtrate) and larger size fraction (located in the retentate).

Our findings showing the disappearance of a gold surface plasmon resonance (SPR) peak in our size fraction between 0.5 and 3 nm are in fair agreement with findings from literature on ligand-capped Au NCs,[32] though some deviations occur. Zhou et al. experimentally observed disappearance of SPR in particles smaller than 2.3 nm (Au_{333}) followed by a transition regime where neither plasmonic nor luminescence are observable, followed by a particle diameter smaller 1.7 nm (Au_{144}), where distinctive emissions are dominant.[33] Another study even suggests the occurrence of plasmon resonance for particles with average diameters of 1.3 nm, although these samples also contained significant amounts of particles >2 nm.[34] Furthermore, these differences in the threshold diameter for SPR disappearance may also be attributed to different surface ligands and solvents used. It is yet unknown how the absence of organic surface adsorbates on Au NCs and high surface charge densities affect the size-dependent onset size threshold of SPR. In future, such ligand-free Au NC size series could be fabricated based on modified parameters within the fragmentation and centrifugation method established here.

The particle sizes were analyzed using analytical ultracentrifugation (AUC), and in the case of the smaller particles, electrospray ionization mass spectrometry (ESI-MS) was additionally employed. A narrow size distribution (Figure 1B) was found in each case. Note that particles were produced in ultrapure water without the addition of organic stabilizers. Therefore, one novelty of this study is that the optical properties of the Au NCs were investigated without any cross-effects caused by ligand–metal charge transfer (LMCT), which are induced by organic ligands. This allowed for a direct investigation of the surface charge density effects altered by the addition of inorganic surface adsorbates.

We observed a strong absorbance in the UV region (277 nm) for particles with mean diameters of 1 nm, which could not be detected for larger NCs with mean diameters of 2–2.5 nm (Figure 1C). This absorbance peak for particles smaller than 1 nm probably originates from the well-known onset of energy state quantization and, thus, a discretization of the energy levels.[35] These findings are in qualitative accordance with the absorbance behavior of small ligand-capped Au NCs after wet-chemical synthesis,[36] which supports that this absorbance is linked to the quantized energy state of the Au NC metal core. When both smaller particles (1 nm) and larger particles (2–2.5 nm) were optically excited by UV-light, a pronounced and clearly distinguishable photoluminescence could be detected (Figure 1C–E). The smaller size fraction was found to emit light between 300 and 350 nm and at ≈610 nm with a large Stokes shift, whereby the large fraction emitted light between 350 and 400 nm (peak maxima consideration). This observation clearly verifies that completely inorganic colloidal Au NCs can be fluorescent, which is still considered a controversial topic in literature.[24–26] Quantum yield analysis of a colloid containing all cluster sizes between 0.5 and 3 nm (Figure S1, Supporting Information) indicated that 2% of all absorbed photons were emitted (measured at pH 8), which is 8 orders of magnitude higher than that for pure gold and in a comparable range to some studies of Au NCs in aqueous solutions bearing organic surface ligands.[1,2,37] Even though a QY of 2% can be considered moderate, it should be noted that this value was measured for a particle ensemble with sizes 0.5–3 nm and not on size selected fractions. Based on similar findings on ligand-capped Au NC,[38] it may be anticipated that higher QY for optical applications could be possible for smaller particles, however, a systematic study on the QY-particle size-correlation was not the focus of this study.

In summary, we can state that the laser-generated fully inorganic Au NCs showed a pronounced photoluminescence, which differs between smaller and larger particle sizes. The particles free of organic ligands were produced through LFL followed by ultrafiltration. However, it is well known that Au NPs obtained from laser processing in liquids have partially oxidized particle surfaces, leading to a pH-dependent equilibrium of AuO^-/AuOH groups on the particle surface in aqueous solution,[39–41] which can be varied through simple pH alteration.[42] In the basic range, the AuO^- group is favored, which directly correlates with a better colloidal stability, as caused by electrostatic repulsion. Based on these findings, it may be concluded that the surface charge density of our Au NCs (derived from zeta potentials as specified by Makino and Ohshima[43]) can be tuned by the pH value (**Figure 2**A; Figures S5–S7, Supporting Information). This gives the opportunity to correlate surface charge density with photoluminescence, which is systematically examined in the following paragraph.

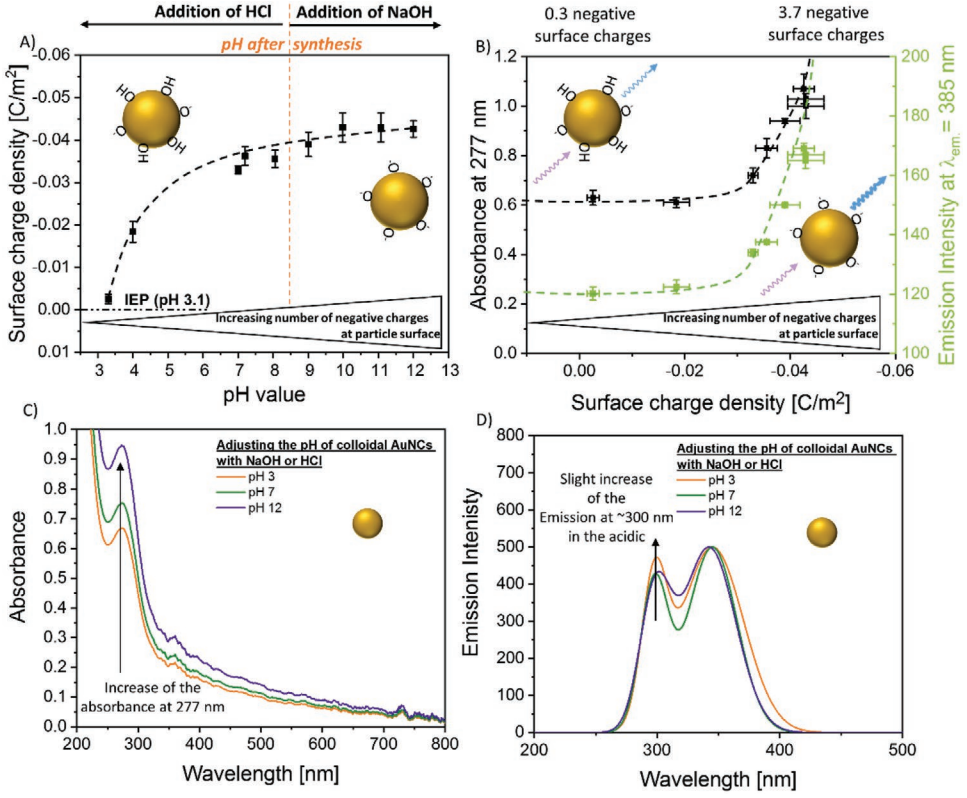

Figure 2. Surface charge density effects. A) Electronic and B) optical behavior of the large Au NC size fraction after the addition of NaOH and HCl. Absorbance was measured at 277 nm, emission intensity was measured at 385 nm after excitation at a wavelength of 277 nm. The inset sketches illustrate the increased emission intensity at high surface charge densities. C) Absorbance spectra and D) emission spectra of the small NC size fraction after pH adjustment. To exclude peaks associated with the excitation wavelength, we performed a multiple peak fit routine using a Gaussian peak function. The inset sketches in (C) and (D) remind that small particles are discussed within these graphics.

2.1. Influence of Ion-Induced Surface Charge Density on Photoluminescence

We experimentally investigated the effect of surface charge density on the large size fraction, as shown in Figure 1B in gray color. Here, NaOH and HCl were used to deprotonate and protonate surface-bound hydroxide groups (AuO^-/AuOH equilibrium), respectively, and to control the number of negative surface charges on the particles' surfaces.[39,41] By varying the pH from the acidic to the strongly basic regime (pH < 3 was not achievable as particles aggregated), we observed a pronounced increase of the surface charge density with increasing pH (Figure 2A). Based on this, we calculated the number of elemental charges per Au NCs by normalizing the surface charge density by the surface area of one larger Au NC (2 nm) and the elemental charge. This yielded 0.3 to 3.7 elementary charges per particle (more information can be found in Section SII in the Supporting Information). Consecutively, we examined the optical properties of the corresponding particles at different pH values. We observed an increase in the broad absorbance band (200–600 nm) (Figure S6A, Supporting Information) with increasing number of negative charges. The increased absorbance was accompanied by an elevated emission intensity at 385 nm after excitation at 277 nm, while the emission wavelength at 385 nm remained constant (Figure 2B). To rule out side effects due to particle aggregation by pH alteration, which could also result in a decreased photoluminescence intensity[44] or aggregation-induced emission,[45] we checked the particle size distributions at different pH values using AUC and found no differences (Figure S7, Supporting Information).

Therefore, we can conclude that changes in photoluminescence intensity of larger Au NCs can be attributed to solvent effects influencing the surface charge density. Such effects have already been reported to influence the emission intensity, but were mostly studied in context with polarization of the solvent.[46] We changed the polarization of the particles via deprotonation/protonation (OH^-/H_3O^+) and observed an emission intensity increase with increasing surface charge density. Note that the photophysical properties both at moderate and at significantly increased surface charge densities are long-term stable (see Section SII in the Supporting Information). Though not directly measured here, the increased fluorescence intensity with surface charge density might be a useful tool to increase the QY of the fully inorganic Au NC for applications. However, we did not aim at increasing the QY but want to strengthen the fundamental knowledge on the fluorescence origin in Au NCs.

Following Scanlon et al.,[47] anion adsorption leads to a slightly positive particle surface, as excess electron density is transferred to the interior of the particle.[47] This affects the local charge density of the surface, leading to an alteration of the surface potential.[47] A partially electron-deprived (positive) surface would hence increase the absorption[48] and the emission intensity, since reduced electronic density on the particle surface would decrease the probability of nonradiative transitions.[49]

For the smaller Au NCs (Figure 2C,D), we observed an increase of the absorbance at 277 nm with the pH value, which seems to indicate similar charge-induced phenomena as those seen for the larger particles. The emission spectra, on the other hand, revealed a constant emission intensity at 350 nm, while the higher energy emission at 300 nm increased when changing the medium to an acidic pH. However, the impact of the surface charge density on the optical properties of the smaller particles could not be determined experimentally, as colloidally stable Au NCs in this size regime had concentrations too low for realistic zeta potential measurements, despite the charge states observed in nanoelectrospray ionization (nano-ESI)-MS being between 4 and 7 (see Figure S2 in the Supporting Information).

In order to explain the experimentally observed increase in the absorption intensity and to establish a relation between the emission behavior and the total surface charge in those small Au NCs, we performed DFT calculations for a series of $Au_{38}(OH)_{24-x}(O)_x^{x-}$ model particles ($X = 0, 2, 4$) differing in the total (negative) charge of the system obtained by abstracting protons from the hydroxy groups on the Au NC surface. As the Au_{38}NC core has a diameter of about 1 nm (8000 kDa), it closely matches the size regime determined experimentally (Figure 1; Figure S3, Supporting Information). The calculations were performed with aid of the wB97X-D range-separated hybrid exchange–correlation functional,[50] the conductor-like screening model (COSMO)[51,52] with parameters for water to simulate the solvent effects at the single-particle level, as well as a dhf-SVP-2c basis set,[53,54] including spin–orbit effects (more computational details are given in the Supporting Information). We additionally performed SCIS calculations[55] to obtain the excited state properties as a function of the total charge (or equivalently the degree of deprotonation). The obtained theoretical absorbance spectra (**Figure 3**A) are shown for three different charge states, i.e., 0, −2, and −4, which were chosen based on previous experiments on the larger particle size fraction (Figure 2B).

The calculated absorption spectra show one absorption band at 293 nm for the neutral structure (Figure 3A), which is in very good agreement with the absorption peak at 277 nm for the experimental spectra of small Au NCs (Figure 2C). Further, the experimentally observed increase in the absorption with increasing negative charge (or increasing degree of deprotonation) is well reproduced by the model system. While we found a blueshift of up to 10 nm for the negatively charged structures with respect to the neutral structure, this blueshift was noticeably smaller than the one obtained with DFT. This could potentially be a result of the basis set choice, which is assumed to be sufficient for neutral systems. Comparatively, anions ideally require basis sets with diffuse basis functions according to the literature,[56] yet, no diffuse basis sets are currently available for spin–orbit calculations.

By analyzing the excited states with respect to their respective transition-dipole moments, we discovered that the 32nd excited state is strongly dominant for the neutral and twofold negatively charged structure. This dominant state corresponds to an exciton with dominant contributions from HOMO–2 and LUMO+2 (Table S1, Supporting Information). The varied intensity of the absorption peak from the 0 to −2 charge state can be tentatively explained by the observation that HOMO–2 and LUMO+2 tend to become more localized when the charges are added to the structure (Figures S9 and S10, Supporting Information). Furthermore, the much stronger increase of intensity when going from the −2 to −4 structures can be

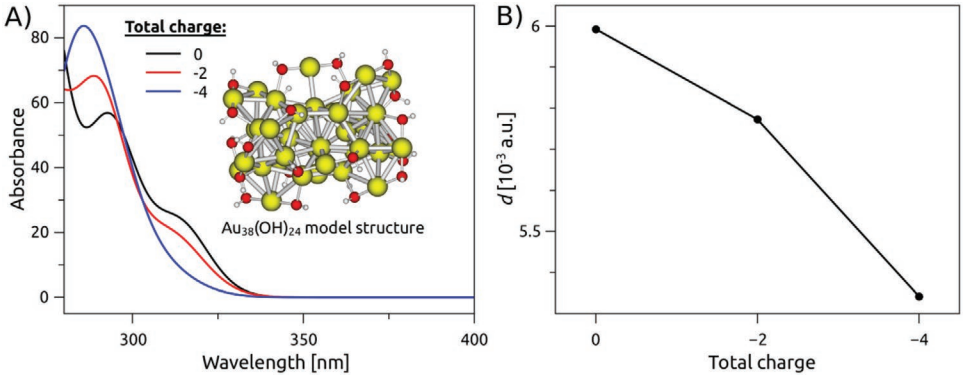

Figure 3. Calculated absorbance spectra depending on the degree of deprotonation (where we explicitly remove H^+ and thereby increase the size of negative total charges on the Au NC). A) Absorption spectrum calculated with SCIS and wB97X-D/dhf-SVP-2c/COSMO (water) employing a Gaussian broadening with a half width at half maximum of 120 meV. B) Transition-dipole moments of the lowest excitonic emitting state as a function of the total charge.

explained by the appearance of a second optical transition with large intensity for the −4 structure. This additional absorption peak mainly stems from a HOMO−2 → LUMO+1 excitation. When comparing the LUMO+2 with the LUMO+1, it can be deduced that both have very similar shapes in the −4 charged structures (see Figures S9 and S10 in the Supporting Information), which is then reflected in the emergence of a new bright HOMO−2 → LUMO+1 transition. The energetic difference between the transition energies of the two bright states in the −4 structure is only around 50 meV (see Table S1 in the Supporting Information) and cannot be resolved in Figure 3 due to the broadening.

Finally, the pH-dependent emission observed for the small Au NCs (Figure 2D) was approached by considering the lowest excited state as the emissive state, also known as Kasha's rule.[57] It should be noted that this is a rather rough assumption because the exact kinetics of the emission process requires the study of the excited-state dynamics in these systems, which is out of the scope of this work. In agreement with experiment, we find that the transition-dipole moments d (the intensity is proportional to d squared) is decreasing with increasing negative total charge (Figure 3B). In all cases, the lowest exciton state is dominated by the HOMO → LUMO single-particle states. By inspecting the shapes of the HOMO and LUMO (Figure S10 and S11, Supporting Information), it can be seen that when the negative charge is increased, the HOMO shows larger contributions from the deprotonated oxygen atoms on the surface, while the LUMO becomes more localized on the gold core. Consequently, the overlap of the HOMO–LUMO decreases, resulting in lower transition-dipole moments with respect to the charge.

Summarizing the experimental results in the surface anion adsorbate effects: the fully inorganic particles with a mean size of 1 and 2–2.5 nm react differently to altered surface charge densities. While both species show an increased absorbance behavior with increasing negative charges around 277 nm, an optical excitation at this wavelength leads to an increased emission intensity for the larger Au NCs, which cannot be observed for the smaller Au NCs. The latter, however, show a decrease of the emission intensity around 300 nm, verified by DFT and SCIS calculation (Figure 3B). For both sizes, the observed changes in the emission intensity are influenced by the increased surface charge density (with opposite trends for both size regimes) while no influence on the emission energy could be observed. It indicates that the gold (surface) lattice structure of the particles is not changed by the addition of inorganic additives.

However, irrespective of the surface charge density influence, the absorbance and emission behavior of the two studied size fractions (1 nm vs 2–2.5 nm) of totally inorganic Au NCs was fundamentally different. This could originate from I) a difference in the crystal structures, or II) a change in the quantization of energy states. A detailed investigation of these two effects in inorganic Au NCs as well as their interplay is documented in the following paragraphs.

2.2. Structural Resolution of Larger and Smaller NCs

To study the lattice structure of Au NCs, we utilized X-ray absorption spectroscopy (XAS), including X-ray absorption near edge structure (XANES) and extended X-ray absorption fine structure (EXAFS). The averaged gold valency can be deduced from the XANES spectrum (**Figure 4**A). While monovalent gold shows a spectrum very similar to metallic (fcc) gold, trivalent gold exhibits a marked difference with a distinct peak around 11.92 keV that can be modified by the amount of charge transfer when coordinated with chlorine, bromine, or water.[58] Fits of the XANES spectra for both size distributions (1 nm vs 2–2.5 nm) reveal that a fraction of 30–35% for <1 nm Au NCs and 20–30% for >1 nm may be oxidized. However, the portion of Au(I) could not be determined with sufficient accuracy due to the similarity of the spectrum to metallic gold. The atomic correlation as derived from EXAFS is surprisingly similar for both the NCs samples and metallic gold (Figure 4B). Therefore, we conclude that even the small-sized fraction shows an fcc-like local order seen at the expected atomic distances of 2.88 and 4.08 nm (Figure S17, Supporting Information). The correlation for larger distances is naturally dampened due to the finite size of the clusters and possibly some disorder.

The results also interestingly reveal that even the smaller Au NCs (consisting of about 40 gold atoms) exhibit a pronounced fcc-like structure similar to bulk gold, while the more

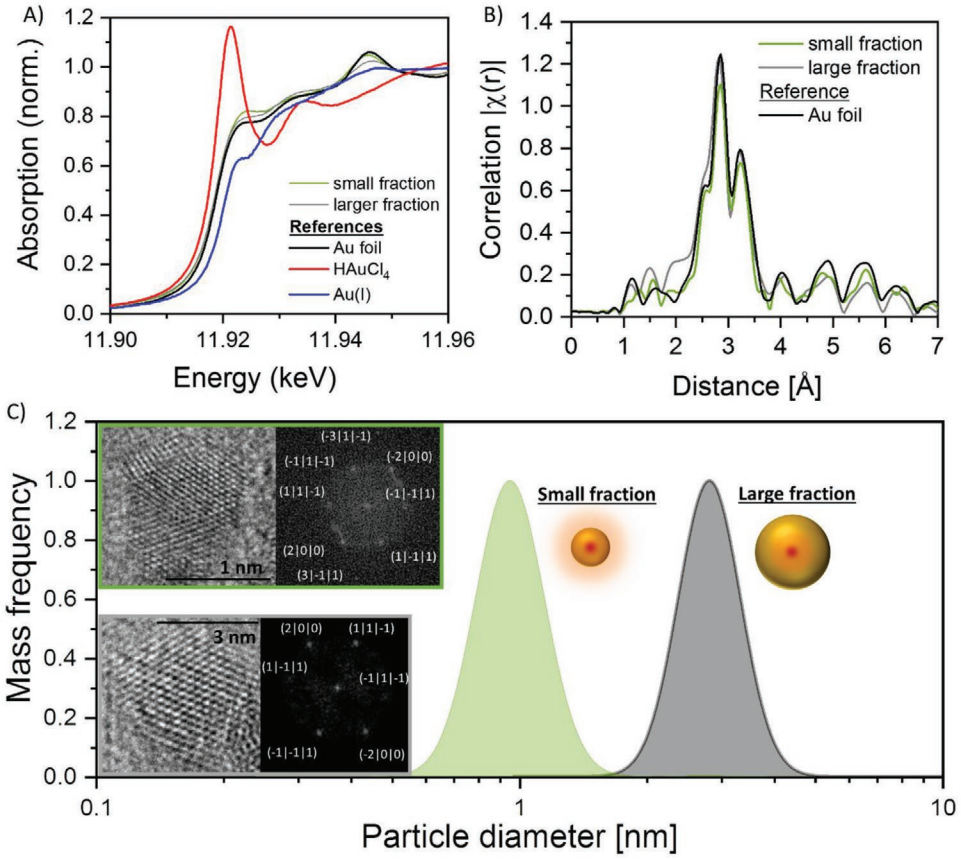

Figure 4. Structural characterization. A,B) Results from XAS measurements with: A) the XANES part around the L(III) absorption edge of both NC size fractions as well as references of a gold foil, aqueous $HAuCl_4$, and reduced Au(I) stabilized by CTAB and B) Fourier transform $\chi(r)$ of the cube weighted oscillation $\chi(k)$ extracted from the EXAFS signal for both size fractions as well as the gold foil. C) Ultracentrifuge-fractionated particle size distributions with HR-TEM images and Fourier transforms as inset. Both particles are in a [011] zone axis.

frequently discussed metal–organic compounds with thiolated ligands have very unique crystal structures.[59] Note that XAS is not a surface sensitive technique. In addition, surface defects could contribute to the optical properties of Au NCs and are expected as the laser-based synthesis technique involves an extremely fast cooling of the vaporized material and can freeze metastable crystal structures.[29,30] To probe more sensitively for potential surface defects, we performed high-resolution transmission electron microscopy (HR-TEM) measurements with consecutive image analysis. In accordance with the EXAFS, we found a global fcc-like structure (Figure 4B; Figure S17, Supporting Information). A more detailed examination of the HR-TEM images (Figure 4C; Figure S14, Supporting Information) reveals a more frequent occurrence of (3|1|1) crystal facets in the smaller Au NCs. This seems to indicate that the surface of the small-sized fraction Au NCs is more distorted and causes one crystal facet to preferentially adsorb on the TEM grid (statistic evaluation can be found in Figure S12 in the Supporting Information).

In the previous paragraphs, we concentrated on the observation of two Au NC colloids with clearly distinguishable, nonoverlapping particle size distributions. In the subsequent experiments, we used adapted particle size separation techniques to systematically elucidate whether there is a clear particle size effect on the optical properties of the fully inorganic Au NCs and whether we can use the findings to deduce a quantum-size effect.

2.3. Elucidation of Quantum-Size Effects in Fully Inorganic Colloidal Au NCs

We measured the emission of 17 different monodisperse, but not atomically precise, gold nanocluster colloids after excitation at 275 nm. A total of six different emission wavelengths were obtained (**Figure 5**A; Figures S15 and S16, Supporting Information), which varied in occurrence and intensities with particle size. The most frequently occurring emission peak was located between 350 and 400 nm, which can be observed for all particle sizes. An increased particle size resulted in a redshift of the measured emission. A comparable behavior of organometallic gold clusters was previously reported in the literature.[17,60] By reducing the number of atoms in precise clusters, the energy of the emission will increase, which can be explained by the decreasing particle volume, inducing a larger optical bandgap. Based on these findings, we conclude that the origin of this emission is probably related to the particle core. Besides, we measured the lifetime of 1.1 nm particles, which show a core emission around 340 nm (for

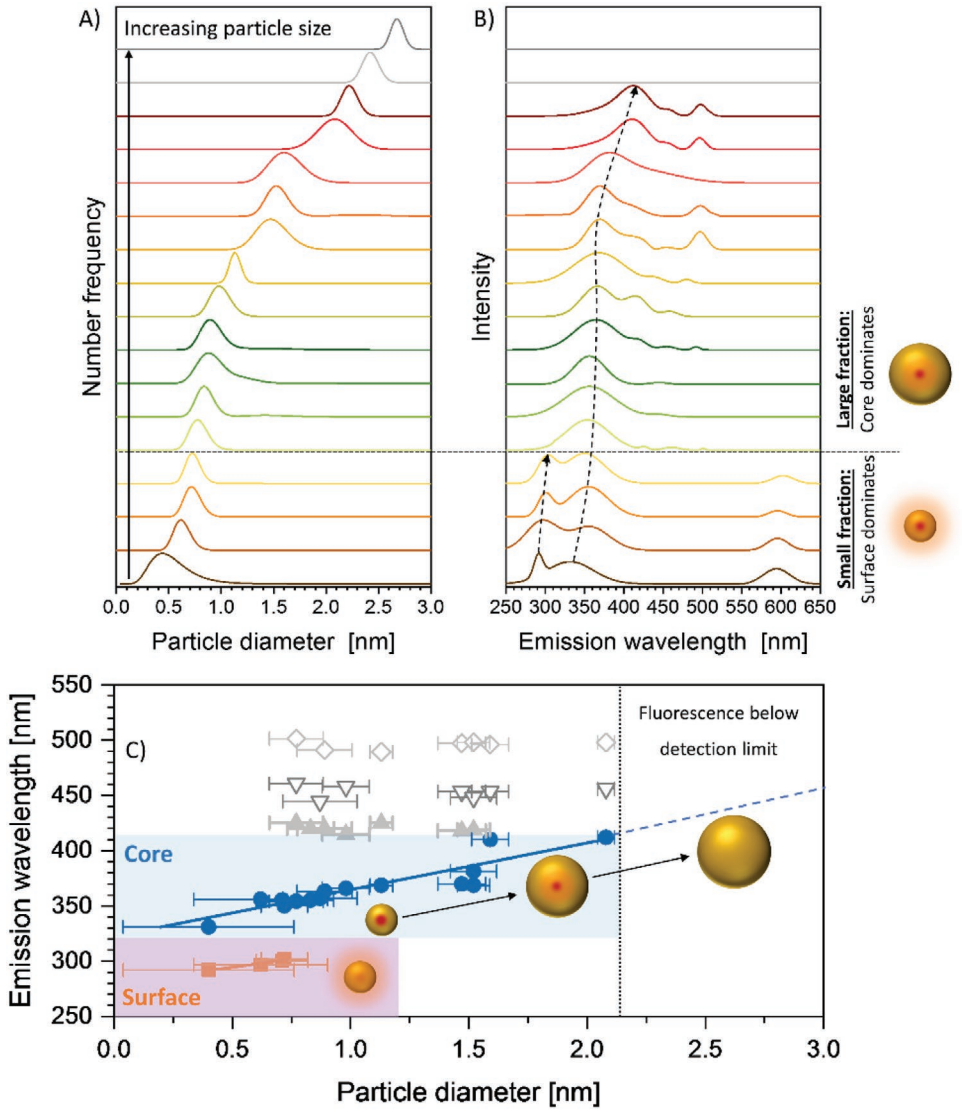

Figure 5. Particle surface and core contribution to the photoluminescence of fully inorganic Au NCs: A) Number-weighted size distribution of the investigated samples as obtained by AUC measurements. B) Emission spectra after excitation at 275 nm using the same color code as in (A). C) Position of the emission wavelength after excitation with 275 nm as function of mean particle diameter. The individual contribution of surface states (orange) and core states (blue) can be influenced by particle size. The additional emission wavelengths are indicated in gray.

further description, see Section SVI in the Supporting Information). The decay profiles (Figure S18C, Supporting Information) can be fitted with a triexponential decay, which gives lifetimes of 2.20 ± 0.01 ns (60.5%), 1.01 ± 0.01 ns (36.1%), and 0.09 ± 0.01 ns (3.4%). Such small lifetimes were expected as longer lifetimes primarily correlate with a ligand–metal charge transfer in ligand-capped Au NC systems.[38]

Further dominant emission peaks were found at 300 and 610 nm and were only visible for particles smaller than 1 nm (Figure 5B,C). The main characteristic of these smaller particles is that their specific surface area in the colloid was large. Basic calculations of these smaller particles, assuming sphericity, indicate that the majority of atoms are located at the interface to the dispersion medium. Based on these findings, we hypothesize that these emission features are connected to surface states and could be further linked to the occurrence of a structural surface deformation, as indicated by the HR-TEM measurements. It is well known that the presence of surface defects coincides with distinctive surface features, which can influence electron–phonon coupling and energy relaxation.[61] Such defects could be responsible for the occurrence or amplification of these surface state emission lines. As already mentioned, three other emission wavelengths (420, 450, and 490 nm) were detected, but only contribute significantly for particle diameters larger than 0.7 nm. The wavelength of these contributions showed no size dependence.

A compilation of all spectra can be found in Figure 4C, where only Au NCs in the size range 0.5–2.2 nm show emission, thus the occurrence and energies are dependent on the particle size. While core-emission was energetically sliced off, the surface emission possessed the largest bandgap, indicating a high-energy emission or small Stokes shift to the excitation.

3. Conclusion

Fully inorganic, colloidal NCs are an underexplored new class of nanomaterials that allow the investigation of surface charge effects on the optical properties, excluding ligand–metal charge transfer effects from organic molecules. Such inorganic Au NCs are accessible through pulsed laser fragmentation in liquids and size-controlled via fractionation procedures. They exhibit pronounced photoluminescence even in the absence of organic ligands with quantum yields comparable to those of their ligand-capped counterparts. Herein, we demonstrated that their emission behavior is size-dependent and dominated by core state emission for larger particles (2–2.5 nm) and by surface state emission for smaller particles (<1 nm). Within this fundamentally based study, we found that their emission intensity is a direct function of the surface charge density and is easily controllable by the pH of the surrounding medium. While the deprotonation of hydroxide groups on the larger NCs leads to an increase of the emission, the same leads to hardly any effect with the small particles' core emissions. However, we observe a small decrease of the more energy-rich surface emission. To explain this effect, we have performed supporting DFT simulations on an $Au_{38}(OH)_{24-x}(O)_x^{x-}$ model particle. The theoretical insight allows an explicit explanation of this observation. It shows that the HOMO is dominated by contributions from the deprotonated hydroxide at the particles surface, whereas the LUMO is localized closer to the particles' core. The overlap of both decreases, resulting in the lower experimentally observed surface emission intensity. These findings not only deepen our understanding of the origin of photoluminescence in Au NCs, but they also reveal that core state emission from metal atoms is a major contributor to the photoluminescence in Au NCs. The latter phenomenon has only been predicted by theory until now—this work experimentally verifies that an overlap with organometallic charge transfer bands in chemically generated NCs could be responsible for the photoluminescence. Hence, fully inorganic NCs are an excellent model to bridge the gap between theory and experiment. Furthermore, our results stress the importance of surface-dominated emission states, which emerge even in the absence of organic surface adsorbates and become particularly dominant for particles <1 nm. Another interesting finding is the direct correlation between surface charge density and photoluminescence intensity, as demonstrated by successive particle surface deprotonation. As the mechanism is based on anion adsorption, this phenomenon may be transferrable to the specific adsorption of ions, which is relevant for optical sensing. Furthermore, a suitable concentration technique, e.g., by adsorbing those particles on support materials could aid in harvesting their unique optical properties in different applications. One example is the field of scintillation, where the short emission lifetime of the cluster composed of a material with a large atomic number (gold atoms) makes them particularly attractive. In advanced medical imaging technologies, fast scintillators are required to achieve high-resolution imaging at the millimeter length scale.[62] This supporting procedure of inorganic Au NC also leads to excellent model material for heterogeneous catalysis, which benefits from the high specific surface area of the inorganic metal NC as well as from their high surface charge.[63] Synthesis of supported catalysts from laser-based synthesis routes was already demonstrated to be scalable to kilograms of catalysts for larger noble metal NPs[64] and transferability to Au NC with higher specific surface areas could be highly interesting. Note that surface charge tuning of ligand-free, laser-generated Au NCs has recently been demonstrated as an approach to understand the role of surface charge and size in heterogeneous catalysis of gold clusters supported on titania, evaluated for four different oxidation catalytic reactions.[41] Here, naked Au NCs are in general beneficial as no energy-intensive calcination to remove ligands is required, which could cause particle ripening and aggregation and impede catalytic activity.

4. Experimental Section

Synthesis: Laser-generated Au NPs with an average particle diameter of 53 nm were used as the educt of the fragmentation process. These particles were synthesized via laser ablation in liquids (LAL) following a protocol described in ref. [27]. In short, LAL was performed using a picosecond-pulsed Nd:YAG laser (Ekspla, Atlantic Series, 10 ps, 1064 nm, 8.8 mJ, 100 kHz, 10 min) in an ablation chamber filled with 30 mL deionized water and subsequent centrifugation (73 × *g*, 90 min), and then the colloidal particles were separated from the pellet. The gold concentration after centrifugation was 150 mg L^{-1} and was diluted to 7.5 mg L^{-1} for the fragmentation procedure. The LFL was conducted with a nanosecond laser (Innolas, Spitlight, 9 ns, 100 Hz, 84 mJ, 532 nm) in a free liquid jet reactor. The thickness of the fluid jet was 1.1 mm. The laser beam was focused by a cylindrical lens. LFL was conducted in front of the geometrical focus of the lens at a fluence of 1.5 J cm^{-2}. Each experiment included four irradiation cycles (passages).

Colloid Characterization: The NPs generated by LAL were analyzed by UV–vis extinction spectroscopy (Thermo Scientific, Evolution 201) and analytical disc centrifugation (ADC, CPS Instruments DC 24000, 24 000 rpm). The separation of the Au NCs from the remaining colloid after the fragmentation was done by ultrafiltration (1145 g, 20 min) at pH 9.5 (changed using NaOH) with centrifugal filters (Amicon Ultra, Z648000-8EA, 50 kDa). The resulting Au NCs were characterized by UV–vis extinction spectroscopy (Thermo Scientific, Evolution 201) and fluorescence spectroscopy (Varian Eclipse) at a constant mass concentration of dispersed Au NCs of 1.5 mg L^{-1}. The zeta potential was recorded with a Zetasizer (Malvern, Nano ZS) at different pH values (changed using NaOH or HCl). The surface charge density was evaluated from the zeta potential. Due to the low ionic strengths and small particle sizes, the Hückel model was used for the conversion of electrophoretic mobilities into zeta potentials.[65] The mass of the NCs was determined by inductively coupled plasma mass spectrometry (ICP-MS, Perkin Elmer Sciex - ELAN 6000). Their diameters and crystal structures were identified by TEM (Zeiss EM 910 and JEM 2200FS) by either measuring the particle size or performing a fast Fourier transformation. Additionally, AUC (Beckmann Coulter, optima XLI) was performed, which gave access to the hydrodynamic particle diameter. Measurements were performed in the sedimentation-velocity mode under centrifugal field conditions of 11 290 × *g*, 20 °C, and 100 scans were performed for each sample. To measure the molecular weight of the particles, nano-ESI was further conducted on a quadrupole time-of-flight mass spectrometer (micro-qTOF, Bruker-Daltonics, Bremen, Germany, mass resolution 10 000). The samples were recorded at a final concentration of ≈1 mg Au mL^{-1}. The samples were analyzed in positive and negative ion modes: each data point was the summation of spectra over 5 min. Interestingly, an ion signal was only observed in negative mode. External calibration was carried out with a set of synthetic peptides. The nano-ESI method considerably increased the signal intensity and yielded stable signals at 3 µL h^{-1}. The molecular weight

distribution was determined by a multiplicative correlation algorithm (MCA). The multiplicative correlation was designed to enhance the deconvoluted signal when the parent molecule was distributed into several charge states in the measured spectrum.[66] Molecular weight spectra were converted into particle diameter (nm) as described in the Supporting Information.

Quantum Yield Measurement: The QY of the NCs was measured following reported methodology[67] using an Agilent 8453 UV-visible Spectroscopy System and Horiba Fluorolog-3 instrument. Quinoline sulfate (in 0.1 M H_2SO_4) was chosen as the reference dye with a known QY of 0.54.

Computation Methodology: All ground-state calculations were carried out with the TURBOMOLE 7.3 program package.[68] The structure optimizations were carried out with a single-zeta basis set with polarization functions on all atoms, def2-SVP,[69] employing the Perdew–Burke–Ernzerhof generalized-gradient approximation (GGA) exchange-correlation functional,[70] the COSMO[51] with parameters for water (dielectric constant: 78.39; radius of solvent: 1.93 Å) to take into account the solvent effects at the single-particle level, using the m4 grid space option for integration. On top of the optimized structures, two-component calculations were carried out using the dhf-SVP-2c basis set[53,54] with corresponding relativistic effective core potentials for gold and the range-separated wB97X-D exchange–correlation functional.[50] On top of the two-component calculations, the excitonic states were calculated with the in-house implementation of SCIS, employing bulk screening with an approximate dielectric constant of 9.84 from ref. [71]. The frequency dependence of the dielectric constant (which also accounts for the size dependence) was neglected, employing 16 valence and 16 conduction states (a change of below 0.1 meV in the lowest excitonic state was considered as the convergence criterium for the CI space). It should be noted that such a highly approximate screening model might not be ideal, however, because only one gold nanocluster size was considered, the qualitative trends were expected to be stable with respect to that choice.

Time-Correlated Single-Photon Counting (TCSPC): TCSPC was used to record the time decay profiles. The setup for these measurements is shown in Figure S18 in the Supporting Information. The samples were excited after focusing the laser beam with a fused silica lens on a Suprasil quartz glass cuvette (Hellma Analytics, Germany). The excitation wavelength λ_{ex} = 254 nm was obtained from a frequency tripled titanium–sapphire laser (Tsunami, Spectra Physics Lasers Inc., USA) with a pulse width of 1.7 ps and a repetition rate of 80 MHz. A photodiode (PMA-200, PicoQuant, Germany) was used for the trigger signal. A bandpass filter (254/10 Metal-UV ET, AHF analysentechnik AG, Germany) was placed after the flexible harmonic generator (GWU2 23-PS, Spectra Physics Lasers Inc., United States) to ensure that only the tripled frequency (3ω) excites the AuNCs. Selection of the emission wavelength at λ_{em} = 340 nm was achieved by using a scanning monochromator with a 1200 g mm^{-1} grating blazed at 250 nm (2035, McPherson, USA). The monochromator was connected to a hybrid photomultiplier detector assembly (PMA hybrid series 06, PicoQuant, Germany), which is sensitive in the range of 220 to 650 nm. This detector was connected to a single-photon counting PCI express card (TimeHarp260P, PicoQuant, Germany) inside the PC setup. The resolution was 0.025 ns. The maximum laser power was 3.1 mW. An optical density filter, optimized for the UV-range, was used to reduce the power to around 0.3 mW. To analyze the obtained data, the software FluoFit (PicoQuant, Germany) was used. To consider the instrument response function (IRF), a numerical reconvolution algorithm was applied. The IRF (full width at half maximum: 92 ps) was recorded by using a diluted suspension of colloidal silica (Ludox, Sigma-Aldrich).

X-ray Absorption Spectroscopy (XAS): The colloids were adsorbed onto carbon (Vulcan, Cabot Corporation), dried, and pressed into pellets of 3 mm thickness. XAS was performed at the SUL-X beamline of the Karlsruhe Light Source. The X-ray beam around the Au-L(III) edge of about 1 mm × 1 mm size was measured in transmission by a pair of ionization chambers, and X-ray fluorescence emission was recorded on a multielement silicon drift detector (7 element SiriusSD, Rayspec with Falcon electronics, XIA). After standard corrections, both spectra matched well. The near-edge structure (XANES) provided information on the lowest unoccupied electronic states, as well as symmetry-related selection rules. Spectra were compared to reference compounds (gold foil, aqueous gold (III) chlorate $HAuCl_4$, and CTAB-bound monovalent gold, CTAB: cetyl triammoniumbromide), according to established procedures.[72] In the extended absorption spectrum (EXAFS), emitted electrons probed the next neighbors to reveal information on atomic correlations in the cluster using Fourier inversion as described in the Supporting Information.

Supporting Information

Supporting Information is available from the Wiley Online Library or from the author.

Acknowledgements

The authors gratefully acknowledge the Deutsche Forschungsgemeinschaft (DFG) for its financial support under Project Nos. BA 3580/22-1 and PA 794/28-1. B.G.-L. gratefully acknowledges the Bundesministerium für Bildung und Forschung (BMBF) for funding under project 05K19GU5. The authors also thank Jurij Jacobi and Dr. Marcus Heidelmann for their experimental support in producing the HR-TEM images.

Open access funding enabled and organized by Projekt DEAL.

Conflict of Interest

The authors declare no conflict of interest.

Data Availability Statement

The data that support the findings of this study are available from the corresponding author upon reasonable request.

Keywords

core effect, density functional theory, ligand-free Au nanoclusters, origin of Au nanocluster fluorescence, surface charge, surface effect, ultrasmall gold nanoparticles

Received: February 24, 2021
Revised: April 8, 2021
Published online: June 24, 2021

[1] I. Chakraborty, T. Pradeep, *Chem. Rev.* **2017**, *117*, 8208.
[2] R. Jin, C. Zeng, M. Zhou, Y. Chen, *Chem. Rev.* **2016**, *116*, 10346.
[3] T. Huang, R. W. Murray, *J. Phys. Chem. B* **2001**, *105*, 12498.
[4] H. Liu, G. Hong, Z. Luo, J. Chen, J. Chang, M. Gong, H. He, J. Yang, X. Yuan, L. Li, X. Mu, J. Wang, W. Mi, J. Luo, J. Xie, X.-D. Zhang, *Adv. Mater.* **2019**, *31*, 1901015.
[5] a) D. Shen, M. Henry, V. Trouillet, C. Comby-Zerbino, F. Bertorelle, L. Sancey, R. Antoine, J.-L. Coll, V. Josserand, X. Le Guével, *APL Mater.* **2017**, *5*, 053404; b) W.-F. Lai, W.-T. Wong, A. L. Rogach, *Adv. Mater.* **2020**, *32*, 1906872; c) C. N. Loynachan, A. P. Soleimany, J. S. Dudani, Y. Lin, A. Najer, A. Bekdemir, Q. Chen, S. N. Bhatia, M. M. Stevens, *Nat. Nanotechnol.* **2019**, *14*, 883.

[6] Y. Liu, K. Ai, X. Cheng, L. Huo, L. Lu, *Adv. Funct. Mater.* **2010**, *20*, 951.
[7] T. Higaki, Y. Li, S. Zhao, Q. Li, S. Li, X.-S. Du, S. Yang, J. Chai, R. Jin, *Angew. Chem., Int. Ed.* **2019**, *58*, 8291.
[8] M.-M. Shi, Di Bao, B.-R. Wulan, Y.-H. Li, Y.-F. Zhang, J.-M. Yan, Q. Jiang, *Adv. Mater.* **2017**, *29*, 1606550.
[9] a) N. A. Sakthivel, M. Shabaninezhad, L. Sementa, B. Yoon, M. Stener, R. L. Whetten, G. Ramakrishna, A. Fortunelli, U. Landman, A. Dass, *J. Am. Chem. Soc.* **2020**, *142*, 15799; b) H. Kawasaki, K. Hamaguchi, I. Osaka, R. Arakawa, *Adv. Funct. Mater.* **2011**, *21*, 3508.
[10] C. Helmbrecht, D. Lützenkirchen-Hecht, W. Frank, *Nanoscale* **2015**, *7*, 4978
[11] a) M. Eichelbaum, K. Rademann, A. Hoell, D. M. Tatchev, W. Weigel, R. Stößer, G. Pacchioni, *Nanotechnology* **2008**, *19*, 135701; b) X. Le Guével, B. Hötzer, G. Jung, K. Hollemeyer, V. Trouillet, M. Schneider, *J. Phys. Chem. C* **2011**, *115*, 10955; c) K. Lemke, C. Prietzel, J. Koetz, *J. Colloid Interface Sci.* **2013**, *394*, 141; d) F. Bertorelle, C. Moulin, A. Soleilhac, C. Comby-Zerbino, P. Dugourd, I. Russier-Antoine, P.-F. Brevet, R. Antoine, *ChemPhysChem* **2018**, *19*, 165.
[12] a) L. D'Souza, M. Noeske, R. M. Richards, U. Kortz, *J. Colloid Interface Sci.* **2013**, *394*, 157; b) M. Farrag, M. Tschurl, U. Heiz, *Chem. Mater.* **2013**, *25*, 862; c) K. Kimura, N. Sugimoto, S. Sato, H. Yao, Y. Negishi, T. Tsukuda, *J. Phys. Chem. C* **2009**, *113*, 14076; d) Y. Negishi, Y. Takasugi, S. Sato, H. Yao, K. Kimura, T. Tsukuda, *J. Am. Chem. Soc.* **2004**, *126*, 6518; e) J. Polte, X. Tuaev, M. Wuithschick, A. Fischer, A. F. Thuenemann, K. Rademann, R. Kraehnert, F. Emmerling, *ACS Nano* **2012**, *6*, 5791; f) H. Qian, M. Zhu, Z. Wu, R. Jin, *Acc. Chem. Res.* **2012**, *45*, 1470; g) X. Kang, H. Chong, M. Zhu, *Nanoscale* **2018**, *10*, 10758.
[13] a) S. Link, A. Beeby, S. FitzGerald, M. A. El-Sayed, T. G. Schaaff, R. L. Whetten, *J. Phys. Chem. B* **2002**, *106*, 3410; b) J. Zheng, P. R. Nicovich, R. M. Dickson, *Annu. Rev. Phys. Chem.* **2007**, *58*, 409.
[14] T.-Q. Yang, B. Peng, B.-Q. Shan, Y.-X. Zong, J.-G. Jiang, P. Wu, K. Zhang, *J. Nanomater.* **2020**, *10*, 261.
[15] Z. Wu, R. Jin, *Nano Lett.* **2010**, *10*, 2568.
[16] V. Bonačić-Koutecký, R. Antoine, *Nanoscale* **2019**, *11*, 12436.
[17] J. Zheng, C. Zhou, M. Yu, J. Liu, *Nanoscale* **2012**, *4*, 4073.
[18] J. Jiang, C. V. Conroy, M. M. Kvetny, G. J. Lake, J. W. Padelford, T. Ahuja, G. Wang, *J. Phys. Chem. C* **2014**, *118*, 20680.
[19] C. Zhou, C. Sun, M. Yu, Y. Qin, J. Wang, M. Kim, J. Zheng, *J. Phys. Chem. C* **2010**, *114*, 7727.
[20] S.-H. Cha, J.-U. Kim, K.-H. Kim, J.-C. Lee, *Chem. Mater.* **2007**, *19*, 6297.
[21] C. Zhou, J. Yu, Y. Qin, J. Zheng, *Nanoscale* **2012**, *4*, 4228.
[22] E. M. Goldys, M. A. Sobhan, *Adv. Funct. Mater.* **2012**, *22*, 1906.
[23] J. A. Lopez-Sanchez, N. Dimitratos, C. Hammond, G. L. Brett, L. Kesavan, S. White, P. Miedziak, R. Tiruvalam, R. L. Jenkins, A. F. Carley, D. Knight, C. J. Kiely, G. J. Hutchings, *Nat. Chem.* **2011**, *3*, 551.
[24] P. Londoño-Larrea, J. P. Vanegas, D. Cuaran-Acosta, E. Zaballos-García, J. Pérez-Prieto, *Chem. - Eur. J.* **2017**, *23*, 8137.
[25] J. M. J. Santillán, D. Muñetón Arboleda, D. Muraca, D. C. Schinca, L. B. Scaffardi, *Sci. Rep.* **2020**, *10*, 8217.
[26] J. M. J. Santillán, D. M. Arboleda, D. Muraca, D. C. Schinca, L. B. Scaffardi, *J. Nanotechnol. Nanomater.* **2020**, *1*, 65.
[27] A. R. Ziefuß, S. Reichenberger, C. Rehbock, I. Chakraborty, M. Gharib, W. J. Parak, S. Barcikowski, *J. Phys. Chem. C* **2018**, *122*, 22125.
[28] a) A. R. Ziefuß, S. Barcikowski, C. Rehbock, *Langmuir* **2019**, *35*, 6630; b) M. Lau, I. Haxhiaj, P. Wagener, R. Intartaglia, F. Brandi, J. Nakamura, S. Barcikowski, *Chem. Phys. Lett.* **2014**, *610–611*, 256.
[29] A. R. Ziefuss, S. Reich, S. Reichenberger, M. Levantino, A. Plech, *Phys. Chem. Chem. Phys.* **2020**, *22*, 4993.
[30] A. Kanitz, M.-R. Kalus, E. L. Gurevich, A. Ostendorf, S. Barcikowski, D. Amans, *Appl. Surf. Sci.* **2019**, *28*, 103001.
[31] a) L. Delfour, T. E. Itina, *J. Phys. Chem. C* **2015**, *119*, 13893; b) S. Hashimoto, D. Werner, T. Uwada, *J. Photochem. Photobiol., C* **2012**, *13*, 28; c) A. Pyatenko, M. Yamaguchi, M. Suzuki, *J. Phys. Chem. C* **2009**, *113*, 9078; d) K. Yamada, Y. Tokumoto, T. Nagata, F. Mafuné, *J. Phys. Chem. B* **2006**, *110*, 11751.
[32] F. Naz, V. Koul, A. Srivastava, Y. K. Gupta, A. K. Dinda, *J. Drug Targeting* **2016**, *24*, 720.
[33] M. Zhou, C. Zeng, Y. Chen, S. Zhao, M. Y. Sfeir, M. Zhu, R. Jin, *Nat. Commun.* **2016**, *7*, 13240.
[34] L. B. Scaffardi, J. O. Tocho, *Nanotechnology* **2006**, *17*, 1309.
[35] R. Jin, *Nanoscale* **2010**, *2*, 343.
[36] G. Schmid, B. Corain, *Eur. J. Inorg. Chem.* **2003**, *2003*, 3081.
[37] a) A. Mooradian, *Phys. Rev. Lett.* **1969**, *22*, 185; b) L. Shang, S. Brandholt, F. Stockmar, V. Trouillet, M. Bruns, G. U. Nienhaus, *Small* **2012**, *8*, 661.
[38] D. Bain, S. Maity, B. Paramanik, A. Patra, *ACS Sustainable Chem. Eng.* **2018**, *6*, 2334.
[39] V. Merk, C. Rehbock, F. Becker, U. Hagemann, H. Nienhaus, S. Barcikowski, *Langmuir* **2014**, *30*, 4213.
[40] J.-P. Sylvestre, A. V. Kabashin, E. Sacher, M. Meunier, J. H. T. Luong, *J. Am. Chem. Soc.* **2004**, *126*, 7176.
[41] A. R. Ziefuß, I. Haxhiaj, S. Müller, M. Gharib, O. Gridina, C. Rehbock, I. Chakraborty, B. Peng, M. Muhler, W. J. Parak, S. Barcikowski, S. Reichenberger, *J. Phys. Chem. C* **2020**, *124*, 20981.
[42] C. Pfeiffer, C. Rehbock, D. Hühn, C. Carrillo-Carrion, D. J. de Aberasturi, V. Merk, S. Barcikowski, W. J. Parak, *J. R. Soc., Interface* **2014**, *11*, 20130931.
[43] K. Makino, H. Ohshima, *Langmuir* **2010**, *26*, 18016.
[44] Y. Bao, C. Zhong, D. M. Vu, J. P. Temirov, R. B. Dyer, J. S. Martinez, *J. Phys. Chem. C* **2007**, *111*, 12194.
[45] a) A. Tahmasbi Rad, Y. Bao, H.-S. Jang, Y. Xia, H. Sharma, E. E. Dormidontova, J. Zhao, J. Arora, V. T. John, B. Z. Tang, T. Dainese, A. Hariri, J. V. Jokerst, F. Maran, M. Y. P. E. Nieh, *Adv. Funct. Mater.* **2021**, *31*, 2009750; b) M.-M. Zhang, K. Li, S.-Q. Zang, *Adv. Opt. Mater.* **2020**, *8*, 1902152.
[46] a) Y. Ling, J. J. Wu, Z. F. Gao, N. B. Li, H. Q. Luo, *J. Phys. Chem. C* **2015**, *119*, 27173; b) I. Díez, H. Jiang, R. H. A. Ras, *ChemPhysChem* **2010**, *11*, 3100.
[47] M. D. Scanlon, P. Peljo, M. A. Méndez, E. Smirnov, H. H. Girault, *Chem. Sci.* **2015**, *6*, 2705.
[48] E. Rosenkrantz, S. Arnon, *Opt. Lett.* **2010**, *35*, 1178.
[49] P. Avouris, B. N. J. Persson, *J. Phys. Chem.* **1984**, *88*, 837.
[50] J.-D. Chai, M. Head-Gordon, *Phys. Chem. Chem. Phys.* **2008**, *10*, 6615.
[51] A. Klamt, G. Schüürmann, *J. Chem. Soc.* **1993**, *2*, 799.
[52] a) A. Klamt, *J. Phys. Chem.* **1995**, *99*, 2224; b) A. Klamt, V. Jonas, *J. Chem. Phys.* **1996**, *105*, 9972.
[53] F. Weigend, A. Baldes, *J. Chem. Phys.* **2010**, *133*, 174102.
[54] D. Figgen, G. Rauhut, M. Dolg, H. Stoll, *Chem. Phys.* **2005**, *311*, 227.
[55] a) A. Franceschetti, H. Fu, L. W. Wang, A. Zunger, *Phys. Rev. B* **1999**, *60*, 1819; b) G. Bester, *J. Phys.: Condens. Mater.* **2009**, *21*, 023202.
[56] G. W. Spitznagel, T. Clark, J. Chandrasekhar, P. V. R. Schleyer, *J. Comput. Chem.* **1982**, *3*, 363.
[57] M. Kasha, *Discuss. Faraday Soc.* **1950**, *9*, 14.
[58] H. Duggal, P. Rajput, I. Alperovich, T. Asanova, D. Mehta, S. N. Jha, S. Gautam, *Vacuum* **2020**, *176*, 109294.
[59] M. Hesari, M. S. Workentin, Z. Ding, *ACS Nano* **2014**, *8*, 8543.
[60] J. Zheng, C. Zhang, R. M. Dickson, *Phys. Rev. Lett.* **2004**, *93*, 77402.
[61] P. Yu, X. Wen, Y.-R. Toh, X. Ma, J. Tang, *Part. Part. Syst. Charact.* **2015**, *32*, 142.
[62] R. M. Turtos, S. Gundacker, S. Omelkov, B. Mahler, A. H. Khan, J. Saaring, Z. Meng, A. Vasil'ev, C. Dujardin, M. Kirm, I. Moreels, E. Auffray, P. Lecoq, *npj 2D Mater. Appl.* **2019**, *3*, 37.

[63] S. Reichenberger, G. Marzun, M. Muhler, S. Barcikowski, *ChemCatChem* **2019**, *11*, 4489.
[64] S. Dittrich, S. Kohsakowski, B. Wittek, C. Hengst, B. Gökce, S. Barcikowski, S. Reichenberger, *Nanomaterials* **2020**, *10*, 1582.
[65] T. L. Doane, C.-H. Chuang, R. J. Hill, C. Burda, *Acc. Chem. Res.* **2012**, *45*, 317.
[66] M. Waszkielewicz, J. Olesiak-Banska, C. Comby-Zerbino, F. Bertorelle, X. Dagany, A. K. Bansal, M. T. Sajjad, I. D. W. Samuel, Z. Sanader, M. Rozycka, M. Wojtas, K. Matczyszyn, V. Bonacic-Koutecky, R. Antoine, A. Ozyhar, M. Samoc, *Nanoscale* **2018**, *10*, 11335.
[67] J. Hühn, C. Carrillo-Carrion, M. G. Soliman, C. Pfeiffer, D. Valdeperez, A. Masood, I. Chakraborty, L. Zhu, M. Gallego, Z. Yue, M. Carril, N. Feliu, A. Escudero, A. M. Alkilany, B. Pelaz, P. del Pino, W. J. Parak, *Chem. Mater.* **2017**, *29*, 399.
[68] TURBOMOLE V7.3 2018, a development of University of Karlsruhe and Forschungszentrum Karlsruhe GmbH, 1989–2007,TURBOMOLE GmbH, since 2007; available from https://www.turbomole.com (accessed: May 2021).
[69] a) D. Andrae, U. Huermann, M. Dolg, H. Stoll, H. Preu, *Theor. Chim. Acta* **1990**, *77*, 123; b) F. Weigend, R. Ahlrichs, *Phys. Chem. Chem. Phys.* **2005**, *7*, 3297.
[70] a) J. P. Perdew, K. Burke, M. Ernzerhof, *Phys. Rev. Lett.* **1996**, *77*, 3865; b) J. P. Perdew, Y. Wang, *Phys. Rev. B* **1992**, *45*, 13244; c) P. A. M. Dirac, *Proc. R. Soc. London, Ser. A* **1929**, *123*, 714; d) J. C. Slater, *Phys. Rev.* **1951**, *81*, 385.
[71] A. Derkachova, K. Kolwas, I. Demchenko, *Plasmonics* **2016**, *11*, 941.
[72] B. Abécassis, F. Testard, Q. Kong, B. Francois, O. Spalla, *Langmuir* **2010**, *26*, 13847.

3.3.2 Highly Fluorescent Surfactant-Free Gold Nanocluster with Efficient Photon Memory

Synopsis:

The previous chapter demonstrated that fully inorganic and ligand-free Au NCs are highly fluorescent. Larger and core-dominating NCs (> 1 nm) show a size-dependent specific emission around 350–400 nm, while smaller, surface-dominating nanoclusters (< 1 nm) exhibit an additional energy-rich emission state at around 300 nm. In both cases, the emission intensity is a function of the surface charge density. Thereby, the core emission of the larger-sized fraction increases with an increasing number of surface charges. The smaller-sized fraction does not show this behavior. Here we do not observe any differences at the core emission. We found the HOMO is dominated by contributions from the surface located deprotonated oxygen (which is responsible for the increased surface charge density). The lower observed surface emission intensity can be explained by an overlap of this HOMO with the LUMO which is primarly located at the particles core.

In the following, we employed systematic pump-probe emission spectroscopy to document a critical interdependence between irradiation intensity and changes in surface-based fluorescence emission intensity. A detailed understanding of this correlation is vital for the potential application of these fully inorganic clusters in imaging. We associate the occurring changes in intensity to a photo-induced re-structuring of the surface atoms.

Highly Fluorescent Surfactant-Free Gold Nanocluster with Efficient Photon-Density Memory *(unpublished results)*

Anna. R. Ziefuss[1], Melissa Teubner[2], Christoph Rehbock[1], Michael Rübhausen[2], Wolfgang J. Parak[3], Stephan Barcikowski[1]*

[1] Technical chemistry I and Center for Nanointegration Duisburg-Essen (CENIDE), Unibversity Duisburg-Essen 45141 Essen, Germany

[2] Institue for applied physics, University Hamburg, Jungiusstraße 9, D-20355 Hamburg, Germany
[3] Department of physics and chemistry, University Hamburg, Hamburg, Germany

Gold nanocluster (Au NCs) tend to show quantum size effects with properties connected to a molecule-like behavior rather than bulk properties.[1,2] Especially, their optical properties make them interesting for a broad research area not only related to applications like optical sensing[3] and catalysis[4] but also fundamentally[1,5]. One of the most frequently asked fundamental questions concerns the origin of the fluorescence. Is the fluorescence a core effect of the particle itself, or is it caused by ligand-metal-charge transfer? So far, the evidence for the fluorescence origin was only indirect as typical synthesis routes required organic molecules known to contribute to the emission via HOMO-LUMO interactions.[6] Until now, techniques such as ligand exchange[5,7] and surface[8] or kernel[9] alloying have been used to alter the ligand's capability of donating charges or the electropositivity of the metal-core. While the role of ligands in the fluorescence of NCs has been widely studied, there is limited experimental work in the literature on the role of the NC core in photoluminescence phenomena. In 2019 Li et al.[10] were able to demonstrate a major contribution of the Au(0) core HOMO-LUMO transition, however, a comprehensive mechanistic understanding of the general fluorescence origin is still hampered by the available synthesis routes, which are limited to metal-organic compounds.

In our working group[6], we have recently succeeded in producing colloidal NC in high purity without the use of organic components. This has been achieved by employing pulsed laser fragmentation in liquids, which consists essentially of the re-irradiation of larger nanometer-sized particles present in water with high-intensity laser pulses. A precise description of this process can be found elsewhere.[11,12] The mechanism is proposed to be a phase explosion of larger Au particles followed by rapid cooling of produced smaller particles in the colloidal nano environment. To suppress particle growth sufficiently, we used ionic additives acting as an electrostatic stabilizer of the colloidal NCs.[13] In our previous study on fully inorganic Au NCs[6], we suspected a surface deformation in smaller Au NCs (< 1 nm) while larger (~2 nm), core-dominated particles were subject to secondary particle nucleation[12]. We found special optical features for both particle sizes (surface dominating Au NCs and their larger counterparts).[6] We discussed further that in all cases the emission was most pronounced after excitation in the ultra-violet (250 nm). The emission of the surface state in the surface dominating particles appeared to be linked to an energy-rich emission (~300 nm) while the emission of the larger and thus core-dominating particles seems to be in the range of 400-500 nm, and showed thus a large Stokes-shift with

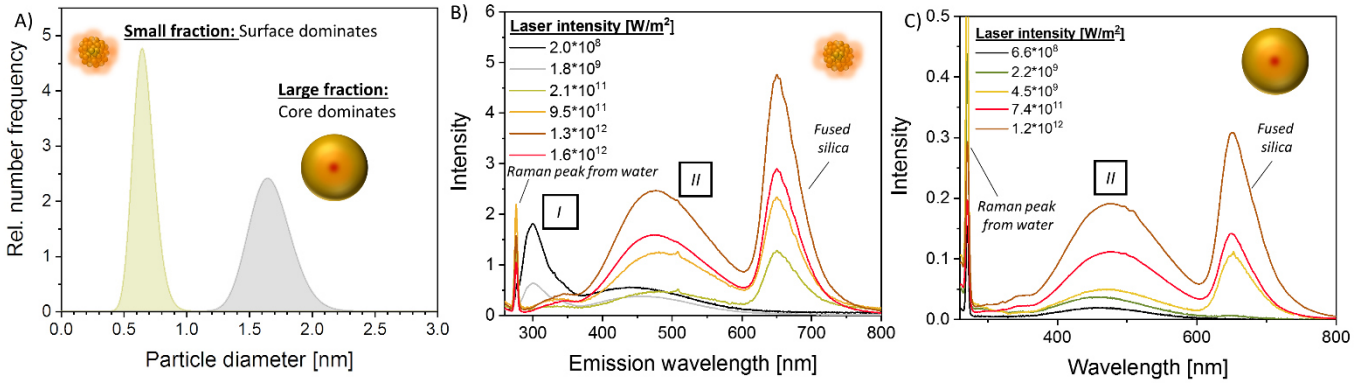

Figure 1: *Size-distribution of laser-generated surfactant-free gold nanocluster determined with analytical ultracentrifugation (AUC) (A) and pump-power dependent emission spectra of surface dominating, smaller AuNCs (B) and core dominating, larger spheres (C). Surface emission states are marked with (I) and core-states are marked with (II).*

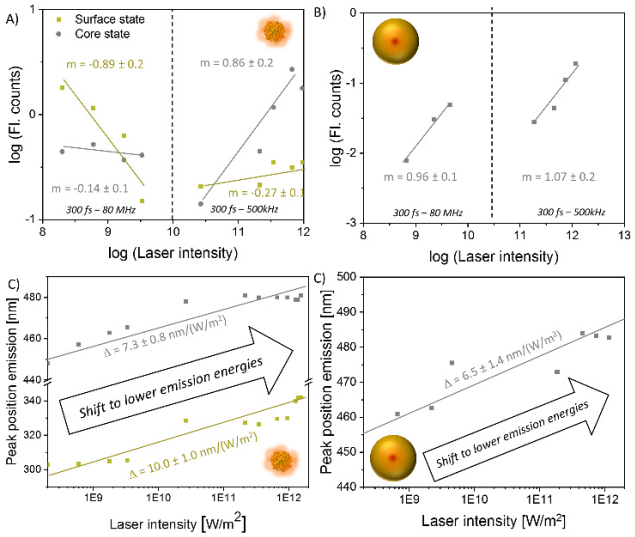

Figure 2: *Emission behavior after excitation with 250 nm and increasing pump energy. Laser-intensity dependency of surface dominating (A) and core-dominating surfactant-free AuNCs and position of the emission wavelength in C) for the smaller size fraction and D) for larger AuNCs.*

respect to the excitation wavelength. The surface-dominant properties were not observed for this larger size fraction which we referred to the surface constitution and the lower abundance of surface atoms, however, low-intensity core emission has been detected for particles < 1 nm as well.[6] From a thermodynamic point of view, it can be expected that surface atoms in a gold nanocluster formed by a rapid cooling process far from thermodynamic equillibrium are rich in defects and these defects could be prone to photo-induced re-crystallization. Consequently, a detailed pump-power-dependent emission study was conducted to examine this hypothesis experimentally. Furthermore, the implications of a photo-induced re-structuring and hence a change in correlated optical properties is critical for the utilization of Au NC in imaging. Here it is necessary to establish irradiation parameters suitable for stable emission properties. In this context, we have synthesized Au NCs < 1 nm and Au NCs > 1 nm (Fig. 1A) and investigated their emission behavior after excitation at 250 nm using different pump laser intensities. Furthermore, the present research aims to understand the photostability of surface and core emission to get an in-depth understanding of both emission states. The emission spectra of the surface dominating Au NCs using low pump intensities $2.0*10^8$ W/m^2 match well with our previous report (Fig. 1B) and show a dominating emission at ~300 nm coupled with a second emission located at ~460 nm. All measurements conducted with different laser intensities were performed using a fresh sample aliquot as we wanted to avoid cross-effects from previous irradiations. Increasing the intensity of the excitation source to $2.1*10^{11}$ W/m^2 leads to a decrease in the surface-emission state without any observable effect on the emission intensity of the particle core. On the one hand, this implies a change of the surface, but on the other hand, it confirms the existence of two distinguishable emission states. A further increase of the laser intensity increases the core emission intensity while the surface-emission intensity stabilizes at a value close to zero. Here we can identify two distinctively different processes occurring at low fluence, where emissions from surface states continuously decrease and a second regime at higher intensity, where we observe an increase in the core emission intensity and a fully quenched surface state.

The pump-power dependent emission behavior of Au NCs > 1 nm is comparable to the behavior of core emission in the smaller fractions; however, the surface-emission is missing, and we observe an influence of the laser intensity on the core emission instead even at low pump intensities (Fig.1 C). The extracted information on the emission behavior after pumping with different laser intensities can be found in a double logarithmic manner in Fig. 2A and B. The core-emission shows predominantly a slope of ~1 indicating a one-photon excited emission. This emission behavior of ligand-free Au NC is more related to quantum dots rather than metal-organic compound NC as the latter, in this size range, are known to possess a distinctive two-photon cross-section.[14]

Conspicuous and highly interesting, however, is the pump-power emission behavior of the surface-emission at lower laser intensities (Fig. 2A) which follows a slope of ~ (-1). Therefore, the portion of photons re-emitted as radiation is reduced and an energy transfer due to non-radiative processes becomes more pronounced. This can be either explained by I) The higher amount of excited electrons, which would lead to a stronger electron-electron interaction and hence more non-radiative energy transfer or II) by a transfer of photon energy into the particle, inducing a photo-induced re-structuring. This transformation occurs slowly, with increasing laser intensity, and is irreversible at any time (Fig. S2). The Au NCs < 1 nm, thus, seems to have a photon density memory, which basically excludes mechanism I and makes a structural change in the clusters, for example, a change in the surface defect structure more probable, so that we can conclude that laser-generated surface-dominating surfactant-free AuNCs can be described as a photon counter. Meanwhile, the corresponding core emission of surface

dominating particles at low laser intensities stays unchanged, which additionally demonstrates that absorbed photons are primarily used to re-structure the crystal structure of the nanoclusters. The threshold fluence needed for full re-crystallization is in the order of 10^{10} W/m^2. We cannot further detect the surface state emission for higher laser intensities and only obtain a pump-power dependent emission with a slope of ~ 1 from the core.

Next to the behavior of the pump-power-dependent emission intensity, we observe a shift of the emission wavelength to smaller emission energies for both particle sizes and for both emission states (Fig. 2C and D), which is also permanent as long as we perform further excitation with lower laser energies. The photon memory is thus also noticeable by the energy of the emitted photons and not only by the emission intensity/quantum yield. A change of the core emission energy while maintaining the chemistry of the colloidal environment is so far known to correlate with a change of the NCs size[6]. Measurements of the particle size after excitation with the highest laser intensity confirm this for the core dominating particles (Fig. S1B); however, in the case of the surface dominating NCs, the pump-power dependent emission is not accompanied by a change of the NCs size (Fig. S1A). We believe that especially the change of the surface will lead to a change of the interaction between metal-surface and metal-core (MMCT), resulting in lower emission energies, a factor that has already been discussed for AuNCs with organic surface ligands.[1]

In summary, our results have shown that surface dominating and core dominating surfactant-free laser-generated AuNCs show a photon memory in terms of pronounced phonon counter ability, although their optical behavior is distinguishable. Surface dominating AuNCs < 1 nm show a negative slope of the pump power-dependent surface-emission below a threshold laser intensity of 10^{10} W/m^2, which is permanent and could correlate with a relaxation of the distorted fcc surface lattice. Although the particle size did not change, we observed a change of the emission position for both – surface and core state further in the visible range. Therefore, we consider this kind of new matter as highly interesting for a broad community.

Supporting Information Available: Experimental procedure, Size distributions before and after laser excitation.

References

[1] I. Chakraborty, T. Pradeep, *Chemical reviews* **2017**, *117*, 8208.

[2] a) R. Jin, C. Zeng, M. Zhou, Y. Chen, *Chemical reviews* **2016**, *116*, 10346; b) Y. Zhang, C. Zhang, C. Xu, X. Wang, C. Liu, G. I. N. Waterhouse, Y. Wang, H. Yin, *Talanta* **2019**, *200*, 432.

[3] Y. Liu in *Springer Theses, Recognizing Outstanding Ph.D. Research* (Ed.: Y. Liu), Springer Singapore, Singapore, **2018**, pp. 51–64.

[4] a) Z. Wu, S. H. Overbury (Eds.) *Catalysis by materials with well-defined structures*, Elsevier Academic Press, Amsterdam, **2015**; b) Y. Chen, G. Li, H. Qian, R. Jin in *Catalysis by materials with well-defined structures* (Eds.: Z. Wu, S. H. Overbury), Elsevier Academic Press, Amsterdam, **2015**, pp. 239–262; c) T. Higaki, Y. Li, S. Zhao, Q. Li, S. Li, X.-S. Du, S. Yang, J. Chai, R. Jin, *Angewandte Chemie (International ed. in English)* **2019**, *58*, 8291.

[5] Z. Wu, R. Jin, *Nano letters* **2010**, *10*, 2568.

[6] A. R. Ziefuss, M. Teubner, C. Rehbock, C. Zerbino, D. Amans, M.Rübhausen, I. Chakraborty, W. J. Parak, S. Barcikowski, Photoluminescence of fully inorganic colloidal gold nanocluster and their manipulation using surface charge effects. (unpublished), **2020**.

[7] S.-H. Cha, J.-U. Kim, K.-H. Kim, J.-C. Lee, *Chem. Mater.* **2007**, *19*, 6297.

[8] a) Z. Gan, J. Chen, L. Liao, H. Zhang, Z. Wu, *The journal of physical chemistry letters* **2018**, *9*, 204; b) R. Kazan, U. Müller, T. Bürgi, *Nanoscale* **2019**, *11*, 2938.

[9] X. Kang, M. Zhu, *Chemical Society reviews* **2019**, *48*, 2422.

[10] Q. Li, M. Zhou, W. Y. So, J. Huang, M. Li, D. R. Kauffman, M. Cotlet, T. Higaki, L. A. Peteanu, Z. Shao et al., *Journal of the American Chemical Society* **2019**, *141*, 5314.

[11] a) A. R. Ziefuß, S. Reichenberger, C. Rehbock, I. Chakraborty, M. Gharib, W. J. Parak, S. Barcikowski, *J. Phys. Chem. C* **2018**, *122*, 22125; b) A. R. Ziefuss, S. Reich, S. Reichenberger, M. Levantino, A. Plech, *Physical chemistry chemical physics : PCCP* **2020**, *22*, 4993.

[12] A. R. Ziefuß, S. Barcikowski, C. Rehbock, *Langmuir : the ACS journal of surfaces and colloids* **2019**, *35*, 6630.

[13] a) *IEEE J. Select. Topics Quantum Electron.* **2014**, *20*, 45; b) J. I. Gonzalez, T.-H. Lee, M. D. Barnes, Y. Antoku, R. M. Dickson, *Physical review letters* **2004**, *93*, 147402; c) P. N. Day, K. A. Nguyen, R. Pachter, *Journal of chemical theory and computation* **2008**, *4*, 1094; d) R. Khandelia, S. Bhandari, U. N. Pan, S. S. Ghosh, A. Chattopadhyay, *Small (Weinheim an der Bergstrasse, Germany)* **2015**, *11*, 4075.

3.3.3 How the charging effects through ligand-metal charge transfer processes influence the photoluminescence of fully inorganic gold nanoclusters

Synopsis:

Despite the considerable theoretical and experimental work on the photoluminescence properties of NCs carried out to date, a fundamental understanding of the origin of their optical properties is still lacking. This is predominantly attributed to the fact that particle oxidation and ligand coverage cannot be altered independently up to now, as oxidized gold clusters are primarily available with thiolated ligands. Of course, the ligands can be exchanged, but these processes are only partially successful[1,2] and can force either etching[2] or aggregation[3] of the NCs.

In this thesis (chapter 5.3.1), totally inorganic colloidal Au NCs were synthesized for the first time, and it was found that the emission intensity is a function of the surface charge density. Thus, an ion-metal charge transfer process could be elucidated as an effector of the NC's emission. Besides, those inorganic NC serve as ideal reference materials to systematically evaluate charge transfer effects from organic ligands as the consideration does not require exchange reactions.

Therefore, the present chapter aims to study the interactions of organic surface ligands with the inorganic colloidal Au NCs. Here, one approach entails a systematic variation of the ligand's anchor group directly bound to the particle surface (amine and thiolated carboxylic acids), which may transfer charge density directly to the NC's core, possibly resulting in an altered emission behavior. A second approach addresses a systematic variation of head groups, where electron acceptor or donor moieties may indirectly influence charge density and hence the NC's' optical properties.

References

(1) Smith, A. M.; Marbella, L. E.; Johnston, K. A.; Hartmann, M. J.; Crawford, S. E.; Kozycz, L. M.; Seferos, D. S.; Millstone, J. E. Quantitative analysis of thiolated ligand exchange on gold nanoparticles monitored by 1H NMR spectroscopy. *Analytical chemistry* **2015**, *87* (5), 2771–2778. DOI: 10.1021/ac504081k. Published Online: Feb. 6, 2015.

(2) Zhou, S.; Huo, D.; Goines, S.; Yang, T.-H.; Lyu, Z.; Zhao, M.; Gilroy, K. D.; Wu, Y.; Hood, Z. D.; Xie, M.; Xia, Y. Enabling Complete Ligand Exchange on the Surface of Gold Nanocrystals through the Deposition and Then Etching of Silver. *Journal of the American Chemical Society* **2018**, *140* (38), 11898–11901. DOI: 10.1021/jacs.8b06464.

(3) Viudez, A. J.; Madueño, R.; Pineda, T.; Blázquez, M. Stabilization of gold nanoparticles by 6-mercaptopurine monolayers. Effects of the solvent properties. *The journal of physical chemistry. B* **2006**, *110* (36), 17840–17847. DOI: 10.1021/jp062165l.

How the charging effects through ligand-metal charge transfer processes influence the photoluminescence of fully inorganic gold nanoclusters

(unpublished results)

Anna. R. Ziefuss[1], Christoph Rehbock[1], I. Chakraborty[2], Wolfgang J. Parak[2], Stephan Barcikowski[1]*

1 Technical chemistry I and Center for Nanointegration Duisburg-Essen (CENIDE), Unibversity Duisburg-Essen 45141 Essen, Germany

[2] Department of physics and chemistry, University Hamburg, Hamburg, Germany

While metallic nanoparticles (NPs) are known for their surface plasmon resonance, non-metallic nanoclusters (NCs) < 2.3 nm lack this feature and show, instead, a pronounced fluorescence.[1] The origin of this fluorescence and the influence of surface ligands is yet not fully understood.[2] The mechanistic elucidation becomes complicated because almost all observations and results concerning the fluorescence of nanoclusters were gathered for wet-chemical synthesized Au NCs, which i) differ in their geometry[1,2], ii) their oxidation state[2,3], and iii) are (electro-) sterically stabilized by organic ligands[2–4], dependent on the synthesis route. However, all these factors can influence the electronic density of the particles' core and surface, which directly correlates with the observed emission behavior.[3,5–9]

If the influence of organic ligands on the emission is to be considered, this requires a ligand exchange in any case since typical synthesis routes always lead to organo-metallic compounds instead of pure NC.[10–13] In most cases, ligand exchange on NPs is only partially successful[14,15] and, dependent on the types of ligands, an exchange can lead to altered particle sizes by either etching[15] or aggregation[16]. Despite these problems, the role of organic ligands on the NC fluorescence has been studied by many groups[1–4,17] and the findings remain diverse as a multitude of electronic processes seem to be involved. Yet, the following two influence factors for

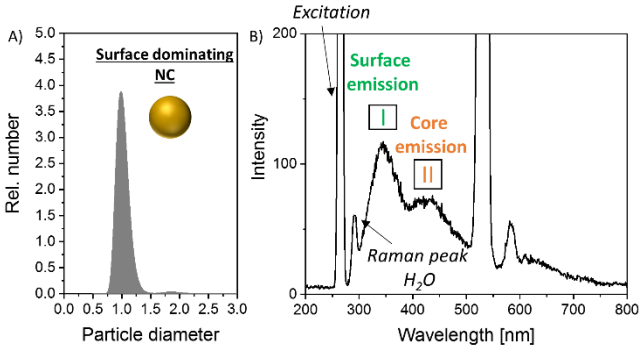

Figure 1: *Particle size (A) and optical properties after excitation at 275 nm of fully inorganic Au NCs.*

surface ligands on the emission intensity behavior of Au NCs are widely accepted in the literature:[3,9,18]

i) **Influence of the anchor group** (pointing towards NC): charge transfer from the ligand anchor group (e.g. Au-S) to the metal core (LMCT)[3]

ii) **Influence of the head group** (pointing towards the solution): Contribution of electron-rich ligand groups or atoms by donation of delocalized electrons (Increased capability of the ligands to donate charge density to the NCs)[3].

In both cases, a drastic increase of the fluorescence quantum yield (QY) can be observed, which is referable

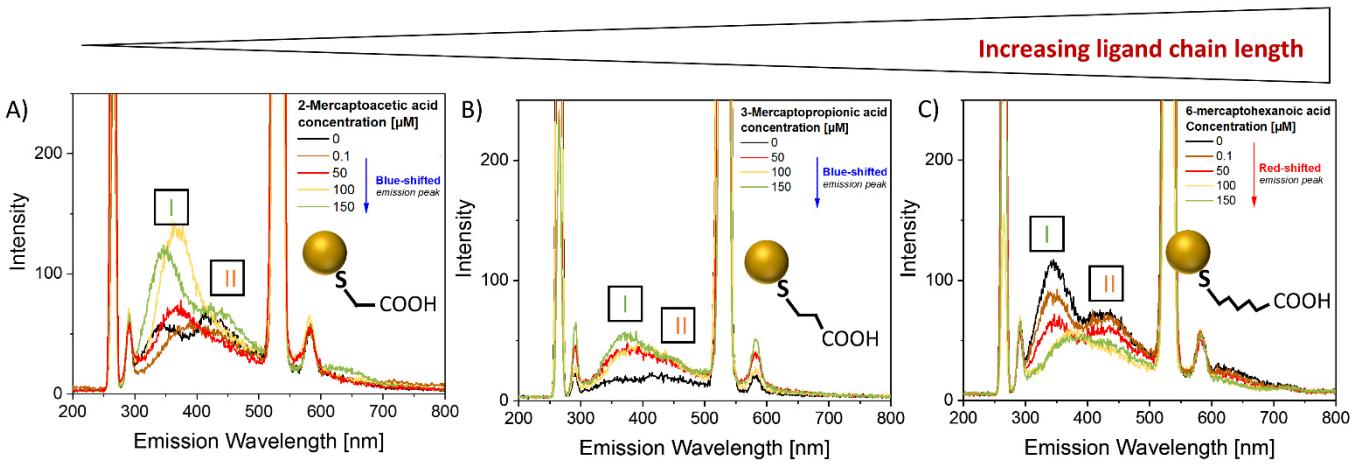

Figure 2: *Emission behavior of fully inorganic Au NCs (excitation at 275 nm) after the addition of different kind of carboxylic acids with the same anchor group (S) and different carbon chain length A) 2-Mercaptoacetic acid, B) 3-Mercaptopropionic acid, C) 6-Mercaptohexanoic acid. All ligands are added in different concentrations from 0.1 – 150 µM.*

to an increased probability of photon emission by reducing the number of non-radiative transitions [3,18] Changes of the latter are often attributed to a change in the particle size[19] or crystal structure[18] which both leads to altered energy levels. Zheng et al.[19] found that the energy of an emitted photon is a function of particle size and increases with an increasing number of atoms within the NCs. Wu et al.[20] reported on the reversible structural transformation of fcc to non-fcc NCs and found a pronounced, red-shifted emission. However, the transformation from fcc to non-fcc NCs required a ligand exchange, making it difficult to differentiate between charging and structural influence factors. Indeed, charging the surface goes along with a partially positive NC surface, as electron density is shifted to the particle's interior.[21] Aparticle engineering required a ligand exchange in all cases, it has been difficult to distinguish between surface and core emission yet. Recently, Ziefuß et al.[22] were able to synthesize fully inorganic colloidal Au NCs (size distribution can be found in Fig. 1A) and found an individual contribution from the NC's core (II) and surface (I) on the emission behavior after excitation at 275 nm (Fig. 1B). This new kind of matter allows a systematic study of LMCT processes without the need of ligand exchange, as the particles are initially free of organic ligands. Further, the emission of the core (~400 nm) and the surface (~350 nm) can be analyzed independently, making this kind of matter to an interesting model material for LMCT process elucidation in Au NCs.

Within this study, we investigate the influence of the ligand anchor and head group on the emission intensity and emission energy of fully inorganic NC (Fig. 1), while adding carboxylic thiolated (Fig. 2) or aminated ligands (Fig. 3) with chain lengths from 2-6 carbon atoms under

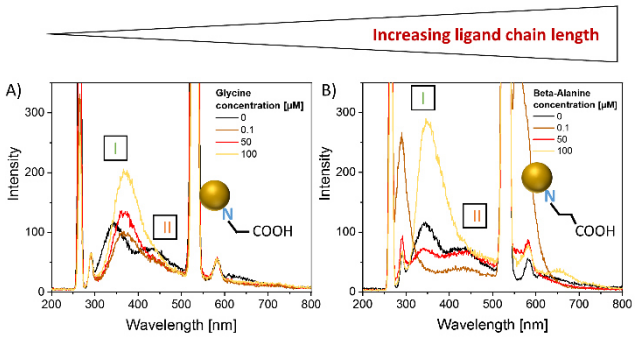

Figure 3: *Emission behavior of fully inorganic Au NCs (excitation at 75 nm) after the addition of different kind of carboxylic acids with the same anchor group (N) and different carbon chain length A) Glycine, B) Beta-Alanine*

variation of the ligand concentration. Following Fig. 2

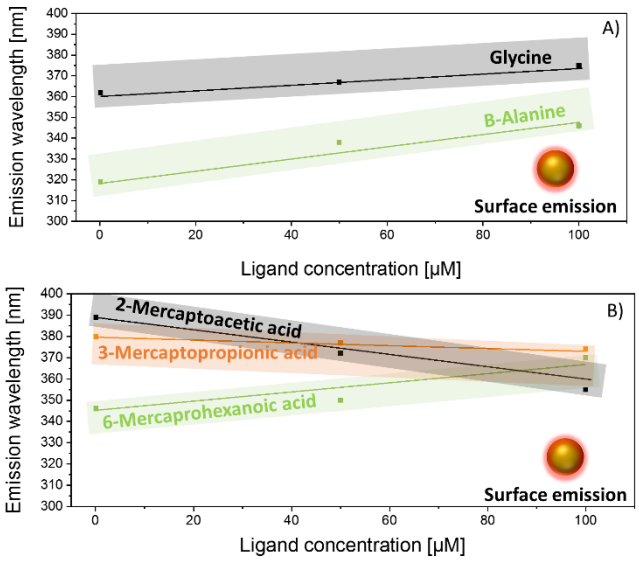

Figure 4: *Summary of the emission wavelength position in dependence of the carboxylic ligand concentration. A) Aminated ligands, B) Thiolated ligands.*

and 3, the addition of the different ligands greatly affects the emission behavior. It seems that core and surface emission merge into one peak (at around 400 nm) with increasing ligand concentration. This is highly interesting and could possibly explain why it was not possible so far to detect the two separate emission peaks attributed to the metallic nanocluster alone, which were previously differentiated into a metal core and metal surface emission. However, it also complicates the optical detection of charging effects through LMCT processes in this study as it is not clear if the peak fusion is based on a broader surface-emission peak accompanied by a decrease or blue-shifted core-emission or even the other way around. Nevertheless, it is intuitive that the surface reacts more sensitive to external charging effects so that we assume in the following that the addition of ligands will lead to a quenching of the core emission, which goes along with the fact that the remaining pronounced emission peak belongs to the surface emission. In a later step, we will look at the charge distributions in the particle and will be able to tighten the validity of this assumption.

To better illustrate the influence of ligands on the surface emission, we plotted the emission wavelength (Fig. 4) and intensity (Fig. S1) with increasing ligand concentration, and we found a nearly linear behavior. Note that we excluded the spectra bevor ligand addition (lowes ligand concentration amounts to 0.1 µM). The addition of 0.1 µM 2-Mercaptoacetic acid, for example, leads to a red-shifted emission, while with increasing ligand concentration, the peak shows a pronounced,

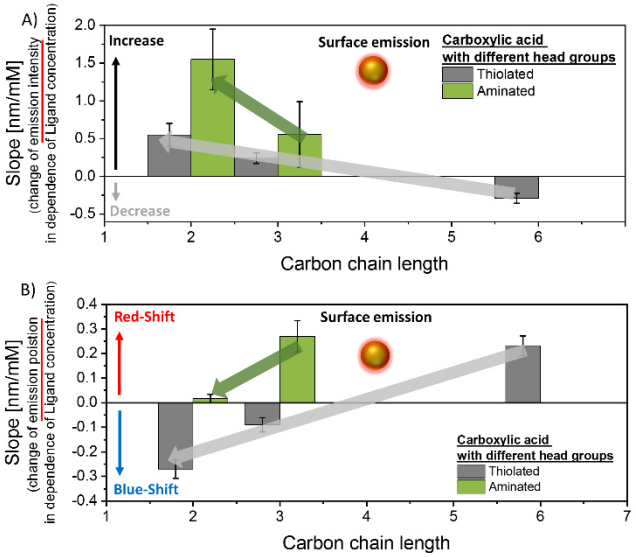

Figure 5: *Summary of emission Intensity (A) and position (B) after addition of different ligands. Both plots show the slope of the emission variation at different ligand concentration assuming linear behavior with the standard deviation plotted as error.*

blue-shifted emission. To further extract suitable trends in the emission behavior, we plotted the slope of the linear regression in Fig 4 (and Fig S1) with the standard deviation indicated as error (see Fig. 5). With this, the effect of the ligands in dependence of their carbon chain length on the surface emission becomes visible, and we observe (for ligands with both anchor groups) an elevated emission intensity with decreasing C content in the head group which is accompanied by a blue-shift of the emission wavelength (up to ~40 nm). A more detailed discussion on the effects caused by head and anchor groups is given in the consecutive paragraphs:

- **Influence of the ligand head group on the surface emission**

  For shorter chain lengths, the contribution of the carboxyl group increases, resulting in an increased electron density donation to the Au surface (directly or via the Au-S bond). The Au surface reacts with a shift of the electron density into the Au core, which results in a partially positive particle surface and a partially negative particle core.[21] As the electronic density on the surface is reduced, an increase of the emission intensity and hence the quantum yield is to be expected as non-radiative processes are reduced. This is observable by an increased emission intensity in Fig. 5A. Note that the core emission should react with a decreased emission, as the amount of non-radiative processes should be increased, a fact that strengthens the previously made assumption that the core emission disappears and become negligible in the presence of electron-donating ligands.

Additionally, this ligand-forced charge injection into the NC core will influence the surface potential of the Au NCs and thus the position of the Fermi level [21] so we have to ask the question to what extent this effect can have an impact on energy levels and thus influence the emitted energy. The charge injection should lead to an energetic lowering of the ground state so that even with an unchanged excited state, a blue shift of the emission would be expected. Indeed, following Fig. 5B, we observe a blue-shifted emission with an increasing charging effect from the ligands, which would fit perfectly in the above assumption. However, structural changes are also known to force an altered emission.[18] Note that ligand addition does not alter the hydrodynamic particle diameter (Fig S2). Investigations varying the excitation wavelength could contribute to a better understanding of the position of energy states. Overall, we found a charging effect in Au NCs through the carboxylic head group of aminated and thiolated organic ligands. The charging effect increases with decreasing distance from the Au surface, leading to a charge-injection within the particle observable by an increased and blue-shifted surface emission (while looking from long-chained to short-chained ligands).

- **Influence of the ligand anchor group on the surface emission**

  Following Fig. 5A, the aminated ligand shows an even stronger influence on the emission intensity than the thiolated ligand. Although both primarily show an increase in emission, long thiolated ligands lead to a decrease in emission. This finding is of great interest because with a longer carbon chain length, the distance of the carboxyl group to the Au surface increases, and the charging effect can be assigned more and more to the anchor group. If we now look at the wavelength of the emission maximum, we generally see a blue shift for both ligands (from C6 to C2). However, if the influence of the anchor group is predominant (for long C-chained ligands), a red shift can be seen. This observation supports the theory of the charging effect because with increasing distance between the carboxyl group and the Au surface, the direct charge density donation efficiency of the carboxyl group to the Au surface decreases. Instead, donative effects of the anchor group prevail, which in both cases lead to a reduction of the electron density. This seems to provoke the opposite effect in the Au - electron density is pulled out of the core, which partially

charges the surface negatively, reducing the emission intensity and causing a redshift of the emitted light. It is noticeable that particularly aminated ligands show a strong red-shift, which is very pronounced, even for only 3 carbon atoms. While thiol binding is predominantly described as covalent and electron density is pushed into the metalcore, there is only electrostatic interaction between an amine and Au. Here, the large electron negativity differences between Au and N are probably the most important effector, which causes electrons to be pulled from the gold cluster, which induces a redshift as previously described. These effects are probably only compensated at low distances, where the electron-donating effect of the carboxyl group prevails.

***Table 1**: Summary of the influence of ligand anchor and head group on the emission of fully inorganic Au NCs.*

	Carboxylic ligand	**Aminated ligand**
Head group	**Short distance**	
	direct electron injection (**blue shift and emission intensity increase**)	
	Long-distance	
	Electron withdrawal at larger distances **(red-shift and emission intensity decrease)**	Not part of this work
Anchor group	electron injection **(blue shift)**	Electron withdrawal by strong electronegativity difference (dominates over electron induction by binding **(red-shift)**

In summary, we have shown that inorganic Au NCs work as good model material to understand charge effects through LMCT processes on the fluorescence behavior (Tab. 1). Although those particles show a pronounced fluorescence, their emission intensity can be increased with short carboxylic organic ligands. This can be justified by a charge injection within the NCs which is predominantly triggered by the donation of electron density by the functional group. Additionally, the emission wavelength can be adjusted. When the charge density is donated to the particle, the ligands force a blue-shifted emission, while the emission is red-shifted when donative effects from the anchor group prevail.

References

(1) Zhou, M.; Zeng, C.; Chen, Y.; Zhao, S.; Sfeir, M. Y.; Zhu, M.; Jin, R. Evolution from the plasmon to exciton state in ligand-protected atomically precise gold nanoparticles. *Nature communications* **2016**, *7*, 13240. DOI: 10.1038/ncomms13240. Published Online: Oct. 24, 2016.

(2) Yang, T.-Q.; Peng, B.; Shan, B.-Q.; Zong, Y.-X.; Jiang, J.-G.; Wu, P.; Zhang, K. Origin of the Photoluminescence of Metal Nanoclusters: From Metal-Centered Emission to Ligand-Centered Emission. *Nanomaterials (Basel, Switzerland)* **2020**, *10* (2). DOI: 10.3390/nano10020261. Published Online: Feb. 4, 2020.

(3) Wu, Z.; Jin, R. On the ligand's role in the fluorescence of gold nanoclusters. *Nano letters* **2010**, *10* (7), 2568–2573. DOI: 10.1021/nl101225f.

(4) Zeng, Y.; Havenridge, S.; Gharib, M.; Baksi, A.; Weerawardene, K. L. D. M.; Ziefuß, A. R.; Strelow, C.; Rehbock, C.; Mews, A.; Barcikowski, S.; Kappes, M. M.; Parak, W. J.; Aikens, C. M.; Chakraborty, I. Impact of Ligands on Structural and Optical Properties of Ag29 Nanoclusters. *Journal of the American Chemical Society* **2021**, *143* (25), 9405–9414. DOI: 10.1021/jacs.1c01799. Published Online: Jun. 17, 2021.

(5) Westcott, S. L.; Averitt, R. D.; Wolfgang, J. A.; Nordlander, P.; Halas, N. J. Adsorbate-Induced Quenching of Hot Electrons in Gold Core−Shell Nanoparticles. *J. Phys. Chem. B* **2001**, *105* (41), 9913–9917. DOI: 10.1021/jp011213t.

(6) Aruda, K. O.; Tagliazucchi, M.; Sweeney, C. M.; Hannah, D. C.; Schatz, G. C.; Weiss, E. A. Identification of parameters through which surface chemistry determines the lifetimes of hot electrons in small Au nanoparticles. *Proceedings of the National Academy of Sciences of the United States of America* **2013**, *110* (11), 4212–4217. DOI: 10.1073/pnas.1222327110. Published Online: Feb. 25, 2013.

(7) Cowan, M. J.; Mpourmpakis, G. Structure–property relationships on thiolate-protected gold nanoclusters. *Nanoscale Adv.* **2019**, *1* (1), 184–188. DOI: 10.1039/C8NA00246K.

(8) Yu, H.; Rao, B.; Jiang, W.; Yang, S.; Zhu, M. The photoluminescent metal nanoclusters with atomic

precision. *Coordination Chemistry Reviews* **2019**, *378*, 595–617. DOI: 10.1016/j.ccr.2017.12.005.

(9) Zheng, J.; Zhang, C.; Dickson, R. M. Highly fluorescent, water-soluble, size-tunable gold quantum dots. *Physical review letters* **2004**, *93* (7), 77402. DOI: 10.1103/PhysRevLett.93.077402. Published Online: Aug. 13, 2004.

(10) Cui, M.; Zhao, Y.; Song, Q. Synthesis, optical properties and applications of ultra-small luminescent gold nanoclusters. *TrAC Trends in Analytical Chemistry* **2014**, *57*, 73–82. DOI: 10.1016/j.trac.2014.02.005.

(11) Liu, H.; Hong, G.; Luo, Z.; Chen, J.; Chang, J.; Gong, M.; He, H.; Yang, J.; Yuan, X.; Li, L.; Mu, X.; Wang, J.; Mi, W.; Luo, J.; Xie, J.; Zhang, X.-D. Atomic-Precision Gold Clusters for NIR-II Imaging. *Advanced materials (Deerfield Beach, Fla.)* **2019**, *31* (46), e1901015. DOI: 10.1002/adma.201901015. Published Online: Oct. 1, 2019.

(12) Yang, Y.; Han, A.; Li, R.; Fang, G.; Liu, J.; Wang, S. Synthesis of highly fluorescent gold nanoclusters and their use in sensitive analysis of metal ions. *The Analyst* **2017**, *142* (23), 4486–4493. DOI: 10.1039/C7AN01348E.

(13) Sokołowska, K.; Malola, S.; Lahtinen, M.; Saarnio, V.; Permi, P.; Koskinen, K.; Jalasvuori, M.; Häkkinen, H.; Lehtovaara, L.; Lahtinen, T. Towards Controlled Synthesis of Water-Soluble Gold Nanoclusters: Synthesis and Analysis. *J. Phys. Chem. C* **2019**, *123* (4), 2602–2612. DOI: 10.1021/acs.jpcc.8b11056.

(14) Smith, A. M.; Marbella, L. E.; Johnston, K. A.; Hartmann, M. J.; Crawford, S. E.; Kozycz, L. M.; Seferos, D. S.; Millstone, J. E. Quantitative analysis of thiolated ligand exchange on gold nanoparticles monitored by 1H NMR spectroscopy. *Analytical chemistry* **2015**, *87* (5), 2771–2778. DOI: 10.1021/ac504081k.

(15) Zhou, S.; Huo, D.; Goines, S.; Yang, T.-H.; Lyu, Z.; Zhao, M.; Gilroy, K. D.; Wu, Y.; Hood, Z. D.; Xie, M.; Xia, Y. Enabling Complete Ligand Exchange on the Surface of Gold Nanocrystals through the Deposition and Then Etching of Silver. *Journal of the American Chemical Society* **2018**, *140* (38), 11898–11901. DOI: 10.1021/jacs.8b06464.

(16) Viudez, A. J.; Madueño, R.; Pineda, T.; Blázquez, M. Stabilization of gold nanoparticles by 6-mercaptopurine monolayers. Effects of the solvent properties. *The journal of physical chemistry. B* **2006**, *110* (36), 17840–17847. DOI: 10.1021/jp062165l.

(17) Zhang, B.; Chen, J.; Cao, Y.; Chai, O. J. H.; Xie, J. Ligand Design in Ligand-Protected Gold Nanoclusters. *Small (Weinheim an der Bergstrasse, Germany)* **2021**, *17* (27), e2004381. DOI: 10.1002/smll.202004381. Published Online: Jan. 28, 2021.

(18) Kang, X.; Zhu, M. Tailoring the photoluminescence of atomically precise nanoclusters. *Chemical Society reviews* **2019**, *48* (8), 2422–2457. DOI: 10.1039/c8cs00800k.

(19) Zheng, J.; Nicovich, P. R.; Dickson, R. M. Highly fluorescent noble-metal quantum dots. *Annual review of physical chemistry* **2007**, *58*, 409–431. DOI: 10.1146/annurev.physchem.58.032806.104546.

(20) Dong, H.; Liao, L.; Wu, Z. Two-Way Transformation between fcc- and Nonfcc-Structured Gold Nanoclusters. *The journal of physical chemistry letters* **2017**, *8* (21), 5338–5343. DOI: 10.1021/acs.jpclett.7b02459.

(21) Scanlon, M. D.; Peljo, P.; Méndez, M. A.; Smirnov, E.; Girault, H. H. Charging and discharging at the nanoscale: Fermi level equilibration of metallic nanoparticles. *Chemical science* **2015**, *6* (5), 2705–2720. DOI: 10.1039/C5SC00461F.

(22) Ziefuss, A. R.; Steenbock, T.; Benner, D.; Plech, A.; Göttlicher, J.; Teubner, M.; Grimm-Lebsanft, B.; Rehbock, C.; Comby-Zerbino, C.; Antoine, R.; Amans, D.; Chakraborty, I.; Bester, G.; Nachev, M.; Sures, B.; Rübhausen, M.; Parak, W. J.; Barcikowski, S. Photoluminescence of Fully Inorganic Colloidal Gold Nanocluster and Their Manipulation Using Surface Charge Effects. *Advanced materials (Deerfield Beach, Fla.)* **2021**, *33* (31), e2101549. DOI: 10.1002/adma.202101549. Published Online: Jun. 24, 2021.

3.3.4 Influence of Pt alloying on the fluorescence of fully inorganic gold nanocluster

Synopsis:

Besides the production of elemental, inorganic gold nanoclusters, combining two or more elements in one cluster is a recent research topic. Within such particles, the properties of two or more metals are combined, leading to a synergetic strengthening of some material properties. For example, the addition of very small amounts of Pt to Au NCs may significantly increase catalytic activity.

Also, the fluorescent behavior can be influenced as well by alloying Au NCs with elements such as Ag or Pt, which makes such materials both photo catalytically and fundamentally interesting. Since studies have been performed exclusively on organic ligand capped metal nanocluster systems, it is difficult to differentiate between ligand-induced effects and metal-induced effects. For this reason, synergetic effects could not be clearly reduced to one parameter. In addition to the (i) altered electropositivity of the metal core, alterations in the (ii) crystal structure and (iii) charge effects due to ligands on the surface are considered as possible triggers for this phenomenon.

However, predicting new multi-metallic nanocluster types is still difficult as understanding pure metal-based interactions is hampered by ligands bound to the surface due to the typical wet-chemical synthesis routes. In the following work, we transferred the LFL synthesis of Au NCs to gold-rich bi-metallic AuPt nanoclusters and compared their optical behavior with that of their elemental counterparts. We found that even minor amounts of Pt atoms in the AuPt NC lead to a quenched surface emission and are accompanied by a red-shift, which may be attributed to (i) and (ii) but excludes (iii) since we have entirely dispensed the use of organic ligands. With this, LFL is a fast and efficient way to produce molar fraction series of alloy NCs.

ChemPhysChem

Research Article
doi.org/10.1002/cphc.202200033

Chemistry Europe
European Chemical Societies Publishing

Special Collection

Influence of Pt Alloying on the Fluorescence of Fully Inorganic, Colloidal Gold Nanoclusters

Anna R. Ziefuss,[a] Michael Willeke,[a] Matthias Miertz,[a] Alexander Heinemann,[a] Christoph Rehbock,[a] and Stephan Barcikowski*[a]

Noble metal alloy nanoclusters (NCs) are interesting systems as the properties of two or more elements can be combined in one particle, leading to interesting fluorescence phenomena. However, previous studies have been exclusively performed on ligand-capped NCs from wet chemical synthesis. This makes it difficult to differentiate to which extent the fluorescence is affected by ligand-induced effects or the elemental composition of the metal core. In this work, we used laser fragmentation in liquids (LFL) to fabricate colloidal gold-rich bi-metallic AuPt NCs in the absence of organic ligands and demonstrate the suitability of this technique to produce molar fraction series of 1nm alloy NC. We found that photoluminescence of ligand-free NCs is not a phenomenon limited to Au. However, even minute amounts of Pt atoms in the AuPt NCs lead to quenching and red-shift of the fluorescence, which may be attributed to the altered surface charge density.

Introduction

Monometallic metal nanoclusters (NC) have attracted strong interest in a variety of scientific research fields due to their characteristic quantum confinement, which leads to discrete structure,[1] size,[2] and surface coverage[3] dependent electronic transitions. This results in extraordinary physicochemical and molecular-like properties, directly affecting the discrete photoluminescence phenomena observed in these materials.[3–5] Scientists have successfully modified electronic transitions and related optical properties of NC by combining two or more metal species to form alloy NCs (e.g., AuAg,[6,7] AuCu,[8] AuPt[9,10]). Next to a combination of different material properties, bi-metallic NC can induce synergistic effects, resulting in enhanced catalytic activity or significantly shifted fluorescence signals.[11] Andolinia et al.[12] found that even small amounts of Cu in AuCu NCs can lead to a dramatic red-shift of the emission wavelength and an increased emission intensity. In contrast, Negishi et al.[7] observed a blue shift after doping Au NCs with Ag. Kothalawala et al.[13] incorporated up to 3 Pd atoms into the $Au_{144}(SR)_{60}$ icosahedral NC structure and found a decreased absorbance in the visible spectrum attributed to the inclusion of Pd atoms into the metal core rather than the staple motifs. Alloying Au NCs with Pt was reported to increase the catalytic activity without affecting the fluorescence behaviour.[10] Contrary, Feng et al.[14] detected a decrease in emission and absorbance by successfully alloying glutathione-stabilized Au NCs with Pt, accompanied by increased peroxidase-like activity. Due to many existing monometallic NC systems with strongly deviating crystal structures, number of atoms, and surface ligand types, it is difficult to systematically predict the influence of heteroatoms on their intrinsic properties. However, some influencing factors could already be determined. The influence of heteroatoms on fluorescence is currently explained by a changed electronegativity of the metal core,[15] deviating crystal structures,[16] different numbers of valence electrons,[17] or charge effects on the surface.[18] The latter, however, is often not caused by the metal alone; covalently bound organic ligands are also known to cause ligand-metal-charge-transfer (LMCT) effects with the metal surface.[19] Such ligands are necessarily present during typical wet chemical synthesis based on the reduction of a metal precursor[5] and tend to dominate the features of the NCs. For example, $Au_{25}(HSG)_{18}$ (with HSG = glutathione) contains only 3.75% of gold atoms.[20] This makes it difficult to clearly assign the above effects to either LMCT or metal-metal charge-transfer (MMCT) effects.

Recently, Ziefuss et al.[21] have successfully prepared monometallic, completely inorganic NC using a laser-based approach without organic ligands. They first irradiated a solid Au target using the laser ablation in liquids (LAL) method to obtain a well-dispersed nanoparticle (NP) colloid. The colloid was then re-irradiated using laser fragmentation in liquids (LFL), and protoplasmonic Au NCs smaller than 3 nm were obtained after centrifugation. A detailed description of the LAL[22] and the followed LFL[23,24] process can be found elsewhere. Here, LFL leads to particles with a mean diameter of 2.9 nm[23] without an observable fluorescence behaviour. However, a mechanical ultracentrifugation step enables a proper size separation.[21] Larger and core-dominated NCs (> 1 nm) showed size-dependent specific emission around 350–400 nm, while smaller, sur-

[a] Dr. A. R. Ziefuss, M. Willeke, M. Miertz, Dr. A. Heinemann, Dr. C. Rehbock, Prof. Dr. S. Barcikowski
Technical Chemistry I and Center for Nanointegration Duisburg–Essen (CENIDE),
University Duisburg–Essen
Universitätsstraße 7, 45141 Essen (Germany)
E-mail: stephan.barcikowski@uni-due.de

Supporting information for this article is available on the WWW under https://doi.org/10.1002/cphc.202200033

An invited contribution to a Special Collection on Synthesis and Modeling of Alloy Nanoparticles.

face-dominated nanoclusters (<1 nm) exhibited an additional energy-rich emission state at around 300 nm. In both cases, the emission intensity has been a function of the surface charge density.[21] Thereby, the core emission of the larger-sized fraction increases with an increasing number of surface charges. The smaller-sized fraction does not show this behaviour. Here, no differences in the core emission could be observed. We found the HOMO is dominated by contributions from the surface located deprotonated oxygen (which is responsible for the increased surface charge density). The lower observed surface-emission intensity can be explained by an overlap of this HOMO with the LUMO, which is primarily located at the particle's core.[21] However, the influence of heteroatoms on the LFL synthesis and on the photoluminescence properties of fully inorganic NCs has not been determined to date.

Hence, we generated ligand-free monometallic Au NCs, Pt NCs, and gold-rich bimetallic AuPt NCs with composition of $Au_{98}Pt_2$ and $Au_{90}Pt_{10}$. We compared the optical behaviour with that of their monometallic equivalents and an *ex-situ* mixture of monometallic Au and Pt NC with the same global elemental composition as the alloy.

Results and Discussion

The production of AuPt alloy NC is a three-step procedure, starting with LAL of a sintered metallic target produced by mixing Au and Pt micro powders in a defined ratio (see method part) as previously described in the literature.[25] The process leads to colloidal nanoparticles (NP) with a broad hydrodynamic size distribution. Hence, these nanoparticles require further downsizing steps to reach the NCs size range. However, LFL requires particles larger than the fragmentation threshold diameter (for Au, $d > 13.4$ nm[23]), so that separation of smaller particle fractions was necessary before LFL. Here, we used centrifugation as described in Ref. [23]. The resulting particle size distributions with mean diameter 50–60 nm can be found in Figure S2A. We have determined the actual composition of the produced NPs for the 90:10 (Au:Pt) composition by TEM-EDX single particle analysis (see EDX summed up line spectrum in Figure 1). Note that the EDX-mapping pixel intensity is not linearly correlated with the composition, a pixel is displayed where the elemental threshold count rate is exceeded, showing homogeneous elemental distribution in the particle volume but no direct quantitative information. Such solid-solution structure has been reported earlier for laser-generated AuPt particles.[25–27]

In addition, we prepared a 98:2 (Au:Pt) atomic mixture target and EDX-analysis of this target verified the 98:2 atomic ratio (Figure 1B). The Pt content in the nanoparticles fabricated from these targets was too low to be verifiably measured via EDX. However, following Ref. [25,28–30] the composition of the nanoparticles after laser processing equals the mixing ratio of the micro powder for target preparation and can thereby be easily tuned by the mixing ratio[31] For example, Neumeister et al.[29] verified this for $Ag_{100-x}Au_x$-alloys (x = 10 to 90% in 10% intervals), and Waag et al.[28] expanded this knowledge to even

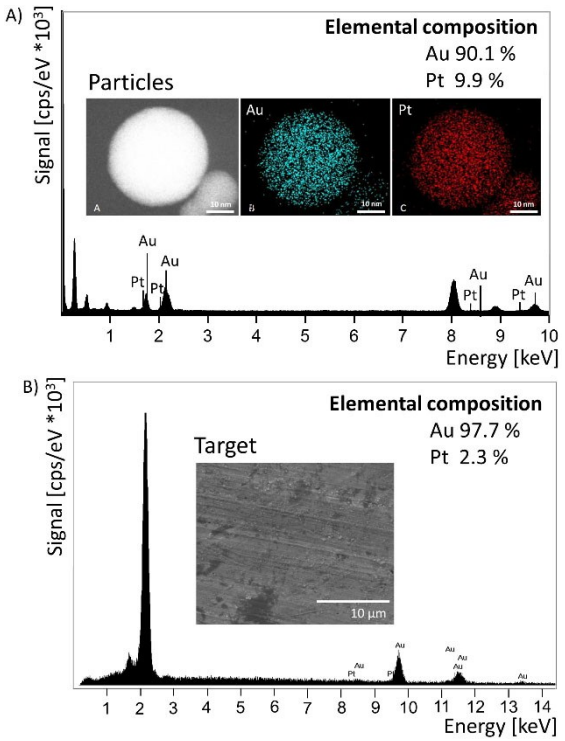

Figure 1. A) EDX results of $Au_{90}Pt_{10}$ NPs after LAL incl. TEM-EDX mapping of this particle to show the homogeneity of the elemental composition. B) EDX results of the $Au_{98}Pt_2$ sintered powder target.

quinary alloys, at the example of high entropy CoCrFeMnNi-alloy systems. Furthermore, the pronounced differences in the absorbance spectra of the Au, Pt, $Au_{98}Pt_2$, and $Au_{90}Pt_{10}$ colloids (Figure S3) suggest a difference in composition. Note that the differences in the absorbance spectra[32] (Figure S3) will also affect the LFL process, especially its efficiency since the energy input critically depends on the absorption at the LFL wavelength (intensity and absorption cross-section). To overcome these limitations, we have performed the LFL in a free-liquid jet with single pulse per volume element (PPV)[23] conditions and cycled the colloid as long as we could detect changes in the absorbance spectra (Figure S3). The resulting mean diameter determined by analytical disk centrifugation (ADC) varied from 2.7 nm (Au NPs) to 3.1 nm (Pt NPs) (see also Figure S4); however, ultracentrifugation steps enable access to monodisperse NC with a similar size distribution for all produced NCs (see Figure 2). Please note that we used analytical ultracentrifugation (AUC) to determine the resulting hydrodynamic particle size distribution of the NCs, which is a powerful tool with a resolution in the Angström range.[21,33] Here, the particle size determination is based on a measurement of the sedimentation behaviour of the particles, which can be influenced by the particles' density, diffusion, and surface charge in addition to the particle size. While charge effects (as a directed counter-force to sedimentation) can reduce the sedimentation velocity, diffusion should lead to a broadening of the sedimentation velocity distribution. Since different materials are compared with each other here, these influencing factors can become

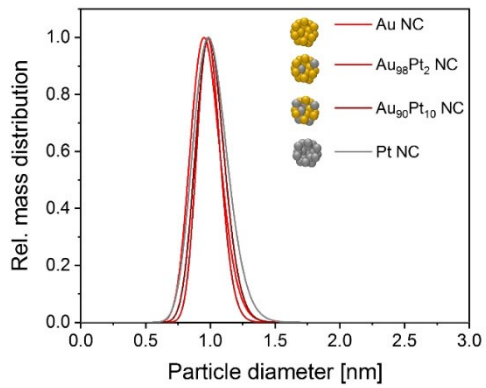

Figure 2. Normalized mass-weighted particle size distribution of inorganic Au NCs, Pt NCs, and AuPt NCs with different Pt molar fractions produced with laser fragmentation in the absence of organic ligands.

quite relevant and lead to slight deviations in the distribution. Therefore, we will not discuss the minor differences in detail and assume comparable particle sizes for the NC, in particular as the density of Au and Pt is almost the same.

Although all analysed samples possess a comparable mean diameters (1 nm) and size distribution widths (Figure 2), we found a distinguishable optical behavior (Figure 3A, B). The Au NCs show an absorbance peak at 277 nm, which cannot be observed for Pt NC. The gold-rich bi-metallic AuPt NCs also show this absorbance peak; however, a slight decrease with increasing Pt content can be observed (Figure 3A). This is in good agreement with the study of Kothalawala et al.[13] as they found that alloying of $Au_{144}(SR)_{60}$ with Pd leads to a diminution of the Au NCs absorbance features.

Besides, we found a change in the fluorescence emission with increasing Pt content in the NCs. The emission behaviour of ligand-free Au NCs has been discussed previously.[21] A size-tuneable core emission between 350 nm and 400 nm and a surface-related emission at 300 nm were detected for Au NCs smaller than 1 nm, originating from changed crystal structures or quantization of energy states.[21] The emission at around 300 nm decreases in the case of $Au_{98}Pt_2$ and $Au_{90}Pt_{10}$ NCs (Figure 3B), which could be due to a lower absorption efficiency

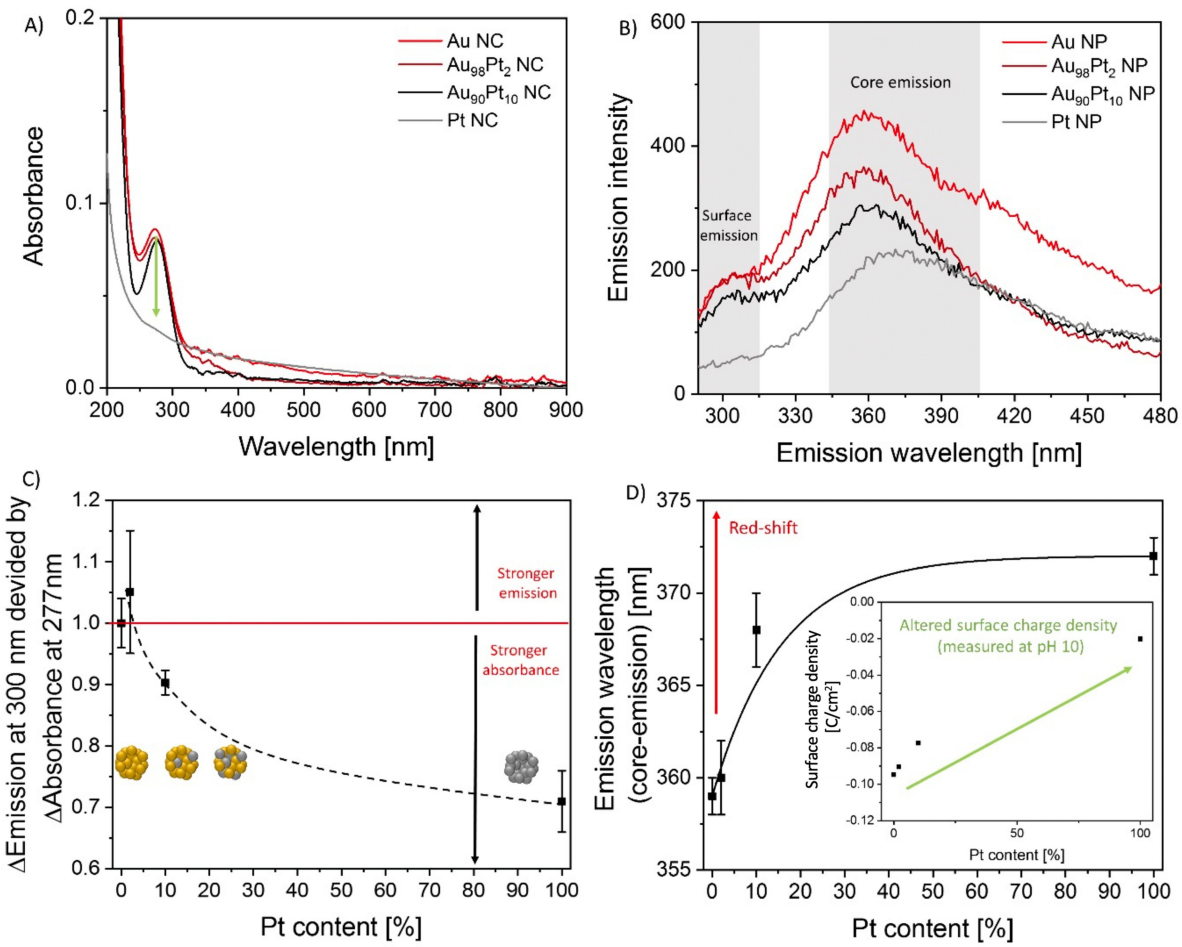

Figure 3. Characterisation of optical properties of Au and Pt NCs and two Au-rich AuPt-alloy NCs at a concentration of 0.5 mg/L. A) absorbance spectra, B) emission spectra after excitation at 250 nm. (Emission plotted excluding the excitation wavelength range). C) Relative change of normalized emission intensity divided by a decrease of normalized absorbance using Au NCs as a reference. D) An increasing Pt content leads to a red shift of the emission between 355 and 375 nm. Error bars correspond to the standard deviation after measurement of three samples each.

(Figure 3A). These findings, showing a reduction of absorbance and emission intensity with increasing Pt content triggered the question of whether these phenomena are directly proportional, and the reduced absorbance is the only cause for lower emission intensities. To tackle this question, we calculated the quotient between the emission intensity at 300 nm (ΔEmission) and the absorbance at 277 nm (ΔAbsorbance) and normalized it by the corresponding quotient for pure AuNC. Consequently, a quotient >1 corresponds to an intensified emission intensity, while a quotient <1 would indicate an emission intensity quenching. For the sample with 2% Pt content, a value close to 1 is found. However, the addition of 10% Pt to the AuNC leads to a drastic reduction of this value, which gets more pronounced for pure Pt. From these findings we can conclude: I) The strong reduction in emission intensity following the alloying of AuNC with Pt is not only caused by the reduced absorbance. II) Non-radiative decay channels for the absorbed light get more pronounced with increasing Pt content, a phenomenon which could be related to surface defects or different electron densities due to the laser-fabricated alloy NCs (hypotheses discussed below in more detail). In this context, it should be noted that these phenomena were only found for the surface-attributed emission peaks at 300 nm. Hence the presented ratio does not correspond to the total quantum yield as it is usually calculated by integrating the entire absorbance and emission spectra. Similarly, the core emission intensity at ~350 nm decreases significantly and shows an exponential red shift with increasing Pt content (Figure 3D). Please note that we could not determine the exact composition of the alloy NCs as the particle size was too small to get an appropriate signal during EDX measurements. However, to exclude a separation of the pure elements and the formation of individual monometallic PtNC and AuNC, we compared the absorbance of the alloy particles after LFL with a mixture of the corresponding monometallic NC at the same elemental ratio and found a clearly distinguishable optical behaviour. While the $Au_{90}Pt_{10}$ particles prepared by LFL from $Au_{90}Pt_{10}$ alloy target still show an absorbance peak at 277 nm, the mixture of the pure elements in the same ratio lacks this feature. Furthermore, time-resolved measurements of the individual single element particle mixtures show no changes over time. Hence, we can exclude atom exchange reactions between single metallic alloy NCs in solution as a competing particle formation mechanism (Figure S5).

These observations are highly interesting, and we must consider the following two factors, which can influence the intensity and position of the core or surface emission in alloyed NCs. Note that we can exclude a particle size effect as all particles show comparable size distributions (Figure 2).

(i) Au and Pt are known to crystalize in an fcc crystal structure. We may assume a solid solution structure in the NC as Pt is well soluble in Au at these low Pt contents as already verified for the educt nanoparticles (Figure 1). However, the unit cells show a different physical dimension caused by different lattice constants (Au: 408.0 pm, Pt: 392.4 pm)[34] and different atomic radii (Au: 144 pm, Pt: 138.5 pm).[35] Hence, we can assume that the unit cell shrinks due to the incorporation of Pt into the Au fcc. On the other hand, it is known that lattice constant dilatation of some percent happens for very small NPs.[36] The introduction of small amounts of Pt in Au-based NC is further expected to stabilize defects in the crystal structure, mainly referable to the different atomic radii.[34,35] Even small amounts of Pt <10% in the NC lead to a red-shifted core emission, non-linearly correlated with the Pt content. Hence, we could speculate on a potential correlation between an increasing defect density and a change of the optical properties. The defects of AuPt NCs may originate from or could be further intensified by the LFL synthesis process. Re-irradiation of larger NPs initiates a phase explosion,[24,37] followed by sudden cooling of the fragmentation plume,[24] causing the spontaneous solidification in the thermodynamically unfavoured distorted (3|1|1) surface lattice structure.[21]

It has been reported that laser-generated NPs are often defect-rich, caused by cooling rate of 10^{12}–10^{13} K/s during this kinetically-controlled synthesis.[31] Recently, Zhigilei et al. reported that NCs are ejected directly into the dense cold water during LFL,[37] indicating even faster cooling-rates. The distortion depends on the cooling rate, atomic radius, and material-dependent properties. Since the surface-emission vanishes completely in Pt NCs, it can be presumed that the Pt NCs solidify differently compared to Au NCs during LFL. Unfortunately, it has not been possible to determine the crystal structure of the particles (e.g. by XRD or XAS) as the concentration of the particles is too low. However, in our previous work on Au NCs,[24] we performed in-situ X-ray absorption spectroscopy to determine the structure of the particle's core and found clear evidence of an fcc.

(ii) Moreover, different energy states and (Highest Occupied Molecular Orbital) HOMO – (Lowest Unoccupied Molecular Orbital) LUMO gaps could result in different electronic states. In this context, particularly the fact that Pt atoms possess less valence electrons than Au atoms should be relevant and would result in an alloy NC with a pronounced electron deficiency, which would go along with a reduced surface charge density. According to Ohshima et al.[38] the surface charge density can be correlated to the zeta potential. Hence, we performed zeta potential measurements of our AuPt NC and found a decreasing zeta potential (surface charge density) with increasing Pt content (inset Figure 2D), which confirms our hypothesis even though the zeta potential was measured using dynamic light scattering at 633 nm, and the signal was noisy as the colloid's absorbance at this wavelength is very low. These findings are in accordance with our previous work on Au NCs,[21] where reduced surface charge density went along with a quenched fluorescence emission intensity, a trend similar to the one reported here for AuPt alloy NC.

Conclusions

In summary, we succeeded in producing fully inorganic bimetallic AuPt and monometallic Pt NCs and compared their properties with fully inorganic Au NCs. Minute amounts of Pt doping to create PtAu NCs lead to a (i) quenched energy-rich

surface emission, (ii) a red-shifted and quenched core emission, and (iii) a drastic decrease of the surface charge density. Point (i) and (iii) are possibly correlated and indicate the surface charge density-dependent emission that was already found in Ref. [13]. Point (ii), the red-shifted emission with increasing Pt content could be due to distortions in the crystal structure and the formation of defects, a hypothesis to be further examined in follow-up experiments. Here, suitable concentration techniques are to be developed to allow crystal structure evaluations e.g., by XAS. These studies further highlight the suitability of the LFL technique to produce alloy NCs with controlled composition and free of organic surface adsorbates. This trend should be explored in producing AuPt alloy series over a broader range of compositions as well as the transfer to other alloy NCs like AgAu or CuAu to further understand correlations between core composition and photoluminescence of fully inorganic NCs.

Experimental Section

The laser-based production of fully inorganic NC is a three-step procedure containing laser ablation in liquids (LAL), laser fragmentation in liquids (LFL), and a subsequent ultrafiltration step. All steps, including the characterization of intermediate products, will be explained in the following.

Pulsed LAL

A ps-pulsed laser (Ekspla, Atlantics series, 10 ps, 1064 nm, 8.8 mJ, 100 kHz) is focused on a bulk target (Au in case of Au NCs and Pt in case of Pt NCs) or a sintered powder target in case of bi-metallic NC, which was in each case located in a 30 mL batch chamber filled with ultra-pure water. The sintered powder targets contained micro powders in an atomic ratio of 98% Au and 2% Pt in the case of $Au_{98}Pt_2$ NC and 90% Au and 10% Pt in the case of $Au_{90}Pt_{10}$ NC. The sintering was carried out at 800 °C (which is 80% of the melting point so that the highest yield of alloy particles with the narrowest composition range can be expected[39]) for 24 h. It was required to densify the target surface to prevent fragments from detaching during the LAL process and to ensure that particles with an even elemental distribution ruled by the target composition are obtained. We produced colloids with broad size distributions and centrifuged the as produced colloidal solutions (Hettich, 67.1 g-force, 70 min) to separate particles smaller than 20 nm because we know – at least for Au – that the absorption cross-section of those particles is too small to absorb enough energy for a successively required LFL process.[23] The size distribution of as produced particles can be found in Figure S1. Even small amounts of Pt dramatically affect the colour of the colloidal solutions (Figure S1 B–D). We observed a drastic decrease in the Au NP surface plasmon resonance intensity even for the sample with 2% Pt (Figure 1C). This indeed influences the amount of absorbed light, which will, following Ref. [23], affect the LFL efficiency in the successive LFL.

Pulsed LFL

The LFL was performed in a free-liquid jet as already described in Ref. [21,23]. In short, we re-irradiated the colloids depicted in Figure 1A with a ns-pulsed laser (Innolas, 9, ns, 100 Hz, 84 mJ, 1.6 J/m^2) at 532 nm. The laser spot diameter and the jet dimensions were adjusted so that each volume element of the liquid jet was hit at least once by the laser (PPV; pulses per volume element). However, because of the gaussian laser profile and the attenuation of the laser beam in the axial direction, some particles stay unirradiated, so we needed multiple cycles to reach fragmentation of each educt NP (Figure S2). As soon as no change in absorption could be detected, the fragmentation was stopped, and we measured the particle size (Figure S3 D) using the analytical disc centrifuge (ADC, CPS Instruments DC 24000, 24000 rpm). In Ref. [23,40], we have determined a lower measurement limit of 2 nm, so this method is a first approximation to identify particle fractions >3 nm, which must be removed by ultrafiltration. The fragmentation was done using a colloidal solution at a mass concentration of 7.5 mg/L. Measurements of the particle composition were not possible yet, as typical characterization methods require much higher concentrations. However, while working with bimetallic particles, the mass composition of the elements is an important factor. The scale-up of particle production and increasing the concentration through supporting the product particles on microparticles or embedding them in gels is necessary for follow-up studies. However, that the bimetallic character is preserved is already indicated recognized by the colloid's color after LFL. Au NCs are orange (Figure 1A), whereas the bimetallic equivalents show a rather greyish shade (Figure 1B–C). An aggregation of particles could also explain a greyish color but, we can observe this neither in the UV-Vis nor in ADC measurements.

The colloidal solution after LFL contained particles that are larger than typical nanocluster sizes. We performed ultra-filtration using centrifugal filters (Merk-millipore) to remove this size fraction with a molecular weight cut-off of 50 kDa. The centrifugation was done in a Hettich centrifuge at 4000 rpm (15 min). The filtrate was removed and used as a educt for a second centrifugal step using filters with a MWCO of 3 kDa. The filtrate contains the final product in a very low concentration. To concentrate these particles, we used a rotary evaporator (7 mbar, 45 °C). We determined the particle mass concentration with an inductively coupled plasma with mass spectrometric detection (ICP-MS, Perkin Elmer Sciex – ELAN 6000).

Nanocluster Characterization

The particle sizes were analyzed using an analytical ultracentrifuge (AUC) (Beckman-Coulter). We measured the sedimentation profile with an absorbance optic at 280 nm (12 h, 20 °C) and evaluated the sedimentation behaviour with the license-free software "Sedfit". The absorbance spectra were measured in the range of 190 nm–900 nm using a tabletop device from Thermo Scientific (Evolution 201). The emission behaviour was measured in the range of 200–800 nm after excitation at 250 nm (Variant Eclipse). Zeta-potential measurements were done with the Nano ZS (Malvern). Here, the surface charge density was calculated following Ref. [38].

Acknowledgements

We gratefully acknowledge the DFG Deutsche Forschungsgemeinschaft for its financial support under Project No. BA 3580/22-1. We further acknowledge Prof. Sures and Milen Nachev for access and support in ICP-MS measurements. Open access funding enabled and organized by Projekt DEAL. Open Access funding enabled and organized by Projekt DEAL.

Conflict of Interest

The authors declare no conflict of interest.

Data Availability Statement

The data that support the findings of this study are available from the corresponding author upon reasonable request.

Keywords: laser based synthesis · colloidal alloy nanocluster · analytical ultracentrifugation · surfactant free photoluminescence · surface charge density

[1] L. Zhang, E. Wang, *Nano Today* **2014**, *9*, 132–157.
[2] J. Zheng, C. Zhang, R. M. Dickson, *Phys. Rev. Lett.* **2004**, *93*, 77402.
[3] Z. Wu, R. Jin, *Nano Lett.* **2010**, *10*, 2568–2573.
[4] R. Jin, C. Zeng, M. Zhou, Y. Chen, *Chem. Rev.* **2016**, *116*, 10346–10413.
[5] I. Chakraborty, T. Pradeep, *Chem. Rev.* **2017**, *117*, 8208–8271.
[6] a) R. D. Corpuz, Y. Ishida, M. T. Nguyen, T. Yonezawa, *Langmuir* **2017**, *33*, 9144–9150; b) K. Loza, M. Heggen, M. Epple, *Adv. Funct. Mater.* **2020**, *30*, 1909260.
[7] X. Dou, X. Yuan, Y. Yu, Z. Luo, Q. Yao, D. T. Leong, J. Xie, *Nanoscale* **2014**, *6*, 157–161.
[8] a) G. Barcaro, A. Fortunelli, G. Rossi, F. Nita, R. Ferrando, *J. Phys. Chem. B* **2006**, *110*, 23197–23203; b) P.-C. Chen, J.-Y. Ma, L.-Y. Chen, G.-L. Lin, C.-C. Shih, T.-Y. Lin, H.-T. Chang, *Nanoscale* **2014**, *6*, 3503–3507.
[9] N. Xu, L. Meng, H.-W. Li, D.-Y. Lu, Y. Wu, *Mikrochim. Acta* **2018**, *185*, 294.
[10] Y. Chen, X.-Y. Ge, S.-Y. Cen, A.-J. Wang, X. Luo, J.-J. Feng, *Sens. Actuators B* **2020**, *311*, 127931.
[11] X. Yuan, X. Dou, K. Zheng, J. Xie, *Part. Part. Syst. Charact.* **2015**, *32*, 613–629.
[12] C. M. Andolina, A. C. Dewar, A. M. Smith, L. E. Marbella, M. J. Hartmann, J. E. Millstone, *J. Am. Chem. Soc.* **2013**, *135*, 5266–5269.
[13] N. Kothalawala, C. Kumara, R. Ferrando, A. Dass, *Chem. Commun.* **2013**, *49*, 10850–10852.
[14] J. Feng, P. Huang, F.-Y. Wu, *Analyst* **2017**, *142*, 4106–4115.
[15] X. Kang, M. Zhu, *Chem. Soc. Rev.* **2019**, *48*, 2422–2457.
[16] Z. Gan, J. Chen, L. Liao, H. Zhang, Z. Wu, *J. Phys. Chem. Lett.* **2018**, *9*, 204–208.
[17] X. Kang, Y. Li, M. Zhu, R. Jin, *Chem. Soc. Rev.* **2020**, *49*, 6443–6514.
[18] R. Kazan, U. Müller, T. Bürgi, *Nanoscale* **2019**, *11*, 2938–2945.
[19] a) R. R. Nasaruddin, T. Chen, N. Yan, J. Xie, *Coord. Chem. Rev.* **2018**, *368*, 60–79; b) M. B. Newmai, P. S. Kumar, *AIP Conf. Proc.* **2016**, *1728*, 1, 050111.
[20] M. Zhou, Y. Song, *J. Phys. Chem. Lett.* **2021**, *12*, 1514–1519.
[21] A. R. Ziefuss, T. Steenbock, D. Benner, A. Plech, J. Göttlicher, M. Teubner, B. Grimm-Lebsanft, C. Rehbock, C. Comby-Zerbino, R. Antoine, et al., *Adv. Mater.* **2021**, *33*, e2101549.
[22] S. Scaramuzza, M. Zerbetto, V. Amendola, *J. Phys. Chem. C* **2016**, *120*, 9453–9463.
[23] A. R. Ziefuß, S. Reichenberger, C. Rehbock, I. Chakraborty, M. Gharib, W. J. Parak, S. Barcikowski, *J. Phys. Chem. C* **2018**, *122*, 22125–22136.
[24] A. R. Ziefuss, S. Reich, S. Reichenberger, M. Levantino, A. Plech, *Phys. Chem. Chem. Phys.* **2020**, *22*, 4993–5001.
[25] J. Zhang, D. N. Oko, S. Garbarino, R. Imbeault, M. Chaker, A. C. Tavares, D. Guay, D. Ma, *J. Phys. Chem. C* **2012**, *116*, 13413–13420.
[26] F. Waag, R. Streubel, B. Gökce, S. Barcikowski, *Appl. Nanosci.* **2021**, *11*, 1303–1312.
[27] a) D. N. Oko, S. Garbarino, J. Zhang, Z. Xu, M. Chaker, D. Ma, D. Guay, A. C. Tavares, *Electrochim. Acta* **2015**, *159*, 174–183; b) D. N. Oko, J. Zhang, S. Garbarino, M. Chaker, D. Ma, A. C. Tavares, D. Guay, *J. Power Sources* **2014**, *248*, 273–282.
[28] F. Waag, Y. Li, A. R. Ziefuß, E. Bertin, M. Kamp, V. Duppel, G. Marzun, L. Kienle, S. Barcikowski, B. Gökce, *RSC Adv.* **2019**, *9*, 18547–18558.
[29] A. Neumeister, J. Jakobi, C. Rehbock, J. Moysig, S. Barcikowski, *Phys. Chem. Chem. Phys.* **2014**, *16*, 23671–23678.
[30] D. Tiedemann, U. Taylor, C. Rehbock, J. Jakobi, S. Klein, W. A. Kues, S. Barcikowski, D. Rath, *Analyst* **2014**, *139*, 931–942.
[31] S. Reichenberger, G. Marzun, M. Muhler, S. Barcikowski, *ChemCatChem* **2019**, *11*, 4489–4518.
[32] a) S. Moniri, M. Reza Hantehzadeh, M. Ghoranneviss, M. Asadi Asadabad, *Eur. Phys. J. Plus* **2017**, *132*, 13413; b) A. Joplin, S. A. Hosseini Jebeli, E. Sung, N. Diemler, P. J. Straney, M. Yorulmaz, W.-S. Chang, J. E. Millstone, S. Link, *ACS Nano* **2017**, *11*, 12346–12357.
[33] K. L. Planken, H. Cölfen, *Nanoscale* **2010**, *2*, 1849–1869.
[34] S. M. Foiles, M. I. Baskes, M. S. Daw, *Phys. Rev. B: Condens. Matter Mater. Phys.* **1986**, *33*, 7983–7991.
[35] L.-Q. Chen, Y. Gu, *Physical Metallurgy* **2014**, 2807–2835.
[36] C. Solliard, M. Flueli, *Surf. Sci.* **1985**, *156*, 487–494.
[37] H. Huang, L. V. Zhigilei, *J. Phys. Chem. C* **2021**, *125*, 13413–13432.
[38] K. Makino, H. Ohshima, *Langmuir* **2010**, *26*, 18016–18019.
[39] F. Waag, W. I. M. A. Fares, Y. Li, C. Andronescu, B. Gökce, S. Barcikowski, *J. Mater. Sci.* **2022**, *57*, 3041–3056.
[40] A. R. Ziefuß, S. Barcikowski, C. Rehbock, *Langmuir* **2019**, *35*, 6630–6639.

Manuscript received: January 14, 2022
Revised manuscript received: March 31, 2022
Accepted manuscript online: April 5, 2022
Version of record online: April 25, 2022

3.4 – PART III

Catalytic application of fully inorganic and ultra-small gold nanoparticles

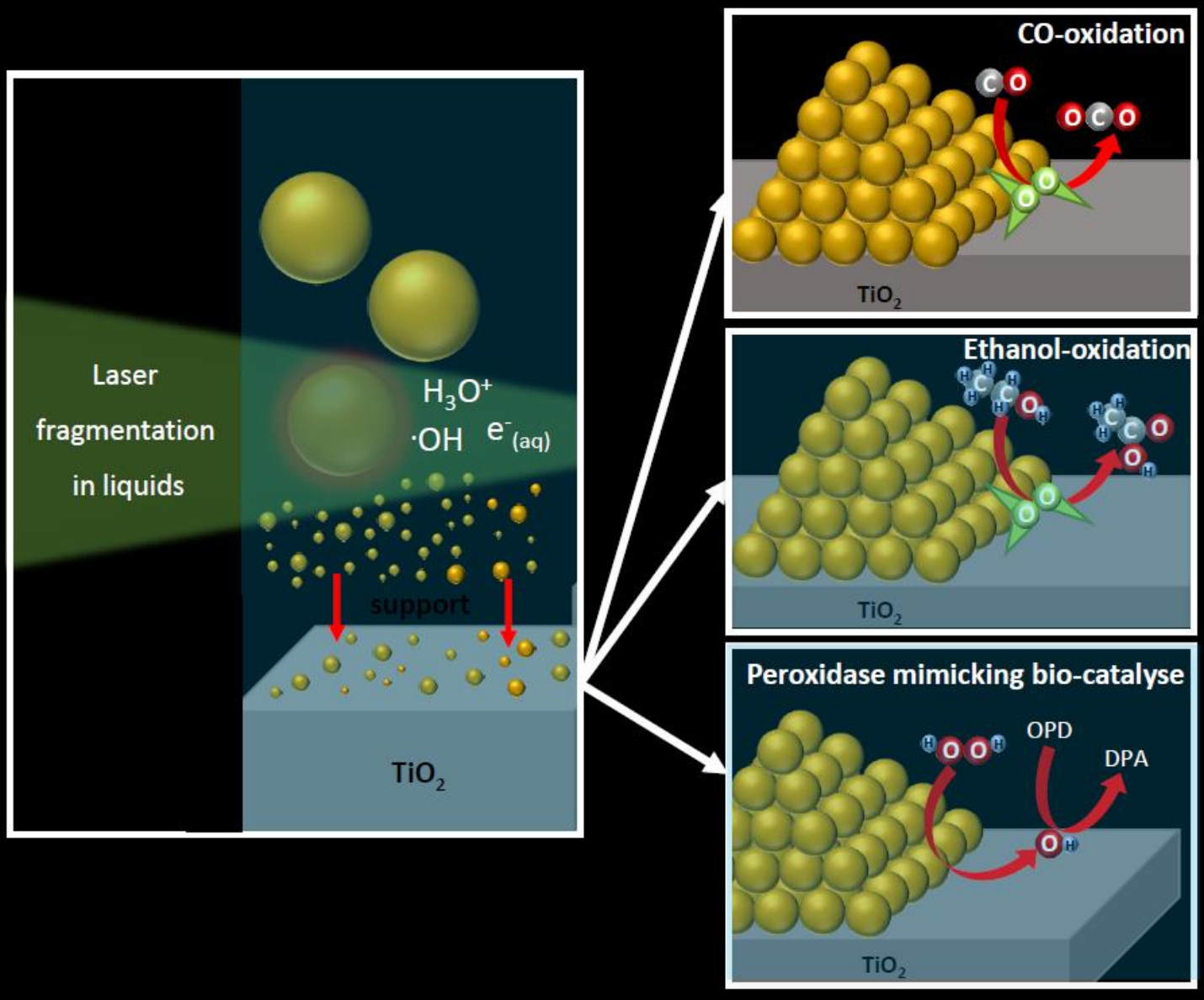

3.4.1 Origin of Laser-Induced Colloidal Gold Surface Oxidation and Charge Density, and Its Role in Oxidation Catalysis

Synopsis:

In catalysis, ultra-small nanoparticles' size and surface oxidation are linked to the electronic surface effects that drive the adsorption enthalpies of the reactants and products. Since no organic molecules are involved, the fragmentation of colloidal nanoparticles with high-intensity, pulsed lasers allows the fabrication of cluster-sized nanoparticles with outstanding purity. This unique quality spectrum renders laser-generated nanoparticles especially useful for catalytic studies since no surface-altering calcination is required, and the properties of the particles can be tuned before they are immobilized on the support. This allows a precise correlation between the catalytic activity and size of the nanoparticles, surface oxidation, and anions used for size quenching in laser fragmentation.

In this context, we found a fundamental link between the gold particle surface properties and the presence of hydroxyl radicals during laser fragmentation, yielding charge-tuned, 3 nm gold nanoclusters. We extensively tested the gold nanoparticles after adsorption onto TiO_2 (without calcination) in three different catalytic model reactions (CO oxidation, selective ethanol oxidation, and peroxidase-like oxidation) and observed that the surface charge density of the laser-generated nanoclusters appeared to be strongly linked to the oxidation activity of the catalysts. These results provide physico-chemical insights into the properties of particles in the colloidal state, which can be linked to catalytic activity and suggested for application in different areas.

This paper was published in the Journal of Physical Chemistry C on August 24, 2020. It was featured on the journal's front cover.

THE JOURNAL OF PHYSICAL CHEMISTRY C

pubs.acs.org/JPCC Article

Origin of Laser-Induced Colloidal Gold Surface Oxidation and Charge Density, and Its Role in Oxidation Catalysis

Anna R. Ziefuß, Ina Haxhiaj, Stefan Müller, Mustafa Gharib, Olga Gridina, Christoph Rehbock, Indranath Chakraborty, Baoxiang Peng, Martin Muhler, Wolfgang J. Parak, Stephan Barcikowski,* and Sven Reichenberger

Cite This: J. Phys. Chem. C 2020, 124, 20981–20990

Read Online

ACCESS | Metrics & More | Article Recommendations | Supporting Information

ABSTRACT: Laser fragmentation in liquids (LFL) allows the synthesis of fully inorganic, ultrasmall gold nanoparticles, usAu NPs (<3 nm). Although the general method is well established, there is a lack of understanding the chemical processes that are triggered by the laser pulses, which may dictate the surface properties that are highly important in heterogeneous oxidation catalytic reactions. We observed the formation of radical oxygen species during LFL, which suggested that LFL is a physicochemical process that leads to particle size reductions and initiates oxidative processes. When the ionic strength in the nanoenvironment was increased, the oxidation of the first atomic layer saturated at 50%, whereby the surface charge density increases continuously. We found a correlation between the surface charge density after synthesis of colloidal nanoparticles and its behavior in catalysis. The properties of the laser-generated nanoparticles in the colloidal state appear to have predetermined the catalytic performance. We found that a smaller surface charge density of the usAu NPs was beneficial for the catalytic activity in CO and ethanol oxidation, while their peroxidase-like activity was affected less. The catalytic activity was 2 times higher for samples prepared by chloride-free LFL after ozone pretreatment compared to samples prepared in pure water.

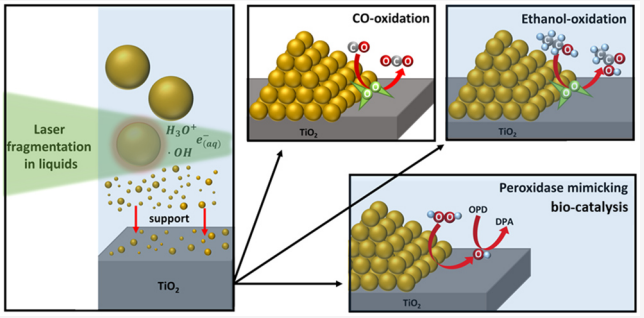

INTRODUCTION

During the past few decades, the synthesis of usAu NPs[1−5] has received increasing attention, which has been especially due to their unique optical and electronic properties that are of particular importance in the fields of biomedicine[1,2] and catalysis.[3−5] The surface properties of Au NPs are essential parameters because both the catalytic activity[4] and the cytotoxicity[6] are dictated by particle size and/or the related density of active sites on the surface of the catalyst as well as by other factors.[7,8] It is frequently reported that the catalytic activity in oxidation catalysis increases as the sizes of the Au NPs decrease on oxide supports, such as Au/TiO_2.[4,9−11] Also, it is generally accepted that the catalytic activity in selective oxidation reactions using reducible oxides, such as TiO_2, is caused by the active sites located at the interface between the Au NPs and the partially reduced (oxygen-deficient) surface of the TiO_2 support.[12,13] The charge transfer between the Au NPs and TiO_2 is promoted if the surfaces of the Au NPs are partially oxidized. For CO oxidation[8,14] and selective alcohol oxidation,[15] a high degree of surface oxidation and the small sizes of the Au NPs were also found to be beneficial.

The wet-chemical synthesis[16] of heterogeneous catalysts commonly is achieved by impregnation[17,18] or coprecipitation methods,[19−21] followed by calcination of the catalyst to remove surfactants and/or excess reduction media, both of which result in changes in the surface properties and/or specific surface area of the particles. In turn, the method of laser ablation in liquids (LAL) to prepare surfactant-free colloids and catalysts has been established as an alternative synthesis route.[22−24] Because of the synthesis-related electrostatic surface charges, quantitative adsorption of the laser-generated NPs on oxide-, carbon-, or metal-based supports with controllable mass load is possible.[22] Supported LAL-generated NPs were found to be catalytically active even without additional calcination steps.[5,22,25−29] Adding anions in micromolar concentrations to the ablation medium and/or adjustment of its pH value were shown to induce growth quenching of particles and their diameter could be tuned in the range of 6-30 nm.[30,31] In turn, the synthesis of surfactant-free, usAu NPs was recently achieved by using pulsed laser fragmentation in liquids (LFL).[32,33] In this process, the colloids that initially

Received: July 8, 2020
Revised: August 24, 2020
Published: August 24, 2020

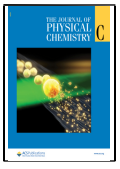

are prepared by laser ablation in water were fragmented into sub-3 nm particles by high-intensity picosecond-laser or nanaosecond-laser pulses using electrosteric (anionic) stabilizers to inhibit the growth of the particles.[34] This ion-mediated reduction in the size of the Au NPs at a constant mass concentration results in the Au NPs having a larger surface area[5,9] and a larger surface charge density, and it also has the potential to alter the total number of active sites, binding strength, and activation of the reactants on the surfaces of the NPs.[4,35] The adsorption of the laser-generated Au NPs to oxides supports potentially leads to strong metal−support interactions, especially when reducible oxides are used as the support materials.[36,37] Note, that the electrostatic double layer was reported to alter the charge transfer between the metal and the oxide support.[38] Because surface hydroxides and adsorbed ions (used for size-quenching) increase the density of the surface charge of the surfactant-free, laser-generated Au NPs, the hydration shell of laser-generated catalysts also should be considered in catalytic liquid-phase reactions.[39] Even so, the interplay between oxidation, anion adsorption, and size quenching during LFL, as well as the implications of the surface properties on laser-generated catalysts and the catalytic activity, remain unexplored. Note, that while the inhibiting effect (poisoning) by halides has been addressed extensively in the literature on oxidation catalysis, the concentrations of the halides used in laser-based synthesis always have been at the micromolar scale, which is far less than the concentrations used in poisoning studies.[40,41] Consequently, in the first part of this study, we aim to explore the extent to which surface properties, such as surface oxidation and surface charge density of surfactant-free (that is, free of any organic molecular adsorbates) usAu NPs gained by LFL, are altered by the presence of anions in micromolar concentration during LFL. Thus, the role of radical chain reactions started by the fragmentation process itself and the effect of oxidative pretreatment conducted with the Au NPs used for LFL will be considered. In the second part, the overall catalytic activity of synthesized usAu NPs will be evaluated in three catalytic model reactions directly after colloidal adsorption to nanoparticulate TiO_2 without any further pretreatments. The catalytic model reactions were chosen to address different types of reactions (gas vs liquid phase) such as CO oxidation (with O_2) in the gas phase, selective ethanol oxidation (with O_2) in an aqueous phase, and peroxidase-like reaction (with H_2O_2). To summarize, we will highlight that the surface charge density of laser-generated colloidal usAu NPs, which was predetermined during LFL in the colloidal state, affects multiple catalytic reactions, even after supporting and phase transfer.

MATERIALS AND METHODS

The Au NPs were produced by using the LAL and the subsequent LFL technique. In brief, 53 nm particles gained from LAL were used as educt material for the LFL process after dilution to 7.5 mg/L by using water that contains ionic additives as specified in Table S1 of the Supporting Information. The LFL was performed in a free liquid jet by using the second harmonics of an Nd:YAG laser with a pulse duration of 9 ns (100 Hz and 85 mJ). A detailed description has been provided in the first section of the Supporting Information.

Gas-Phase Oxidation of CO. The catalytic oxidation of CO was done in a microreactor at atmospheric pressure. A mixture consisting of 20 mg of Au/TiO_2 (255−350 μm sieve fraction) diluted in 80 mg of SiC was placed in a U-tube glass reactor. A gas mixture (96% He, 2% CO, and 2% O_2) flowed over the catalyst at the flow rate of 50 mL/min. First, the reactor was heated at the rate of 1 K/min to a temperature of 300 °C, and the reactor was held at this temperature for 1 h. Subsequently, the reactor was cooled to room temperature with a cooling rate of 1 K/min. A calibrated, two-channel, nondispersive IR detector (Hartmann & Braun, URAS 14) was used to measure the concentrations of CO and CO_2 in the effluent gas stream. The CO conversion was referenced to the total surface area of the usAu NPs present during resting. The latter was calculated from the mass load of gold on the TiO_2 (1 wt %), the mass of catalyst used during testing (20 mg, see above), and the specific surface area of the Au NPs from the size analyses of the respective samples.

Liquid-Phase Ethanol Oxidation. The liquid-phase ethanol oxidation was performed in a multiple reactor system (Parr 5000 series). In a typical run, each reactor was filled with 15 mL of a 3.3 wt % ethanol (absolute, Fisher Scientific U.K. Limited) aqueous solution and 100 mg of the catalyst. Then, the reactors were pressurized to 30 bar with synthetic air and were heated to 160 °C at a constant stirring speed of 350 rpm. After the reaction was allowed to proceed for 4 h, the reactors were cooled to 70 °C in air and then to <5 °C in an ice bath. After centrifugation to separate the catalyst, liquid samples were taken for quantitative GC analysis to analyze the ethanol conversion and the yield of acetic acid (product) and acetaldehyde and ethyl acetate (side-products). The GC measurement was performed by using a 7820 A GC system from Agilent Technologies equipped with an Agilent DB-WAX column (30 m × 0.25 mm × 0.25 μm) and an FID detector. Because the active sites were located in the perimeter and not fully understood yet, the yield of acetic acid (CH_3COOH) was referenced to the total reaction time and surface area of the Au NPs during testing. The latter was calculated from the mass load of gold on the TiO_2 (1 wt %), the mass of catalyst used during testing (100 mg, see above), and the specific surface area of the Au NPs based on the analysis of the sizes of the NPs in the sample. This reaction time and the Au NPs' surface-normalized yield of acetic acid were referenced to the term turnover frequency (TOF).

Peroxidase-like Catalytic Activity. The peroxidase-like activity of the Au/TiO_2 catalyst nanocomposites was assessed by investigating their ability to oxidize the almost colorless peroxidase substrate, *o*-phenylenediamine (OPD), in the presence of hydrogen peroxide (H_2O_2) to the yellow oxidized OPD product, 2,3-diaminophenazine (DAP). In a typical experiment, 250 μL of Au/TiO_2 (300 μg mL^{-1})[42] or 250 μL of horseradish peroxidase (HRP, 0.1 nM) was mixed with 3 mL of sodium acetate buffer (pH = 4) and H_2O_2 solution (284 mM, final concentration). Subsequently, the OPD substrate solution (2.9 mM, final concentration) was added, and the UV−vis absorption spectra were collected for 30 min while the reaction was performed at 37 °C. Control experiments were conducted by replacing the NPs with Milli-Q water. The reaction rates (V) of OPD oxidation, which corresponded to the amount of DAP produced in a unit time using the different Au/TiO_2 catalysts and different concentration of the substrates (OPD and H_2O_2), were calculated by plotting the absorption values at λ = 450 nm as a function of time, and then, the data points were fitted using a second-order polynomial fit. V was calculated by dividing the

https://dx.doi.org/10.1021/acs.jpcc.0c06257
J. Phys. Chem. C 2020, 124, 20981−20990

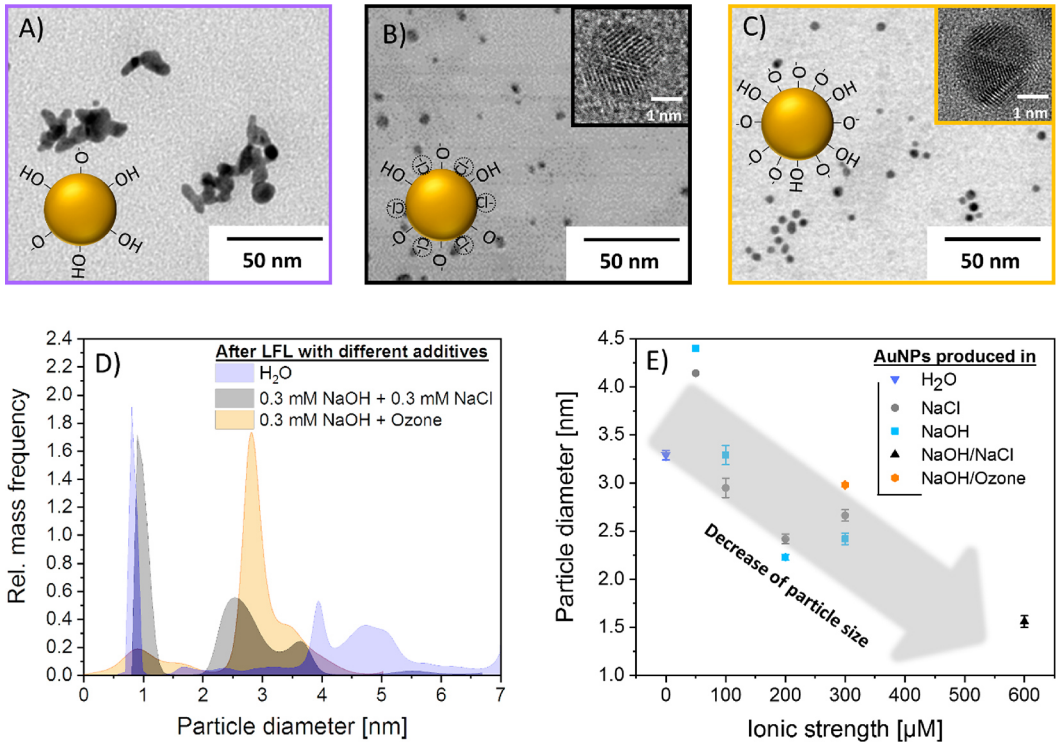

Figure 1. TEM images of respective Au NPs after LFL in (A) pure water, (B) 300 μM NaOH + 300 μM NaCl solution, and (C) 300 μM NaOH containing ozone. The inset is a corresponding sketch of the relevant stabilizing mechanisms of the additive that was used. (D) Corresponding mass-weighted size distributions measured by the AUC. (E) Effect of ionic strength on the diameters of the NPs obtained by LFL.

values of the regression coefficient (B_1) extracted from the quadratic equation (y = intercept + B_1x + B_2x^2) of the fit model by the extinction coefficient of DAP.

The steady-state kinetic parameters of the OPD oxidation reaction, K_m and V_{max}, were evaluated by plotting the reaction rate values that were obtained while varying the concentration of either the peroxidase substrate, OPD, or H_2O_2 and keeping the other two constant. The K_m and V_{max} values were generated after fitting the substrate concentration-dependent reaction rate curves to the Michaelis–Menten fit model.

RESULTS AND DISCUSSION

Laser fragmentation was performed starting from the colloidal educt Au NPs (53 nm) synthesized by LAL and subsequent centrifugation to attain the desired particle size fraction allowing particularly high fragmentation efficiency.[32,43,44] However, to produce usAu NPs and inhibit the growth of secondary particles, the addition of electrostatic stabilizers (anions, e.g., OH^- and Cl^-) improves the size quality and yield of LFL.[34] The anions discussed here either were adsorbed on the surfaces of the Au NPs[45] or they caused the pH-dependent deprotonation of hydroxide groups due to the partial oxidation caused by the laser synthesis, resulting in an increased charge density on the surfaces.[45] While the anionic species adsorbed on the surfaces of the particles had no influence on the optical absorption cross section, oxidation generally is known to affect the latter, and therefore it could influence the fragmentation efficiency and surface chemistry.[46−48] Overall, in this study we investigated usAu NPs prepared from educt Au NPs with two different oxidation degrees, i.e., 4% and 15% (Figure S1B), as well as different anionic additives at micromolar concentrations (compare experimental details in the Supporting Information).

Figure 1A shows that the LFL in ultrapure water (without inorganic additives) resulted in usAu NPs that were prone to ripening and coalescence. However, using inorganic additives (Figure 1B) or educt particles with higher surface oxidation (Figure 1C) yielded well-dispersed particles with far smaller particle sizes, well in line with the literature.[34] Figure 1D shows the exemplary particle size distribution measured by analytical ultracentrifugation (AUC) of the colloids, and the presence of multimodal particle size distributions is evident. Note, that AUC allowed the quantification of the size distribution with atomic precision (Δx < 0.1 nm) similar to the HR-TEM analysis and high statistical robustness, with more than 10^{13} NPs being detected during one measurement (assuming ~3 nm Au NPs diameter, a concentration of 7.5 mg/L, and an analyzed volume of 350 μL).[49] Further information about both methods are given in the Supporting Information (section II). To qualitatively compare the resulting distributions, we calculated the hydrodynamic diameter with respect to the mass-specific surface area of the usAu NPs determined from AUC results. (An example calculation is provided in the second section of the Supporting Information.) Figure 1E summarizes the results. As qualitatively deduced above, the addition of anions in the micromolar concentration regime indeed led to a significantly reduced mean particle diameter after LFL (Figure 1E). However, note that an excessive increase of ionic strength above several millimolar will cause colloidal instability due to cation-induced screening of the double layer, as reported previously.[34] Colloidal instability also can occur when the acidic ozone-enriched water is added, so that the maintaining neutral to alkaline pH values are important when pretreating the surfactant-free gold nanoparticles with ozone.

https://dx.doi.org/10.1021/acs.jpcc.0c06257
J. Phys. Chem. C 2020, 124, 20981−20990

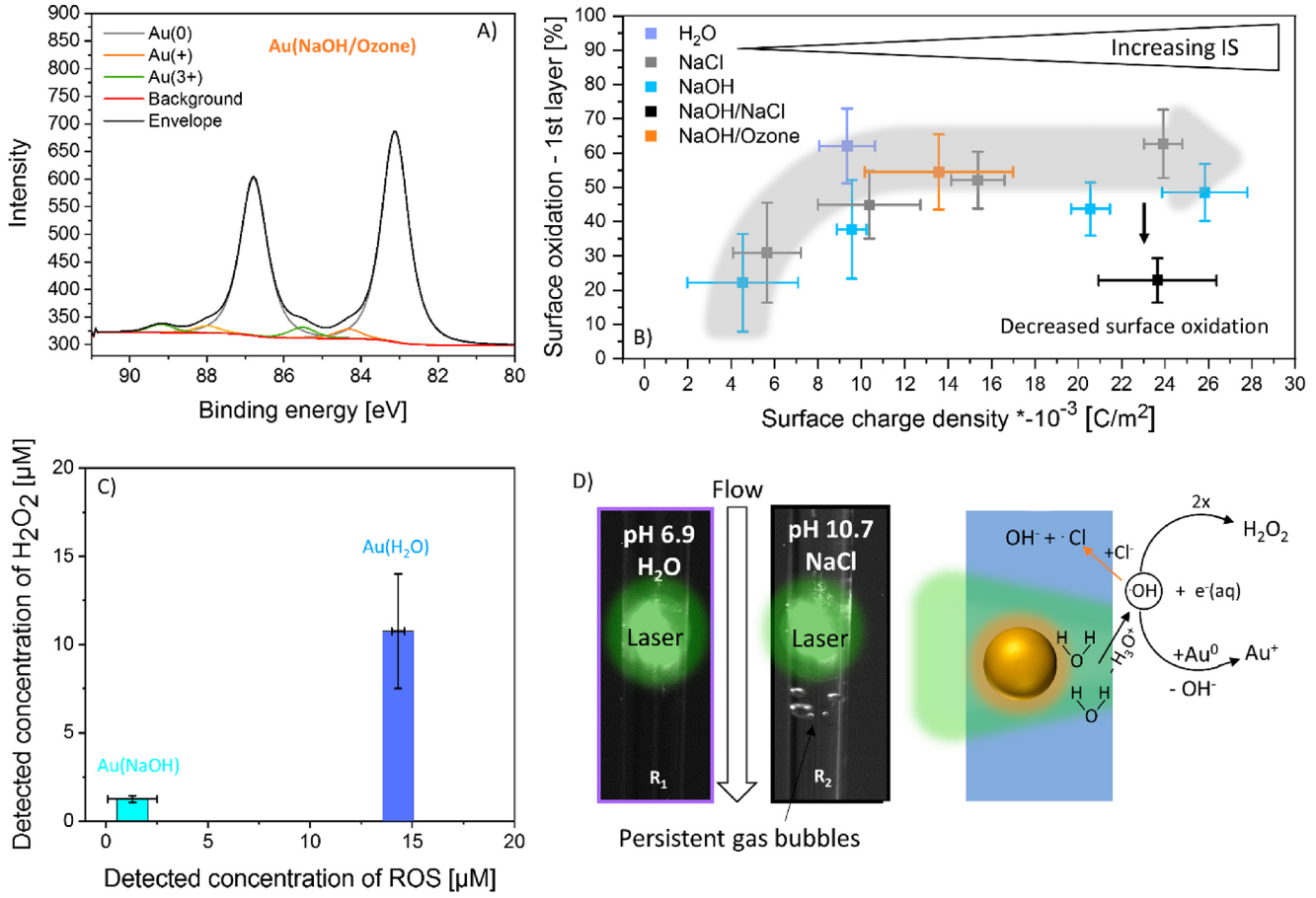

Figure 2. Characterization of radical-mediated surface properties of Au NPs after LFL. Exemplary XPS spectra of the sample in 0.3 mM NaOH/Ozone are shown in (A), whereby the relation between surface oxidation of the first atomic layer and surface charge density is printed in (B). (C) Detected concentration of H_2O_2 and ROS after LFL of Au NPs in H_2O and NaOH. (D) *In situ* image of LFL performed in a capillary to demonstrate the formation of persistent gas bubbles during LFL in NaOH/NaCl with the corresponding formation mechanism of radical species by photothermal ionization of water molecules according to eq 1.

Interestingly, Figure 1 shows that the preoxidation of the educt Au NPs before LFL only had a minor effect on the resulting particle size and/or was superimposed by the effect that anions with the same ionic strength tend to have. Consequently, and consistent with the previous literature, the presence of anions in the Gouy−Chapman layer surrounding the NPs[31,34] tailors the colloidal stability and growth tendencies of the Au NPs during the laser fragmentation process.[34] Also, according to Scanlon et al.,[38] the adsorption of anions on the surfaces of the Au NPs leads to an altered electron density distribution with a slightly positive Au surface, whereas electron density is increased at the interior of the particle. This affects both the zeta potential and the surface potential, which increases the Fermi level until an electrochemical equilibrium with the surrounding is reached.[38]

Hence, we investigated the surface chemistry of the Au NPs obtained after LFL more closely by X-ray photoelectron spectroscopy (XPS) and zeta potential measurements. The percentage of oxidized Au atoms on the Au NPs was quantified based on the XPS Au 4f region after deconvolution of the former into the respective individual contributions from Au^0, Au^+, and Au^{3+} (Figure 2A).

The percentage accounts for all atoms that contributed to the Au 4f peak. Because oxidized Au atoms will be located on the outer surface of the NPs, which is in contact with the surrounding environment, we converted the overall percentage of oxidation of the usAu NPs derived from XPS into the surface oxidation of the first atomic layer. Details on the calculation are described in the third section of the Supporting Information. Figure 2B summarizes the correlation between the surface oxidation of the first layer of Au NPs (XPS) with respect to the surface charge density of colloidal Au NPs (zeta potential). The latter was calculated according to Ohshima et al.[50] using the zeta potential measured at the slipping plane in a colloidal solution at pH 9. Evidently, at low surface charge densities (correlated to low ionic strengths of NaCl and NaOH), the surface oxidation and surface charge density appear to be linearly correlated. Here, the surface oxidation is linked directly to the formation of amphoteric hydroxides at oxidized gold atoms.[34,51] Consequently, the effect of adsorbing anions and the contribution of amphoteric hydroxides to the increasing surface charge density cannot be distinguished.

Yet, when the surface oxidation of the first atomic layer reaches about 50% (Figure 2B), further addition of anions continues to increase the surface charge density, while the surface oxidation after LFL remains constant. We attributed the increase of surface charge density to an accumulation of anions in the Helmholtz layer, considering that we calculated the former from the zeta potential at the slipping plane in a colloidal solution showing the same trend (Figure S5).[50] This is a clear indication that in the micromolar salinity regime investigated here, anion adsorption, not surface oxidation, is

https://dx.doi.org/10.1021/acs.jpcc.0c06257
J. Phys. Chem. C 2020, 124, 20981−20990

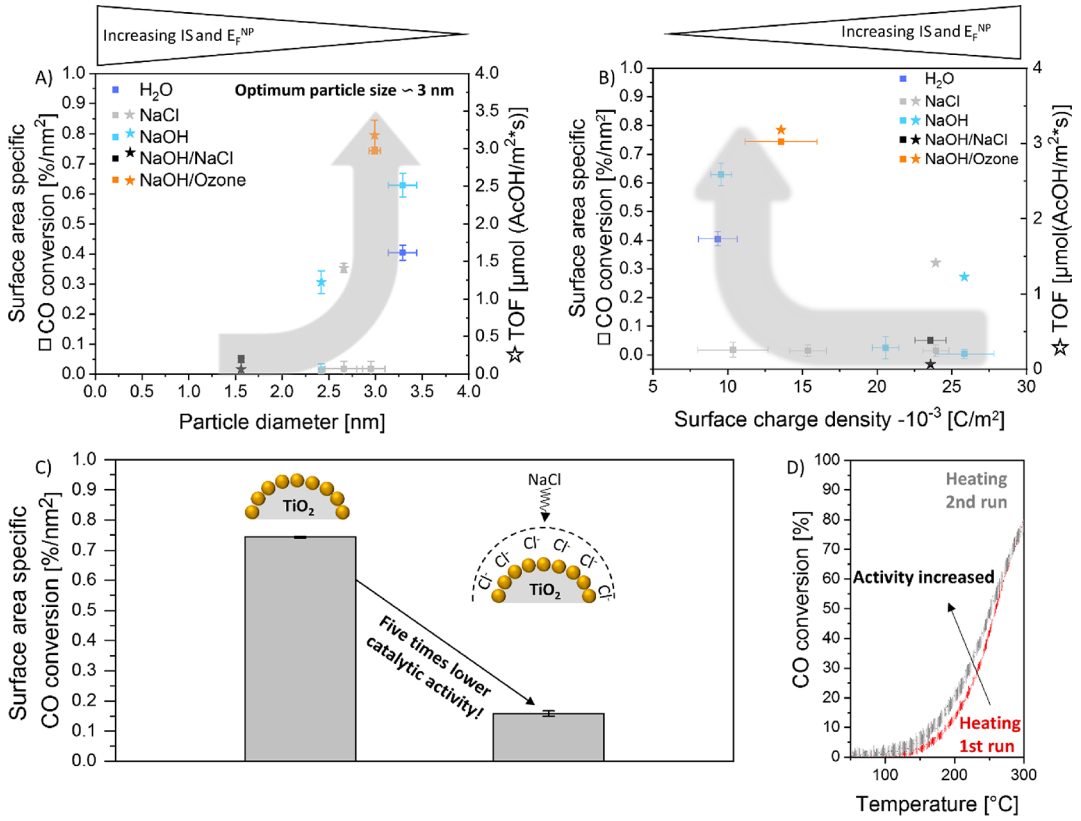

Figure 3. Surface area-specific CO conversion (squares) and turnover frequency (with respect to geometric UsAu NPs surface area), monitored during ethanol oxidation (stars) related to (A) particle diameter and (B) the surface charge density of the Au NPs. (C) Impact of chloride on the surface area-specific CO conversion. (D) CO conversion for catalyst prepared with Au NPs produced in NaOH/ozone monitored for two heating cycles.

the main mechanism that controls the high density of the surface charges of ligand-free NPs. An exception can be found for the sample produced in the presence of both NaOH and NaCl. As described by Ziefuss et al., both additives influence each other synergetically.[34] This is in agreement with the higher Fermi level that makes the Au NPs appear less noble after anion adsorption,[38] which will be discussed in detail in the following.

In accordance with the literature on optical breakdown-induced photochemical redox reactions and radical formation,[52] we investigated the role of reactive oxygen species (ROS) during the fragmentation of Au NPs. Radicals are likely induced through a two-step, multiphoton ionization from water molecules[53] at the surface of the Au NPs initiated by a thermally induced plasma during LFL (eq 1).[54,55]

$$H_2O \xrightarrow{h\nu} H_2O^+ + e^-_{(aq)} \xrightarrow{+H_2O} H_3O^+ + \cdot OH + e^-_{(aq)} \qquad (1)$$

Despite the short lifetime of the OH radicals (approximately nanoseconds), the oxidation of the surfaces of the Au NPs appears to be linked to their presence, providing a redox potential of 2.31 V,[56] which is more than 30% higher than the standard potential of Au^0.[57] Note that the temperature dependence of the oxidation potential is a potentially important aspect, too, as indicated in a previous general calculation performed in a recent review. These calculations showed a reduction of oxidation potential with increasing particle temperature.[22] By recombining two OH radicals, H_2O_2 is formed, which has a redox potential that is of the same order of magnitude as that for bulk Au.[58]

According to Scanlon et al., 500 negative charges on 10 nm Au NPs are sufficient to lower the standard potential to that of the H^+/H_2 redox couple.[38] Although the ionic strength of the added anions only is in the micromolar range, still a clear excess of the number of anions compared to the usAu NPs can be expected (>2000 anions per 3 nm Au NPs at 100 μM). Hence, we assume that it is likely that oxidation processes during LFL processing will be facilitated due to the reduced oxidation potential of Au NPs in the presence of adsorbed anions.

We determined the amounts of reactive oxygen species and H_2O_2 by using two commonly applied radical probes, i.e., 2,9-dimethyl-1,10-phenanthroline (DMP) for detecting H_2O_2[59] and dichlorofluorescein (DCF) to detect ROS.[60] Both are highly sensitive to light, so calibration of the optical signal after LFL in the aqueous solution (containing no Au NPs) was necessary (see the fourth section of the Supporting Information). Note that the ROS and H_2O_2 detection methods were biased in the presence of chloride, which most likely was due to a dissociation of the dyes by chlorine radicals.[61] Figure 2C shows drastic decreases in the concentrations of H_2O_2 and ROS when more hydroxide anions were present during the LFL process.

When chloride ions are present during LFL, radical chain reactions may lead to a production of chlorine radicals, thereby enabling additional termination reactions. The occurrence of persistent gas bubbles has only been observed in the presence of dissolved chloride ions, even at micromolar concentrations (Figure 2D). Similar observations also were discussed recently in terms of laser ablation studies,[55] where the persistent

https://dx.doi.org/10.1021/acs.jpcc.0c06257
J. Phys. Chem. C 2020, 124, 20981−20990

microbubbles contain oxygen and hydrogen in the stoichiometric composition of 1:2.[52] Hence, the persistent microbubbles, which do not occur in pure water but do occur when there are micromolar concentrations of Cl^- (Figure 2D), indicate an increased rate of redox reactions. In this context, the fate of the solvated electrons created photochemically (eq 1) also must be considered because they potentially can exhibit a non-negligible reduction potential.

When performing LFL in NaOH, a lower oxidation of the gained gold nanoparticles can be observed compared to pure water (Figure 2B). This is in line with solvated electrons being coordinated in basic solutions, which leads to a prolonged lifetime[62] and improves the likelihood to in turn reduce the partially oxidized gold surface after LFL in NaOH. On the basis of these findings, we concluded that LFL initiates oxidative processes both of the nanoparticle (surface) and inside the liquid (vapor) that are affected by the lifetime of the electrons and mediated by radicals. Hence, particle size, surface oxidation, and the surface charge density can be tuned during LFL of Au NPs by adding different ionic strengths of NaCl or NaOH as mediators of these reaction channels. This also explains why the extent of the oxidation of the educt particles is of minor importance.

We aimed to elucidate to what extent these particle surface properties determined in the colloidal state correlate with their activity in three different catalytic model reactions performed in different reaction media after supporting them on titania. The surfactant-free usAu NPs obtained by LFL were adsorbed on TiO_2 (P25) with 1 wt % mass loading and used without further calcination. First, two oxidation model reactions were examined, i.e., CO oxidation performed in the gas phase and selective ethanol oxidation performed in the liquid phase. The individual catalytic runs for CO oxidation are summarized in the fifth section of the Supporting Information (Figure S9). Concerning Figure 3A, the highest Au surface area-related CO conversion and TOF in selective ethanol oxidation (time- and gold surface area-normalized formation of acetic acid; see the Materials and Methods section) was observed for the usAu NPs that were pretreated in ozone-saturated water, yielding a particle diameter of around 3 nm. Interestingly, Figure 3A shows that for both reactions the catalytic activity decreased exponentially as the particle size decreased. Note that the decrease of activity was significantly more pronounced for gaseous CO oxidation than for selective ethanol oxidation conducted in the liquid phase. While decreases in the sizes of the NPs (even down to single atoms) commonly are associated with improved catalytic activity,[11,63] CO oxidation has been reported to be inhibited when atom cluster-sized particles were used.[64,65] Via Raman studies, such size effects were linked directly to a decreasing adsorption rate of CO on Au (following Au_{Atom} < $Au_{Cluster}$ < Au NPs) correlated to an increasing Au oxidation degree with Au_{Atom} > $Au_{Cluster}$ > Au NPs measured by *in situ* X-ray absorption fine structure (XANES)[64] and *in situ* diffuse reflectance infrared Fourier transformation spectroscopy (DRIFTS) studies.[66]

While these examples address the effect of particle size-dependent surface oxidation on catalytic reactivity, Figure 2B shows that we also found a correlation between surface oxidation and surface charge density for our colloidal Au NPs. Figure 3B indicates that samples prepared from Au NPs that possessed a high surface charge density had rather low oxidation activity in gas-phase CO and liquid-phase ethanol oxidation. Apart from the well-described importance of the perimeter at the contact of Au NPs and TiO_2,[67] it has been reported previously that the hydration shell is crucial for oxygen activation (hydrated proton transfer to O_2) and hence hydrocarbon oxidation in the liquid phase.[39] Interestingly, even in the gaseous phase reaction that was conducted without extensive drying (meaning there was a possibility of remaining water molecules), the surface charge density of the usAu NPs that was measured in the colloidal form before adsorption on TiO_2 was correlated directly with the catalytic activity. Although small NPs generally are favored concerning the high specific surface area,[68] the present results with laser-generated NPs indicated that the surface charge density of Au NPs gained by LFL should not exceed $(13.6 \pm 2.4) \times 10^{-3}$ C/m^2 to obtain sufficiently active catalysts. The results in Figure 3B for the oxidation of CO and ethanol appear to follow a volcano-like trend concerning the surface charge density when no halides were present during the synthesis. Additional theoretical studies are required to validate this trend.

To date, our results have shown that an optimal ratio between surface charge density and particle diameter is required to ensure high catalytic activity. Interestingly, this condition should also apply to particles produced in the presence of NaCl, which, however, shows intermediate activity for ethanol oxidation but no activity during CO oxidation, irrespective of the density of the surface charge. While chloride acted as an efficient size quencher during LFL, the absence of any CO oxidation activity is linked in the literature to the well-accepted, but surprisingly rarely published, effect of halides, such as Cl^-, acting as catalytic poisons during CO oxidation over Au-based catalysts.[69] The deactivating effect of Cl^- was much less pronounced during the oxidation of ethanol. The fact that the reaction was performed in the liquid phase probably led to washing of the catalyst, which significantly reduced the chloride content on the surfaces of Au NPs surface during the reaction. At this point, it is important to mention that our catalysts were used directly and without further calcination or washing steps.

To exclude the influence of the particle diameter and highlight the inhibiting effect of Cl^- in a more suitable way, we also recorded the CO conversion of Au NPs produced by LFL after incubation of educt Au NPs with ozone and subsequent addition of 0.3 mM NaCl after LFL followed by supporting the Au NPs on TiO_2 to obtain the final catalyst. Figure 3C shows that the addition of 0.3 mM NaCl was enough to decrease the catalytic activity during CO oxidation by a factor of 5, which can be assigned directly to the poisoning effect of chloride.[40,41] In turn, the sample prepared in ozone-saturated water without the addition of chloride had the highest catalytic activity. This observation highlights the important role of oxidative LFL, both to yield usAu NPs increasing the colloidal stability through the partial surface oxidation without chloride and to guarantee the high purity of the contaminant-free catalysts and hence ensure appropriate catalytic activity.

Again, we want to highlight that the Au/TiO_2 catalyst prepared by using Au NPs pretreated in NaOH/ozone before LFL had more than double the activity compared with the catalyst prepared without ozone pretreatment, and it also showed good recycle stability and even a slightly higher activity for CO oxidation (Figure 3D). The better stability indicates that the ligand-free usAu NPs are anchored strongly on the TiO_2 support, which hinders rapid aging in the first run. Further stability-oriented studies are still required to conduct a more detailed investigation. While the previous reactions were

https://dx.doi.org/10.1021/acs.jpcc.0c06257
J. Phys. Chem. C 2020, 124, 20981−20990

performed with oxygen as the oxidant, we also investigated how the trends changed when using other oxidizing agents, such as H_2O_2. Hence, a peroxidase-mimicking experiment was conducted since Au NPs are known for such enzyme-mimicking activities in the presence of H_2O_2.[70,71] The peroxidase-like activity of NPs was evaluated by measuring the ability of the NPs to oxidize the typical peroxidase substrate, *o*-phenylenediamine (OPD), which is colorless, into the yellow-orange 2,3-diaminophenazine (DAP) in the presence of hydrogen peroxide (H_2O_2).[72,73] The catalytic oxidation reaction of OPD molecules proceeds after the enhanced decomposition of H_2O_2 on the surfaces of Au/TiO_2 catalysts, leading to the formation of the highly oxidizing OH radicals. The OH radicals initiate a radical chain reaction, during which OPD radicals are formed, which ultimately are transformed into DAP.[73] The time-dependent formation of DAP was monitored to calculate the rate constant of this peroxidase-mimicking reaction. The steady-state kinetic parameters (such as the Michaelis–Menten constant (K_m) and the maximum reaction velocity (V_{max})) were evaluated by using the rate equation.[73] The value of K_m reflects the affinity of an enzyme (or a compound an enzyme mimic) to its substrate(s), and V_{max} denotes the maximum catalytic activity exhibited by an enzyme during the saturation with its substrate(s). Our results indicated that both parameters (K_m and V_{max}) have a clear dependence of the peroxidase-like catalytic reaction on the particle size and surface charge density of the Au NPs used during the catalytic oxidation reaction of OPD, which is consistent with the catalytic reactions discussed previously. In contrast to the previous results on CO and ethanol oxidation with oxygen, Figure 4 shows that usAu NPs that have a high surface charge density also have enhanced peroxidase-like activity, as indicated by the relatively higher V_{max} values and lower K_m values. Interestingly, the sample that was prepared by LFL in ozone-saturated water again showed high activity, but it seems that Cl^- poisoning did not occur.

Hence, for the preparation of a biocatalyst, either chloride or ozone can be added to induce surface oxidation and increased surface charge density to reduce the effective diameter of the particles. The relative enhancement of the catalytic parameters in the case of smaller NPs with high surface charge density seems to be linked to the increased specific surface-to-volume ratio, which favors more binding sites for H_2O_2, thereby controlling its decomposition and enhancing the oxidation of OPD.

CONCLUSION

The laser-based synthesis of ultrasmall Au NPs by LFL and the subsequent colloidal adsorption of the Au NPs on TiO_2 results in catalysts that have a unique surface chemistry. As shown in this paper, anionic additives (NaOH and/or NaCl) at micromolar concentrations decreased the gained size of the usAu NPs (<3 nm) and increased their surface oxidation and colloidal surface charge density. We found evidence for the OH radical-mediated oxidation of the surfaces of the Au NPs after LFL, which affected the surface oxidation and charge density of the usAu NPs that were obtained. We found that the surface charge density of the usAu NPs had a linear correlation with the oxidation of the surface when the ionic strength was increasing in the micromolar regime. Above 50% oxidation of the first atomic gold layer, only the accumulation of anions that acted as surface adsorbates increased the surface charge density (zeta potential) further and, hence, also increased the work function of the usAu NPs colloids, while the surface oxidation remained constant.

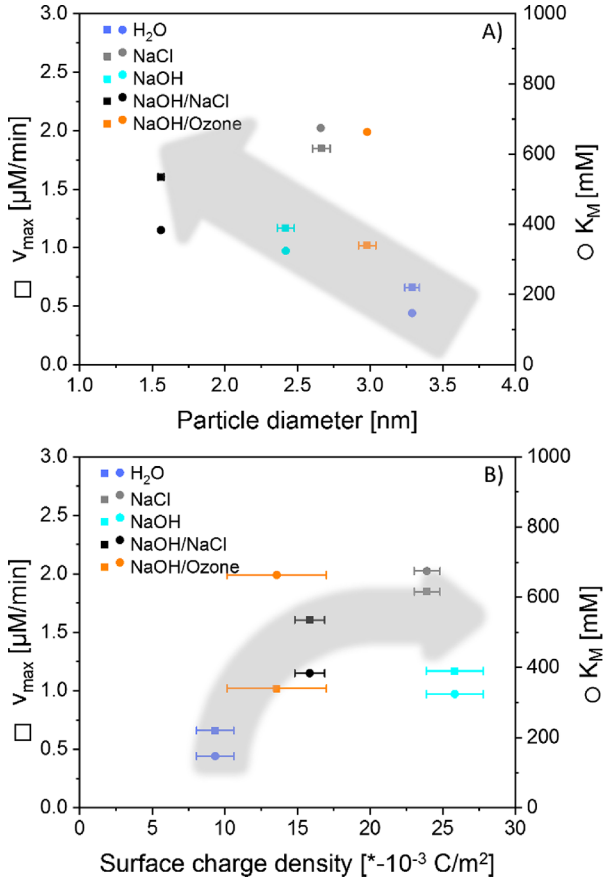

Figure 4. Steady-state kinetics of the enzyme-like catalytic oxidation of OPD into DAP in the presence of H_2O_2 by using Au/TiO_2 catalysts with different particle sizes (A) and surface charge densities (B). Anions used during the laser-based synthesis of the catalysts are indicated in the legends of the graphs.

Initially, active usAu NPs/TiO_2 catalysts were synthesized from the colloidal adsorption of usAu NPs on colloidal TiO_2 after drying (<100 °C) but without any calcination required or performed. Considering three different oxidation model reactions, we found that smaller sizes (<3 nm) of the usAu NPs obtained by LFL did not correlate with the higher activity of the Au/TiO_2 catalyst in the gas-phase CO and selective liquid-phase ethanol oxidation as one would also expect considering the general trends in the literature. Interestingly, extensive catalytic activity was found when the surface charge density of the laser-generated colloidal usAu NPs before adsorption on TiO_2 was in the range of $(13.6 \pm 2.4) \times 10^{-3}$ C/m^2, but higher values appeared to be detrimental for the oxidation of CO and ethanol. Micromolar concentrations of halides had a similar poisoning effect. Generally, there is agreement concerning the latter, although most studies have been done with millimolar or molar halide concentrations. The highest catalytic activity was observed in the case of the chloride-free size quenching by ozone pretreatment of the educt Au NPs, and the activity was about 2 times higher than the sample gained by the LFL of the untreated samples. In this case, ozone pretreatment resulted in surface oxidation of the Au NPs prior to LFL that was more than 3 times higher than the oxidation without ozone pretreatment. Contrary to the previously discussed oxidation reactions, we found an

https://dx.doi.org/10.1021/acs.jpcc.0c06257
J. Phys. Chem. C 2020, 124, 20981–20990

enhanced turnover frequency for the peroxidase-like oxidation conducted with the same catalysts when using Au NPs that obtained a high surface charge density in the colloidal state. Chloride had no impeding effect in this case, and catalysts were obtained that were as active as the catalysts after ozone treatment.

To summarize, this study provides evidence that LFL initiates oxidative process driven by OH-radical species. In this study, the surface oxidation and surface charge density of colloidal usAu NPs gained by LFL were found to be linked and driven by the anionic additives used for size-quenching purposes. In addition, both the surface charge density of the laser-generated, colloidal Au NPs and the presence of anions were found to affect the catalytic activity ambivalently. Our findings could lead to an improved, laser-based catalyst design in which catalytic activity is predetermined by synthesis parameters in the colloidal state. Further consideration of the density of the surface charge in theoretical studies and how the former affects the adsorption strength of educts and products in heterogeneous catalysis were beyond the scope of this publication. Laser fragmentation in the presence of anionic additives or by using ozone-pretreated educt Au NPs provides a unique set of routes to synthesize initially active, size, and surface property-selected NPs for catalytic studies. Other material systems, such as alloy NPs, will be ideal candidates for future studies.

■ ASSOCIATED CONTENT

Supporting Information

The Supporting Information is available free of charge at https://pubs.acs.org/doi/10.1021/acs.jpcc.0c06257.

Section I: laser-based synthesis of ligand-free gold nanoclusters (Figure S1: overview of the educt Au NP size distribution and surface oxidation from XPS before and after ozone treatment; Table S1: concentrations of additive added before LFL; Figure S2: change of ozone concentration during treatment of AuNP over time); section II: particle size characterization (Figure S3: mass-weighted hydrodynamic Au NP diameter after LFL in the presence of ionic additives; Figure S4: size histograms of corresponding to the TEM images in Figure 2 C,D); section III: calculation of surface oxidation and surface charge density based on the XPS and zeta potential (Figure S5: zeta potential of all AuNP colloids presented in Figure 1E; Table S2: summary of constants and assumption used to calculate the oxidation of the first atomic layer; Figure S5: Au 4f signals (XPS) and pH-dependent titrations of the zeta potential of the samples presented in Figure 2C,D); section IV: correlation between the emission intensity of DCF and H_2O_2 concentration (Figure S7: titration of DCF and DCFH with H_2O_2 to calibrate the optical emission intensity and radical concentration); section V: catalytic raw data (Figure S8: CO conversion; Figures S9–S12: peroxidase reaction) (PDF)

■ AUTHOR INFORMATION

Corresponding Author

Stephan Barcikowski − *Department of Technical Chemistry I, University of Duisburg-Essen and Center for Nanointegration Duisburg-Essen (CENIDE), Essen, Germany;* orcid.org/0000-0002-9739-7272; Email: stephan.barcikowski@uni-due.de

Authors

Anna R. Ziefuß − *Department of Technical Chemistry I, University of Duisburg-Essen and Center for Nanointegration Duisburg-Essen (CENIDE), Essen, Germany*

Ina Haxhiaj − *Department of Technical Chemistry I, University of Duisburg-Essen and Center for Nanointegration Duisburg-Essen (CENIDE), Essen, Germany*

Stefan Müller − *Laboratory of Industrial Chemistry, Ruhr-University Bochum, Bochum, Germany*

Mustafa Gharib − *Department of Physics and Center for Hybrid Nanostructure (CHyN), University of Hamburg, Hamburg, Germany*

Olga Gridina − *Department of Technical Chemistry I, University of Duisburg-Essen and Center for Nanointegration Duisburg-Essen (CENIDE), Essen, Germany*

Christoph Rehbock − *Department of Technical Chemistry I, University of Duisburg-Essen and Center for Nanointegration Duisburg-Essen (CENIDE), Essen, Germany;* orcid.org/0000-0002-4708-5246

Indranath Chakraborty − *Department of Physics and Center for Hybrid Nanostructure (CHyN), University of Hamburg, Hamburg, Germany;* orcid.org/0000-0003-4195-9384

Baoxiang Peng − *Laboratory of Industrial Chemistry, Ruhr-University Bochum, Bochum, Germany*

Martin Muhler − *Laboratory of Industrial Chemistry, Ruhr-University Bochum, Bochum, Germany;* orcid.org/0000-0001-5343-6922

Wolfgang J. Parak − *Department of Physics and Center for Hybrid Nanostructure (CHyN), University of Hamburg, Hamburg, Germany;* orcid.org/0000-0003-1672-6650

Sven Reichenberger − *Department of Technical Chemistry I, University of Duisburg-Essen and Center for Nanointegration Duisburg-Essen (CENIDE), Essen, Germany*

Complete contact information is available at: https://pubs.acs.org/10.1021/acs.jpcc.0c06257

Notes

The authors declare no competing financial interest.

■ ACKNOWLEDGMENTS

We gratefully acknowledge the Deutsche Forschungsgemeinschaft (DFG) for its financial support under Projects BA 3580/22-1 and PA 794/28-1. M.M., S.B., and S.R. further acknowledge funding of the project CRC 247, subproject C5, grant number 388390466, by the Deutsche Forschungsgemeinschaft. I.H. thanks the German Federal Environment Foundation (DBU) for financial support. The authors thank Jurij Jacobi for support in TEM. We further acknowledge Anton Plech and Stefan Reich for support in recording *in situ* images during LFL.

■ REFERENCES

(1) Das, N. K.; Ghosh, S.; Priya, A.; Datta, S.; Mukherjee, S. Luminescent Copper Nanoclusters as a Specific Cell-Imaging Probe and a Selective Metal Ion Sensor. *J. Phys. Chem. C* **2015**, *119*, 24657−24664.

(2) Zheng, K.; Setyawati, M. I.; Leong, D. T.; Xie, J. Antimicrobial Gold Nanoclusters. *ACS Nano* **2017**, *11*, 6904−6910.

(3) Heeskens, D.; Aghaei, P.; Kaluza, S.; Strunk, J.; Muhler, M. Selective Oxidation of Ethanol in the Liquid Phase Over Au/TiO2. *Phys. Status Solidi B* **2013**, *250*, 1107−1118.
(4) Hvolbæk, B.; Janssens, T. V.W.; Clausen, B. S.; Falsig, H.; Christensen, C. H.; Nørskov, J. K. Catalytic Activity of Au Nanoparticles. *Nano Today* **2007**, *2*, 14−18.
(5) Dong, W.; Reichenberger, S.; Chu, S.; Weide, P.; Ruland, H.; Barcikowski, S.; Wagener, P.; Muhler, M. The Effect of the Au Loading on the Liquid-Phase Aerobic Oxidation of Ethanol Over Au/TiO_2 Catalysts Prepared by Pulsed Laser Ablation. *J. Catal.* **2015**, *330*, 497−506.
(6) Pan, Y.; Neuss, S.; Leifert, A.; Fischler, M.; Wen, F.; Simon, U.; Schmid, G.; Brandau, W.; Jahnen-Dechent, W. Size-Dependent Cytotoxicity of Gold Nanoparticles. *Small* **2007**, *3*, 1941−1949.
(7) Campbell, C. T. Physics. The Active Site in Nanoparticle Gold Catalysis. *Science* **2004**, *306*, 234−235.
(8) Schlögl, R. Catalysis 4.0. *ChemCatChem* **2017**, *9*, 533−541.
(9) Shao, B.; Zhang, J.; Huang, J.; Qiao, B.; Su, Y.; Miao, S.; Zhou, Y.; Li, D.; Huang, W.; Shen, W. Size-Dependency of Gold Nanoparticles on TiO2 for CO Oxidation. *Small Methods* **2018**, *2*, 1800273.
(10) Haruta, M. Spiers Memorial Lecture. Role of Perimeter Interfaces in Catalysis by Gold Nanoparticles. *Faraday Discuss.* **2011**, *152*, 11.
(11) Haruta, M. When Gold is not Noble: Catalysis by Nanoparticles. *Chem. Rec.* **2003**, *3*, 75−87.
(12) Farnesi Camellone, M.; Marx, D. Nature and Role of Activated Molecular Oxygen Species at the Gold/Titania Interface in the Selective Oxidation of Alcohols. *J. Phys. Chem. C* **2014**, *118*, 20989−21000.
(13) Tosoni, S.; Pacchioni, G. Oxide-Supported Gold Clusters and Nanoparticles in Catalysis: A Computational Chemistry Perspective. *ChemCatChem* **2019**, *11*, 73−89.
(14) Klyushin, A. Y.; Greiner, M. T.; Huang, X.; Lunkenbein, T.; Li, X.; Timpe, O.; Friedrich, M.; Hävecker, M.; Knop-Gericke, A.; Schlögl, R. Is Nanostructuring Sufficient To Get Catalytically Active Au? *ACS Catal.* **2016**, *6*, 3372−3380.
(15) Pakrieva, E.; Ribeiro, A. P. C.; Kolobova, E.; Martins, L. M. D. R. S.; Carabineiro, S. A. C.; German, D.; Pichugina, D.; Jiang, C.; Pombeiro, A. J. L.; Bogdanchikova, N. Supported Gold Nanoparticles as Catalysts in Peroxidative and Aerobic Oxidation of 1-Phenylethanol under Mild Conditions. *Nanomaterials* **2020**, *10*, 151.
(16) Xia, Y.; Xiong, Y.; Lim, B.; Skrabalak, S. E. Shape-Controlled Synthesis of Metal Nanocrystals: Simple Chemistry Meets Complex Physics? *Angew. Chem., Int. Ed.* **2009**, *48*, 60−103.
(17) Masoud, N.; Delannoy, L.; Schaink, H.; van der Eerden, A.; de Rijk, J. W.; Silva, T. A. G.; Banerjee, D.; Meeldijk, J. D.; de Jong, K. P.; Louis, C.; et al. Superior Stability of Au/SiO_2 Compared to Au/TiO_2 Catalysts for the Selective Hydrogenation of Butadiene. *ACS Catal.* **2017**, *7*, 5594−5603.
(18) Alshammari, A.; Köckritz, A.; Kalevaru, V. N.; Bagabas, A.; Martin, A. Potential of Supported Gold Bimetallic Catalysts for Green Synthesis of Adipic Acid from Cyclohexane. *Top. Catal.* **2015**, *58*, 1069−1076.
(19) Liu, Y.; Jia, C.-J.; Yamasaki, J.; Terasaki, O.; Schüth, F. Highly Active Iron Oxide Supported Gold Catalysts for CO Oxidation: How Small Must the Gold Nanoparticles be? *Angew. Chem., Int. Ed.* **2010**, *49*, 5771−5775.
(20) Kung, H. H.; Kung, M. C.; Costello, C. K. Supported Au catalysts for low temperature CO oxidation. *J. Catal.* **2003**, *216*, 425−432.
(21) Zhang, J.; Wang, H.; Wang, L.; Ali, S.; Wang, C.; Wang, L.; Meng, X.; Li, B.; Su, D. S.; Xiao, F.-S. Wet-Chemistry Strong Metal-Support Interactions in Titania-Supported Au Catalysts. *J. Am. Chem. Soc.* **2019**, *141*, 2975−2983.
(22) Reichenberger, S.; Marzun, G.; Muhler, M.; Barcikowski, S. Perspective of Surfactant-Free Colloidal Nanoparticles in Heterogeneous Catalysis. *ChemCatChem* **2019**, *11*, 4489−4518.
(23) Zeng, H.; Du, X.-W.; Singh, S. C.; Kulinich, S. A.; Yang, S.; He, J.; Cai, W. Nanomaterials via Laser Ablation/Irradiation in Liquid: A Review. *Adv. Funct. Mater.* **2012**, *22*, 1333−1353.
(24) Scaramuzza, S.; Zerbetto, M.; Amendola, V. Synthesis of Gold Nanoparticles in Liquid Environment by Laser Ablation with Geometrically Confined Configurations: Insights To Improve Size Control and Productivity. *J. Phys. Chem. C* **2016**, *120*, 9453−9463.
(25) Haxhiaj, I.; Tigges, S.; Firla, D.; Zhang, X.; Hagemann, U.; Kondo, T.; Nakamura, J.; Marzun, G.; Barcikowski, S. Platinum Nanoparticles Supported on Reduced Graphene Oxide Prepared in Situ by a Continuous One-Step Laser Process. *Appl. Surf. Sci.* **2019**, *469*, 811−820.
(26) Zhang, J.; Chen, G.; Chaker, M.; Rosei, F.; Ma, D. Gold Nanoparticle Decorated Ceria Nanotubes with Significantly High Catalytic Ativity for the Reduction of Nitrophenol and Mechanism Study. *Appl. Catal., B* **2013**, *132*−*133*, 107−115.
(27) Vassalini, I.; Borgese, L.; Mariz, M.; Polizzi, S.; Aquilanti, G.; Ghigna, P.; Sartorel, A.; Amendola, V.; Alessandri, I. Enhanced Electrocatalytic Oxygen Evolution in Au-Fe Nanoalloys. *Angew. Chem., Int. Ed.* **2017**, *56*, 6589−6593.
(28) Lv, J.; Wu, S.; Tian, Z.; Ye, Y.; Liu, J.; Liang, C. Construction of PdO−Pd Interfaces Assisted by Laser Irradiation for Enhanced Electrocatalytic N2 Reduction Reaction. *J. Mater. Chem. A* **2019**, *7*, 12627−12634.
(29) Kohsakowski, S.; Streubel, R.; Radev, I.; Peinecke, V.; Barcikowski, S.; Marzun, G.; Reichenberger, S. First PEM Fuel Cell Based on Ligand-Free, Laser-Generated Platinum Nanoparticles. *Appl. Surf. Sci.* **2019**, *467*−*468*, 486−492.
(30) Itina, T. E. Ultra-Short Laser Interactions with Nanoparticles in Different Media: from Electromagnetic to Thermal and Electrostatic Effects. *Proc. SPIE* **2017**, 100930A.
(31) Rehbock, C.; Merk, V.; Gamrad, L.; Streubel, R.; Barcikowski, S. Size Control of Laser-Fabricated Surfactant-Free Gold Nanoparticles with Highly Diluted Electrolytes and their Subsequent Bioconjugation. *Phys. Chem. Chem. Phys.* **2013**, *15*, 3057−3067.
(32) Ziefuß, A. R.; Reichenberger, S.; Rehbock, C.; Chakraborty, I.; Gharib, M.; Parak, W. J.; Barcikowski, S. Laser Fragmentation of Colloidal Gold Nanoparticles with High-Intensity Nanosecond Pulses is Driven by a Single-Step Fragmentation Mechanism with a Defined Educt Particle-Size Threshold. *J. Phys. Chem. C* **2018**, *122*, 22125−22136.
(33) Ziefuss, A. R.; Reich, S.; Reichenberger, S.; Levantino, M.; Plech, A. In Situ Structural Kinetics of Picosecond Laser-Induced Heating and Fragmentation of Colloidal Gold Spheres. *Phys. Chem. Chem. Phys.* **2020**, *22*, 4993−5001.
(34) Ziefuß, A. R.; Barcikowski, S.; Rehbock, C. Synergism between Specific Halide Anions and pH Effects during Nanosecond Laser Fragmentation of Ligand-Free Gold Nanoparticles. *Langmuir* **2019**, *35*, 6630−6639.
(35) Zhang, X.; Shi, H.; Xu, B.-Q. Catalysis by Gold: Isolated Surface Au3+ Ions are Active Sites for Selective Hydrogenation of 1,3-Butadiene over Au/ZrO2 Catalysts. *Angew. Chem., Int. Ed.* **2005**, *44*, 7132−7135.
(36) Farnesi Camellone, M.; Zhao, J.; Jin, L.; Wang, Y.; Muhler, M.; Marx, D. Molecular Understanding of Reactivity and Selectivity for Methanol Oxidation at the Au/TiO_2 Interface. *Angew. Chem., Int. Ed.* **2013**, *52*, 5780−5784.
(37) Widmann, D.; Behm, R. J. Active Oxygen on a Au/TiO_2 Catalyst: Formation, Stability, and CO Oxidation Activity. *Angew. Chem., Int. Ed.* **2011**, *50*, 10241−10245.
(38) Scanlon, M. D.; Peljo, P.; Méndez, M. A.; Smirnov, E.; Girault, H. H. Charging and Discharging at the Nanoscale: Fermi Level Equilibration of Metallic Nanoparticles. *Chem. Sci.* **2015**, *6*, 2705−2720.
(39) Muñoz-Santiburcio, D.; Farnesi Camellone, M.; Marx, D. Solvation-Induced Changes in the Mechanism of Alcohol Oxidation at Gold/Titania Nanocatalysts in the Aqueous Phase versus Gas Phase. *Angew. Chem., Int. Ed.* **2018**, *57*, 3327−3331.

https://dx.doi.org/10.1021/acs.jpcc.0c06257
J. Phys. Chem. C 2020, 124, 20981−20990

(40) Diao, P.; Wang, J.; Zhang, D.; Xiang, M.; Zhang, Q. The Effect of Halide Ions on the Electrooxidation of CO on Gold Particles Supported by Indium Tin Oxide. *J. Electroanal* **2009**, *630*, 81−90.
(41) Chandler, B. D.; Kendell, S.; Doan, H.; Korkosz, R.; Grabow, L. C.; Pursell, C. J. NaBr Poisoning of Au/TiO2 Catalysts: Effects on Kinetics, Poisoning Mechanism, and Estimation of the Number of Catalytic Active Sites. *ACS Catal.* **2012**, *2*, 684−694.
(42) Peng, X.; Wan, G.; Wu, L.; Zeng, M.; Lin, S.; Wang, G. Peroxidase-Like Activity of Au@TiO_2 Yolk-Shell Nanostructure and its Application for Colorimetric Detection of H_2O2 and Glucose. *Sens. Actuators, B* **2018**, *257*, 166−177.
(43) Amendola, V.; Amans, D.; Ishikawa, Y.; Koshizaki, N.; Scirè, S.; Compagnini, G.; Reichenberger, S.; Barcikowski, S. Room-Temperature Laser Synthesis in Liquid of Oxide, Metal-Oxide Core-Shells, and Doped Oxide Nanoparticles. *Chem. - Eur. J.* **2020**, *26*, 1−38.
(44) Delfour, L.; Itina, T. E. Mechanisms of Ultrashort Laser-Induced Fragmentation of Metal Nanoparticles in Liquids: Numerical Insights. *J. Phys. Chem. C* **2015**, *119*, 13893−13900.
(45) Merk, V.; Rehbock, C.; Becker, F.; Hagemann, U.; Nienhaus, H.; Barcikowski, S. In situ non-DLVO Stabilization of Surfactant-Free, Plasmonic Gold Nanoparticles: Effect of Hofmeister's Anions. *Langmuir* **2014**, *30*, 4213−4222.
(46) Metwally, K.; Mensah, S.; Baffou, G. Fluence Threshold for Photothermal Bubble Generation Using Plasmonic Nanoparticles. *J. Phys. Chem. C* **2015**, *119*, 28586−28596.
(47) Jain, P. K.; Lee, K. S.; El-Sayed, I. H.; El-Sayed, M. A. Calculated Absorption and Scattering Properties of Gold Nanoparticles of Different Size, Shape, and Composition: Applications in Biological Imaging and Biomedicine. *J. Phys. Chem. B* **2006**, *110*, 7238−7248.
(48) Maximova, K.; Aristov, A.; Sentis, M.; Kabashin, A. V. Size-Controllable Synthesis of Bare Gold Nanoparticles by Femtosecond Laser Fragmentation in Water. *Nanotechnology* **2015**, *26*, 065601.
(49) Cölfen, H.; Pauck, T. Determination of Particle Size Distributions with Angström Resolution. *Colloid Polym. Sci.* **1997**, *275*, 175−180.
(50) Makino, K.; Ohshima, H. Electrophoretic Mobility of a Colloidal Particle with Constant Surface Charge Density. *Langmuir* **2010**, *26*, 18016−18019.
(51) Pfeiffer, C.; Rehbock, C.; Hühn, D.; Carrillo-Carrion, C.; de Aberasturi, D. J.; Merk, V.; Barcikowski, S.; Parak, W. J. Interaction of Colloidal Nanoparticles with their Local Environment: the (Ionic) Nanoenvironment around Nanoparticles is Different from Bulk and Determines the Physico-Chemical Properties of the Nanoparticles. *J. R. Soc., Interface* **2014**, *11*, 20130931.
(52) Meader, V. K.; John, M. G.; Rodrigues, C. J.; Tibbetts, K. M. Roles of Free Electrons and H_2O2 in the Optical Breakdown-Induced Photochemical Reduction of Aqueous AuCl4. *J. Phys. Chem. A* **2017**, *121*, 6742−6754.
(53) Doñate-Buendía, C.; Fernández-Alonso, M.; Lancis, J.; Mínguez-Vega, G. Overcoming the Barrier of Nanoparticle Production by Femtosecond Laser Ablation in Liquids Using Simultaneous Spatial and Temporal Focusing. *Photonics Res.* **2019**, *7*, 1249.
(54) Serkov, A. A.; Kuzmin, P. G.; Rakov, I. I.; Shafeev, G. A. Influence of Laser-Induced Breakdown on the Fragmentation of Gold Nanoparticles in Water. *Quantum Electron.* **2016**, *46*, 713−718.
(55) Kalus, M.-R.; Lanyumba, R.; Lorenzo-Parodi, N.; Jochmann, M. A.; Kerpen, K.; Hagemann, U.; Schmidt, T. C.; Barcikowski, S.; Gökce, B. Determining the Role of Redox-Active Materials during Laser-Induced Water Decomposition. *Phys. Chem. Chem. Phys.* **2019**, *21*, 18636−18651.
(56) Koppenol, W. H.; Stanbury, D. M.; Bounds, P. L. Electrode Potentials of Partially Reduced Oxygen Species, From Dioxygen to Water. *Free Radical Biol. Med.* **2010**, *49*, 317−322.
(57) HO, K.; YEUNG, K. Effects of Ozone Pretreatment on the Performance of Au/TiO_2 Catalyst for CO Oxidation Reaction. *J. Catal.* **2006**, *242*, 131−141.
(58) Wu, L.; Shoesmith, D. W. An Electrochemical Study of H_2O2 Oxidation and Decomposition on Simulated Nuclear Fuel (SIMFUEL). *Electrochim. Acta* **2014**, *137*, 83−90.
(59) Kosaka, K.; Yamada, H.; Matsui, S.; Echigo, S.; Shishida, K. Comparison among the Methods for Hydrogen Peroxide Measurements To Evaluate Advanced Oxidation Processes: Application of a Spectrophotometric Method Using Copper(II) Ion and 2,9-Dimethyl-1,10-phenanthroline. *Environ. Sci. Technol.* **1998**, *32*, 3821−3824.
(60) Elder, A.; Yang, H.; Gwiazda, R.; Teng, X.; Thurston, S.; He, H.; Oberdörster, G. Testing Nanomaterials of Unknown Toxicity: An Example Based on Platinum Nanoparticles of Different Shapes. *Adv. Mater.* **2007**, *19*, 3124−3129.
(61) Halliwell, B.; Whiteman, M. Measuring Reactive Species and Oxidative Damage in Vivo and in Cell Culture: How Should you do it and What do the Results Mean? *Br. J. Pharmacol.* **2004**, *142*, 231−255.
(62) Siefermann, K. R.; Liu, Y.; Lugovoy, E.; Link, O.; Faubel, M.; Buck, U.; Winter, B.; Abel, B. Binding Energies, Lifetimes and Implications of Bulk and Interface Solvated Electrons in Water. *Nat. Chem.* **2010**, *2*, 274−279.
(63) Reske, R.; Mistry, H.; Behafarid, F.; Roldan Cuenya, B.; Strasser, P. Particle Size Effects in the Catalytic Electroreduction of CO_2 on Cu Nanoparticles. *J. Am. Chem. Soc.* **2014**, *136*, 6978−6986.
(64) Guo, L.-W.; Du, P.-P.; Fu, X.-P.; Ma, C.; Zeng, J.; Si, R.; Huang, Y.-Y.; Jia, C.-J.; Zhang, Y.-W.; Yan, C.-H. Contributions of Distinct Gold Species to Catalytic Reactivity for Carbon Monoxide Oxidation. *Nat. Commun.* **2016**, *7*, 13481.
(65) Du, M.; Sun, D.; Yang, H.; Huang, J.; Jing, X.; Odoom-Wubah, T.; Wang, H.; Jia, L.; Li, Q. Influence of Au Particle Size on Au/TiO 2 Catalysts for CO Oxidation. *J. Phys. Chem. C* **2014**, *118*, 19150−19157.
(66) Wei, S.; Fu, X.-P.; Wang, W.-W.; Jin, Z.; Song, Q.-S.; Jia, C.-J. Au/TiO2 Catalysts for CO Oxidation: Effect of Gold State to Reactivity. *J. Phys. Chem. C* **2018**, *122*, 4928−4936.
(67) Widmann, D.; Behm, R. J. Dynamic Surface Composition in a Mars-Van Krevelen Type Reaction: CO Oxidation on Au/TiO_2. *J. Catal.* **2018**, *357*, 263−273.
(68) Yao, Q.; Wang, C.; Wang, H.; Yan, H.; Lu, J. Revisiting the Au Particle Size Effect on TiO2 -Coated Au/TiO2 Catalysts in CO Oxidation Reaction. *J. Phys. Chem. C* **2016**, *120*, 9174−9183.
(69) Oxford, S. M.; Henao, J. D.; Yang, J. H.; Kung, M. C.; Kung, H. H. Understanding the Effect of Halide Poisoning in CO Oxidation over Au/TiO_2. *Appl. Catal., A* **2008**, *339*, 180−186.
(70) Jv, Y.; Li, B.; Cao, R. Positively-Charged Gold Nanoparticles as Peroxidase Mimic and their Application in Hydrogen Peroxide and Glucose Detection. *Chem. Commun. (Cambridge, U. K.)* **2010**, *46*, 8017−8019.
(71) Huang, Y.; Ren, J.; Qu, X. Nanozymes: Classification, Catalytic Mechanisms, Activity Regulation, and Applications. *Chem. Rev.* **2019**, *119*, 4357−4412.
(72) Gao, L.; Zhuang, J.; Nie, L.; Zhang, J.; Zhang, Y.; Gu, N.; Wang, T.; Feng, J.; Yang, D.; Perrett, S.; et al. Intrinsic Peroxidase-Like Activity of Ferromagnetic Nanoparticles. *Nat. Nanotechnol.* **2007**, *2*, 577−583.
(73) Gharib, M.; Kornowski, A.; Noei, H.; Parak, W. J.; Chakraborty, I. Protein-Protected Porous Bimetallic AgPt Nanoparticles with pH-Switchable Peroxidase/Catalase-Mimicking Activity. *ACS Mater. Lett.* **2019**, *1*, 310−319.

4. Summary

Proto-plasmonic ultra-small Au NCs, bridging the plasmonic and the quantized world, allow to study the intrinsic nanoparticle properties (e.g., fluorescence) in the colloidal state. But experimental access to pure colloidal gold is limited due to the employment of organic ligands, inducing ligand effects potentially contributing to the electronic properties of the gold atoms. LFL is a suitable method to produce ultra-small (< 3 nm) colloidal Au NCs free of organic ligands. With a sufficient size reduction, the optical properties of gold fundamentally change as the energy levels are quantized, and quantum mechanical features prevail, leading to discrete fluorescence phenomena. Even though theory predicts the occurrence of fluorescence in gold clusters, it has not been observed experimentally. Though numerous studies claim to have examined the optical properties of Au NCs, they predominantly only address “metal-organic compounds” where the number of heteroatoms is far higher than that of gold atoms. As a result, it has not been possible to investigate surface charge effects by inorganic surfactants (e.g., anions). In these studies, optical properties are dominated by ligand-metal charge transfer phenomena. However, the optical properties of purely inorganic ligand-free gold nanoclusters have not been examined before in detail, primarily because no synthesis methods have been available to generate this class of nanomaterial.

To this end, this work aimed to establish a synthesis of completely inorganic Au NCs based on laser synthesis in liquids to fundamentally understand the origin of fluorescence appearances of such ultra-small colloidal particles. In addition to this fundamental question about the origin of NC emission, the LFL process had to be examined more closely to deal with the interaction between gold and light in several aspects. In this work, six key achievements were obtained.

The first two achievements can be subordinated to the field of LFL, where the interaction between Au and high-intensity coherent light needed further consideration. Since tuning particle sizes using a laser as a post-processing method requires an effective and generalized process control strategy, a comprehensive grasp of the underlying fragmentation and ripening mechanisms is needed. Yet, when performing fragmentation with high-intensity pulsed lasers, individual mechanistic differentiation between the effects of the energy deposition kinetics (pulse duration) and the driving

force of the fragmentation (laser intensity) is a prerequisite for further development of the method. This work showed for the first time that LFL of Au NPs is a one-pulse and one-step event yielding monomodal ultra-small nanoparticles at a pulse peak power exceeding 1.62×10^{12} W/m^2, in case the educt particles are larger than 13.4 ± 2.1 nm. Furthermore, strong evidence has been achieved that the number of irradiation cycles can be used to tune the surface charge density of the resulting ultra-small nanoparticles in the aqueous medium, verified by charge titration curves and zeta potential measurements. To explain these data, a mechanism known as phase explosion was attributed, which has been rarely attributed to LFL before and was verified using time-resolved *in-situ* X-ray scattering analysis. Using synchrotron SAXS, it was possible to track the particle growth on ultrashort time scales, revealing NCs after just a few µs. However, the generated particles were then subjected to growth processes, which could be arrested by anions' in-situ delivery of surface charge density. Thereby, the second achievement is the understanding of the influence of purely electrostatic stabilizers on the resulting particle size after LFL, which shows an anion-specific behavior and follows a direct Hofmeister series (HS) in the neutral pH range. In contrast, the stabilization follows an inverse HS in the basic pH range. This fundamental knowledge addresses a core discipline of physical chemistry and related fields and can be highly relevant for future studies in bioimaging and catalysis.

Interestingly, we observed significant synergism between the pH and ionic strength, which yielded the smallest particles after LFL (<1 nm) at a high mass yield (>70%). Furthermore, optical pump-probe experiments at lower laser intensity indicated that the presence of micromolar saline during LFL further reduces the electron cooling rate due to the adsorbed anions, leading to a slightly positive surface charge caused by a shift of electron density to the interior of the particle. The resulting alteration of the surface potential influences the position of the Fermi level, accelerating the excited electron cooling rate. This fundamental knowledge is relevant for mechanistic LFL studies and for a variety of applications, ranging from hot-electron electrochemical catalysis to biomedical optoporation.

The next part of this thesis deals with the interaction of Au with low intensive light and results in three key achievements related to the NC’s optical properties. First, we found that fully inorganic Au NCs show a pronounced fluorescence which is critically

dependent on the surface charge density and the particle size. Please note that the LFL process will result in distributed particle sizes as the particle formation within the phase explosion LFL process could be attributed to being based on the ultra-fast solidification of evaporated particles, which is strongly affected by the surrounding medium. Some parts of the fragmentation plume cool down more abruptly by the high-temperature gradient, thereby forming very small particles with kinetically stabilized, defect-rich crystal structures. Larger particles are subject to slower cooling and can grow on a longer time scale, and may form a thermodynamically favored structure with a lower defect density. Second, we found that core state emission is a major contributor to the optical behavior of Au NCs. Its energy is a direct function of the particle size and ranges between 350 – 400 nm. Besides, for smaller particles (diameter < 1), we found strong evidence for further surface-emission states located at 300 nm and 610 nm. These small particles are dominated by their large specific surface area, and the majority of surface atoms are located at the interface to the colloidal environment. Based on this consideration, the observed emission can be attributed to inorganic surface states.

The next achievement in this section follows directly from this insight. Here we recorded pump-powder-dependent emission spectra and observed a stepwise reduction of the surface-emission intensity already at low pump-power (< 10^{10} W/m^2) and suspect a thermal transformation to the thermodynamic more favored defect-free structure. For higher laser intensities, we cannot further detect the surface-emission state's emission. However, we obtain a pump-powder-dependent increase of the particles' core emission intensity. Here, we suspect a one-photon excitation process as the slope amounts to ~1. Both observations occur slowly, with increasing laser intensity, and are irreversible at any time so that we can attribute this kind of matter with a pronounced photon counter ability.

The next achievement is transferring the knowledge gained on fully inorganic Au NCs to further mono- and bimetallic NC type series. A proof-of-concept on platinum nanoclusters and gold-platinum alloy clusters revealed that the photoluminescence of ligand-free NCs is not a phenomenon limited to gold. Instead, the significant differences between the emission properties of Pt and Au are most likely attributed to different band structures, crystallinity, and their surface charge density, which are controllable via the LFL process. For AuPt alloys, we found an exponential red-shift of

the core emission and a drastic decrease of the energy-rich surface-related emission with increasing Pt content in the NCs. As with monometallic Au NCs, predicting the properties of new multi-metal NCs is difficult since a contribution of organic ligands to the properties of wet-chemical NC cannot be excluded.

The last achievement in this work is the proof of the applicability of fully inorganic Au NCs in three different catalytic model reactions (CO oxidation, selective ethanol oxidation, and peroxidase-like oxidation). We found that the LFL process itself already predetermines the catalytic activity. We found evidence for an OH radical-mediated oxidation of the Au NP surface during LFL affecting the surface charge density and the particle size, which are shown to be the decisive parameters for predetermining the catalytic activity.

Overall, this work gives access to charge-tunable and size-selected inorganic, colloidal Au NCs. This includes inorganic mono- and bimetallic NC, which are unique model materials for fundamental studies in physical chemistry and application-oriented research such as catalysis. Furthermore, this work sheds light on the laser fragmentation in liquids process. It is an indispensable prerequisite for the synthesis of completely inorganic Au NCs but also leads to the formation of hot electrons whose lifetime are a key factor for light-triggered process studies in aqueous media, such as catalysis and biophysics.

German version:

Proto-plasmonische ultrakleine Au-NCs bilden eine Brücke zwischen der plasmonischen und der quantisierten Welt und ermöglichen dadurch die Untersuchung der intrinsischen Eigenschaften von Nanopartikeln (z. B. Fluoreszenz) im kolloidalen Zustand. Der experimentelle Zugang zu reinem kolloidalem Gold ist jedoch durch oberflächenaffine organische Liganden eingeschränkt. Diese Liganden rufen Effekte hervor, die zu den elektronischen Eigenschaften der Goldatome beitragen. Die LFL ist eine anerkannte und die einzige Methode zur Herstellung ultrakleiner (< 3 nm) kolloidaler Au NCs, die frei von solchen organischen Liganden sind. Bei einer ausreichenden Verkleinerung ändern sich die optischen Eigenschaften von Gold grundlegend, da die Energieniveaus quantisiert werden und quantenmechanische Eigenschaften vorherrschen, was zu diskreten Fluoreszenzphänomenen führt. Obwohl die Theorie das Auftreten der Fluoreszenz in rein anorganischen kolloidalen Goldclustern vorhersagt, wurde es bisher nicht experimentell beobachtet. Obwohl zahlreiche Studien behaupten, die optischen Eigenschaften von Au NCs untersucht zu haben, befassen sie sich überwiegend nur mit "metallorganischen Verbindungen", bei denen die Anzahl der Heteroatome weitaus höher ist als die der Goldatome. Infolgedessen war es bisher nicht möglich, Oberflächenladungseffekte durch anorganische Zusätze (z. B. Anionen) zu untersuchen. In diesen Studien werden die optischen Eigenschaften von Ligand-Metall-Ladungsübertragungsphänomenen dominiert. Die optischen Eigenschaften von rein anorganischen, ligandenfreien, kolloidalen Gold-Nanoclustern wurden jedoch bisher nicht systematisch untersucht, vor allem weil es keine zufriedenstellenden Synthesemethoden zur Herstellung dieser Klasse von Nanomaterialien gab.

Ziel dieser Arbeit war es daher, eine Synthese vollständig anorganischer Au NCs auf der Basis von Lasersynthese in Flüssigkeiten zu etablieren, um den Ursprung der Fluoreszenzerscheinungen solcher ultrakleinen kolloidalen Partikel grundlegend zu verstehen. Zusätzlich zu dieser grundlegenden Frage nach dem Ursprung der NC-Emission musste der LFL-Prozess genauer untersucht werden, um die Wechselwirkung zwischen Gold und Licht in mehreren Aspekten zu untersuchen. In dieser Arbeit wurden sechs wichtige Ergebnisse erzielt.

Die ersten beiden Ergebnisse lassen sich dem Bereich der LFL zuordnen, wo die Wechselwirkungen zwischen Au und hochintensivem kohärentem Licht näher

untersucht werden mussten. Da die Einstellung der Partikelgröße mit Hilfe eines Lasers als Nachbearbeitungsmethode eine wirksame und allgemeine Prozesssteuerungsstrategie erfordert, ist ein umfassendes Verständnis der zugrunde liegenden Fragmentierungs- und Reifungsmechanismen erforderlich. Bei der Fragmentierung mit hochintensiv gepulsten Lasern ist eine individuelle mechanistische Differenzierung zwischen den Auswirkungen der Energiedepositionskinetik (Pulsdauer) und der treibenden Kraft der Fragmentierung (Laserintensität) eine Voraussetzung für die Weiterentwicklung der Methode. In dieser Arbeit konnte erstmals gezeigt werden, dass die LFL von Au-Nanopartikeln ein Ein-Puls- und Ein-Schritt-Ereignis ist, das bei einer Pulsspitzenleistung von mehr als $1{,}62 \times 10^{12}$ W/m^2 zu monomodalen ultrakleinen Nanopartikeln führt, wenn die Eduktpartikel größer als $13{,}4 \pm 2{,}1$ nm sind. Darüber hinaus konnte eindeutig nachgewiesen werden, dass die Anzahl der Bestrahlungszyklen dazu verwendet werden kann, die Oberflächenladungsdichte der resultierenden ultrakleinen Nanopartikel im wässrigen Medium einzustellen, was durch Ladungstitrationskurven und Zetapotenzialmessungen bestätigt wurde. Zur Erklärung dieser Daten wurde ein als Phasenexplosion bekannter Mechanismus herangezogen, der bisher nur selten mit LFL in Verbindung gebracht worden ist und durch zeitaufgelöste in-situ-Röntgenstreuungsanalysen verifiziert werden konnte. Mithilfe von Synchrotron-SAXS konnte das Partikelwachstum auf ultrakurzen Zeitskalen verfolgt werden, wobei NCs bereits nach wenigen ps sichtbar wurden. Die erzeugten Partikel waren dann jedoch Wachstumsprozessen unterworfen, die durch die adsorption von Anionen gestoppt werden konnten. Die zweite Errungenschaft ist somit das Verständnis des Einflusses rein elektrostatischer Stabilisatoren auf die resultierende Partikelgröße nach LFL, die ein anionenspezifisches Verhalten zeigt und im neutralen pH-Bereich einer direkten Hofmeister-Reihe (HS) folgt. Im Gegensatz dazu folgt die Stabilisierung im basischen pH-Bereich einer inversen HS. Dieses grundlegende Wissen betrifft eine Kerndisziplin der physikalischen Chemie und verwandter Gebiete und kann für künftige Studien in den Bereichen der biomedizinischen Bildgebung und Katalyse von großer Bedeutung sein.

Interessanterweise wurde ein signifikanter Synergismus zwischen dem pH-Wert und der Ionenstärke beobachtet, der zu den kleinsten Partikeln nach der LFL (< 1 nm) bei einer hohen Massenausbeute (> 70 %) führte. Darüber hinaus zeigten optische Pump-Probe-Experimente bei geringerer Laserintensität, dass die Anwesenheit von

mikromolarer Kochsalzlösung während der LFL die Kühlrate der Elektronen aufgrund der adsorbierten Anionen weiter reduziert, was zu einer leicht positiven Oberflächenladung führt, die durch eine Verschiebung der Elektronendichte ins Innere des Partikels verursacht wird. Die daraus resultierende Änderung des Oberflächenpotenzials beeinflusst die Position des Fermi-Niveaus und beschleunigt die Abkühlung der angeregten Elektronen. Dieses grundlegende Wissen ist für mechanistische LFL-Studien und für eine Vielzahl von Anwendungen von Bedeutung, die von der elektrochemischen Katalyse mit heißen Elektronen bis zur biomedizinischen Optoporation reichen.

Der nächste Teil dieser Arbeit befasst sich mit der Wechselwirkung von Au mit weniger intensivem Licht und führt zu drei wichtigen Ergebnissen im Zusammenhang mit den optischen Eigenschaften der NC. Erstens konnte festgestellt werden, dass vollständig anorganische Au NCs eine ausgeprägte Fluoreszenz aufweisen, die entscheidend von der Oberflächenladungsdichte und der Partikelgröße abhängt. Es ist zu beachten, dass der LFL-Prozess zu einer Partikelgrößenverteilung führt, da die Partikelbildung innerhalb des Phasenexplosions-LFL-Prozesses auf der ultraschnellen Erstarrung der verdampften Partikel beruht, die stark vom umgebenden Medium beeinflusst wird. Einige Teile kühlen durch den Hochtemperaturgradienten abrupter ab und bilden dabei sehr kleine Partikel mit kinetisch stabilisierten, defektreichen Kristallstrukturen. Größere Teilchen werden langsamer abgekühlt und können auf einer längeren Zeitskala wachsen und eine thermodynamisch günstigere Struktur mit einer geringeren Defektdichte bilden. Zweitens haben wir festgestellt, dass die Kernzustandsemission einen wesentlichen Beitrag zum optischen Verhalten von Au NCs leistet. Ihre Energie ist eine direkte Funktion der Partikelgröße und liegt zwischen 350 und 400 nm. Außerdem fanden wir bei kleineren Partikeln (Durchmesser < 1) starke Hinweise auf weitere Oberflächenemissionszustände bei 300 nm und 610 nm. Diese kleinen Partikel werden von ihrer großen spezifischen Oberfläche dominiert, und die Mehrzahl der Oberflächenatome befindet sich an der Grenzfläche zur kolloidalen Umgebung. Aufgrund dieser Überlegung kann die beobachtete Emission auf Oberflächenzustände zurückgeführt werden.

Die nächste Errungenschaft in diesem Teil folgt direkt aus dieser Erkenntnis. Hier wurden anregugsdichtenabhängige Emissionsspektren aufgenommen und es konnte eine schrittweise Verringerung der Oberflächenemissionsintensität bereits bei niedriger Anregungsleistung (< 10^{10} W/m^2) beobachtet werden, was vermutlich auf

eine thermische Umwandlung in die thermodynamisch günstigere defektfreie Struktur zurückzuführen ist. Bei höheren Laserintensitäten konnte die Emission des Oberflächenemissionszustands nicht mehr nachweisen werden. Es wird jedoch ein anregugsdichtenabhängigen Anstieg der Kernemissionsintensität erhalten (Steigung ~1), sodass dies auf einen Ein-Photonen-Anregungsprozess zurückzuführen ist. Beide Beobachtungen treten langsam, mit zunehmender Laserintensität auf und sind jederzeit irreversibel, so dass dieser Art von Materie eine ausgeprägte Photonenzählfähigkeit zuschrieben werden kann.

Ein Proof-of-Concept an Platin-Nanoclustern und Clustern aus einer Gold-Platin-Legierung zeigte, dass die Photolumineszenz von ligandenfreien NCs kein auf Gold beschränktes Phänomen ist. Stattdessen sind die signifikanten Unterschiede zwischen den Emissionseigenschaften von Pt und Au höchstwahrscheinlich auf unterschiedliche Bandstrukturen, Kristallinität und ihre Oberflächenladungsdichte zurückzuführen, die durch den LFL-Prozess steuerbar sind. Für AuPt-Legierungen konnte eine exponentielle Rotverschiebung der Kernemission und eine drastische Abnahme der energiereichen oberflächenbezogenen Emission mit zunehmendem Pt-Gehalt in den NCs gezeigt werden. Wie bei den monometallischen Au NCs ist die Vorhersage der Eigenschaften neuer Multi-Metall-NCs schwierig, da ein Beitrag der organischen Liganden zu den Eigenschaften der nasschemischen NCs nicht ausgeschlossen werden kann.

Die letzte Errungenschaft dieser Arbeit ist der Nachweis der Anwendbarkeit von vollständig anorganischen Au NCs in drei verschiedenen katalytischen Modellreaktionen (CO-Oxidation, selektive Ethanoloxidation und peroxidaseähnliche Oxidation). Es wurde geziegt, dass der LFL-Prozess selbst bereits die katalytische Aktivität vorgibt. Es konnten Belege für eine durch OH-Radikale vermittelte Oxidation der Au NP Oberfläche während der LFL gefunden werden, die sich auf die Oberflächenladungsdichte und die Partikelgröße auswirken.

Insgesamt eröffnet diese Arbeit einen Zugang zu anorganischen, kolloidalen Au NCs, die in ihrer Ladung und Größe angepasst werden können. Dazu gehören anorganische mono- und bimetallische NC, die einzigartige Modellmaterialien für grundlegende Studien in der physikalischen Chemie und anwendungsnahen Forschungen wie die Katalyse sind. Darüber hinaus wirft diese Arbeit ein Licht auf den Prozess der Laserfragmentierung in Flüssigkeiten. Sie ist eine unabdingbare Voraussetzung für die Synthese vollständiger anorganischer Au NCs, führt aber auch zur Bildung heißer

Elektronen, deren Lebensdauer ein Schlüsselfaktor für lichtausgelöste Prozessstudien in wässrigen Medien ist, etwa in der Katalyse und Biophysik.

5. Appendix

A1: Materials and methods

In this thesis several pulsed laser systems have been used. The application was in the laser-based synthesis of NPs, but also in the analysis by means of pump-probe spectroscopic setups. All lasers, their specification and intended use are summarized in Table 1 and 2. Specifications of further devices are given in Table 3. Further information on methods and chemicals can be found in the corresponding experimental sections in chapter 5. For a better clarity, the specific materials and methods are described in in the related section called “Experimental” of each chapter.

Table 1: *Specifications on pulsed laser systems used in this work.*

Model name	**Laser 1 (Ekspla)**	**Laser 2 (Innolas)**	**Laser 3 (ns-Edgewave)**	**Laser 4 (ps-Edgewave)**
Used in Chapter	All Chapter	All Chapter except 5.1.2	5.1.1	5.1.1 5.1.2
Method	LAL	LFL	LFL	LFL
Pulse duration	10 ps	9 ns	7 ns	10 ps
Wavelength [nm]	1064	532	532	532
Repetition rate [kHz]	100	0.100	2	80
Fluence [J/cm^2]	0.9	1.6	2	0.03
Laser intensity [W/m^2]	$4.4*10^{11}$	$1.6*10^{12}$	$2.8*10^{12}$	$1.6*10^{15}$

Table 2: *Further specifications on pulsed laser systems used in this work.*

	Laser 5 (ERSF)	**Laser 6 (SLAC)**	**Laser 7 (Hamburg 1)**	**Laser 8 (Hamburg 2)**
Used in Chapter	5.1.2	5.1.4	5.2.2	5.2.2
Method	LFL	Pump-probe spectroscopy	Pump-probe spectroscopy	Pump-probe spectroscopy
Pulse duration	1 ps	45 fs	300 fs	300 fs
Wavelength [nm]	532	400, 527	250	250
Repetition rate [kHz]	1	0.12	500	80000
Fluence [mJ/cm^2]	180	0. 3 - 2.5	0.015	0.00039
Laser intensity [W/m^2]	10^{15}	10^{14} - 10^{15}	~10^{11}	~10^{9}

Table 3: *Specifications of the devices used in the experiments.*

Device	Manufacturer	Use
UV-Vis spectrometer	Thermo Scientific Evolution 201	Optical properties
Fluorescence spectrometer	Varian Eclipse	
Zetasizer	Malvern Zetasizer Nano ZS	Electronic properties, surface charges
pH Meter	PCE Inst. PCE PHD 1	
XPS		
STEM	JEOL JSM-7500F	Particle size
TEM	Zeiss EM 910	
Hr-TEM		
Analytical disc centrifuge	CPS Instruments DC 24000	
Analytical ultracentrifuge	Beckman Coulter, optima XPN	
Zentrifugal filters	Amicon Ultra, Z648000-8EA	Others
ICP-MS	Perkin Elmer Sciex - ELAN 6000	

A2 Supporting Information: Chapter 3.1.1

Analytical ultra-centrifugation of fully inorganic gold nanocluster

(unpublished results)

Anna. R. Ziefuss[1], Florian de Kock[1], Christoph Rehbock[1], Stephan Barcikowski[1]*

[1] Technical chemistry I and Center for Nanointegration Duisburg-Essen (CENIDE), Unibversity Duisburg-Essen 45141 Essen, Germany

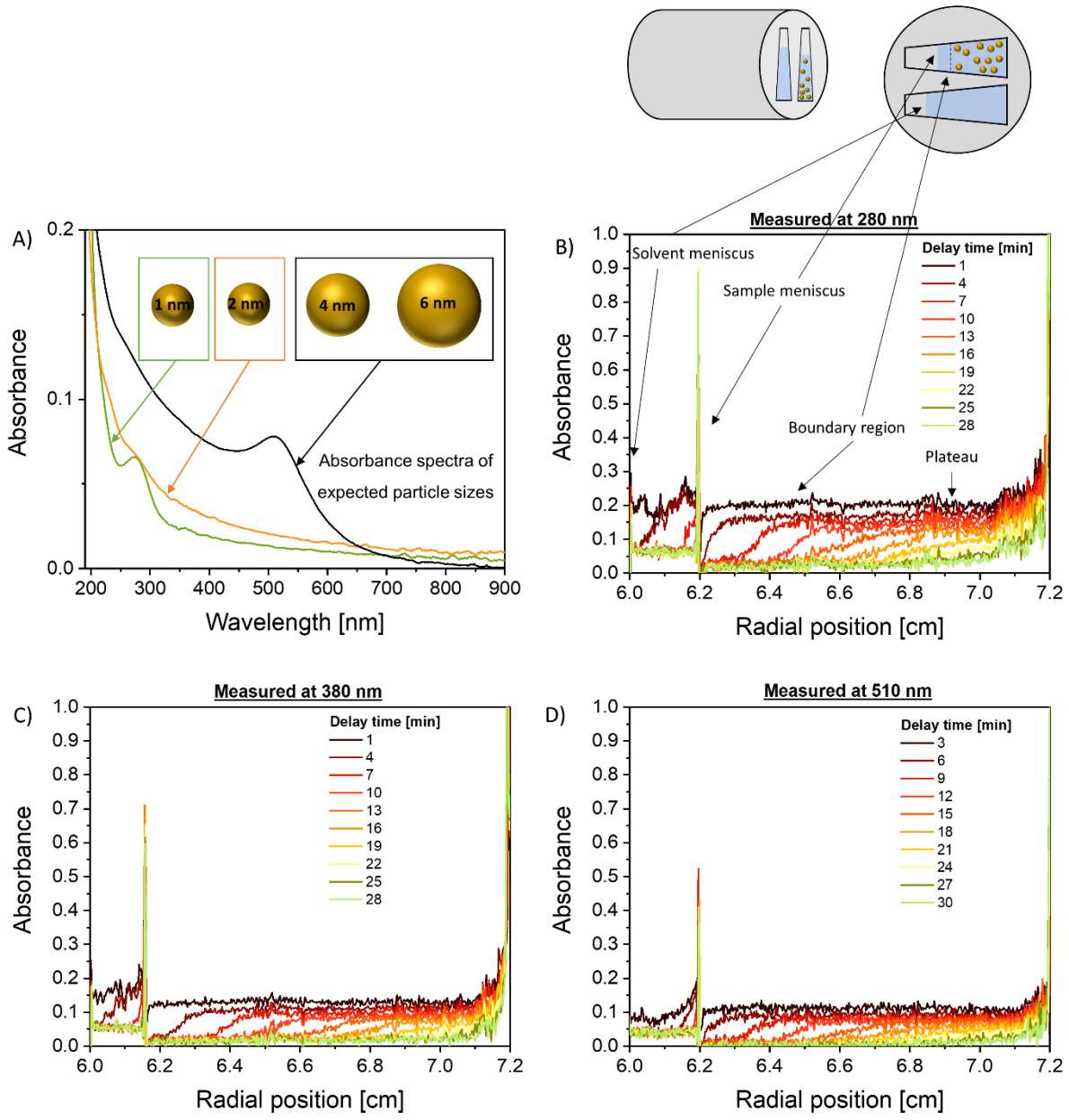

Figure S1: *A) Expected particle sizes and the corresponding absorbance spectra. B)-D) Raw data after measurement of the colloid at 30000 rpm, 20°C and different delay times. B) Measurement at 280 nm, C) Measurement at 380 nm, D) Measurement at 510 nm.*

A3 Supporting Information: Chapter 3.2.1

Associated content

Laser fragmentation of colloidal gold nanoparticles with high-intensity nanosecond pulses driven by a single-step fragmentation mechanism with a defined educt particle-size threshold

Anna R. Ziefuß[1], Sven Reichenberger[1], Christoph Rehbock[1], Indranath Chakraborty[2], Mustafa Gharib[2], Wolfgang J. Parak[2], Stephan Barcikowski[1]*

DOI: 10.1021/acs.jpcc.8b04374

[1] Technical Chemistry I and Center for Nanointegration Duisburg-Essen (CENIDE), University of Duisburg-Essen, Universitaetsstrasse 7, 45141 Essen, Germany

[2]Fachbereich Physik und Chemie, and Center for Hybrid Nanostructure (CHyN), Universität Hamburg, Hamburg, Germany.

* corresponding author: stephan.barcikowski@uni-due.de

Size distribution of the educt particles after PLAL

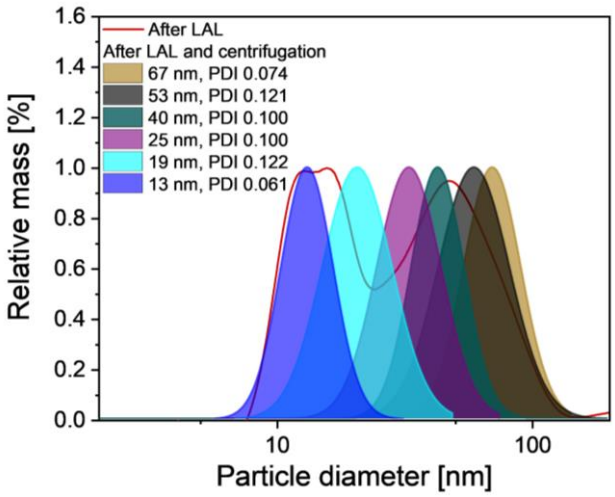

Figure S 1 Relative mass distribution of gold nanoparticles after LAL and fractionated centrifugation. Measured using ADC.

Calculations of the flow behavior of the free liquid jet

The use of a free liquid jet during LFL is an unconventional method that is rarely reported in the literature. Fragmentation typically takes place in a cuvette in which the liquid is stirred, which results in turbulent flow conditions.

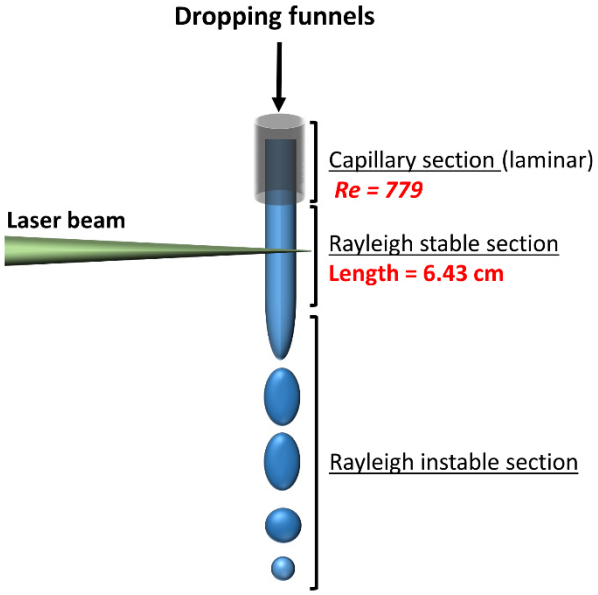

Figure S 2: Schematic diagram of fluid dynamic observation of the free liquid jet

The free liquid jet is characterized in particular by its laminar flow behavior. The Reynolds number inside the nozzle was calculated to be Re = 779. Once the liquid exits the capillary, the gravity, flow velocity ν and the surface tension σ of the medium determine its subsequent fate.

$$v > v_{Min} = 2 \cdot \sqrt{\frac{\sigma}{r_{Jet} \cdot \rho}} \qquad \text{equation 1}$$

Starting from a surface tension of 0.72 N/m and a density ρ of water of 997.04 kg/m^3, the minimum discharge velocity is v_{Min} =0.73 m/s. Since the present flow velocity of 0.63 m/s is lower, decomposition of the liquid jet into droplets is to be expected. In our experiments, the laser pulse irradiates the continuous area before dripping begins (Figure S 2). The drip-off length L of this range can be calculated by multiplying the decay time t by the flow velocity ν_{Jet}:

$$L = t \cdot v_{jet} = \frac{v_{Jet}}{\mu_{opt}} \cdot \ln\left(\frac{r_{Jet}}{\delta_0}\right). \qquad \text{equation 2}$$

Therein, the ratio $\ln\left(\frac{r_{Jet}}{\delta_0}\right)$ depends on the Ohnesorge number Oh, and can be calculated according to Grant and Middleman as follows [1]:

$$\left(\frac{r_{Jet}}{\delta_0}\right) = -2.66 \cdot \ln(Oh) + 7.68 \qquad \text{equation 3}$$

The Ohnesorge number can be calculated $\left[Oh = \frac{\sqrt{We}}{Re} = \frac{\eta}{\sqrt{L \cdot \rho \cdot \sigma}}\right]$. The optimal Rayleigh growth rate for non-viscous jets can be calculated as follows [1]:

$$\mu_{\mathrm{opt}} = 0.97 \cdot \sqrt{\frac{\sigma}{8 \cdot \rho \cdot r_{Jet}^3}} \qquad \text{equation 4}$$

Finally, length of the continuous section, determining the working range is approximated by equation 1 and results in L = 6.4 cm. This was in good agreement with experimental observation.

In our experimental setup the working distance was set at L = 1 cm. To estimate whether the liquid jet is dominated by inertial forces (flow rate) or gravitational forces we calculate the Froude number according to:

$$Fr^2 = \frac{v_{Jet}}{\sqrt{g \cdot L}} \qquad \text{equation 5}$$

Under these conditions we obtain a Froude number of $Fr^2 = 4$. Hence the liquid jet is already strongly dominated by gravitational forces such that we assume plug flow-like conditions and similar residence time of nanoparticles within the irradiated area of the liquid jet.

Consideration of the absorption cross section of gold nanoparticles as a function of the laser wavelength

To decide which wavelength to use for fragmentation, we calculated the absorption cross sections of gold nanoparticles of different sizes using methods adapted from the literature. For the calculation, we used the freely available software MiPlot [2]. The absorption cross section is clearly dependent on the particle size and the wavelength used.

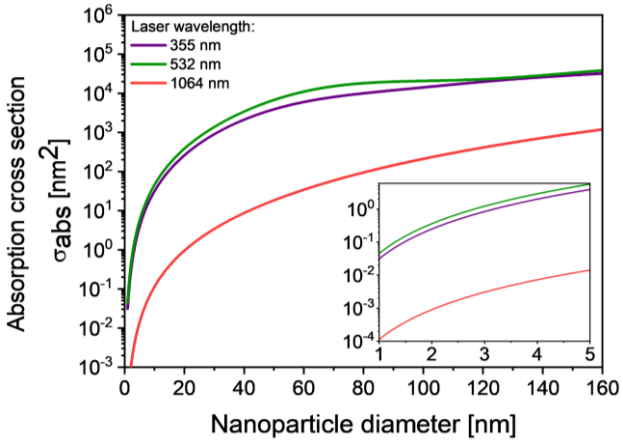

Figure S 3: Absorption cross section of gold nanoparticles of different sizes, calculated using MiePlot [1]. The absorption cross section depends on the excitation wavelength. In the calculations, we used optical data according to Johnson and Christy [2].

The absorption cross section increases with increasing particle size. In addition, it is highest when illuminated with light of 532-nm wavelength. Measured by these values, the laser fragmentation carried out using an excitation wavelength of 532 nm.

Comparison of the quality of three different methods for obtaining particle size distributions of particles after fragmentation

To verify the quality of the ADC in the measurement of particles down to 2 nm diameter, we compared the size distributions with those determined using AUC and TEM (Figure S4). The TEM and ADC distributions show very high comparability, both in the position of the peak maximum (± 0.75%) and the width (± 10.6%) of the distribution. The AUC data show a considerably higher resolution that enables the identification of several peaks. However, such a high resolution is not necessary for this study, as the primary comparison is between different distributions. In Figure 4 the data of the AUC are fitted without consideration of the high resolution to show a fair comparison to the ADC data. Based on this comparison, we assess the ADC as suitable measurement method for the measurement of particles in the range between 2-5 nm.

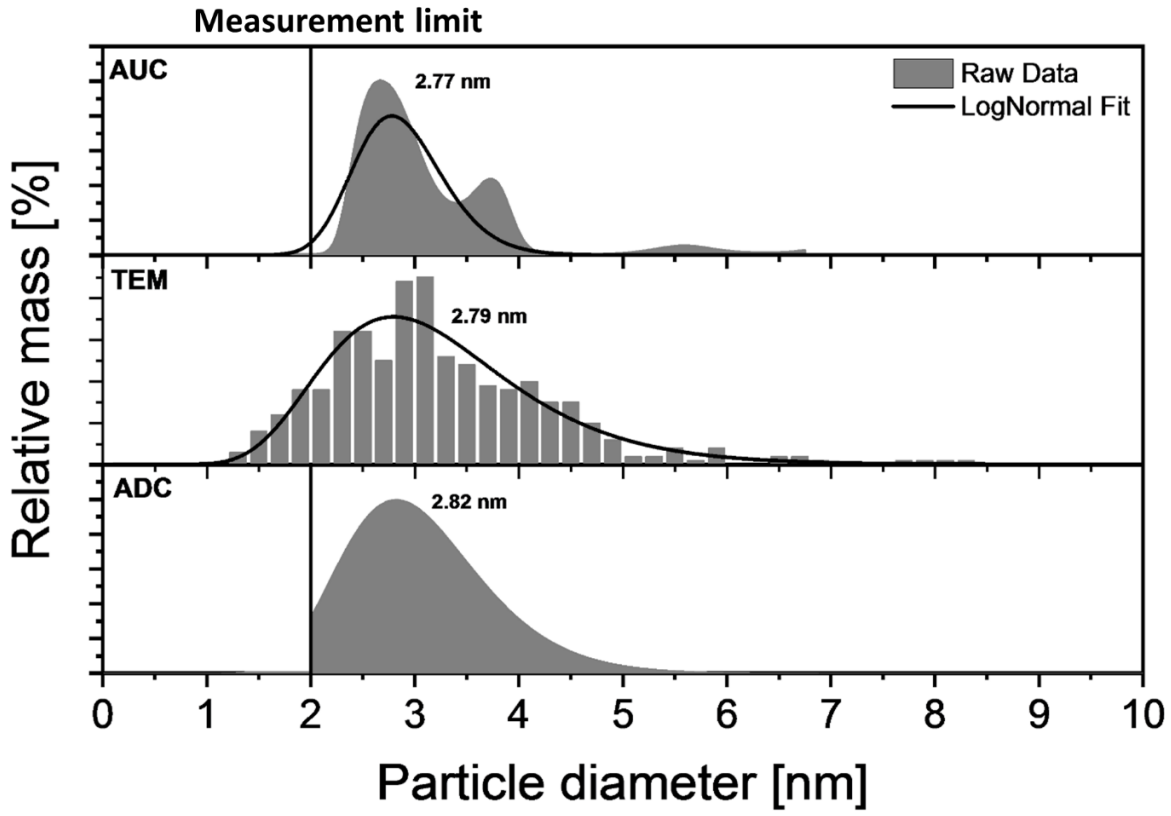

Figure S 4: Comparison of size distributions obtained from TEM, AUC, and ADC

Theoretical consideration of the temperatures in a nanoparticle by LFL

The amount of heat absorbed by a single nanoparticle and its respective temperature increase induced by a single laser pulse depends on the applied laser fluence, absorption efficiency at a given laser wavelength, and the heat-loss kinetics of the liquid. Baffou and co-workers provided a MatLab script that enabled us to estimate the deposited heat and resulting temperature increase of gold nanoparticles based on the Mie theory and heat transfer equations [3]. We performed these calculations based on the laser fluences and pulse durations applied in our experiments, the results of which are shown in Figure S 5. The dotted line in Figure S 5 indicates the energy required to heat the particle to boiling temperature (T_b = 3129 K), considering the heat capacity (129 J $kg^{-1} \cdot K^{-1}$) and the melting enthalpy (12.7 kJ mol^{-1}) [4]. Above this line, the AuNPs absorb enough energy to be partially evaporated. Once the mass-specific thermal energy of the AuNP also exceeds the evaporation enthalpy of gold (324 kJ mol^{-1}), complete evaporation of the AuNPs can be assumed (indicated by the dashed line in Figure S 5). Accordingly, the onset of fragmentation can be considered to occur at this point for the ‘ns-low-RR’ and ‘ns-high-RR’ lasers.

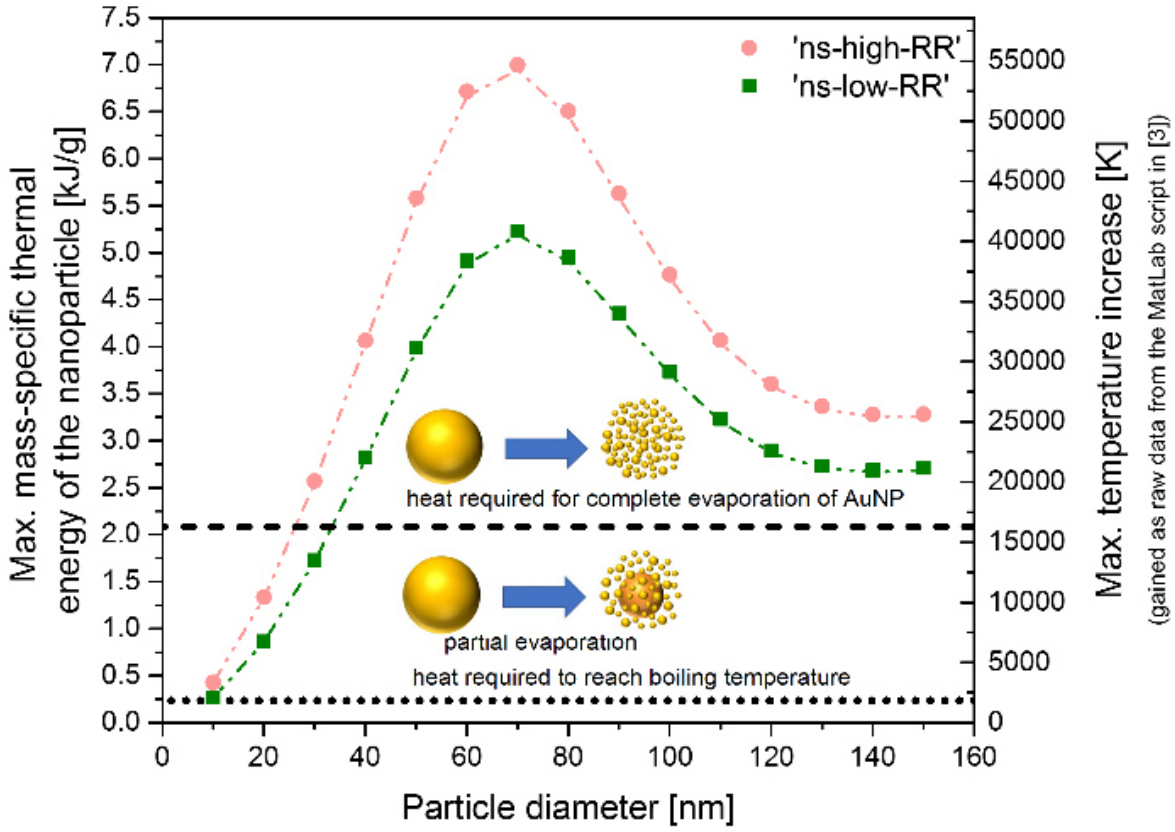

Figure S 5: Mass-specific thermal energy (left axis) absorbed by the AuNP during laser irradiation, as calculated from the virtual temperature increase (right axis) determined by the MATLAB scrip-t from ref. [5]. Data refers to the center of a gold nanoparticle, calculated for single-pulse experiments with the lasers used in this study.

For the sake of transparency, on the right hand site of Figure S 5, we plotted the maximal temperature increase obtained as raw data from the MatLAb script (from ref. [5]). Note that within the model developed by Baffou and co-workers, the temperature increase is calculated solely from the absorbed energy and heat capacity, while neglecting melting and evaporation events [5]. Hence, once the melting temperature is exceeded, the temperature increase from the MatLab script no longer depicts the actual nanoparticle temperature (as melting and later evaporation enthalpy are not considered), but is rather a direct measure of the thermal energy stored in the AuNP. Therefore, we used the thermal energy throughout in our consideration of

the onset and completeness of particle evaporation, rather than the temperature obtained from the MatLab script.

Note that the calculation used by Baffou and co-workers (from ref. [5]) provides a 'best-case-scenario' prediction of the thermal energy absorbed by the AuNP under laser pulse irradiation. That is, as the refractive index of Au was kept constant throughout the whole calculation, no bleaching of surface plasmon resonance as reported by Werner et al. or subsequent drop in absorption efficiency with increasing temperature was neglected [6].

Absorption spectra of nanoparticles before and after LFL

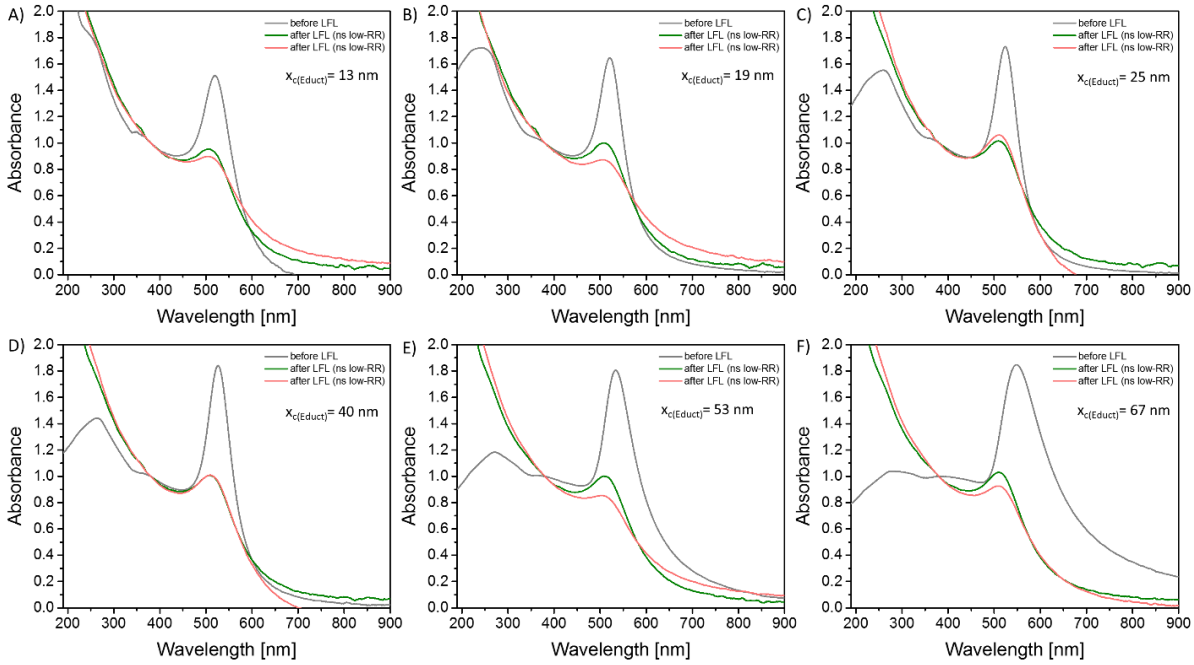

Figure S 6: Absorbance spectra (before and after LFL) in relation to the educt particle size: A) 13 nm, B) 19 nm, C) 25 nm, D) 40 nm, E) 53 nm, and F) 67 nm.

Influence of the number of pulses per volume

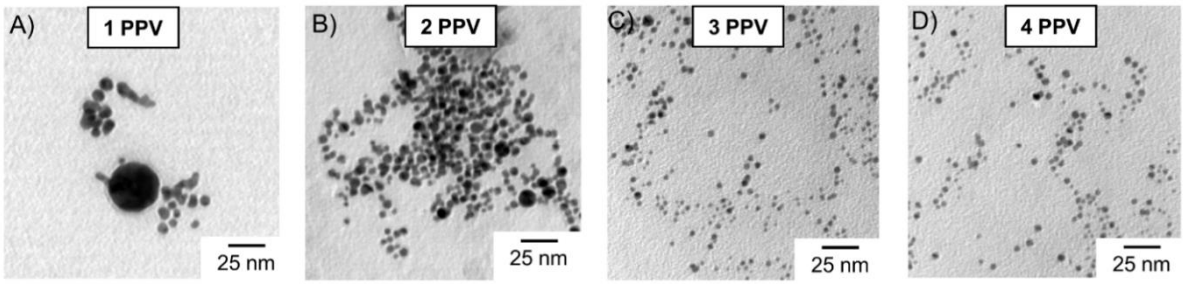

Figure S 7: TEM Images after LFL with 1–4 pulses per volume (PPV). A) 1 PPV, B) 2 PPVs, C) 3 PPVs, and D) 4 PPVs

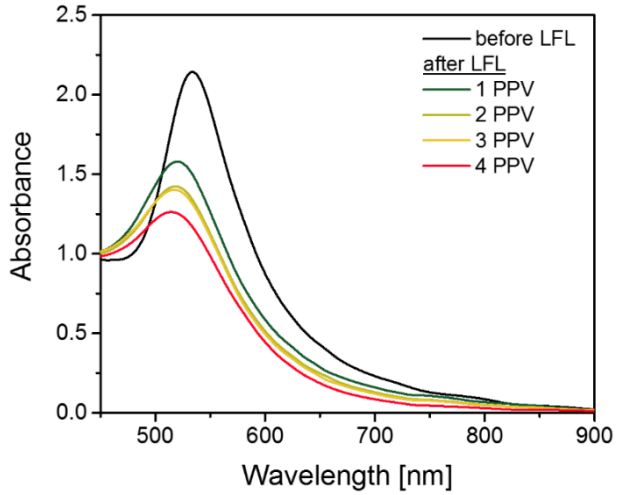

Figure S 8: Comparative UV/Vis-spectra of particles synthesized with a different number of PPVs. The spectra show a gradual blue shift and decrease in surface plasmon resonance (SPR) peak intensity, which confirms the smaller particle formation from 0 to 4 PPVs

Stability experiment against salt concentrations

We checked the colloidal stability of these nanoparticles synthesized via a different number of pulses per volume against the sodium chloride salt concentration. To do so, we titrated suspensions of AuNPs corresponding to different passages against increasing concentrations of

NaCl (0 – 1250 mM) and evaluated their aggregation states (measured after 24 h) by measuring their hydrodynamic diameters (d_h) after 24 h. We determined the hydrodynamic diameters of the nanoparticle suspensions (Figure S9) using the particle analyzer Malvern Zetasizer Nano ZS (Malvern Instruments Limited, UK) at 25 °C. We collected three sets of this data and used the average value in Figures 5 B and 5 D. To better evaluate the stability against salt, in these figures, we show only the changes in the hydrodynamic diameter after the addition of the corresponding aliquot of NaCl.

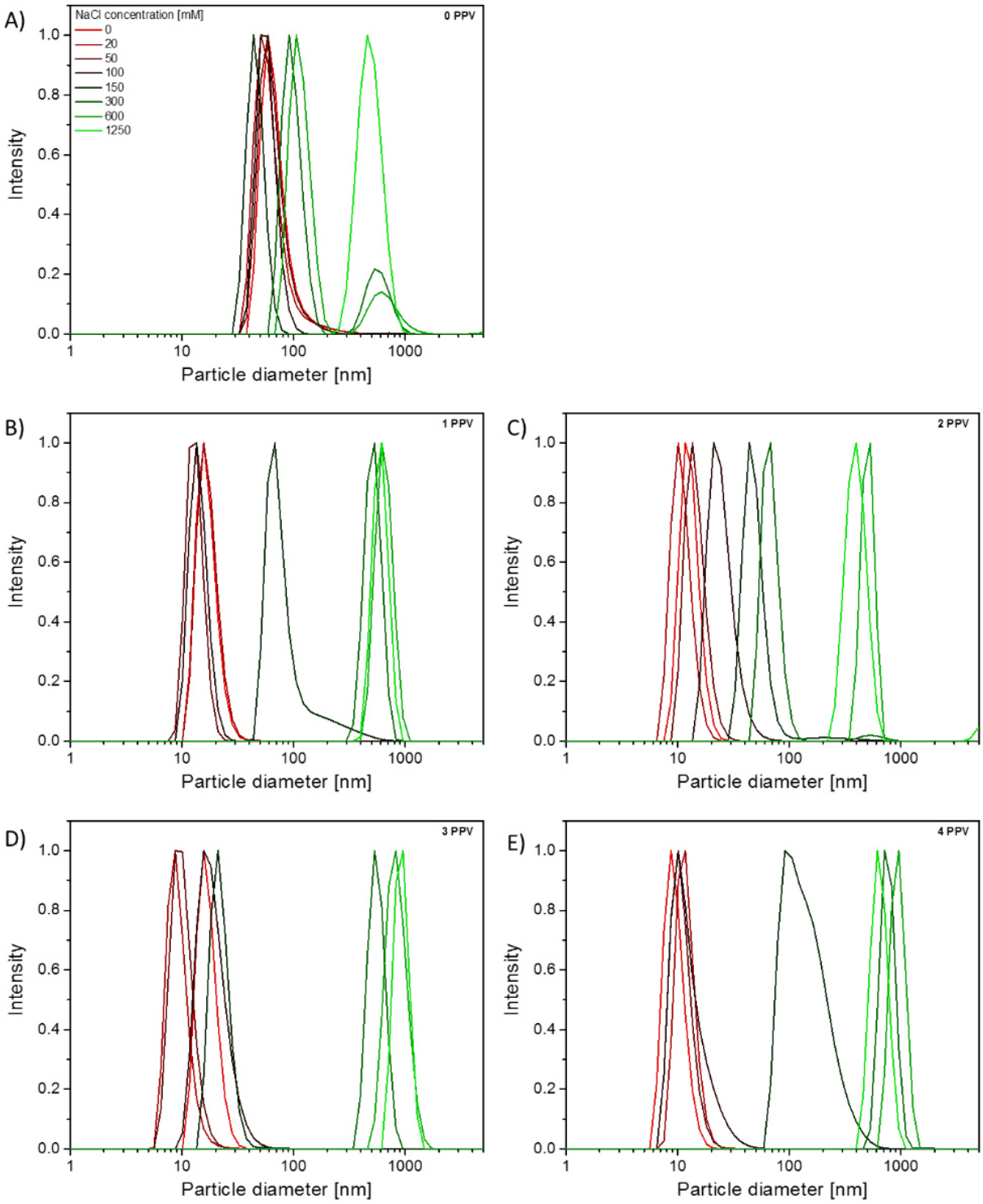

Figure S 9: Size distribution plot of AuNPs after 1 to 4 PPVs in water in the presence of different concentrations of NaCl (recorded after 24 h). The NaCl concentrations ranged from 0.0 M to 1.25 M, as illustrated in the legend.

Experimental observation of the laser intensity

To determine the laser stability, we recorded the laser power over a period of one hour recording the power every 10 ms. Figure S 10 shows the experimentally determined stability of the laser 'ns-high-RR' (the data for laser 'ns-low-RR' are comparable, data not shown). If the laser stability is considered over 60 minutes (long-term) the deviation from the mean value is 1.64% for 'ns-high-RR' (1.40% for laser 'ns-low-RR'). If the laser intensity in the smallest possible measuring range is considered (10 ms), a deviation of 1.19% can be observed for 'ns-high-RR' (1.15% for 'ns-low-RR'). The short-term deviation of the laser intensity is plotted as error bars of the x-axis in Figure 6.

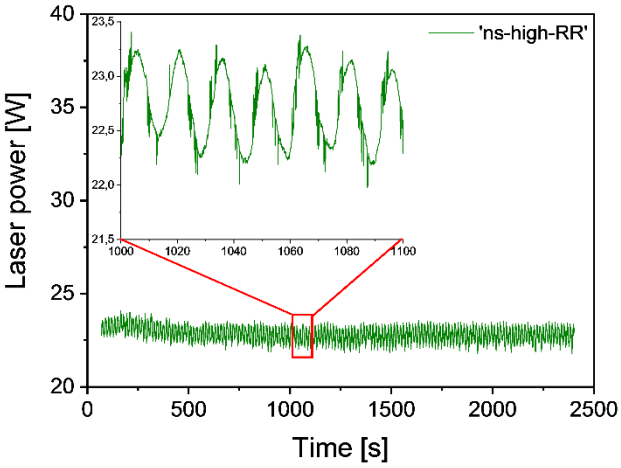

Figure S 10: Long-term stability of the laser power for 'ns-high-RR.'

Influence of pulse intensity on product particle size.

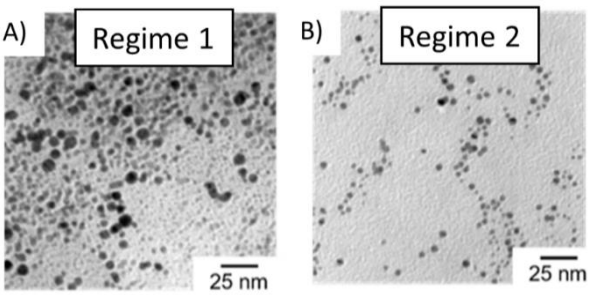

Figure S 11: TEM Images after fragmentation in regimes 1 (A) and 2 (B).

References

[1] R.P. Grant, S. Middleman, Newtonian jet stability, AIChE J. 12 (1966) 669–678.

[2] C.F. Bohren, D.R. Huffman, Absorption and scattering of light by small particles, Wiley-VCH, Weinheim, 2008.

[3] K. Metwally, S. Mensah, G. Baffou, Fluence Threshold for Photothermal Bubble Generation Using Plasmonic Nanoparticles, J. Phys. Chem. C 119 (2015) 28586–28596.

[4] CRC Handbook of Chemistry and Physics, 84th Edition Edited by David R. Lide (National Institute of Standards and Technology). CRC Press LLC. Boca Raton. 2003. 2616 pp. $139.95. ISBN 0-8493-0484-9, J. Am. Chem. Soc. 126 (2004) 1586.

[5] G. Baffou, H. Rigneault, Femtosecond-pulsed optical heating of gold nanoparticles, Phys. Rev. B 84 (2011).

[6] L.C. Groff, X. Wang, J.D. McNeill, Measurement of Exciton Transport in Conjugated Polymer Nanoparticles, J. Phys. Chem. C 117 (2013) 25748–25755.

A4 Supporting Information: Chapter 3.2.2

Electronic Supplementary Material (ESI) for Physical Chemistry Chemical Physics.

Electronic supplementary information for: *In situ* structural kinetics of picosecond laser-induced heating and fragmentation of colloidal gold spheres

Anna Ziefuß,[†] Stefan Reich,[‡] Sven Reichenberger,[†] Matteo Levantino,[¶] and Anton Plech[*,‡]

Department of Technical Chemistry I and Center for Nanointegration Duisburg-Essen, University of Duisburg-Essen, Universitätsstrasse 7, D-45141 Essen, Institute for Photon Science and Synchrotron Radiation, KIT Karlsruhe, Germany, and ESRF, BP 220, F-38043 Grenoble

E-mail: anton.plech@kit.edu

[*]To whom correspondence should be addressed
[†]UDE
[‡]KIT
[¶]ESRF

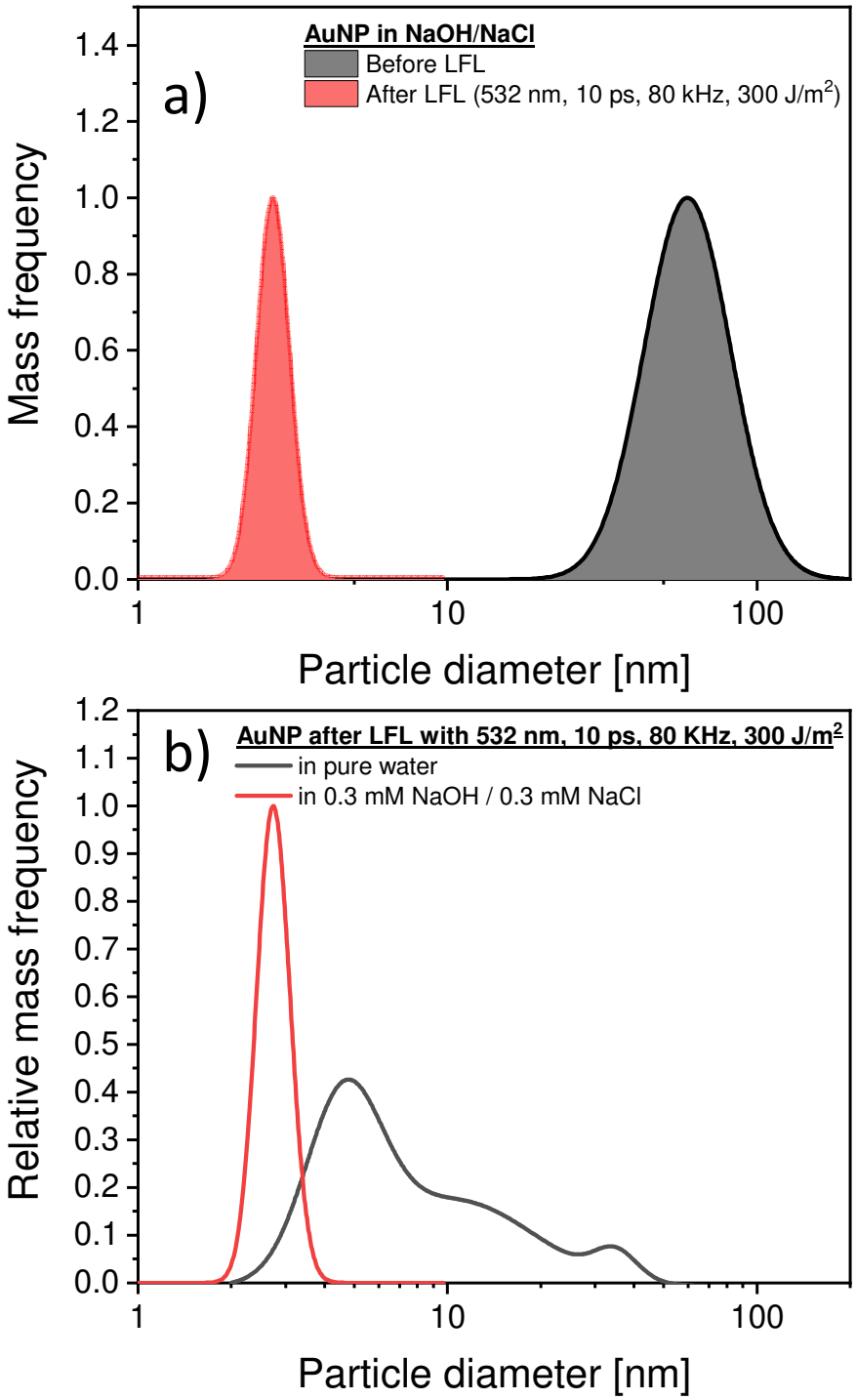

Figure 1: (Supplemental figure 1) a) Mass-weighted particle size distribution of educt and product particles (in 0.3 mM NaOH/NaCl) as derived by analytical ultracentrifugation (ADC). b) Mass-weighted size distribution of product particles in NaOH/NaCl as well as in pure water. The fragmentation has been performed with 10 ps pulses at 532 nm with 80 kHz repetition rate.

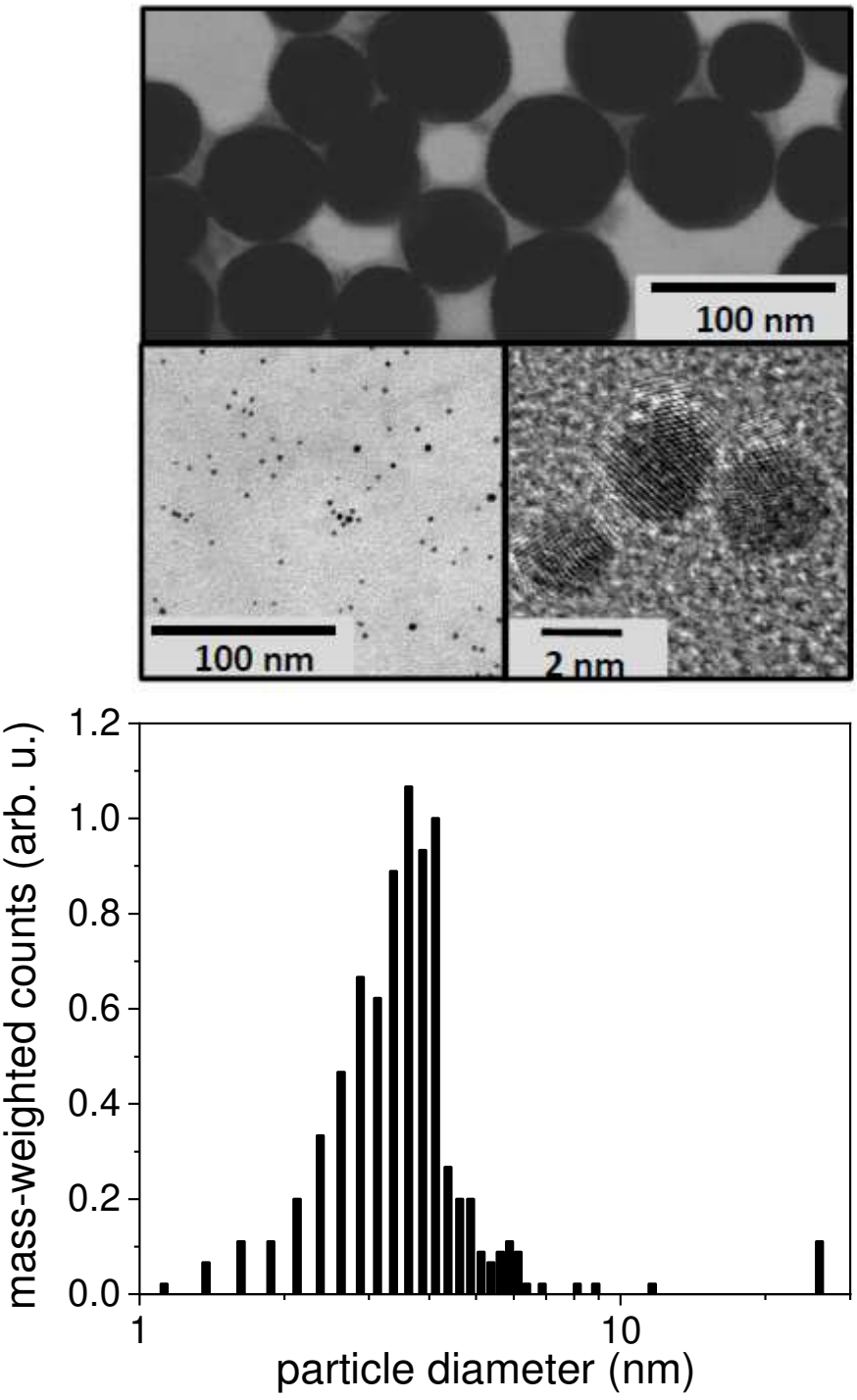

Figure 2: (Supplemental figure 2) TEM images of the educt and product particles as in fig. 1 and S1 together with a size histogram.

A5 Supporting Information: Chapter 3.2.3

Associated content

Synergism between specific halide anion and pH effects during nanosecond laser fragmentation of ligand free gold nanoparticles

Anna Rosa Ziefuß[1], Stephan Barcikowski[1]*, Christoph Rehbock[1*]

DOI: http://dx.doi.org/10.1021/acs.langmuir.9b00418

[1] University of Duisburg-Essen and Center for Nanointegration Duisburg-Essen (CENIDE), Essen 45145, Germany.

* corresponding author: Stephan.barcikowski@uni-due.de; Christoph.rehbock@uni-due.de

Educt particles for LFL

As described in [1], LFL requires a gold colloid that does not contain particles smaller than 13.1 nm in order to achieve full educt particle conversion. This colloid is separated after LAL in water by a double centrifugation step. Then, the colloid is highly-concentrated and can promote the coalescence of small particles to form larger particles [2,1].

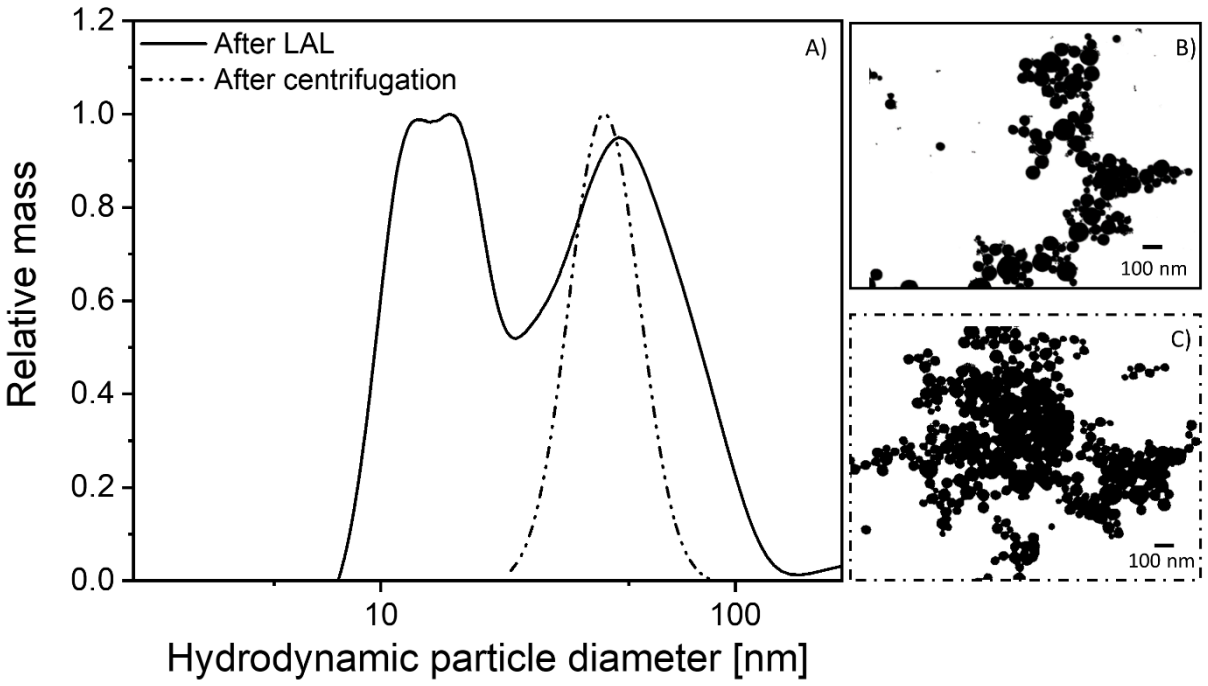

Figure S1: A) Relative mass distribution of the gold nanoparticles after LAL and subsequent centrifugation (dashed line); data determined by ADC measurements: B) STEM images of the nanoparticles after LAL; C) after subsequent centrifugation

Influence of pulses per volume element

As shown in our previous publication [1], the LFL is a one-pulse, one-step event. Higher number of pulses are necessary only because of statistical reasons caused by beam diffraction and attenuation [3] to ensure that each particle is hit at least once. Small particles have a higher

heat loss and a reduced cross section for absorption, so the laser energy that was used was not high enough to fragment the particles further.

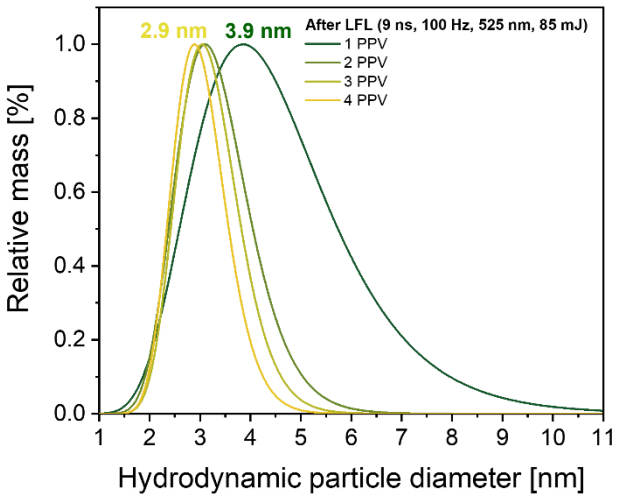

Figure S2: Relative mass distribution acquired from ADC measurements after 1-4 pulses per volume (PPV)

Influence of pH and ions on the zeta potential

The zeta potential of colloids correlates directly with their stability. Stable gold colloids show a zeta potential of > |30| at room temperature. It is well known that the zeta potential of colloids depends on the pH value of the solution, so, to get comparable results, we adjusted the pH value to 9-10 after LFL for all of the colloids before measuring.

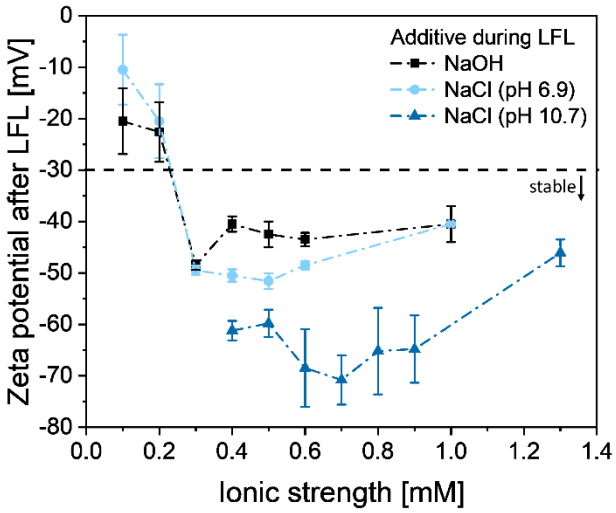

Figure S3: Zeta potential (Hückel regime) for samples after LFL in NaOH and in NaCl (at pH 6.9 and 10.7) with different ionic strengths

Effect of different pH values on the particle diameter after LFL

To stabilize the small particles after LFL, we examined the effect of different amounts of NaOH as a stabilizing agent. Figure S4 shows the mean diameters of the particles after LFL with NaOH.

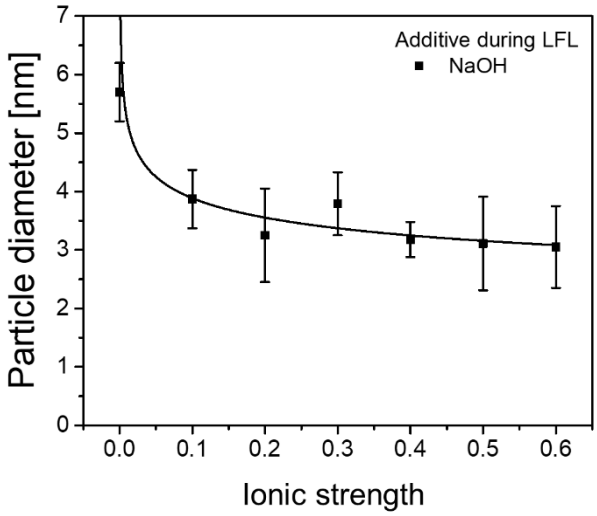

Figure S4: Hydrodynamic particle diameter after LFL with different amounts of NaOH

Influence of different halide salts on the properties of the particles after LFL

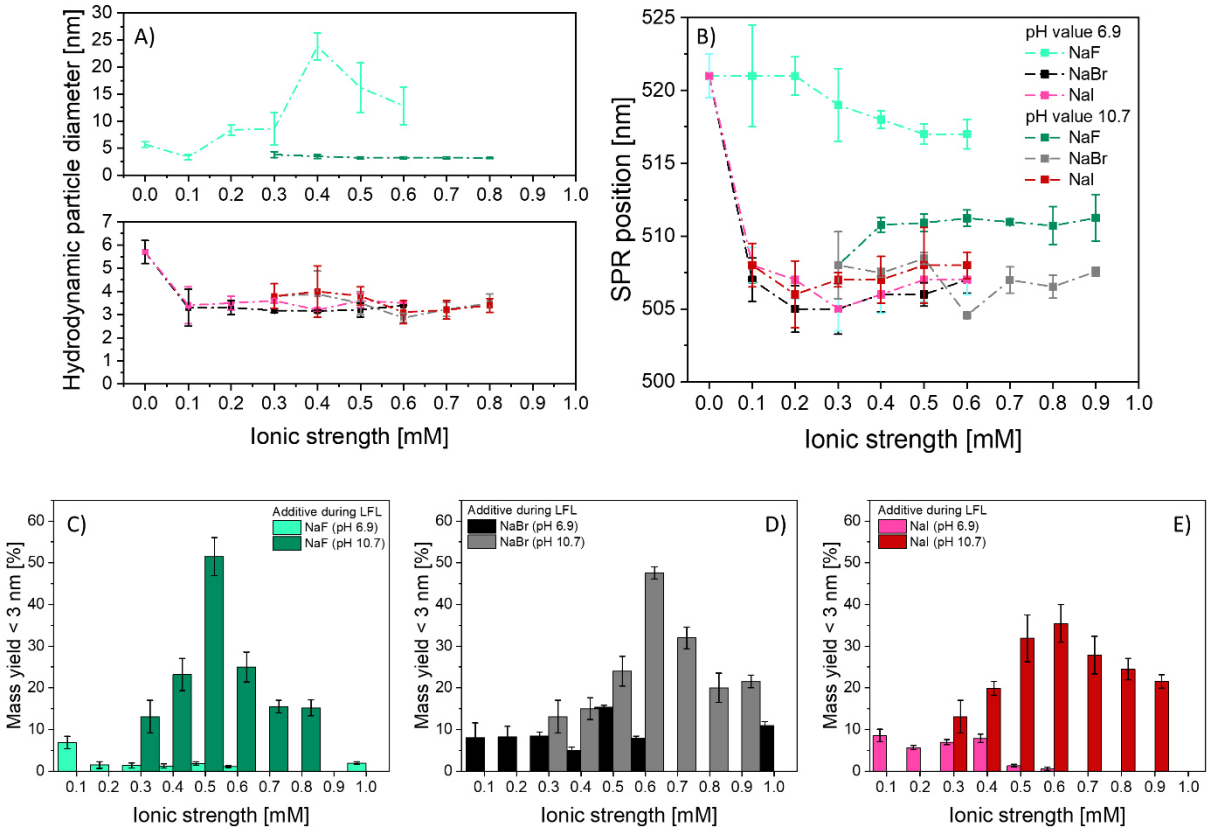

Figure S5: Influence of the ionic strength of NaF, NaBr, and NaI at pH 6.9 and pH 10.7 on A) the hydrodynamic product particle diameter (x_c value of the mass-weighted hydrodynamic particle diameteras determined by ADC); B) position of the SPR peak of particles obtained by LFL; C-E) mass yields smaller than 3 nm (determined by ADC)

Figure S5 provides a comparison of the mass-weighted and number-weighted size distributions after the ex situ addition of salts.

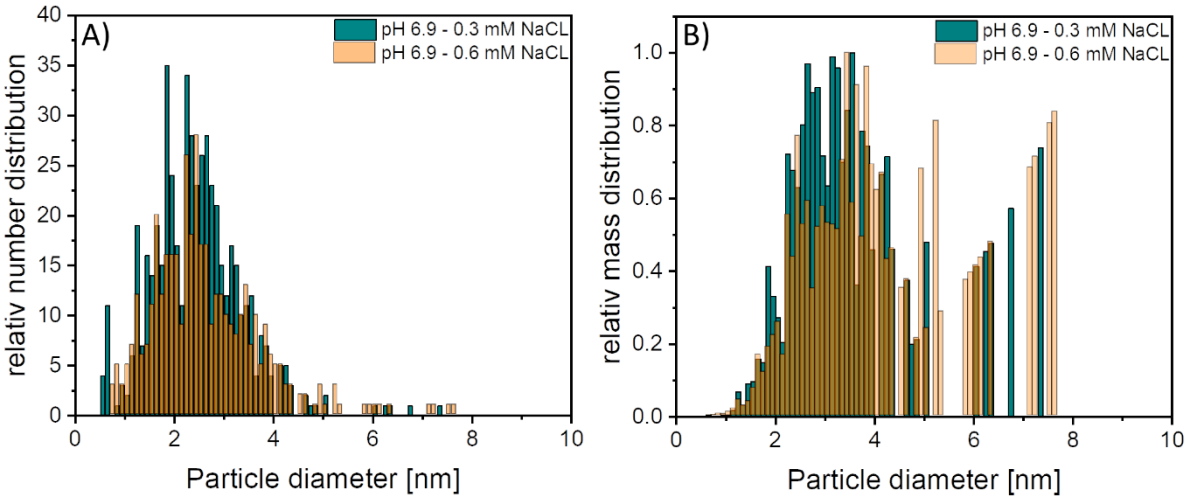

Figure S6: TEM histograms before and after ex situ addition of 0.3 mM NaCl to colloids that were fragmented in aqueous 0.3 mM NaCl: A) Number-weighted hydrodynamic size distributions; B) mass-weighted hydrodynamic size distributions

Surface oxidation of ultra-small AuNPs after LFL with NaCl in the basic and neutral pH ranges

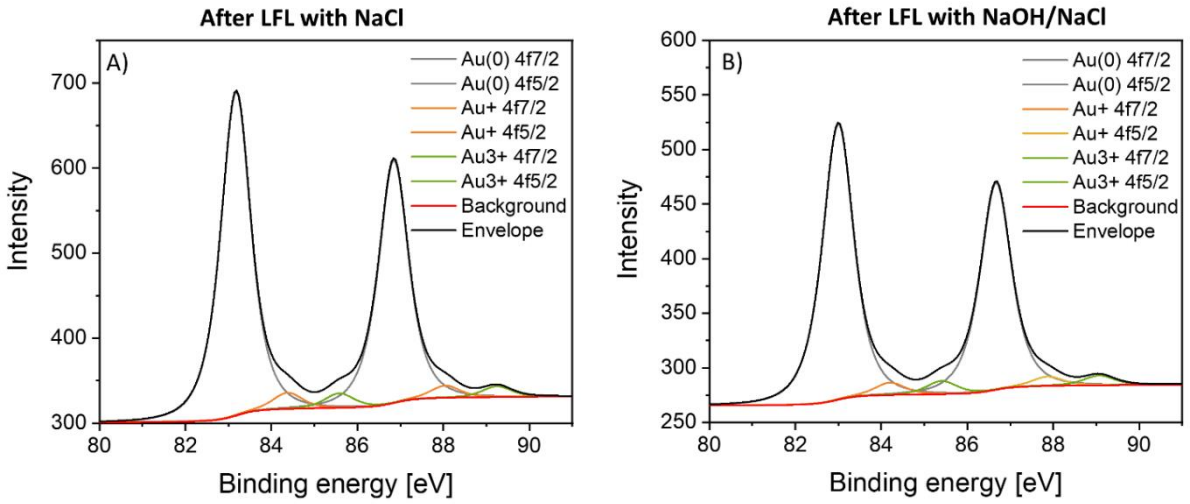

Figure S7: XPS spectra of ultra-small AuNPs after LFL with A) 0.3 mM NaCl; B) 0.3 mM NaOH + 0.3 mM NaCl

Transfer of the experimental findings to LFL in the batch process

All experiments in the main manuscript are conducted via irradiation of a vertically flowing liquid jet. We found that the resulting particle size after LFL of AuNPs is influenced by the amount and kind of anions, that can be used to stabilize the produced particles. We focused on the halide anions and found a stabilizing effect according to the direct HS while LFL in the neutral pH regime and a reversed behavior when LFL is conducted in the basic range. However, in most of the literature, the LFL is described after irradiating a colloid in a cuvette. Such experiments are usually multiple pulse events. According to the literature [1], the surface properties of the resulting ultra-small particles depends critically on the number of pulses. Especially in the context of anionic stabilization events, this could cause different phenomena's and therefore we decided to validate our findings with cuvette experiments.

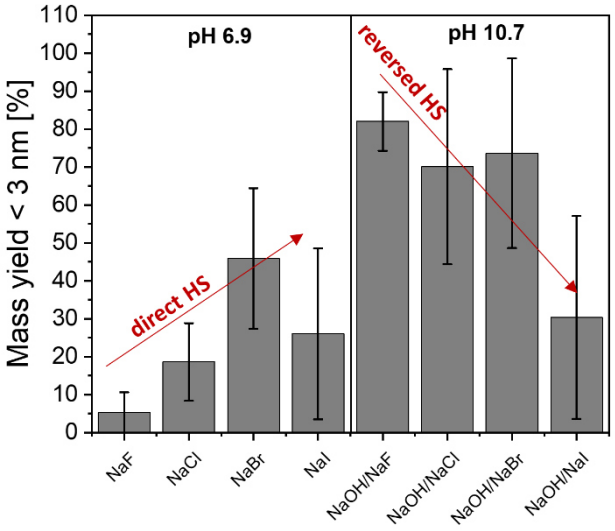

Figure S1: Influence of halide salts LFL results of the different pH values on the A) mass yield of particles smaller than 3 nm. Experiments conducted as a batch process. Error bars obtained by performing the experiments three times.

The experimental setup is similar to the one described in the experimental section, but we replaced the liquid jet by 4 mL clear glass threaded bottles (17,7 x 45 mm) and filled them with 2 mL colloidal educt solution. The laser was adjusted comparable to the liquid jet experiments,

the point where it first met the liquid jet was adjusted to the center of the liquid. The duration time of irradiation was 14 sec and leads to an overall energy input comparable to the experiments in the liquid jet. Our findings can be found in Figure S8.

With this experiment, we confirm the validity of our results in batch experiments. The stability can be enhanced according to the HS in the basic and we found a reverved behavior.

References

[1] Ziefuß, A. R.; Reichenberger, S.; Rehbock, C.; Chakraborty, I.; Gharib, M.; Parak, W. J.; Barcikowski, S. Laser Fragmentation of Colloidal Gold Nanoparticles with High-Intensity Nanosecond Pulses is Driven by a Single-Step Fragmentation Mechanism with a Defined Educt Particle-Size Threshold, J. Phys. Chem. C, **2018**, 122 (38), 22125–22136.

[2] Jendrzej, S.; Gökce, B.; Amendola, V.; Barcikowski, S. Barrierless growth of precursor-free, ultrafast laser-fragmented noble metal nanoparticles by colloidal atom clusters - A kinetic in situ study, J. Colloid Interface Sci., **2016,** 463, 299–307.

[3] Waag, F.; Gökce, B.; Kalapu, C.; Bendt, G.; Salamon, S.; Landers, J.; Hagemann, U.; Heidelmann, M.; Schulz, S.; Wende, H.; et al. Adjusting the catalytic properties of cobalt ferrite nanoparticles by pulsed laser fragmentation in water with defined energy dose, Sci. Rep., **2017**, 7, 13161.

A6 Supporting Information: Chapter 3.2.4

Inorganic anions linearly tune the electron-phonon coupling time of colloidal gold nanoparticles

Anna R. Ziefuß[1], Christoph Rehbock[1], Sven Reichenberger[1], Alexander Letzel[1], Zhijiang Chen[2], Benjamin K. Ofori-Okai[2], Matthias Hoffmann[2], Chandra B. Curry[2,3], Siegfried H. Glenzer[2], Stephan Barcikowski[1]*

[1] Technical Chemistry I and Center for Nanointegration Duisburg-Essen (CENIDE), University of Duisburg-Essen, Universitaetsstrasse 7, 45141 Essen, Germany

[2] High Energy Density Science Division, SLAC National Accelerator Laboratory, Menlo Park, California 94025, USA

[3] Department of Electrical and Computer Engineering, University of Alberta, Edmonton, Alberta T6G 1H9, Canada

* corresponding author: stephan.barcikowski@uni-due.de

Section I: Additional experimental details

Laser ablation of solids in ultra-pure water leads to particles with a broad size distribution.[1] To select narrowed size fractions, further centrifugal steps are necessary. After 70 min centrifugation with a relative centrifugal force (RCF) = 67.1 x g (1.5 mL), the larger size fraction formed a pellet at the bottom of the centrifugation tube (size distribution can be found in Fig. *1*A). The supernatant was removed to retrieve the pellet, which was subsequently dispersed in ultra-pure water. The supernatant was additionally centrifuged (20 min RCF = 645 x g resulting in a redispersible pellet containing the desired 23 nm fraction. For their use in further optical pump-probe experiments, both colloids were diluted to a mass concentration of 100 mg/L for their use in optical pump-probe spectroscopy.

The hydrodynamic particle diameter was estimated using an analytical disk centrifugation (ADC, CPS Instruments) at 24 000 rpm. Additionally, trans electron microscopy (TEM) was done at a Zeiss EM 910. Absorbance spectra in Fig 1 B are measured with an Thermo Scientific, Evolution 201 UV-Vis spectrometer in a wavelength range from 190 - 900 nm (with $\Delta\lambda = 1$ nm). Further static abosrbance measuremnts were done at the same device with a higher resolution of $\Delta\lambda = 0.1$ nm.

Numbers on the surface charge density are calculated[2] from the zetapotential which we measured at a Malvern Zetasizer Nano Z.

The absorbance behavior of the 53 nm An NPs over a broad concentration range is shown in Fig. S1. We cannot observe a change of the absorbance at the SPR (neither in the absorbance intensity nor in the position of the SPR).

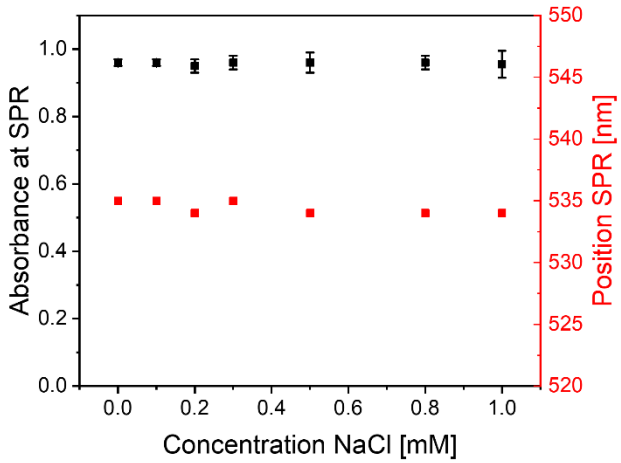

Figure S 1: *Absorbance at SPR (blck) and the position of the SPR (red) after addition of different NaCl concentrations.*

Section II: Geometrical consideration of the number of surface atoms and number of Cl^- per Au NP

Anionic species show a stronger influence on the $\tau_{e\text{-}ph}$ of larger NPs than on smaller NPs, explainable by the different mass-specific surface areas. We used 23 nm and 53 nm particles at identical mass concentrations of 40 mg/L within our experiments. Note that the number concentration of the smaller particles is thus higher (Figure S2A), resulting in a larger specific surface area which is equal to an increased number of surface atoms per mass (Figure S2B). In each case, we discussed the influence of the anion dose on the electron density of the gold surface, which is, under the given conditions, increased for the larger spheres (Figure S2C).

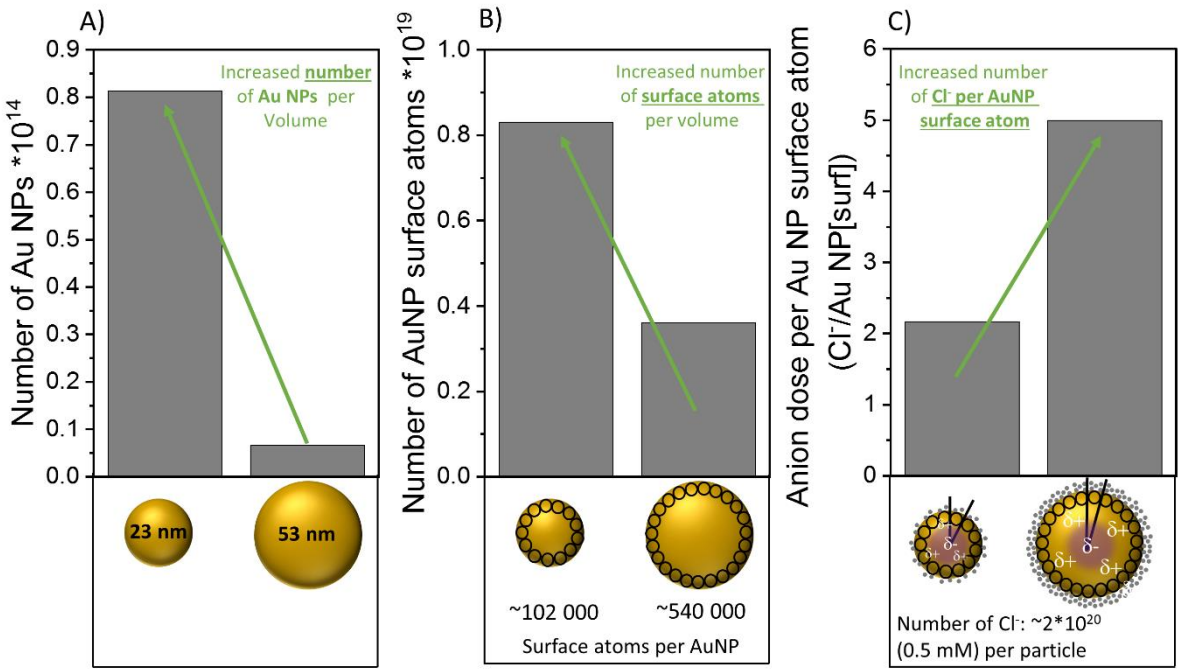

Figure S2: *Graphical illustration of the surface-specific anion dose per liter, via particle number and surface effects at a constant gold mass concentration of 40 mg/L for both sized colloids (A) total number of particles per colloid volume. The calculation follows geometrical consideration:* $N_{Au\ NPs} = \frac{c}{\pi/6 \cdot d^3 \cdot \rho}$. *(B) Total number of gold surface atoms per colloid and therefore probed sample volume. Calculation of surface atoms was done by dividing the projected area of a sphere by the total surface area.[2] (C) Calculation of the total number of* Cl^- *anion dose (at an ionic strength of 0.5 mM) per gold surface atom.*

Note that the calculated number of the nominal Cl^- dose per AuNP surface atom will exceed a monolayer adsorption. Considering the anion diameter[3] and the surface area of a particle, ~12500 Cl^- (for a 23 nm particle) and ~67000 Cl^- (for a 53 nm particle) would maximal fit on the surface of one particle. However, the adsorption of anions on gold surfaces is a reversible equilibrium process, where the adsorption coefficient (K) based on a Langmuir adsorption model would rule the process. In case we drastically reduce the surface area of the particles at the same overall ionic strength the ratio of ions per free gold surface sites would increase. As the K value is supposed to be the same for 23 and 53 nm gold nanoparticles (no significant differences in surface defects or curvature) this would result in a higher anion surface coverage in the larger nanoparticles. However, the anion excess is in part located in the electrochemical double layer as well. The latter is generally formed if electrolytes (in our case Cl^-) come into contact with a metal surface[4] (See also Figure 2 in the manuscript). However, the double layer thickness depends on the electrolyte concentration, and the

electrochemical potential depends on the distance of the electrolytes to the surface[4]. Following Ohshima et al.[5], the charge density in the electrochemical double layer can be calculated by measuring the zeta potential. Following Table 1, the surface charge density is increased for the larger spheres, which proves our initial assumption of more anions next to the particle surface of larger particles."

Table 4: *Measured zeta potential and calculared surface charge density of different sized Au NPs in 0.5 mM aqueous NaCl*

Mean particle diameter [nm]	Zeta potential [mV]	Surface charge density [C/m^2]
23	-20	$-8.11*10^{-4}$
53	-48	$-9.63*10^{-4}$

Section III: Additional information on the laser stability

An analysis of the laser stability of the pump and sample laser shows a fluctuation of the probe beam, which was probably generated during the passing of the OPA. To reduce the effect on the measurement data and to generate a good signal to noise ratio, the data of at least 5 measurements were averaged.

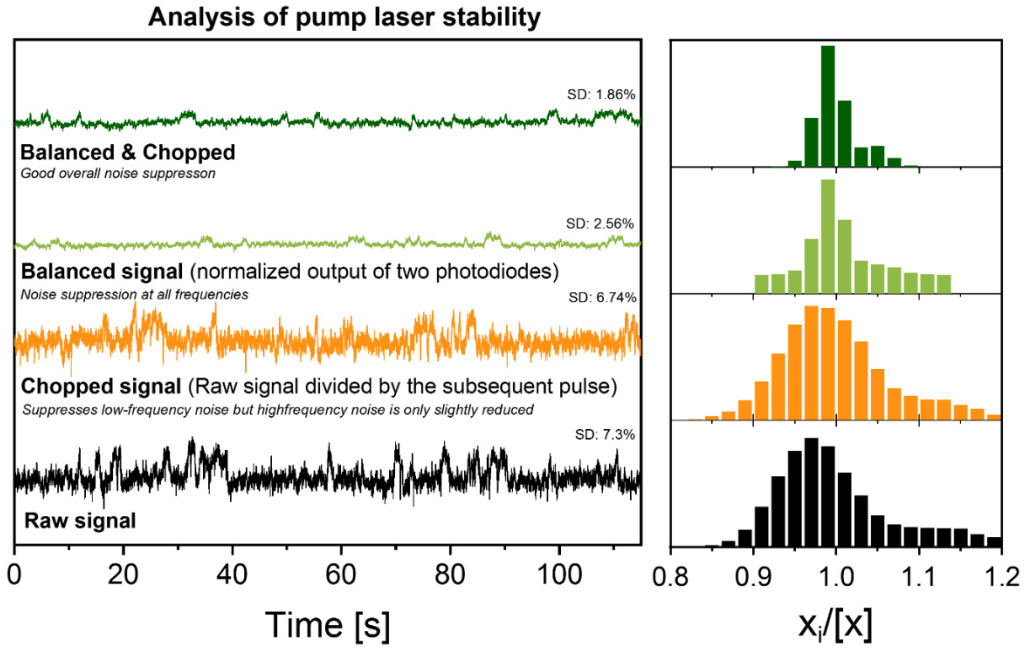

Figure S3: *Raw signal (black), chopped signal (orange), balanced signal (light green), and balanced and chopped (dark green) signal of the pump laser with corresponding standard deviation. The balanced signal was recorded by dividing the raw signal of a pulse with the subsequent pulse to suppress low-frequency noise, while the high-frequency noise is only slightly reduced. A noise signal suppression is achieved by normalizing the output signal of two photodiodes (balanced signal) and overall noise suppression is gained by combining the balanced and chopped signal. More information can be found in ref*[7]

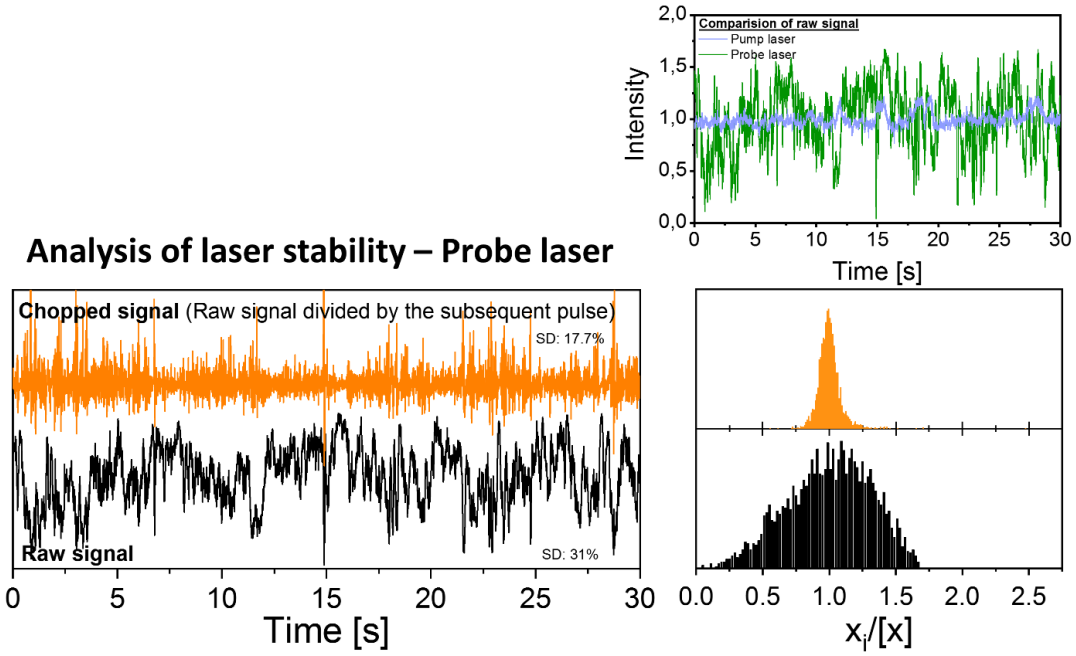

Figure S4: *Raw signal (black) and chopped signal (orange), of the probe laser with corresponding standard deviation. The latter was recorded by dividing the raw signal of a pulse with the subsequent pulse to suppress low-frequency noise, while the high-frequency noise is only slightly reduced. Further, a comparison of the pump and probe raw signal can be found.*

Section IV: Calculations according to the TTM

To determine the energy absorbed by the particles, the knowledge of the absorption cross-section is of crucial importance. We calculated the latter using the license-free software MiePlot (screenshots can be found in S4 and S5). The calculation was done at 400 nm (pump wavelength in our experiments). Additionally, we used optical constants reported by Johnson and Christy in ref[8])

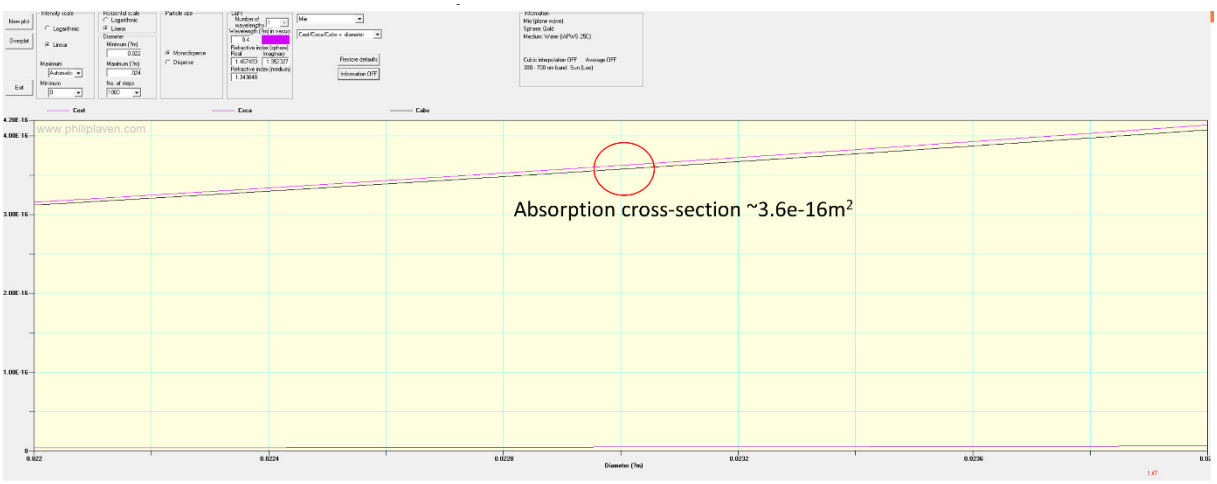

Figure S5: *Screenshot of the calculation of the absorption cross-section of a 23 nm Au NP using MiePlot (the license free software can be found elsewhere: http://www.philiplaven.com)*

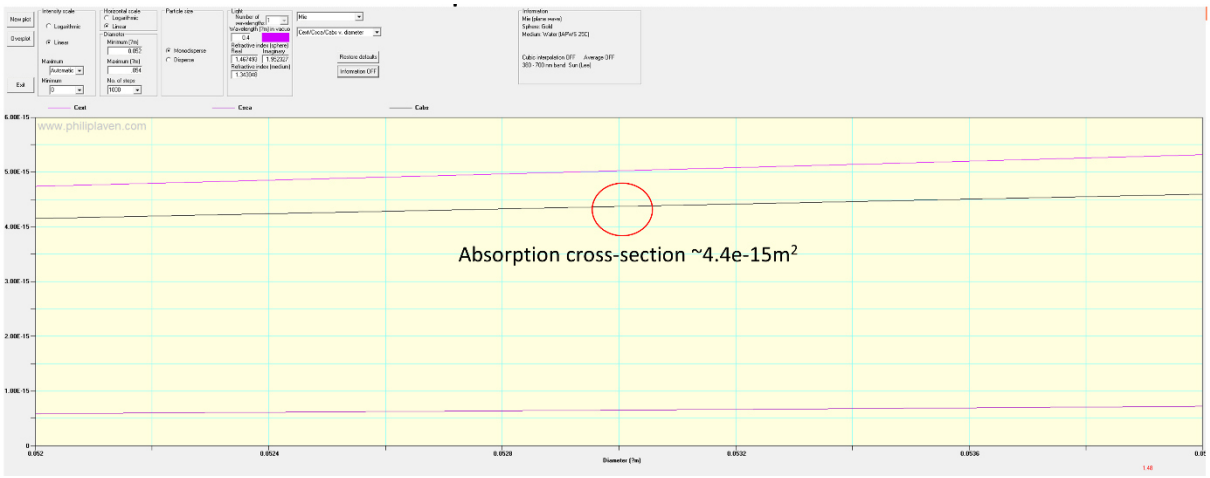

Figure S6: *Screenshot of the calculation of the absorption cross-section of a 53 nm Au NP using MiePlot (the license-free software can be found elsewhere: http://www.philiplaven.com)*

Multiplying the absorption cross-section by the laser fluence gives the total absorbed energy in Joules.

Section V: Optical pump-probe spectroscopy

Raw data of the pump-probe spectroscopy that are not given in the manuscript are shown below.

Fig. S6 shows raw data for 23 nm particles. The corresponding $t_{e\text{-}ph}$ is given in the manuscript in Fig 1D. The coupling time $t_{e\text{-}ph}$ between electrons and phonons was determined by fitting the exponential decay between 1-10 ps with $\frac{\Delta Tr}{Tr} = A \cdot \exp\left(-\frac{t_{Delay}}{\tau_{e-ph}}\right) + \left(\frac{\Delta Tr}{Tr}\right)_0$.

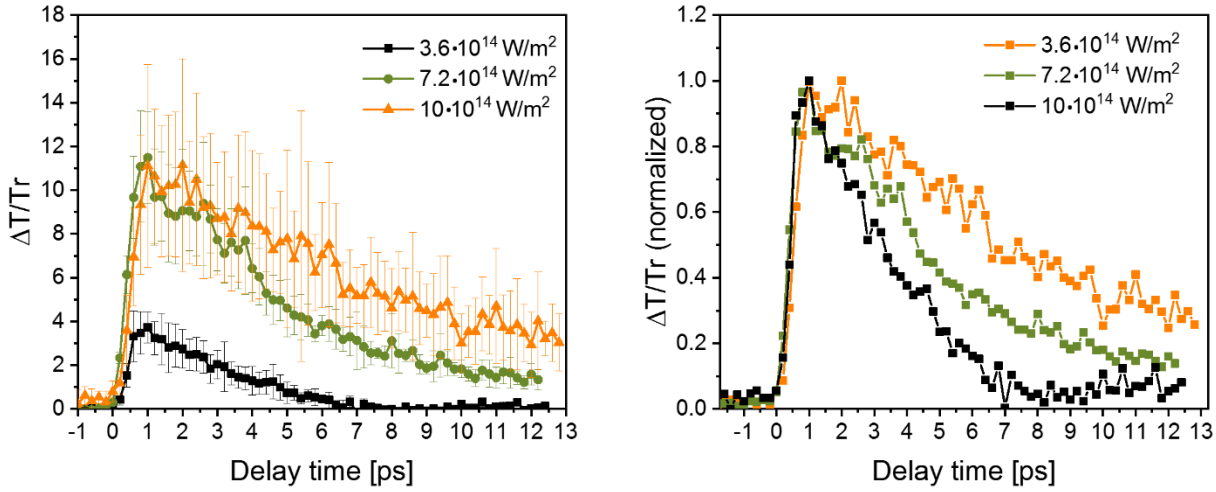

Figure S7: *A) Transient transmission change after excitation of 23 nm AuNPs in H_2O (black)) as a function of delay time with different Laser intensity, B) Normalized data set.*

Fig S7 includes data obtained on 23 nm Au NPs and Fig S8 includes data on 53 nm particles. Both figures are the basis for Fig 2 in the manuscript.

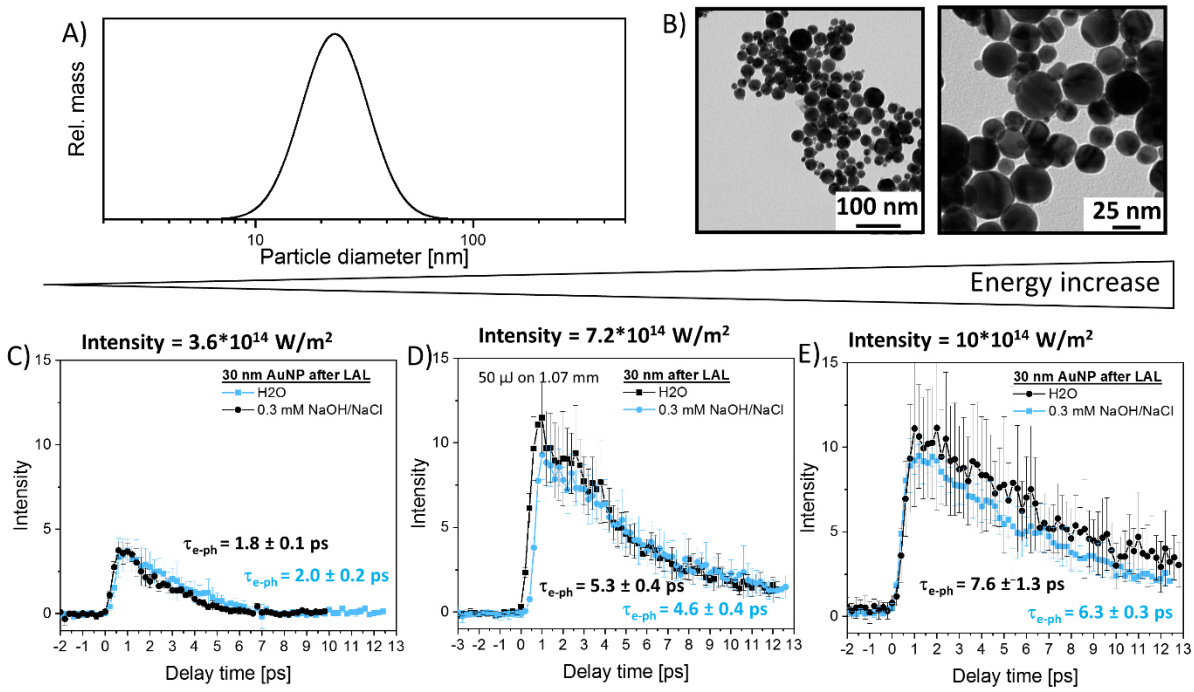

Figure S8: *Particle size analysis after LAL and subsequent centrifugation (23 nm particles) A) ADC mass-weighted size distribution B) TEM Image. C-E) Transient transmission change after excitation of 23 nm AuNPs in H_2O (black) and 0.3 mM* NaOH/NaCl (blue) as a function of delay time with increasing pulse energy from C to E.

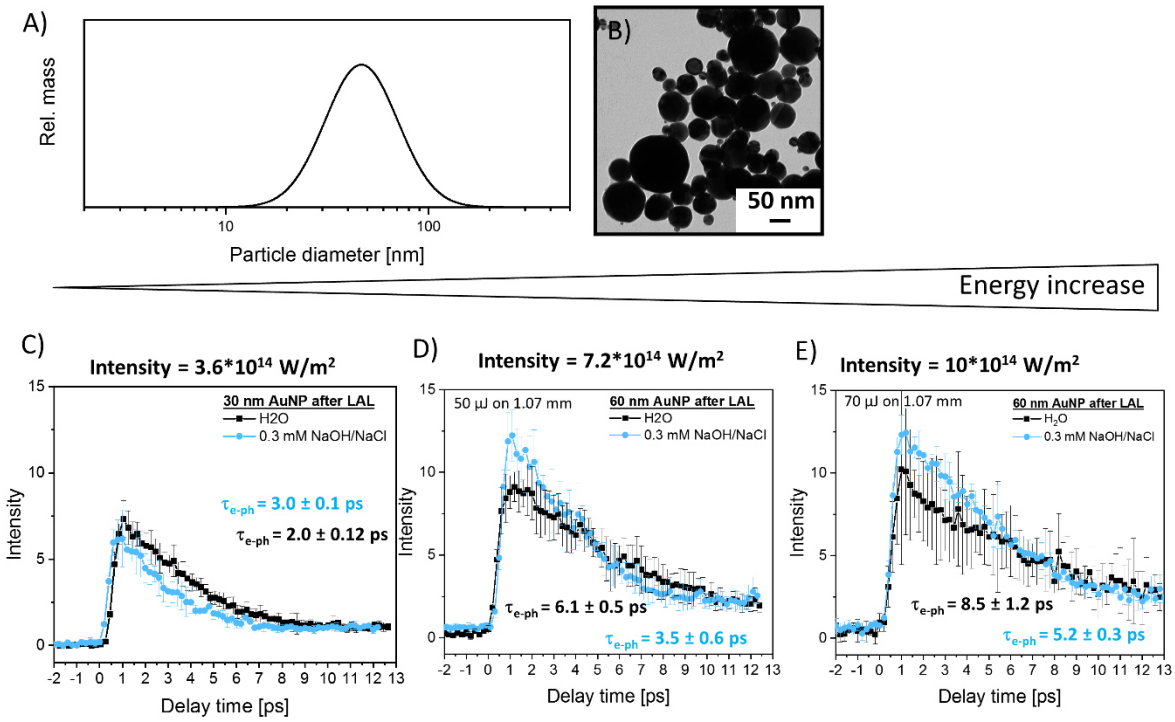

Figure S9: *Particle size analysis after LAL and subsequent centrifugation (53 nm particles) A) ADC mass-weighted size distribution B) TEM Image. C-E) Transient transmission change after excitation of 53 nm AuNPs in H_2O (black) and 0.3 mM NaOH/NaCl (blue) as a function of delay time with increasing pulse energy from C to E.*

Section VI: Static UV-Vis measurements and pump-probe experiments to evaluate the effect of monovalent Hofmeister series of anions

"Anion adsorption leads to a partial positive surface charge while electron density is transferred to the interior of the particle. The influence of the anions on the electron density of the particle surface should be observable in static UV-Vis measurements as Au NP show a pronounced surface plasmon resonance in the visible regime. Here, we added 0.5 mM NaX with X = F^-, Cl^-, Br^-, I^- (Hofmeister series of anions, sorted from kosmotropic to chaotropic) to colloids with 23 nm and 53 nm Au NPs and measured the absorbance at the SPR. The results are shown in Figure S10.

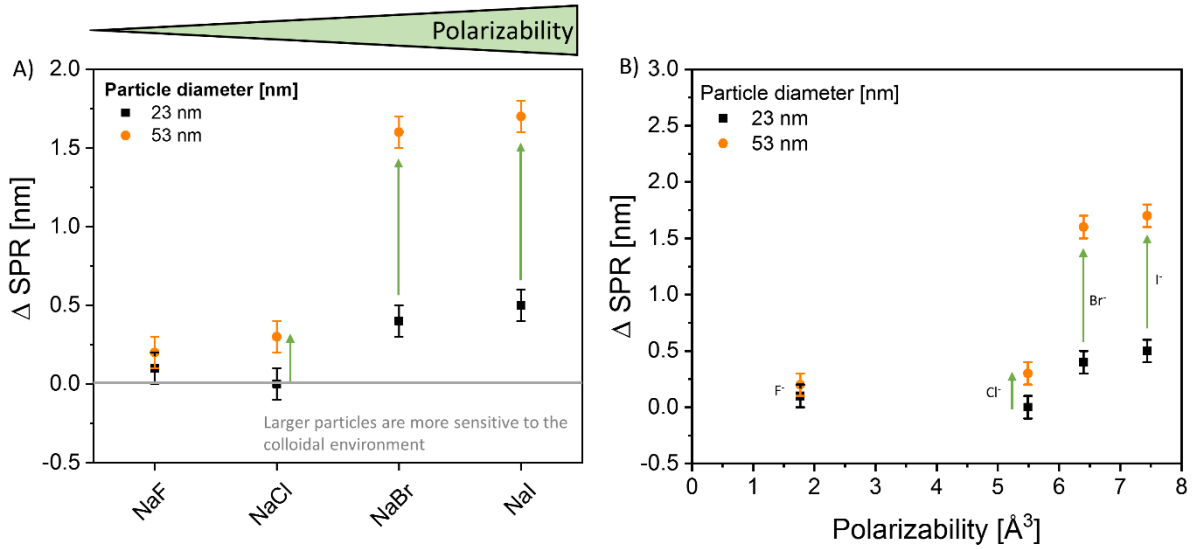

Figure S10: *SPR shift of different sized gold colloids (23 nm particles, black and 53 nm, orange) after ex-situ addition of a Hofmeister anion series of sodium salts. Shifts are calculated by subtracting the SPR position of the respective particles in ultra-pure water. (A) Δ SPR vs. kind of sodium salt, (B) Δ SPR vs. polarizability of the anion (F- [9], Cl- [4], Br- [10], I- [11]).*

Overall, we found that kosmotropic anions like F^- show a minor effect on the position of the SPR. Chaotropic anions like Br^- show a stronger influence which is even stronger for larger spheres. The chosen anions can be differentiated by their polarizability. Following Figure S10B, the polarizability of at least 5 $Å^3$ is needed to induce a measurable effect on the electronic structure of the Au surface (observable by the altered SPR position). Further, the red-shifted SPR with increasing polarizability of the SPR is stronger for larger particles, validating the initial assumption of anion polarizability effects on the AuNP electron density (see also section II). As another control experiment, we adjusted the absolute surface value of the smaller and larger-sized particles to the sample value (4.5±0.5 cm^2/mL) and evaluated the influence of the anions in the position of the SPR. We found no significant differences in the SPR red-shifts caused by the anions if the surface values are the same at the two different particle diameters, even for the bromine anion causing the strongest effect in the probed Hofmeister series. Note that a red-shift of the SPR could also be explained by altered hydrodynamic particle size, by aggregation-induced plasmon coupling. To exclude any influence by the latter, we determined the hydrodynamic particle size both

before and after the addition of 0.5 mM NaBr (Figure S11) and found no significant changes (below 4 ± 0.5%).

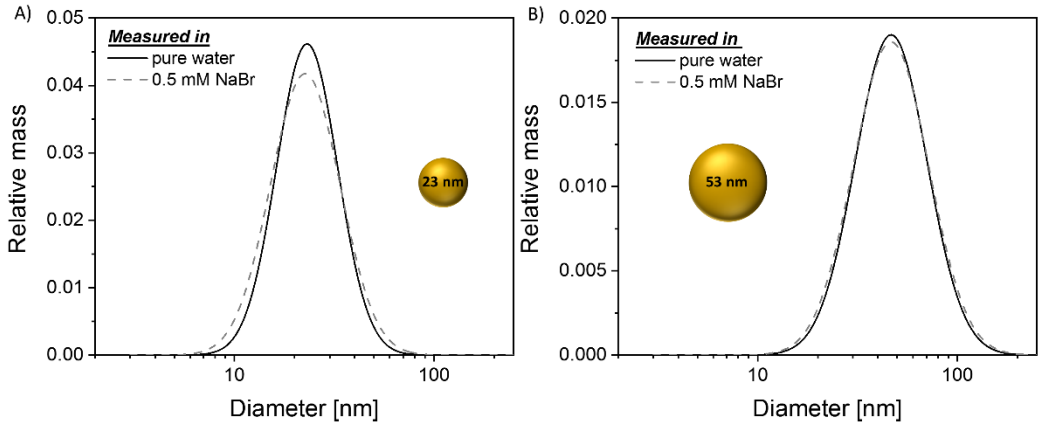

Figure S11: *Mass-weighted hydrodynamic particle size distribution before (solid line) and after (dashed line) addition of 0.5 mM NaBr. A) 23 nm particles, B) 53 nm particles.*

In a second step, we evaluated the influence of the monovalent anions within dynamic pump-probe measurements (Figure S12). We observed the trends expected from the Hofmeister series, with more chaotropic anions having significantly stronger effects on the electron phonon coupling lifetime, shown in Figure S10.

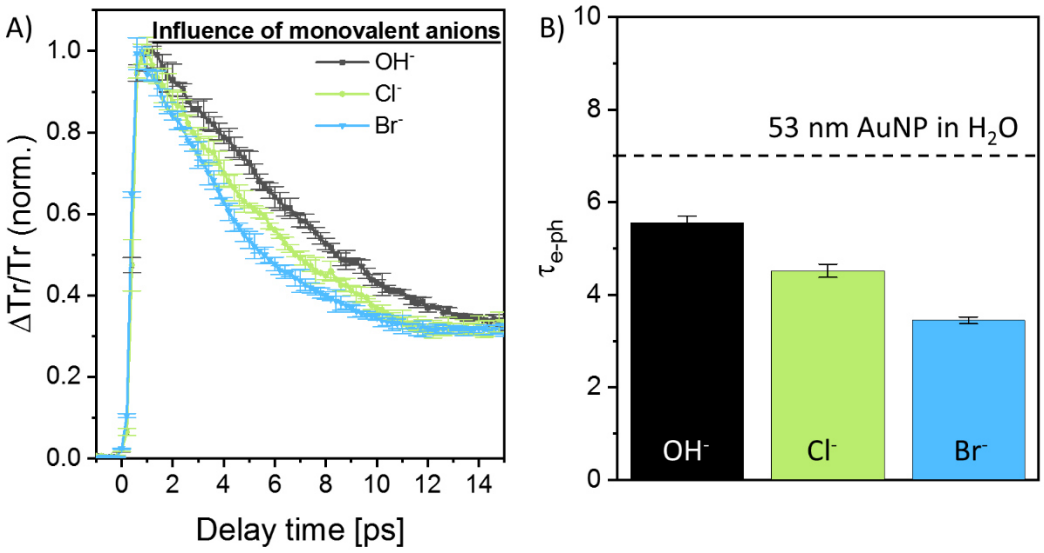

Figure S12: *A) Influence of monovalent anions with increased anion polarizability on the decay curve of 53 nm Au NPs at a laser pulse energy of 50 µJ. B) Comparison of* $\tau_{e\text{-}ph}$ *of Au NPs in* H_2O*, NaCl, and NaBr, showing that increased anion polarizability causes significantly faster electron-phonon coupling.*

We further tested the influence of multivalent salts in the position of the SPR and found no significant differences (Figure S14). Besides polarisation and ionic strength, the number of hydration is critically discussed in the manuscript. The adsorption capacity for strongly hydrated ions on metal surfaces is usually decreased, which we were able to confirm by absorbance measurements (Figure S13).

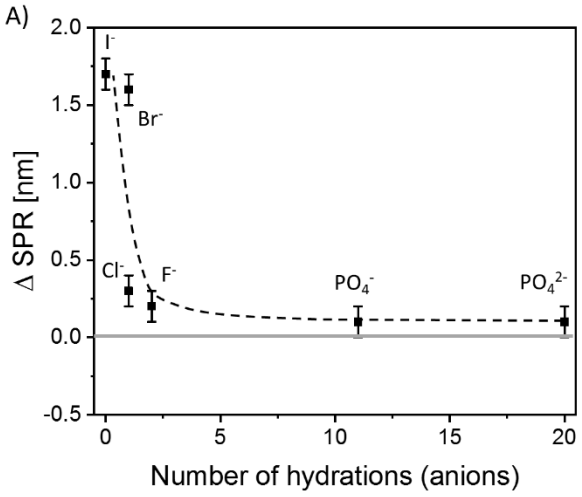

Figure S13: *Plot of SPR shift as a function of the number of hydrations of the anions added to the Au NP colloid.*

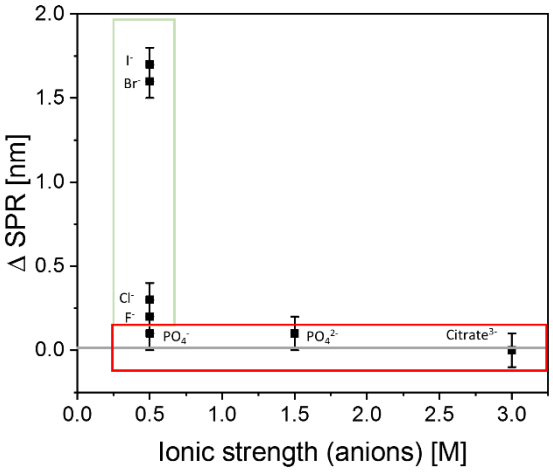

Figure S14: *SPR shift after addition of different monovalent (green box) and multivalent (red box) anions. The SPR shift indicates the position of the SPR in relation to the particles in ultra-pure water in dependency of the ionic strength.*

Section VII: Theoretical consideration of the process based on the TTM

TTM predicts non-exponential decay of T_e for all excitation powers. In the case of a nanoparticle, the TTM reduces to $C_e(T_e)\frac{\partial T_e}{\partial T} = -G(T_e)(T_e - T_l), C_l(T_l)\frac{\partial T_l}{\partial T} = -G(T_e)(T_e - T_l)$ as there is no need to consider thermal conductivity.

Defining $\Delta T = T_e - T_l$ and subtracted one equation from another, leads to: $\frac{\partial \Delta T}{\partial t} = -G(T_e)\frac{C_e(T_e)+C_l(T_l)}{C_e(T_e)C_l(T_l)}\Delta T$. The solution of this differential equation is $\Delta T = exp\left(-\frac{t}{\tau}\right)$, where $\tau = \frac{C_e(T_e)C_l(T_l)}{G(T_e)(C_e(T_e)+C_l(T_l)}$.

Since $C_l \gg C_e$ one can approximate $\tau = \frac{C_e(T_e)}{G(T_e)}$. In general, both G and C_e are functions of T_e. For Au, the dependence of G on T_e is very weak (essentially absent) up to ~4000 K. To proof this, we performed two-temperature model simulations and fit the early times of the calculated traces to exponential functions, and plotted them a function of the absorbed energy density and the max electron temperature for different values of G (Figure S15).

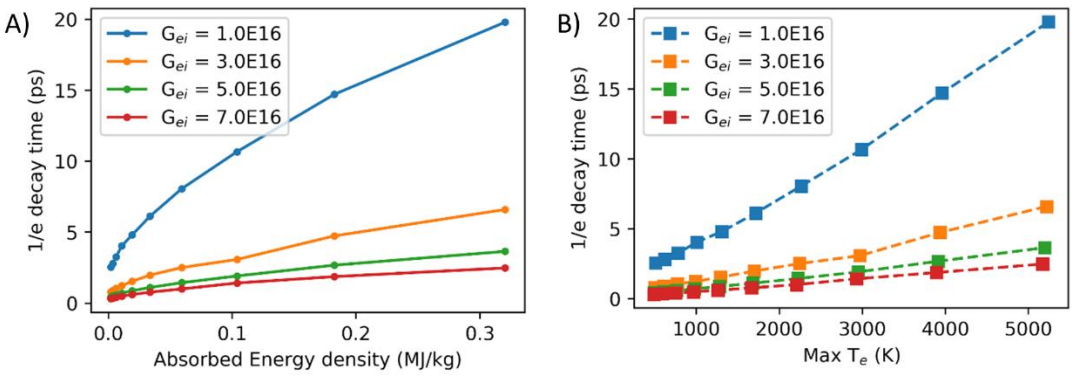

Figure S15: *Early times of the exponential decay in dependency on G as a a function of A) the absorbed energy density and B) the max electron temperture.*

Thus, for moderate excitations, we assume a constant value of G. However, C_e is not constant and has an approximately linear dependence on T_e, i.e., $C_e = \gamma T_e$. Thus, despite the exponential form of the solution $\Delta T = exp\left(-\frac{t}{\tau}\right)$, the value of $\tau = \frac{\gamma T_e}{G}$ is not constant and changes linearly with T_e, which leads to a non-exponential time dependence of ΔT. Note that previous optical pump-probe transient absorption measurements have studied the electron-phonon coupling strength of nanoparticles.[12-13] In these cases, the data were fit to exponential functions and the decay times were used to infer the electron-phonon coupling parameter. These have been compared against results obtained from independent measurements using other ultrafast techniques on nanoparticles[12], with excellent agreement observed[13].

References

1. Zhang, D., Gökce, B. Barcikowski, S. Laser Synthesis and Processing of Colloids: Fundamentals and Applications. *Chem. Rev.* **117,** 3990–4103; 10.1021/acs.chemrev.6b00468 (2017).

2. Makino, K. & Ohshima, H. Electrophoretic mobility of a colloidal particle with constant surface charge density. *Langmuir* **26,** 18016–18019; 10.1021/la1035745 (2010).

3. Ziefuß, A. R.*, I. Haxhiaj, S. Mueller, M. Gharib, O. Gridina, C. Rehbock, I. Chakraborty, B. Peng, M. Muhler, W. Parak et al.,* Origin of Laser-Induced Colloidal Gold Surface Oxidation and Charge Density, and Its Role in Oxidation Catalysis. *J. Phys. Chem. C* **124,** 20981–20990; 10.1021/acs.jpcc.0c06257 (2020).

4. Jungwirth, P. & Tobias, D. J. Chloride Anion on Aqueous Clusters, at the Air−Water Interface, and in Liquid Water: Solvent Effects on Cl - Polarizability. *J. Phys. Chem. A* **106,** 379–383; 10.1021/jp012059d (2002).

5. Li, Z., Ruiz, V. G., Kanduč, M. & Dzubiella, J. Ion-Specific Adsorption on Bare Gold (Au) Nanoparticles in Aqueous Solutions: Double-Layer Structure and Surface Potentials. *Langmuir* **36,** 13457–13468; 10.1021/acs.langmuir.0c02097 (2020).

6. Brown, M. A. *et al.* Determination of Surface Potential and Electrical Double-Layer Structure at the Aqueous Electrolyte-Nanoparticle Interface. *Phys. Rev. X* **6,** 1753; 10.1103/PhysRevX.6.011007 (2016).

7. Werley, C. A., Teo, S. M. & Nelson, K. A. Pulsed laser noise analysis and pump-probe signal detection with a data acquisition card. *Rev. Sci. Instrum.* **82,** 123108; 10.1063/1.3669783 (2011).

8. Johnson, P. B. & Christy, R. W. Optical Constants of the Noble Metals. *Phys. Rev. B* **6,** 4370–4379; 10.1103/PhysRevB.6.4370 (1972).

9. Bryce, R. A., Vincent, M. A., Malcolm, N. O. J., Hillier, I. H. & Burton, N. A. Cooperative effects in the structuring of fluoride water clusters: Ab initio hybrid quantum mechanical/molecular mechanical model incorporating polarizable fluctuating charge solvent. *J. Chem. Phys.* **109,** 3077–3085; 10.1063/1.476900 (1998).

10. Ayala, R. *et al.* Development of first-principles interaction model potentials. An application to the study of the bromide hydration. J. Phys. Chem. **117,** 10512–10524; 10.1063/1.1519843 (2002).

11. Archontis, G., Leontidis, E. & Andreou, G. Attraction of iodide ions by the free water surface, revealed by simulations with a polarizable force field based on Drude oscillators. *J. Phys. Chem. B* **109,** 17957–17966; 10.1021/jp0526041 (2005).

12. Perner, M. *et al.* Optically Induced Damping of the Surface Plasmon Resonance in Gold Colloids. *Phys. Rev. Lett.* **78,** 2192–2195; 10.1103/PhysRevLett.78.2192 (1997).

13. Hartland, G. V., Hodak, J. H. & Martini, I. Comment on “Optically Induced Damping of the Surface Plasmon Resonance in Gold Colloids”. *Phys. Rev. Lett.* **82,** 3188; 10.1103/PhysRevLett.82.3188 (1999).

A7 Supporting Information: Chapter 3.3.1

ADVANCED MATERIALS

Supporting Information

for *Adv. Mater.,* DOI: 10.1002/adma.202101549

Photoluminescence of Fully Inorganic Colloidal Gold Nanocluster and Their Manipulation Using Surface Charge Effects

*Anna R. Ziefuss, Torben Steenbock, Dominik Benner, Anton Plech, Jörg Göttlicher, Melissa Teubner, Benjamin Grimm-Lebsanft, Christoph Rehbock, Clothilde Comby-Zerbino, Rodolphe Antoine, David Amans, Indranath Chakraborty, Gabriel Bester, Milen Nachev, Bernd Sures, Michael Rübhausen, Wolfgang J. Parak, and Stephan Barcikowski**

Supporting Information

Photoluminescence of fully inorganic colloidal gold nanocluster and their manipulation using surface charge effects

*Anna. R. Ziefuss, Torben Steenbock, Dominik Benner, Anton Plech, Jörg Göttlicher, Melissa Teubner, Benjamin Grimm-Lebsanft, Christoph Rehbock, Clothilde Comby-Zerbino, Rodolphe Antoine, David Amans, Indranath Chakraborty, Gabriel Bester, Milen Nachev, Bernd Sures, Michael Rübhausen, Wolfgang J. Parak, Stephan Barcikowski**

Section I: Laser-based synthesis of ligand-free Au NCs

LFL leads to a colloid containing plasmonic and proto-plasmonic particles.[1] A detailed description of the laser-based fragmentation can be found in the following references.[1,2]. In brief, the interaction of nanoparticles with a high-intensity laser pulse leads to a temperature increase within the particles and the medium, causing phase transitions leading to phase explosion and fragmentation. The efficiency of laser fragmentation measured by the average product particle diameter and mass yield of particles smaller than 3 nm increases with increasing laser intensity. In recent in situ investigations, we could shed light on the phase-explosion mechanism during fragmentation and the subsequent ripening.[2] This secondary particle growth after LFL is favored as it will reduce the specific surface area, which is thermodynamically driven as it results in a decreased free Gibbs enthalpy. To avoid particle growth, a stabilization strategy is required, which could be i) dilution to increase the mean free path length and thereby decrease the collision rate or ii) addition of electrostatic stabilizers which can 'shield' the particles by electrostatic repulsion and increase the Debye length. Note that the addition of organic ligands would also reduce secondary particle growth by steric stabilization. However, the omission of organic ligands is a central point in this work. In previous work, we have already demonstrated that the yield of Au NCs can be synergistically increased when LFL takes place in the presence of the two electrostatic stabilizers NaOH and NaCl.[3] However, as this procedure does not guarantee a 100 % yield of particles smaller than 3 nm, and we observe an optical signal of larger, plasmonic particles (Figure S1A) 50 kDa centrifugal filters were used to separate remaining plasmonic particles. The separation was successful (Figure S1C) and no more plasmonic particles could be detected in the absorbance measurements (Figure S1B).

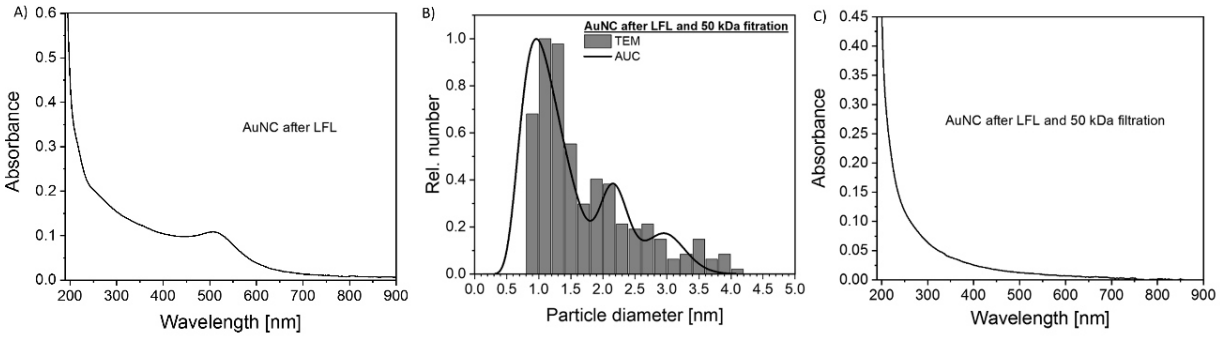

Figure S 1: A) Absorbance spectra after LFL of AuNPs with 0.3 mM NaOH and 0.3 mM NaCl B) Size distribution of Au NCs after LFL and subsequent filtration with 50 kDa centrifugal filter. The filtrate contains particle sizes between 0.4 – 4 nm. C) Corresponding absorbance spectrum.

Further size separation was conducted by using smaller MWCO centrifugal filters (10, 3, 1 kDa). Using 3 kDa filter, we were able to produce ultra-small particles (Figure 1B), which could be additionally analysed using ESI-MS. While the size distribution is given in Figure 1B of the main manuscript, additional information on this method can be found in the following section.

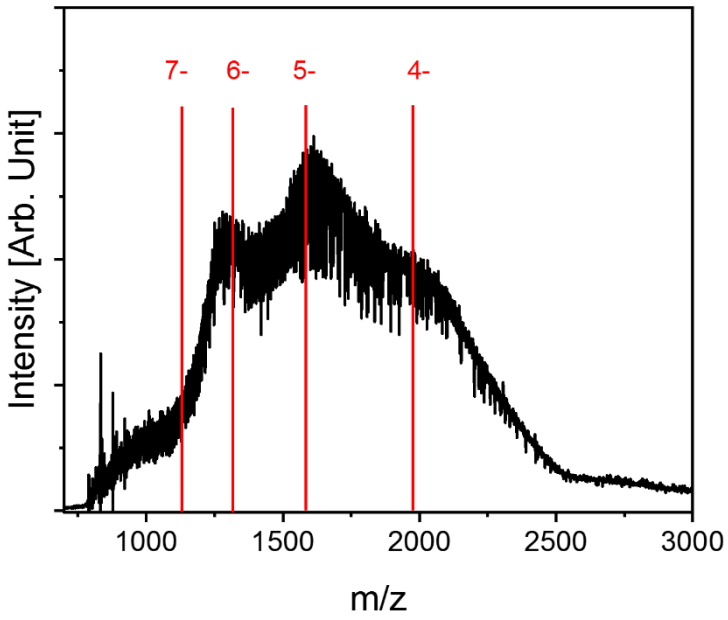

Figure S2: Nano ESI mass spectra of Au NCs in water recorded in negative mode. The red number assignment (at the red vertical lines) corresponds to charge states of the MW=7900 Da.

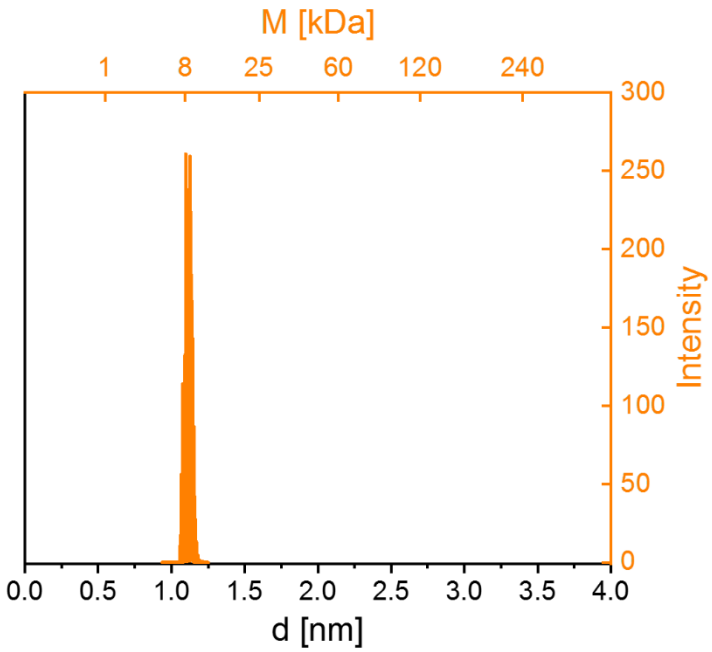

Figure S3: Spectra corresponding to deconvoluted nano ESI mass spectra between the charges states 4 and 7, rescaled with the formula $D_{Nanoparticles} = \sqrt[3]{\frac{\text{Mw nanoparticles}}{\text{MAu}*30.89602}}$. We are assuming spherical shape and face centered cubic crystal structure.[4]

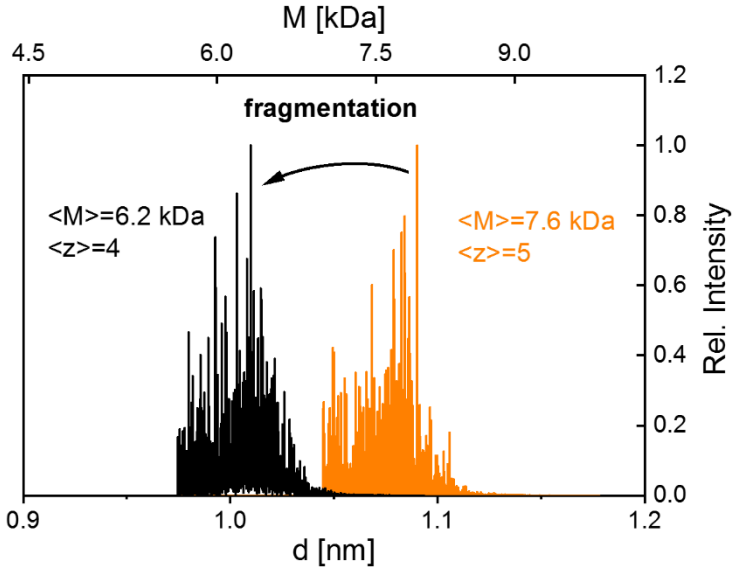

Figure S4: Deconvoluted nanoESI mass spectra of precursor NCs (orange) and of fragmented NCs (black). The precusors' ions undergo collisions with argon in the collision cell device on

the MS instrument. The difference between fragments and parents corresponds to the evaporation of around seven gold atoms and one negative charge.

Section II: Surface adsorbates effect

The variation of the pH value forces a pronounced alteration of the gold surface charge density as it leads to protonation or deprotonation of surface adsorbates (OH/O^-).[5] Following Ohshima et al.[6], the surface charge density can be described as a function of the zeta potential, a factor that can be determined experimentally (see experimental section of the main manuscript) and describes the electric charge in Coulomb per surface area. Based on this it is possible to calculate absolute values of negative surface charges by simply dividing the surface charge density by the elementary charge and subsequently multiplying it by the mean particle surface. The mean particle surface is calculated from the experimentally obtained particle size distribution shown in Figure 1B (green curve) in the main manuscript. A comparison with the charge quantity of the elementary charge finally results in the number of free charge carriers on the particle surface.

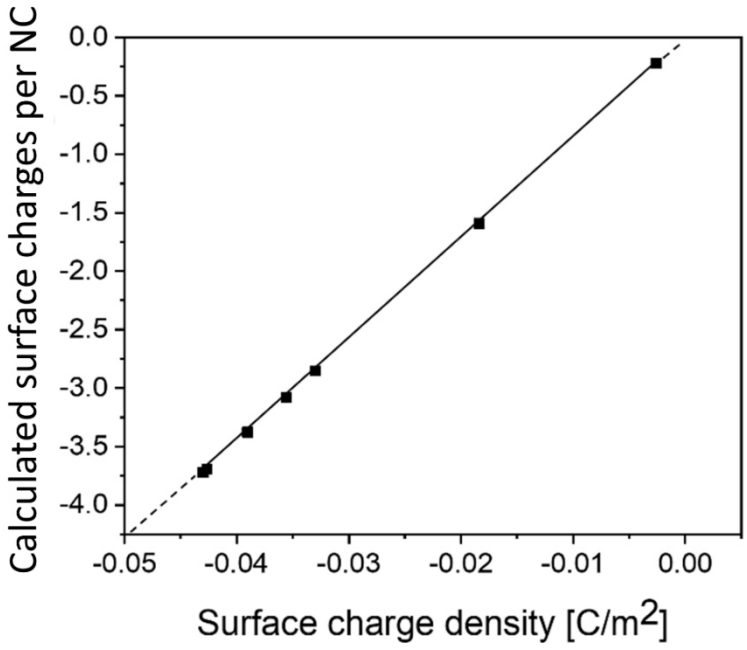

Figure S5 Correlation between total number of surface charges and the surface charge density, calculated for LFL generated NCs with a mean diameter of 2.1 nm.

In addition, the change of the pH value shows an influence on the emission. To determine this, different ionic strengths of NaOH and HCl were added. All raw data can be found in Figure S6. Note that adjusting the pH value in a range between pH 4 and 12 does not influence the particle diameter (Figure S7).

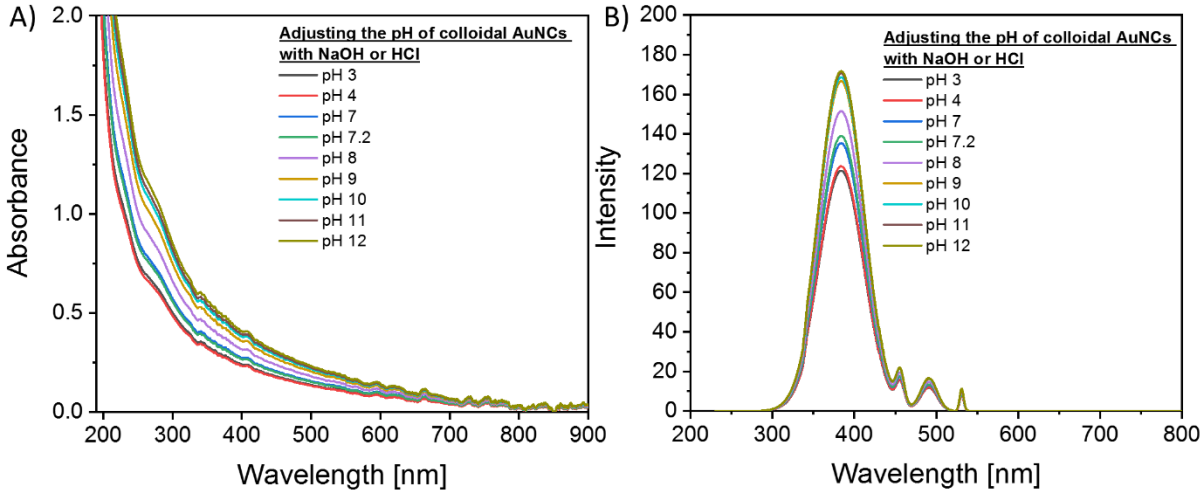

Figure S6: Absorbance and emission intensity of Au NCs after adjusting the pH value in the range of pH 3 to pH 12.

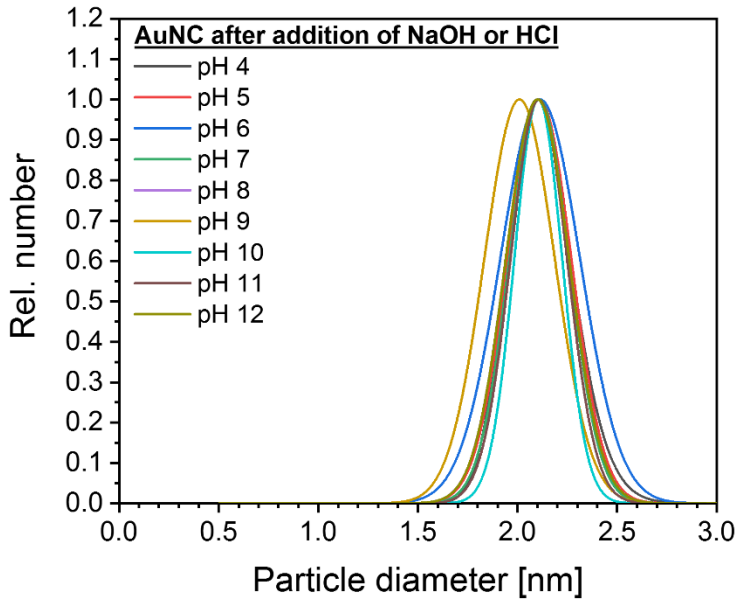

Figure S7: Hydrodynamic particle diameter distribution of Au NCs after adjusting the pH value with HCl or NaOH.

Additionally, we checked the photophysical long-term stability of the particle's emission at two different surface charge densities of -0.031 C/m^2 and -0.059 C/m^2, corresponding to a solution pH of 7 and 10, respectively. Size distributions of the corresponding particles are depicted in Figures S8 A and D. The size distribution evaluated by AUC is unchanged after photoexcitation and after 1 week of storage.
Even though we found no significant differences in the particles' size distributions at pH=7 and pH=10 small deviations occurred even though the particles were taken from the same synthesis batch. Here, we cannot discriminate whether these differences are due to an impact of the charge on particle size or whether the charge density affects the measurement. We

measured the particle size with the AUC, which detects the movement of a sedimentation front which is formed after radial acceleration of a sample rotor. The temporal displacement of the sedimentation front allows the determination of the sedimentation coefficient. The sedimentation distribution can be described by the Lamm equation and is a function of the particle size. However, the sedimentation behavior can be influenced by charging effects.[7] Surface charges can act as a counterforce to sedimentation[7] so that particles could be perceived as smaller, as observed at pH=10. However, these slight differences do not impede the consecutive evaluation of particle stability.

Figures S8 B and E show the emission behavior measured at different times, and Figures S8 C and F show a summary of the emission intensity measured at 350 nm. Following this, the emission intensity changed neither for particles with 1 negative charge per particle (-0.031 C/m^2) nor for particles with doubled negative surface charges per particle (-0.059 C/m^2). Based on this, we conclude that the photophysical properties of fully inorganic gold nanoclusters are long-term stable."

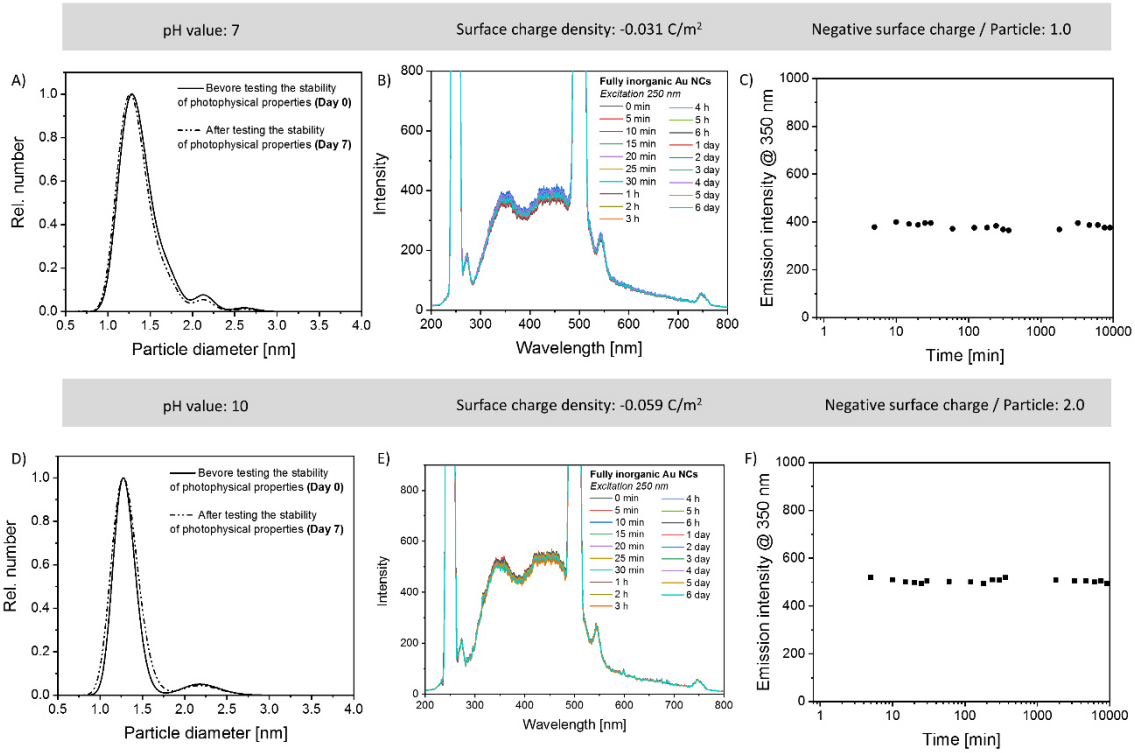

Figure S8: Investigation of the photophysical stability at different surface charges. A-C) surface charge adjusted to -0.031 C/m^2, D-F) surface charge adjusted to -0.059 C/m^2. A) and D) particle size distribution of the particles measured before and after photoexcitation and storage for 7 days. B) and E) Emission spectra recorded after different times. C) and F) Emission intensity at 350 nm in correlation with storage time. Note that the emission intensity for particles increases with higher surface charge density (see also Figure 2 in the manuscript)

Section III: Additional information on the theoretical calculations

In the following, we will provide the details on the theoretical calculations carried out on the $Au_{38}(OH)_{24}$ gold nanocluster and the subsequently deprotonated species.

Analysis of excited states from SCIS

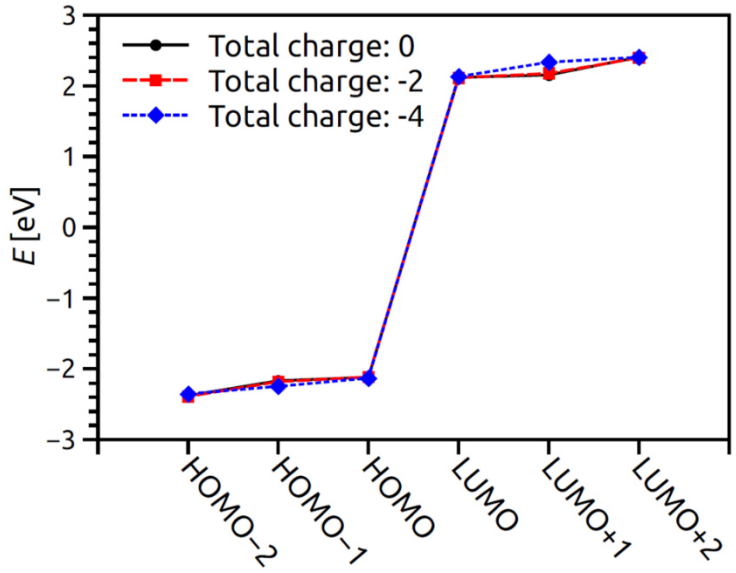

Figure S 9: Single-particle energies calculated with BHLYP/dhf-SVP-2c/COSMO(water) including spin-orbit coupling.

Table S 1: Analysis of excited states according to the SCIS results. The values in parenthesis after the single-particle excitations represent the contribution of a given single-particle excitation to a given excited state in percent.

Excited state number	**Energy [eV]**	**Transition dipole moment [a.u.]**	**Composition**
Total charge: 0			
32	4.24653	3.56×10^{-1}	HOMO-2 → LUMO+2 (66%) HOMO-2 → LUMO (14%)
Total charge: -2			
32	4.28637	4.29×10^{-1}	HOMO-2 → LUMO+2 (52%) HOMO-2 → LUMO (24%)
Total charge: -4			
32	4.37497	3.53×10^{-1}	HOMO-2 → LUMO+1 (44%) HOMO-2 → LUMO+2 (18%) HOMO-1 → LUMO+2 (18%)
36	4.41981	1.04×10^{-1}	HOMO-2 → LUMO+2 (66%) HOMO-2 → LUMO+1 (44%)

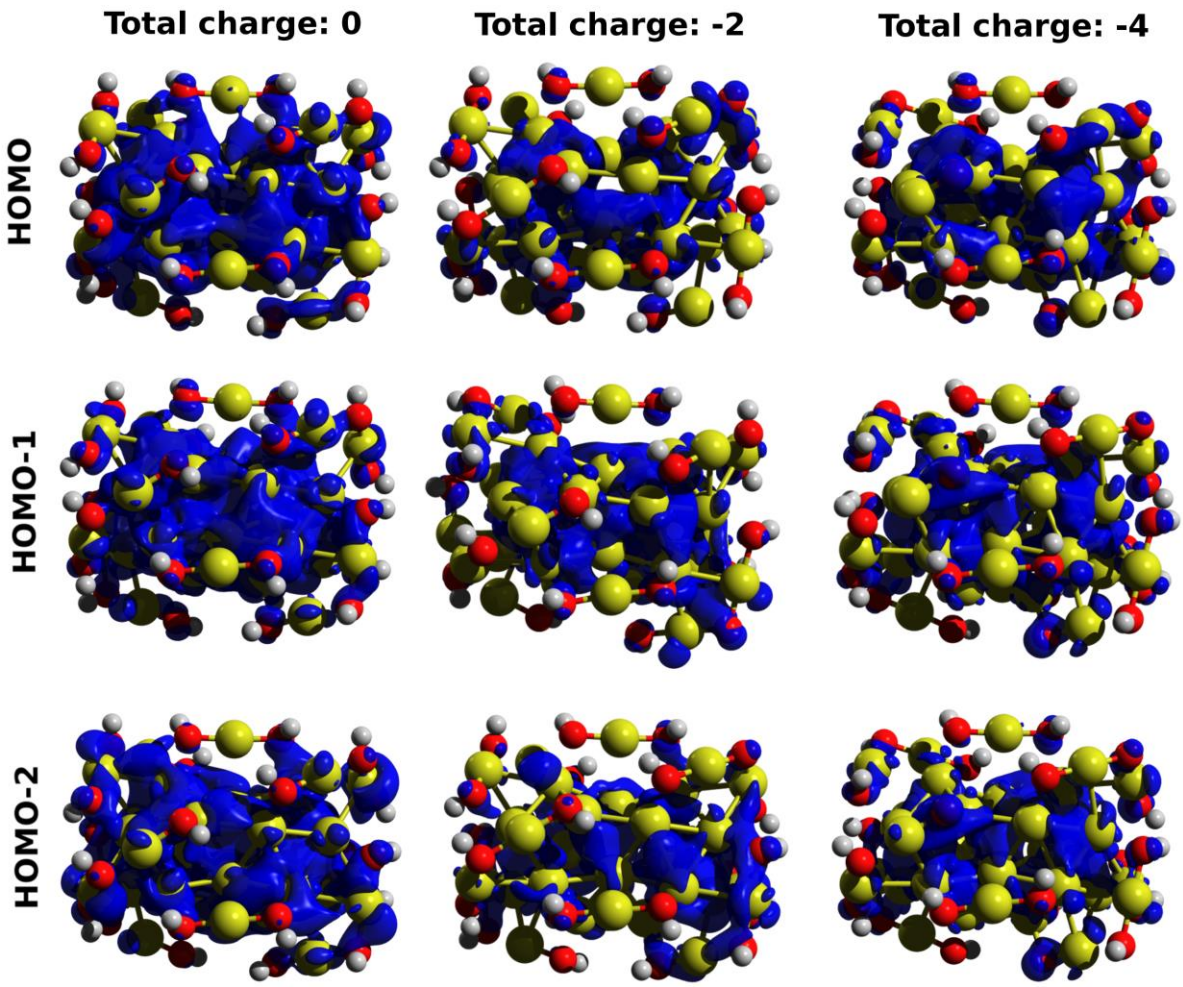

Figure S10: Electron densities of the valence states for three different charge states calculated with wB97X-d/dhf-SVP-2c and the COSMO model with parameters for water.

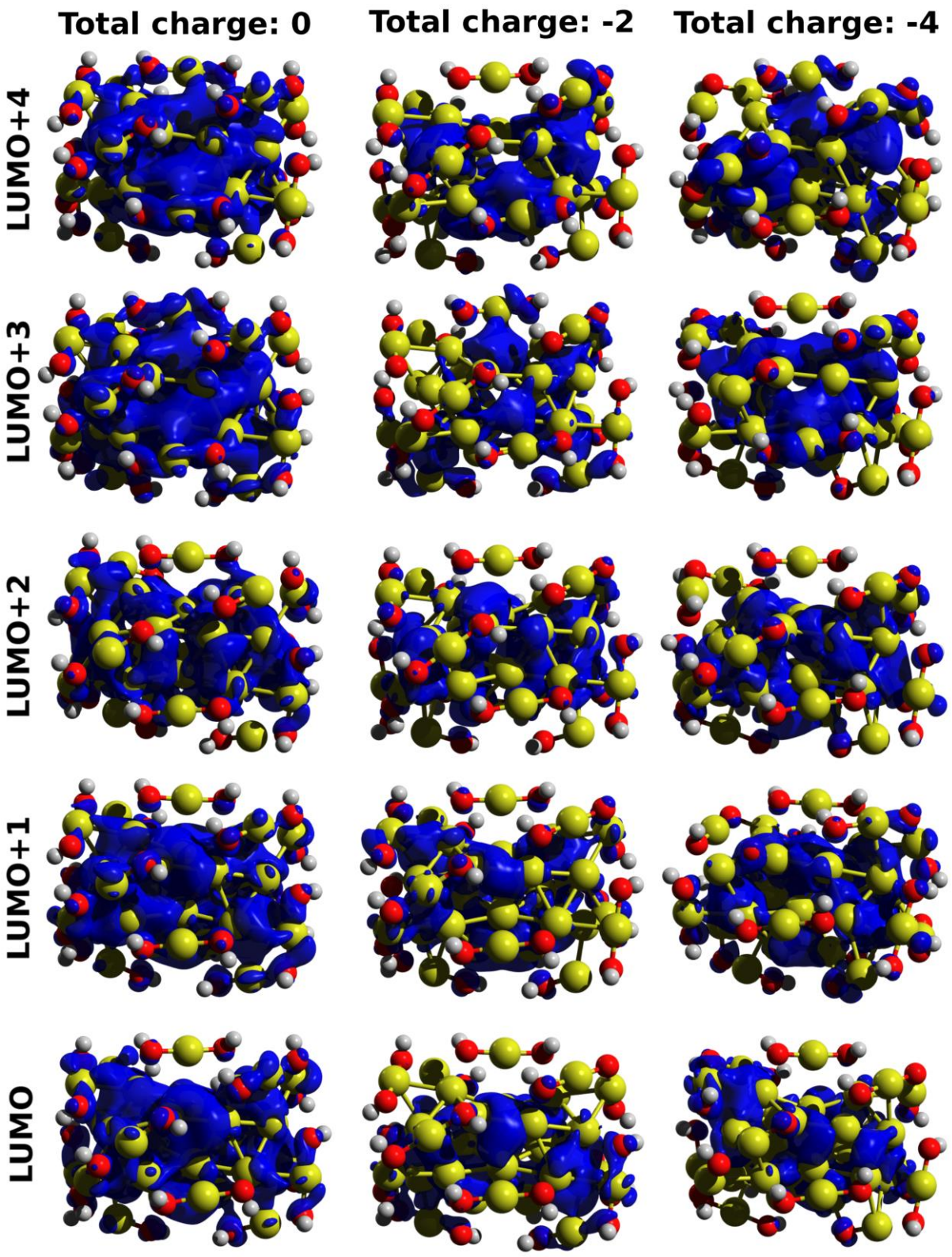

Figure S 11: Electron densities of the conduction states calculated for different charge states calculated with wB97X-d/dhf-SVP-2c and the COSMO model with parameters for water.

Section IV: Structural resolution

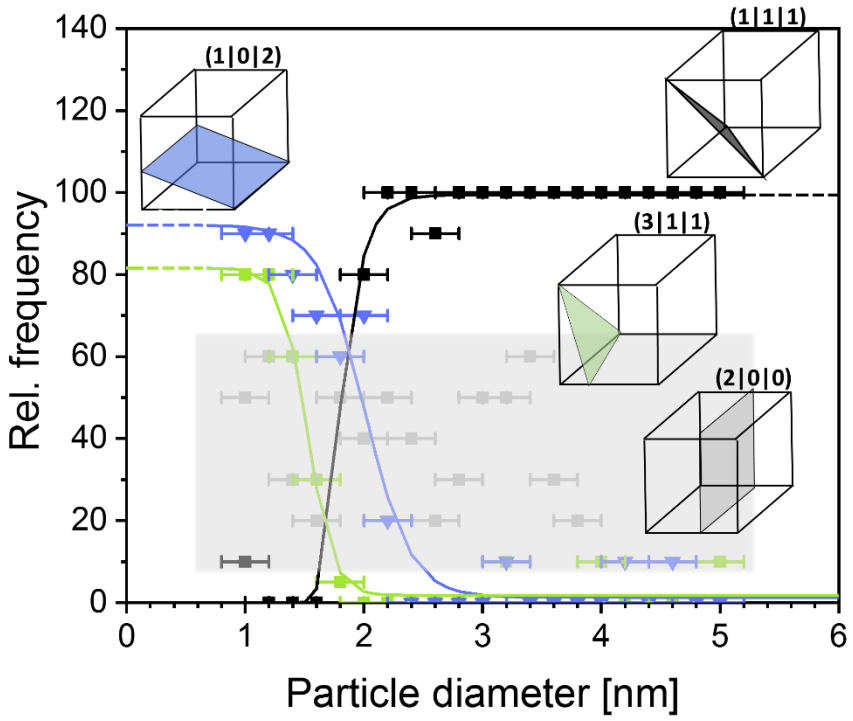

Figure S12: Single-particle measurement of the observed crystal planes in HR-TEM measurements. The crystal structure is determined by a single particle fast Fourier transformation on the HR-TEM images in Figure S13 after measuring 60 individual particles. The x-error corresponds to the histogram Δd and amounts to 0.2 nm.

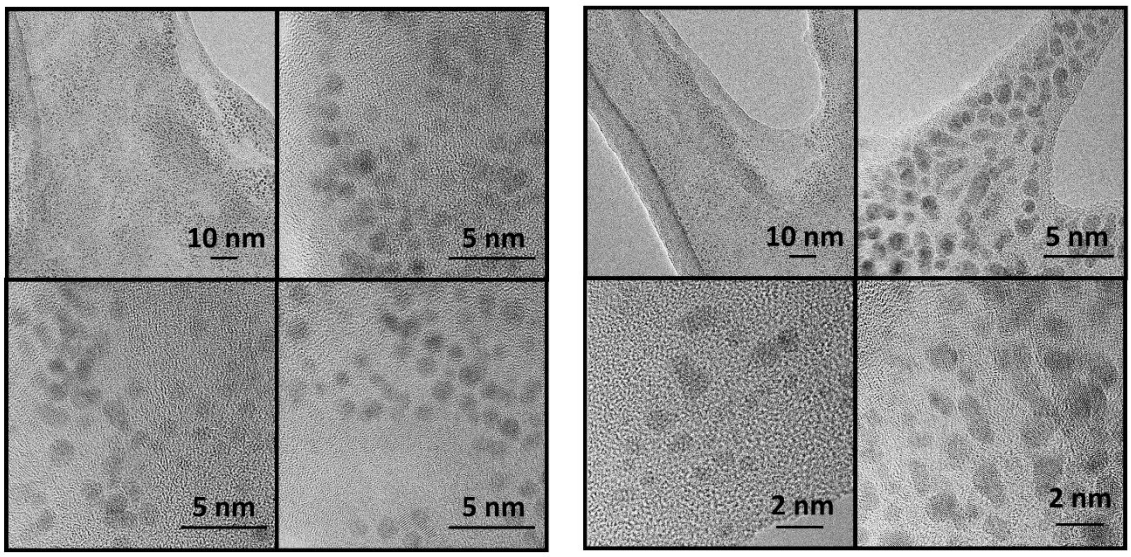

Figure S13: Representative HR-TEM images of Au NCs after LFL and ultracentrifugation using 50 kDa centrifugal filters.

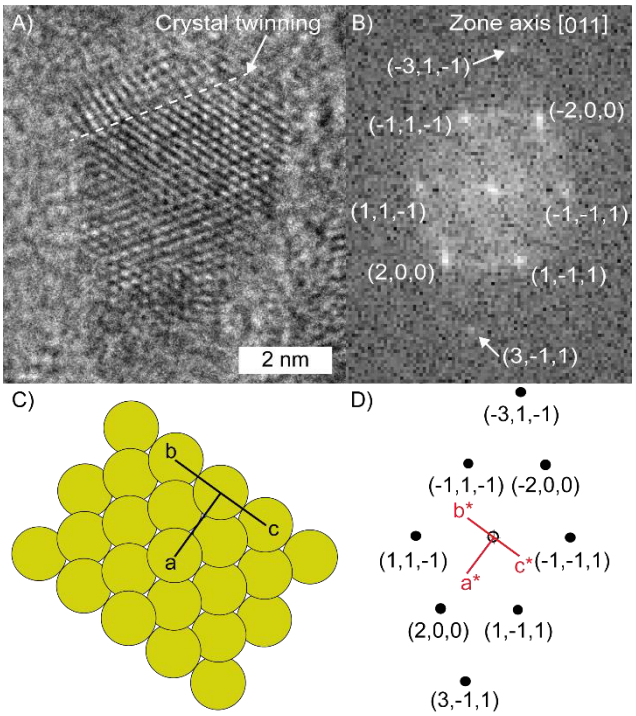

Figure S14: A) HR-TEM image and B) corresponding Fast Fourier Transform. A crystal twinning is observed on the particle. The particle shows reticular planes consistent with the [011] zone axis. C) Observed cubic crystal structure (gold, Fm-3m) and D) corresponding reciprocal lattice.

Section V: Size effect on the photoluminescence behaviour

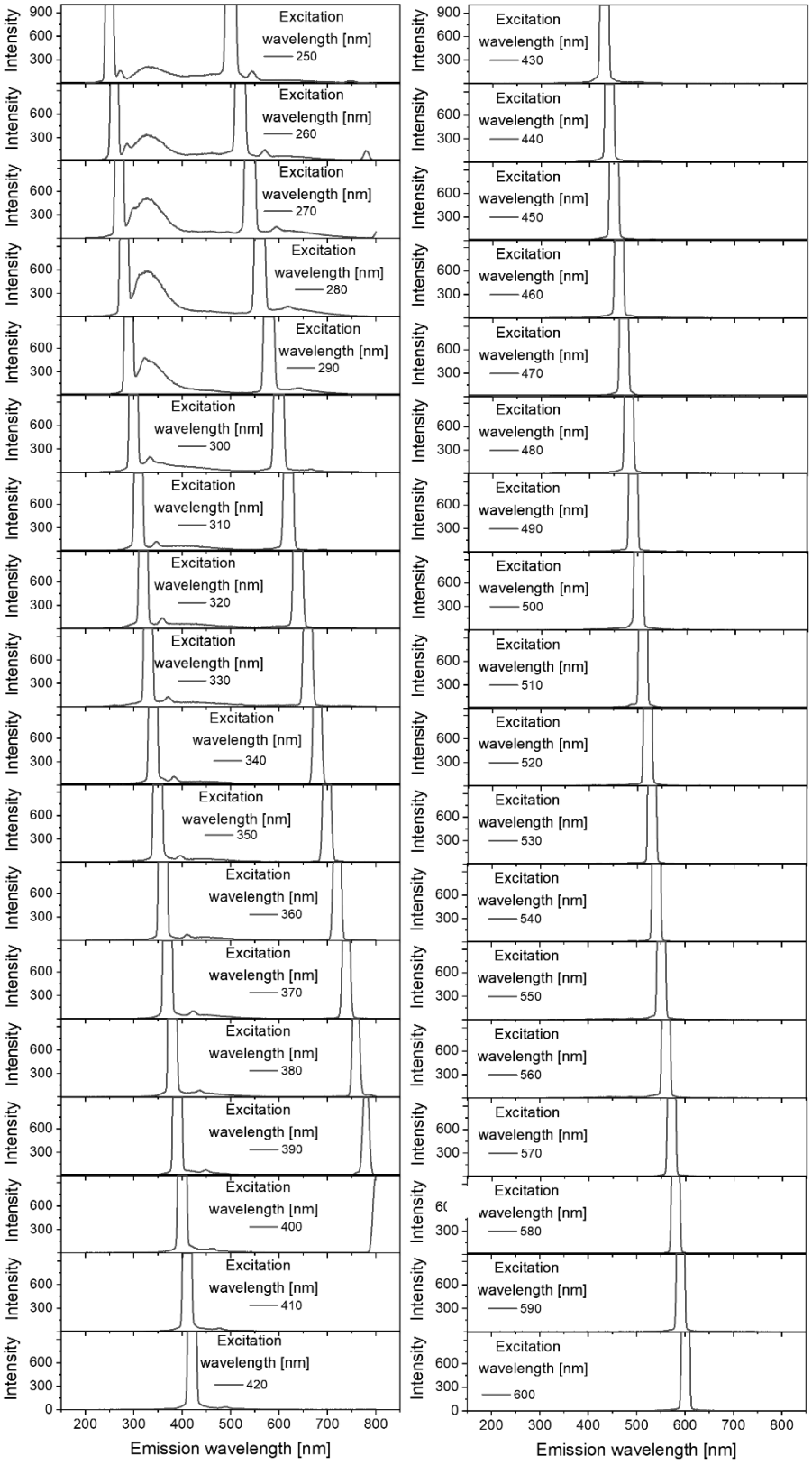

Figure S 15: Emission detected for surface dominated Au NCs after excitation with different wavelengths. Corresponding particle size distributions can be found in Figure 1 of the main manuscript.

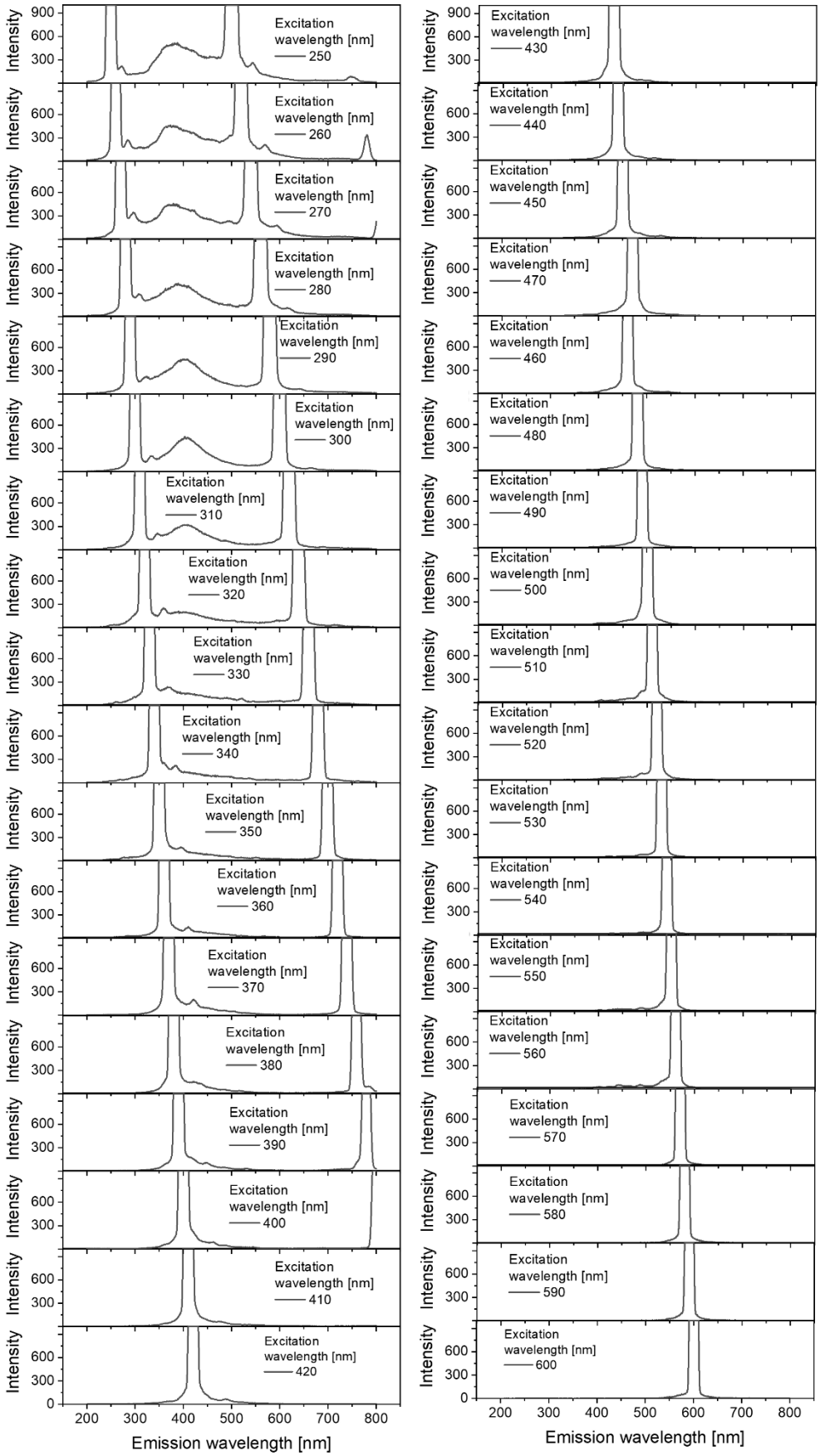

Figure S 16: Emission detected for core-dominated Au NCs after excitation with different wavelengths. Corresponding particle size distributions can be found in Figure 1 of the main manuscript.

X-ray absorption and fluorescence spectra are corrected for background with polynomial functions in the Athena software of the ifeffit package.[8] The oscillatory EXAFS information χ(k) as a function of electron momentum k was derived by subtracting a spline-fitted step function at the L(III) edge. A spectrum of a gold foil in transmission and the large colloids together with the pure χ(k) function are shown in Figure. S14. The EXAFS data were analysed by Fourier transforming the modulation in absorption χ(k) with a k^2 weight in the range of k = 1.5 and 15 $Å^{-1}$.

Reference samples for the XANES analysis were 2 mM aqueous $HAuCl_4$ (Chempur) in 3-valent state with chloride nearest neighbors, 2mM aqueous $HAuCl_4$ (Chempur) in 100 mM cetyl trimethyl ammonium bromide (CTAB, Chempur) reduced by 2 mM sodium ascorbate (Roth chemicals) in 1-valent state with bromide neighbors.[9,10]

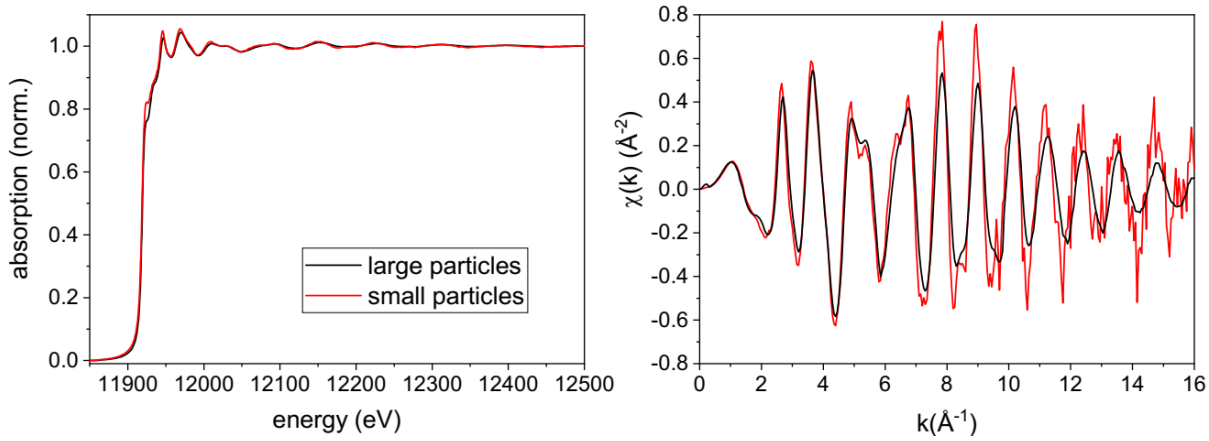

Figure S17: Normalized X-ray absorption of the small and large particles as a function of X-ray energy (left) and k^2 weighted EXAFS oscillations as a function of electron momentum k (right).

Section VI: Emission lifetime of core dominated Au NCs

We measured the lifetime of 1.1 nm fully inorganic gold nanocluster with the particle size distribution presented in Figure S18 A. Here, we focused our lifetime measurements on the most stable and most reproducibly found emission at 340 nm (core emission). The summarized lifetimes can be found in Table S2.

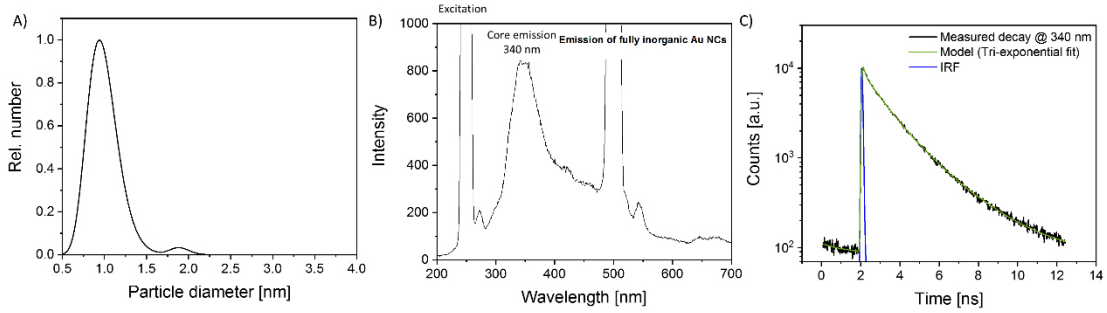

Figure S18: Determination of the lifetime of fully inorganic NCs: A) Size distributions of the measured Au NC. B) Fluorescence spectrum. C) Time-resolved decay of the fluorescence measured at 340 nm.

Table S2: Summary of measured lifetimes τ_i and fractional intensities I_i after tri-exponential fitting of the decay curves in Figure S 18C

Emission centered at	τ_1 (I_1)	τ_2 (I_2)	τ_3 (I_3)
340 nm	2.20 ± 0.01 ns (60.5%)	1.01 ± 0.01 ns (36.1%)	0.09 ± 0.01 ns (3.4%)

References

[1] A. R. Ziefuß, S. Reichenberger, C. Rehbock, I. Chakraborty, M. Gharib, W. J. Parak, S. Barcikowski, J. Phys. Chem. C, **2018**, 122, 22125.

[2] A. R. Ziefuss, S. Reich, S. Reichenberger, M. Levantino, A. Plech, Phys. Chem. Chem. Phys., **2020**, 22, 4993.

[3] A. R. Ziefuß, S. Barcikowski, C. Rehbock, *Langmuir,* **2019**, *35*, 6630.

[4] X. Liu, M. Atwater, J. Wang, Q. Huo, Colloids Surf. B.: Biointerfaces **2007**, 58, 3.

[5] C. Pfeiffer, C. Rehbock, D. Hühn, C. Carrillo-Carrion, D. J. de Aberasturi, V. Merk, S. Barcikowski, W. J. Parak, J. R. Soc. Interface, **2014**, 11, 20130931.

[6] K. Makino, H. Ohshima, Langmuir, **2010**, 26, 18016.

[7] K. L. Planken, H. Cölfen, Nanoscale, **2010**, 2, 1849.

[8] B. Ravel, M. Newville, J. Synchrotron Radiat., **2005**, 12, 537.

[9] B. Abécassis, F. Testard, Q. Kong, B. Francois, O. Spalla, Langmuir, **2010**

[10] F. Farges, J. A. Sharps, G. E. Brown, Geochim. Cosmochim. Acta, **1993**, 57, 1243.

A8 Supporting Information: Chapter 3.3.2

Highly Fluorescent Surfactant-Free Gold Nanocluster with Efficient Photon-Density Memory

(unpublished results)

Anna. R. Ziefuss[1], Melissa Teubner[2], Christoph Rehbock[1], Michael Rübhausen[2], Wolfgang J. Parak[3], Stephan Barcikowski[1]*

[1] Technical Chemistry I and Center for Nanointegration Duisburg-Essen (CENIDE), University of Duisburg-Essen, Universitaetsstrasse 7, 45141 Essen, Germany

[2] Institue for applied physics, University Hamburg, Jungiusstraße 9, D-20355 Hamburg, Germany

[3] Department of physics and chemistry, University Hamburg, Hamburg, Germany

Experimental procedure: The experimental setup was adopted from REF[213]. In short, we synthesized 53 nm AuNP through laser ablation in liquids (LAL). We irradiated, therefore, an Au-targed with an Nd:YAG laser (Ekspla, Atlantic series, 10 ps, 1064 nm, 8,8mJ, 1064 nm) in a 30 mL batch chamber for 10 min followed by centrifugation (73*g, 90 min) to get a monomodal size separated 60 nm colloidal pellet. The latter was diluted to 7.5 mg/mL using ultrapure water and a mixture of NaCl/NaOH with a final concentration of 0.3 mM of both NaCl and NaOH. The fragmentation was conducted with a nanosecond laser (Innolas, Spotlight, 9 ns, 100 Hz, 84 mJ, 532 nm) in a free liquid jet reactor, which was established and described in more detail in previous works.[153,218] LFL leads to colloids with protoplasmonic and plasmonic particles. To separate both, we used centrifugal filters with an MWCO of 50 kDa. The filtrate was then filtered again with 3 kDa filters, whereby the retentate contained the core dominating fraction and the filtrate the surface dominating fraction.

Particle analysis: The particle size analysis of AuNCs was performed using analytical ultracentrifugation (Beckman coulter, optima XLI) under experimental field conditions (11290*g, 20 °C, 100 scans). Particle size distributions before fluorescence measurements are shown in the manuscript. The comparison of particle sizes before and after fluorescence measurements at 10^{12} W/m^2 can be found in Fig. S1.

Fluorescence measurements: The fluorescence was measured after excitation at 250 nm using two different 300 fs pulsed lasers (500 kHz and 80MHz) as light sources to cover a laser intensity range from 10^8 -10^{12} W/m^2. We used a new sample aliquot for each measurement.

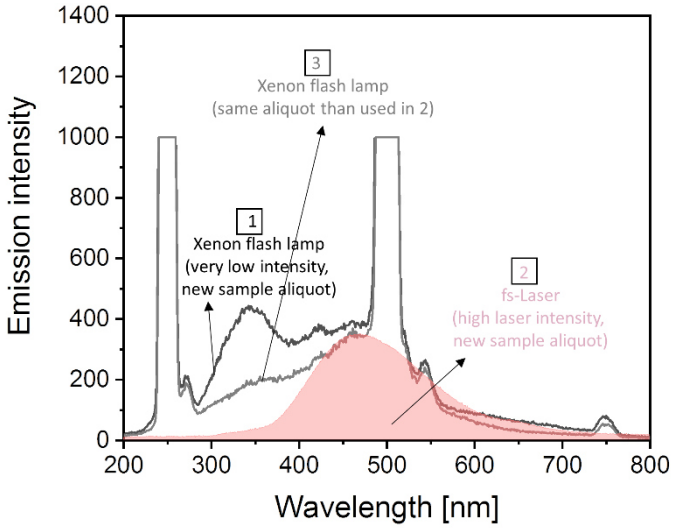

Figure S1: *Emission behavior after excitation at 250 nm with a low intensity xenon flash lamp (1) and a high intensity pulsed-fs laser (2). For both measurements we have used a new sample aliquot. The pump-power emission dependency is highly interesting. Renewed measurement of sample aliquot 2 (after fs irradiation) with the less intensive xenon lamp shows an existing emission change. Since not the whole volume of aliquot 2 was irradiated before, a mixture of the previous spectra is visible. However, an irreversible pump-power intensity change can be observed.*

As an additional recommendation, the hypotheses presented in this chapter should be investigated further by supporting experiments, including but not limited to the following:

Fully inorganic gold nanoclusters show a pronounced photon density memory. This study helps to clearly differentiate between core and surface states and is also interesting from a technical application perspective. However, before a publication of this work can be considered, the results must be supported by measuring the surface structure after irradiation with different laser intensities. If the colloidal concentrations are high, in-situ XAS measurements would be suitable. In addition, it would be useful to saturate the surface with organic ligands prior to the measurement to verify if the emission loss of the surface can be suppressed.

A9 Supporting Information: Chapter 3.3.3

How charging effect through ligand-metal charge transfer processes influence the photoluminescence of fully inorganic gold nanoclusters

(unpublished results)

Anna. R. Ziefuss[1], Christoph Rehbock[1], I. Chakraborty[2], Wolfgang J. Parak[2], Stephan Barcikowski[1]*

[1] Technical Chemistry I and Center for Nanointegration Duisburg-Essen (CENIDE), University of Duisburg-Essen, Universitaetsstrasse 7, 45141 Essen, Germany

[2] Department of physics and chemistry, University Hamburg, Hamburg, Germany

The production of fully inorganic Au NCs was done via laser fragmentation in liquids (synthesis route described in chapter xx). To investigate the influence of LMCT processes under variation of the anchor group (S, N) and the headgroup (carboxcylic acid with C =2, 3, 6) we added the following ligands in different concentrations:

Table S1: *Investigated type of ligands including used concentrations.*

Number of C	Thiolated ligands	Aminated ligands
2	2-Mercaptoacetic acid 0, 0.1, 50, 100, 150 µM	Glycine 0,0.1,50, 100 µM
3	3-Mercaptopropionic acid	Beta-Alanine 0, 0.1, 50, 100 µM
6	6-Mercaptohexanoic acid	

The incubation time for all ligands was different (…more specialize…) which can be considered as draw back as it can be expected that the system need a certain time to get to the thermodynamic equilibrium. We will therefore not looking at relative relations rather than absolute values.

We measured the emission after excitation at 270 nm using a common UV-Vis spectrometer with a xxx lamp. The raw data can be found in the main part of this work. Fig. S1 summarized the emission intensity changes of surface states in dependence of the ligands carbon chain length. A summary of the emission position change can be found in the main manuscript. Probably due to the unequal incubation time; we observe a big deviation for the single datapoints. Nevertheless, we fitted the single data points linearly to get a feeling for certain trends. Further measurements with a fixed incubation time are necessary to improve the fit quality.

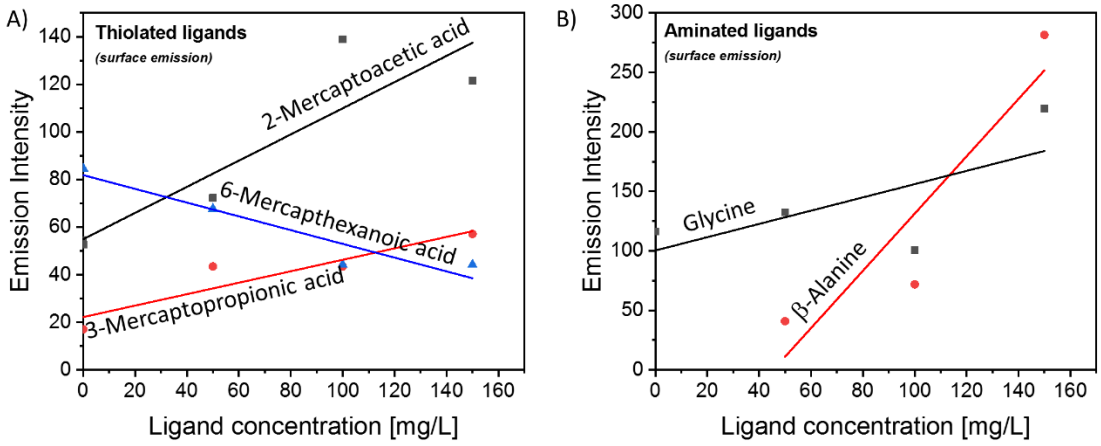

Figure S1: Summary of the emission intensity in dependence of the carboxylic ligand concentration. Black: C = 2, red: C = 3, Blue C = 6. A) Influence of thiolated ligands on the surface emission, B) Influence of aminated ligands on the surface emission.

As an additional recommendation, the hypotheses presented in this work should be investigated further by supporting experiments, including but not limited to the following:

The emission intensity and energy of fully inorganic metal NCs can be controlled by targeted addition of organic ligands depending on the ligand head and anchor group. Further statistical measurements are needed prior to submission. It would be especially interesting to further increase the concentration of ligands with a large spacing between the head and anchor groups, which lead to a red-shift of the emission. A red-shift is favored for biomedical applications as the emission can be detected with conventional microscopes. Furthermore, a consideration of the best excitation conditions would be useful considering that excitation in the UV range will lead to the destruction of healthy tissue and should thus be avoided for biological measurements.

A10 Supporting Information: Chapter 3.3.4

ChemPhysChem

Supporting Information

Influence of Pt Alloying on the Fluorescence of Fully Inorganic, Colloidal Gold Nanoclusters

Anna R. Ziefuss, Michael Willeke, Matthias Miertz, Alexander Heinemann, Christoph Rehbock, and Stephan Barcikowski*

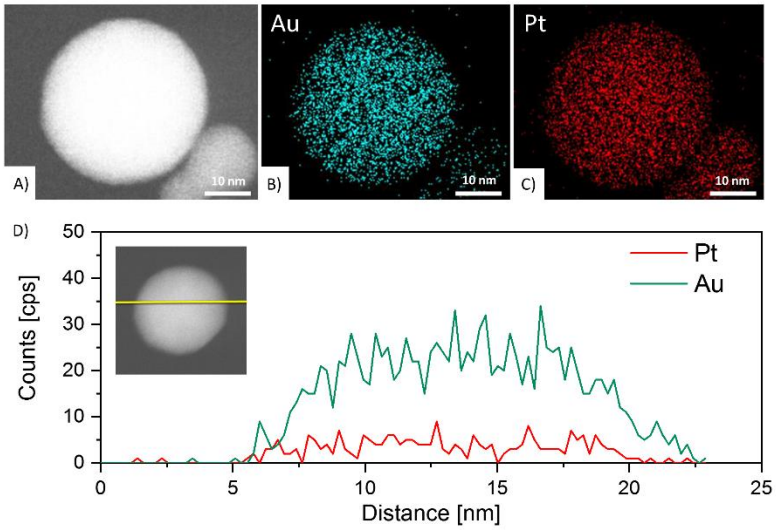

***Figure S1**: Elemental analysis of the nanoparticles produced with LAL before LFL. A) exemplary TEM image of a single alloy NP, B,C) TEM-EDX mapping of this particle, D) EDX line scan. The summed up spectrum can be found in Figure 1A, revealing a 90:10 composition.*

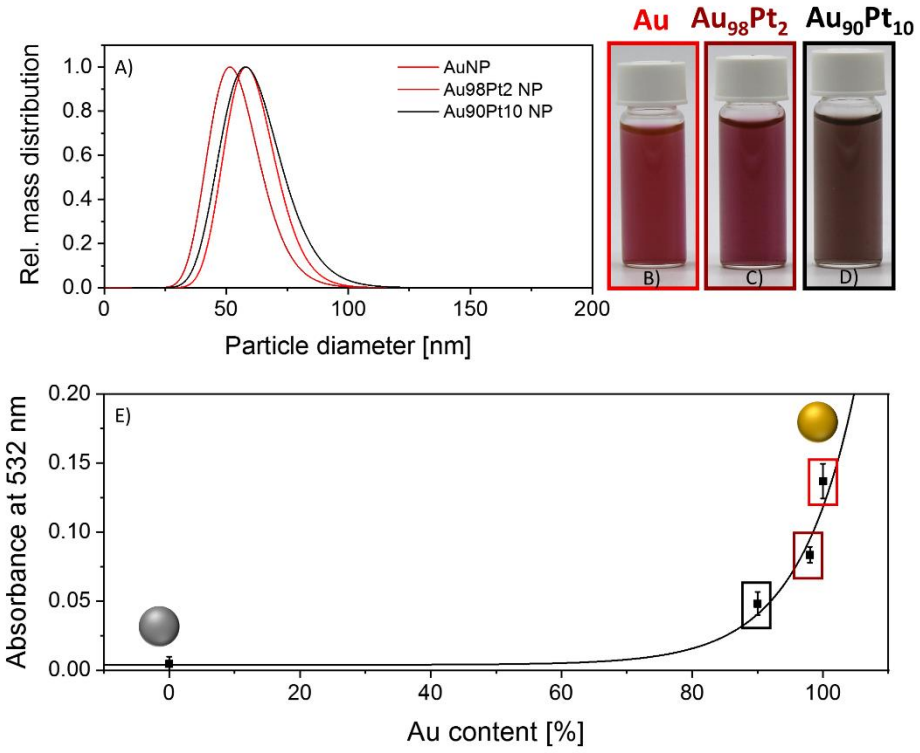

Figure S2: *Characterization of NP colloids before LFL. A) Particle size distribution after LAL and centrifugation B) – D) Pictures of the colloids with (B) Au, (C) $Au_{98}Pt_2$, (D) $Au_{90}Pt_{10}$ E) Absorbance at 532 nm as a function of the Au content in the colloid.*

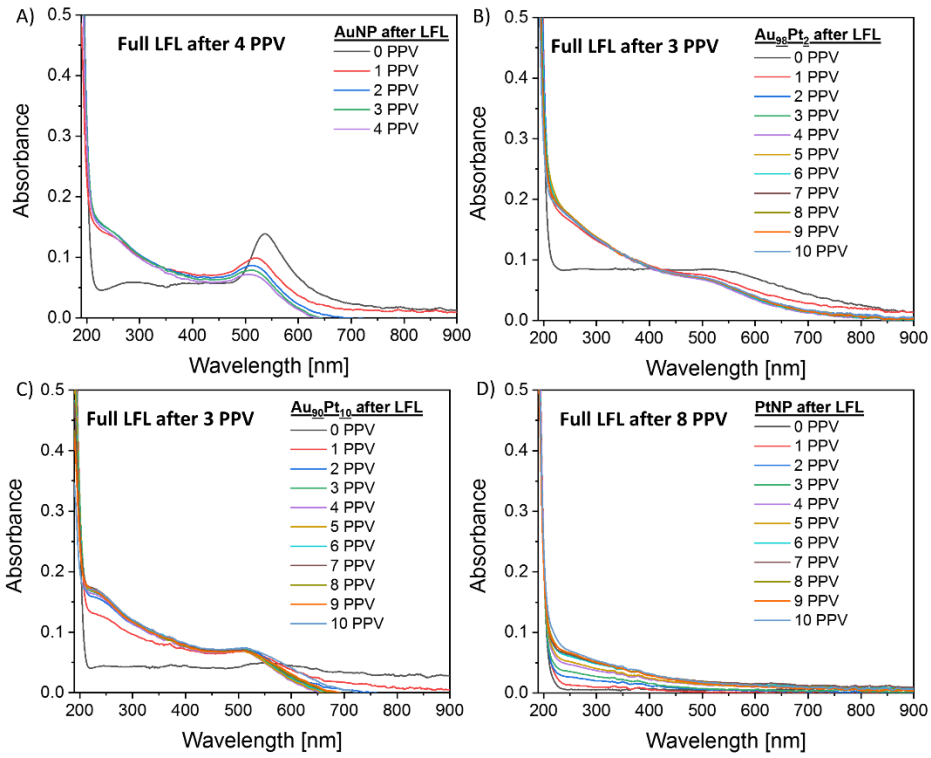

Figure S3: *Absorbance spectra of Au NPs, Pt NPs, and the bi-metallic NPs before and after fragmentation. PPV represents the pulses per volume element and indicates the number of irradiation cycles.*

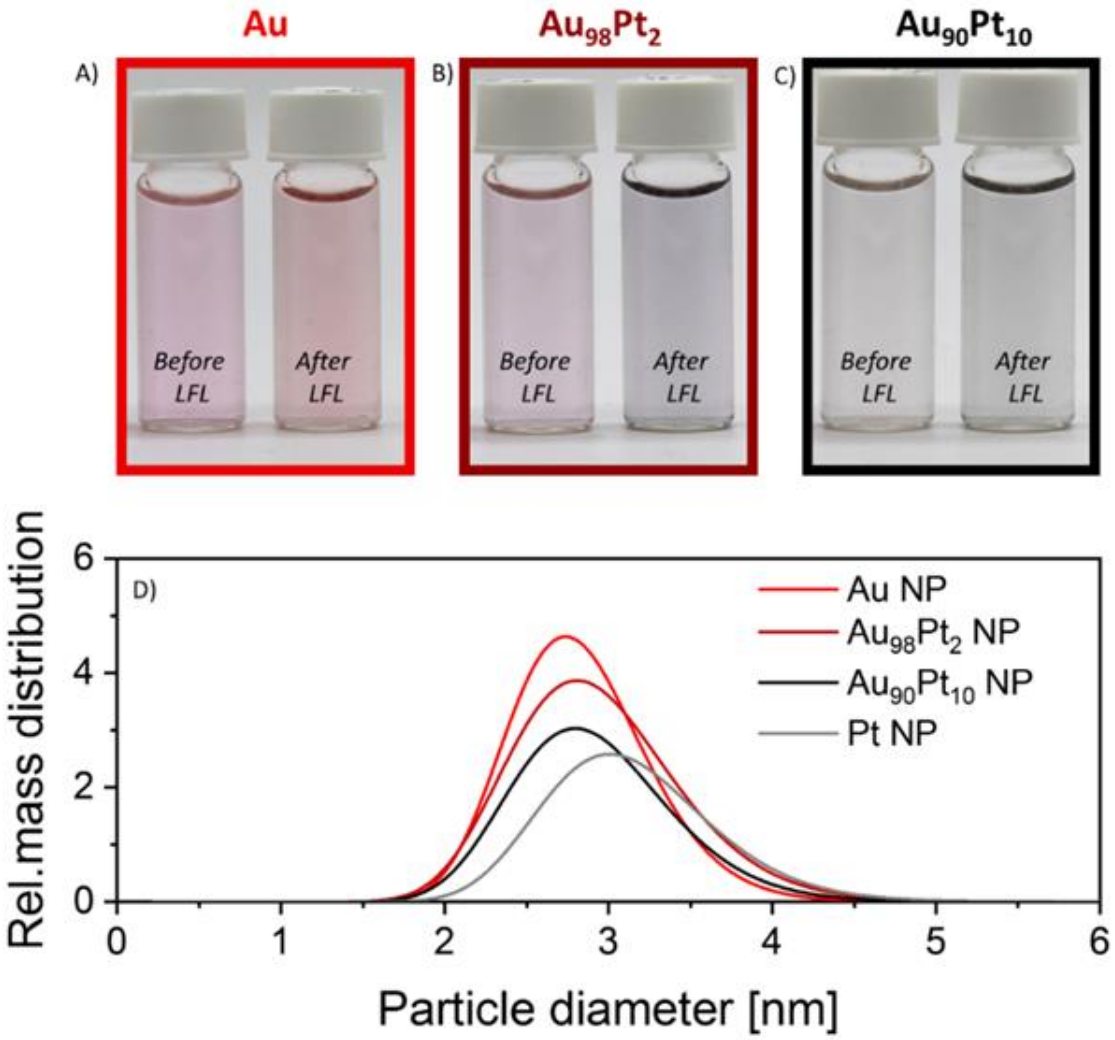

Figure S4: *A)-C) Pictures of colloids before and after LFL at concentrations of 7.5 mg/L. D) The size distribution of particles after LFL measured with the analytical disc centrifugation. Please note that the small size fraction (found after centrifugation) does not show prior to centrifugation, because the analytical disk centrifugation in contrast to AUC cannot detect such small particles.*

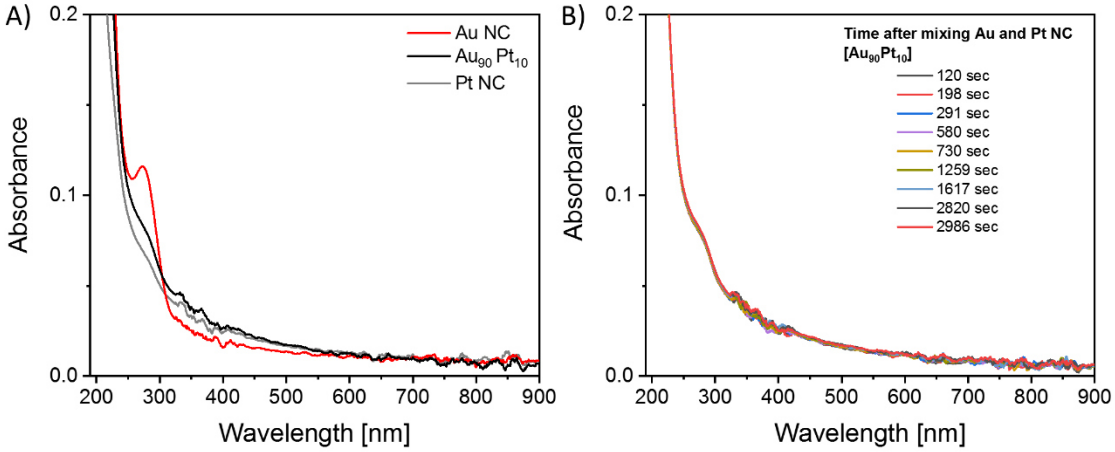

Figure S5: *Absorbance behavior of a mixture of 90% AuNCs and 10%PtNCs (A) in comparison to pure AuNCs and Pt NCs and (B) as a function of the time after mixing.*

A11 Supporting Information: Chapter 3.4.1

Supporting Information

The Origin of Laser-Induced Colloidal Gold Surface Oxidation and Charge Density, and Its Role in Oxidation Catalysis

Anna R. Ziefuß[1], Ina Haxhiaj[1], Stefan Müller[2], Mustafa Gharib[3], Olga Gridina[1], Christoph Rehbock[1], Indranath Chakraborty[3], Baoxiang Peng[2], Martin Muhler[2], Wolfgang J. Parak[3], Stephan Barcikowski[1]*, Sven Reichenberger[1]

[1] University of Duisburg-Essen, Technical Chemistry I and Center for Nanointegration Duisburg-Essen (CENIDE), Essen, Germany.

[2] Ruhr University Bochum, Laboratory of Industrial Chemistry, Bochum, Germany

[3] Department of Physics and Center for Hybrid Nanostructure (CHyN), University of Hamburg, Hamburg, Germany

* corresponding author: stephan.barcikowski@uni-due.de

Supporting Information

Section I: Laser-based synthesis of ligand-free gold nanoclusters

The first step is the fabrication of the educt using LAL, performed in a batch chamber with an Nd:YAG laser (Ekspla, Atlantic series, 10 ps, 1064 nm, 8.8 mJ, 100 Hz, 10 min), followed by a centrifugal step (Hettich, 70 min, 1.5 mL, 67.1 x g) to separate a particle size fraction which contains no particles with diameter less than 13.4 nm. Due to a low absorption-cross-section, particles smaller than these values cannot be fragmented, and would, therefore, remain as larger particles in the product solution [1]. The produced educt particles show a particle size distribution with an average diameter of 53 nm (σ = 19.25 nm) (Figure S1A).

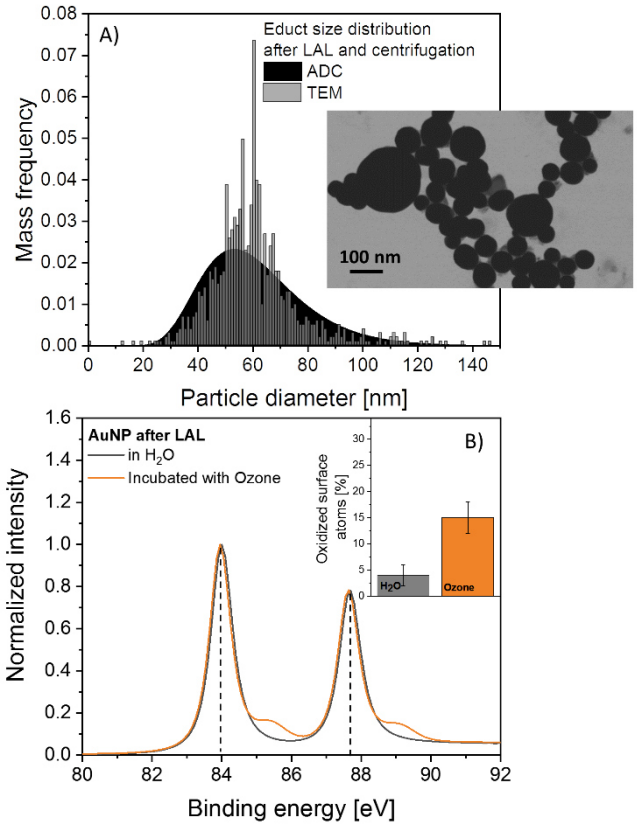

Figure S1: Overview of the educt Au NP properties after LAL and centrifugation for subsequent LFL. A) Mass-weighted size distribution from ADC and TEM (normalized integral) with corresponding TEM image. B) Binding energies of the 7/2f and 5/2f orbitals and corresponding oxidation before and after ex-situ oxidation with O_3.

The third step is LFL, performed in a free liquid jet with a Nd:YAG laser (Innolas, 9 ns, 532 nm, 85 mJ, 100 Hz). To avoid statistical uneven energy transfer to the particles in the axial direction due to absorption events of frontal particles, we diluted all solutions before LFL to 7.5 mg/L, to reduce the number of particles per volume unit in the solutions. The concentration was determined by inductively coupled plasma mass spectroscopy (ICP-MS, PerkinElmer Sciex-ELAN 6000). For the subsequent LFL process, the colloids were diluted using water, containing the respective ionic additives to yield the concentrations given in Table 2.

Table S1: Concentrations of additives, added before LFL if not otherwise stated

Additive	**Concentration [mM]**
Ultra-pure water	0
NaOH	0.025, 0.05, 0.1, 0.2, 0.3
NaOH/O_3	0.3 / 0.045
NaCl	0.025,0.05,0.1, 0.2, 0,3
NaOH/NaCl	0.3/ 0.3

In the case of the sample containing ozone, water was previously saturated using an ozone generator (BMT Messtechnik, BMT 802X). Due to the strong loss of ozone over time, detected by absorption spectroscopy, the concentration reaches nearly a steady-state after ~80 min (Figure S2), so that we defined a working window between 80 and 140 min. To determine the concentration of ozone-enriched ultrapure water, we measured the absorbance at 258 nm in constant time intervals within an overall time of 150 min. According to [2] the concentration c of ozone can be determined from the measured absorbance as follows ($A_{258\,nm}$= absorbance at 258 nm, ε = extinction coefficient, d = layer thickness):

$$c = \frac{A_{258\,nm}}{\varepsilon \cdot d}$$

The change of the ozone concentration is given in Figure S2. The concentration decreases exponentially within the observed time interval. The changes after 80 minutes are marginal. To get comparable results, we decided to do the LFL between 80-140 min.

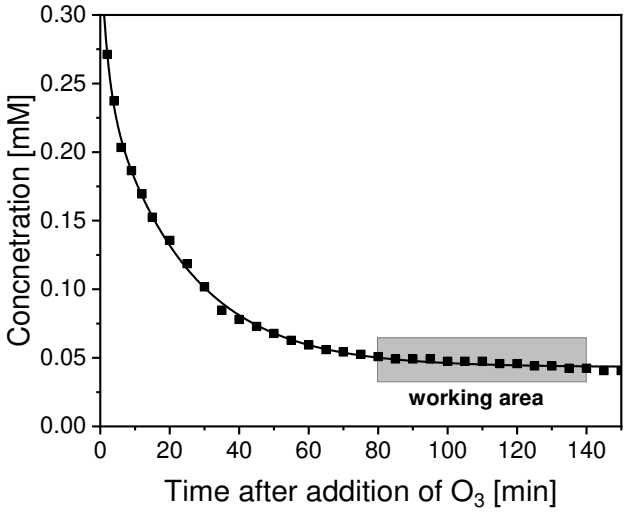

Figure S2: Change in ozone concentration over time. The grey area marks the working-time window of LFL. The cuvette was closed during measurement, to create real measuring conditions.

The acidic nature of the ozone leads to a pH shift of the colloid during the incubation time. To prevent that, we added 300 µM NaOH to the solution before adding the ozone. The addition of ozone before

LFL leads to a significant oxidation of the Au NPs surface which was confirmed by XPS measurements (Figure S1B), performed on Au NPs in ultra-pure water and after subsequent incubation in an ozone enriched solution. Prior to the XPS measurements, we drop-casted the samples on a SiO_2 wafer. The measurement required a monochromatic aluminum anode with a Kα line at 1486.6 eV and a spot size of 100 µm. We used a hemispherical analyzer (angle between the sample surface and the analyzer was 45°) and dual-beam charge neutralization. All spectra are referenced to the 2p3/2 Cu peak. The reference was introduced into the vacuum together with the sample and was sputtered with Ar-Ions, to avoid contaminations and to get a clean surface. The software Casa XPS was used for analyzing the spectra. The oxide peaks were fitted with symmetrical Gauß-Lorentz peak shape with a relative weight of 80% and 20%.

LFL of all colloids took place in a free liquid jet. The laser was focused on the jet generated by a dropping funnel. The colloid was cycled four times to maintain quantitative LFL of the educt particles [1]. The laser fluence was set to 1.6 J/cm^2 at each fragmentation passage. The illuminated surface of the liquid jet is 5.7x10^{-6} m^2 (detected by a picture of the laser spot on photo paper). The volume flow of the liquid was 6.0x10^{-7} m^3/s. A more detailed description of the setup can be found in [1].

All absorbance measurements were performed using an UV-Vis extinction spectrometer (Thermo Scientific, Evolution 201, wavelength range 190 – 900 nm). Particle size was determind by analytical ultracentrifuge (AUC, Beckman Coulter, Proteomlab XL-I) and transmission electron microscopy (TEM, JEM 2200FS and Zeiss EM 910). With the AUC the hydrodynamic particle diameter was measured. A sample of 350 µL is required. The sample is accelerated in the centrifuge to 16350 G and absorption measurements are performed every 60 s at 380 nm. The data evaluation is carried out using the software Sedfit. The sedimentation coefficient is obtained which can be converted into the hydrodynamic diameter according to [3]. The primary particle diameter of the particles is obtained by TEM measurement, after drying the colloids on a carbon-coated copper 400-mesh grid. Additionally, we determined the surface charge density according to [4] from the zeta potential, measured by a Malvern Zetasizer Nano ZS 90.

Section II: Particle size characterization

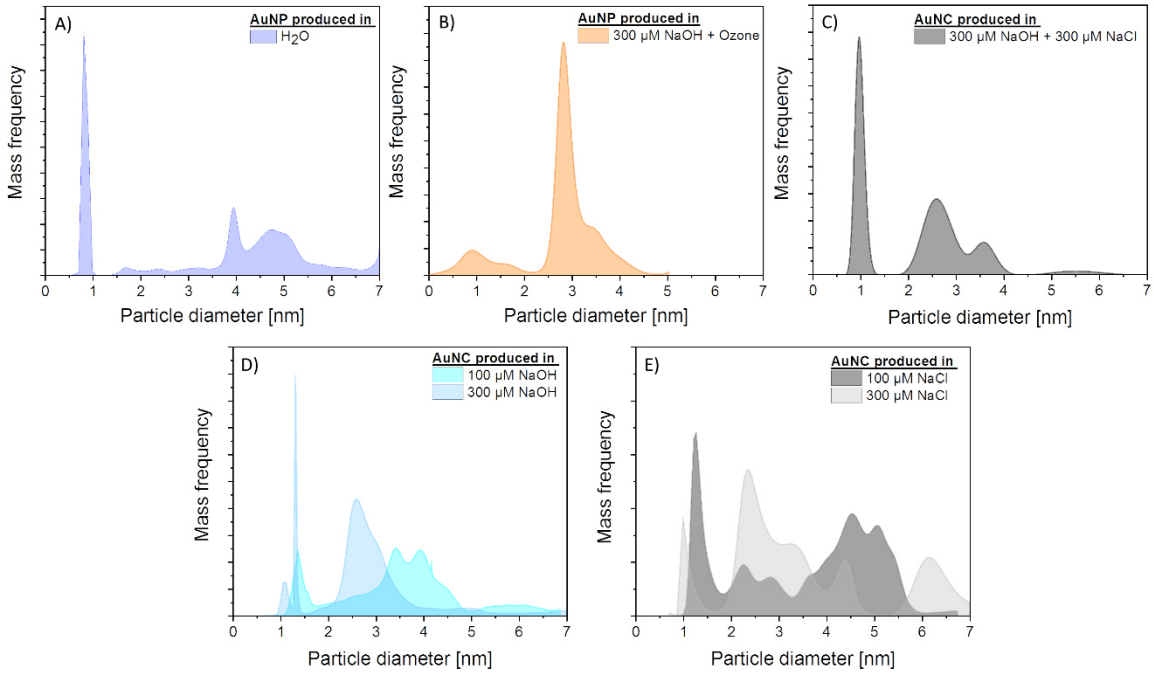

Figure S3: Mass-weighted hydrodynamic Au NP diameter after LFL with A) H_2O, B) 300 µM NaOH + Ozone, C) 300 µM NaOH + 300 µM NaCl, D) 100 µM NaOH and 300 µM NaOH, and E) 100 µM NaCl and 300 µM NaCl.

To measure the particle size distribution of the prepared gold nanoparticles, we recorded the hydrodynamic particle diameter of colloidal AuNP using the AUC (Fig. S3) in line with a previous study.[8] In general, HRTEM is the more prominent and often applied method to characterize the particle size (e.g. Ferret diameter) with atomic precision, while the sedimentation-based AUC method as an alternative approach has been highlighted about a decade ago by Planken and Cölfen.[9] Here, AUC is a standard method for the characterization of ultrasmall nanoparticles, and even superior to TEM regarding size resolution, as has been systematically shown for a comparative HRTEM/AUC study of gold nanoclusters.[10] The comparably poor statistics of HR-TEM has always been a major drawback, as only a few hundred nanoparticles represent the ensemble of billions of nanoparticles used for preparing the TEM grid. In turn, the AUC method is a powerful and non-invasive (no electron beam damage or drying artifacts) technique to determine the hydrodynamic particle diameter of the whole ensemble of nanoparticles in a colloidal state and with atomic-scale precision. Additionally, the colloid is characterized without any pretreatment.

During AUC measurement, the colloid is filled into a measuring cell and accelerated by a centrifugal field which forces the formation of a sedimentation front. This front is temporarily tracked by optical components that allow an absorbance measurement over the whole radial field of the cell. With the Lamm-equation, the particle size distribution of spherical and colloidal stable nanoparticles can be calculated from the sedimentation front. In the case of non-spherical particles or coalescence during the measurement more sophisticated analysis of sedimentation and diffusion coefficients from different experimental runs and concentration series is required as described by Planken and Cölfen, which were not used here.[9] Since the measured particle diameter of non-spherical particles resembles the hydrodynamically equivalent sphere, the aspect ratio needs to be assessed by the frictional ratio from two-dimensional analysis of the sedimentation velocity data which however is very heavy on computation. Alternatively, a combination of TEM analysis to determine the form factor and subsequent AUC provides a less complicated alternative. Due to the presence of charged ligands on the surface and/or ions in the Gouy-Chapman double layer, the sedimentation velocity is potentially

affected too, since the electrostatic force will oppose and partially reduce the sedimentation speed.[9] Since highly diluted samples (< 7 mg/L) were measured here and hydrodynamic particle sizes were in accordance with Ferret diameters from TEM the effect is likely to be negligible. Yet, for higher particle concentrations this should theoretically lead to an underestimation of the sedimentation, an aspect that is rarely studied in literature so far. Additionally, AUC does not allow to characterize the nanoparticle size when they are present on a support (the final catalysts).

Hence, to characterize the Au/TiO_2 catalysts, and investigate wether the supporting of Au NPa causes a difference to the particle diameter or not, we have performed high-resolution transmission electron microscopy (HR-TEM) of selected catalysts. We found no significant differences of the particle sizes (Fig. S4 a-c) in comparison to the measured size distribution of particles in their colloidal state (Fig. S3 a-c). It should be mentioned that we measured the hydrodynamic diameter by AUC, while we measured the primary particle diameter with TEM. While using inorganic additives, small differences in the absolute values are to be expected [8]. The statistics in TEM measurements are quite bad as compared to AUC measurements, so that we decided to use AUC dada to calculate the particle diameter.

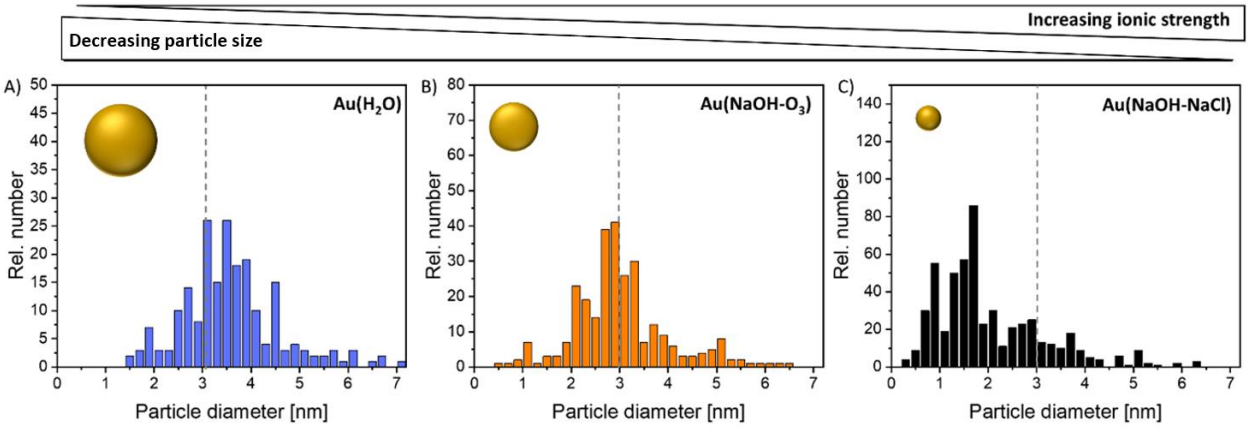

Figure S4: Size histograms corresponding to images shown in Figure 2C-D. Particles measured by TEM after being supported on TiO_2 (1 wt%). More than 200 particles were measured in each case.

Section III: Calculation of surface oxidation and surface charge density based on the XPS and zeta potential

The surface charge density (according to Ohshima et al. [4]) was calculated based on the zeta potential of the as-prepared colloids. The absolute values are shown in Figure S6 and were recorded at a pH value of 9.

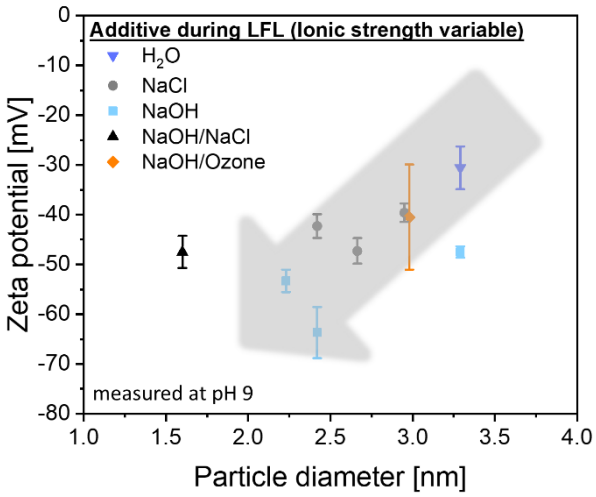

Figure S5: Zeta potential (measured at pH 9) of all synthesized AuNP colloids measured after LFL and before supporting on TiO_2.

From XPS (Figure S5) it is generally accepted, that the oxidation signal is specified by dividing the integral of the peak corresponding to the oxidized species by the integral of the peak corresponding to the neutral Au species. We assume that the upper atomic layer oxidizes first (layer-by-layer), as it is the one directly exposed to the oxidant in solution. We believe it is a probable hypothesis to assume that all oxidation signals measured in XPS originate from atoms in the first outer atomic layer.

Table S2: Summary of all constant parameters and assumptions, which are required to calculate the surface oxidation of the first atomic layer on the example of 53 nm particles.

Constant parameters		**Assumptions**	
Particle diameter	53 nm	**Signal depth XPS**	3 nm (15 atomic layers, assuming spherical particles)
Atomic radius	197 pm	**Atomic layers within the signal depth**	15
Projection area sphere (πd^2)	0.49 nm^2	The upper atomic layers of the gold nanoparticles oxidizing first (layer-by-layer) and homogeneously.	

Within the 15 atomic layers (signal depths 3 nm), 257670 atoms of the 53 nm diameter particle contribute to the XPS signal resulting in oxidization of 4 ± 2 % of these atoms. If only the first atomic layer is oxidized (and not the first 15 layers), this is equal to an oxidation of 57 ± 29 percent. If the 15 atomic layers result in an oxidization of 16 percent, that would theoretically account for a first-layer-oxidation of 230 %. This is a clear indication, that more than 1 atomic layer of gold atoms is oxidized, and it probably indicates that the first and second atomic layers are 100 % oxidized while the third atomic layer is estimated to contain 28% of oxidized gold atoms.

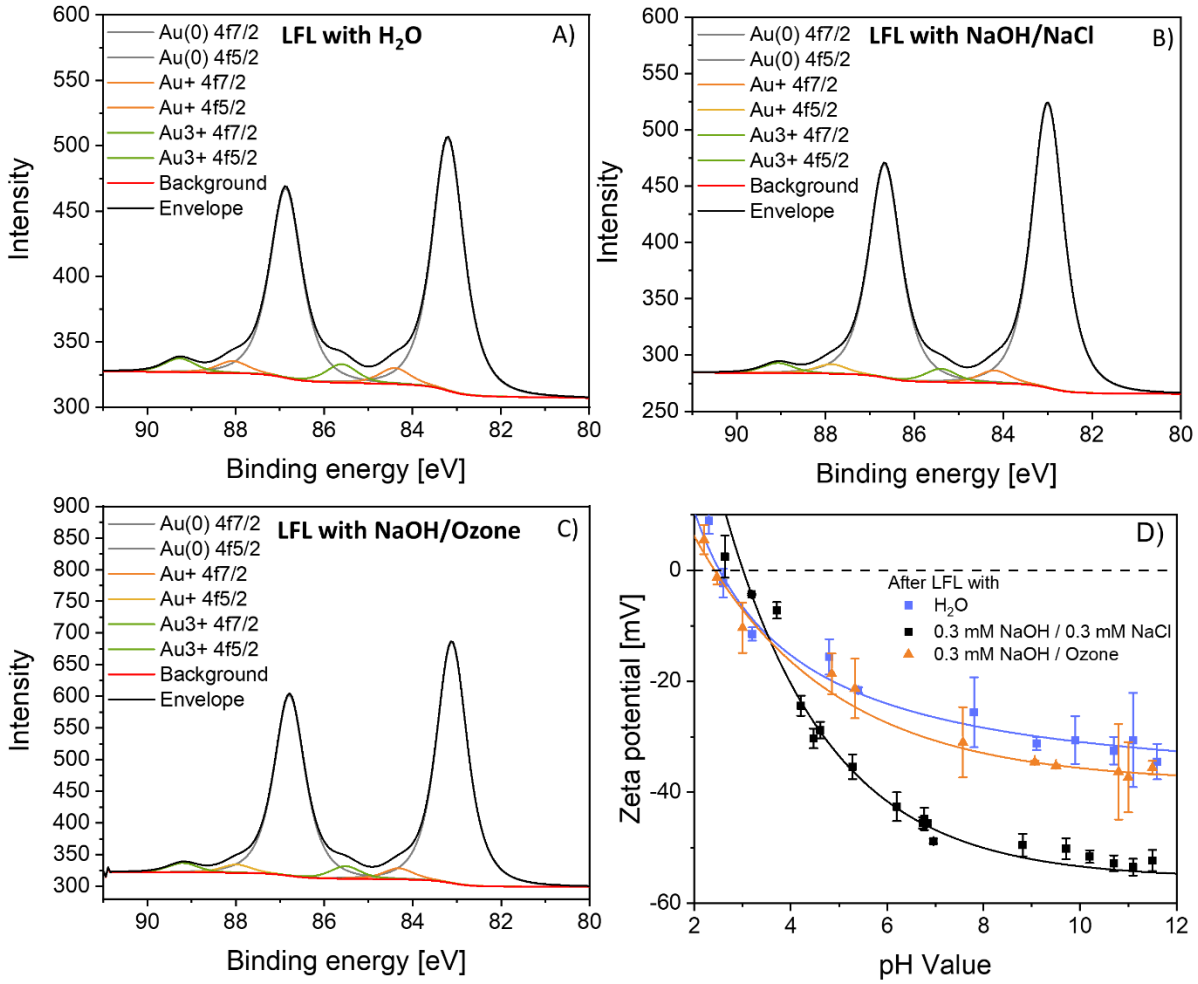

Figure S6: Electronic properties of AuNPs after LFL with XPS spectra after LFL in A) water, B) 300 µM NaOH + 300 µM NaCl, and C) in 300 µM NaOH + Ozone. D) Zeta potential measurements at different pH values adjusted with 0.1 M NaOH and 0.1 M HCl solution of the three corresponding samples.

Section IV: Correlation between the emission intensity of DCF and H_2O_2 concentration

The formation of H_2O_2 during fragmentation was examined spectrometrically by fluorescence measurements. Dichlorodihydrofluorescein diacetate (DCFH-DA), purchased from Sigma Aldrich, was dissolved in Ethanol. The concentration of this stock solution is 1 M. The deacetylation is carried out by adding a 1 M NaOH solution. After 1 h a large fraction is converted to Dichlorodihydrofluorescein DCFH. The activated stock solution is diluted to 0.1 M and added to the educt particles, which are then laser-fragmented. The final concentration of DCFH in the colloid is 10 µM. In the presence of reactive oxygen species, DCFH is oxidized and the highly fluorescent Dichlorofluorescin DCF is formed [5]. Both before and after LFL the emission is detected (Varian, Cary eclipse) at 521 nm (excitation at 500 nm). In order to be able to calculate the concentration of reactive oxygen species, the fluorescence intensity of DCF was calibrated in the presence of known quantities of H_2O_2 (Figure S8). The formation of all ROS was recorded using a protocol described in [6]. According to this protocol, we prepared a 0.01 M DMP and a 10 mM phosphate buffer solution (pH 9) stock solution and dissolved 5.9 mg copper sulfate pentahydrate in 2 mL ultra-pure water.

The addition of H_2O_2 leads to the oxidation of H-DCF to DCF. The latter shows a fluorescence at 521 nm after excitation at 500 nm, which intensity is dependent on the concentration of DCF. The correlation shows a linear trend until the hole H-DCF is oxidized. At this point, saturation is to be expected (Figure S 8). We decided to work with a concentration of the H-DCF stock solution of 120 µM. Note, that it is not possible to detect H_2O_2 concentrations larger than 20 µM, because at this point H-DCF is fully oxidized.

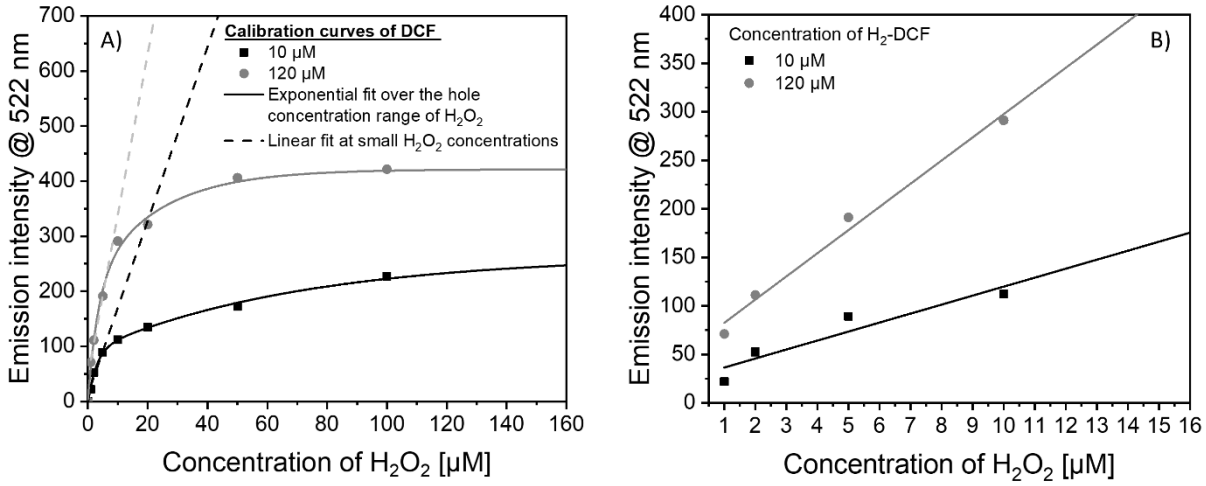

Figure S7: Calibration of the emission intensity of DCF at 522 nm after the addition of different amounts of H_2O_2 to the unoxidized DCFH. A) Representation of the full concentration range measurement B) Zoom in the linear regime at low H_2O_2 concentrations.

Section V: Catalytic raw data.

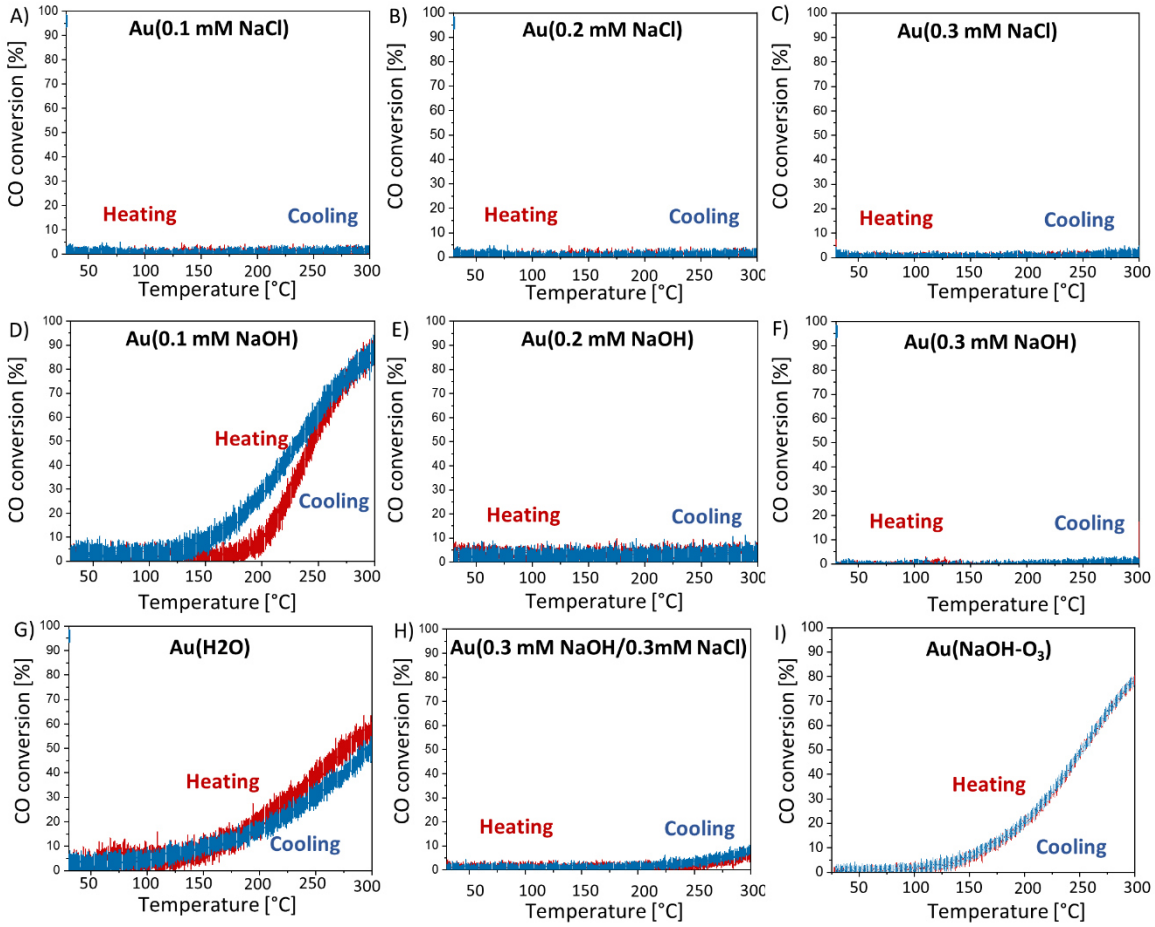

Figure S8: CO conversion in dependence of the temperature (increase and decrease) for all tested Au/TiO_2 catalysts.

Peroxidase-like activity of Au/TiO_2 NPs

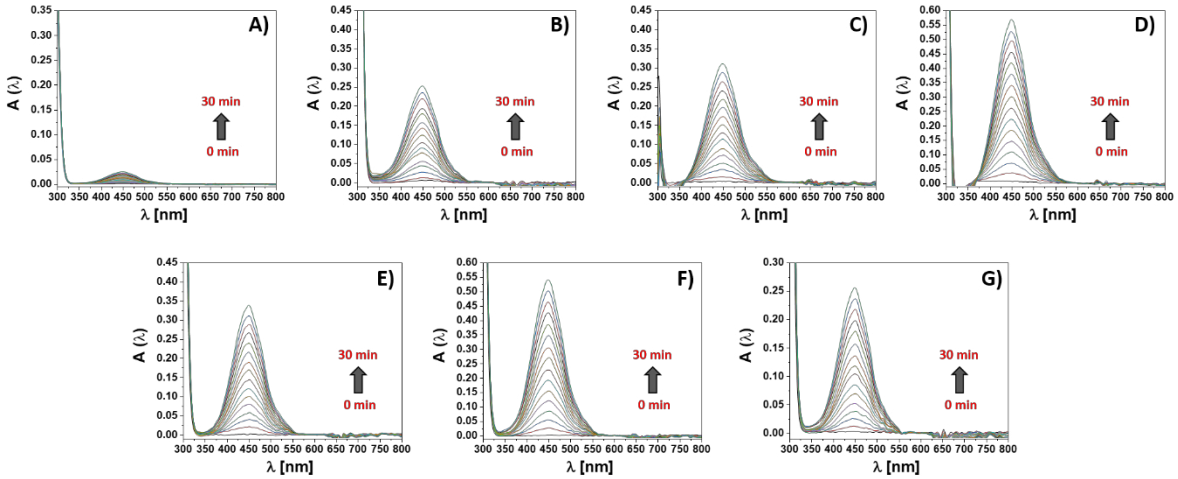

Figure S9: Time-dependent absorbance spectra A(λ) of DAP generated during the peroxidase-like catalytic reaction in absence of catalyst (A), in presence of HRP (B) and different Au/TiO_2 catalysts; Au(H_2O) (C), Au(NaCl) (D), Au(NaOH-NaCl) (E), Au(NaOH) (F) and Au(NaOH-O_3) (G).

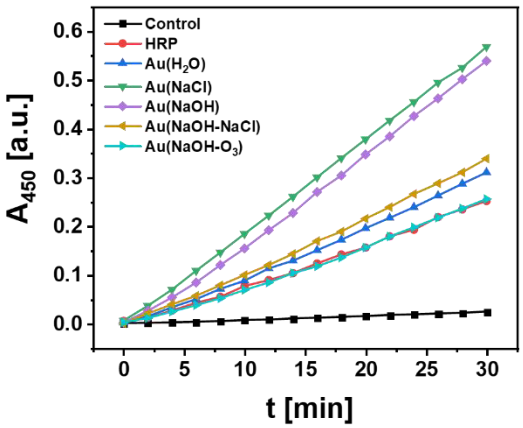

Figure S10: Time-dependent absorbance changes at λ = 450 nm of DAP generated during the peroxidase-like catalytic reaction using different Au/TiO_2 catalysts.

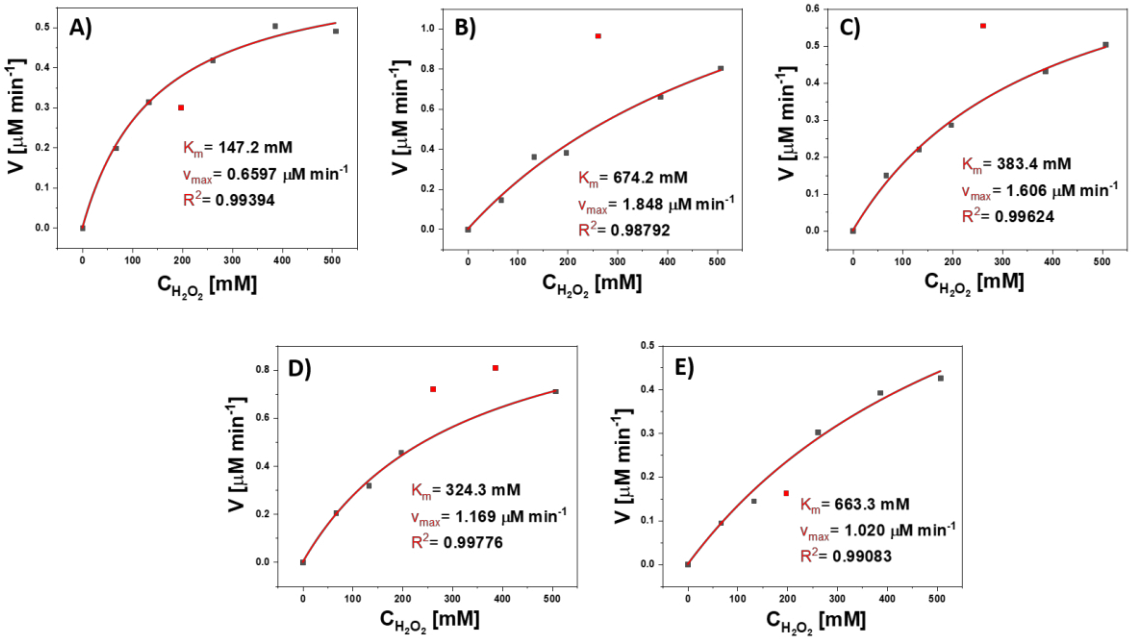

Figure S11: Steady-state kinetics of the peroxidase-like catalytic reaction in presence of different Au/TiO_2 catalysts; Au(H_2O) (A), Au(NaCl) (B), Au(NaOH-NaCl) (C), Au(NaOH) (D) and Au(NaOH-O_3) (E), using different concentrations of H_2O_2 ($c_{H_2O_2}$) while keeping the concentration of OPD fixed. Red points are excluded from the fitting.

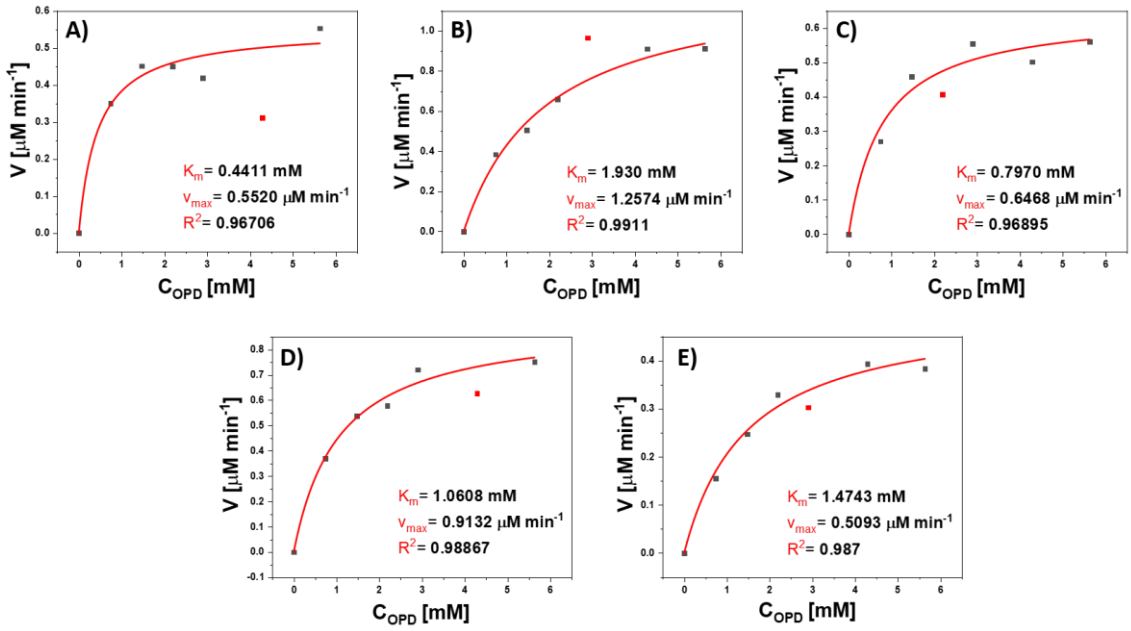

Figure S12: Steady-state kinetics of the peroxidase-like catalytic reaction in presence of different Au/TiO_2 catalysts; Au(H_2O) (A), Au(NaCl) (B), Au(NaOH-NaCl) (C), Au(NaOH) (D) and Au(NaOH-O_3) (E), using different concentrations of OPD (c_{OPD}) while keeping the concentration of H_2O_2 fixed. Red points are excluded from the fitting.

References

[1] Ziefuß, A. R.; Reichenberger, S.; Rehbock, C.; Chakraborty, I.; Gharib, M.; Parak, W. J.; Barcikowski, S. Laser Fragmentation of Colloidal Gold Nanoparticles with High-Intensity Nanosecond Pulses is Driven by a Single-Step Fragmentation Mechanism with a Defined Educt Particle-Size Threshold. *J. Phys. Chem. C* **2018**, *122*, 22125–22136.

[2] Singer, P.C., Harrington, G.W., Cowman, G.A., Smith M.E., Schechter, D.S., Harrington, L. J., Impacts of Ozonation on the Formation of Chlorination and Chloramination By-Products, AWWA Research Foundation and American Water Works Association, **1999**.

[3] Planken, K.L., Cölfen, H., Analytical Ultracentrifugation of Colloids, *Nanoscale* **2010**, *2*, 1849.

[4] Makino, K., Ohshima, H., Electrophoretic Mobility of a Colloidal Particle with Constant Surface Charge Density, Langmuir, 2010, 26, 18016-18019

[5] Elder, A., Yang, H., Gwiazda, R., Teng, X., Thurston, S., He, H., Oberdörster, G., Testing Nanomaterials of Unknown Toxicity: An Example Based on Platinum Nanoparticles of Different Shapes, *Adv. Mater.* **2007**, *19*, 3124.

[6] Kosaka, K., Yamada, H., Matsui, S., Echigo, S., Shishida, K., Comparison among the Methods for Hydrogen Peroxide Measurements To Evaluate Advanced Oxidation Processes of a Spectrophotometric Method Using Copper(II) Ion and 2,9-Dimethyl-1,10-phenanthroline, *Environ. Sci. Technol.* **1998**, *32*, 3821.

[7] X. Peng, G. Wan, L. Wu, M. Zeng, S. Lin, G. Wang, *Sensors and Actuators B: Chemical* **2018**, *257*, 166.

[8] Ziefuß, A. R.; Barcikowski, S.; Rehbock, C. Synergism between Specific Halide Anions and pH Effects during Nanosecond Laser Fragmentation of Ligand-Free Gold Nanoparticles. *Langmuir* **2019**, *35*, 6630–6639.

[9] K. L. Planken, H. Cölfen, *Nanoscale* **2010**, *2*, 1849–1869.

[10] R. P. Carney, J. Y. Kim, H. Qian, R. Jin, H. Mehenni, F. Stellacci, O. M. Bakr, *Nat. Commun.* **2011**, *2*, 335, DOI 10.1038/ncomms1338.

Acknowledgment

The compilation of this work was linked with many emotions. I have learned a lot and developed as a person. A variety of people have been involved and supported me on my journey. Today, I would like to express my deepest appreciation to all of these people.

I want to thank Stephan Barcikowski for giving me the opportunity to work in his group on a fundamentally exciting topic. *Stephan, thank you for igniting the spark for fundamental science in me that I thought I had lost long ago. Thank you for the many conversations and discussions that have helped me sort out my thoughts and clearly see the path.*

Furthermore, I would like to thank Christoph Rehbock, who always supported me as my group leader. *Christoph, we discussed a lot and did not always agree. Until today we could not find out if the egg or the hen came first. But maybe that was a good thing because we got deeper into topics than we ever suspected. Thank you.*

Of course, I would also like to thank the whole department of Technical Chemistry. *You make it worth getting up in the morning. I know that I can rely on each and every one of you.* Particularly noteworthy here are Andreas Schielke, Florian De Kock, Jurij Jakobi, René Streubel, Alexander Heinemann, and Sven Reichenberger. Not to forget my office partners, Dieter Jacobi, Tim Hupfeld, and Sandra Zwiehoff. *Dieter, Tim, and Sandra.*

I would also like to thank Wolfgang Parak and Leonid Zhigilei for reviewing this dissertation.

My research work was not possible without cooperation with others. The following scientists have helped me in my work and have also left their mark on me. Therefore, I would like to express my gratitude to: David Amans, Clothilde Comby-Zerbino, Melissa Teubner, Banjamin Grimm-Lebsanft, Michael Rübhausen, Torben Steenbock, Gabriel Bester, Milen Nachev, Bernd Sures, Baoxiang Peng and Martin Muhler. Furthermore, I thank Leonid Zhigilei, Wolfgang Parak, Indranath Chakraborty, and Mustafa Gharib for their intense collaboration within our DFG funded project. Thanks to Siegfried Glenzer, Ben, Zhijiang Chan, and Chandra for their great kindness and welcome in the USA. *Thanks for your support and all the cold drinks in sunny*

California. In addition to the scientists already mentioned, I would like to thank Anton Plech. *Anton, many thanks for the countless discussions at different X-ray sources. You played a special role as you helped me step outside the box and open my eyes to other scientific disciplines.*

I want to extend my thanks to a variety of students that played a decisive role in my research: Andreas Schielke, Michael Willeke, Max Reuschenbach, Dario Becker, Ibrahim Tan, Dominik Wäsche, and David Köhler.

I also gratefully acknowledge the Faculty of Chemistry, the German research foundation (DFG), the German academic exchange service (DAAD), and the center of nanointegration Duisburg-Essen (CENIDE) for financial support of my research.

Finally, I want to thank my family and friends for their never-ending support. *Mom and Dad, I thank you for your open arms, warm words, and your love*. I also thank my brother and his family*. Sebi, Jessy, Lena, Moritz, thank you that I can always rely on you.* I would like to thank my girls, Sandra and Selina, for their support; and I thank my best friend. *Goran, thank you for your love, your patience, and your talent to make me the best person I can be.*

Curriculum vitae

Der Lebenslauf ist in der Online-Version aus Gründen des Datenschutzes nicht enthalten.

Der Lebenslauf ist in der Online-Version aus Gründen des Datenschutzes nicht enthalten.

Der Lebenslauf ist in der Online-Version aus Gründen des Datenschutzes nicht enthalten.

Declaration of scientific contribution

Parts of this work have been published or were prepared in cooperation with co-authors, with my own contribution declared as follows:

Chapter 3.1.1

Anna. R. Ziefuss, Florian de Kock, Stephan Barcikowski: How to determine suitable parameters for AUC of inorganic gold colloids (unpublished results)

- Declaration of own contribution: The laser-based particle synthesis as well as data evaluation and the paper draft preparation, including the figures, was done by AZ. Fdk performed all centrifugal runs. SB inspired the work.

Chapter 3.2.1

A. Ziefuß, S. Reichenberger, C. Rehbock, I. Chakraborty, M. Gharib, W. Parak, S. Barcikowski: Laser fragmentation of Colloidal Gold Nanoparticles with High-Intensity Nanosecond Pulses is Driven by a Single-Step Fragmentation Mechanism with a Defined Educt Particle-Size Threshold, JPCC, 2018, 122, 22125-22136

- Declaration of own contribution: The experimental design, the laser-based particle synthesis, characterization (except recording of NaCl titration curves, which was done by IC and MG), as well as data evaluation and the paper draft preparation including the figures was done by AZ. All was conducted under the supervision of SB and CR, who also revised the manuscript. SR and WP have also revised the manuscript, and all of them improved the manuscript in the review process.

Chapter 3.2.2

A.R. Ziefuß, S. Reich, S. Reichenberger, M. Levantino, A. Plech: In situ structural kinetics of picosecond laser-induced heating and fragmentation of colloidal gold spheres, PCCP, 2019, accepted 2020

- Declaration of own contribution: The particle preparation and colloidal analysis were performed by AZ. SAXS and WAXS measurements and data evaluation at the ERSF were performed by AP and SReich, while AZ helped with the laser settings and experimental set-up just-in-time. The draft was written by AP with help from AZ and SR. SB supervised the study and revised the final manuscript.

Chapter 3.2.3

A. Ziefuß, S. Barcikowski, C. Rehbock: Synergism between specific halide anion and pH effects during nanosecond laser fragmentation of ligand-free gold nanoparticles, Langmuir, 2019, 35, 6630-6639

- Declaration of own contribution: The experimental design, all experiments, data evaluation and interpretation of the data as well as the preparation of the draft including figures, was done by AZ. CR and SB supervised the study and revised the manuscript.

Chapter 3.2.4

A. R. Ziefuß, C. Rehbock, S. Reichenberger, A. Letzel, Z. Chen, B. Ofori-Okai, S. H. Glenzer, S. Barcikowski: Tuning the electron screening effect in colloidal gold nanoparticles sets the energy coupling time between electrons and phonons (unpublished)

- Declaration of own contributions: The experimental design, all experiments, data evaluation and interpretation of the data as well as the preparation of the draft including figures, was done by AZ. The experimental set-up was designed and set by BO, CC, ZC. AL helped with particle preparation. CR, SR, SG, and SB supervised the study and revised the manuscript.

Chapter 3.3.1

Anna. R. Ziefuss, Melissa Teubner, Christoph Rehbock, Clothilde Zerbino, David Amans, Michael Rübhausen, Indranath Chakraborty, Wolfgang J. Parak, Stephan Barcikowski: Photoluminescence of fully inorganic colloidal gold nanocluster and their manipulation using surface charge effects (unpublished)

- Declaration of own contributions: The experimental design, the production of Au NCs including data analysis (except ESI-MS, which was performed by CZ under supervision of DA and lifetime measurements which was done by MT under supervision of MR) as well as the preparation of the draft including full data analysis and preparation of figures was done by AZ. CR, IC, WP, and SB revised the manuscript.

Chapter 3.3.2

Anna. R. Ziefuss, Melissa Teubner, Christoph Rehbock, Michael Rübhausen, Wolfgang J. Parak, Stephan Barcikowski: Highly Fluorescent Surfactant-Free Gold Nanocluster with Efficient Photon-Density Memory (unpublished results)

- Declaration of own contributions: The experimental design, the production of Au NCs including data analysis as well as the preparation of the draft including full data analysis

and preparation of figures was done by AZ. MT performed the pump-power-dependent emission spectra under the supervision of MR. CR and SB revised the manuscript.

Chapter 3.3.3

Anna. R. Ziefuss, Michael Willeke, Alexander Heinemann, Christoph Rehbock, Stephan Barcikowski: Influence of Pt atoms on the fluorescence of fully inorganic gold nanocluster (unpublished results)

- Declaration of own contributions: The experimental design, data analysis as well as preparation of the draft, including preparation of figures, was done by AZ. AZ and MW produced metallic mono and bimetallic NC and performed characterization. AH prepared the powder targets. CR and SB revised the manuscript.

Chapter 3.4.1

Anna R. Ziefuß, Ina Haxhiaj, Stefan Müller, Mustafa Gharib, Olga Gridina, Christoph Rehbock, Indranath Chakrabort[3], Baoxiang Peng, Martin Muhler, Wolfgang J. Parak, Stephan Barcikowski, Sven Reichenberger

- Declaration of own contributions: The experimental design, the production of catalysts data analysis as well as the preparation of the draft, including preparation of figures, was done by AZ. IH organized the preparation for catalysts used in Ethanol oxidation and prepared the catalysts together with AZ. The implementation of CO and Ethanol oxidation was done by SM, BP, and MM. The peroxidase-like catalytic activity was determined by MG, IC, and WP. SR, CR, and SB revised the manuscript.

Eigenständigkeitserklärung (Declaration)

Hiermit bestätige ich, dass ich die vorliegende Arbeit selbst verfasst habe und keine außer den angegeben Hilfsmitteln und Quellen benutzt habe.

Ort, Datum	Anna Rosa Ziefuß